# X-RAY REFLECTIONS ON AGN

**A.C. Fabian**

Institute for Astronomy, Madingley Road, Cambridge CB3 0HA, UK

## ABSTRACT

X-ray reflection generates much of the spectral complexity in the X-ray spectra of AGN. It is argued that strong relativistic blurring of the reflection spectrum should commonly be expected from objects accreting at a high Eddington rate. The good agreement found between the local density in massive black holes and the energy density in quasar and AGN light requires that the accretion which built massive black holes was radiatively efficient, involving thin discs extending within 6 gravitational radii. The soft excess found in the spectra of many AGN can be explained by X-ray reflection when such blurring is included in the spectral analysis. Some of the continuum variability and in particular the puzzling variability of the broad iron line can be explained by the strong light bending expected in the region immediately around a black hole. Progress in understanding this behaviour in the brightest sources can be made now with long observations using instruments on XMM-Newton and Suzaku. Future missions like Xeus and Con-X, with large collecting areas, are required to expand the range of accessible objects and to make reverberation studies possible.

## 1. INTRODUCTION

In this brief review, I consider the spectra and spectral variability of unobscured Active Galactic Nuclei such as Seyferts and quasars. They typically have the spectral components identified in Fig. 1, namely a) an underlying power-law, b) a soft excess above the power-law at low energies below 1 keV, c) an iron line (which may have a broad component), and d) a Compton hump. Traditionally these components have been considered as a) thermally Comptonized soft photons originating from b) thermal (blackbody) emission from an optically-thick accretion disc about the central black hole, together with the line c) and Compton-scattered d) parts of X-ray reflection from that disc or more distant matter. An important parameter when model-fitting such sources is the inner radius of the accretion disc, which determines how much relativistic blurring is applied to the reflection components. It is often assumed to be greater than 6 gravitational radii ($6r_{\rm g} = 6GM/c^2$) around the black hole, which is the innermost stable circular orbit around a non-spinning Schwarzschild black hole. Spectral deviations from this picture are often taken into account by adding additional emission and/or absorption components, some of which cover only part of the source.

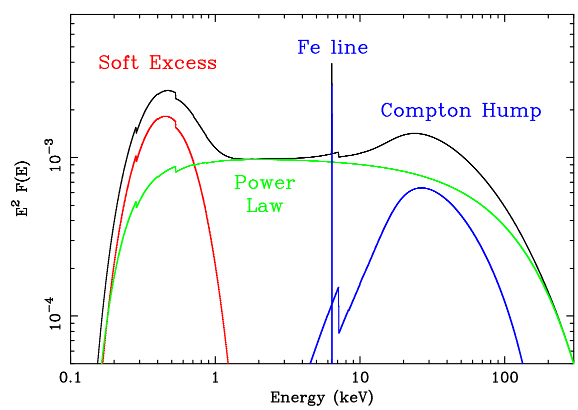


*Figure 1. Model X-ray spectrum of an AGN. Galactic absorption causes the flux to decrease steeply below 0.3 keV.*

There are problems with this traditional picture which suggest that it is at least incomplete. For several well-studied sources there are modifications to the above model which seem to fit the data, in particular the spectral variability, better. The main modification is to allow the inner radius of the disc to go to $2r_{\rm g}$, meaning the black hole is spinning. This introduces the possibility of very strong gravitational effects on the spectrum. The second consideration is to allow the atomic abundances to be different from the solar value. A more detailed review is given in Fabian & Miniutti (2005).

Note that most bright AGN *must* have a radiatively efficient accretion flow or the Soltan (1982) argument relating the energy density of accretion radiation and the local mean density in black holes would yield a low efficiency. The good agreement between the observations of quasar/Seyfert light and local black holes with an accretion efficiency of at least 10 per cent (Yu & Tremaine 2002; Fabian 2003; Marconi et al 2004) strongly argues for radiatively efficient flows with an inner disc radius within $6r_g$. The agreement, at all mass ranges, would not happen if the discs in quasars and luminous Seyfert galaxies stopped at several tens of $r_g$ or indeed larger than $6r_g$. Any power lost in winds and jets only strengthens these arguments. Massive black holes in galactic nuclei are likely to be rapidly spinning (Volonteri et al 2004) so small disc inner radii should be the norm and we should seriously consider that much of the X-ray emission from objects accreting at a high ($\gg 0.01$) Eddington fraction emerges from within a few $r_g$.

## 2. THE PROBLEMS

### 2.1. The soft excess

Several studies culminating in the work of Gierlinski & Done (2004) show that the temperature of the excess emission, if characterized as blackbody, seems to be the same in systems where the accretion rates and/or masses differ by several orders of magnitude. This is not expected from an accretion disc.

### 2.2. The iron line

Many sources show a narrow iron line component which is undoubtedly due in many cases to reflection on distant gas. Broad components, as expected from reflection by the inner accretion disc, are seen, but are not always present or at least not evident. Such components can sometimes be fitted away with partial-covering models.

### 2.3. Variability

Where sources are highly variable so that the emission region must be very small, partial covering models present physical problems for understanding the geometry of the situation. Only very occasionally can we be in a preferred line of sight; the covering material has to be randomly placed. What this matter is, where it lies and why it only partly covers the source are unknown.

### 2.4. Iron line variability

MCG–6-30-15 has a robust broad iron line (Tanaka et al 1995; Wilms et al 2001; Fabian et al 2002). Chandra grating observations and RXTE data have sufficient resolution and coverage to rule out partial covering solutions (Young et al 2005). A problem emerges with the lack of variability seen in the line, if the effects of strong gravity are ignored. The strength of the iron line should follow the brightness of the power-law component, but it does not. The iron line does vary on short timescales but not in any simple manner (Iwasawa et al 1996, 1999; Nandra & Edelson 2000; Matsumoto et al 2002; Fabian et al 2002).

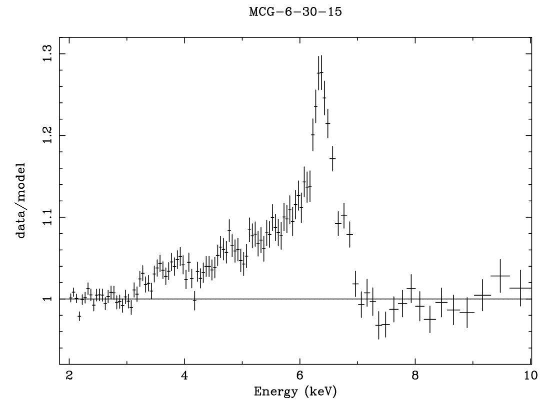


*Figure 2. The broad iron line seen in the XMM-Newton spectrum of MCG–6-30-15 (see Fabian et al 2002; this spectrum was produced from reprocessed data by S. Vaughan).*

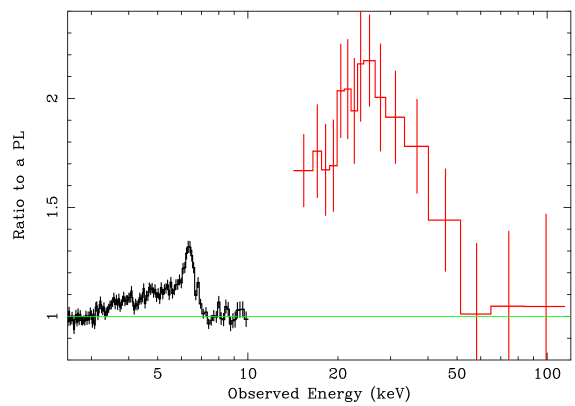


*Figure 3. The iron line and Compton hump in MCG–6-30-15 shown as deviations from a simple power-law spectrum. The data below 10 keV are from XMM-Newton and the data above from BeppoSAX (kindly prepaqred by G. Miniutti).*

## 3. THE TWO-COMPONENT MODEL OF SPECTRAL VARIABILITY

A simple phenomenological model which fits the spectral variability of several bright Seyferts well has two main components (McHardy et al 1998; Shih et al 2001; Fabian & Vaughan 2003). A simple power-law decription of the spectrum often shows the source to be harder when faint and softer when bright. The photon index of the source may limit to some fixed value at the highest fluxes. This behaviour can be modelled well in terms of two components; a soft power-law of fixed spectral index and variable intensity plus a hard component which varies little. The model accounts for the rms variability spectrum and spectral behaviour of many sources.

The shape of the quasi-constant hard component can be extracted in several ways, using a) flux-flux plots in which the flux in various energy bands is correlated with the flux in another band (say 1–2 keV) with the con-

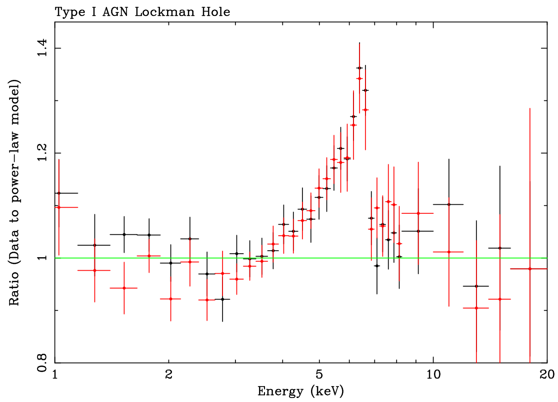


*Figure 4. Broad iron line seen in the rest-frame shifted, summed spectra of 51 Seyfert 1 galaxies in the XMM-Newton observations of the Lockman Hole (Streblyanska et al 2005).*

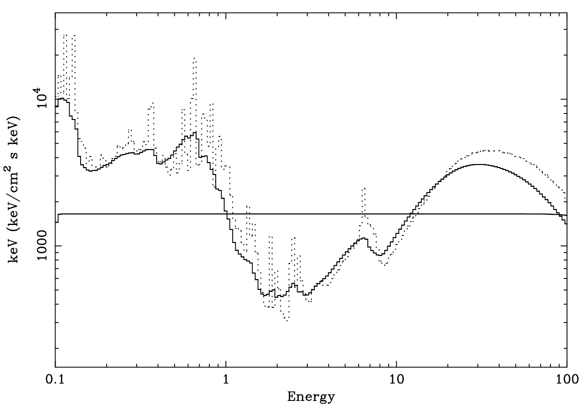


*Figure 5. Two-component model. The horizontal line is the power-law component which varies significantly in amplitude. The solid curved line is the relativistically-blurred reflection spectrum (shown dotted).*

stant component appearing as the intercept (e.g. Taylor et al 2004); b) difference plots where the spectrum of the faintest flux state is subtracted from that of the brightest (Fabian et al 2002); or c) straight model fitting (Vaughan et al 2004). When applied to MCG–6-30-15 all these methods indicate that the hard component has the shape of blurred reflection and the variable soft component is a power-law. Similar results are found for NGC 4051 (Ponti et al 2005).

## 4. SOLUTIONS INVOVING STRONG GRAVITY

An alternative interpretation of the soft excess, hinted at in earlier papers (Czerny et al 2003; Ross & Fabian 2005) is for it to be the blurred soft part of the ionized reflection spectrum. This has been tested by Crummy et al (2005) and generally found to give better fits to spectra of PG quasars and various Seyferts than a simple blackbody disc does. The reflection spectrum needs to be significantly blurred, requiring that much of the emission arises from

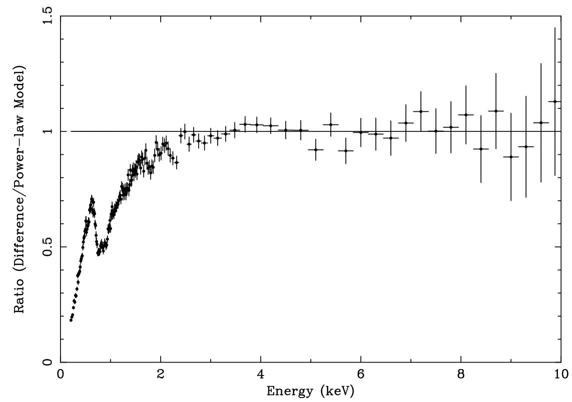


*Figure 6. Difference spectrum from MCG–6-30-15 (Turner et al 2004). It shows the ratio of the spectrum, made by subtracting low from high flux data, to a simple power-law. Note that it has no broad iron line and shows that the component which varies is a simple power-law in the 3–10 keV band). Assuming that it remains a power-law to low energies, the deviations there show the absorption components (mostly due to a warm absorber).*

near the centre of an accretion disc about a spinning black hole. The blurred reflection spectrum has a ’boxy’ shape better suited to the soft excess than a blackbody which then requires fewer, if any, additional absorption components for a good fit.

The iron abundance needs also to be a free parameter. Extreme blurring together with low iron abundance can make most broad iron lines undetectable with current instruments.

If much of the X-ray emission emerges from the innermost parts of the disc around a spinning black hole then light bending needs to be taken into account. This has a strong effect on the brightness of the primary power-law source, making it appear faint to a distant observer when it is close to the hole and bright when further away. Some of the variability of the power-law continuum can thus be due to the position of the source relative to the hole, rather than any intrinsic effect. The strong light bending causes much of the flux variability.

Consider a constant power-law source which is brought down the spin axis from 20 to $1r_{\rm g}$. It would appear to an observer seeing the disc at an inclination of say 30 degrees to decrease dramatically in flux. The reflection component would however change little until the source is below about $4r_{\rm g}$. Although the reflection is becoming more concentrated at the centre of the disc the increase in power-law flux bent down onto the disc compensates for any loss of flux.

This ’light-bending’ model (Miniutti et al 2003, 2004) is a simple consequence of strong gravity close to the black hole and predicts effects that have to be taken into account.

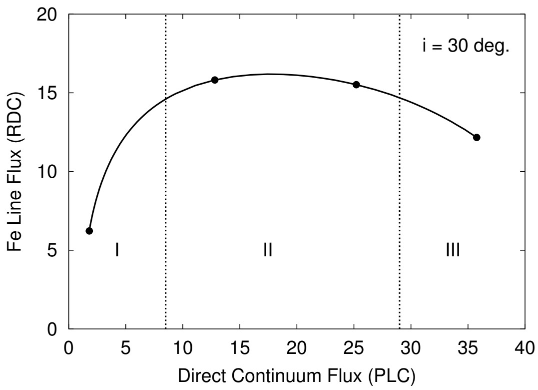


*Figure 7. The response of the reflection component (RDC) to the power-law continuum (PLC) in the light bending model. The height of the PLC above the hole is 20, 10, 5 and 1$r_g$ at the 4 marked points on the curve going from right to left.*

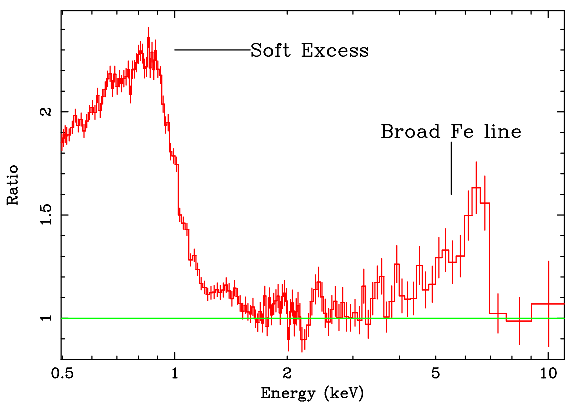


*Figure 8. The XMM-Newton spectrum of 1H 0707 shown as the ratio to a power-law fitted in the 2–3 and 8–10 keV energy bands. The spectral features resemble blurred reflection, although absorption models can be made to fit (Boller et al 2002).*

## 5. APPLICATIONS TO A RANGE OF SOURCES

The light-bending model has been applied to an increasing range of AGN, particularly NLS1 (MCG–6-30-15, Fabian & Vaughan 2003; NGC 4051, Ponti et al 2005; 1H0707, Fabian et al 2004; 1H0439, Fabian et al 2005) and at least one Galactic Black Hole ( GRO J1650, Rossi et al 2005). Future challenges are to see whether it fits just a class of AGN or its relevance is more widespread.

Is it consistent, for example, with the variable, red or blue-shifted, emission features occasionally seen in some objects (e.g. NGC 3516, Iwasawa et al 2004)? A possibility in those cases is that indeed most of the primary emission raises from close to the centre of the disc but, due to the rapid rotation there, it is beamed along the disc and illuminates transient 'bumps' or waves on the surface of the disc, causing transient reflection there.

What we need to do next is to see whether the reflection does follow the variation expected to occur as the power-law continuum moves and varies (Fig. 7). Subtle changes are expected in the degree of extreme blurring which occurs when the power-law source is closest to the black hole. This requires more data from the parts of the lightcurve when the flux is low. These occur infrequently but are accessible in MCG–6-30-15 by long observations with XMM-Newton and Suzaku. Testable variations of the reflection from the strong gravity regime around black holes should be detectable now with long dedicated observations.

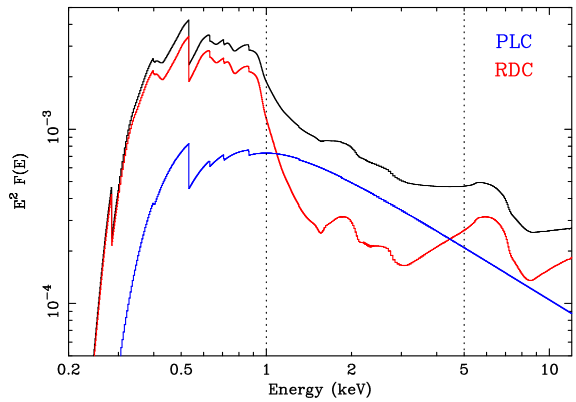


*Figure 9. The spectral components in the 2 component model for 1H 0707 (Fabian et al 2002. In this state the power-law component dominates the spectrum in the 1–5 keV band.*

On the longer term we look to the next generation of detectors to measure the reverberation of the reflection. This needs to be done in a light crossing time and requires a large collecting area. AGN detect 100s of times more photons per light crossing time than Galactic black holes so are the preferred targets. At a flux of about 2 photon per square metre per second from the brightest iron lines, this requires a collecting area of at least two square metres at 6 keV. We look forward to such observations with Xeus and Con-X.

## ACKNOWLEDGMENTS

I thank Giovanni Miniutti for help and discussion and the Royal Society for support.

## REFERENCES

Boller T., et al 2002, MNRAS, 329, L1

Crummy J.C., Fabian A.C., Gallo L., Ross R.R., 2005, MNRAS, submitted

Czerny B., Nikolajuk M., Róźańska A., Dumont A.-M., 2003, A&A, 412, 317

Fabian A.C., et al. 2002a, MNRAS, 335, L1

Fabian A.C., Vaughan S., 2003, MNRAS, 340, L28

Fabian A.C., Miniutti G., Gallo L., Boller Th., Tanaka Y., Vaughan S., Ross R.R., 2004, MNRAS, 353, 1071

Fabian A.C., Miniutti G., Iwasawa K., Ross R.R., 2005, MNRAS in press, astro-ph/0504472

Fabian A.C., 2003, astro-ph/0304122

Fabian A.C., Miniutti G., 2005, astro-ph

Gierlinski M., Done C., 2004, MNRAS, 349, L7

Iwasawa K., Fabian A.C., Mushotzky R.F., Brandt W.N., Awaki K., Kunieda H., 1996, MNRAS, 279, 837

Iwasawa K., Fabian A.C., Young A.J., Inoue H., Matsumoto C., 1999, MNRAS, 307, 611

Iwasawa K., Lee J.C., Young A.J., Reynolds C.S., Fabian A.C., 2004, MNRAS, 347, 411

Marconi A., Risaliti G., Gilli R., Hunt L.V., Maiolino R., Salvati M., MNRAS, 351, 169

Matsumoto C., Inoue H., Fabian A.C., Iwasawa K., 2003, PASJ,

McHardy I.M., Papadakis I.E., Uttley P., 1998, Nucl. Phys. B, 69, 509

Iwasawa K., Miniutti G., 2004, Progr. Theor. Phys., S155, 247

Iwasawa K., Miniutti G., Fabian A.C., 2004, MNRAS, 355, 1073

Miniutti G., Fabian A.C., Goyder R., Lasenby A.N., 2003, MNRAS, 344, L22

Miniutti G., Fabian A.C., 2004, MNRAS, 349, 1435

Ponti G., et al 2005, MNRAS submitted

Reynolds C.S., Wilms J., Begelman M.C., Staubert R., Kendziorra E., 2004, MNRAS, 349, 1153

Ross R.R., Fabian A.C., 2005, MNRAS, 358, 211

Rossi S., Homan J., Miller J.M., Belloni T., 2005, MNRAS, 360, 763

Soltan A., 1982, MNRAS, 200, 115

Yu Q., Tremaine S., 2002, MNRAS, 335, 965

Shih D.C., Iwasawa K., Fabian A.C., 2001, MNRAS, 333, 687

Streblyanska A., Hasinger G., Finoguenov A., Barcons X., Mateos S., Fabian A.C., 2005, A&A, 432, 395

Tanaka Y., et al 1995, Nature, 375, 659

Taylor R.D., Uttley P., McHardy I.M., 2003, MNRAS, 342, L31

Turner A.K., Fabian A.C., Vaughan S., Lee J.C., 2003, MNRAS, 346, 833

Turner A.K., Fabian A.C., Lee J.C., Vaughan S., 2004, MNRAS, 353, 319

Vaughan S., Edelson R., 2001, ApJ, 548, 694

Vaughan S., Fabian A.C., Nandra K., 2003, MNRAS, 339, 1237

Vaughan S., Fabian A.C., 2004, MNRAS, 348, 1415

Vaughan S., Fabian A.C., Ballantyne D.R., de Rosa A., Piro L., Matt G., 2004, MNRAS, 351, 193

Volonteri M., Madau P., Quataert E., Rees M.J., 2005, ApJ, 620, 69

Wilms J., et al., 2001, MNRAS, 328, L27

Young A.J., Lee J.C., Fabian A.C., Reynolds C.S., Gibson R.R., Canizares C.R., 2005, ApJ, 631, 733

# MAPPING THE INNERMOST REGIONS OF AGNS WITH SHORT TIMESCALE FE LINE VARIABILITY

**Giovanni Miniutti, Kazushi Iwasawa, and Andrew C. Fabian**

Institute of Astronomy, Madingley Road, Cambridge CB3 0HA, UK

## ABSTRACT

A relatively narrow emission line feature is seen at 6.1 keV in the X–ray spectrum of the Seyfert galaxy NGC 3516 with *XMM–Newton*. The energy of the feature does not correspond to atomic transitions with large enough probability to occur and is most likely redshifted iron emission (6.4 keV). We study its short timescale variability which reveals both flux and energy modulations on a characteristic timescale of 25 ks. The variations agree with an orbiting spot model in which an Fe line is emitted from a localized spot on the accretion disc, illuminated by a corotating flare above it. The spot is located at about 10 $r_g$ from the black hole and almost four cycles of orbital modulation are seen. By combining the spot location with the orbital timescale we can estimate the black hole mass in NGC 3516 which turns out to be in excellent agreement with reverberation mapping results, supporting our interpretation in terms of relativistic effects close to the black hole. *XMM–Newton* proves here able to map with high accuracy the inner accretion flow in AGNs down to the relativistic region of the curved spacetime in the immediate vicinity of the accreting black hole.

Key words: X–rays: galaxies; galaxies: active; galaxies: individual: NGC 3516; relativity.

## 1. INTRODUCTION: FE EMISSION FROM ACCRETION DISCS

A substantial fraction of the accretion energy in luminous Active Galactic Nuclei (AGNs) is thought to be dissipated in the inner regions of the accretion flow around the central black hole. Most bright AGNs are believed to have accretion efficiencies of at least 10 per cent which requires the flow to be radiatively efficient down to only few gravitational radii ($r_g = GM/c^2$ where M is the black hole mass) from the black hole, where both special and general relativity are likely to play a fundamental role. X–rays provide a unique vue of the innermost regions of accreting black holes and time–resolved spectroscopy has the great potential of mapping the accretion flow and even the spacetime geometry in the immediate vicinity of black holes.

One of the most powerful tool we have to investigate the nature of the innermost accretion flow in AGNs is provided by the X–ray reflection spectrum from the accretion disc. The main feature of the reflection spectrum is the iron (Fe) K fluorescent line with rest–frame energy between 6.4 keV and 6.96 keV depending on the ionization state of the reflector. If the Fe line originate from the accretion disc, high velocities and strong gravity effects produce distortions on the line profile that can be used to infer the main properties of the accretion flow and the geometry of the spacetime close to the black hole. In fact, each ring on the accretion disc produces a symmetric double–horned line profile corresponding to emission from the approaching and receding sides of the disc with respect to the observer. As one approaches the central black hole, orbital velocities become relativistic and relativistic beaming enhances the blue peak of the line with respect to the red one. Finally, transverse Doppler and gravitational redshift produce a shift to lower energies of the emission from each ring on the disc. The overall line profile from the accretion disc is obtained by summing the contributions from all radii. The resulting line profile is asymmetric and broad.

The best example of a broad relativistic line in an AGN is that of MCG–6-30-15 (Tanaka et al 1995; Wilms et al 2001; Fabian et al 2002 and many others). In this case, the red wing of the line extends below 4 keV implying that the accretion disc extends within the innermost stable circular orbit of a non–rotating black hole and thus strongly suggesting that the black hole in MCG–6-30-15 is rapidly spinning, providing evidence for the astrophysical relevance of the Kerr solution of the Einstein's field equations. In Fig. 1 we show another example of a broad relativistic Fe line from a stellar–mass Galactic black hole in outburst, XTE J1650–500. The broad line was discovered by *XMM–Newton* (Miller et al 2004) and we show the result of a *BeppoSAX* observation performed 10 days later during the same 2001 outburst (Miniutti, Fabian & Miller 2004). The detection of a high frequency QPO during the time of the *BeppoSAX* observation (Homan et al 2003) strongly argues in favour of small accretion disc radii. Indeed, the extent of the red wing in the *BeppoSAX*

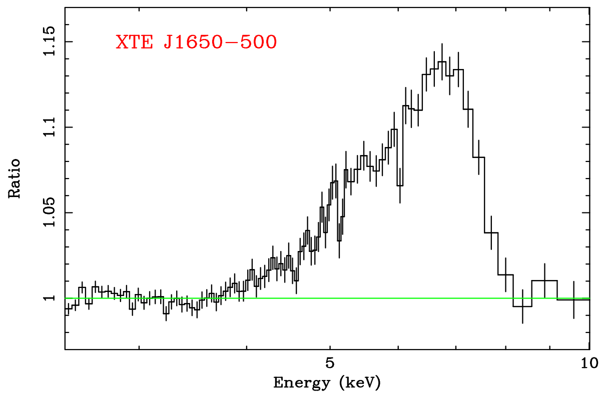


*Figure 1. We show the broad Fe line in the Galctic black hole XTE J1650–500. The data were collected by BeppoSAX on 2001 September 21 (Miniutti, Fabian & Miller 2004). See also Miller et al (2004) for the same broad line detected with XMM–Newton 10 days earlier during the same outburst and Rossi et al (2005) for a spectral and variability analysis based on RXTE data.*

and *XMM–Newton* data suggest that the accretion disc extends down to about 2 $r_g$ from the black hole, indicating, once again, that the black hole is rapidly spinning.

## 2. ENERGY–SHIFTED EMISSION LINES

In addition to the major Fe K line at 6.4 keV (often narrow and coming from distant material, sometimes broad and coming from the inner accretion disc), emission features at energies generally lower than 6.4 keV have been observed in the X–ray spectra of several AGNs. An early example was seen with *ASCA* in MCG–6-30-15 (Iwasawa et al 1999) in which the redshifted emission was associated to Fe fluorescence from a localized spot on the disc induced by irradiation from a flare located only few $r_g$ from the black hole. More detections followed in recent years mainly thanks to the improved sensitivity of present X–ray mission such as *Chandra* and *XMM–Newton*. The most remarkable cases reported so far are those of NGC 3516 (Turner et al 2002; Dovčiak et al 2004; Iwasawa, Miniutti & Fabian 2004), NGC 7314 (Yaqoob et al 2003), ESO 198–G24 (Guainazzi 2003; Bianchi et al 2004), Mrk 766 (Turner, Kraemer & Reeves 2004), ESO 113–G10 (Porquet et al 2004), and AX J0447–0627 (della Ceca et al 2005). In all the above cases, the energy at which these emission features are detected does not correspond to any atomic transition with large enough probability to occur to be detected in the X–ray spectra of AGNs. The most natural and likely explanation is that these features are Fe K emission lines which have been redshifted to the observed energies by a kinematical and/or gravitational mechanism.

In Fig. 2 we show two examples of redshifted detected features. In the left panel we show the hard spectrum and data to model ratio from the first *XMM–Newton* observation of ESO 198–G24 (Guainazzi 2003). Besides emission around 6.4 keV, an emission line is detected at 5.7 keV. In a subsequent observation, the line was found at 5.9 keV but only in the second half of the observation suggesting a transient nature and short–timescale variability (Bianchi et al 2004). In the right panel of the same figure, we show the spectrum and data to model ratio (a simple power law is assumed) for the *XMM–Newton* observation of ESO 113–G10 (Porquet et al 2004). An emission feature is clearly seen at 5.4 keV in the source rest–frame and a detailed statistical analysis shows it is significantly detected (about 99 per cent confidence level according to Montecarlo simulations, see Porquet et al 2004).

### 2.1. Short–timescale variability: orbiting spots?

A tentative, exciting, but not unique explanation for the observed redshifted emission features is that we are looking at Fe emission originating in a localized region on the accretion disc (hereafter "spot"). In this picture, the spot is produced by irradiation from a localized magnetic flare above the disc which produces the Fe line by fluorescence in the surface layers of the disc. The redshift of the observed lines is due to the location and velocity of the flare/spot system, combined with the disc inclination with respect to the observer. The simplest assumption is that the flare, linked by magnetic fields to the disc, participates to the disc Keplerian motion. As shown in Dovčiak et al (2004) and Pecháček et al (2005), such a model could indeed explain most of the observed features. The idea is that if the integration time is longer than the spot orbital period, emission from a narrow ring will be seen. The Fe line emitted from such a ring is generally narrow and redshifted, as seen in most data. If the data are interpreted in this framework, relevant parameters such as flare/spot location and disc inclination can be extracted.

As mentioned, the orbiting spot model is not unique. Energy–shifted lines can be produced for example in outflows as well (see Turner, Kraemer & reeves 2004). However, the spot model makes definite predictions on the short timescale variability of the features. In this respect, it is much more appealing than other models because predictions can be tested and falsified. If the redshifted lines are really due to orbiting spots on the disc, they should vary on the orbital timescale at the spot location. If the flare/spot system lasts for more than one orbital period periodic modulations on both the emission line flux and energy should be seen, reflecting the orbital motion of the emitting spot and the different Doppler and beaming effects as the spot's orbit proceeds.

The Keplerian orbital timescale around a typical $10^7\ M_\odot$ black hole is about $10^4$ s at 10 $r_g$. Therefore, some of the long and uninterrupted *XMM–Newton* observations (lasting about $10^5$ s) potentially contains several cycles of orbital modulation. The orbiting spot model can then be tested by using long *XMM–Newton* observations of AGNs in which the redshifted features have been de-

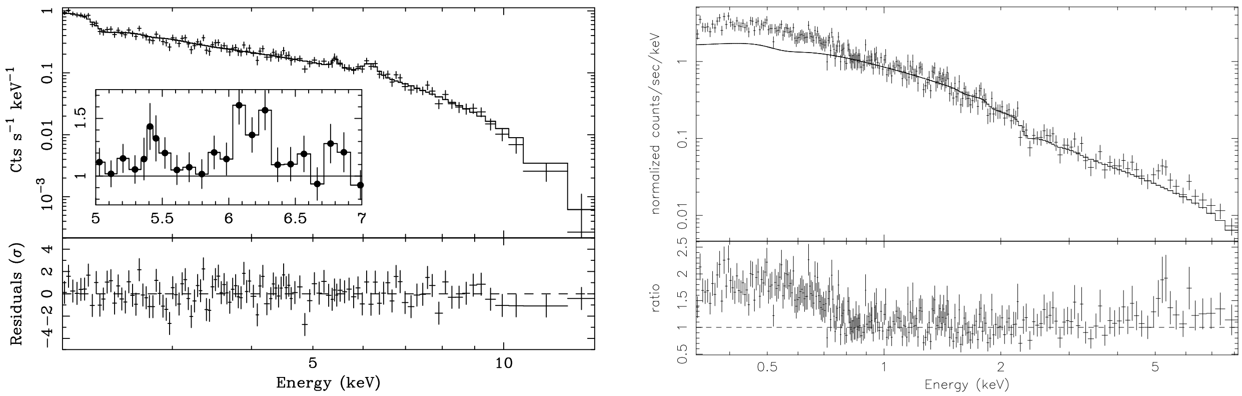


*Figure 2. In the left panel we show the hard spectrum and data to model ratio from the first XMM–Newton observation of ESO 198–G24 where, besides emission around 6.4 keV, a feature is detected in emission around 5.7 keV (from Guainazzi 2003). In the right panel, we show a power law fit to the broadband XMM–Newton spectrum of ESO 113–G10. The emission line visible above 5 keV has a rest–frame energy of 5.4 keV and is detected at the 99 per cent level (from Porquet et al 2004). Long XMM–Newton follow–up observations are planned during AO4 to study the short timescale variability of the redshifted features in both sources.*

tected.

## 3. THE CASE OF NGC 3516

We select one of the XMM-Newton observations of the bright Seyfert galaxy NGC3516 in which Bianchi et al (2004) reported the presence of an emission feature around 6.1 keV in addition to a stronger 6.4 keV Fe K$\alpha$ line in the time-averaged spectrum. This is one of the most robust detection of a redshifted feature so far and the existence of a long *XMM–Newton* observation prompted us to study the short timescale variability in the Fe K band as a test for the orbiting spot model. Dovčiak et al (2004) have already studied the same dataset by splitting the observation in three time intervals about 27 ks long and they found that the feature is present in all intervals. However, if the orbiting spot model has to be tested, it is clear that a study at much shorter time–resolution is required.

There is another long *XMM–Newton* observation of NGC 3516 in which Turner et al (2002) reported the presence of a 6.2 keV emission feature which is however not present in the time–averaged spectrum but only towards the end of the observation indicating its transient nature. Since we want to study the variability of the feature on short timescales but for the longest possible period of time, we decided to study the first observation in which the feature seems to last for most of the exposure (Dovčiak et al 2004).

The time–averaged line profile of NGC 3516 during the selected observation is shown in Fig. 3. Two clear emission features are seen. The higher energy one is at 6.4 keV and is easily identified with a narrow Fe K$\alpha$ emission line from a distant reflector such as the torus. The lower energy one is the feature we are interested in and is detected at 6.1 keV (hereafter the “red feature”).

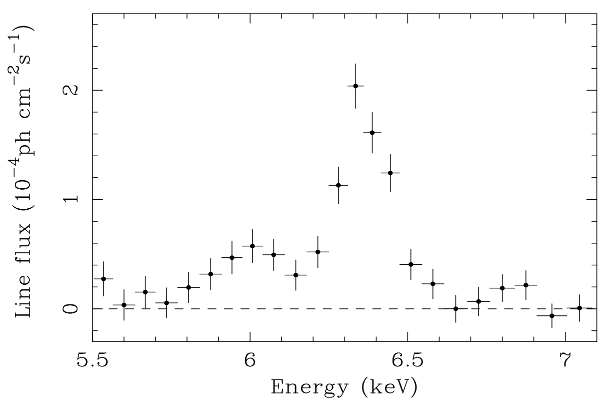


*Figure 3. The time–averaged line profile of NGC 3516. Besides the Fe K$\alpha$ line at 6.4 keV a redshifted emission feature is clearly seen around 6 keV (6.1 keV in the source rest–frame).*

### 3.1. Variability analysis

The broad-band X-ray spectrum of NGC3516 is complex, as a result of modification by absorption and reflection components (Turner et al 2004). Since our interest is on the behaviour of the 6.1 keV feature only, we design our analysis method to avoid unnecessary complication: i) the energy band is restricted to 5.0–7.1 keV; ii) the continuum is determined by fitting an absorbed power-law to the data excluding the Fe line band (6.0–6.6 keV). In this way any spectral curvature induced by either a broad relativistic Fe line or absorption is modelled out and we are left with the narrow emission features only (the 6.4 keV Fe K line and the red feature).

To study the short timescale variability we first investigate time–resolved spectra at 5 ks resolution in time. Each individual 5 ks spectrum is fitted with the absorbed power law model and any excess emission above this con-

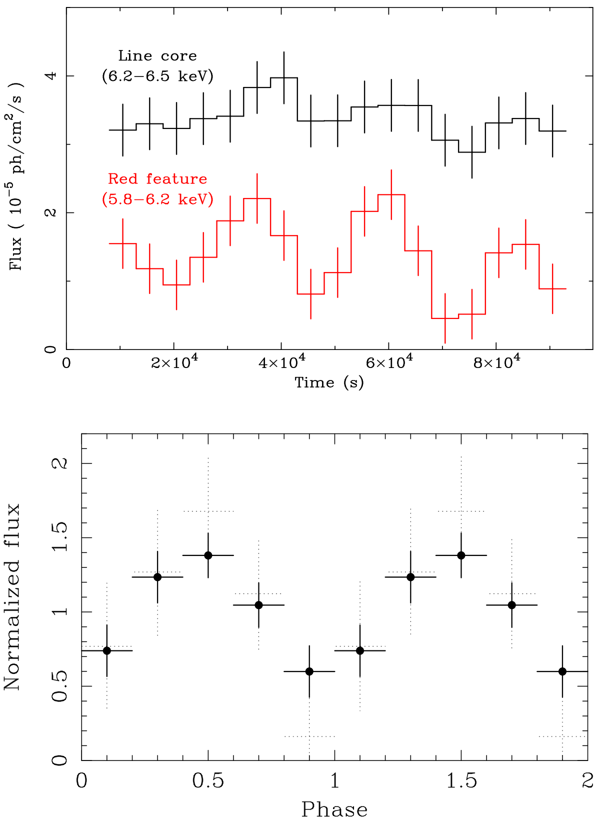


*Figure 4. In the top panel we show two light curves extracted from the time–energy map of the excess emission. Each data point corresponds to a 5 ks time interval. Two energy bands are selected corresponding to the Fe K$\alpha$ line core at 6.4 keV and to the red feature at 6.1 keV. The red feature light curve exhibits systematic variations suggesting a cyclic behaviour on a 25 ks timescale. In the bottom panel the red feature light curve is folded at 25 ks. The solid data refers to the folded light curved as extracted from the smoothed time–energy map of the excess emission, the dotted ones are from the original unsmoothed map. This shows that smoothing does not introduces spurious variability but only reduces the errors, as expected.*

tinuum is recorded, corrected for the detector response, and used to construct a map of the excess emssion in the time–energy plane which is slightly smoothed to reduce intra–pixel noise (see Iwasawa, Miniutti & Fabian 2004 for details). The map suggests that systematic variation are taking place in the red feature energy band (5.8–6.2 keV in the observer frame).

In the top panel of Fig. 4 we show the light curves of the excess emission in two energy bands selected around the Fe K line core (6.2–6.5 keV band) and the red feature (5.8–6.2 keV) respectively. Errors are estimated via simulations as explained in Iwasawa, Miniutti & Fabian (2004). A simple $\chi^2$ test reveals that the line core is well fitted by a constant while the same fit results in $\chi^2 = 36$ for 16 degrees of freedom for the red feature. The above results are confirmed through simulations. Moreover, as mentioned, the red feature appears to vary in a systematic way, the peaks and dips being always spaced by 25 ks. In the bottom panel of the same Figure, we show the result of folding the red feature light curve by using the evident 25 ks characteristic timescale. The light curve and the folding procedure suggest a cyclic behaviour with a 25 ks timescale. However, this result is based on four cycles only and it is difficult to secure any periodicity with such a small number of cycles. To investigate in more detail wheter noise can produce spurious cyclic variability we make use of Montecarlo simulations as detailed below.

### 3.2. Significance of the cyclic behaviour

Fitting the folded light curve with a constant provides an unacceptable fit of $\chi^2 = 24.5$ for 4 degrees of freedom. We do not consider this result as a clear indication for a periodicity, but we use it as a figure for Montecarlo simulations that are performed to assess the significance of the cyclic variability suggested by the data. We proceed as follows: in each simulation run, both the 6.4 keV line core and the red feature are assumed to remain constant at the flux observed in the time–averaged spectrum. The normalisation of the power law continuum is set to follow the 0.3–10 keV light curve. Each run consists of seventeen 5 ks spectra reproducing collectively the total exposure which is about 85 ks. From the simulated spectra, an image of the excess emission in the time–energy plane is obtained and smoothed, from which a light curve in the red feature energy band is extracted following exactly the same procedure as applied for the real data. The light curve is then folded at six trial periods between 15 ks and 40 ks with a 5 ks time–step (since the observation is about 85 ks long it does not make sense to consider longer trial periods) and the $\chi^2$ value for a constant–fit is recorded and compared with that from the real data. The procedure is repeated 1000 times.

We find that only 0.2 per cent of the simulations show comparable or larger significance compared to the real data. Moreover, this is limited to the largest trial period of 40 ks (two cycles in the 85 ks long observation). None of the 1000 simulations show comparable periodic signals to the real data for the trial periods of 35 ks or shorter (i.e. we never observe spurious variability producing more than two cycles). The above test indicates it is unlikely for random noise to produce the cyclic patterns at the intervals of 25 ks as observed, providing a significance of 99.8 per cent for the cyclic behaviour. This result remains unchanged if the red feature light curve is characterized by red noise with the same power law slope and r.m.s. variability amplitude (2–3 per cent) as the continuum in NGC 3516. If the r.m.s. amplitude is artificially (and probably unreasonably) increased up to 35 per cent, the significance is reduced, but is still of about 98 per cent (see Iwasawa, Miniutti & Fabian 2004 for more details).

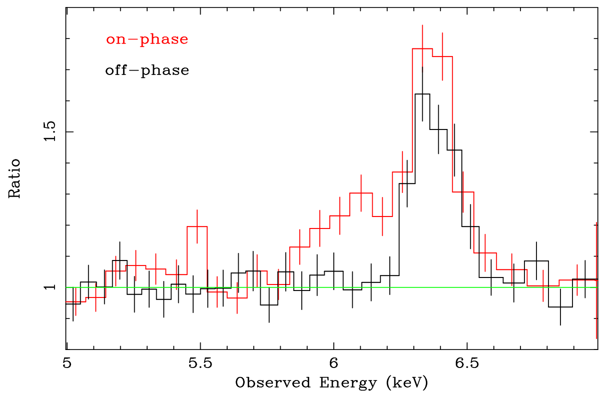


*Figure 5. The two line profiles are obtained by performing phase–resolved spectroscopy following the light curve of the red feature. The red feature is detected only in the on–phase spectrum. It is absent in the off-phase spectrum the difference between the two being significant at the 4σ level.*

### 3.3. Line profile variation in the on and off phases

Using the red feature light curve (top panel of Fig. 4) as a guide, we construct two spectra by selecting time–intervals in a periodic manner from the 'on' and 'off' phases to verify the implied variability in the red feature. The line profiles obtained from the two spectra are shown in Fig. 5. The two line profiles can be modelled with a double Gaussian model. The 6.4 keV core is found in both spectra with an equivalent width (EW) of 110 eV. While the 6.4 keV core remains similar between the two, there is a clear difference in the energy range of 5.7–6.2 keV due to the presence/absence of the red feature. In the on–phase spectrum, the red feature is centred at $6.13^{+0.10}_{-0.07}$ keV and has a flux of $2.1^{+1.3}_{-0.8} \times 10^{-5}$ ph cm$^{-2}$ s$^{-1}$ corresponding to an equivalent width of about 65 eV with respect to the continuum at the centroid energy. On the other hand, the red feature is not detected in the off–phase spectrum. If a line with the same centroid and width as in the on–phase spectrum is fitted to the off–phase data we only obtain a 90 per cent upper limit of $< 0.7 \times 10^{-5}$ ph cm$^{-2}$ s$^{-1}$ corresponding to an equivalent width $<$ 20 eV. The variability detected between the two spectra is significant at $4\sigma$ confirming that the variability is real and present in the data.

### 3.4. Shorter timescales: flux and energy orbital modulation

The observed cyclic behaviour is exactly what is expected in the orbiting spot model: a periodic modulation should be seen corresponding to the orbital period of the spot and a cyclic behaviour is indeed observed. If this interpretation is correct the observed 25 ks characteristic timescale is the orbital period of the emitting spot. However, if the red feature is due to emission from an orbiting spot on the accretion disc, we do expect to see not only a periodic

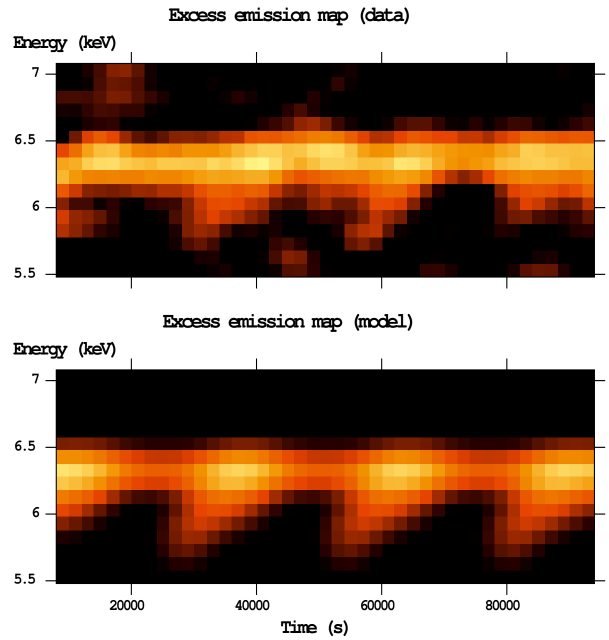


*Figure 6. In the top panel we show the observed excess emission map at 2 ks resolution in time. In the bottom panel we show one of the theoretical maps constructed with the orbiting spot model. The brightest pixels correspond to about 15 counts of excess emission. The data–model agreement is surprisingly good and allows us to infer the parameters of the orbiting spot with good accuracy.*

modulation in flux, but also in energy. This is because, as the spot orbits the black hole, it samples different regions of the accretion disc where different Doppler shifts are imprinted. As an example, when the spot is approaching to the observer, we expect a brighter and higher energy line, while when it is receading we should observe a fainter and lower energy line, due to the combined effect of relativistic Doppler and beaming effects. The image constructed from individual 5 ks spectra does not show any energy evolution. We therefore decided to investigate the feature evolution at a shorter timescale (2 ks).

The resulting (smoothed) image of the excess emission in the time–energy plane is shown in the top panel of Fig. 6 and exhibits further interesting behaviour. Beside the horizontal strip (representing the stable 6.4 keV Fe line) a saw–tooth pattern appears in the red feature energy band suggesting its energy evolution with time. The red feature emerges at about 5.7 keV and then increases its energy with time to merge with the 6.4 keV line. This behaviour appears to be repeated in each 'on' phase. If the characteristic variability timescale of 25 ks is interpreted as the orbital period of the emitting orbiting spot, this behaviour can be easily understood. Only the bright emission from the approaching side of the disc is seen and flux and energy both increase with time during the on phase. On the other hand, when the spot is on the receading side of the disc,the line emission is too faint to be detected (because of relativistic beaming away from the observer) and we cannot see the opposite trend (flux and energy of the line decreasing with time during the off phase). However, this naive interpretation has to be tested with a model that takes into account all the relativistic effects on the emission from the spot on the disc.

To extract as much information as possible from the observed image, we adopt a simple model in which a flare is located above an accretion disc, corotating with it at a fixed radius. The flare illuminates an underlying region on the disc (or spot) which produces a reflection spectrum, including an Fe K$\alpha$ line. The disc illumination is computed by integrating the photon geodesics in a Kerr spacetime from the flare to the disc, and is converted to local line emissivity. Then, the observed emission line profile is computed through the ray–tracing technique including all special and general relativistic effects (see Miniutti et al 2003; Miniutti & Fabian 2004). The main parameter of the model are the flare location, specified by its distance $r$ from the black hole axis, its height above the accretion disc ($h$), and the accretion disc inclination $i$. We have computed the evolution of Fe K emission induced by an orbiting flare and simulated time-energy maps with the same resolution and smoothing as in the excess emission map of Fig. 6 (top panel) exploring the parameter space. A constant, narrow 6.4 keV core representing the Fe K$\alpha$ line from distant material was also added to the model.

The bottom panel of Fig. 6 shows one of the theoretical time-energy maps we produced. This particular example assumes a flare with $(\,r\,,\,h\,)\,=\,(\,9\,,\,6\,)\;r_g$ and a disc inclination of 20°. By comparing the theoretical maps obtained with different spot's parameters with the data, we estimate that the flare must be located at a radius $r = (7-16)\;r_g$. The location of the flare (and of the irradiated spot on the disc) can be combined with the orbital timescale to provide an estimate of the black hole mass in NGC 3516. This is because the orbital period of the corotating flare/spot is related to its radial position by

$$T = 310\,[\,a + (\,r/r_g\,)^{3/2}\,]\,M_7 \quad [\,\mathrm{seconds}\,]\,, \qquad (1)$$

where $M_7$ is the black hole mass in units of $10^7\,M_\odot$ and $a$ is the dimensionless black hole spin.

The most natural interpretation for the characteristic 25 ks timescale we observe is that it is the orbital period $T$ of the emitting spot on the accretion disc. Therefore the only unknown in the above equation are the black hole spin and mass. Taking into account the uncertainty in $a$ (which can take any value from 0 to 1), we estimate that the black hole in NGC 3516 has a mass of $M_{\rm BH} = (1-5)\times 10^7\;M_\odot$. This result is in very good agreement with reverberation mapping estimates ($1.7\times 10^7\;M_\odot$ Onken et al 2003; $2.3\times 10^7$ Ho 1999) providing further support for our interpretation.

Our results indicate that present X-ray missions such as *XMM–Newton* are already probing the spacetime geometry in the vicinity of supermassive black holes if their observational capabilities are pushed to the limit. Future observatories such as *XEUS* and *Constellation-X*, which are planned to have much larger collecting area at 6 keV, will be able to exploit this potential and map the strong field regime of general relativity with great accuracy.

## ACKNOWLEDGMENTS

We thank the European Space Astronomy Centre (ESAC) and the Organizing Committee for organizing such a beautiful conference in El Escorial. The work presented here is based on observations obtained with *XMM-Newton*, an ESA science mission with instruments and contributions directly funded by ESA Member States and NASA. GM and KI thank the PPARC for support. ACF thanks the Royal Society for support.

## REFERENCES

[1] Bianchi S. et al, 2004, A&A, 422, 65

[2] della Ceca R. et al, 2005, ApJ, 627, 706

[3] Dovčiak M. et al, 2004, MNRAS, 350, 745

[4] Fabian A.C. et al, 2002, MNRAS, 335, L1

[5] Guainazzi M., 2003, A&A, 401, 903

[6] Ho L.C., 1999, in Observational Evidence for BHs in the Universe, ed. S.K. Chakrabarti (Dordrecht: Kluwer), 157

[7] Homan J. et al, 2003, ApJ, 586, 1262

[8] Iwasawa K. et al 1999, MNRAS, 306, L19

[9] Iwasawa K., Miniutti G., Fabian A.C., 2004, 355, 1073

[10] Miller J.M. et al, 2002, ApJ, 570, L69

[11] Miniutti G. et al, 2003, MNRAS, 344, L22

[12] Miniutti G., Fabian A.C., 2004, 2004, MNRAS, 349, 1435

[13] Miniutti G., Fabian A.C., Miller J.M., 2004, 351, 466

[14] Onken C.A. et al, 2003, ApJ, 585, 121

[15] Pecháček T. et al, 2005, A&A, 441, 855

[16] Porquet D. et al, 2004, A&A, 427, 101

[17] Rossi S. et al, 2005, MNRAS, 360, 763

[18] Tanaka Y. et al, 1995, Nature, 375, 659

[19] Turner T.J. et al, 2002, ApJ, 574, L123

[20] Turner T.J., Kraemer S.B., Reeves J.N., 2004, ApJ, 603, 62

[21] Turner T.J. et al, 2004, ApJ, 618, 155

[22] Wilms et al, 2001, MNRAS, 328, L27

[23] Yaqoob T. et al, 2003, ApJ, 596, 85

# A CHANDRA HETGS SPECTRAL STUDY OF THE IRON K BANDPASS IN MCG–6-30-15: A NARROW VIEW OF THE BROAD IRON LINE

**A. J. Young[1], J. C. Lee[2], A. C. Fabian[3], C. S. Reynolds[4], R. R. Gibson[1], and C. R. Canizares[1]**

[1]MIT Kavli Institute for Astrophysics and Space Research, 77 Massachusetts Avenue, Cambridge, MA 02139, USA
[2]Harvard-Smithsonian Center for Astrophysics, 60 Garden Street, Cambridge, MA 02138, USA
[3]Institute of Astronomy, University of Cambridge, Cambridge, CB3 0HA, UK
[4]Department of Astronomy, University of Maryland, College Park, MD 20742

## ABSTRACT

We present a 522 ksec Chandra High Energy Transmission Grating Spectrometer (HETGS) observation of the Fe K bandpass of MCG–6-30-15. The Chandra spectrum shows a broad Fe K$\alpha$ line, consistent with a relativistic disk line. Narrow, blue-shifted H- and He-like Fe absorption lines are detected, with a likely origin in a $\simeq 2000\,\mathrm{km\,s^{-1}}$ outflow. No other narrow absorption lines are detected in the Fe K bandpass. The gas giving rise to the H- and He-like Fe absorption lines is very highly ionized and does not affect the $\sim 2-6\,\mathrm{keV}$ continuum shape. Less highly ionized absorption could alter the $\sim 2-6\,\mathrm{keV}$ continuum shape and reduce the extent of the red wing of the iron line but a generic prediction of such models are narrow absorption lines between $\sim 6.4-6.5\,\mathrm{keV}$ which are inconsistent with the Chandra spectrum. Furthermore, the difference spectrum between the high flux and low flux states shows no deviation from a power law between 2 and 6 keV, contrary to the predictions of simple absorption models. These are compelling arguments that the broad iron K$\alpha$ line is *not* significantly affected by complex ionized absorption. We conclude that the relativistic disk line interpretation of the broad iron K$\alpha$ line in MCG–6-30-15 is robust.

Key words: accretion disks — black hole physics — galaxies: active — galaxies: Seyfert — galaxies: individual (MCG–6-30-15) — X-rays: galaxies.

## 1. INTRODUCTION

Broad iron lines are a potentially powerful probe of the accretion flow and space-time within a few Schwarzschild radii of a black hole (e.g. Fabian et al., 2000; Reynolds & Nowak, 2003). A major discovery of the ASCA observatory was a relativistically broadened Fe K$\alpha$ fluorescence line from the black hole accretion disk in the Seyfert 1 galaxy MCG–6-30-15 (Tanaka et al., 1995). The broad iron line in MCG–6-30-15 has since been confirmed and extensively studied by many different X-ray observatories.

It has been proposed, however, that ionized absorption can affect the continuum shape in the $\sim 2-6\,\mathrm{keV}$ bandpass and significantly reduce the extent of the broad red wing of the iron line. Ionized absorption models do not require the effects of strong gravity to explain the iron line profile (e.g. Kinkhabwala, A. A., 2003).

One of the science goals of future missions such as Constellation-X or XEUS is to map the accretion flow and space-time in the immediate vicinity of the black hole hole by studying the iron line and its variability. It is, therefore, crucial to test the robustness of the relativistic disk-line interpretation of broad iron K features.

In these proceedings we present the Chandra HETGS observation of MCG–6-30-15 and discuss the implications for broad iron line models. A more general discussion can be found in Young et al. (2005).

## 2. OBSERVATIONS

MCG–6-30-15 was observed by the Chandra HETGS for 522 ksec. We restrict our attention to the hard X-ray spectrum above 2 keV as our conclusions do not depend on the detailed properties of the warm absorber below 2 keV (i.e. our results are robust to the choice of *any* reasonable warm absorber model). A full analysis of the warm absorber will be presented by Lee et al. (2005).

If the Chandra HETGS spectrum is heavily binned the broad iron K$\alpha$ line is evident, and consistent with the one seen by XMM-Newton even though these observations were not contemporaneous (Fig. 1).

Looking at the $5.5-7.5\,\mathrm{keV}$ bandpass in more detail, the Chandra High Energy Gratings (HEG) spectrum shows

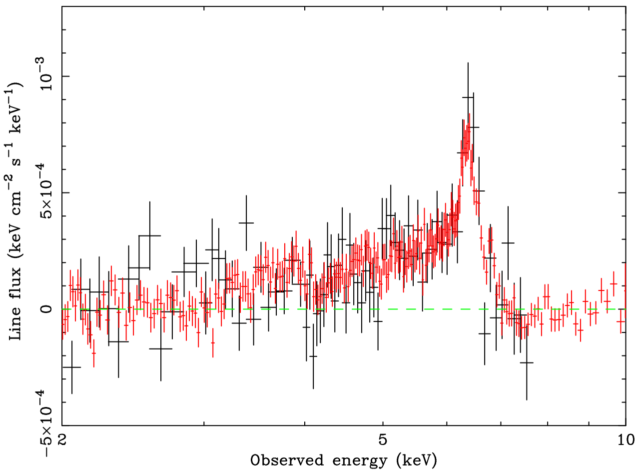


*Figure 1. The broad iron line in MCG–6-30-15 observed with the Chandra High Energy Gratings (HEG, black points) and XMM-Newton EPIC-pn (Vaughan & Fabian, 2004, red points). The Chandra spectrum has been heavily binned. There is good agreement between the two line profiles even though these spectra were not contemporaneous.*

three narrow lines (Fig. 2). There is a narrow component of the Fe K$\alpha$ fluorescence line that probably arises in cold material some distance from the nucleus. There are narrow absorption lines from H- and He-like Fe, blueshifted with respect the source frame by approximately $2000\,\mathrm{km\,s^{-1}}$ . These probably originate in an outflow.

The continuum light curve of MCG–6-30-15 shows variability by a factor of $\sim 2$ about the mean. The difference spectrum formed by subtracting low flux states from high flux states is well described by a power law between 2 and 6 keV (Fig. 3).

## 3. DISCUSSION

In this section we investigate the robustness of the relativistic disk line interpretation of the broad iron K$\alpha$ line.

The absorbing gas giving rise to the H- and He-like Fe absorption (§2, Fig. 2) is very highly ionized and does not have a significant affect on the $2-6\,\mathrm{keV}$ continuum. This is because most of the ions that can absorb soft X-ray photons (and hence affect the $2-6\,\mathrm{keV}$ continuum) are completely ionized or, in the case of iron, do not have the necessary L-shell electrons.

Less highly ionized gas can, however, affect the continuum shape between 2 and 6 keV, as illustrated in Fig. 4. The effect of this absorption is to reduce the extent of the red wing of the broad iron line to the point where relativistic effects of strong gravity are not required to explain the line profile. To significantly affect the $2-6\,\mathrm{keV}$ continuum the gas cannot be too highly ionized, and Fe ions must have L-shell electrons. On the other hand, the gas

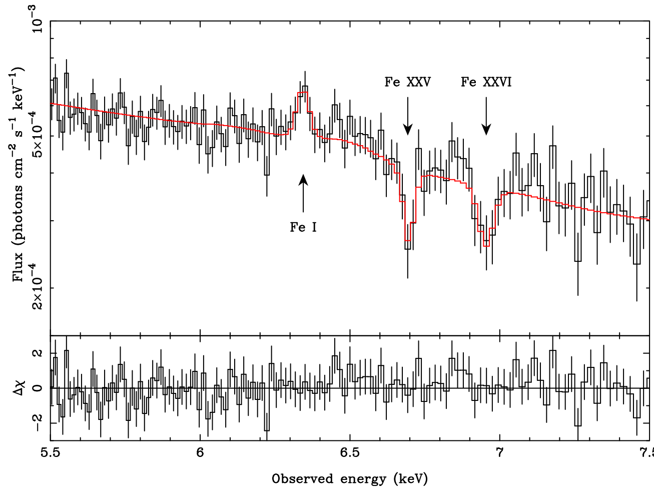


*Figure 2. Chandra HEG spectrum of the iron K bandpass in MCG–6-30-15. There is narrow iron K$\alpha$ emission at 6.34 keV (i.e. at rest in the source frame) and narrow absorption features from He-like iron at 6.69 keV and H-like iron at 6.96 keV. The absorption lines are blue-shifted with respect to MCG–6-30-15 by approximately* $2000\,\mathrm{km\,s^{-1}}$ *. No other narrow absorption lines are seen in this band.*

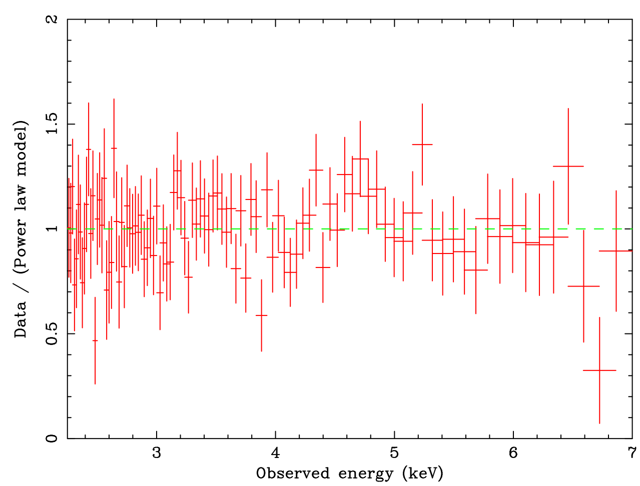


*Figure 3. Ratio of the difference spectrum between the high and low flux states of MCG–6-30-15 to a power law model with photon index* $\Gamma = 2$*. There is no evidence of absorption affecting the continuum shape between 2 and 6 keV, consistent with previous findings (e.g. Fabian et al., 2002). If the red wing of the broad iron line is significantly affected by absorption, that absorption should also be present in the difference spectrum. This implies that the broad, red wing of the iron line is* not *significantly affected by absorption.*

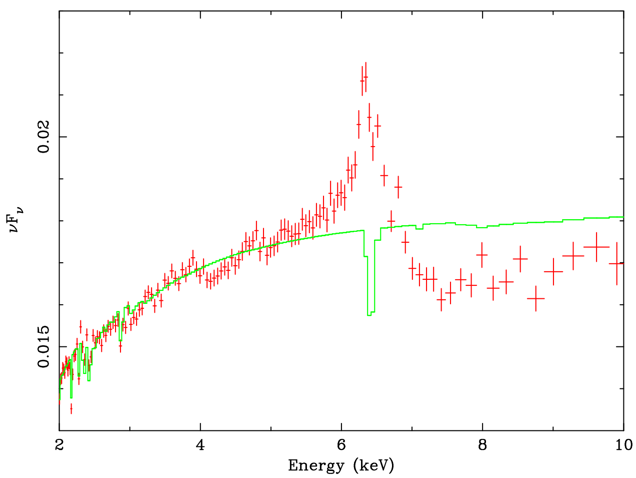


*Figure 4. An example of an ionized absorption model fit to the XMM-Newton spectrum. This unfolded spectrum shows how absorption causes curvature of the continuum spectrum below 6 keV that can mimic the broad red wing of the iron line.*

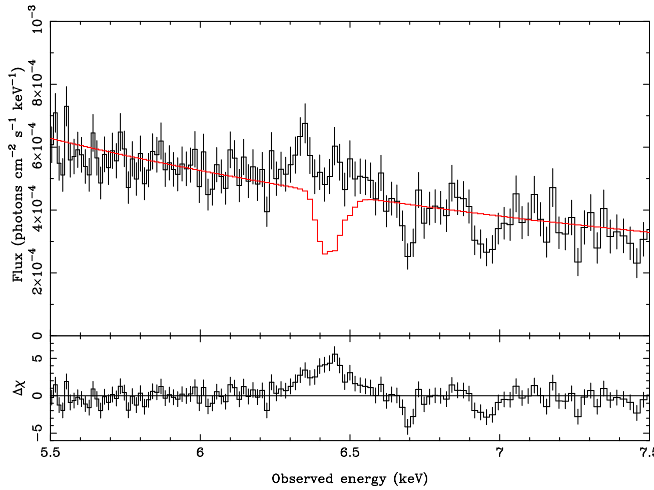


*Figure 5. Comparison of an ionized absorption model (red line) with the Chandra HEG spectrum (black points). The ionized absorption model reduces the extent of the red wing of the iron line but predicts strong iron absorption lines around $6.4 - 6.5\,\mathrm{keV}$ that are clearly inconsistent with the Chandra spectrum. We conclude that a simple ionized absorption model* cannot *account for the red wing of the broad iron line in MCG–6-30-15.*

cannot be neutral because its spectrum would be inconsistent with the RXTE spectrum above 10 keV (Reynolds et al., 2004). As a result, ionized absorption models of the red wing of the broad iron line predict narrow absorption lines between $\sim 6.4$ and 6.5 keV. Simple ionized absorption models can therefore be ruled out by the Chandra HEG spectrum (Fig. 5) in which the narrow absorption lines predicted by these models between 6.4 and 6.5 keV are not seen.

## 4. CONCLUSIONS

1. Narrow H- and He-like Fe absorption lines are detected in the Chandra HETGS spectrum of MCG–6-30-15, with an outflow velocity of $\sim 2000\,\mathrm{km\,s^{-1}}$.
2. No other absorption lines are seen in the Fe K band, ruling out simple ionized absorption models for the red wing of the broad iron K$\alpha$ line.
3. The difference spectrum between the high and low flux states does not show any deviations from a power law between 2 and 6 keV, further supporting the conclusion that absorption does not significantly affect this band.
4. We conclude that the relativistic disk line interpretation of the broad iron K$\alpha$ line in MCG–6-30-15 is robust.

## ACKNOWLEDGMENTS

We thank the conference organizers for an enjoyable and interesting meeting. Support for this work was provided by NASA through the Smithsonian Astrophysical Observatory (SAO) contract SV3–73016 to MIT for support of the Chandra X-ray Center which is operated by the SAO for and on behalf of NASA under contract NAS8–03060. JCL thanks and acknowledges support from the Chandra fellowship grant PF2–30023 – this is issued by the Chandra X-ray Observatory Center, which is operated by SAO for an on behalf of NASA under contract NAS8–39073.

## REFERENCES

Fabian, A. C., et al., 2000, PASP, 112, 1145

Fabian, A. C., et al., 2002, MNRAS, 335, L1

Kinkhabwala, A. A., 2003, Ph. D. thesis, Columbia Univ.

Lee, J. C., et al., 2005, in prep.

Reynolds, C. S. & Nowak, M. A., 2003, Phys. Rep. 377, 389

Reynolds, C. S., et al., 2004, MNRAS, 349,1153

Tanaka, Y., et al., 1995, Nature, 375, 659

Vaughan S. & Fabian A. C., 2004, MNRAS, 348,1415

Young, A. J., et al., 2005, ApJ, 631, 733

# A NEW INTERPRETATION OF THE X-RAY SPECTRAL VARIABILITY OF NGC 4051

**G. Ponti[1,2,3], G. Miniutti[1], M. Cappi[3], L. Maraschi[4], A.C. Fabian[1], and K. Iwasawa[1]**

[1]Institute of Astronomy, Madingley Road, Cambridge CB3 0HA
[2]Dipartimento di Astronomia, Università di Bologna, Via Ranzani 1, I–40127, Bologna, Italy
[3]INAF–IASF Sezione di Bologna, Via Gobetti 101, I–40129, Bologna, Italy
[4]Osservatorio Astronomico di Brera, via Brera 28, 20121 Milan, Italy

## ABSTRACT

We study the X–ray spectral variability of the Narrow Line Seyfert 1 galaxy NGC 4051 as observed during two *XMM–Newton* observations. The data show evidence for a neutral and constant reflection component and for constant emission from photoionized gas. The nuclear emission can be modelled both in terms of a "standard model" (pivoting power law plus a black body component for the soft excess) and of a two–component one (power law plus ionized reflection from the accretion disc). Both models reproduce the source spectral variability and cannot be distinguished on a statistical ground. The distinction has thus to be made on a physical basis. The standard model results indicate that the soft excess does not follow the standard black body law. The resulting temperature is consistent with being constant and has the same value as observed in PG quasars which have a much larger black hole mass than NGC 4051. Moreover, although the spectral slope is correlated with flux (consistent with spectral pivoting) the hardest photon indexes are so flat as to require rather unusual scenarios. Furthermore, the very low flux states exhibit an inverted Γ–flux behaviour which disagrees with a simple pivoting interpretation. These problems can be solved in terms of the two–component model in which the soft excess is not thermal, but due to the ionized reflection component. The variability of the reflection component from the inner disc closely follows the predictions of the light bending model, suggesting that most of the primary nuclear emission is produced in the very innermost regions, only a few gravitational radii from the central black hole.

Key words: X-rays; galaxies: active; galaxies: individual: NGC 4051.

## 1. INTRODUCTION

NGC 4051 is a nearby (z=0.0023) low–luminosity Narrow–Line Seyfert 1 (NLS1) galaxy which exhibits extreme X–ray variability in flux and spectral shape on both long and short timescales. The source sometimes enters relatively long and unusual low flux states in which the hard spectrum becomes very flat ($\Gamma \sim 1$) while the soft band is dominated by a much steeper component ($\Gamma \sim 3$, or blackbody with $kT \sim 0.12$ keV). Most remarkable is the 1998 *BeppoSAX* observation reported by Guainazzi et al (1998) in which the source reached its minimum historical flux state and the overall spectrum was best explained by assuming that the nuclear emission had switched off leaving only a reflection component from distant material.

NGC 4051, like many other Seyfert 1 and NLS1 galaxies, shows a 2–10 keV spectral slope that is well correlated with flux. However, the correlation is not linear with the slope hardening rapidly at low fluxes and reaching an asymptotic value at high fluxes (see e.g. Lamer et al 2003). This behaviour might be due to flux–correlated variations of the power law slope produced in a corona above an accretion disc as originally proposed by Haardt & Maraschi (1991; 1993) and related to changes in the input soft seed photons (e.g. Haardt, Maraschi & Ghisellini 1997, Poutanen & Fabian 1999). On the other hand, such slope–flux behaviour can be explained in terms of a two–component model (Shih, Iwasawa & Fabian 2002) in which a constant slope power law varies in normalisation only, while a harder component remains approximately constant hardening the spectral slope at low flux levels only, when it becomes prominent in the hard band.

Uttley et al (2004) have analysed the same *XMM–Newton* data we are presenting here. They showed that the source spectral variability is consistent with a Comptonization scenario and that the same process causing the spectral variability in high and intermediate flux states continues to operate even at the very low flux levels probed by the *XMM–Newton* data). This evidence seems to challenge the interpretation of the spectral variability as due to variable absorption by a substantial column of gas partially covering the source and affecting the spectral shape above 3 keV (Pounds et al. 2004).

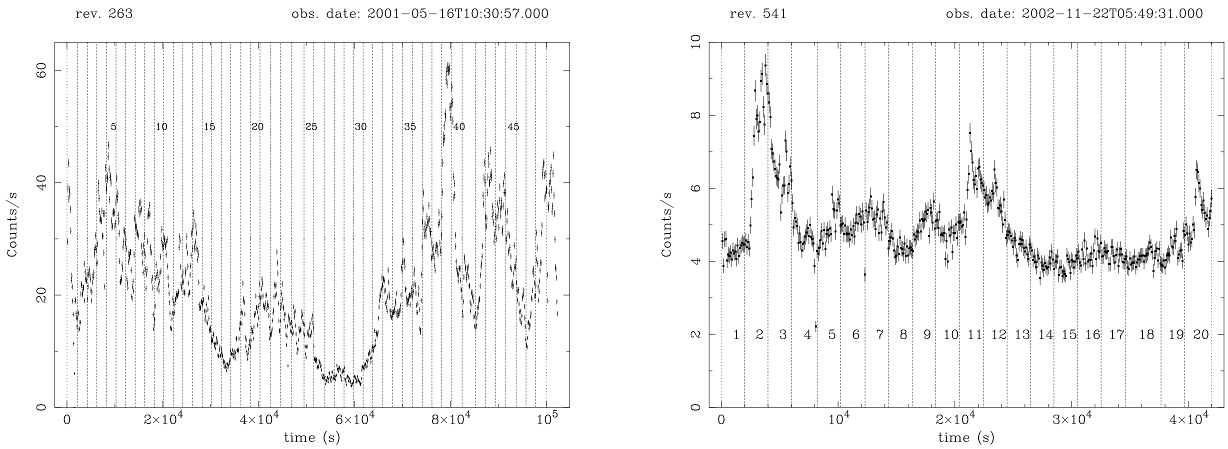


*Figure 1. The broadband 0.2–10 keV XMM–Newton EPIC–pn light curves of NGC 4051 for the first (left panel, rev. 263) and the second (right panel, rev. 541) observations. The 2 ks time slices used in the time–resolved spectroscopic analysis are also shown.*

## 2. SPECTRAL VARIABILITY: RMS SPECTRA

NGC 4051 has been observed twice by *XMM-Newton*. During the first observation (rev. 263, 2001 May) the source flux was comparable to the historical average, while during the second (rev. 541, 2002 November) it was much lower. The *XMM–Newton* broadband light curve of NGC 4051 (see Fig. 1) exhibits an extraordinary variability with variations up to a factor of 3 in few thousands seconds. We observe that not only the flux, but also the spectral slope changes in the same short timescale. To study the spectral variability, we start our analysis calculating the RMS spectrum, which measures the total amount of variability as a function of energy (Edelson et al. 2002; Vaughan et al. 2004; Ponti et al. 2004).

During the high flux observation of rev. 263 (Fig. 2) the variability rapidly increases toward softer energies, i.e. the broadband emission tends to steepen as it brightens. Some reduction in the variability is seen below about 800 eV followed by a plateau below 500 eV. A similar RMS shape has been observed in other sources (Ponti et al. 2005; Vaughan et al. 2003; Vaughan et al. 2004) and the two simplest explanations for the broadband trend invoke either spectral pivoting of the variable component, or the two–component model (see e.g Markowitz, Edelson & Vaughan 2003). Another important feature of the RMS spectrum is a drop of variability at 6.4 keV. Such a drop shows that the narrow Fe line (and therefore the associated reflection continuum) is much less variable than the continuum indicating an origin in distant material. Some structure is also present around 0.9 keV, with the possible presence of either a drop at that energy or two peaks.

The right panel of Figure 1 shows the RMS spectrum obtained for the low flux observation (rev 541). The variability below 3 keV is strongly suppressed with respect to the high flux observation. Moreover, the shape of the RMS spectrum is totally different and rather unusual. The trend of increasing variability toward softer energies breaks down completely and the most striking feature is the marked drop of variability around 0.9 keV. This feature, as well as the other drop of variability at ~0.55 keV, could have the same nature as the structure seen in the high flux RMS spectrum, but is much more significant and prominent here. As in the high flux observation, the variability is also suppressed around 6.4 keV.

The drops of variability at the energy of the narrow component of the Fe K line suggest that it comes from material distant from the variable illuminating source. In the time–averaged spectra the narrow component of the Fe line is clearly detected. In the low flux one, the line is unresolved, has an energy of $6.42 \pm 0.015$ keV, a flux of $(1.5 \pm 0.2) \times 10^{-5}$ ph s$^{-1}$ cm$^{-2}$, and an equivalent width of about 260 eV. The line energy and flux are consistent with measurements obtained in the high flux observation and also with previous data from *Chandra* (Collinge et al 2001) and *BeppoSAX* (Guainazzi et al 1998). Since the Fe line must be associated with a reflection continuum, in all subsequent fits we always include a constant and neutral reflection model from Magdziarz & Zdziarski (1995) and a narrow Fe line. The reflection continuum normalization is chosen such that the Fe line equivalent width (with respect to such continuum only) is consistent with the *BeppoSAX* observation (EW$_{FeK}$ ~700 eV) by Guainazzi et al (1998).

The strongest feature in the rms spectrum during the low flux observation (right panel of Fig. 2) is the drop of variability at ~0.9 keV. In the pn spectrum of the low flux observation an emission–like feature with energy of $0.88 \pm 0.02$ keV and a flux of $(1.2 \pm 0.2) \times 10^{-4}$ ph s$^{-1}$ cm$^{-2}$ is present. This emission line is present also in previous *Chandra* low flux spectra as well (Collinge et al 2001; Uttley et al 2003). The energy of the feature in the pn spectrum is consistent with Ne IX (and possibly Fe emission plus O VIII recombination continuum, or RRC). A second feature is also detected around 0.5–0.6 keV, where emission from O VII and O VIII is expected. As already shown by Pounds et al (2004) the high–resolution RGS

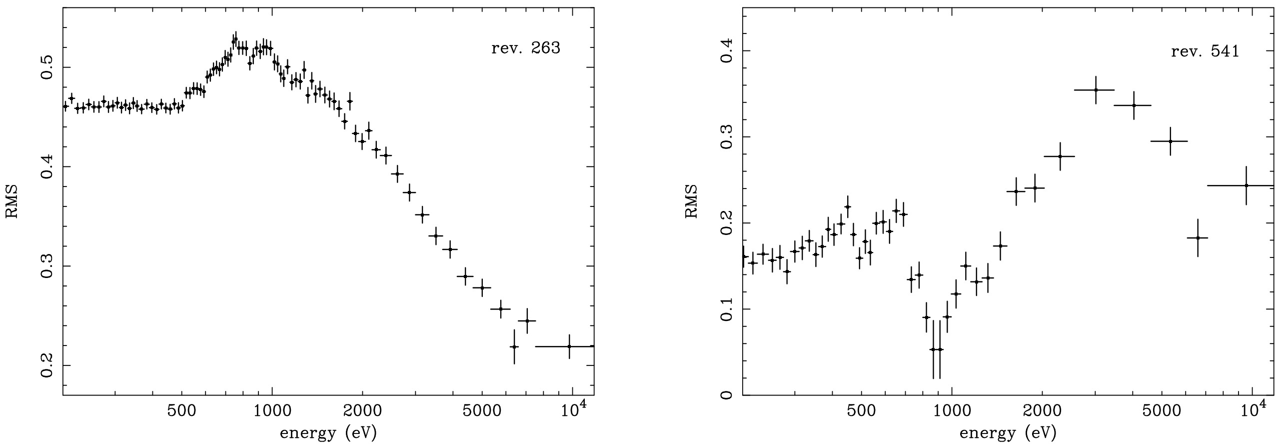


*Figure 2. The RMS spectra of the rev. 263 (left panel) and rev. 541 (right panel). The RMS spectra are computed with time bins of 2 ks with a minimum of 300 counts per energy bin.*

data during the same low flux *XMM–Newton* observation indeed show an emission line spectrum which is very similar to that of typical Seyfert 2 galaxies. The most prominent emission lines are due to the O VII triplet , the O VIII K$\alpha$ line and the N VII K$\alpha$ line. The Ne IX (forbidden) line is also clearly detected at 0.905 keV with a flux of $(3.5 \pm 1.0) \times 10^{-5}$ ph s$^{-1}$ cm$^{-2}$. The intensity of this line is not enough to account for the pn feature around 0.9 keV. However, the Ne line sits on top of a broad feature most likely due to O VIII RRC and possibly unresolved Fe emission lines. When fitted with a crude Gaussian model in the RGS data, such a feature has an energy of $0.88 \pm 0.01$ keV and a flux of $(5.0 \pm 1.5) \times 10^{-5}$ ph s$^{-1}$ cm$^{-2}$. By combining the Ne line with this broad feature ($\sigma \simeq 20$ eV) we obtain a flux of (0.7-1.1)$\times 10^{-4}$ ph s$^{-1}$ cm$^{-2}$ around 0.9 keV consistent with the pn lower limit. As mentioned in Pounds et al (2004) excess absorption might be present around 0.76 keV (possibly related to a M–shell unresolved transition array from Fe). If included in both CCD and RGS data, this has the effect of reducing the broad 0.9 keV feature intensity, making so more difficult to reproduce the variability drop in the RMS spectra.

## 3. TIME–RESOLVED SPECTRAL ANALYSIS

We then explore time–resolved spectroscopy on the shortest possible timescale (set by requiring good quality time–resolved individual spectra). In the following, we present results obtained by performing such an analysis on a 2 ks timescale (about four dynamical timescales at 10 $r_g$). The 2 ks slices that have been used in the analysis are shown in Fig. 1 and have been numbered for reference.

### 3.1. The 2–10 keV $\Gamma$–flux relationship

It is well known that the 2–10 keV spectral slope in NGC 4051 (and other sources) is correlated with the source flux. In Fig. 3, we show such a correlation when all the 2 ks spectra are fitted with a simple power–law model in the 2–10 keV band (including the constant reflection component from distant material discussed in Sec. 2). Data for the two observations are shown with different symbols.

The photon index increases with flux and seems to saturate at high flux around $\Gamma \simeq 2.2$ and at low fluxes to $\Gamma = 1.3$–$1.4$, with a $\Delta\Gamma \simeq 0.8$. Since the two asymptotes are not extremely well defined, such behaviour could still be consistent with spectral pivoting. On the other hand, the $\Gamma$–flux relationship can be explained if an additional and weakly variable component is present in the 2–10 keV band. If so, such a component dominates the low flux states and the hard photon index measured there is just a measure of its intrinsic spectral shape in the 2–10 keV band, while it is overwhelmed by the power law at high fluxes where $\Gamma \simeq 2.2$ is then the intrinsic power law photon index. In other words, as an alternative to spectral pivoting, the $\Gamma$–flux relationship can be explained by assuming the presence of i) a variable power law with constant or weakly variable slope $\Gamma \simeq 2.2$; ii) an additional less variable component with approximate spectral shape of $\Gamma = 1.3$–$1.4$ in the 2–10 keV band.

### 3.2. Broadband analysis I: the standard model

As a first step, we consider a simple continuum model comprising a power law plus black body (BB) emission to model the prominent soft excess. This is, in many respects, the “standard model” to fit AGN X–ray spectra and, though often crude and phenomenological, provides useful indications that can guide further analysis. The power law slope is free to vary to account for possible spectral pivoting. We add to the model neutral photoelec-

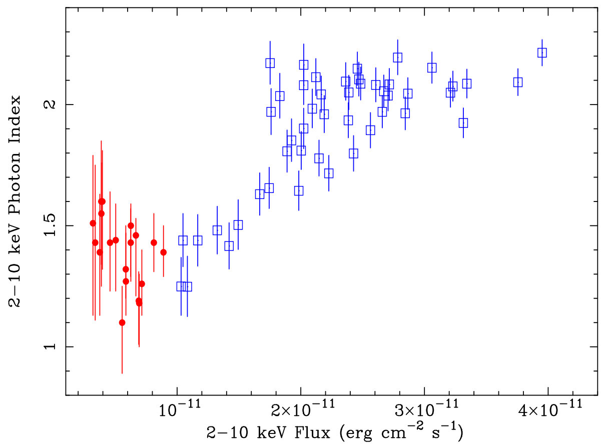


*Figure 3. The best fit spectral index vs. flux in the 2–10 keV band. The contribution of the constant reflection (including a narrow Fe line) coming from distant material is considered in the model.*

tric absorption with column density fixed to the Galactic value. To account for the presence of absorbing ionized gas in the line of sight we include two edges (O VII and O VIII). We searched for possible variations of their energies without finding any evidence, so we fixed the absorption energies to the rest–frame ones. This is clearly a crude approximation for the effects of the warm absorber in NGC 4051, but the quality of the individual 2 ks spectra is not such as to suggest the use of more sophisticated models. In addition, the constant components discussed above (reflection from distant matter and emission from photoionized gas) are also included in the spectral model. The overall model has six free parameters only. The resulting fits are very good with a reduced $\chi^2$ ranging between 0.9 and 1.2 with a mean close to unity. Therefore, from a statistical point of view, a single model is able to describe the spectral variability of the source in a very satisfactory way.

In Fig. 4 (left panel) we show the relation between the measured BB temperature and its intensity, which is proportional to the luminosity (in the present case $A_{BB}=10^{-4}$ correspond to $L_{BB}=9.7\times10^{40}$ ergs s$^{-1}$, assuming $H_0=71$ Mpc km$^{-1}$ s$^{-1}$). The BB luminosity spans about one order of magnitude, while the BB temperature ranges from about 90 eV to 140 eV with an average of 110–120 eV. Such a temperature is somewhat high, but can still be consistent with that expected from a black hole with mass $\simeq 5\times10^5\ M_\odot$ (Shemmer et al 2003; M$^c$Hardy et al 2004) accreting at high rate. If the soft excess in NGC 4051 is really due to BB emission from a constant area, we should be able to detect the BB law ($L_{BB}\propto T^4$) in data spanning one order of magnitude in BB luminosity. However, such a relation is ruled out ($\chi^2=1552$ for 67 degrees of freedom). The relation appears to be much steeper (with an index of 6.3–6.4 rather than 4), but even so, a power law fit is unacceptable. Moreover the measured temperature appears to be much more constant (the fit with a constant gives a $\chi^2=75$ for 67 degrees of freedom) than predicted by standard disc models.

The properties of the soft excess in NGC 4051 are remarkably similar to those of 26 bright radio–quiet quasars studied e.g. by Gierlinski & Done (2004). The quasar sample spans a wide range of black hole masses and luminosities and should therefore exhibit a wide range of disc temperatures. However, the measured temperature of the soft excess is remarkably constant throughout the sample with a mean of 120 eV (and very small variance). It is a rather surprising coincidence that this is exactly the average temperature we measure for the soft excess in NGC 4051, considering that the black hole mass in NGC 4051 is about 3 orders of magnitude smaller than the typical black hole mass in the quasar sample.

The "standard model" of the source emission seems to be inadequate to describe the corona parameters as well. In the right panel of Fig. 4 we show the power law slope as a function of the 0.5–10 keV flux. In the normal/high flux observation the photon index steepens with flux, as already pointed out in the 2–10 keV analysis. This behaviour is consistent with spectral pivoting, even if the lowest $\Gamma$ require a too hard spectral shape to be accounted for by standard Comptonization models. The main problems arise at very low fluxes, where the $\Gamma$–flux relation is inverted in a manner that is not consistent with simple spectral pivoting. Such behaviour could indicate the presence of an additional soft (steep) component which becomes prominent at low fluxes and is not properly accounted for by the black body component. In fact, the power law is trying to fit the soft data by steepening the index at low fluxes and leaves significant residuals in the hard band where a slope of about 1.3–1.4 would be more appropriate even at very low fluxes (see Fig. 3).

Such discrepancies naturally raises questions on the real nature of the X–ray soft excess and of the soft steep component observed at low fluxes. As pointed out by Gierlinski & Done (2004), the remarkable constancy of the "soft excess temperature" might indicate an origin in atomic rather than thermal physical conditions. Possible candidates seems to be absorption and/or ionized reflection. We investigate here the two–component model in which the soft excess and the soft steep component observed at low fluxes are due to a ionized reflection component.

### 3.3. Broadband analysis II: the two–component model

In the two–component model the variability is dominated by a power law component (PLC) which changes in flux but not in spectral shape ($\Gamma=2.2$). The PLC illuminates the accretion disc giving rise to a reflection–dominated component (RDC, from Ross & Fabian 2005) which is affected by the relativistic effects arising in the inner disc. We take into consideration these effects convolving the ionized reflection spectrum with a LAOR kernel with fixed inner and outer disc radius (to $1.24\ r_g$ and $100\ r_g$ respectively), and fixed disc inclination ($30°$). The inner disc

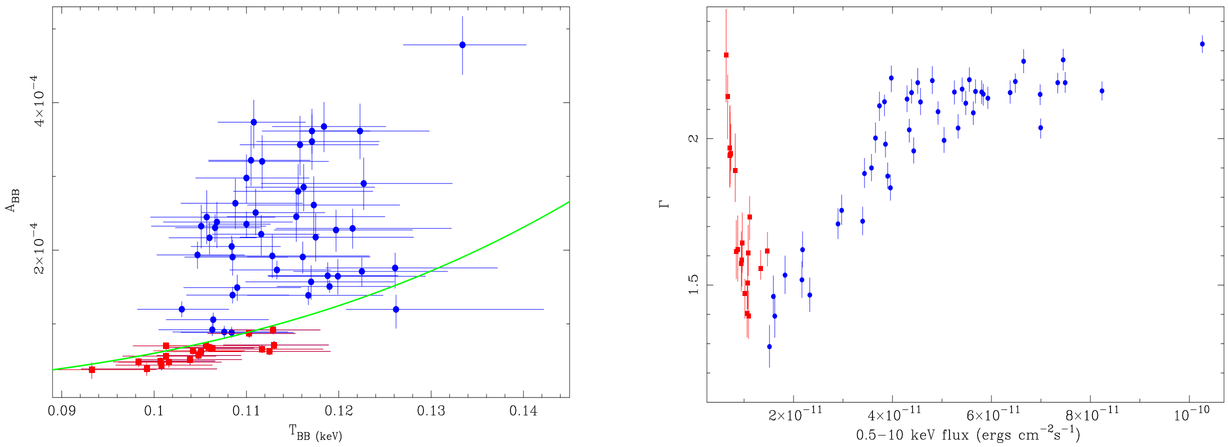


*Figure 4. In the left panel we show the blackbody intensity as a function of its observed temperature. The line shows the best fit relation between the $A_{BB} \propto T^4_{BB}$. In the right panel, we show the broadband $\Gamma$–flux relationship as obtained from the standard model fits (see text for details).*

radius corresponds to the innermost stable circular orbit around a Kerr black hole. The only free parameters of the relativistic kernel is then the index $q$ of the disc emissivity profile ($\epsilon = r^{-q}$). The ionized reflection model is appropriate for solar abundances and has ionization parameter and normalization as free parameters, while the photon index of the illuminating power law in the RDC model is tied to that of the PLC and therefore fixed to $\Gamma = 2.2$. As for the "standard model" discussed in the previous Section, the overall spectral model also includes Galactic absorption, constant emission from photoionized gas and from a distant reflector and the O VII and O VIII edges with fixed energies. The number of free parameters in the model is just the same as in the "standard model" case (6 free parameters).

The model reproduces very well the data at all flux levels with a reduced $\chi^2$ between 0.8 and 1.2. The two–component model is statistically indistinguishable from the standard one and has to be considered as a possible alternative to be accepted or rejected on a physical rather than statistical basis. We would like to stress again that with this interpretation the soft excess is not due to a thermal component anymore. It is the ionized reflection from the disc that naturally produces a soft excess. The reflection can then naturally solve the "constant temperature" problem because of the very non–thermal nature of that component. Moreover, no changes in the PLC slope are required to fit the data and to reproduce the $\Gamma$–flux relation. We tested, in fact, a variable $\Gamma$ fit to the data and found that all the 68 spectra are consistent with $\Gamma$=2.2 with only three exceptions (with $\Delta\Gamma$ <0.1). Thus, the $\Gamma$–flux relation is simply due to the relative contribution of the two components, with the steep and variable PLC dominating the medium and high flux states and with a stronger contribution of the flatter RDC during the low flux ones.

As for the variability of the two components, the RDC is expected to respond to the PLC variations and to be well correlated with it. Fig. 5 shows the 0.5–10 keV flux of the RDC versus the PLC flux in the same band. The RDC is well correlated with the PLC at low flux levels (the solid line represent perfect correlation between the two components). However, as the PLC flux increases, the correlation clearly breaks down and the RDC is much less variable (about a factor 2.5) than the PLC (about a factor 7). A similar behaviour has been observed also in MCG-6-30-15 (Vaughan & Fabian 2004) and has been interpreted in terms of a strong gravitational light bending by Miniutti et al (2003) and Miniutti & Fabian (2004), which predicts an almost stable RDC during normal/high flux periods and a correlation at low flux levels only. The observed variability is therefore in good agreement with the light bending model prediction. The other free parameters of the RDC in our fit are the disc reflection emissivity index of the relativistic blurring model ($q$) and the ionization parameter of the reflection spectrum ($\xi$). The former shows some trend with flux, with low flux states generally corresponding to steeper emissivity profiles than high flux ones (Ponti et al. in prep.). This result is also in line with the predictions of the light bending model (Miniutti & Fabian 2004). The latter, instead, is not very well constrained by the data and most spectra are consistent with $\xi$ between 50 and 300 erg cm s$^{-1}$ with only few exceptions below and above (and no clear trend with flux). We finally remark that, if the light bending interpretation is correct, the RDC versus PLC behaviour requires the primary source of PLC to be centrally concentrated above the accretion disc within 15 gravitational radii at most from the central black hole (see Miniutti & Fabian 2004). In particular, the correlation between the two component is predicted to occur only if the primary source of the PLC is within $\sim$ 5 gravitational radii from the hole. Therefore, one consequence of this interpretation is that low flux states are characterised by an extremely compact region of primary emission, well inside the relativistic region around the black hole.

As a final comment, the mean optical depth of the ionized absorber, here modelled crudely by the O VII and O VIII edges, is of the order of 0.1–0.2. These values are

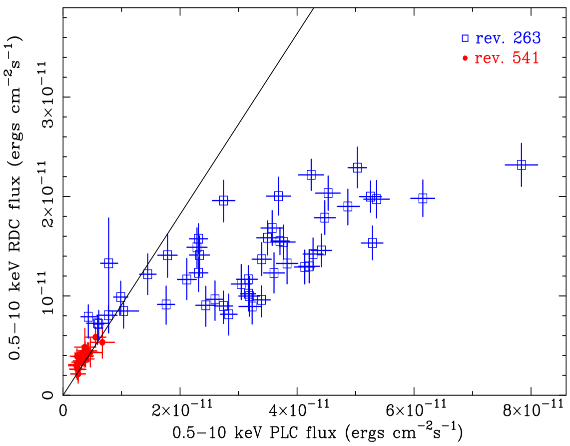


*Figure 5. RDC vs. PLC 0.5–10 keV fluxes. The data clearly rule out a perfect correlation between the two components (solid line). The RDC is well correlated with the PLC at low fluxes only and varies with smaller amplitude in normal/high flux states.*

left free to vary and they seem to suggest some variations during the two observations (in agreement with the evidences presented by Elvis et al. during this conference). Nevertheless, the uncertainties associated with our measurements are so large that a fit to the optical depth with a constant during the first observation results in a $\chi^2$ of 26 (O VII) and 47 (O VIII) for 47 degrees of freedom, while during the second low flux observation the $\chi^2$ are 29 and 7 for 19 degrees of freedom, preventing us from claiming the variation.

## 4. CONCLUSIONS

We investigated the X–ray spectral variability of the Narrow Line Seyfert 1 galaxy NGC 4051 with model independent techniques (RMS spectra and Flux–Flux plots) and with time resolved spectral variability. NGC 4051 show evidence for a distant neutral and constant reflection component contributing by about 10 per cent in the 4–10 keV band at mean fluxes and constant emission from photoionized gas.

The nuclear emission has been interpreted both in a “standard scenario” (consisting of BB plus power law emission) and by a two–component (PLC plus ionized RDC from the disc). Both models reproduce the RMS spectra, and describe the time–resolved spectra in a comparable way from a statistical point of view, thus the dinstinction has to be made on a physical basis. In the framework of the two–component model the soft excess is interpreted as the soft part of ionized reflection from the accretion disc. The constant temperature problem is then solved in terms of atomic rather than truly thermal processes. Moreover, the RDC explains the Γ–flux relationship at all flux levels in terms of the relative contribution of a PLC with constant slope $\Gamma = 2.2$ and the RDC.

## REFERENCES


Collinge M.J. et al, 2001, ApJ, 557, 2

Edelson et al, 2002, ApJ, 568, 610

Gierliński, M., & Done, C., 2004, MNRAS, 349, L7

Guainazzi M. et al, 1998, MNRAS, 301, L1

Haardt, F., & Maraschi, L., 1991, ApJL, 380, L51

Haardt, F., & Maraschi, L., 1993, ApJ, 413, 507

Haardt, F., Maraschi, L., & Ghisellini, G., 1997, ApJ, 476, 620

Lamer G. et al., 2003, MNRAS, 338, 323

M$^c$Hardy I.M. et al., 2004, MNRAS, 348, 783

Magdziarz P., Zdziarski A.A., 1995, MNRAS, 273, 837

Markowitz A., Edelson R., Vaughan S., 2003, ApJ, 598, 935

Miniutti, G., Fabian, A. C., Goyder, R., & Lasenby, A. N. 2003, MNRAS, 344, L22

Miniutti, G., & Fabian, A. C., 2004, MNRAS, 349, 1435

Ponti, G., Cappi, M., Dadina, M., & Malaguti, G., 2004, A&A, 417, 451

Ponti, G., et al, 2005, Proceedings of the 6th Italian Conference on Active Galactic Nuclei, http://www.arcetri.astro.it/ agn6/

Pounds K.A., Reeves J.N., King A.R., Page K.L., 2004, MNRAS, 350, 10

Poutanen, J., & Fabian, A. C. 1999, MNRAS, 306, L31

Ross, R. R., & Fabian, A. C., 2005, MNRAS, 358, 211

Shemmer O., Uttley P., Netzer H., M$^c$Hardy I.M, 2003, MNRAS, 343, 1341

Shih, D. C., Iwasawa, K., & Fabian, A. C., 2002, MNRAS, 333, 687

Uttley P., Fruscione A., M$^c$Hardy I.M., Lamer G., 2003, ApJ, 595, 656

Uttley P., et al, 2004, MNRAS, 347, 1345

Vaughan, S., Edelson, R., Warwick, R. S., & Uttley, P., 2003, MNRAS, 345, 1271

Vaughan, S., & Fabian, A. C., 2004, MNRAS, 348, 1415

# THE HIGH-VELOCITY OUTFLOW OF PG 1211+143: AN UNBIASED VIEW BASED ON SEVERAL OBSERVATIONS

**S. Kaspi**[1,2] **and E. Behar**[1]

[1]Department of Physics, Technion, Haifa 32000, Israel
[2]School of Physics and Astronomy and the Wise Observatory, Tel-Aviv University, Tel-Aviv 69978, Israel

## ABSTRACT

We present and discuss high-resolution grating spectra of the quasar PG 1211+143 obtained over three years. Based on an early observation from 2001, we find an outflow component of about 3000 km s$^{-1}$ in contrast with the much higher velocity of about 24000 km s$^{-1}$ reported earlier for this source, and based on the same data set. Subsequent grating spectra obtained for PG 1211+143 are consistent with the first observation in the broad-band sense, but not all narrow features used to identify the outflow are reproduced. We demonstrate that the poor S/N and time variability seen during all existing observations of PG 1211+143 make any claims about the outflow precariously inconclusive.

## 1. INTRODUCTION

Typical mass outflow velocities of a few hundreds to a few thousands km s$^{-1}$ have been measured by now in numerous Active Galactic Nuclei (AGNs; Crenshaw et al. 2003 and references therein). Recent studies of the X-ray spectra of certain quasars have led to claims of much higher outflow velocities reaching a significant fraction of the speed of light, e.g., APM 08279+5255 — Chartas et al. (2002) claim speeds of $\sim 0.2c$ and $\sim 0.4c$[1], PG 1115+080 — Chartas et al. (2003) find two X-ray absorption systems with outflow velocities of $\sim 0.10c$ and $\sim 0.34c$. These measurements, however, were carried out using spectra obtained with CCD cameras and hence at moderate spectral resolving powers of $R \sim 50$. Using the *XMM-Newton* reflection gratings ($R$ up to 500), high resolution X-ray spectra for several quasars have been obtained. For PG 1211+143 Pounds et al. (2003a, 2005) find a rich, well resolved spectrum featuring absorption lines of several ions, which they interpret as due to an outflow of $\sim$ 24000 km s$^{-1}$. A similar interpretation was applied to a similar observation of PG 0844+349, where Pounds et al. (2003b) report even higher velocities reaching $\sim$ 60000 km s$^{-1}$. In NGC 4051, Pounds et al. (2004) find a single absorption line at $\sim$ 7.1 keV, which they suggest may be Fe XXVI Ly$\alpha$ at an outflow velocity of $\sim$ 6500 km s$^{-1}$, or the He$\alpha$ resonance absorption line of Fe xxv in which case the outflow velocity is $\sim$ 16500 km s$^{-1}$. Yet another ultra-high-velocity (UHV, i.e., sub-$c$) wind of 50000 km s$^{-1}$ was reported by Reeves et al. (2003) for PDS 456. In all of these sources, the inferred hydrogen column densities through the wind is of the order of $10^{23}$ cm$^{-2}$, which is about an order of magnitude higher than the typical values measured for the nearby Seyfert sources.

If indeed UHV outflows are common to bright quasars, this could have far reaching implications on our understanding of AGN winds and AGNs in general. For instance, if these winds carry a significant amount of mass as the high column densities may suggest, they would alter our estimates of the metal enrichment of the intergalactic medium by quasars. It remains to be shown theoretically what mechanism (e.g., radiation pressure) can drive these intense winds. Since the amount of mass in the wind is not well constrained, it is still unclear what effect it may have on the energy budget of the AGN. King & Pounds (2003) note that UHV winds have been found mostly for AGNs accreting near their Eddington limit. They provide a theory by which the UHV outflows are optically thick producing an effective photosphere, which is also responsible for the UV blackbody and soft X-ray (excess) continuum emission observed for these sources.

## 2. PG 1211+143 — FIRST OBSERVATION — SECOND VIEW

PG 1211+143 was observed with *XMM-Newton* during 2001 June 15 for about 55 ks. We retrieved the data for this observation from the *XMM-Newton* archive and reduced them using the Science Analysis System (SAS v5.3.0) in the standard processing chains as described in the data analysis threads and the ABC Guide to *XMM-*

[1]Though Hasinger et al. (2002) using a different instrument prefer a more conservative interpretation by which the X-ray wind is much slower and consistent with the well known, UV broad absorption line wind of that source, outflowing at velocities of up to 12000 km s$^{-1}$.

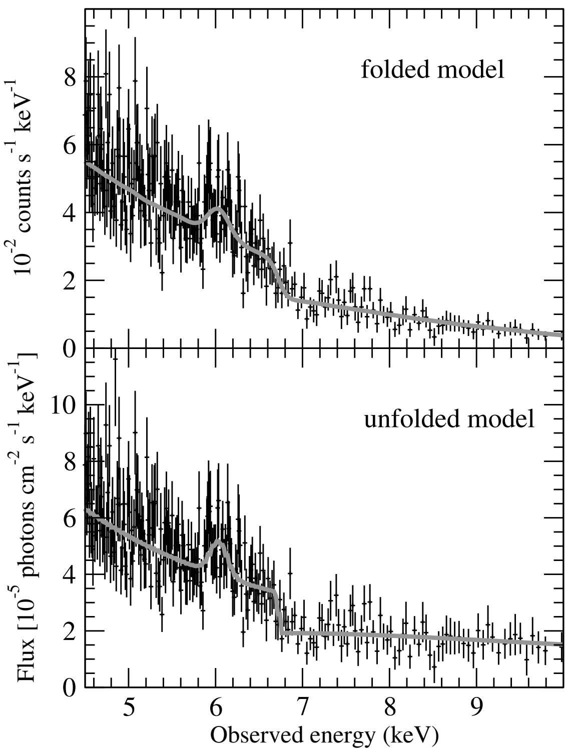


*Figure 1. The EPIC-pn data and a simple fitted model, which is discussed in § 2.1. The upper panel shows the model folded through the instrument response and compared with the data. Bottom panel shows the unfolded model.*

*Newton* Data Analysis. Overall, our data reduction results agree well with that of Pounds et al. (2003a, 2005) except for a few minor features which appear to be slightly different between the two reductions. We attribute these discrepancies to the different binning methods used and to the averaging of RGS1 and RGS2 in this work (see below). The results described in this section are presented in details in Kaspi & Behar (2006).

### 2.1. EPIC-pn

For the EPIC-pn data we first fitted the (line-free) rest-frame 2–5 keV energy range with a simple power law. The best fitted power law has a photon index of $\Gamma = 1.55 \pm 0.05$ and a normalization of $(6.6 \pm 0.4) \times 10^{-4}$ ph cm$^{-2}$ s$^{-1}$ keV$^{-1}$ and gives $\chi^2_\nu = 0.74$ for 487 degrees-of-freedom (d.o.f.). Extrapolating this power law up to a rest-frame energy of 11 keV, we find a flux excess above the power law at around 6.4 keV, which is indicative of an iron K$\alpha$ line, and a flux deficit below the power law at energies above 7 keV. We add to the model a Gaussian emission line to account for the Fe K$\alpha$ line and a photoelectric absorption edge to account for the deficit. Fitting for all parameters simultaneously, we find the best-fit Gaussian line center is at $6.04 \pm 0.04$ keV (or $6.53 \pm 0.05$ keV in the rest frame) and a line width ($\sigma$) of $0.096 \pm 0.067$ keV. The total flux in the line is $(2.9 \pm 1.4) \times 10^{-6}$ ph cm$^{-2}$ s$^{-1}$. For the edge, we find a threshold energy of $6.72 \pm 0.10$ keV, which is translated to a rest frame energy of $7.27 \pm 0.11$ keV. The optical depth at the edge is $\tau = 0.56 \pm 0.10$. The power law model with the Gaussian line and the absorption edge gives a $\chi^2_\nu = 0.983$ for 613 d.o.f. This model is plotted in Figure 1 where we show the model, both folded through the instrument and fluxed (i.e., unfolded). We stress that this edge does not necessarily contradict the presence of the line detected by Pounds et al. (2003a, 2005), since K$\alpha$ edges have lines right next to them.

We also observe the lines at 2.68 keV and 1.47 keV claimed by Pounds et al. (2003a, 2005) to be from S and Mg, only we identify them as different lines at much lower velocities. The 2.68 keV line is identified here as S XV He$\beta$ and the 1.47 keV line is identified as Mg XI He$\beta$.

### 2.2. RGS

The RGS1 and RGS2 were operated in the standard spectroscopy mode resulting in an exposure time of $\sim 52$ ks. The spectra were extracted into uniform bins of $\sim 0.04$ Å (which is about the RGS resolution and is 4 times the default bin width) in order to increase the signal-to-noise ratio (S/N). For the purpose of modeling narrow absorption lines, this rebinning method is better than the method used by Pounds et al. (2003a) of rebinning the spectrum to a minimum of 20 counts per bin, which distorts the spectrum especially around low-count-rate absorption troughs. To flux calibrate the RGS spectra we divided the count spectrum of each instrument by its exposure time and its effective area at each wavelength. Each flux-calibrated spectrum was corrected for Galactic absorption and the two spectra were combined into an error-weighted mean. At wavelengths where the RGS2 bins did not match exactly the wavelength of the RGS1 bins, we interpolated the RGS2 data to enable the averaging. The sky-subtracted combined RGS spectrum has in total $\sim 8900$ counts and its S/N ranges from $\sim 2$ around 8 Å to $\sim 5$ around 18 Å with an average of 3. Statistics in the second order of refraction are insufficient, hence we did not include it in our analysis.

The combined RGS spectrum (RGS1 and RGS2) of PG 1211+143 is presented in Figure 2. Numerous absorption lines and several emission lines are detected. We identify K-shell lines of C, N, O and Mg and L-shell lines of O, Mg, Si, Ar, and Fe. The absorption line widths are consistent with the RGS resolution, and with the present S/N we are not able to resolve the intrinsic velocity widths. In emission, we identify significantly broadened lines of N VII Ly$\alpha$, O VIII Ly$\alpha$, the forbidden line of O VII and its He$\alpha$ resonance line, the forbidden line of Ne IX, and the Mg XI He$\alpha$ resonance line, all in the rest frame of the source with no velocity shift.

In order to quantitatively explore the emission and absorption lines, we have constructed a model for the entire

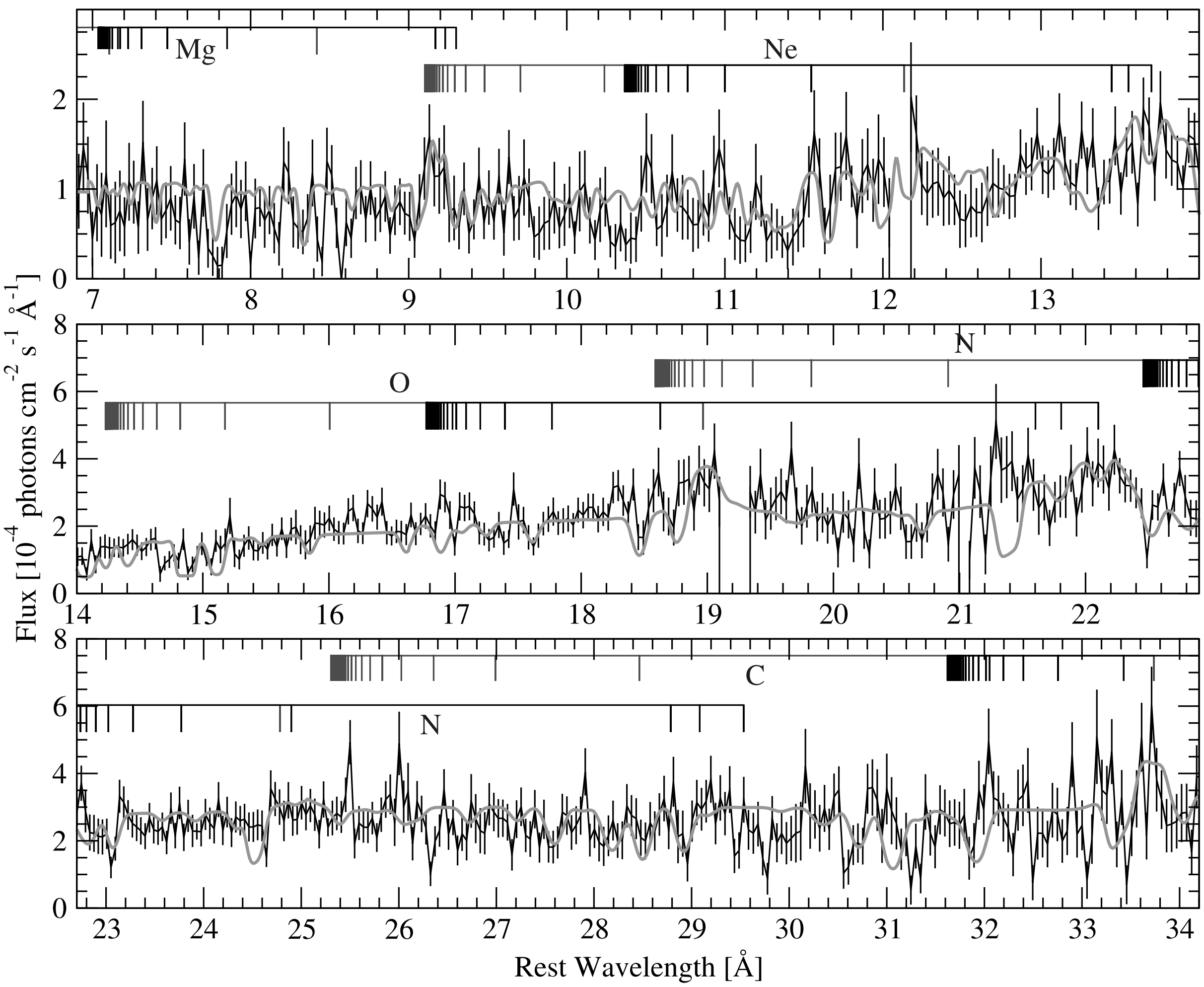


*Figure 2. Combined RGS1 and RGS2 spectrum of PG 1211+143 binned to $\sim 0.04$ Å. The spectrum has been corrected for Galactic absorption and for the redshift of the source. The rest-frame positions of lines from H-like and He-like ions of N, O, Ne, and Mg are marked above the spectrum. The lines from the lower ionization states of O and Mg, and the L-shell lines of Fe are not marked. Gaps in the spectrum are due to chip gaps and have zero flux. The model is marked as the solid gray curve.*

RGS spectrum. The present method is an ion-by-ion fit to the data similar to the approach used in Sako et al. (2001) and in Behar et al. (2003). We first use the continuum measured from the EPIC-pn data, but renormalized to the RGS flux level. This continuum is then absorbed using the full set of lines for each individual ion. Our absorption model includes the first 10 resonance lines of H- and He- like ions of C, N, O, Ne, and Mg as well as edges for these ions. The model also includes our own calculation for the L-shell absorption lines of Fe (Behar et al. 2001) as well as of Si, S, and Ar corrected according to laboratory measurements (Lepson et al. 2003, 2005). Finally, we include inner-shell K$\alpha$ absorption lines of O and Mg (Behar & Netzer 2002), which we detect in the spectrum. The absorbed spectrum is complemented by the emission lines mentioned above, which are observed in the RGS spectrum.

By experimenting with the absorption line parameters, we find that the observed lines are all blueshifted by about 3000 km s$^{-1}$ with an uncertainty of 500 km s$^{-1}$. In the model we used a turbulence velocity of 1000 km s$^{-1}$ to broaden the absorption lines. This width includes the instrumental broadening, which as noted above, we could not separate from the intrinsic broadening. Since the lines appear to be saturated, but no line goes to zero intensity in the trough, we obtain the best fit by assuming a covering factor of 0.7 for the X-ray continuum source. The best-fit column densities that we find for the different ions are consistent with a hydrogen column density of about $10^{21}$–$10^{22}$ cm$^{-2}$. The emission lines are modeled using Gaussians with uniform widths of $\sigma = 2500$ km s$^{-1}$ (resolved, but again, including the instrumental broadening), with no velocity shift, and assumed to be unabsorbed. These lines at FWHM $\simeq 6000 \pm 1200$ km s$^{-1}$ are even broader than those observed from the broad line region in the visible band ($\sim 2000$ km s$^{-1}$; Kaspi et al. 2000). The entire best-fit spectrum is shown in Figure 2 (gray curve). The spectrum beyond 25 Å is particularly challenging as it comprises many unresolved lines from

L-shell ions of Si, S, and Ar while the RGS effective area drops rapidly. Several predicted lines may be observed here (e.g., Ar XIII - 28.92 Å, Si XII - 30.71 Å, Ar XII - 31.06 Å, S XIII - 31.93 Å; these wavelengths include the 3000 km $s^{-1}$ shift). We are still unable to explain several features seen in the data, e.g., around 8.5 Å, 10.4 Å, or 29.8 Å, but the model gives a good fit to the data overall.

### 2.3. Conclusions - First Observation

We have provided a self consistent model to the ionized outflow of PG 1211+143 revealing an outflow velocity of approximately 3000 km $s^{-1}$. Our model reproduces many absorption lines in the RGS band, although the S/N of the present data set is rather poor and some of the noise might be confused with absorption lines.

The present approach is distinct from the commonly used global fitting methods and also from the line-by-line approach used by Pounds et al. (2003a). It allows for a physically consistent fit to the spectrum and is particularly appropriate for a broad-ionization-distribution absorber as observed here for PG 1211+143.

The present model also features several broad (FWHM = 6000 km $s^{-1}$) emission lines, which are observed directly in the data.

A broad and relatively flat ionization distribution is found throughout the X-ray outflow consistent with a hydrogen column density of roughly $10^{21}$–$10^{22}$ cm$^{-2}$. This is reminiscent of the outflow parameters measured in other well studied Seyfert galaxies.

We also detect Fe-K absorption, which was identified by Pounds et al. (2003a, 2005) as a strongly blueshifted Fe XXVI absorption line. We find that most of the Fe-K opacity can alternatively be attributed to several consecutive, low charge states of Fe, although it can not be assessed whether the absorber is co-moving with the outflow or not. Future missions with microcalorimeter spectrometers on board might be able to address this interesting question.

## 3. A SECOND OBSERVATION OF PG 1211+143

A second *XMM-Newton* observation of PG 1211+143 for $\sim$ 50 ks was carried out on 2004 June 21, three years after the first observation of 2001 June 15 which is described above. We have retrieved the data of this second observation from the *XMM-Newton* archive and reduced it in exactly the same way described above for the first observation. The data of the second RGS observation are plotted (gray line) in Figure 3 over the first observation (black line). The broad-band spectra of the two observations are generally consistent. However, not all narrow features are consistently reproduced. The total flux in the RGS band is the same in the two observations, though the continuum slope in the second observation the spectrum is somewhat harder.

When inspecting the detailed narrow features in the spectrum some have changed while others remain the same. For example, the second observations shows features which appear to be emission lines around 8 Å where the first observation had absorption lines. Also, around 15 Å the absorption lines seem to have disappeared in the second observation. Conversely, some features are the same in the two spectra, for example, the emission O VII triplet around 22 Å and the Ne IX triplet around 13.5 Å. From Figure 3, it can be seen that due to the poor S/N in both spectra, it is extremely hard to determine whether the differences between the two spectra are real, or a mere result of the data's poor S/N.

## 4. SIMULTANEOUS OBSERVATIONS OF *XMM-NEWTON* AND *CHANDRA*

Simultaneously with the 2004 June 21 *XMM-Newton* observation, PG 1211+143 was also observed with the Low Energy Transmission Grating (LETG) on board the *Chandra* X-ray observatory. The LETG observation of $\sim$ 45 ks has made use of the ACIS CCDs as the detector. We retrieved the data of this observation from the *Chandra archive* and reduced it using CIAO 3.2.1 and CALDB version 3.01, according to the updated CIAO threads. We have combined the +1 and -1 orders of the LETG spectrum using a weighted mean and the combined spectrum is represented in Figure 4 by a black line. The simultaneous RGS observation (the gray data in Figure 3) is shown in gray in Figure 4.

Although the simultaneous data from the two X-ray observatories are consistent overall, they differ in many details. For example, the RGS data between 7 to 9 Å show several emission-like features which the LETG data do not. Also, around 16.4 Å the LETG data show absorption-like features which are not present in the RGS data. These differences are consistent to within about $3\sigma$ and are probably a result of the poor S/N of the observations

After the first $\sim$ 45 ks LETG observation of PG 1211+143 on 2004 June 21, which is described above, there were two more observations in consecutive orbits of the *Chandra* observatory. The second $\sim$ 45 ks observation took place on 2004 June 23 and the third observation was on 2004 June 25. These data are not presented here, but their spectra is in overall agreement with the first LETG observation, *except* that the flux level in the last two observations was twice that of the first observation, i.e., during a period of $\sim$ 2 days the flux level doubled. This is somewhat unexpected for a source that had retained its flux level of three years earlier (see Figure 3). Besides the change in flux between the three LETG observations, there is also a change in the absorption features seen between the first observation and the other two. Some of these features have disappeared between the first low-flux

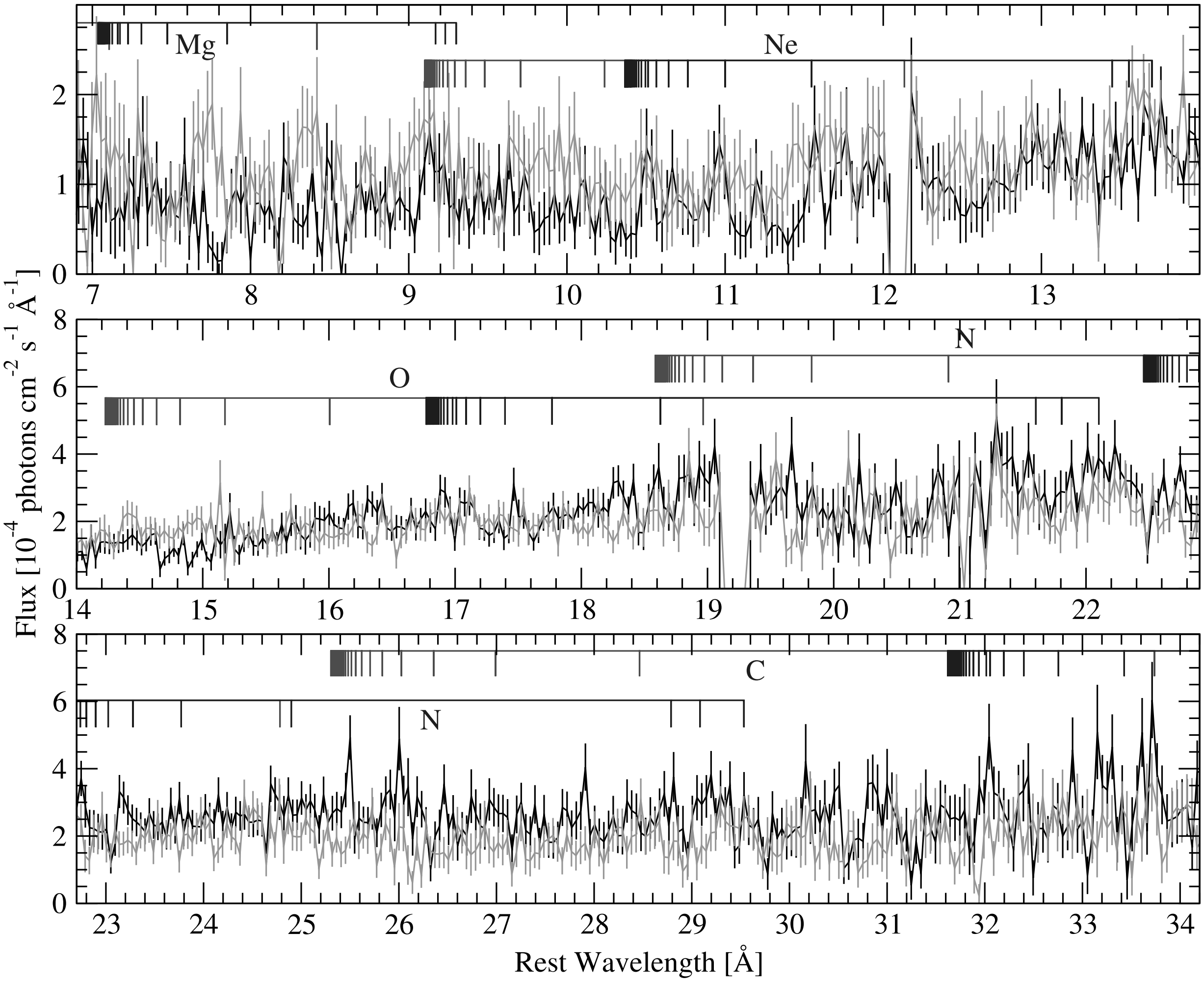


*Figure 3. Two RGS spectra of PG 1211+143 obtained three years apart. The first observation (in black) was carried out on 2001 June 15 and is also presented in Figure 1. The second observation (in gray) took place on 2004 June 21.*

observation and the high-flux observations taken 2 days later, while other features seems to appear. The absorption features interpreted by Reeves et al. (2005) as evidence for sub-c gravitational infall are seen only in the second observation and not in the first or third ones. The fact that, again, absorption features are not reproduced in different spectra is rather confusing. If these lines are statistically significant (see Reeves et al. 2005) then they represent a transient flow.

## 5. SUMMARY AND CONCLUSIONS

We claim in Kaspi & Behar (2006) that an outflowing absorber at a velocity of 3000 km s$^{-1}$ fits the first (2001) RGS data of PG 1211+143 better than a 24000 km s$^{-1}$ model. Admittedly though, the poor S/N of those data can tolerate more than one interpretation.

A second RGS observation taken three years after the first observation shows general consistency with the first observation, but differs in important details of the absorption lines relevant to the outflow. Some features that appear in the first RGS observation disappear in the second one and vice versa. This could be a result of either short-time variability of the absorber (almost impossible to prove or refute) or the poor S/N of the data. Even more confusing is the fact that *simultaneous* observations of PG 1211+143 with RGS and LETG produce spectra that are partially incompatible in their absorption lines. This significantly reduces our confidence in the existence of the absorption lines and even more so in their identification. The poor S/N of the data calls for extra caution and careful modeling.

The three LETG observations indicate that the continuum source changes on a timescale of days. If the discrete features seen in these spectra are real, they too vary on short timescales. With the loss of the high-resolution X-ray spectrometer (XRS) on board *Astro-E2*, a very long observation of a good, bright UHV-wind source with *Chandra* or *XMM-Newton* gratings remains as the most viable approach toward testing what we feel is still a putative phenomenon of high velocity outflow.

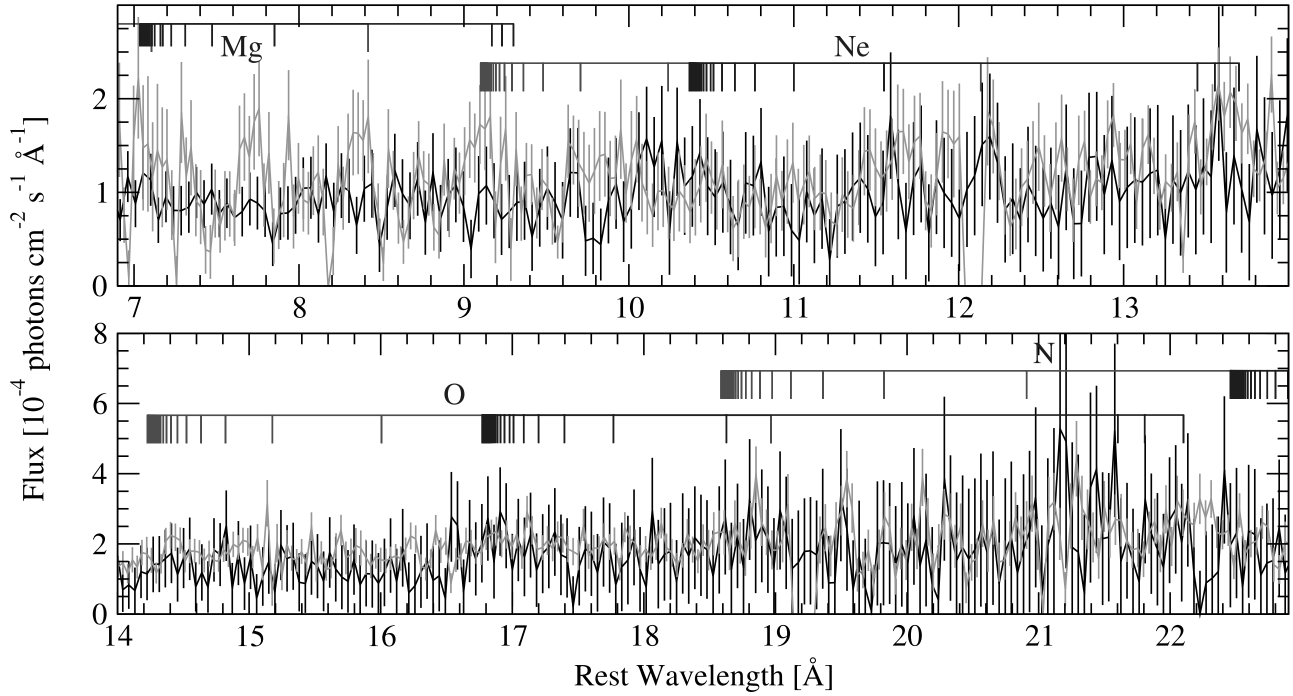


*Figure 4. PG 1211+143 spectrum taken by the RGS on board XMM-Newton (gray line) on 2004 June 21 shown together with a spectrum taken simultaneously by the LETG on board Chandra (black line). Although the data are taken at the same time, discrepancies between the spectra are evident, probably as a result of the poor S/N of the data.*

**ACKNOWLEDGMENTS**

This research was supported by the Israel Science Foundation (grant no. 28/03), and by a Zeff fellowship to S.K.

**REFERENCES**

Behar, E., Cottam, J. C., & Kahn, S. M. 2001, ApJ, 548, 966

Behar, E., & Netzer, H. 2002, ApJ, 570, 165

Behar, E., Rasmussen, A. P., Blustin, A. J., Sako, M., Kahn, S. M., Kaastra, J. S., Branduardi-Raymont, G., & Steenbrugge, K.C. 2003, ApJ, 598, 232

Chartas, G., Brandt, W. N., Gallagher, S. C., & Garmire, G. P. 2002, ApJ, 579, 169

Chartas, G., Brandt, W. N., & Gallagher, S. C. 2003, ApJ, 595, 85

Crenshaw, D. M., Kraemer, S. B., & George, I. M. 2003, ARA&A, 41, 117

Hasinger, G., Schartel, N., & Komossa, S. 2002, ApJ, 573, L77

Kaspi, S., & Behar, E. 2006, ApJ, 636, in press

Kaspi, S., Smith, P. S., Netzer, H., Maoz, D., Jannuzi, B. T., & Giveon, U. 2000, ApJ, 533, 631

King, A. R. & Pounds, K. A. 2003, MNRAS, 345, 657

Lepson, J. K., Beiersdorfer, P., Behar, E., & Kahn, S. M. 2003, ApJ, 590, 604

Lepson, J. K., Beiersdorfer, P., Behar, E., & Kahn, S. M. 2005, ApJ, 625, 1045

Pounds, K. A., Reeves, J. N., King, A. R., Page, K. L., O'Brien, P. T., & Turner, M. J. L. 2003a, MNRAS, 345, 705

Pounds, K. A., King, A. R., Page, K. L., & O'Brien, P. T. 2003b, MNRAS, 346, 1025

Pounds, K. A., Reeves, J. N., King, A. R., & Page, K. L. 2004, MNRAS, 350, 10

Pounds, K. A., Reeves, J. N., King, A. R., Page, K. L., O'Brien, P. T., & Turner, M. J. L. 2005, MNRAS, 356, 1599

Reeves, J. N., O'Brien, P. T., & Ward, M. J. 2003, ApJ, 593, 65

Reeves, J. N., Pounds,K., Uttley, P., Kraemer, S., Mushotzky, R., Yaqoob, T., George, I. M., and Turner, T. J. 2005, ApJL, 633, L81

Sako, M., et al. 2001, A&A, 365, L168

# ENERGY-SHIFTED LINES IN XMM-NEWTON EPIC SPECTRA OF SEYFERT GALAXIES

**A.L.Longinotti[1,2], S. Sim[1,3], K.Nandra[1], P. O'Neill[1], and M.Cappi[4]**

[1]Astrophysics Group, Imperial College London, Blackett Laboratory Prince Consort Rd, SW7 2AZ London, UK
[2]XMM-Newton Science Operation Centre, ESAC, Apartado 50727 E-28080, Madrid
[3]Max-Planck-Institut für Astrophysik, 85741 Garching, Germany
[4]INAF-IASF Sezione di Bologna, VIa Gobetti 101, I-40129 Bologna, Italy

## ABSTRACT

In the recent literature on AGNs it has been often reported that spectra of Seyfert 1 Galaxies show resonant absorption lines of Fe K which are redshifted from the rest frame position. Such lines are often found with marginal significance but, if real, could potentially open up new avenues to study the circumnuclear gas in the black hole environment. It is also extremely important to take them into account in X-ray spectral analysis because of the influence they have in the correct estimation of spectral parameters, Fe K$\alpha$ line *in primis*. An *XMM-Newton* observation of Mrk 335 is reported here as a case study: a narrow feature has been detected at 5.9 keV, i.e. with a redshift corresponding to a velocity of v$\sim$ 0.15c. Preliminary results on the statistical significance of narrow absorption and emission lines in a sample of PG QSOs observed by *XMM-Newton* are also included.

Key words: AGN, X-rays, spectroscopy.

## 1. INTRODUCTION

Since Active Galactic Nuclei have been discovered, it has been postulated that the powering mechanism is likely to be the release of gravitational energy of matter accreted on a supermassive black hole. Observational evidence for this was found in the redshifted and broad Fe K disc line seen in bright Seyfert galaxies (1). The picture on hard X-ray spectra has been made even more complex by the recent detection of narrow lines shifted from their rest-frame position in the Fe K band spectra of many Seyfert 1 galaxies which may affect modeling of the Fe K emission line. Previous cases of highly ionised redshifted absorption Fe K lines were in fact found superimposed to the broad wing of the Fe K$\alpha$ line in NGC 3516 (2) with *ASCA* data, and in E 1821+643 (3) with *Chandra* data. (4) reported on the presence of an unshifted Fe K absorption line superimposed on the relativistic Fe K line in IRAS13349+2438, with *XMM-Newton* data. High confidence detections of such features would be of crucial importance in testing the black hole paradigm for AGN and would provide a new additional tool to be used alongside the broad Fe K$\alpha$ line. In fact, although the exact nature of the energy shift of such lines is as yet unclear, the most likely scenario for producing the observed features would involve a combination of gas orbiting in highly relativistic motion and/or gravitational shifts of the photons (2; 5). With the advent of *XMM-Newton* and *Chandra*, the number of *absorption* features in active galaxies spectra have considerably increased (6; 3; 7; 8). Narrow energy-shifted *emission* lines have also been detected in the hard X-ray spectra of many AGN (9; 10; 11; 12; 13; 14). Theoretical models have predicted the possibility that Fe K emission lines from the disc can be observed with a narrow profile if the X-ray reflection arises as a result of magnetic flares in localized regions on the disc (15; 16).

## 2. MRK 335 CASE STUDY

### 2.1. Spectral analysis

Mrk 335 is a bright Seyfert 1 Galaxy at $z$=0.026, which was observed by *Xmm-Newton* for about 30 ks. A previous analysis was reported by (17), who found evidence for a broad Fe K$\alpha$ line associated to an ionised reflection component. Here, the data from the pn camera are presented. A fit on the 2-10 keV data with a simple power law model yields a steep spectrum, with $\Gamma$=$2.13^{+0.04}_{-0.02}$. The pn residuals from 3-9 keV are plotted in Fig. 1: the energy band of the Fe K$\alpha$ emission line is pictured on the data showing the presence of broad excess in flux not only above the position of the neutral line (6.4 keV), but even up to $\sim$ 7.3 keV and down to $\sim$ 5.9 keV. A deficit of counts in a notch-shape is also present at $\sim$ 5.9 keV. A Gaussian line is added to the power law, with energy, width and flux free to vary. The line is highly significant with $\Delta\chi^2$=33 for 3 d.o.f, indicating an ionized and broad line. The line parameters are found to

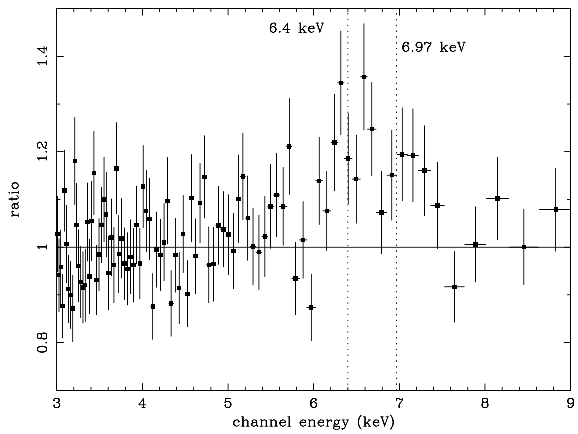


*Figure 1. Data to model ratio: the 2-10 keV spectrum is fitted by a power law with $\Gamma$= 2.15$^{+0.04}_{-0.03}$ . The plot is in the source rest frame and the Fe K$\alpha$ energy band is labelled for clarity.*

be E=6.63$^{+0.16}_{-0.14}$ keV (rest-frame), $\sigma$=0.40$^{+0.32}_{-0.13}$ keV and EW=245$^{+123}_{-126}$ eV. Although the residuals shape may suggest the presence of another Gaussian line, any attempt to fit the data with 2 emission lines failed. To fit the notch-shaped feature another Gaussian line with negative intensity has been added. The fit yields $\chi^2$=738/731 d.o.f. and the lines parameters are found to be E=6.31$^{+0.20}_{-0.20}$ keV, $\sigma$=0.78$^{+0.21}_{-0.26}$ keV, EW=468$^{+250}_{-175}$ eV for the broad component and as for the narrow one, E=5.92$^{+0.05}_{-0.05}$ keV with an EW=52 $^{+18}_{-18}$ eV (measured in absorption with negative intensity with respect to the continuum). The width of the absorption line is unresolved with CCD resolution and therefore it is kept fixed to 50 eV. The improvement in $\chi^2$ is $\Delta\chi^2$~14 for 2 degrees of freedom, corresponding to a level of confidence higher than 99.7 percent according to the F-test. This is an extremely basic parametrization of the spectrum, meant purely to show the main features in the spectral curvature above $\sim$ 5 keV. The line profile in fig. 1 appears complex not only for the presence of the absorption feature, but also because the residuals show a double-peak structure. As reported before, fitting *two* emission lines is not required by the fit so we have included only one broad Gaussian in our basic parametrization. When the spectrum is fitted with two Gaussian lines (emission and absorption), the energy of the broad line is consistent with 6.4 keV. A close look to fig.1, reveals that the profile is very different from a Gaussian and that in this case the use of such model could be quite misleading. The profile is asymmetrical and skewed suggesting that if there is a broad line it could be modified by relativistic effects. We used the DISKLINE model in Schwarzschild metric (18) where the line parameters other than the energy are: *q*, the line emissivity index, where the line emissivity *j* is a function of the emission radius *r* according to $j \propto r^{-q}$; the inner radius $r_{in}$ and the outer radius $r_{out}$ of the accretion disc which define the area of the disc where the line is emitted; the inclination of the disc *i*, set as to be the angle between the line of sight and the normal to the disc. Fitting the broad line in this way yields E=7.12$^{+0.27}_{-0.21}$ keV and EW=407$^{+102}_{-109}$ eV, $q$=3.98$^{+2.45}_{-0.77}$, $i$=21$^\circ$$^{+8}_{-16}$ and $\chi^2$/d.o.f.=735/730. The absorption line is included in this fit as a negative Gaussian, as previously described.

The presence of a diskline suggests that a reflection component should be included. Since the line energy is clearly indicative of a high ionisation state for Iron, the XION model developed by (19) was used to fit the spectrum. In this way, the reflected spectrum is computed in hydrostatic balance, taking into account the ionization instability in the disc. After choosing one of the available geometries, this model calculates the distance between the disc and the source of X-ray photons, the accretion rate, the luminosity of the X-ray source, the inner and outer disc radii and the spectral index as free parameters. Relativistic smearing is included for a non-spinning black hole. We resolved to assume the simplest geometrical configuration (lamppost). After adding an absorption Gaussian line, the model provides a fairly good fit, yielding $\chi^2$/d.o.f. = 738/730.

We try to model the absorption line by adding an appropriate warm absorber to the best fitting reflection model XION. In order to do that, a grid of XSTAR photoionization model was generated with solar elemental abundances and turbulence velocity of 100 km/s. Then, such model has been incorporated in XSPEC as a table model with 3 additional free parameters: i) the column density $N_w$ ii) the ionization parameter $\xi$, which describes the state of the photoionized medium; iii) a redshift parameter which includes all the redshift contributions, namely the cosmological redshift ($z_{source}$), the velocity of the absorber ($z_{inflow}$) and the gravitational shift which the gas may be subjected to, if close enough to the black hole ($z_{grav}$). The best-fitting parameters are consistent with a very ionized absorber, with log$\xi$ $\sim$ 3.9 ergs cm s$^{-1}$ where it is most likely that only the H-like and He-like Fe ions survive. The fit yields $\chi^2$/d.o.f.=735/728. Four main absorption features are imprinted on the continuum (see Fig. 2): the K$\alpha$ and K$\beta$ transitions of Fe XXV and XXVI produce the absorption lines, but only the K$\alpha$ ones are sufficiently strong to be interesting for our purposes here. The absorption line detected in the data is consistent with the Fe XXVI K$\alpha$, whereas the other ones are too weak to be detected at the CCD resolution. Most striking is that, if such feature is identified as we propose, it requires to be redshifted corresponding to an inflow velocity of $\sim$ 0.14 *c*. Such value is inferred by measuring the energy shift of the Gaussian line peak ($\sim$5.92 keV) from the rest-frame position of 6.90 keV.

### 2.2. A simple model for the inflow

To further investigate the inflow hypothesis, a simple physical model has been developed and used to synthesise X-ray spectra for qualitative comparison with the observed absorption feature (a more thorough description of the model is included in the paper Longinotti et al. in prep.) Spectra were synthesised for the 2 – 10 keV re-

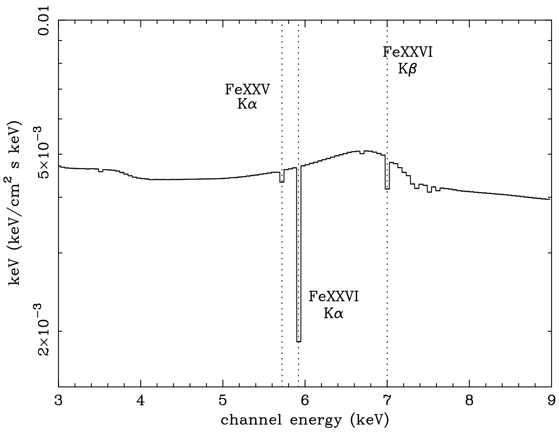


*Figure 2. Rest frame plot of the model used to fit the data on the left. The combination of the effects of the reflection spectrum and the highly photoionized gas is visible: the first one reproduces the spectral curvature between 5 and 7 keV, the latter imprints redshifted absorption features on the continuum. In our data, we observe the Fe XXVI K$\alpha$ only, the other ones being too weak.*

gion using a Monte Carlo radiative transfer code based closely on that discussed by (20). For the computation presented here, the power-law photon index was fixed at $\Gamma = 2.2$ (based on fits to the data) and the normalisation fixed by requiring the total 2 – 10 keV X-ray flux to match the observed luminosity of $1.8 \times 10^{43}$ ergs s$^{-1}$. The disc luminosity was set to 60 per cent of the Eddington luminosity for the central black-hole, close to the value $L/L_{\rm edd} = 0.62$ reported for Mrk 335 by (21). The soft-excess was modelled as a black-body with temperature $1.3 \times 10^6$ K and normalisation fixed to the power-law component. In contrast to that presented by (20), the code used here includes the full special relativistic expression for the Doppler shift and approximately accounts for gravitational redshift using

$$\gamma(1 - \mu v(r)/c)\nu = \nu' \sqrt{1 - 2R_g/r} \qquad (1)$$

where $\nu'$ is the frequency of a photon at radius $r$ as measured in the comoving frame, $\mu$ is the usual direction cosine, $\gamma = (1 - v^2/c^2)^{-1/2}$ and $\nu$ is the photon frequency that would be recorded by an infinitely distant observer at rest relative to the black-hole. Other relativistic effects are neglected. A simple spherical geometry for the gas in a radial inflow has been considered. It is assumed that the gas occupies a region which extends from inner radius $r_{\rm in}$ to outer radius $r_{\rm out}$ from the central black-hole. Here only the main results from such model are described. From a qualitative comparison to the computed spectra, the data can rule out an inflow model of a continuous flow extending from the vicinity of the central black-hole to much greater distances. The left panel in Figure 3 shows the 3–9 keV spectrum computed for a model of this sort with $r_{in} = 20\ R_g$, $r_{out} = 10^3\ R_g$, and a mass infall rate $\Phi = 0.2\ M_\odot$ yr$^{-1}$. This model predicts very few spectral features since the ionisation state of the gas is very high. The dominant feature is a broad inverse P Cygni Fe XXVI K$\alpha$ line, but a weaker feature due to the K$\beta$ line of the same ion appears at harder energies. The computed absorption line is very broad, extending from around 5.5 keV to $\sim 6.5$ keV, where the deepest absorption occurs. The large line width in the model is therefore the result of the large radial extent of the absorbing gas and of the large velocity range present in the flow. If the infalling gas is instead distributed over a narrow range of radii, the model is found to be a good description of the data (right panel in Figure 3). A possible configuration could be described as a discontinuous infalling of shells or blobs of gas at different densities. With the model considered here, this was obtained by limiting the radial range occupied by the flow.

## 2.3. Significance of the narrow line in Mrk 335

The problem of the reality and significance of narrow features such as the one detected in Mrk 335, has been pointed out in the most recent cases of narrow line detections by (3) for an absorption line, and by (13) for an emission line. These authors have employed realistic Montecarlo simulations for testing the reality of the lines, which have been found significant at a level in between 2-3 $\sigma$. Moreover, the employment of the F-test to test the significance of X-ray spectral lines has been recently put into question by rigourous statistical arguments (22). Therefore, we try to assess whether the line in Mrk 335 could be due to statistical fluctuations through Montecarlo simulations. The phenomenological model (power law +broad em. line) used in the spectral analysis section, is taken as a “baseline” model and the $\Delta\chi^2$ for adding an absorption line is measured to be 14.37 in the real spectrum. In this way, 10000 fake background-subtracted data sets have been obtained. Each of these spectra is fitted with the baseline model (power law + broad Gaussian line) and only then, a narrow absorption line with $\sigma$=50 eV is added to the fit, in order to measure the improvement in $\chi^2$ with respect to the $\chi^2$ value obtained by fitting the baseline model with no absorption. We obtain a $\Delta\chi^2$ larger than in the baseline model in 263 cases, yielding a significance for the absorption line of 97.37 percent.

## 3. SEARCH FOR ENERGY-SHIFTED NARROW LINES: SIMULATION PROCEDURE

All narrow lines detected in the literature have been found in individual sources, as the one discussed for Mrk 335 and many of them have been found marginal. Marginal detections could possibly arise due to random deviations in the spectra. Quantifying the significance of such deviations in a large number of X-ray spectra would provide an estimate of the robustness of the detections. To date, a systematic search for the presence of such features in a sample of objects has not been performed. An attempt to do that is presented in the following. A sample of archival PG quasars observed by *XMM-Newton* has been chosen.

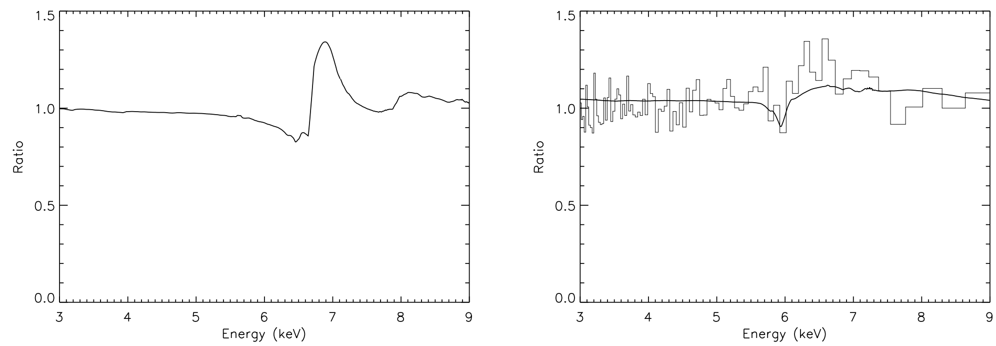


*Figure 3. The plot shows the ratio of the computed 3 – 9 keV flux to a power-law with index $\Gamma = 2.2$ (rest frame energy). Left: inflow with $r_{in} = 20\ R_g$, $r_{out} = 10^3\ R_g$, $\Phi = 0.2\ M_\odot$ yr$^{-1}$, neglecting radiation pressure. The absorption features are predominantly due to Fe* XXVI *K$\alpha$ [around 6.5 keV] and K$\beta$ [around 7.7 keV]. Right: inflow with $r_{in} = 24\ R_g$, $r_{out} = 48\ R_g$, $\Phi = 0.3\ M_\odot$ yr$^{-1}$, accounting for radiation pressure due to electrons at 60 per cent of the Eddington limit. The absorption feature is due to FE* XXVI *K$\alpha$. The light histogram shows the observational data for Mrk 335, also normalised to a power-law fit*

For completeness, the description of the X-ray properties of this sample is reported by (23) and (24). In the present analysis instead, only the sources with more than 800 counts above 5 keV are included in order to insure good statistics in the Fe K region. The list of the sources is shown in Table 1. A blind search for positive and negative flux deviations has been performed in the simulated spectra. This procedure is addressed to test for the presence of a narrow line in each of the spectra in the sample. We shall distinguish between unshifted Fe K lines (i.e. emission lines in the range 6.4-7 keV) and those which we will call energy-shifted lines, i.e. any absorption line and emission lines shifted out of this range.

- For each spectrum, 10000 spectra have been simulated with XSPEC assuming a baseline model *without* any narrow line, folding it through the same instrumental response and adding Poisson noise. Such spectra have then been grouped according to the same criterion adopted for the real data set, i.e. 20 counts per spectral bin. In this way, 10000 synthetic background-subtracted spectra were generated, with photon statistics corresponding to the exposure in the pn detector (see second column in Table 1).

- Each of these spectra was fitted first with the baseline model. Then, each of them was fitted a second time with a model consisting of the baseline model plus a narrow line. The narrow line parameters were set as follows. Positive and negative deviations were allowed for the line flux. The width of the narrow line was fixed to 50 eV during the fitting and the energy of the line was stepped in steps of 70 eV, corresponding approximately to the instrumental resolution. To avoid any calibration uncertainties at the boundaries of the instrumental response, the line is searched across the energy range 2.5–9.5 keV. For each energy on this grid, the value of the $\Delta\chi^2$ for adding the narrow line to the data was calculated with respect to the baseline model. When the minimum $\Delta\chi^2$ was found, the values of the corresponding energy and line flux were recorded. in this way, the most significant narrow lines in the data were detected.

- The presence of a narrow feature has been tested in the *real* spectrum applying the same grid of energy, so that the comparison is made consistently.

- The procedure of fitting the spectrum with the baseline model and then adding a narrow line with the same grid of energies described above, has been repeated for each simulated spectrum. In each of the fake data sets, the greatest improvement in $\chi^2$ for adding the narrow feature, $\Delta\chi^2$(sim), is recorded, along with the energy and the flux of the line, providing a list of 10000 detections. Then, the number of spectra where $\Delta\chi^2$(sim) $>$ $\Delta\chi^2$(data) is counted. This quantifies the probability that an apparent feature as significant as that in the real data could be the result of random noise.

Two runs of simulations have been performed. The first run picks up the most significant line in each spectrum, with the adopted baseline model. The second run is performed for a limited number of spectra where an unshifted emission Fe K$\alpha$ line has been detected at $>$90% in the first run. In these cases, the Fe K line has been added to the baseline model and the procedure has been run again. Table 2 summarises the final results and the baseline model used for each spectrum. This table comprises the list of the 10 detections significant at $>$90% selected in the following way:

- Energy-shifted features significant at $>$90% from the first run of simulations

- Energy-shifted features significant at $>$90% from the second run of simulations (i.e. after including significant Fe K$\alpha$ lines in the baseline model)

*Table 1. List of the PG QSOs sample where the narrow lines blind search has been performed. The sources have been fitted with a power law in the 2-10 keV range.*

| Quasar | Exposure | Gamma | Flux | $\chi^2$/d.o.f. |
|---|---|---|---|---|
| - | s | - | ($10^{-12}$ cgs) | - |
| Mrk 335 | 28401 | $2.12^{+0.02}_{-0.02}$ | 11.81 | 815/742 |
| IIIZW2 | 10141 | $1.62^{+0.04}_{-0.04}$ | 6.78 | 344/349 |
| I Zw 1 | 18189 | $2.29^{+0.03}_{-0.03}$ | 7.73 | 529/450 |
| PG 0844+349 | 9230 | $2.07^{+0.07}_{-0.07}$ | 4.69 | 169/172 |
| PG 0947+396 | 17392 | $1.90^{+0.06}_{-0.05}$ | 1.75 | 197/217 |
| PG 0953+414 | 10211 | $2.07^{+0.05}_{-0.05}$ | 2.92 | 194/225 |
| PG 1048+342 | 19801 | $1.82^{+0.06}_{-0.07}$ | 1.32 | 196/197 |
| PG 1114+445 | 34902 | $1.46^{+0.03}_{-0.04}$ | 2.23 | 363/386 |
| PG 1115+080 | 37082 | $1.89^{+0.06}_{-0.06}$ | 0.26 | 178/184 |
| PG 1202+281 | 11448 | $1.72^{+0.05}_{-0.05}$ | 3.60 | 216/241 |
| PG 1211+143 | 46884 | $1.73^{+0.02}_{-0.02}$ | 3.06 | 741/638 |
| PG 1407+265 | 46124 | $2.45^{+0.02}_{-0.02}$ | 1.34 | 465/490 |
| PG 1415+451 | 20569 | $1.99^{+0.07}_{-0.08}$ | 1.09 | 151/159 |
| PG 1425+267 | 29394 | $1.48^{+0.04}_{-0.04}$ | 1.65 | 337/312 |
| PG 1427+480 | 30763 | $1.98^{+0.06}_{-0.06}$ | 1.04 | 246/251 |
| Mrk 478 | 18037 | $2.12^{+0.06}_{-0.06}$ | 1.84 | 189/202 |
| PG 1448+273 | 17840 | $2.23^{+0.06}_{-0.06}$ | 2.09 | 239/245 |
| Mrk 841(*) | 7609 | $1.92^{+0.03}_{-0.03}$ | 14.80 | 468/492 |
| PG 1512+370 | 13503 | $1.81^{+0.06}_{-0.06}$ | 1.86 | 226/216 |
| PG 1634+716 | 12207 | $2.25^{+0.06}_{-0.06}$ | 0.74 | 267/207 |
| UGC 11763 | 23579 | $1.63^{+0.04}_{-0.04}$ | 3.68 | 361/423 |
| Mrk 304 | 6945 | $0.88^{+0.06}_{-0.08}$ | 3.41 | 224/115 |

(*)3 spectra in the archive

In total, 10 detections out of 24 spectra have been found at a significance higher than 90%.

To estimate the probability to detect 10 features by random chance, it is assumed a null hypothesis in which the sample comprises 24 featureless spectra. The probability that this hypothesis can be rejected in the present data is then calculated assuming the binomial distribution as a probability distribution:

$$P = \frac{n!}{x!(n-x)!}p^x(1-p)^{n-x} \qquad (2)$$

In the present case, the parameters of the distribution correspond to $n$=24 (number of spectra), $x$=10 (number of successes i.e. detections at >90%), $p$=0.1 (i.e. the probability to have a detection at more than 90% in the case of the null hypothesis). The cumulative probability for a given number of random detections defines the probability to have *up* to that number of random detections in the sample and it is defined as:

$$P_c = \sum_{k=0}^{x} p_f$$

The probability to find 10 or more random detections in the sample is calculated to be 1-$P_c$=5.25×$10^{-5}$. This number is very small, implying that it is very unlikely that 10 detections in a sample of 24 spectra are all due to random noise. Therefore, the possibility that none of them is real can be ruled out, i.e. the null hypothesis is rejected. From statistical considerations, it is reasonable saying that out of 10 detections *some* are real. From a more speculative point of view, let us considering the number of successful events characterised by the average cumulative probability $P_c$=0.5. At this point, it is as likely to have *more* than $x$ false detections, as to have *less* than $x$ false detections, because obviously they have the same cumulative probability. For 24 number of trials, the probability calculation shows that such number is between 2 and 1. So, one could draw an approximate conclusion by saying that the majority of the 10 detections are real, at a level of confidence of 90% and 2-3 of them are false.

*Table 2. List of the shifted features detected at > 90% in each spectrum with the corresponding baseline model*

| Quasar | Baseline | Energy (*) | Intensity (*) | Significance |
|---|---|---|---|---|
| - | - | (keV) | (Ph $s^{-1}$ $cm^{-2}$) | - |
| Mrk 335 | plaw+broad gau | 5.93 | -7.422e-06 | 95.82% |
| IIIZW2 | plaw | 9.01 | -5.870e-06 | 90.93% |
| I Zw 1 | plaw | 3.20 | -1.187e-05 | 96.34% |
| PG 1211+143 | plaw+zwabs | 7.61 | -2.9541e-06 | 100% |
| PG 1211+143 | plaw+zwabs+2 zgau | 2.92 | -7.411e-06 | 99.96% |
| PG 1407+265 | plaw | 7.89 | 3.794e-06 | 92.2% |
| Mrk 841 (I) | plaw | 6.28 | 1.504e-05 | 98.26% |
| PG 1634+716 | plaw | 4.11 | -1.109e-5 | 96.99% |
| UGC 11763 | plaw | 6.28 | 3.781e-06 | 94.21% |
| Mrk 304 | plaw+zwabs +zgau | 4.46 | 9.986e-06 | 100% |

## 4. SUMMARY OF RESULTS

A narrow absorption line has been detected at ∼5.9 keV with a significance of ∼97% in the EPIC pn spectrum of Mrk 335; if interpreted as Fe XXVI K$\alpha$ and if the effect of the gravitational field is neglected, the observed redshift of the line corresponds to a receding velocity of 50000 km $s^{-1}$ in the absorbing gas. The comparison to a physical inflow model shows that the line is consistent with being produced in a discontinuous flow of material dragged in high velocity motion towards the nucleus, rather than in a spherical flow. Arguably, the fact that the line is not smeared nor broad is a strong indication against the hypothesis of matter in orbit at a few gravitational radii, as suggested for other similar cases.

The blind search for energy shifted features carried out in the sample of PG quasars provided an encouraging result on the statistical significance of the narrow lines, in general. The majority of the detections are in fact believed to be real in the *XMM-Newton* data. This preliminary result should be investigated using a much larger sample of spectra.

## ACKNOWLEDGMENTS

The AstroGroup at Imperial College London is acknowledged for financial support. A.L.L. is grateful to Giovanni Miniutti for many stimulating discussions during this conference.

## REFERENCES

[1] Nandra, K., George, I. M., Mushotzky, R. F., Turner, T. J., and Yaqoob, T. ASCA Observations of Seyfert 1 Galaxies. II. Relativistic Iron K alpha Emission. *ApJ*, 477:602–+, March 1997.

[2] Nandra, K., George, I. M., Mushotzky, R. F., Turner, T. J., and Yaqoob, T. The Properties of the Relativistic Iron K-Line in NGC 3516. *ApJ*, 523:L17–L20, September 1999.

[3] Yaqoob, T. and Serlemitsos, P. Iron K Features in the Quasar E1821+643: Evidence for Gravitationally Redshifted Absorption? *ApJ*, 623:112–122, April 2005.

[4] Longinotti, A. L., Cappi, M., Nandra, K., Dadina, M., and Pellegrini, S. The complex FeK line of the Narrow-Line Seyfert 1 galaxy IRAS 13349+2438. *A&A*, 410:471–479, November 2003.

[5] Ruszkowski, M. and Fabian, A. C. On the influence of resonant absorption on the iron emission-line profiles from accreting black holes. *MNRAS*, 315:223–228, June 2000.

[6] Matt, G., Porquet, D., Bianchi, S., Falocco, S., Maiolino, R., Reeves, J. N., and Zappacosta, L. A changing inner radius in the accretion disc of Q0056-363? *A&A*, 435:857–861, June 2005.

[7] Dadina, M., Cappi, M., Malaguti, G., Ponti, G., and De Rosa, A. X-ray absorption lines suggest matter infalling onto the central black-hole of mrk 509. *astro-ph/0506697*, 2005.

[8] Reeves, J. N. et al. Evidence for gravitational infall of matter onto the super- massive black hole in the quasar pg 1211+143? 2005.

[9] Turner, T. J., Mushotzky, R. F., Yaqoob, T., George, I. M., Snowden, S. L., Netzer, H., Kraemer, S. B., Nandra, K., and Chelouche, D. Narrow Components within the Fe K$\alpha$ Profile of NGC 3516: Evidence of the Importance of General Relativistic Effects? *ApJ*, 574:L123–L127, August 2002.

[10] Turner, T. J., Kraemer, S. B., and Reeves, J. N. Transient Relativistically Shifted Lines as a Probe of Black Hole Systems. *ApJ*, 603:62–66, March 2004.

[11] Guainazzi, M. The history of the iron K line profile in the Piccinotti AGN ESO 198-G24. *A&A*, 401:903–910, April 2003.

[12] Yaqoob, T., George, I. M., Kallman, T. R., Padmanabhan, U., Weaver, K. A., and Turner, T. J. Fe XXV and Fe XXVI Diagnostics of the Black Hole and Accretion Disk in Active Galaxies: Chandra Time-resolved Grating Spectroscopy of NGC 7314. *ApJ*, 596:85–104, October 2003.

[13] Porquet, D., Reeves, J. N., Uttley, P., and Turner, T. J. XMM-Newton observation of the Seyfert 1.8 ESO 113-G010: Discovery of a highly redshifted iron line at 5.4 keV. *A&A*, 427:101–105, November 2004.

[14] Gallo, L. C., Fabian, A. C., Boller, T., and Pietsch, W. A possible line-like emission feature at 8 keV in the Seyfert 1.2 UGC 3973. *MNRAS*, pages 732–+, August 2005.

[15] Nayakshin, S. and Kazanas, D. Narrow Moving Fe K$\alpha$ Lines from Magnetic Flares in Active Galactic Nuclei. *ApJ*, 553:L141–L144, June 2001.

[16] Dovčiak, M., Bianchi, S., Guainazzi, M., Karas, V., and Matt, G. Relativistic spectral features from X-ray-illuminated spots and the measure of the black hole mass in active galactic nuclei. *MNRAS*, 350:745–755, May 2004.

[17] Gondoin, P., Orr, A., Lumb, D., and Santos-Lleo, M. XMM-Newton observations of the Seyfert 1 galaxy Mrk 335. *A&A*, 388:74–87, June 2002.

[18] Fabian, A. C., Rees, M. J., Stella, L., and White, N. E. X-ray fluorescence from the inner disc in Cygnus X-1. *MNRAS*, 238:729–736, May 1989.

[19] Nayakshin, S. and Kallman, T. R. Accretion Disk Models and Their X-Ray Reflection Signatures. I. Local Spectra. *ApJ*, 546:406–418, January 2001.

[20] Sim, S. A. Modelling the X-ray spectra of high-velocity outflows from quasars. *MNRAS*, 356:531–544, January 2005.

[21] Gierliński, M. and Done, C. Is the soft excess in active galactic nuclei real? *MNRAS*, 349:L7–L11, March 2004.

[22] Protassov, R., van Dyk, D. A., Connors, A., Kashyap, V. L., and Siemiginowska, A. Statistics, Handle with Care: Detecting Multiple Model Components with the Likelihood Ratio Test. *ApJ*, 571:545–559, May 2002.

[23] Piconcelli, E., Jimenez-Bailón, E., Guainazzi, M., Schartel, N., Rodríguez-Pascual, P. M., and Santos-Lleó, M. The XMM-Newton view of PG quasars. I. X-ray continuum and absorption. *A&A*, 432:15–30, March 2005.

[24] Jiménez-Bailón, E., Piconcelli, E., Guainazzi, M., Schartel, N., Rodríguez-Pascual, P. M., and Santos-Lleó, M. The XMM-Newton view of PG quasars. II. Properties of the Fe K$\alpha$ line. *A&A*, 435:449–457, May 2005.

# AN EXPLANATION FOR THE SOFT X-RAY EXCESS IN AGN

**J. Crummy[1], A.C. Fabian[1], L. Gallo[2], and R.R. Ross[3]**

[1]Institute of Astronomy, Madingley Road, Cambridge, UK. CB3 0HA
[2]Max-Planck-Institut für extraterrestrische Physik, Postfach 1312, 85741 Garching, Germany
[3]Physics Department, College of the Holy Cross, Worcester, MA 01610, USA

## ABSTRACT

We present a large sample of type 1 AGN spectra taken with XMM-Newton. We fit them with the relativistically blurred photoionized disc model of Ross & Fabian (2005). This model is based on an illuminated accretion disc of fluorescing and Compton-scattering gas, and includes relativistic Doppler effects due to the rapid motion of the disc and general relativistic effects such as gravitational redshift due to presence of the black hole. The disc model successfully reproduces the X-ray continuum shape, including the soft excess, of all the sources. It provides a natural explanation for the observation that the soft excess is at a constant temperature over a wide range of quasar properties. The model also reproduces many features that would conventionally be interpreted as absorption edges. We use the model to measure properties of the quasars such as inclination, black hole rotation, and metallicity.

Key words: accretion; accretion discs; active galactic nuclei; X-rays.

## 1. INTRODUCTION

The soft excess is an important component of the X-ray spectra of many AGN and is present in every source in this survey. The soft excess is defined as the enhanced emission below ~2 keV compared to an extrapolation of the approximately power law spectrum in the 2 – 10 keV band. This extra emission is generally approximately thermal in shape, and well fit with a black body of energy 0.1 – 0.2 keV. This result stands over several decades in AGN mass, e.g. Walter & Fink (1993), Gierliński & Done (2004), Porquet et al. (2004). This poses problems for the thermal interpretation of the data, as the temperature does not scale in the expected way with luminosity ($L \propto T^4$), as well as being too high for the standard model of Shakura & Sunyaev (1973). Several alternative models have been proposed to account for one or both of these results, none of which have yet been broadly accepted by the community. This paper investigates photoionized emission blurred relativistically by motion in an accretion disc, which has been previously studied by e.g. Ballantyne, Iwasawa & Fabian (2001). We use the latest models from Ross & Fabian (2005), which include more ionization states and more recent atomic data than earlier versions (Ross & Fabian 1993).

## 2. THE RELATIVISTICALLY BLURRED PHOTOIONIZED DISC MODEL

In the model of Ross & Fabian (2005) a semi-infinite slab of cold optically thick gas of constant density is illuminated by a power law, producing a Compton component and fluorescence lines from the ionized species in the gas. To produce the relativistically blurred photoionized disc model this reflected emission is added to the illuminating power law and the summed emission is convolved with a Laor (1991) profile to simulate the blurring from an accretion disc around a maximally rotating (Kerr) black hole. This assumes a geometrically thin and flat accretion disc with clearly defined inner and outer radii, and that the emissivity of the disc as a function of radius is described by a power law. This combined model allows fitting to the inclination of the disc, the inner and outer radii (the outer radius is generally poorly constrained as emission is centrally concentrated), the emissivity index of the disc, the iron abundance of the gas, the spectral index of the illuminating power law and the ionization parameter (which we define as $\xi = 4\pi F/n_H$, where $F$ is the illuminating energy flux and $n_H$ is the hydrogen number density in the illuminated layer, a measure of the ratio of the energy density in the illuminating radiation to the atomic number density in the gas). Since the model is physically motivated measuring these free parameters can give us information about the sources. An example of the model is shown in Figure 1 (bottom right panel).

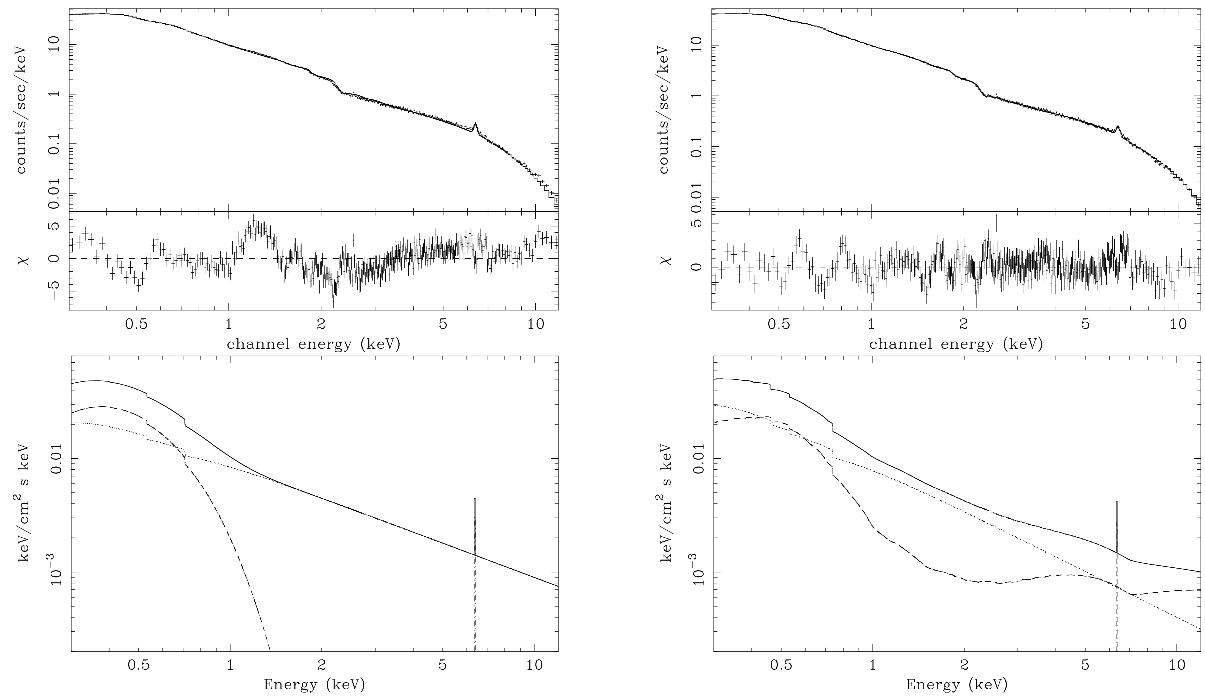


*Figure 1. This figure shows a comparison between the thermal model and the relativistically blurred photoionized disc reflection model for NGC 4051. The top panels show spectra and residuals to the thermal (left) and disc reflection (right) models, and the bottom panels show the components of the thermal (left) and disc reflection (right) models. Both include a power law (dotted line) and narrow iron emission (sharp line at ∼6.4 keV), the components shown in dashed lines are a black body and the relativistically blurred disc reflection respectively. As the residuals show, the disc reflection model is a much better fit. Most of the remaining residuals to NGC 4051 in the soft band (top right panel, 0.5 – 1.0 keV) have been shown to be due to narrow line emission (Ponti et al., in prep).*

## 3. DATA

We used publicly available archival *XMM-Newton* data on 22 type 1 AGN from the Palomar-Green (PG) sample and a selection of 12 other Seyfert 1 galaxies with high-quality observations available. The sample includes several well-studied AGN, such as NGC 4051, PG 1211+143 and I Zw 001. We analyse the longest available observation where the EPIC pn camera took data. We reduced the Observation Data Files in the standard way using SAS 6.0 to produce spectra (See Crummy et al. (in prep) for details), taking the range 0.3 – 12.0 keV as the region in which the pn is accurately calibrated. We do not include MOS data in our fits. We grouped the spectra so each bin includes at least 20 source counts, so $\chi^2$ statistics are applicable. Quoted errors are 90 per cent limits on one parameter ($\Delta\chi^2$ = 2.706).

## 4. ANALYSIS

We fit the data with two classes of model using xspec, the standard power law with a black body to model the soft excess, and the relativistically blurred photoionized disc reflection model. Both models are subject to absorption from cold gas in our Galaxy, we fix the amount of absorption at the value given by the nh ftool (Dickey & Lockman 1990). We also allow for absorbing matter at the AGN by fitting for extra cold absorption and up to two absorption edges in the 0.45 – 1.1 keV band. These components are redshifted such that they are local to the AGN. We finally allow for cold reflection (e.g. from distant gas such as a torus) by including a narrow iron line at 6.4 keV (in the source frame). We are concerned primarily with the underlying continuum rather than these features, so we include in our final model only those components which improve the overall $\chi^2$ by $> 2.7$ per lost degree of freedom. Since we are performing fits over the entire *XMM-Newton* band, we only report lines for which xspec reports a non-zero minimum equivalent width, this avoids fitting spurious lines due to a curvature in the continuum not addressed by the model. This conservative procedure means faint lines are likely to be missed, although any line that significantly affects the overall goodness of fit will be included. In xspec terminology our models are phabs * zphabs * zedge * zedge * (powerlaw + zbbody + zgauss and phabs * zphabs * zedge * zedge * (kdblur(powerlaw + atable {reflion }) + zgauss), where kdblur is a convolution model using a Laor line and reflion is a table model of reflection from cold gas (including a

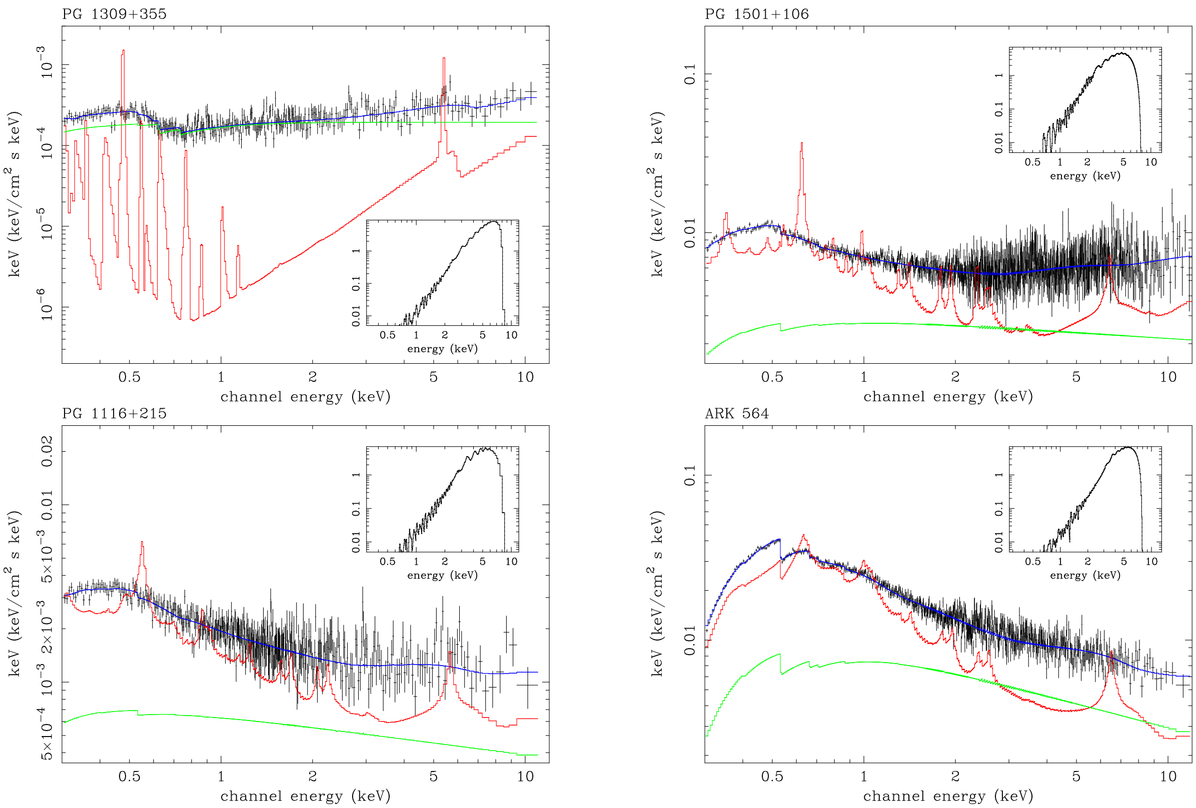


*Figure 2. Example disc reflection model fits plotted in $\nu F_\nu$, showing the amount of flux emitted as a function of energy. The crosses are data, the data-following (blue) line is the fit, the smooth (green) line the power law component and the spiky (red) line the reflection component. The inserts show the shape of the Laor line used in the convolution. The soft excess is shown to be the result of blurred line emission, and the extreme blurring effect on the iron lines around 6.4 keV is visible. The figure also illustrates the effect of ionization parameter on reflection spectra, for PG 1309+355, $\xi = 3$, PG 1501+108, $\xi = 510$, PG 1116+215, $\xi = 1270$ and ARK 564, $\xi = 3120$. A colour version is available online.*

redshift)[1].

## 5. RESULTS & DISCUSSION

Our results are presented in full in Crummy et al. (in prep). One of the sources in the sample, PG 1404+226, has been investigated with the same model in a previous paper (Crummy et al. 2005). We find that in general the relativistically blurred photoionized disc reflection model is a better fit to the data, with 25 of the 34 sources showing an improvement in $\chi^2 > 2.7$ per degree of freedom (note that this does not correspond to 90 per cent probability, the $\chi^2$ distribution is not calibrated across models). 6 sources show a significant worsening and 3 sources are inconclusive. In some sources the improvement is very marked, see Figure 1.

The disc reflection model reproduces the shape of the continuum well, and naturally explains the constant temperature of the soft excess; see Figure 2. The model also reproduces many features that would be otherwise interpreted as absorption edges in medium resolution pn data. When the thermal model is used, 17 of the 34 sources appear to have an absorption edge. This reduces to just 7 sources when the disc reflection model is used. The disc reflection model is somewhat less smooth than the thermal model (see Figure 1), and bumps on the scale of absorption edges are possible. Absorption lines cannot be reproduced by the model, therefore the possibility of outflows from absorption edges should be checked by investigating reflection models, or by detecting absorption lines from outflowing matter. This has implications for the energetics and cosmological evolution of these systems, as some measured outflows can involve similar amounts of power as the radiation e.g. Pounds et al. (2003). The model also explains the apparent lack of broad iron lines in most AGN spectra. Very few broad iron lines have been clearly detected (the most well studied being MCG –6-30-15, Tanaka et al. 1995), which is unexpected since it is believed that these systems are powered by accreting matter near the black hole, where broad iron lines are formed. Our results suggest that the broad iron lines do occur, but are broadened to the point of near undetectability. A previous paper by Gallo et al. (2004) supports this hypothesis, they fit an extremely broad excess of counts in the hard band of MRK 0586

[1]Models available from
http://www-xray.ast.cam.ac.uk/~jc/kdblur.html and
http://heasarc.gsfc.nasa.gov/docs/xanadu/xspec/models/reflion.html

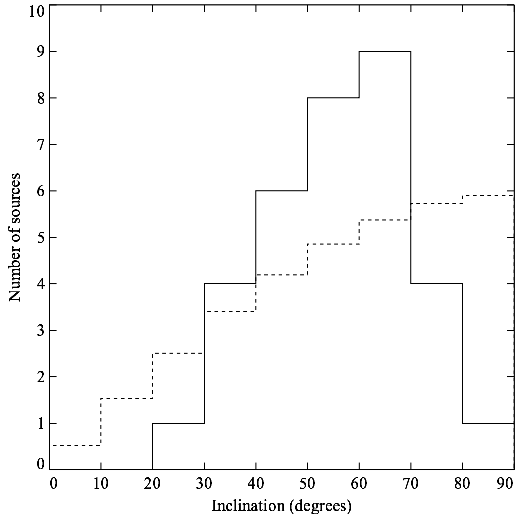


*Figure 3. This histogram shows the measured inclinations of the sources (the solid line) and the expected distribution if the inclinations were random (the dashed line). There is a deficit at high inclinations.*

with a Laor profile. MRK 0586 is included in our sample, and we find an inclination consistent with theirs; we even fit consistent inclinations when we exclude the hard band from the fit and determine the inclination purely from the blurring effects on the soft excess. This illustrates how the hard and soft bands are connected, they key to the absence of obvious broad lines is in the shape of the soft excess. Conversely, it is clear that the soft excess is nothing more than a blend of many broad lines.

As noted in the previous paragraph, it is also possible to measure the inclination of the central disc using the disc reflection model. Our measured inclinations are plotted in Figure 3. We find that the inclinations are inconsistent with being random, with a Kolmogorov-Smirnov (K-S) test probability of 0.06. Performing a K-S test against a distribution which is random over $0^{\circ}$ – $81^{\circ}$ (ignoring any data points above $81^{\circ}$) gives a probability of 0.34, so the data is somewhat consistent with being random over this range. The deficit at low inclinations may be a selection effect, discs at $\sim 0^{\circ}$ Doppler beam all of their emission along the plane of the disc and so would appear dim. The model also takes no account of limb darkening, which is strong at low inclinations. At high inclinations the deficit could be due to torus obscuration, with the sources that do have high inclination perhaps not having a torus, or with the torus unaligned with the central disc.

Abundances may also be measured with the model. The model assumes a fixed, solar abundance for all elements except iron, for which the abundance is a free parameter. The measured abundance is consistent with being between solar and $1/3$ solar for 28 of the 34 sources. No sources have measured abundances below $1/3$ solar, and 6 have abundances which are clearly above solar. These fairly low iron abundances are another factor in the apparent absence of broad iron lines. The inability to fit more than one element abundance means these results are tentative, but show that in principle the composition of AGN accretion discs can be measured from their X-ray spectra. Finally, the rotation of the central black hole may be measured using this model. The model uses convolution with a Laor line, which is based on a maximally rotating (Kerr) black hole. It is equally possible to use a model based on a non-rotating (Schwarzschild) black hole (`diskline` in `xspec` , Fabian et al. 1989). We also performed fits to all our sources using this non-rotating model, and found that in all cases the non-rotating model has a worse goodness of fit, with only two of the 34 sources where the fit is of comparable quality. This shows that rotating black holes dominate our sample. The black hole rotation is not a free parameter in our analysis, but the inner radius of the accretion disc is. The last stable orbit around a non-rotating black hole is at 6 gravitational radii, and the last stable orbit around a maximally rotating black hole is at 1.235 gravitational radii. Inside this radius matter plunges into the black hole, and does not emit strongly (Section 3.4 of Fabian & Miniutti, 2005). All 34 sources have inner disc radii consistent with being below 6 gravitational radii, and 29 of the 34 have inner radii consistent with being below 1.3 gravitational radii. This is a strong indication that most black holes are maximally rotating, in agreement with theoretical predictions, e.g. Volonteri et al. (2005) predicts that 70 per cent of AGN black holes are maximally rotating.

One further interesting result from the fits is that the illuminating power-law component is often undetected. This seems to be a problem, as it is hard to imagine how the disc could be illuminated by radiation we cannot see. However, it is quite possible for relativistic effects due to the black hole to "hide" the illuminating continuum from us. If the source of the illuminating continuum is above the disc, the light from it will be bent and impact on the disc, with little escaping to be observed (Miniutti & Fabian 2004). Emission from the disc is Doppler beamed away from the black hole and will still escape. This primarily applies to sources which do not share the rotation velocity of the disc, e.g. the base of a weak jet or shocks in a failed jet (Ghisellini, Haardt & Matt 2004).

## 6. CONCLUSIONS

We fit a large number of type 1 AGN with a thermal model and a relativistically blurred photoionized disc reflection model based on Ross & Fabian (2005). We find that:

- The disc reflection model fits the data better.
- The disc reflection model reproduces all the major features of all the sources, including the soft excess and the absence of obvious broad iron lines. The model explains the constant temperature of the soft excess across all the sources, since it is formed from a large number of highly broadened lines. The model reproduces many features that might otherwise be interpreted as absorption edges.
- Black holes in quasars strongly rotate.

- The central discs around type 1 AGN have a wide distribution in inclination, with possible deficits at very low and high inclinations. The high inclination deficit may indicate torus obscuration.
- The elemental abundances in accretion discs can be measured, iron abundances in these sources are solar or mildly sub-solar.

The relativistically blurred photoionized disc reflection model is an important tool in the study of AGN. Taking account of their intrinsically relativistic nature answers several questions about their spectra, as well as providing information about the central regions.

## ACKNOWLEDGMENTS

JC, ACF and RRR thank PPARC, the Royal Society, and the College of the Holy Cross for support respectively. The *XMM-Newton* satellite is an ESA science mission (with instruments and contributions from NASA and ESA member states).

## REFERENCES

Ballantyne D.R., Iwasawa K., Fabian A.C., 2001, MNRAS, 323, 506
Crummy J., Fabian A.C., Brandt W.N., Boller Th., 2005, MNRAS, 361, 1197
Dickey J.M., Lockman F.J., 1990, ARA&A, 28, 215
Fabian A.C., Miniutti G., 2005, astro-ph:0507409
Fabian A.C., Rees M.J., Stella L., White N.E., 1989, MNRAS, 238, 729
Gallo L.C., Boller Th., Brandt W.N., Fabian A.C., Vaughan S., 2004b, MNRAS, 355, 330
Ghisellini G., Haardt F., Matt G., 2004, A&A, 413, 535
Gierliński M., Done C., 2004, MNRAS, 349, L7
Laor A., 1991, ApJ, 376, 90
Miniutti G., Fabian A.C., 2004, MNRAS, 349, 1435
Porquet D., Reeves J.N., O'Brien P., Brinkmann W., 2004, A&A, 422, 85
Pounds K.A., Reeves J.N., King A.R., Page K.L., O'Brien P.T., 2003, MNRAS, 345, 705
Ross R.R., Fabian A.C., 1993, MNRAS, 261, 74
Ross R.R., Fabian A.C., 2005, MNRAS, 358, 211
Shakura N.I., Sunyaev R.A., 1973, A&A, 24, 337
Tanaka Y., et al., 1995, Nature, 375, 659
Volonteri M., Madau P., Quataert E., Rees M.J., 2005, ApJ, 620, 69
Walter R., Fink H.H., 1993, A&A, 274, 105
Wang T., Lu Y., 2001, A&A, 377, 52

# *XMM-NEWTON* OBSERVATIONS OF LUMINOUS NARROW-LINE SEYFERT 1 GALAXIES

**Chiho Matsumoto**[1], **Karen M. Leighly**[2], **and Toshihiro Kawaguchi**[3]

[1]EcoTopia Science Institute, Nagoya University, Furo-cho, Chikusa, Nagoya, 464-8603, Japan
[2]Department of Physics and Astronomy, The University of Oklahoma, 440 West Brooks St., Norman, OK 73019
[3]Optical and Infrared Astronomy Division, National Astronomical Observatory of Japan, Osawa 2-21-1, Mitaka, Tokyo 181-8588, Japan

**ABSTRACT**

We present results from the XMM-Newton observations of four optically-luminous narrow-line Seyfert 1 galaxies. The obtained X-ray spectra showed that intrinsic absorption is unlikely to be present; all the four X-ray spectra are steep, as is typical among narrow-line Seyferts. Utilizing simultaneous UV observations by the OM, we also investigate the spectral energy distributions in the UV–X-ray band. One object (RX J1225.7+2055) of the four was found to be X-ray weak (the spectral energy index between 2500 Å and 2 keV: $\alpha_{\rm ox}\sim2.0$) during our observations. Compiling values of $\alpha_{\rm ox}$ from a larger sample of narrow-line Seyferts, we find that, although the sample is small, the $\alpha_{\rm ox}$ distribution suggests that X-ray weakness may occur more frequently among more luminous objects. This suggest that X-ray weakness may be caused by high accretion rate. We try to interpret the $\alpha_{\rm ox}$ dependence on the optical luminosity, based on simple disk models of an accretion disk sandwiched by coronae.

Key words: X-rays; Narrow-line Seyfert 1 Galaxies.

## 1. INTRODUCTION

The extreme spectral and variability properties of narrow-line Seyfert 1 galaxies (NLS1s) have been the subject of intensive study by virtually every X-ray satellite during the past decade, and are now well established. They frequently show a strong soft excess component, their hard X-ray spectrum tends to be steeper than in similar broad-line Seyfert 1 galaxies, and they show rapid and large-amplitude X-ray variability (e.g. Boller et al. 1996; Leighly 1999). NLS1s, defined by their optical emission-line properties: FWHM H$\beta$ $<$ 2000 km s$^{-1}$ and [O III]$\lambda$5007/H$\beta$ $<$ 3 (Osterbrock & Pogge 1985; Goodrich 1989), are different from type 2 Seyfert galaxies, which generally have [O III]/H$\beta > 3$. NLS1s usually have strong permitted lines of Fe II from broad-line region (BLR), which also discriminate NLS1s from type 2 Seyfert galaxies. The most promising explanation for these X-ray and optical properties is that NLS1s have a higher mass accretion rate compared with the Eddington value.

Luminous AGNs with narrow emission lines are of special interest, because they should have particularly high accretion rates based on the reverberation mapping argument (e.g., Laor 2000). If the motion of the BLR gas is dominated by gravity of the central black hole (BH), the velocity dispersion ($\Delta v$) is expressed by $\Delta v^2 \simeq GM_{\rm BH}/R_{\rm BLR}$, where $R_{\rm BLR}$ is the radius of the emission line in question. The BLR size is expected to be set by the bolometric luminosity ($L$), specifically $R_{\rm BLR} = 0.1\left(\frac{L}{10^{46}\,{\rm ergs\ s^{-1}}}\right)^{0.5}$ pc and this is experimentally verified in reverberation mapping (Kaspi et al. 2000, though with somewhat steeper slope of $\sim$0.7). Combining these two equations reveals $L/L_{\rm Edd} \propto \Delta v^{-2} L^{0.5}$. Therefore, study of luminous NLS1s is particularly important, as it allows examination of the physics under conditions of extremely high $L/L_{\rm Edd}$.

Our study on luminous NLS1s is also inspired by PHL 1811, a quite luminuos ($M_{\rm v} = -26.5$) quasar discovered in the VLA FIRST radio survey. It is extremely bright and optically classified as a NLS1. This object is remarkable because was not a known X-ray source, being undetected in the *ROSAT* all-sky survey (RASS; Voges et al. 1999), nevertheless its brightness (m=13.7). Followup *BeppoSAX* observations detected the quasar in the X-rays, but discovered that it is remarkably X-ray weak (Leighly et al. 2001a). During followup *Chandra* observations in 2001, it was again observed to be X-ray weak. Significant variability was observed between the two observations separated by 12 days, and an observed steep X-ray spectrum shows that it is not absorbed (Leighly et al. 2004; Leighly et al. in prep.). The UV emission line property observed with the *HST* STIS is unusual in that the spectrum is dominated by Fe II and there is no prominent broad emission line; it is consistent with weak X-ray emission(Leighly et al. 2004; Leighly et al. in prep.). These observations argues that PHL 1811 is intrinsically

X-ray weak. Still it is not clear whether or not intrinsic X-ray weakness is common among luminous NLS1s.

In order to begin to generalize the properties of luminous NLS1s (narrow-line quasars, hereafter NLQSOs), we proposed to observe handful NLQSOs with luminosity of $M_{\rm v} < -25$, and four of them are approved and observed (Table 1).

Throughout this paper, uncertainties quoted in the body and tables are 90 % confidence for one parameter of interest.

## 2. THE *XMM-NEWTON* OBSERVATIONS

We carried out *XMM-Newton* observations of four NLQSOs with scheduled duration of 12 ks for each in 2003. The observation date and fundamental informations of the sources are summarized in Table 1. The EPIC instruments were operated in Full-frame mode for all observations. We used medium filter for most observations; only for the MOS instrument in the RX J2241.8−4405 observation, thick filter is used to suppress events from bright star in the F.O.V. With the optical monitor onboarded *XMM-Newton*, we also scheduled UV photometry with two filters. The RGS was also operated, however, these objects are too faint to investigate with the RGS. We also performed UV photometric observation by the optical monitor (OM; Mason et al. 2001) with two filters for each object. Details of the UV observations are described later in §3.2.

We analyzed pipeline processed products using SAS 5.4.1 and HEAsoft 5.2 and 5.3 packages. We selected only the events with "flag=0" and "pattern=0–4 (pn) or 0–12 (MOS)".

Unfortunately, most of observations happened to be done in the period with quite high background rate. We discarded such data using the method described in the *XMM-Newton* SAS users' guide: First we extracted light curves of the "pattern=0" events with the energy greater than 10 keV, and the quiet background period was defined when the count rate was lower than the recommended values of 0.35 c $s^{-1}$ and 1.0 c $s^{-1}$ for the MOS and the pn, respectively. For most instruments, "good" exposures are 30–70 % of the total pipeline processed durations. The length is summarized in Table 1. In the worst case of the pn observation of RX J2241.8−4405, no good exposure is obtained with the above criterion. If we increased the threshold five times higher than the users' guide value, exposure of 0.6 ks is selected. We used this pn data of RX J2241.8−4405 only for the purpose to check whether the MOS results is consistent with that.

The sources are clearly seen at the positions which are consistent with the optical positions. We made plots of the point spread function (radial profile of the count rate) of the sources; The plots show no signature of spatial extension for all sources, and also show that photons from the source are dominating background photons at radii smaller than several ten arcseconds even for the faintest source. Thus, the source photons are collected from the region of $r < 35''$ for all. The background photons are collected from the near region avoiding serendipitous sources.

To look at variability, we extracted "cleaned" X-ray light curves in the 0.3–10 keV band. The fit to each light curve with a constant model is not rejected, hence, significant short-term variability is not detected during our observations. This is not surprising because our observations were pretty short in duration, and because the photon-statistics are not so great. The light curve with the highest photon-statistics from PG 2233+134 suggests marginal variability with time-scale of $\sim$1000 s.

## 3. ANALYSES & RESULTS

### 3.1. X-ray Spectra

The extracted pn and MOS spectra are grouped so that each energy bin has 20 photons at least; then, we used $\chi^2$ fitting method. The detector response matrices were created by rmfgen and arfgen in SAS.

First, we fitted each spectrum in the whole energy band (0.3–10 keV) with a model of a power law attenuated by Galactic absorption. After confirming that the results from each detector are consistent among them, we fitted the pn and MOS spectra simultaneously[1] with the same model. For RX J2241.8−4405 and PG 2233+134, this model was rejected at 90 % confidence level. We also made fits with the same model only in the 2–10 keV band, this fit was acceptable for every target. The obtained power-law indices from both fits are summarized in Table 1. The results shows that all the X-ray spectra are pretty steep with $\Gamma > 2$, as is typical among NLS1s (e.g. Pounds et al. 1995; Boller et al. 1996; Brandt et al. 1997; Leighly 1999).

The observed steep X-ray spectra strongly implies no significant intrinsic absorption. If there is absorption material with $N_{\rm H}$ of $10^{21-24}$ $\rm cm^{-2}$, the EPIC spectrum should have convex curvature; but it is not observed. One possibility remains not to be rejected, where the absorption column is quite large ($N_{\rm H} \gtrsim 10^{25}$ $\rm cm^{-2}$) and the observed X-rays are not direct emission from the nucleus but the scattered light, as sometimes seen in Seyfert 2 galaxies. In this case, neutral-iron K-emission line with an huge equivalent width (EW) of larger than 1 keV is considered to be accompanied (e.g., Ghisellini, Haardt, & Matt, 1994). The obtained spectra yielded that the upper-limit of a narrow iron-line EW is 0.7, 0.2, 0.8, and 6 keV for RX J2241.8−4405, PG 2233+134, PG 1543+489, and RX J1225.7+2055, respectively. Thus, we can say that

[1] The pn data is not used in the analyses of RX J2241.8−4405, as mentioned before.

*Table 1. Results from the* XMM-Newton *observations of luminous NLS1s.*

| Object Name | $z$ | $M_v$ | $m$ | $N_H{}^a$ | Obs. Date Time | $\Gamma_{0.3-10\mathrm{keV}}$ | $\Gamma_{2-10\mathrm{keV}}$ | $F_{2-10\mathrm{keV}}{}^a$ | $\alpha_{ox}$ |
|---|---|---|---|---|---|---|---|---|---|
| RX J2241.8−4405 | 0.545 | −26.9 | 15.8 | 1.8 | 5/28 15–18(UT) | $(2.64\pm0.10)^b$ | 2.4±0.4 | $4.2\times10^{-13}$ | 1.52 |
| PG 1543+489 | 0.400 | −25.6 | 16.0 | 1.6 | 2/08 20–24(UT) | 2.74±0.07 | 2.6±0.5 | $1.5\times10^{-13}$ | 1.58 |
| PG 2233+134 | 0.325 | −25.2 | 16.0 | 4.8 | 5/17 17–20(UT) | $(2.56\pm0.04)^b$ | 2.2±0.2 | $5.4\times10^{-13}$ | 1.54 |
| RX J1225.7+2055 | 0.335 | −25.1 | 15.9 | 2.4 | 6/12 16–20(UT) | $2.73^{+0.29}_{-0.25}$ | ... | $0.2\times10^{-13}$ | 1.95 |

$a$: The unit of Galactic column density is $10^{20}$ cm$^{-2}$, and that of the 2–10 keV flux is erg cm$^{-2}$ s$^{-1}$.
$b$: The $\chi^2$ value of this fit was unacceptable at 90 % confidence level, and the fit was improved significantly by the addition of a soft excess component.

all but RX J1225.7+2055, at least, are not attenuated by heavy absorption based on the iron-line upper limit.

For RX J2241.8−4405, an iron-emission-line is marginally detected at the central energy of 6.7±0.3 keV with the EW of $300^{+365}_{-260}$ eV; however, because the detection is just based on a single energy bin in the MOS spectrum, this validity should be examined by further observation.

Soft excess component is another common spectral feature among NLS1s; Actually, its existence is implied for some sources in the ratio plots of the data to the extrapolated best-fit power-law model in the 2–10 keV band. As a trial, we fitted the 0.3–10 keV spectra with the power-law plus a blackbody model. By adding a blackbody component, the fits are improved significantly (>99% by F-test) for RX J2241.8−4405 and PG 2233+134. The blackbody temperatures are obtained to be 0.14±0.02 keV and $0.13^{+0.02}_{-0.01}$ keV in the source rest frame for RX J2241.8−4405 and PG 2233+134, respectively. Although the blackbody component is not statistically required, the fit for PG 1543+489 could yield the temperature of $0.16^{+0.07}_{-0.06}$ keV. For RX J1225.7+2055, the temperature was far from being constrained because of poor statistics. These obtained temperatures are again rather typical among NLS1s; e.g., $kT_{\mathrm{diskpn}} = 0.14$–0.20 keV[2] (e.g., Leighly 1999, Porquet et al. 2004). We also tested a broken power-law model for the two sources with significant soft excess feature. For both cases, the obtained $\chi^2$ values were slightly worse than those from the fit with the blackbody model with same degrees of freedom ($\Delta\chi^2 \sim 5$). The break energies in the observed frame were 1.0±0.2 keV and $1.6^{+1.0}_{-0.7}$ keV for RX J2241.8−4405 and PG 2233+134, respectively. The power-law indices below the break energy were 3.2±0.2 and 2.7±0.1 for RX J2241.8−4405 and PG 2233+134, respectively. With physical point of view a Comptonized blackbody model are considered more appropriate, but, we will not report such fits because limited quality of the data prevents us constrain parameters.

[2]The inner disk temperature of a multicolor blackbody model of diskpn in XSPEC. This value is larger by several times ten percent than that from the fit with a single temperature blackbody model.

### 3.2. UV–X-ray Spectral Slopes: $\alpha_{ox}$

One of the great advantage of *XMM-Newton* for this research is that it can perform observation in UV and X-ray bands simultaneously. In order to obtain fluxes and spectral slopes in the UV band, we performed UV photometric observation by the OM with two filters for each object. The choice of filters are yielded by bright stars in the OM field of view; we used the U and UVM2 filters for PG 1543+489 and RX J1225.7+2055, and the UVW1 and UVW2 filters for the others. The effective wavelength of U, UVW1, UVM2, and UVW2 filters are 344, 291, 231, and 212 nm, respectively.

We utilized the pipeline products, and converted the OM counts rate into the fluxes using the method described at an *XMM-Newton* web page.[3] Then, attenuation by Galactic reddening is corrected using a reddening curve[4] and E(B−V) values taken from the NED.

We investigated UV–X-ray spectral slopes of our targets utilizing a parameter of $\alpha_{ox}$, which is conventionally defined as a power-law energy index bridging two points of 2500 Å and 2 keV in the rest frame. The 2 keV fluxes can be directly measured by X-ray spectra, and the fluxes at 2500 Å are estimated by interpolating or extrapolating the observed OM fluxes with a power law. Unfortunately for PG 1543+489, no good data were obtained with U filter, hence we assumed that the spectral slope is the mean value of those from the other three sources.[5] The resulting $\alpha_{ox}$ values are also listed in Table 1.

Contrary the others showed rather normal $\alpha_{ox}\sim$1.5–1.6, RX J1225.7+2055 was found to be X-ray weak ($\alpha_{ox}\sim$2.0) during our observation (See also Figure 1). Thus, our observations show that not all NLQSOs are X-ray weak; at the same time, that not only PHL 1811 is anomalously X-ray weak.

[3]http://xmm.vilspa.esa.es/sas/documentation/watchout/uvflux.shtml
[4]http://idlastro.gsfc.nasa.gov/ftp/pro/astro/ccm_unred.pro
[5]The three spectral slopes range $\alpha_\nu = 0.1$–0.4, and we assumed the slope of PG 1543+489 is $\alpha_\nu = 0.27$. If we assume it is same as the slope from the SDSS composite ($\alpha_\nu = 0.44$; Vanden Berk et al. 2001), the resulting 2500 Åflux gets smaller by 7 %. The difference in the $\alpha_{ox}$ values is as small as $\Delta\alpha_{ox} = 0.01$. Although it is reported that the average NLS1 UV spectrum shows rather red color ($\alpha_\nu \sim 0.8$), there is a trend relating $\alpha_\nu$ and luminosity (Constantin & Shields, 2003). Among the luminous end of their sample, $\alpha_\nu$ is about 0.5.

# 4. DISCUSSION

## 4.1. More Luminous, More Frequently X-ray Weak?

To investigate $\alpha_{\rm ox}$ distribution among luminous NLS1s in general, we compiled a heterogeneous sample of rather luminous AGNs ($M_{\rm v} < -23$) with narrow H$\beta$ line from the literatures (White et al. 2000, Bade et al. 1998, Veron-Cetty & Veron 2001, among others). The 2500 Å flux ($l_o$) was estimated from optical magnitude taken from the references by extrapolating a power law of $f_\nu \propto \nu^{-0.44}$. The assumed spectral index of $\alpha_\nu = 0.44$ is based on that from the SDSS Quasar composite spectrum (Vanden Berk et al., 2001). The 2 keV fluxes were estimated from the count rates or upper limits obtained from RASS, assuming that the X-ray spectrum can be represented by Galactic absorbed power law with photon-index of 2.75 (Williams, Pogge, & Mathur 2002; Williams, Mathur, & Pogge 2004). The resulting values of $\alpha_{\rm ox}$ are plotted as a function of monochromatic luminosity at 2500 Å in Figure 1.

With above analysis, We discovered four additional X-ray weak objects in relatively luminous regime ($\log l_o > 30.6$). If we make statistics of X-ray weak objects in the several luminosity range, for example, $\log(l_o)$ below and above 30.3, only 2 among 18 objects are X-ray weak in the lower luminosity regime, whilst 6 among 17 objects show X-ray weakness in the higher. Although it is not statistically clear, it is suggested that X-ray weak objects might be found more frequently in more luminous regime.

It should be noted that no "X-ray bright" source was found. Variability with large-amplitude is common nature of NLS1s, but, if X-ray weakness is just because of fluctuation of flux around the average flux, we should find "X-ray bright" objects as frequently as X-ray weak ones. Contrary, Figure 1 shows that no source exhibits X-ray brightness with $\Delta\,\alpha_{\rm ox} \gtrsim 0.5$. Thus, X-ray weakness is not just caused by such fluctuation, instead some mechanism is likely to exist to make sources selectively fainter in the X-ray band.

It is true that NLS1s show skewed variability pattern in their light curves, and that they are characterized by flare-like peaked patterns (e.g., McHardy et al. 2004). For such a light curve, the time-averaged flux level is located at the level much lower than the median value. Then, we expect X-ray bright sources at less frequency and with larger amplitude, and X-ray faint sources at more frequency and with less amplitude. At least, from the point of frequency, this trend does not conflict with Figure 1; however, we cannot discuss with respect to the amplitude, because Figure 1 lacks X-ray bright sources. Thus we cannot rule out this explanation completely, but this predicts that the overall amplitude of variability (taking into account the not-yet-observed X-ray bright phase) is as large as several orders of magnitude, which has not been reported so far.

## 4.2. X-ray Weakness in Low-State of Transients?

In our *XMM-Newton* observation RX J1225.7+2055 was X-ray weak; however, during RASS it was 30 times brighter with normal $\alpha_{\rm ox}$. Another X-ray weak object found in our study with larger sample (H1137−127) was also found to have similar large-amplitude long-term variability: It was detected by *HEAO-1* survey with the 2–10 keV luminosity of $\log L_{\rm X} = 46.29$ erg s$^{-1}$ (Remillard et al., 1993), and the RASS count rate predicts the luminosity fainter by 2 orders of magnitude. These facts mean that the some X-ray weak objects are not always to be so, and that they are in a transient state.

As Uttley et al. (2004) show in a NLS1 NGC 4051, hard X-ray spectra of AGN in general tend to be flatter when they are in fainter-state. Unfortunately because the net exposure time of RX J1225.7+2055 was significantly reduced because of background flare, we cannot investigate its power-law index solely in the hard X-ray band. In order to look at this property and also possible time short-variability, further and longer observations are necesarry for RX J1225.7+2055.

## 4.3. Physical Driver of X-ray Weakness

Attenuation by absorber is a way to explain observed X-ray weakness; in fact, We can not rule out this possibility for the other X-ray weak objects estimated by RASS. For RX J1225.7+2055, however, attenuation by absorption is unlikely to be the case because of its steep spectra, and because it was previously observed with "X-ray normal" during RASS. Of course, we cannot rule out completely this possibility, if Compton-thick cold absorption appeared in the our line-of-sight between the RASS and *XMM-Newton* observations separated by 10 years.

Intrinsic X-ray weakness could be more likely. As described in §1, another optically-luminous NLQSO, PHL 1811, is now securely confirmed to be intrinsically X-ray weak (Leighly et al. 2004; Leighly et al. in prep.). Since we selected the sample with relatively narrow H$\beta$ line width, the luminosity axis is considered to be strongly correlated with accretion rate. The observed trend that more X-ray weak objects are found in more luminous regime implies that X-ray weakness is a nature of high $L/L_{\rm Edd}$, though they are not always so.

## 4.4. Implications from a disk-corona model

What is the implications of the X-ray weakness in terms of accretion disk models? Here, we try to interpret the $\alpha_{\rm ox}$ v.s. $l_o$ diagram, based on simple disk models of an accretion disk sandwiched by coronae. The energy dissipation rate at the corona normalized to the total (corona plus disk) dissipated energy (often noted as $f$) can be estimated by considering either gas evaporation rate from the disk (Meyer & Meyer-Hofmeister 1994), or energy

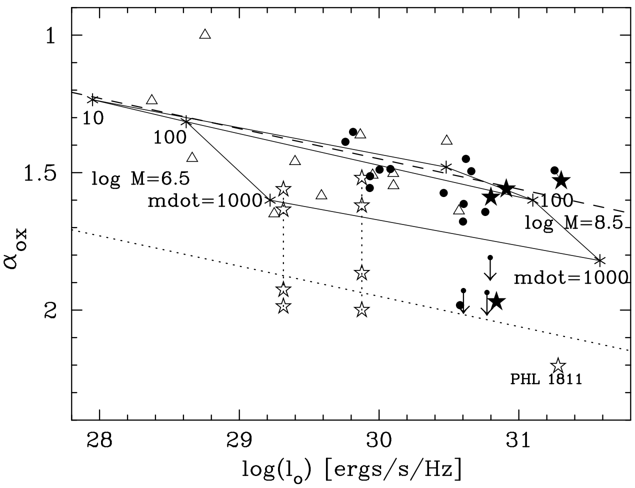


*Figure 1.* $\alpha_{\rm ox}$ *of NLS1s as a function of monochromatic luminosity at 2500 Å from our* XMM-Newton *observations (filled stars) along with those from heterogeneous samples. Filled circles are newly investigated data, using the* ROSAT *all-sky survey (RASS) X-ray fluxes and the optical fluxes in NED database. For the objects which could not be detected in RASS, 3σ upper-limits of* $\alpha_{\rm ox}$ *are shown with arrows. Data marked with open triangles and stars are taken from Leighly (2001b). The dashed line represents the regression among radio quiet quasars (Vignali et al. 2003), and the dotted line is parallel to the dashed done (*$\Delta\,\alpha_{\rm ox} = 0.5$*; the sources at the dotted line have are 20 times X-ray weaker than the sources at the dashed line), and is shown to guide the eye. The results calculated from the disk-corona model are shown with asterisks. Here we show the results in the cases of* $M_{\rm BH} = 10^{6.5}$ *and* $10^{8.5}$ *solar mass, and the accretion rate of* $\dot{m} = 10, 100, 1000$.

leakage due to magnetic buoyancy from the disk. For instance, Janiuk & Czerny (2000) showed that $f$, in the framework of an evaporating disk model, decreases when an gas accretion rate $\dot{M}$ increases (see also Bechtold et al. 2003, their Fig. 7). Similarly, Merloni & Fabian (2002) presented, with magnetic coronal models, a decreasing $f$ for an increasing $\dot{m}$ [where $\dot{m} \equiv \dot{M}/(L_{\rm Edd}/c^2)$].

It is out of the scope of this paper to judge and discriminate various coronal models, and we simply adopt the prescription by Merloni & Fabian (2002):[6] Based on their Fig. 1, the ratio of the coronal power-law X-ray luminosity to the total bolometric one is assumed to be proportional to $\dot{m}^{-0.4} M_{\rm BH}^{-0.06}$. The X-ray luminosity is normalized so that the disk-corona model is consistent with the observed $\alpha_{\rm ox}$ of Ton S 180 (Turner et al. 2002) and PG 1448 (Kawaguchi et al. in prep.), [7] and the X-ray power-law index $\Gamma$ is assumed to be a constant. Optical and bomoletric luminosities for various $\dot{m}$ and $M_{\rm BH}$ are taken from disk models of Kawaguchi (2003) with a constant viscosity parameter $\alpha$ of 0.01. The results are shown in Figure 1.

Firstly, Figure 1 shows that the slope of the regression line by Vignali et al. 2003 ($d\alpha_{\rm ox}/d\log l_o \approx -0.1$) can be explained by changing $M_{\rm BH}$ with a fixed $\dot{m}$. Given a larger $M_{\rm BH}$, an accretion disk becomes cooler, shining at longer wavelength (optical) with smaller $\alpha_{\rm ox}$. On the other hand, a smaller $M_{\rm BH}$ tends to make the disk shine at shorter wavelength (e.g., UV), and hence with larger $\alpha_{\rm ox}$. In other words, accretion disk models predict that bolometric luminosities are not necessarily in proportion to optical luminosities, as emphasized in Hosokawa et al. (2000, §2.3.1). Actually, Collin & Kawaguchi (2004) showed, by using the data of X-ray selected AGNs obtained by Grupe et al. (2004), that optical luminosities roughly scale as $L_{\rm bol}^{0.7}$.

Secondly, the deviation of $\alpha_{\rm ox}$ from the regression relation seems to be controlled by $\dot{m}$. This disk-corona model turns out to cover the distribution of most of the plotted objects (except for the X-ray weak ones, as discussed below). A large offset of $\alpha_{\rm ox}$ happens when $\dot{m}$ changes from 100 to 1000, where the bolometric luminosity increases very little due to saturation of disk emission by photon trapping (Abramowicz et al. 1988; Begelman 1978), while the optical luminosity continues to increase since the outer region of the disk, responsible for optical emission, is still outside the photon trapped region (see Kawaguchi 2003). Observational data seem to support this trend. Wang, Watarai & Mineshige (2004) pointed out that the ratio of X-ray (2–10 keV) luminosity over optical luminosity is anticorrelated with the ratio of optical luminosity over Eddington luminosity. (Note, however, that the anticorrelation is trivial if the 2–10 keV luminosity is roughly in proportion to the BH mass.)

Finally, it is now clear that the X-ray weak objects are located outside the region predicted by this simple disk-corona model. The X-ray weakness could be originated in either (i) an extremely large $\dot{m}$ ($> 1000$), or (ii) an extremely low energy dissipation rate at the corona, $f$ (by some unknown physical mechanisms). Let us go back again to the case of PHL 1811. Its H$\beta$ width and optical luminosity imply (Kaspi et al. 2000; Wandel et al. 1999) that its BH mass is around $10^{8.5}$ to $10^9 M_\odot$. Based on the spectral model in Kawaguchi (2003, Fig. 11), the optical luminosity and inferred BH mass indicate $\dot{m}$ to be between 100 and 1000. Therefore, at least for this object, the hypothesis (i) with an extremely large $\dot{m}$ ($> 1000$) is not likely. Although the second interpretation (ii) is favored, the physical reason behind very low $f$ is still unclear. Frequency of the X-ray weakness (this study), a search for common properties of X-ray weak objects, and detailed observations of the X-ray weak objects who transient between X-ray weak and X-ray normal regimes will help to understand what is going on there. Theoret-

[6] Their model is in principle limited to sub-Eddington accretion rate ($\dot{m} \le 16$). However, the $M_{\rm BH}$-dependency of $f$ found for sub-Eddington rates are likely valid also for super-Eddington rates, since the $M_{\rm BH}$-dependency of physical quantities in super-Eddington disks is identical to that of the standard disk (e.g., Fukue 2000).

[7] Their $M_{\rm BH}$ and $\dot{m}$ are estimated to be $\sim 10^{6.5-7} M_\odot$ and $\sim 1000$, respectively (Kawaguchi, Pierens, & Huré, 2004; Kawaguchi 2004).

ical investigations on a corona above a super-Eddington accretion disk are also insufficient.

## ACKNOWLEDGMENTS

This work is based on observations obtained with *XMM-Newton*, an ESA science mission with instruments and contributions directly funded by ESA Member States and NASA. We acknowledge the great efforts of all the members of the *XMM-Newton* team. This research has made use of the NASA/IPAC Extragalactic Database (NED) which is operated by the Jet Propulsion Laboratory, California Institute of Technology, under contract with the National Aeronautics and Space Administration. CM gratefully acknowledges support through the Grant-in-Aid for Scientific Research (17740104) of the Ministry of Education, Culture, Sports, Science and Technology.

## REFERENCES

Bade, N. et al. 1998, A&AS, 127, 145

Abramowicz, M. A., Czerny, B., Lasota, J. P., & Szuszkiewicz, E. 1988, ApJ, 332, 646

Begelman, M. C. 1978, MNRAS,184, 53

Bechtold, J. et al. 2003, ApJ, 588, 119

Boller, Th., Brandt, W. N., & Fink, H. 1996, A&A, 305, 53

Brandt, W. N., Mathur, S., & Elvis, M. 1997, MNRAS, 285, L25

Collin & Kawaguchi 2004, A&A, 426, 797

Constantin, A. & Shields, J. C. 2003, ApJ, 115, 592

Fukue, J. 2000, PASJ, 52, 829

Goodrich, R. W. 1989, ApJ, 342, 224

Ghisellini, G., Haardt, & F., Matt, G. 1994, MNRAS, 267, 743

Hosokawa, T., Mineshige, S., Kawaguchi, T., Yoshikawa, K., & Umemura, M. 2001, PASJ, 53, 861

Janiuk, A., & Czerny, B. 2000, NewAR, 5, 7

Kaspi, S., Smith, P. S., Netzer, H., Maoz, D., Jannuzi, B. T., & Giveon, U. 2000, ApJ, 533, 631

Kawaguchi, T., Pierens, A., & Huré, J.-M. 2004, A&A, 415, 47

Kawaguchi, T. 2004, Prog. Theor. Phys. Suppl., 155, 120

Grupe, D., Wills, B. J., Leighly, K. M., Meusinger, H. 2004, AJ, 127, 156

Laor, A. 2000, NewAR, 44, 503

Leighly, K. M. 1999, ApJS, 125, 317

Leighly, K. M., Halpern, J. P., Helfand, D. J., Becker, R. H., & Impey, C. D. 2001a, AJ, 121, 2889

Leighly, K. M. 2001b, Proceeding of "X-ray Emission from Accretion onto Black Holes" ADS Bibliographic Code: 2001xeab.confE..38L

Leighly, K. M., Halpern, J. P., & Jenkins E. B. 2004, in "AGN Physics with the Sloan Digital Sky Survey", eds. G. T. Richards & P. B. Hall, ASP, in press

McHardy, I. M., Papadakis, I. E., Uttley, P., Page, M. J., Mason, K. O. 2004, MNRAS, 348, 783

Merloni, A. & Fabian, A. C. 2002, MNRAS, 332,165

Meyer, F., & Meyer-Hofmeister, E. 1994, A&A, 288, 175

Osterbrock, D. E., & Pogge, R. W. 1985, ApJ, 297, 166

Porquet, D., Reeves, J. N., O'Bruien, P., &, Brinkmann, W. 2004, A&A, 422, 85

Pounds, K. A., Done, C., & Osborne, J. P. 1995, MNRAS, 277, L5

Remillard, R. A., Bradt, H. V. D., Brissenden, R. J. V., Buckley, D. A. H., Roberts, W., Schwartz, D. A., Stroozas, B. A., & Tuohy, I. R. 1993, AJ, 105, 2079

Turner, T. J. et al. 2002, ApJ, 568, 120

Uttley, P., Taylor, R. D., McHardy, I. M., Page, M. J., Mason, K. O., Lamer, G., Fruscione, A. 2004, MNRAS, 347, 1345

Vanden Berk, D. E. et al. 2001, AJ, 122, 549

Veron-Cetty M. P. & Veron P. 2001, A&A, 374, 92

Vignali, C., Brandt, W. N., Schneider, D. P. 2003, AJ, 125, 433

Voges, W. et al. 1999, A&A, 349, 389

Wandel, A., Peterson, B. M., & Malkan, M. A. 1999, ApJ, 526, 579

Wang, J., Watarai, K. & Mineshige, S. 2004, ApJ, 607, L107

White, R. L. et al. 2000, ApJS, 126, 133

Williams, R., Pogge, R. W., & Mathur, S. 2002, AJ, 124, 3042

Williams, R., Mathur, S. & Pogge, R. W. 2004, ApJ, 610, 737

# THE *XMM-NEWTON* AND *SPITZER* VIEW OF GALAXY/AGN FORMATION AT $Z = 2 - 3$

**F.J. Carrera, J. Ebrero[1], M.J. Page[2], and J.A. Stevens[3]**

[1]Instituto de Física de Cantabria, Avenida de los Castros, 39005 Santander, Spain
[2]MSSL-UCL, Holmbury St. Mary, Dorking RH5 6NT, UK
[3]U. of Hertfordshire, Hatfield AL10 9AB, UK

**ABSTRACT**

The genesis of spheroids is central to our understanding of galaxy formation. They contain half of the stellar mass of the Universe, and almost all of the black hole mass. According to galaxy formation models, cluster ellipticals form in high density regions through hierarchical merging of gas-rich subcomponents at early epochs. We have used X-ray absorbed QSOs at z 2-3 to signpost these regions, and found 2 proto-clusters of ultraluminous starburst galaxies using submm observations. If these objects are to evolve into elliptical galaxies, they should contain growing massive black holes. These regions of widespread collapse therefore represent a unique laboratory within which we can study the complete sequence of early AGN evolution.

As part of a detailed multiwavelength ongoing programme, we have used XMM-Newton and Spitzer to search for these buried AGN, and determine the evolutionary stage of the galaxies in the proto-clusters. Our observations provide a powerful test for models of black hole growth in galaxy bulges.

Key words: X-rays; submillimetre; Galaxies: active; Star formation.

## 1. INTRODUCTION

There is mounting evidence in favour of a physical relationship between the growth of the spheroids of galaxies through star formation and the growth of supermassive black holes (SMBH) through accretion: most (if not all) galaxies seem to host a supermassive black hole (Yu & Tremaine 2002), and the mass of the galaxy spheroid and the mass of the SMBH are strongly correlated (Merritt & Ferrarese 2001). The cosmic evolutions of the star formation and AGN emissivity follow similar trends, growing from $z = 0$ to $z \sim 2$, and then stabilizing or decreasing (the so called Madau plot, see e.g. Silverman et al. 2005). All this evidence shows that supermassive black holes may be a natural by-product (even a necessary one) in the process of galaxy formation.

In this context, direct studies of objects in the process of building simultaneously their star populations and their central SMBH are essential in order to understand the mechanisms involved, and the possible feedback effects.

Star formation is normally associated with thick molecular clouds that absorbs most of the UV-optical-NIR radiation, which is re-emited in the FIR-submm where it escapes unimpeded from all but the thickest environments. This has been confirmed by the detection of Ultra and Hyper Luminous Infrared Galaxies (ULIRG and HLIRG, respectively) by *IRAS*, in which star formation seems to dominate the bolometric emission, although it is uncertain how many of them are also AGN powered (Sanders & Mirabel 1996, Rowan-Robinson 2000). The K-correction at 850 $\mu$m is strongly negative for thermal dust sources, cancelling the cosmological dimming (Blain & Longair 1993). The transparency of the star forming environment, and the negative K-correction, favour strongly the FIR and the submm as the spectral windows with which to study star formation over the course of cosmic history.

Accretion onto SMBH produces copious X-ray emission, the hardest part of which (at energies above 2-10 keV) can also escape from very obscured environments. The presence of such very heavily obscured AGN is required by the spectrum of the X-ray Background (XRB, Fabian & Iwasawa 1999), and is assumed by all models for the XRB (Gilli et al. 2001), which also require that most accretion power in Universe is absorbed. Indeed, some of them even identify the material responsible for the X-ray absorption as strongly star-forming material (Fabian et al. 1998).

It is then clear that a combination of FIR/submm and hard X-ray observations has the potential to yield direct insights into the very core of the star forming and BH feeding regions, helping to quantify their mutual relationship. Here, we report our work in the past few years on submm, mid-IR, near IR, optical and X-ray observations of a sample of QSOs. In Section 2 we define the sam-

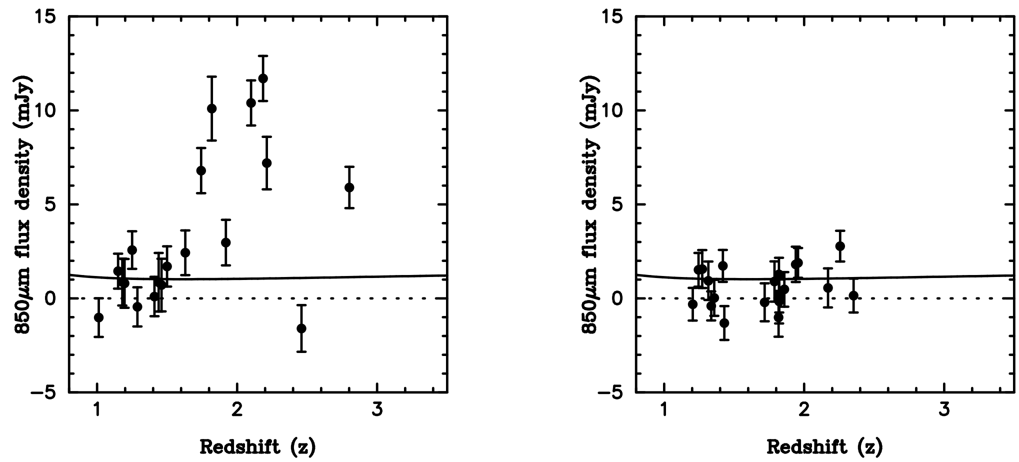


*Figure 1. 850 μm flux vs. $z$ for our sample of 19 X-ray absorbed (left) and unabsorbed (right) QSOs. The solid line is the expected flux from Mrk 231 (a nearby submm luminous X-ray absorbed QSO) if it were viewed at redshift $z$*

ples of X-ray absorbed and unabsorbed QSOs we have used, then in Section 3 we present the submm photometry results on those two samples. The results of submm imaging around some of the X-ray absorbed QSOs are shown in Section 4, and we discuss the possible nature of the submm sources appearing around those QSOs. The available *XMM-Newton* observations are briefly summarized in Section 5 (for a full account see Page et al. 2006, this volume). Finally, the ensemble of results are discussed and interpreted in the framework of a hierarchical evolution of spheroids in Section 6.

## 2. SAMPLE SELECTION

We have assembled two similarly sized samples of broad line QSOs, with similar redshift distributions ($1 < z < 3$) and soft X-ray luminosities ($\log(L_{\rm X,soft} = \log(L^*_{\rm X} \pm 0.7)$, where the bulk of the QSO luminosity density was produced (Page et al. 1997, Miyaji et al. 2001). Most of the objects in both samples are expected to be radio quiet, since the ratio between radio quiet and radio loud objects in the above intervals is 15 to 1 (Ciliegi et al. 1995).

The key difference between the two samples is that one of them is composed of 20 QSOs without absorption in their X-ray spectra, as are most soft X-ray selected AGN (Mateos et al. 2005). The 19 QSOs in the other sample show Compton-thin absorption in their X-ray spectra (Page et al. 2001a). This is in itself rather surprising, since, within unified models for AGN, the material obscuring the central regions is located in a geometrically and optically thick torus, which should block both the X-ray and broad line emitting regions. We will propose a possible way out of this contradiction in Section 5.

Again within the Unified model for AGN, the difference between both samples should be due simply to geometry, hence it would be expected that isotropic properties (such us the submm emission from heated dust) is identical between both samples.

## 3. SUBMILLIMETER PHOTOMETRY

We have performed SCUBA photometry at 450 and 850 $\mu$m (Page et al. 2001b, Page et al. 2004, Stevens et al. 2005) of both samples of objects, finding that 8 out of 19 absorbed QSO were detected at $3\sigma$ in 850 $\mu$m (all at $z > 1.5$), while only 1 of the 20 unabsorbed QSOs was detected (Fig. 1). This difference is significant at $> 3\sigma$, increasing to $> 4\sigma$ if only $z > 1.5$ sources are considered. This difference is completely at odds with the unified models. There must be some physical relationship between the absorbed nature of some of the QSOs and their submm emission.

We have calculated the FIR luminosity of these objects from their observed submm flux using the SED of Mrk 231 (a nearby X-ray abs. Ultra Luminous Infrared Galaxy -ULIRG-) as a template. With this recipe, all the detected absorbed QSO are ULIRG. But, what is the origin of this FIR emission? Could it be due to dust heated by the QSO?

To answer this question, we have also estimated the bolometric luminosities of the QSO, scaling from their soft X-ray luminosities using the QSO template from Elvis et al. (1994). In four of our submm detected absorbed QSO the FIR emission is larger than their bolometric QSO luminosities, in three other objects it is greater than fifty percent, and in the last one it is around thirty percent (Stevens et al. 2005). We conclude then that most of their FIR emission must come form dust heated by starburst

Their detection as strong X-ray and FIR emitters shows that these objects are building up simultaneously their stellar populations and their central SMBH. The deduced star formation rate (Kennicut 1998) is higher than 1000 $M_\odot$/y, sufficient to build a substantial fraction of a galaxy spheroid in only a few 100 Myr.

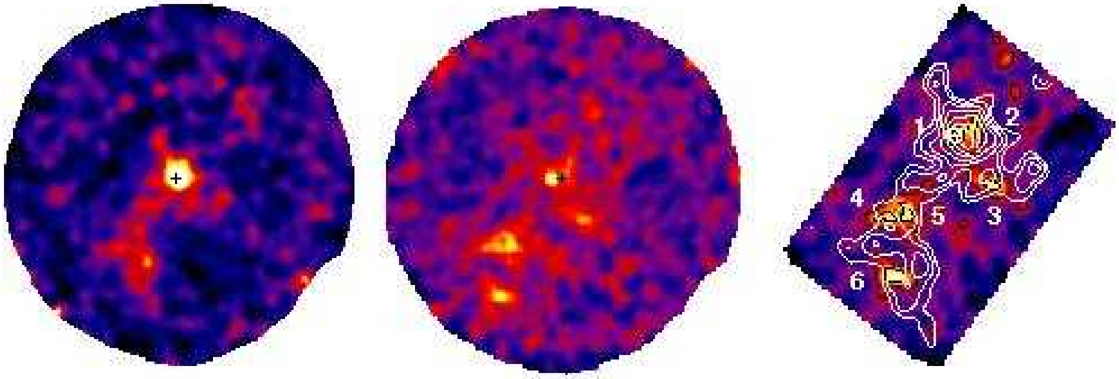


*Figure 2. Submillimeter imaging of the field around RX J094144.51+385434.8. The left-hand panel shows the SCUBA 850 $\mu$m image (diameter ~150", resolution 14.8"). The middle panel shows the corresponding 450 $\mu$m image (diameter ~120", resolution 8.5"). The right-hand panel shows a signal-to-noise image (1.5'×1.0') at 450 $\mu$m (greyscale with black contours at 2, 3, 4 and 5$\sigma$) overlayed with the 850 $\mu$m signal-to-noise contours at 2, 3, 4, 5, 6, 7 and 8$\sigma$. The optical position of the QSO is marked with a cross on the left-hand and middle panels.*

In addition, we have only detected absorbed QSO as submm sources at $z > 1.5$, it is then interesting to check whether they also show significantly higher star formation rates at higher redshifts as radiogalaxies (Archibald et al. 2001). In the full sample of absorbed QSOs both $L_{\rm FIR}$ and $L_{\rm X}$ are correlated with $z$, and between them. If we pick up a subsample of absorbed QSO with $44.5 \leq \log L_{\rm X}({\rm erg/s}) \leq 45$, over which their $\log L_{\rm X}$ is not correlated to $z$ (Stevens et al. 2005), $L_{\rm FIR}$ is still correlated with $z$, but not with $L_{\rm X}$. Therefore, X-ray absorbed QSOs had higher FIR luminosities (and hence star formation rates) in the past.

## 4. THE ENVIRONMENTS OF THE ABSORBED QSOS

As part of an ongoing programme to obtain SCUBA submm imaging in regions (~2 arcmin diameter) around our submm-brighter absorbed QSO, we have found strong overdensities of submm sources around two of them: RX J094144.41+385434.8 (Stevens et al. 2004) and RX J121803.82+470854.6 (Stevens et al., in preparation).

The sky density of submm sources around the first one is $1.4 \pm 0.6$ arcmin$^{-2}$, an order of magnitude higher than in empty fields (Smail et al. 2002), with a probability of a chance superposition of field objects of $\sim 10^{-7}$. This provides very strong evidence that the companion galaxies lie at the same redshift and in the same structure as the QSO. If this were the case, the chain of six submm sources detected in this field would form a ~400 kpc long filament. Each one of them would be itself an ULIRG producing stars at a rate sufficient to build a massive spheroid in less than a Gyr. Some of these sources present complex submm morphologies, indicative of major mergers. Very few of them are detected in X-rays, so they must be heavily obscured if they contain AGN.

We have obtained multiwavelength imaging around those two (and other) QSOs, including $R$, $i$, $J$, $K$ and *Spitzer* 4.5 $\mu$m, 8 $\mu$m and 24 $\mu$m images. We are still analysing them to get photometric redshifts for the detected optical/IR sources, and hence decide which are the most likely counterparts to the submm sources, and to look for structure at the redshift of the central QSO (Ebrero et al. 2006, in preparation). The galaxies closer to the submm sources are mostly faint EROs with $K \geq 19$ and $R > 24$ (Stevens et al. 2004). In Fig. 3, we show $K$ and 450 $\mu$m SNR contours over *Spitzer* 4.5 and 8 $\mu$ images, showing that some of the submm sources have *Spitzer* but no $K$-band counterparts. This probably means that the corresponding galaxies are highly dusty and heavily obscured, contain buried AGN, or both.

## 5. *XMM-NEWTON* OBSERVATIONS

We have so far *XMM-Newton* AO-4 data for three of our absorbed QSOs. Preliminary analysis of the coadded MOS+pn spectra (Page et al. 2006, this volume) show that they can be fit by flat simple powerlaws ($\Gamma \sim 1.4$), much flatter than the "canonical" $\Gamma = 2$ AGN slope (Mateos et al. 2005). Cold absorption of a canonical spectrum is rejected for two of them, while ionized absorbers with that slope, $\log \xi \sim 2$ and column densities $\sim 10^{22.5} - 10^{23.5}$ cm$^{-2}$ are acceptable fits. With these conditions, the absorbers probably originate within the AGN.

Dust (responsible for the optical and UV extinction) would not survive in such ionized X-ray absorbers, solving thus the apparent contradiction between the presence

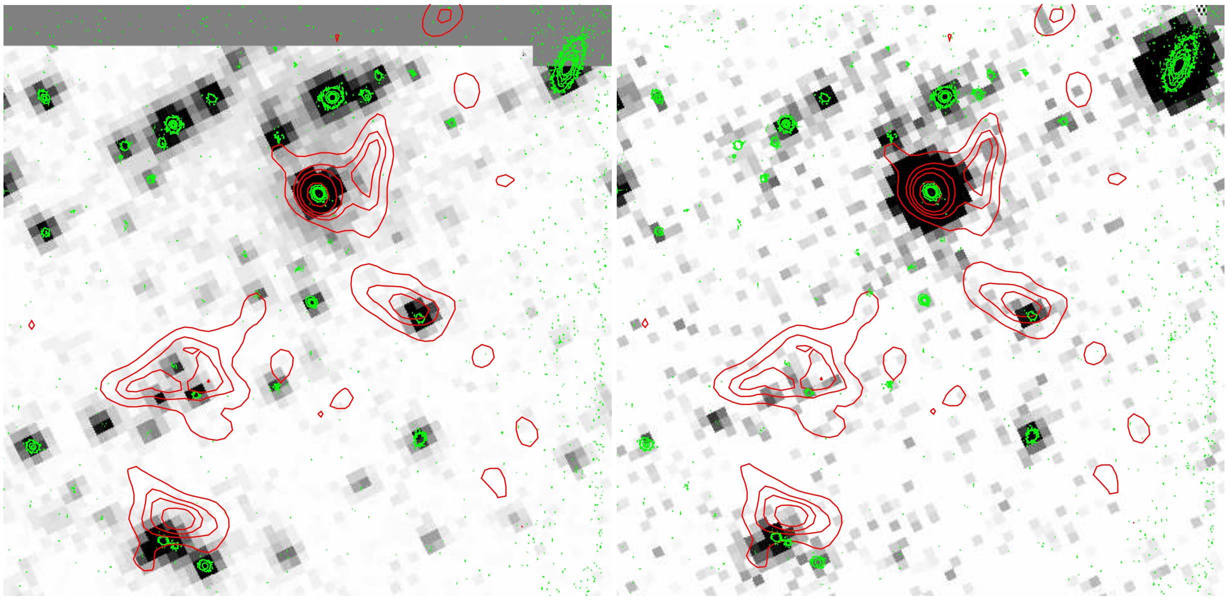

*Figure 3.* **Left***: Spitzer 4.5 $\mu$m image ($\sim (1')^2$) with $K$ (green -light in greyscale-) and 450 $\mu$m (red -dark-, 2, 3, 4, 5$\sigma$) contours.* **Right***: Spitzer 8 $\mu$m image (scale and contours are the same as in the left panel).*

of broad optical/UV lines and strong X-ray absorption within the unified model for AGN (see Page et al. 2006 for a longer discussion).

## 6. DISCUSSION AND CONCLUSIONS

We have found that X-ray absorbed QSO are strong FIR emitters, while unabsorbed QSOs are not. We have shown that the FIR emission must come from star formation, implying that unabsorbed QSO hosts are already formed, while absorbed QSOs are still actively forming stars. At the same time, the BH masses deduced from the X-ray luminosities of the absorbed QSOs are $> 10^8$ M$_\odot$, showing that their BH are already relatively mature. From the relative densities of absorbed and unabsorbed QSOs we infer (Page et al. 2004) that the duration of the absorbed phase is $\sim$15% of the duration of the unabsorbed phase. Finally, there is merger-induced activity in (and around) some of our absorbed QSOs, which seem to inhabit high-density regions of the Universe.

From the above, plus the fact that star formation in absorbed QSOs was stronger in the past, we conclude that the absorbed phase must precede the unabsorbed phase, and star formation and mergers must have something to do with it.

This can be interpreted as an evolutionary sequence within a joint spheroid/QSO evolution in a hierarchical clustering scenario (see Fig. 4, Granato et al. 2004, Silk & Rees 1998, Fabian 1999, Di Matteo et al. 2005): the more massive dark matter halos collapse earlier, giving rise to collisions and mergers, which channel material to the center, triggering star formation and feeding the central BH. This material obscures strongly the optical, UV and X-ray emission, while the heated dust emits FIR radiation which escapes unimpeded.

As star formation progresses, the FIR emission increases, reaching ULIRG luminosities, at which stage these sources could be the bulk of the submm galaxy population discovered by SCUBA (Smail et al. 1997). At the same time the BH keeps growing, reaching Seyfert-like X-ray luminosities (like the objects detected by Alexander et al. 2005, and discussed by Borys et al. 2005), with signatures of buried AGN in their optical spectra (Chapman et al. 2003).

Still forming stars vigorously, the central BH of these objects will eventually reach QSO luminosities. The QSO radiation and star formation processes start sweeping out circumnuclear material, reducing gradually the absorption and the rate of star formation, and giving rise to properties very similar to our absorbed QSOs, or BAL QSOs in slightly later stages (Fabian 1999).

Eventually, the bulk of the circumnuclear material is swept away, leaving a fully grown naked QSO “living off the rents”, with a passively evolving stellar population, like the “standard” unabsorbed QSOs. Eventually the QSO exhausts its fuel reservoir, leaving a dormant SBMH in the center of a “normal” galaxy, like the ones seen in the local Universe.

## REFERENCES

[1] Alexander D., et al., 2005, Nat, 434, 738

[2] Archibald E.N., et al., 2001, MNRAS, 323, 417

[3] Blain A., Longair M., 1993, MNRAS, 264, 509

[4] Borys C., et al., 2005, ApJ, in press (astro-ph/0507610)

[5] Chapman S.C., et al., 2003, Nat, 422, 695

[6] Ciliegi P., et al., 1995, MNRAS, 277, 1463

[7] Di Matteo T., et al., 2005, Nat, 433, 604

[8] Elvis M., et al., 1994, ApJS, 95, 1

[9] Fabian A.C., 1999, MNRAS, 308, L39

[10] Fabian A.C., et al., 1998, MNRAS, 297, L11

[11] Fabian A.C., Iwasawa K., 1999, MNRAS, 303, L34

[12] Gilli R., et al., 2001, A&A, 366, 407

[13] Granato G.L., et al., 2004, ApJ, 600, 580

[14] Kennicut R.C., Jr, 1998, ApJ, 498, 541

[15] Mateos S., et al., 2005, A&A, 433, 855

[16] Merritt D., Ferrarese L., 2001, MNRAS, 320, L30

[17] Miyaji T., et al., 2001, A&A, 369, 49

[18] Page M.J., et al., 1997, MNRAS, 291, 324

[19] Page M.J., et al., 2001a, MNRAS, 325, 575

[20] Page M.J., et al., 2001b, Science, 294, 2516

[21] Page M.J., et al., 2004, ApJ, 611, L85

[22] Rowan-Robinson M., 2000, MNRAS, 316, 885

[23] Sanders D.B., Mirabel F., 1996, ARA&A, 34, 749

[24] Silk J., Rees M., 1998, A&A, 331, L1

[25] Silverman et al., 2005, ApJ, 624, 630

[26] Smail I., et al., 1997, ApJ, 490, L5

[27] Smail I., et al., 2002, MNRAS, 331, 495

[28] Stevens J., et al., 2004, ApJ, 604, L17

[29] Stevens J., et al., 2005, MNRAS, 360, 610

[30] Yu Q., Tremaine S., 2002, MNRAS, 335, 965

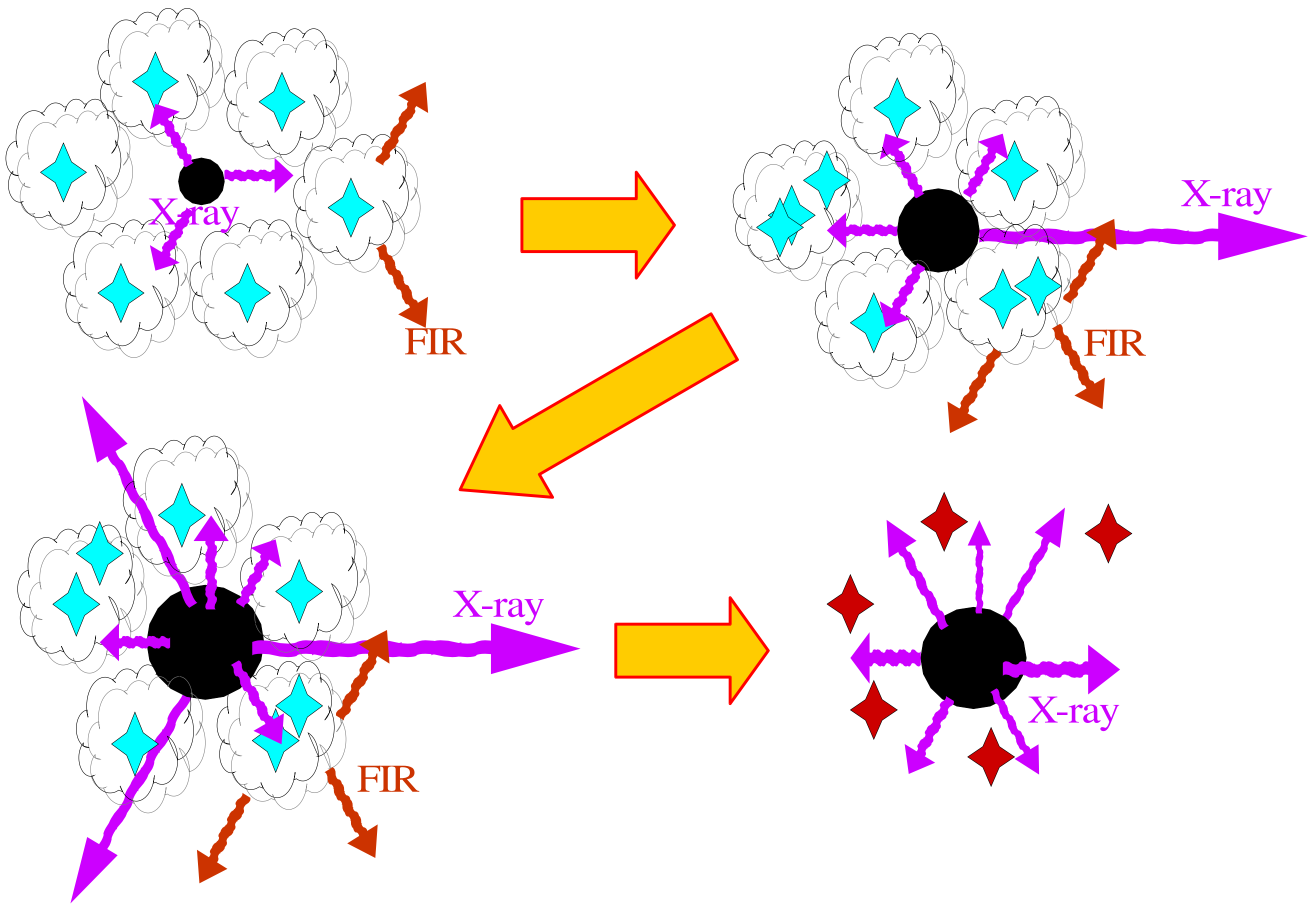


*Figure 4. Joint spheroid/QSO evolutionary sequence:* **Top-left***: Heavily obscured growth of BH, with strong star formation emitting in FIR.* **Top-right***: Star formation reaches ULIRG luminosities, while SMBH reaches Sy-like luminosities, still heavily obscured.* **Bottom-left***: Obscured QSO-like luminosities of SMBH and strong star formation (our absorbed QSO).* **Bottom-right***: Most of the circumnuclear material is swept away, leaving a naked QSO with passively evolving spheroid (standard unabsorbed QSO), which eventually becomes a "normal" galaxy with a SMBH in its centre.*

# TYPE II QUASARS IN THE MOST LUMINOUS GALAXIES

**K. Iwasawa**

Institute of Astronomy, Madingley Road, Cambridge CB3 0HA, UK

## ABSTRACT

An X-ray investigation of Type II active nuclei hosted in the hyperluminous infrared galaxies (HLIGs) is presented. Two classical HLIGs discovered in the IRAS survey, IRAS 09104+4109 and IRAS F15307+3252, are found to share many properties: 1) The active nuclei are absorbed by Compton-thick obscuring matter, and powered by well-grown (billions solar mass) black holes; 2) The large infrared luminosity appears to be due to hot/warm dust heated by the hidden active nuclei; 3) Both galaxies resides in a rich environment and are very luminous. In comparison, the HLIGs might be fundamemntally different from the local lower luminosity counterparts, ultra-luminous infrared galaxies (ULIGs) in their formation. The rich environment suggests that it could be a necessary condition to form the most luminous quasars, and their relation to high redshift radio galaxies is discussed briefly.

Key words: LaTeX; ESA; X-rays.

## 1. INTRODUCTION

The hierarchical assembly in a cold dark matter halo and the apparent relation between massive black holes and their host galaxy spheroids predicts that most luminous quasars (or most massive black holes) would reside in a rich environment such as a galaxy cluster.

It is expected that the early growth of a massive black hole occurs in a dense gaseous environment where star formation is likely to take place at the same time. An active nucleus powered by such a black hole will therefore be observed as an obscured (or Type II) active nucleus. In this context, Type II quasars are part of the evolutionary phase of massive black holes, followed by the optical quasar phase after blowing away the obscuring material (e.g., Sanders etal 1988). On the other hand, as in the unification scheme for the two types of Seyfert galaxies (e.g., Antonucci & Miller 1985), the orientation effect may make a quasar nucleus to manifest itself as a Type II quasar if there are dense clouds in a toroidal form lying along the line of sight.

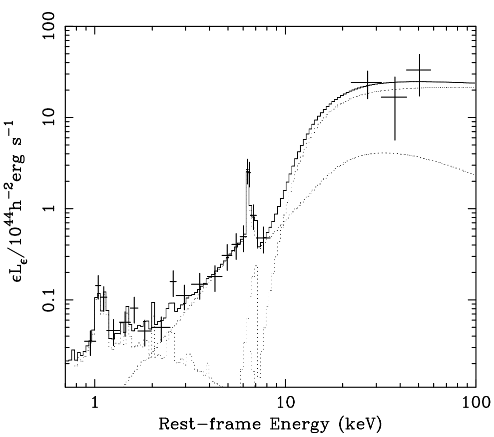


*Figure 1. The energy distribution of IRAS 09104+4109 in the X-ray band derived from the Chandra and BeppoSAX observation. The unresolved nuclear component is plotted in the Chandra bandpass. The energy scale has been corrected for the galaxy redshift.*

We take hyper-luminous infrared galaxies (HLIGs) with infrared luminosities in excess of $10^{13} L_\odot$ as a sub-class of the most luminous galaxies, and investigate the Type II quasars contained in them in relation with the galaxies themselves and their environments. The X-ray results on the two classical, IRAS-selected HLIGs, IRAS 09104+4109 ($z = 0.44$) and IRAS F15307+3252 ($z = 0.93$), and their remarkable similarities are discussed in detail. For calculating luminosities, we adopt the currently popular cosmology with $H_0 = 70$ km s$^{-1}$ Mpc$^{-1}$, $\Omega_{\rm M} = 0.27$ and $\Omega_\Lambda = 0.73$.

## 2. X-RAY DATA

### 2.1. IRAS 09104+4109

This HLIG has been known to be the central galaxy of a rich cluster at $z = 0.44$ since its discovery (Kleinmann

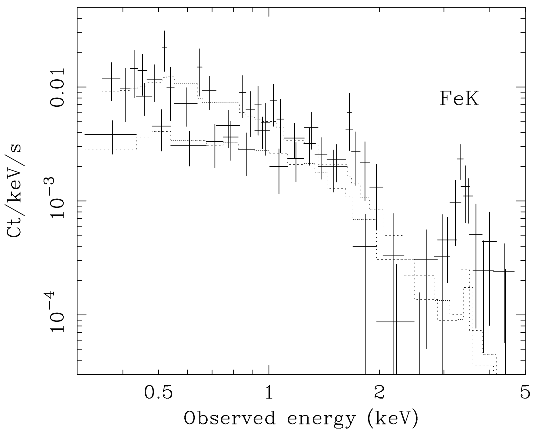


*Figure 2. The X-ray spectrum of IRAS F15307+3252 obtained from the XMM-Newton EPIC cameras (the pn and MOS data are plotted separately). The soft X-ray emission is probably due to the extended cluster emission while the emission peaking in the 3–4 keV band is mostly due to Fe K$\alpha$.*

et al 1988). Extended thermal X-ray emission due to the intracluster medium (ICM) has been imaged by ROSAT (Fabian & Crawford 1995) and the Chandra X-ray Observatory (Iwasawa et al 2001). The ICM has a virial temperature of $kT \simeq 7$ keV with a cooling core of which temperature drops to 2-3 keV towards the cluster centre. The bolometric luminosity of the cluster medium $3\times10^{45}$ erg s$^{-1}$ makes IRAS 09104+4109 one of the most luminous clusters (Allen 2000). The point-like active nucleus is hard in X-ray colour and resolved only with Chandra. The spectrum of the nucleus is characterized by a strong Fe K$\alpha$ emission at 6.4 keV, and together with the hard X-ray detection with the BeppoSAX PDS (Franceschini et al 1999), indicates a Compton thick nucleus (Fig. 1). The absorption-corrected 2–10 keV luminosity is estimated to be $\times10^{45}$ erg s$^{-1}$. With a bolometric correction appropriate for quasars (e.g., Elvis et al 1994), the obscured active nucleus is likely to power most of the bolometric luminosity of this galaxy.

### 2.2. IRAS F15307+3252

The first X-ray detection from this more distant ($z = 0.926$; Cutri et al 1994) galaxy was made with XMM-Newton (Iwasawa et al 2005, and the details are therein) following no detection with the previous X-ray telescopes (Fabian et al 1996; Ogasaka et al 1997). While the data collected from total exposure times of 21 ks and 33 ks from the EPIC pn and MOS detectors, respectively, from three observations are still noisy, they show clear detection of soft X-ray emission up to 2 keV and strong Fe K$\alpha$ emission, redshifted to the 3–4 keV band (Fig. 2). The photometric study combining the both EPIC cameras shows a drop-out in the 2–3 keV band and $4\sigma$ detection in the observed 5–10 keV band (Fig. 3). The Fe K line infers reflection from cold matter.

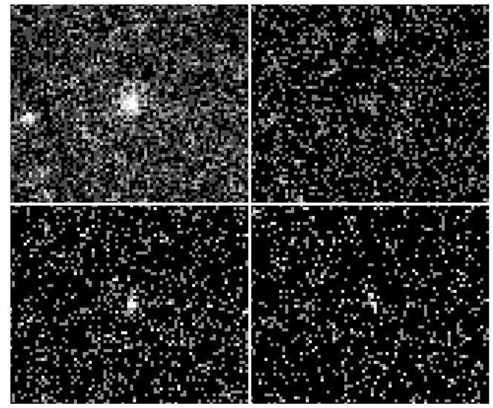

*Figure 3. The X-ray images of IRAS F15307+3252 in the four energy bands, clockwise from upper left: 0.5–2, 2–3, 5–10 and 3–4 keV. The size of the each image is $5 \times 4.5$ arcmin$^2$.*

In the absence of any transmitted emission from the central source, the central source is hidden behind an absorber with a column density larger than $10^{24}$ cm$^{-2}$. For the luminosity of the hidden source, we estimate the X-ray luminosity required to produce the Fe K luminosity $\approx 4 \times 10^{43}$ erg s$^{-1}$ through reflection from cold slab extending over $2\pi$ in solid angle. The value is $\geq 1 \times 10^{45}$ erg s$^{-1}$, which infers the bolometric luminosity of the active nucleus being at least a few times of $10^{46}$ erg s$^{-1}$. This estimate suggests that a significant fraction of the total luminosity can be attributed to the hidden active nucleus.

An unexpected but possibly important finding is an extension of the soft X-ray emission. The image at energies below 2 keV is significantly broader than the point spread function and its intrinsic extension is $21\pm5$ arcsec in FWHM, corresponding to 85 kpc in radius at the distance of the galaxy. Fitting a thermal emission model to the spectrum below 2 keV gives a temperature of $2.1^{+0.6}_{-0.4}$ keV. The bolometric luminosity of this component is estimated to be $1 \times 10^{44}$ erg s$^{-1}$. These values lie on the $L$-$T$X relation of galaxy clusters (e.g., Fukazawa et al 2004). Combinied with the large source extent, the soft X-ray emission may well be due to ICM of a poor cluster. The optical image of the region around the HLIG shows some evidence of galaxy overdensity (Fig. 4).

## 3. DISCUSSION

### 3.1. Common properties

The previous optical spectropolarimetry have already revealed a hidden broad-line regions both in IRAS 09104+4109 and IRAS F15307+3252 (Hines et al 1995). The hidden active nuclei are found to be both Compton thick by the X-ray observations, and they are likely to dominate the energetics of these HLIGs. Their black hole masses are estimated to be $3 \times 10^9 M_{\odot}$ and $1.3 \times 10^9 M_{\odot}$, respectively, using the MgII widths seen in the polarized light and the UV luminosities (McLure & Jarvis 2002). They are efficiently accreting at a large fraction of the Eddington limit. The radio sources are moderately powerful in both galaxies and most likely associated with the active nuclei (Kleinmann et al 1988; Hines & Wills 1993; Drake et al 2003).

The optical images of the two galaxies show well-developed spheroids of a giant elliptical with evidence of minor mergers which lead to the somewhat disturbed morphology (Fig. 5). They are quite luminous in optical (e.g., $M_{\rm I} = -26.4$ for F15307, Farrah et al 2002) compared to the average quasar hosts. There is little evidence for a large reservoir of cold gas, as suggested by no detection of CO (Evans et al 1998; Yun & Scoville 1998) and no detection with SCUBA (Deane & Trentham 2001). This means that a gaseous/dusty condition envisaged for forming galaxies such as high-$z$ SCUBA sources does not apply, and the large X-ray absorbing column and the high accretion onto the black holes are supplied by the gas at small radii in the nuclear region rather than cold gas distributed on the galactic scale. Such cold gas has perhaps been exhausted already after forming stars and/or been expelled by mechanical outflow from the central active nucleus. Cold dust with a temperature around 40 K, typically found in star-forming local ULIGs, are not present in large amount in these galaxies (Deane & Trentham 2001). The dust reradiation responsible for the luminous infrared emission is predominantly due to hot dust, presumably heated by the hidden active nucleus, which peaks in the mid infrared band.

P09104+4109 has been considered peculiar among luminous infrared galaxies, being the central galaxy of a rich cluster, since local ULIGs do not usually reside in a rich environment (Sanders & Mirabel 1996). However, if the possible poor cluster around F15307+3252 suggested by the extended X-ray emission is confirmed, the two earliest examples of HLIGs are found to be in a cluster environment. This means that they are located in a massive dark matter halo, the masses of which are estimated to be in the range of $10^14M_{\odot}$ to $10^15M_{\odot}$ from the temperature-mass relation for clusters (e.g., Finoguenov et al 2001). The galaxies probably grew by the accretion of other galaxies in the respective dark matter halos, and they seem to have a well-grown black hole emitting at the quasar luminosity, as discussed above. In the absense of large amount of cold gas, the classification of Type II quasars is likely to be due to the orientation effect and the central sources are expected to be identical to normal (but powerful) quasars (e.g., Hines et al 1995).

Many pieces of evidence point to that the most massive ($\geq 10^9 M_{\odot}$) black holes are formed early ($z \geq 3$, Merloni 2004) probably behind heavy obscuration of dense gas. Both quasar activity and star formation in the universe peak at around $z = 2$ (e.g., Hasinger et al 2005), but the assembly of cluster central galaxies through hierarchical merging continues afterward. Since star formation induced by minor galaxy mergers does not appear

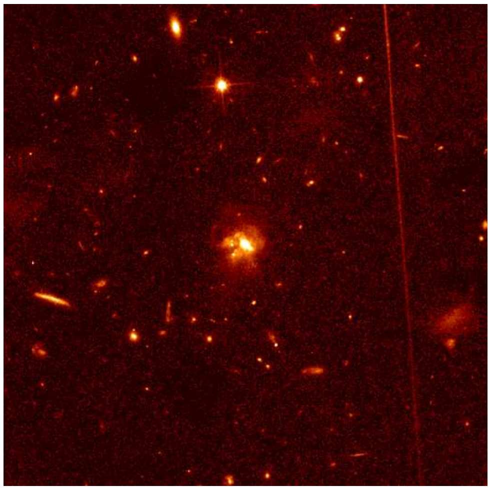

*Figure 4. The HST/ACS image of the $1 \times 1$ arcmin$^2$ region around IRAS F15307+3252, taken through the F814W filter (rest-frame blue). North is up and east to the left. A chain of small galaxies 11–15 arcsec ($\sim$ 100 kpc at $z = 0.93$) lies to the sourth of the IRAS galaxy, which is reminiscent of Markarian's chain of galaxies in the Virgo cluster.*

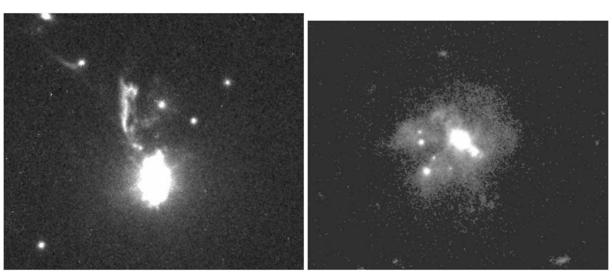

*Figure 5. Left: The HST WFPC2 image of IRAS 09104+4109 with the F814W filter. Right: The HST ACS image of IRAS F15307+3252 (zoom-up of Fig 4).*

to contribute significantly to the final mass of the central galaxies (e.g., Concelice et al 2001), it is expected in those systems that cold gas has been exhausted by vigorous star formation by $z \sim 2$ and the black hole has grown fully (to the mass of $\sim 10^9 M_\odot$) even before. Therefore, for the two HLIGs with $z \leq 1$ we studied, the observed common properties are in agreement with the above scenario.

At least these two HLIGs differ significantly from local ULIGs in all apsects of the massive black holes, galaxies, and environments, and they are probably fundamentally different in formation process. As seen in these cases, massive dark matter halo may be one of the necessary condition to produce the most luminous quasars (and also giant ellipticals). As previously suggested by, e.g., Genzel et al (2001), the local ULIGs will not evolve into such extremely luminous objects.

### 3.2. Relation to high-z radio galaxies

Radio galaxies found at high redshift are considered to be a sign post of massive dark matter concentration. Two radio galaxies at $z > 3$, B2 0902+34 ($z = 3.4$) and 4C+41.17 ($z = 3.8$), which are found to be HLIGs (Huges, Dunlop & Rawlkings 1997; Rowan-Robinson 2000), have been detected in X-ray (Fabian et al 2002; Scharf et al 2003). They are, of course, powerful radio sources. While no clear galaxy overdensity is observed, large rotation measure is observed in both objects. Since strong Faraday rotation is often associated with nearby, strong cooling flow clusters (e.g., Carilli 1995), they might be in a proto-cluster. Unlike P09104+4109 and F15307+3252 at lower redshift, evidence for large amount of cold gas have been reported for both galaxies. At this high redshift, the central black hole may be still in its growth phase, and its activity is of great interest. As shown in Table 1, while they show similar infrared luminosities, observed X-ray luminosities of their nuclei are vastly different: the active nucleus of B2 0902+34 shows strong absorption in the X-ray spectrum, but the quasar luminosity in the X-ray band suggests that a efficiently accreting $10^9 M_\odot$ black hole is already in place in this object (Fabian et al 2002). The weak X-ray nucleus in 4C+41.17 indicates that, if a similarly massive black hole is present, the accretion mode must be radiatively inefficient, most likely dominated by jets. Besides the black hole growth, as proposed by Churazov et al (2005) as in the galactic black hole sources, switching between the two different accretion modes may be occuring in the course of black hole evolution, for which a statistical study will be required to investigate it quantitatively.

## ACKNOWLEDGMENTS

PPARC is thanked for support.

*Table 1. Infrared-Hyperluminous radio galaxies. $*$The absorption-corrected nuclear luminosities.*

| Galaxy | $z$ | log $L_{\rm IR}$ | log $L_{\rm X}^*$ |
|---|---|---|---|
| B20902+34 | 3.4 | 46.74 | 45.60 |
| 4C+41.17 | 3.8 | 46.97 | 43.95 |

## REFERENCES


[1] Allen S.W., 2000, MNRAS, 315, 269

[2] Antonucci R.R.J., Miller J.S., 1985, ApJ, 297, 621

[3] Carillie, C.L., 1995, A&A, 298, 77

[4] Conselice, C.J., Gallaghaer, J.S. III, Wyse, R.F.G., 2001, AJ, 122, 2281

[5] Cutri R.M., Huchra J.P., Low F.J., Brown R.L., van den Bout P.A., 1994, ApJ, 424, L65

[6] Churazov E., Sazonov S., Sunyaev R., Forman W., Jones C., Böhringer H., 2005, MNRAS, 363, L91

[7] Deane J. R., Trentham N., 2001, MNRAS, 326, 1467

[8] Drake C.L., McGregor P.J., Dopita M.A., van Breugel W.J.M., 2003, AJ, 126, 2237

[9] Elvis M., et al, 1994, ApJS, 95, 1

[10] Evans A. S., Sanders D. B., Cutri R. M., Radford S. J. E., Surace J. A., Solomon P. M., Downes D., Kramer C., 1998, ApJ, 506, 205

[11] Fabian A.C., Crawford C.S., 1995, MNRAS, 274, L63

[12] Fabian A. C., Cutri R. M., Smith H. E., Crawford C. S., Brandt W. N., 1996, MNRAS, 283, L95

[13] Fabian A.C., Crawford C.S., Iwasawa K., 2002, MNRAS, 331, L57

[14] Farrah D., Verma A., Oliver S., Rowan-Robinson M., McMahon R., 2002, MNRAS, 329, 605

[15] Finoguenov, A., Reiprich, T.H., Böhringer, H., 2001, A&A, 368, 749

[16] Franceschini A., Bassani L., Cappi M., Granato G. L., Malaguti G., Palazzi E., Persic M., 2000, A&A, 353, 910

[17] Fukazawa Y., Makishima K., Ohashi T., 2004, PASJ, 56, 965

[18] Genzel, R., Tacconi, L.J., Rigopoulou, D., Lutz, D., Tecza, M., 2001, ApJ, 563, 527

[19] Hasinger, G., Miyaji, T., Schmidt, M., 2005, A&A, 441, 417

[20] Hines D. C., Schmidt G. D., Smith P. S., Cutri R. M., Huchra J.P., Low F.J., 1995, ApJ, 450, L1

[21] Hines D.C., Wills B.J., 1993, ApJ, 415, 82

[22] Hughes, D.H., Dunlop, J.S., Rawlings, S., 1997, MNRAS, 289, 766

[23] Iwasawa K., Fabian A. C., Ettori S., 2001, MNRAS, 321, L15

[24] Kleinmann S. G., Hamilton D., Keel W. C., Wynn-Williams C. G., Eales S. A., Becklin E. E., Kuntz K. D., 1988, ApJ, 328, 161

[25] McLure R. J., Jarvis M. J., 2002, MNRAS, 337, 109

[26] Merloni, A., 2004, MNRAS, 353, 1035

[27] Ogasaka Y., Inoue H., Brandt W. N., Fabian A. C., Kii T., Nakagawa T., Fujimoto R., Otani C., 1997, PASJ, 49, 179

[28] Rowan-Robinson M., 2000, MNRAS, 316, 885

[29] Sanders D. B., Soifer B. T., Elias J. H., Madore B. F., Matthews K., Neugebauer G., Scoville N. Z., 1988, ApJ, 325, 74

[30] Sanders D.B., Mirabel F.I., 1996, ARAA, 34, 749

[31] Scharf C., Smail I., Ivison R., Bower R., van Breugel W., Reuland M., 2003, ApJ, 596, 105

[32] Yun M. S., Scoville N. Z., 1998, ApJ, 507, 774

# OBSCURED AGN: CLUES FROM HIGH-RESOLUTION IMAGING AND SPECTROSCOPY

**Stefano Bianchi**[1], **Matteo Guainazzi**[1], **and Marco Chiaberge**[2]

[1]XMM-Newton Science Operations Center, ESAC, ESA, Apartado 50727, E-28080 Madrid, Spain
[2]Space Telescope Science Institute, 3700 San Martin Drive, Baltimore, MD 21218

**ABSTRACT**

We present a sample of 8 Seyfert 2 galaxies observed by *HST*, *Chandra* and XMM-*Newton*. All of the sources present soft X-ray emission which is coincident in extension and overall morphology with the [O III] emission. The spectral analysis reveals that the soft X-ray emission of all the objects is likely to be dominated by a photoionized gas. We tested with the code CLOUDY a simple scenario where the same gas photoionized by the nuclear continuum produces both the soft X-ray and the [O III] emission. Solutions satisfying the observed ratio between the two components exist, and require the density to decrease with radius roughly like $r^{-2}$, similarly to what often found for the Narrow Line Region.

Key words: galaxies: Seyfert - X-rays: galaxies.

## 1. THE SAMPLE

The sample consists of all the Seyfert 2 galaxies included in the Schmitt et al. (2003) catalog, with a *Chandra* observation, with the only exclusion of NGC 1068, which has already been extensively studied. On the other hand, we added another source, NGC 5643. All the sources have also an XMM-*Newton* RGS observation, except for NGC 5347.

## 2. ANALYSIS

### 2.1. Imaging

Figure 1 shows the contours of the *Chandra* soft X-ray emission superimposed on the *HST* [O III] images, for all the sources in our sample. The coincidence between the soft X-ray and [O III] emission is striking, both in the extension and in the overall morphology. Unfortunately, the lower spatial resolution of *Chandra* with respect to *HST* does not allow us to perform a detailed comparison of the substructures apparent in the latter.

### 2.2. Spectral analysis

The spectral analysis of the sources suggests that the most likely origin for the soft X-ray emission is in a gas photoionized by the nuclear continuum. In spectra with CCD resolution, a 'scattering' model (a powerlaw plus emission lines) is to be preferred to a 'thermal' model either on statistical grounds or because of unphysical best fit parameters of the latter (quasi-zero abundances). On the other hand, the RGS spectra are clearly dominated by emission lines, with a very low level of continuum (Fig. 3, 4, 5). This allows us to easily detect strong emission lines even in short observations of objects with relatively low fluxes. The clearest piece of evidence comes from the 190 ks combined RGS spectrum of Mrk 3, which is produced in a photoionized gas with an important contribution from resonant scattering.

The other spectra do not have enough statistics to allow us to draw unambiguous conclusions on any individual object. The predominance of the forbidden transition of the O VII triplet is a common feature of all spectra, except for NGC 5643. Deeper high-resolution observations of our sample will be able to confirm whether photoionization by the AGN is indeed the dominant mechanism responsible for the soft X-ray emission in these objects.

## 3. PHOTOIONIZATION MODELS

The spectral analysis of the sources in our sample suggests that their soft X-ray spectra are likely dominated by emission lines produced in a material photoionized by the central AGN. On the other hand, the striking resemblance of [O III] structures with the soft X-ray emission favors a common origin for both components. Therefore, since the NLR is generally believed to be also produced mainly by photoionization, we generated a number of models in

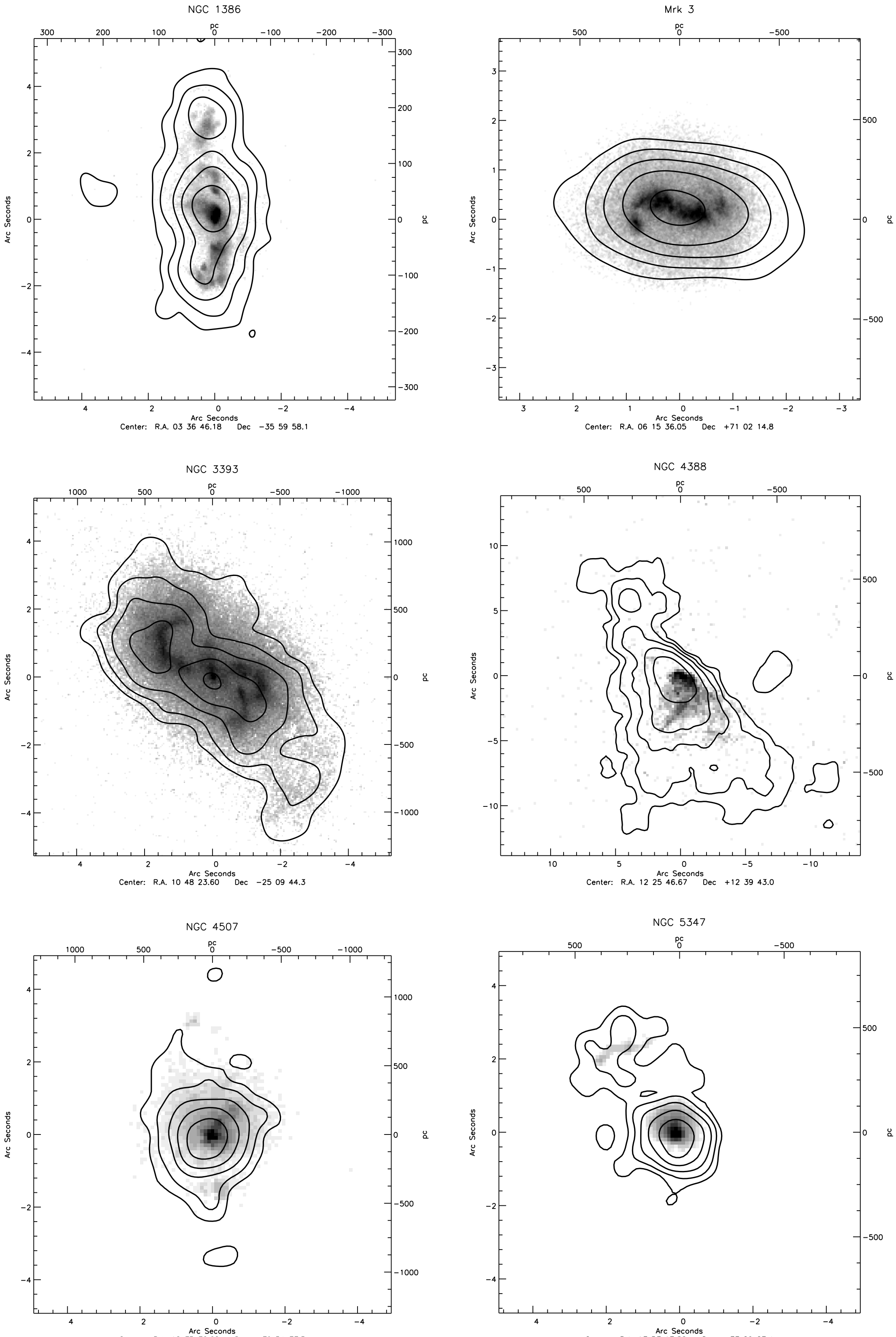


*Figure 1. Chandra soft X-ray contours superimposed on HST [O III] images. The contours correspond to five logarithmic intervals in the range of 1.5-50% (NGC 1386), 5-80% (Mrk 3), 5-90% (NGC 3393), 4-50% (NGC 4388), 0.5-50% (NGC 4507) and 2-50% (NGC 5347) of the peak flux. The HST images are scaled with the same criterion for each source, with the exception of NGC 4388 and NGC 4507, whose [O III] emission goes down to the 2% and the 0.1% of the peak, respectively.*

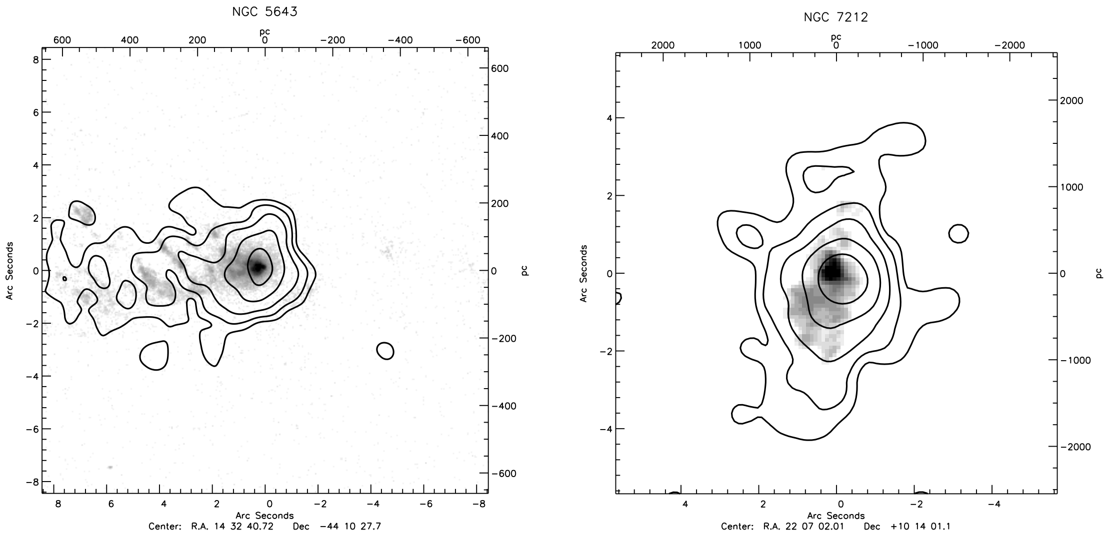


*Figure 2. Same of Fig. 1, but for NGC 5643 (8-80%) and NGC 7212 (1-50%). In the case of NGC 5643, the [O III] emission goes down to the 0.5% of the peak.*

order to investigate if a solution in terms of a single photoionized material to produce the optical NLR and the soft X-ray emission is tenable. Calculations were performed with version 96.01 of CLOUDY, last described by Ferland et al. (1998). The adopted model is represented by a conical geometry, which extends from 1 to 350 pc from the nucleus, with temperature set by photoionization equilibrium under a typical AGN continuum (Korista et al. 1997). We produced a detailed grid of models, as a function of the following parameters: ionization parameter $U$ of the illuminated face of the gas; filling factor of the gas $f$; density of the gas $n_e$. We assume a power-law radial dependence of the density, $n_e(r_0)\left(\frac{r}{r_0}\right)^{-\beta}$, with $\beta = 0$ (constant density) and varying between 1 and 2.4. We limit our models to a minimum total column density of $10^{20}$ cm$^{-2}$.

The ratio between the [O III] $\lambda5007$ line and the soft X-ray emission (defined as the total flux of the K$\alpha$ and K$\beta$ emission lines from N, O, Mg, S, Si in the range 0.5-2.0 keV) was calculated for each set of parameters. In the left panel of Fig. 6, each symbol represents a solution in the $U$ versus $n_e$ plane, where this ratio has a value within 2.8 and 11, as observed in our sample. Different symbols correspond to different values of $\beta$. The net effect of changing the filling factor is simply a shift of the solutions along the density axis, by a factor equivalent to the variation in $f$, thus reproducing the same total column density for each set of three parameters constituting a ‘good’ solution. The solutions occupy well-defined regions in the $n_e - U$ diagram, with those with lower $\beta$ being at larger values of ionization parameters.

The reason for this behaviour becomes clear inspecting the right panel of Fig. 6, where the [O III] to soft X-ray flux ratio is plotted as a function of the radius of the gas. Since $U \propto n_e^{-1} r^{-2}$, all density laws with $\beta < 2$ produce a gas with a ionization parameter decreasing along with the distance. In these cases ($\beta = 1.6$ and 1.8 in Fig. 6), most of the soft X-ray emission is produced in the inner radii of the cone, while the bulk of the [O III] emission is produced farther away, where the gas is less ionized. If $\beta = 2$, the ionization parameter remains fairly uniform up to large radii, so that the total observed ratio between [O III] and soft X-ray is constant with radius. Finally, if $\beta > 2$, the ionization parameter increases with radius, so most of the soft X-rays are actually produced at larger radii, while the [O III] emission line is mostly concentrated around the nucleus (cases $\beta = 2.2$ and 2.4 in Fig. 6). This is the reason why solutions with $\beta < 1.6$ and $\beta > 2.4$ are not plotted in Fig. 6, even if these exist, satisfying the overall [O III] to soft X-ray flux ratio. Their radial behaviour is radically different from what seen in Fig. 1 and 2, where both the [O III] and the soft X-ray emission are produced up to large radii. In particular, it is worth noting that constant-density solutions are totally unacceptable. A detailed analysis, as presented in Bianchi et al. (2005, submitted), suggests that the [O III] to soft X-ray flux ratio observed in the sources of our sample remains fairly constant up to large radii, thus requiring that the density decreases roughly like $r^{-2}$, similarly to what often found for the Narrow Line Region.

**REFERENCES**

Ferland, G. J., Korista, K. T., Verner, D. A., et al. 1998, PASP, 110, 761

Korista, K., Baldwin, J., Ferland, G., & Verner, D. 1997, ApJS, 108, 401

Schmitt, H. R., Donley, J. L., Antonucci, R. R. J., Hutchings, J. B., & Kinney, A. L. 2003, ApJS, 148, 327

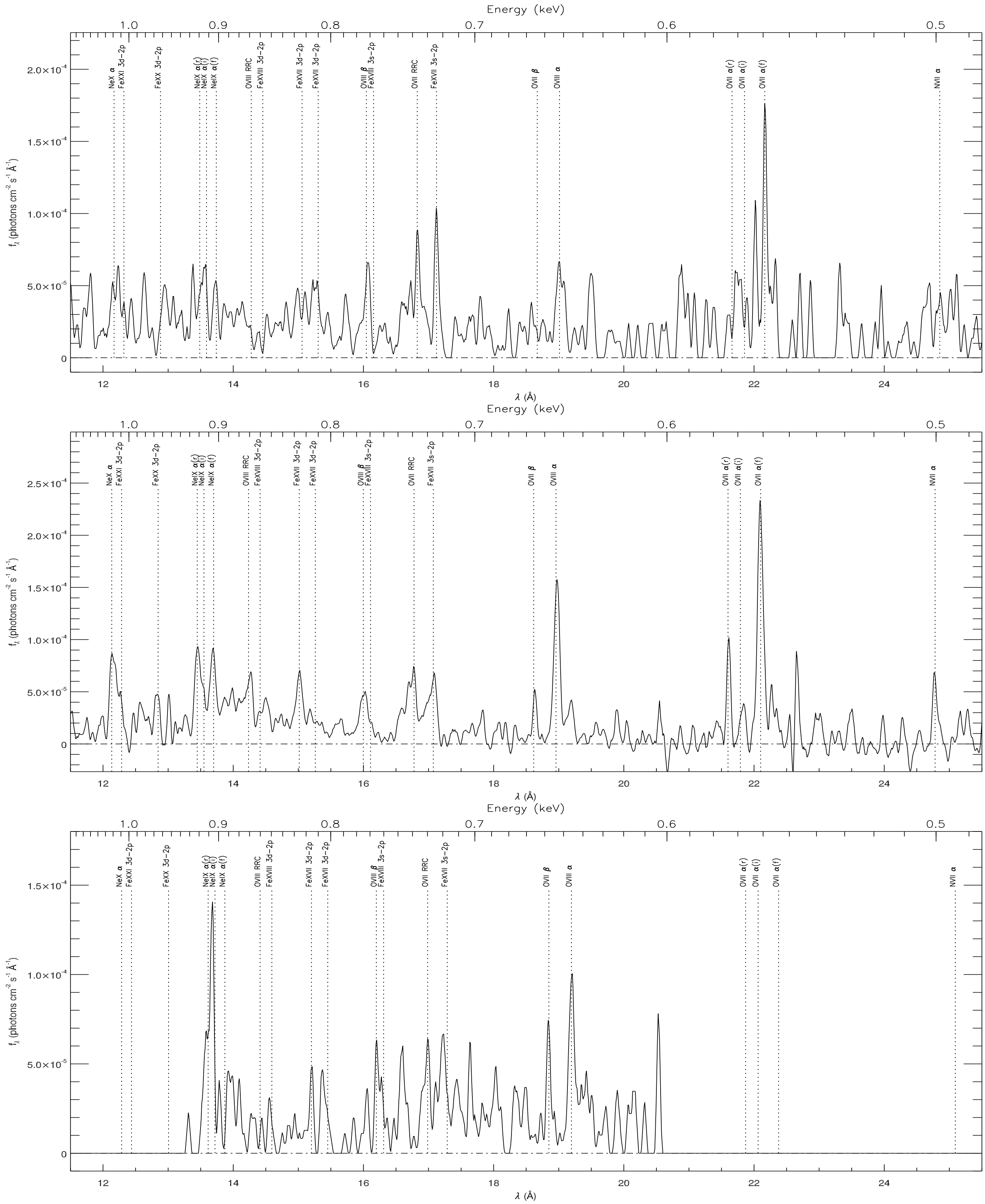


*Figure 3. Combined RGS1/RGS2 spectrum plotted in the rest frame of the source (12-25 Å), for NGC 1386 (17 ks, $F_{0.5-2\,\mathrm{keV}} = 1.8 \times 10^{-13}$ cgs), Mrk 3 (190 ks, 4.7) and NGC 3393 (14 ks, 2.2).*

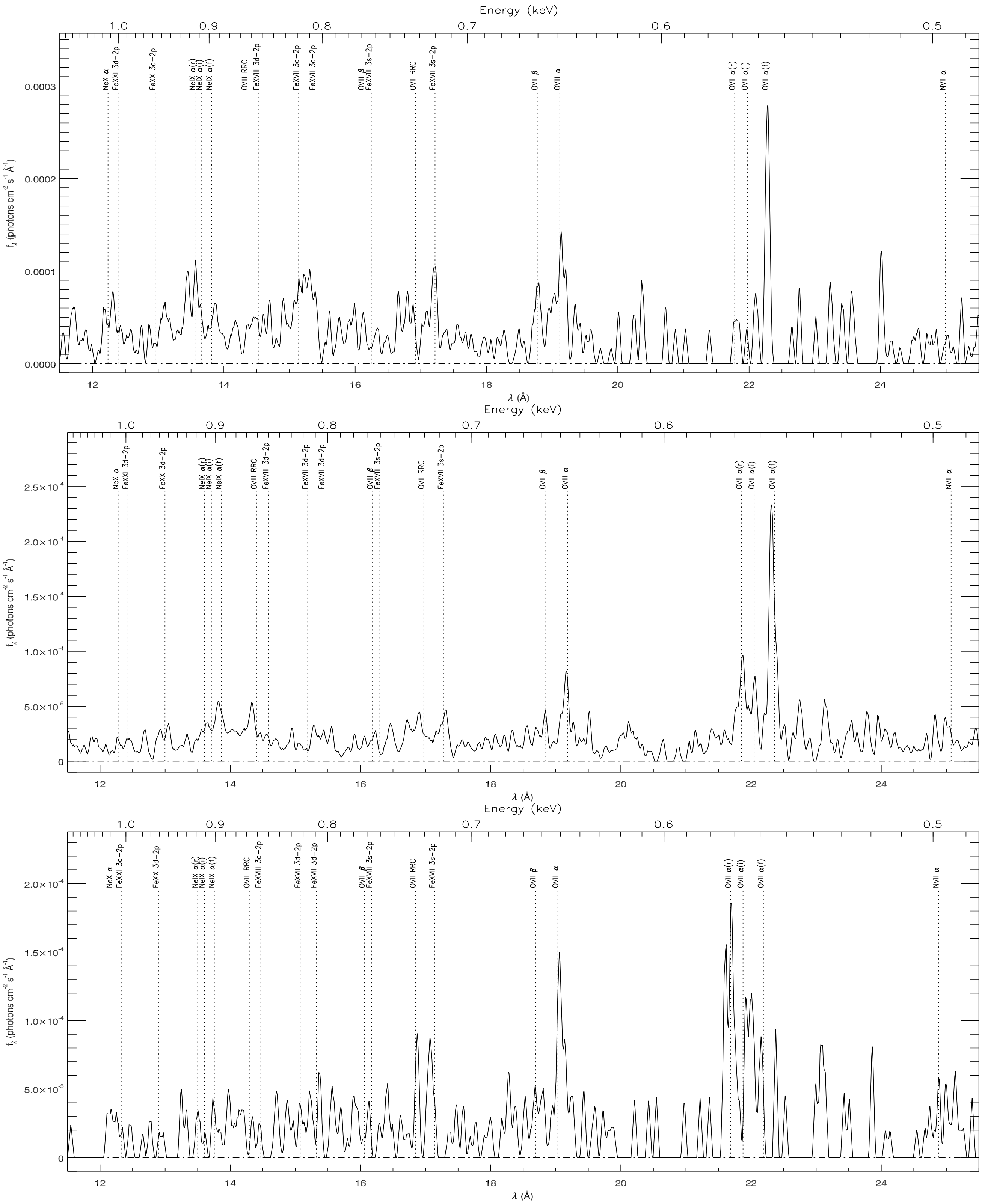


*Figure 4. Same as Fig. 3, for NGC 4388 (12 ks, 3.4), NGC 4507 (46 ks, 3.3) and NGC 5643 (10 ks, 1.4).*

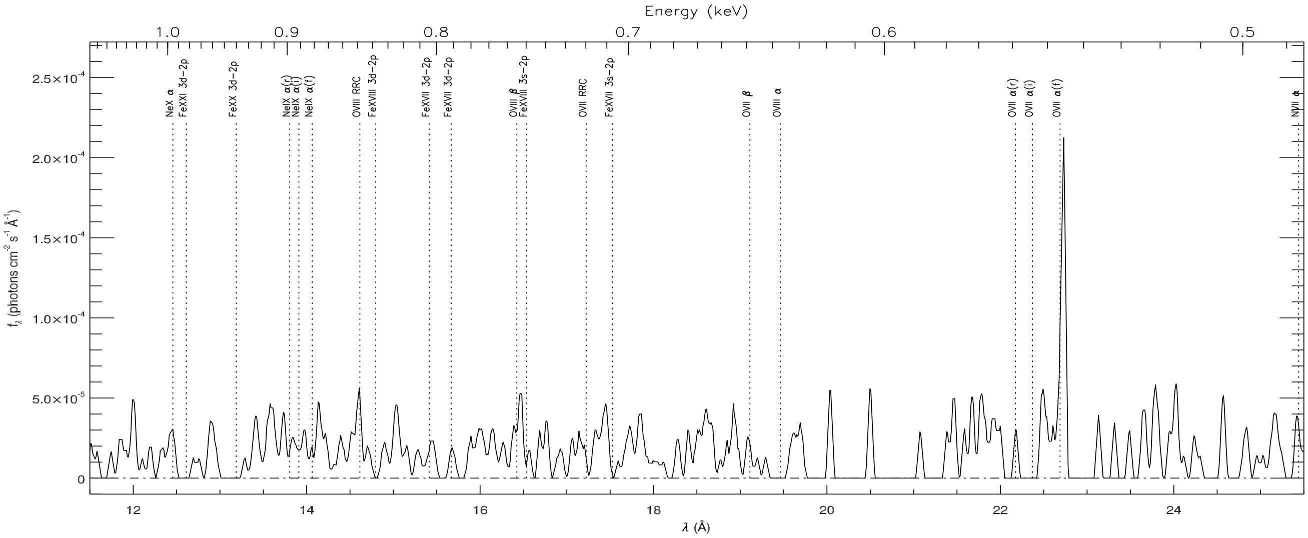


*Figure 5. Same as Fig. 3, for NGC 7212 (14 ks, 0.8).*

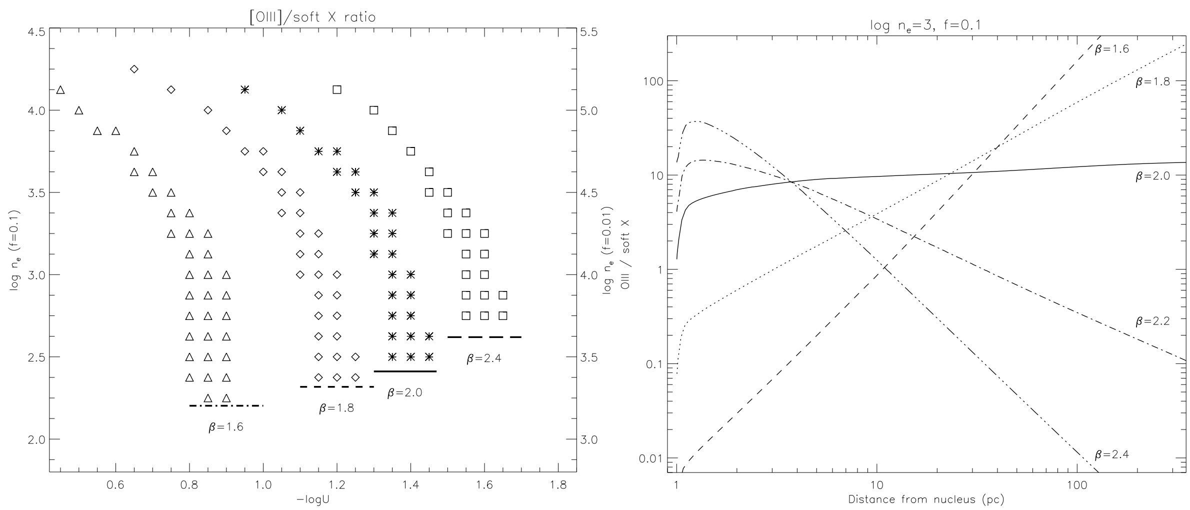


*Figure 6. Left: Each symbol represents one solution in our grid of* CLOUDY *models that satisfies the condition of total [O III] to soft X-ray flux ratio in the range observed in our sample, plotted in a three-parameter space $U$, $n_e$ and $\beta$, i.e. the ionization parameter and the density at the beginning of the cone of gas (1 pc), and the index of the density powerlaw, represented by different symbols (triangles: $\beta = 1.6$, diamonds: $\beta = 1.8$, stars: $\beta = 2.0$, squares: $\beta = 2.4$). The horizontal lines determine the limit corresponding to a total column density of $10^{20}$ cm$^{-2}$ for each index: solutions below this limit are not plotted. Solutions with $\beta = 2.2$ are not plotted for clarity reasons. The net effect of the filling factor $f$ is to shift the density values: the two y axes refer to $f = 0.1$ and $f = 0.01$ (see text for details). Right: The [O III] to soft X-ray ratio plotted as a function of the radius of the gas, for different values of $\beta$, when $\log n_e = 3$ and $f = 0.1$. The corresponding values of $\log U$ for these solutions are (from top to bottom): -0.85, -1.15, -1.4, -1.5, -1.6.*

# X–RAY EMITTING EROS AS TRACERS OF BLACK HOLES-GALAXIES COEVOLUTION

**M. Brusa**[1], **A. Comastri**[2], **E. Daddi**[3], **M. Mignoli**[2], **C. Vignali**[4], **G. Zamorani**[2], **F. Fiore**[5], **and L. Pozzetti**[2]

[1]Max Planck Institut für Extraterrestrische Physik, Garching bei München, Germany
[2]INAF-Osservatorio Astronomico di Bologna, Bologna, Italy
[3]National Optical Astronomical Observatory, Tucson, USA
[4]Dipartimento di Astronomia, Università di Bologna, Bologna, Italy
[5]INAF-Osservatorio Astronomico di Roma, Monteporzio, Italy

## ABSTRACT

The results from massive multiwavelength follow-up campaigns of X–ray sources discovered in both deep and shallow *Chandra* and XMM-*Newton* surveys have revealed a population of X-ray emitting Extremely Red Objects (X-EROs). We present the results obtained from the combined analysis of 80 ks XMM-Newton and 90 ks Chandra observations of a complete sample of optically selected EROs, with particular emphasys on the relationship between X-EROs and high luminosity, obscured quasars (QSO2). We also present several, independent findings indicating that a large fraction of X-EROs are hosted among the most massive galaxies at z=1-2, and thus can be used as lighthouses to investigate the link between the formation of massive ellipticals and the onset of AGN activity.

Key words: X–rays: surveys, galaxies: active, galaxies: Extremely Red Objects.

## 1. INTRODUCTION

Extremely Red Objects (EROs, R$-$K>5, Elston et al. 1988), initially detected in near–infrared ground–based imaging, have the colors expected for high-redshift passive ellipticals and have been used as tracers of distant (z$>1$) and old spheroids. Reproducing their observational properties has probed to be extremely challenging for all current galaxy formation models. However, on the basis of a number of observational results, it has been pointed out that high-redshift passive ellipticals are only one of the various classes of extragalactic sources which make up the ERO population. Deep VLT spectroscopy from the $K20$ `survey` (Cimatti et al., 2002) has indeed shown that EROs are nearly equally populated by old, passively evolving systems and dusty star–forming galaxies over a similar range of redshift ($z = 0.8 - 2$ for both classes) and similar results are confirmed by both colour selection criteria (Mannucci et al., 2002) and by radio observations (Smail et al., 2002). A few individual objects have been also identified as high redshift (z=1–1.5) Active Galactic Nuclei (AGN) on the basis of the detection of strong emission lines in near–infrared and/or optical spectra (see e.g. Pierre et al. 2001).
A population of optically faint X–ray sources without any obvious AGN signature in the optical spectrum and with optical to near–infrared colors typical of high redshift ellipticals and starburst galaxies has been revealed in the deepest *Chandra* and XMM–*Newton* exposures (e.g. Hasinger et al. 2001; Barger et al. 2003; Szokoly et al. 2004). It has been suggested that the AGN population among EROs has the same X–ray properties of high–luminosity, highly obscured (N$_H > 10^{22}$ cm$^{-2}$) Type 2 Quasars (Mainieri et al., 2002; Alexander et al., 2002; Brusa, 2003). Further support for the result that a significant fraction of obscured AGN are hosted in EROs comes from near infrared observations of X–ray sources selected on the basis of their high X–ray to optical flux ratio (X/O$>10$, Mignoli et al. 2004): the hosts of luminous, obscured hard X-ray sources with extreme X/O are among the most massive spheroids at z$>1$.
The observed fraction of AGN among EROs can therefore help constraining models for the joint evolution of supermassive black holes and galaxies bulges (e.g. Granato et al. 2004; Merloni 2004; Marconi et al. 2005). Previous studies on the fraction of AGN among the EROs population, although having deep near–infrared and X–ray observations ($K \sim 21 - 22$ and the Megaseconds *Chandra* exposures) were limited in areal coverage (50–80 arcmin$^2$) and therefore were not suitable for detailed statistical analyses of the AGN EROs population.
We will briefly discuss how it is possible, combining near–infrared and X–ray data over a significantly larger area, to constrain the fraction of AGN EROs in near infrared selected samples and the masses of the black holes powering the X–ray emission in these sources.

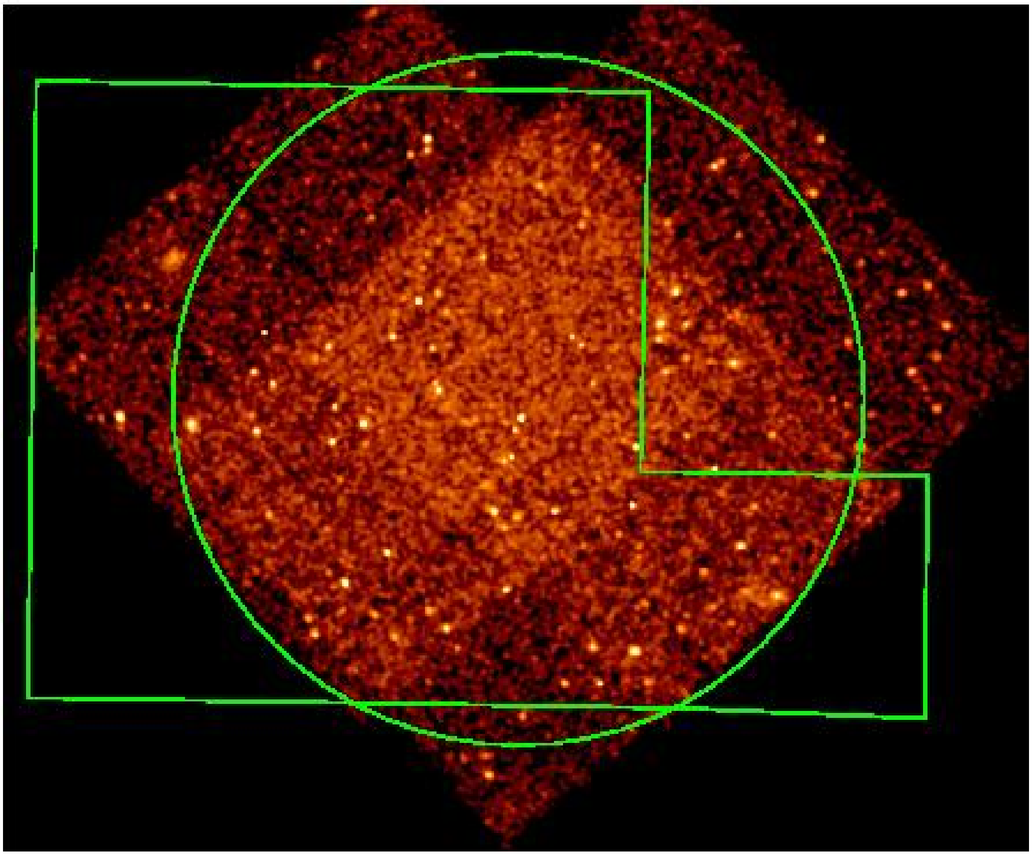

*Figure 1. Chandra 0.5-8 keV image of the central region of the Daddi Field, with superimposed the 11 arcmin radius circle of the XMM-Newton analysis and the deepest region ($\sim 450$ arcmin$^2$) covered with the K-band photometry (polygon). The X–ray image has been smoothed with a gaussian filter of 2 pixels. The central region (where the three pointings overlap) has an effective exposure time of $\sim 85$ ks.*

## 2. THE XMM-NEWTON SURVEY OF EROS IN THE DADDI FIELD

### 2.1. X–ray data

We have started an extensive program of multiwavelength observations of the largest sample of near–infrared selected EROs available to date (∼400 sources), selected over a contiguous field of $\sim$ 700 arcmin$^2$ (the "Daddi field", Daddi et al. 2000). The sample is complete to a magnitude limit of K$s$ ∼19 and the field is covered by deep optical photometry in the R–band (R∼ 26).
We have obtained with XMM–*Newton* a total of about 110 ks observing time, splitted in three different pointings (Brusa et al., 2005). The area analysed in the present work is $\sim$ 380 arcmin$^2$ (see Fig. 1) and covers the region with a uniform coverage in the optical and near–infrared bands. The detection algorithm developed for the `Hellas2Xmm` survey (see Baldi et al. 2002 for details) was run on the 2–10 keV (hard band) cleaned events: 60 sources were detected down to a limiting flux of $S_{2-10} \sim 4 \times 10^{-15}$ erg cm$^{-2}$ s$^{-1}$[1]. The central (380 arcmin2) region of the Daddi Field has been subsequently imaged also by *Chandra*, with a mosaic of 3×30 ks, partially overlapping observatios. Data were processed using version 3.2.1 of the CIAO software and mosaiced with the *merge_all* script. The full band (0.5-7 keV) *Chandra* mosaic is shown in Fig. 1.

### 2.2. Optical identifications

At the faint X-ray and optical fluxes probed by the present survey the identification process of XMM sources is not straightforward due to the positional uncertainties associated with the XMM Point Spread Function. In order to identify the correct optical counterparts and to assess the statistical significance of the X-ray to optical associations we have used the "likelihood ratio technique" (Sutherland & Saunders, 1992). We were able to reliably identify $\sim$ 80% of the X-ray sources, while for the remaining $\sim$ 20% of the sources we were not able to provide an unambiguous association due to the faintness of the

[1] the count rate to flux conversion factor was derived assuming a power law with photon index Γ=1.7, absorbed by the Galactic column density in the direction of the field ($N_H$=5×10$^{20}$ cm$^{-2}$, Dickey & Lockman 1990), and weighted by the effective exposure times of the different EPIC cameras.

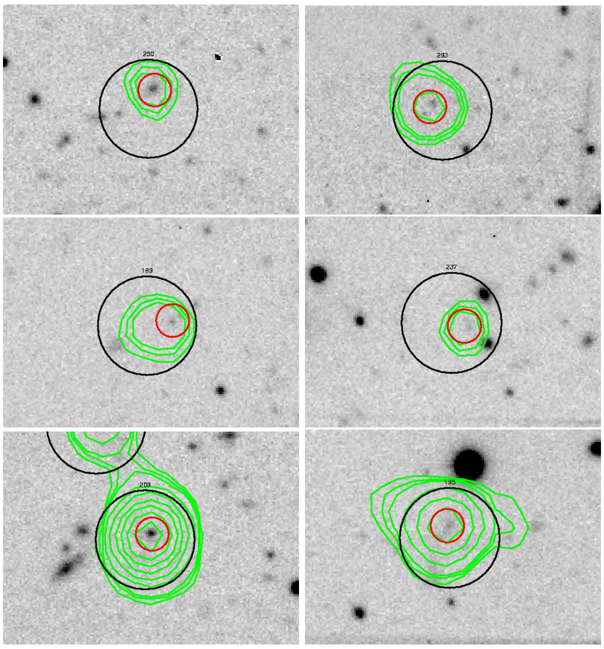

*Figure 2. Finding charts in the R–band of 6 out of the nine X–ray emitting EROs in the Daddi Field. Large open circles (5″ radius) are centered on the XMM-Newton position; small red circles (1″ radius) mark the proposed EROs counterparts; green contours represent the Chandra sources.*

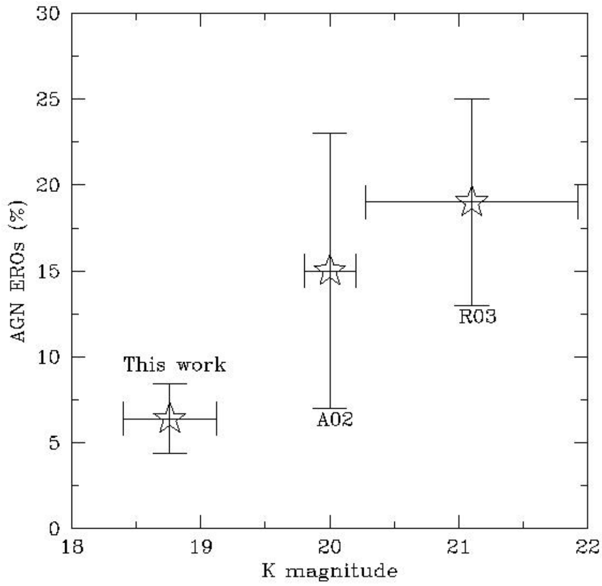


*Figure 3. Fraction of AGN ERO as a function of the K–band magnitudes, as computed from three different samples: this work, the Alexander et al. sample (A02) and the Roche et al. sample (2003). The large errorbars associated with the A02 and R03 points are mostly due to the small area covered*

possible counterparts (R>24) or to the presence of multiple sources, with similar likelihoods of being the correct identification, within the XMM error circles.
The XMM–*Newton* area analysed in this work includes 257 EROs: 173 EROs with $Ks$ <18.8 over $\sim$ 380 arcmin$^2$, and 216 EROs with $Ks$ <19.2 in the area in common with the deeper near–infrared coverage ($\sim 300$ arcmin$^2$, see Fig. 1). Nine of the 257 EROs which fall within the XMM–*Newton* area are individually detected in the hard (2-10 keV) band. We checked our X–ray to EROs associations with the available *Chandra* data: all nine XMM–*Newton* detected EROs have been detected also by *Chandra* and in all the cases, thanks to the much sharper positional accuracy, the *Chandra* X–ray centroid points unambiguously to the candidate optical counterpart, further assessing the reliability of the adopted method for the identification of XMM–*Newton* sources. The finding charts of 6 X–ray emitting EROs in the R–band with superimposed the XMM-Newton error circle (5″) and the *Chandra* contours are shown in Fig. 2.

## 3. RESULTS FROM OUR SURVEY

In the XMM-*Newton* observation, the X–ray limiting flux corresponds to an X–ray luminosity $L_X \sim 10^{43}$ erg s$^{-1}$ for z=1. Thus, the EROs X–ray emission is most likely powered by AGN activity, and the fraction of AGN among EROs in the present sample is *at least* $3.5 \pm 1.7$% (9/257). Conversely, the fraction of EROs among the hard X–ray population is much higher ($\sim 15$%).
The fraction of X–ray detected EROs in K–selected samples has been reported by Alexander et al. (2002; hereinafter A02) and Roche, Almaini & Dunlop (2003; hereinafter R03) at different X–ray and K–band limiting fluxes. Combining the depth of the different samples with the observed X–ray to optical flux ratios distribution (see Next Section), it is possible to derive an estimate of the fraction of AGN EROs among $K$–selected samples as a function of the K–band magnitude only and independently from the X–ray limiting fluxes (see Brusa et al. 2005 for details). Figure 3 compares the fraction of AGN in our sample with those in the A02 and R03 samples and suggests that the fraction of AGN EROs among the K–selected EROs population is an increasing function of the K–band magnitude. The results from hard X–ray surveys indicate a space density of low–luminosity ($10^{42} - 10^{44}$ erg s$^{-1}$) AGN which is almost two orders of magnitudes higher than that of high luminosity sources (Fiore et al., 2003; Ueda et al., 2003). Thus, it is not surprising that the fraction of AGN EROs increases going toward faint fluxes (i.e., lower luminosities). It is worth remarking that the fraction of “active” objects in K–selected EROs samples can be used to constrain models which link the formation and evolution of galaxies and AGN (e.g. Merloni 2004).

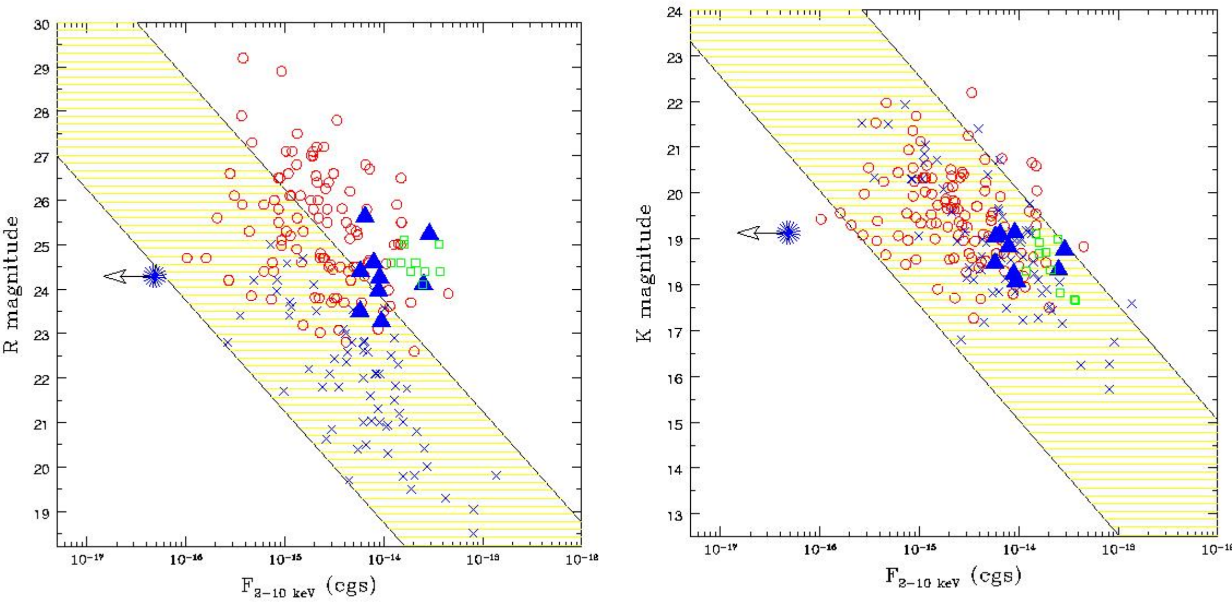


*Figure 4. left panel: R–band magnitude vs. hard X–ray flux for EROs, serendipitously detected in hard X–ray surveys. Large filled triangles are the 9 hard X–ray selected EROs of this work; circles correspond to the EROs in the "literature sample"; squares are sources from the* `Hellas2XMM` *survey. As a comparison, BL AGN detected in the CDF–S and CDF–N surveys are also reported as crosses. The shaded area represents the region typically occupied by known AGN (e.g. quasars and Seyferts) along the correlation log$(X/O) = 0 \pm 1$. For comparison, we report the result of stacking analysis performed on the K20 EROs in the CDF–S field not individually detected in the Chandra observation (Brusa et al. 2002; upper limit at the faintest X–ray flux). Right panel: the same plot but in the K–band.*

## 4. X–RAY TO OPTICAL PROPERTIES

In order to investigate the nature of hard X–ray selected EROs and the link between faint hard X–ray sources and the ERO population, we have collected from the literature a sample of 128 X–ray detected EROs (including the 9 objects previously described). For about half of them (62/128) photometric or spectroscopic redshifts are available (data from: Mainieri et al. 2002; Barger et al. 2003; Willott et al. 2003; Brusa et al. 2005; Crawford et al. 2002; Szokoly et al. 2004; Mignoli et al. 2004). This sample is by no means homogeneous (e.g. the selection criteria for EROs are slightly different, R-K$>5$ or I-K$>4$ depending on the authors; or the K–coverage is not complete), but could be considered representative of EROs individually detected in the X–rays. The R–band magnitudes plotted versus the hard X–ray fluxes are reported in Fig. 4 (left panel): about half of the sources show an X–ray–to–optical flux ratio (X/O) larger than 10, shifted up by one order of magnitude from that of broad-line AGN, confirming independent results from near infrared observations of X–ray sources selected on the basis of their high X/O (e.g. Mignoli et al. 2004; Maiolino et al. 2005). On the contrary, when the X–ray to near–infrared properties are considered, all the X–ray detected EROs in the comparison sample occupy a locus which is indistinguishable from that occupied by unobscured QSO (Fig. 4, right panel). This result further corroborates the hypothesis that AGN EROs are obscured quasars.

## 5. X–RAY PROPERTIES OF AGN EROS

High obscuration in X–ray detected EROs is also revealed in the X–ray band, in agreement with the results from the optical band.
The average hardness ratio of the hard X–ray detected EROs in our XMM–*Newton* observation suggests substantial column densities at the source redshift. We have quantitatively estimated the intrinsic X–ray column densities for the 62 EROs in the comparison sample with a reliable spectroscopic or photometric identification. The results are reported in Fig. 5 (left panel). Almost all of the individually detected EROs have intrinsic $N_H > 10^{22}$ cm$^{-2}$, and they actually *are* heavily obscured AGN. This study confirms previous evidences mainly based on a Hardness Ratio analysis (A02) and on few isolated examples (e.g. Stevens et al. 2003; Severgnini et al. 2005), and unambiguously indicates that large columns of cold gas (even $> 10^{23}$ cm$^{-2}$) are the rule rather than the exception among X–ray bright EROs.

### 5.1. EROs and QSO2: a selection criterion

Given the high–redshift (z$>0.8$) and the average X–ray flux ($\sim 4 \times 10^{-15}$ erg cm$^{-2}$ s$^{-1}$) of these objects, it is not surprising that the majority of X–ray detected EROs have high X–ray luminosities ($L_X > 10^{43}$ erg s$^{-1}$). Moreover, according to our analysis, a significant fraction of them have X–ray luminosities exceeding $10^{44}$ erg s$^{-1}$,

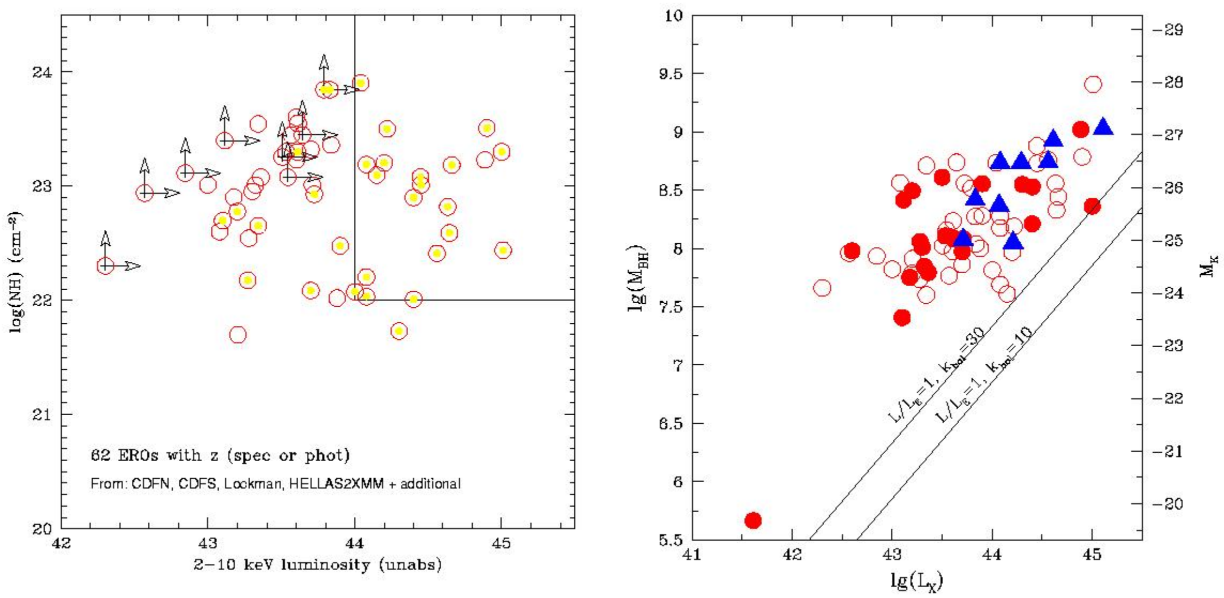


*Figure 5. Left panel: Logarithm of the absorbing column density ($N_H$) versus the logarithm of the unabsorbed X–ray luminosity in the 2-10 keV band for all the X–ray detected EROs with spectroscopic or photometric redshifts from the literature sample. Filled symbols are those with X/O $> 10$ (see text). In the upper right corner the "QSO2 locus" is highlighted. Right panel: The $M_{BH}$ obtained applying the Marconi & Hunt (2003) relation for the identified EROs versus the $L_X$. Symbols as in Fig. 4. Filled circles are sources with spectroscopic redshift. The continuous lines represent the expected correlation between the two plotted quantities for two different assumptions on the bolometric correction and $L_{\rm bol}/L_{\rm E}$=1.*

and therefore lie within the quasar regime (see also Severgnini et al. 2005, and this volume). The large intrinsic column densities further imply that AGN EROs, selected at bright X–ray fluxes, have properties similar to those of QSO2, the high–luminosity, high–redshift Type 2 AGNs required by X–Ray Background synthesis models (Comastri et al., 2001; Gilli et al., 2001). Among the X–ray detected EROs, the higher is the luminosity, the higher is the X–ray to optical flux ratio (filled symbols in left panel of Fig. 5). This confirms that a selection based on X/O $> 10$ is a powerful tool to detect high–luminosity, highly obscured sources (see Fiore et al. 2003) and it is even stronger when coupled with a previous selection on the extremely red colors. Given that the search for QSO2 on the basis of detection of narrow optical emission lines is extremely time consuming and als already challenging the capabilities of the largest optical telescopes, all the findings discussed above support the idea that hard X–ray surveys coupled with near–infrared observations provide an efficient method in detecting QSO2.

### 5.2. The masses and level of activity of X-ray emitting EROs

Indipendent arguments suggest that the near–infrared emission of X–ray selected *obscured* AGN is dominated by their host galaxy starlight (see e.g. Mainieri et al. 2002; Mignoli et al. 2004). Using the correlation between the bulge K–band luminosity and the BH mass published by Marconi & Hunt (2003), it is possible to estimate the masses of the obscured SMBH powering the X–ray emission of the 62 EROs with redshift information in the literature sample and the 9 EROs of the present work for which redshifts and luminosities have been estimated from the Fiore et al. (2003) relation. The BH masses have been computed assuming that 1) the measured K band light is completely due to the bulge component and therefore the AGN emission does not significantly contribute to the near-IR light and that 2) the shape of the Marconi & Hunt (2003) relation does not significantly evolve with redshift and/or luminosity.
The $M_{BH}$ obtained through a chain of assumptions and neglecting the uncertainties associated to the observed relations, are plotted versus the $L_X$ in the right panel of Fig. 5. We note that the presence of a disk or a residual point–source contribution would lower the bulge luminosity and in turn the mass determination, that can therefore be considered as conservative upper limits.
The absorption corrected X–ray luminosity can be translated into a bolometric luminosity assuming a bolometric correction factor ($L_{bol} = k_{bol} \times L_X$)[2]. The continuous lines in the right panel of Fig. 5 represent the relation between the BH mass and the X–ray luminosity in the hypothesis of Eddington limit accretion ($L_{bol}/L_{edd} = 1$) and for two different values ($k_{bol}$=10 and $k_{bol}$=30) of the

[2] A robust estimate for the bolometric correction ($k_{bol} \sim 30$) is available only for bright unobscured quasars (Elvis et al., 1994); lower values ($k_{bol} \sim$ 10–20) appear to better reproduce the observed spectral energy distribution of Seyfert like galaxies (Fabian, 2004) and of a few heavily obscured, luminous sources (Comastri, 2004).

bolometric correction. Despite the large scatter observed in Fig. 5 – for a given BH mass the corresponding luminosity ranges up to 2 orders of magnitudes – there is a clear trend between the X–ray luminosity and the BH mass; the dispersion can be reasonably well explained by a spread in the Eddington ratios in the range $L_{bol}/L_{edd}$=$10^{-3}$–$10^{0}$, most of the sources having $L_{bol}/L_{edd} > 10^{-2}$. Both the BH masses and the Eddington ratios derived above are consistent with a scenario in which X–ray detected EROs are obscured quasars emitting in a radiatively efficient way, in agreement with the results of Merloni (2004) and McLure & Dunlop (2004)).

**REFERENCES**


Alexander, D.M., Vignali, C., Bauer, F.E., et al. 2002, AJ 123, 1149 (A02)

Baldi, A., Molendi, S., Comastri, A., et al. 2002, ApJ, 564, 190

Barger, A.J., Cowie, L. L., Capak, P., et al. 2003, AJ, 126, 632

Brusa, M., Comastri, A., Daddi, E., Cimatti, A., Mignoli, M., & Pozzetti, L. 2002, ApJ, 581, L89

Brusa, M. 2003, AN, 324, 116;

Brusa, M., Comastri, A., Daddi, E., et al. 2005, A&A, 432, 69

Cimatti, A., Daddi, E., Mignoli, M., et al. 2002, A&A 381, L68

Comastri, A., Fiore, F., Vignali, C., et al. 2001, MNRAS, 327, 781

Comastri, A., 2004, in “Supermassive Black Holes in the Distant Universe”, Ed. A. J. Barger. Kluwer Academic Publishers, Chapter 8

Crawford, C.S., Gandhi, P., Fabian, A.C., et al. 2002, MNRAS, 333, 809

Daddi, E., Cimatti, A., Pozzetti, L., et al. 2000, A&A, 361, 535

Dickey, J.M., & Lockman, F.J. 1990 ARA&A, 28, 215

Elston, R., Rieke, G.H., & Rieke, M.J., 1988, ApJ 331, L77

Elvis, M., Wilkes, B.J., McDowell, J.C., et al. 1994, ApJS, 95, 1

Fabian, A.C., 2004, in ”Coevolution of Black Holes and Galaxies”, Carnegie Observatories Astrophysics Series, Vol. 1, pag. 447, ed. L.C. Ho (Cambridge Univ. Press), astro-ph/0304122

Fiore, F., Brusa, M., Cocchia, F. et al. 2003, A&A, 409, 79

Gilli, R., Salvati, M., & Hasinger, G. 2001, A&A, 366, 407

Granato, G.L., De Zotti, G., Silva, L., Bressan, A. & Danese, L., 2004, ApJ, 600, 580

Hasinger, G., Altieri, B., Arnaud, M., et al. 2001, A&A, 365, L45

Mainieri, V., Bergeron, J., Hasinger, G., et al. 2002, A&A, 393, 425

Maiolino, R., Mignoli, M., Pozzetti, L., et al. 2005, A&A, in press, astro-ph/0509244

Mannucci, F., Pozzetti, L., Thompson, D., et al. 2002, MNRAS 329, L57

Marconi, A., & Hunt, L., 2003, ApJ, 589, L21

Marconi, A., Risaliti, G., Gilli, R., Hunt, L.K., Maiolino, R., Salvati, M., 2005, MNRAS, 351, 169

McLure, R.J., & Dunlop. J.S., 2004, to appear in the proceedings of “Multiwavelength AGN Surveys”, astro–ph/0405393

Merloni, A., 2004, MNRAS, 353, 1035

Mignoli, M., Pozzetti, L., Comastri, A., et al. 2004, A&A, 418, 827

Pierre M., et al., 2001, A&A 372, L45

Roche, N., Dunlop, J., & Almaini, O. 2003, MNRAS, 346, 803 (R03)

Severgnini, P., Della Ceca, R., Braito, V. et al. 2005, A&A, 431, 32

Severgnini, P., Della Ceca, R., Braito, V. et al. 2006, this volume

Smail, I., Owen, F.N., Morrison, G.E. et al. 2002, ApJ, 581, 844

Stevens, J.A., Page, M.J., Ivison, R.J., et al. 2003, MNRAS, 342, 249

Sutherland, W. & Saunders, W. 1992, MNRAS, 259, 413

Szokoly, G.P., Bergeron, J., Hasinger, G. et al. 2004, ApJS, check refe

Ueda, Y., Akiyama, M., Ohta, K., & Miyaji, T., 2003, ApJ, 598, 886

Willott, C., Rawlings, S., Jarvis, M.J., Blundell, K.M. 2003, MNRAS, 339, 397

# UNVEILING THE ACTIVE NUCLEUS OF XBONGS

**F. Civano[1,2], A. Comastri[1], M. Mignoli[1], C. Vignali[2,1], F. Fiore[3], and F. Cocchia[4]**

**[*]on behalf of the HELLAS2XMM Collaboration**

[1]INAF – Osservatorio Astronomico di Bologna, Bologna, Italy
[2]Dipartimento di Astronomia, Università di Bologna, Bologna, Italy
[3]INAF – Osservatorio Astronomico di Roma, Monteporzio-Catone , Italy
[4]INAF – Osservatorio Astronomico di Brera, Milano, Italy

## ABSTRACT

We present the results of a detailed morphological analysis of three X–ray Bright Optically Normal Galaxies (XBONGS) detected in the HELLAS2XMM survey and observed with ISAAC@VLT in the $J$ and $K_s$ bands. These sources have relatively high X–ray luminosity and are associated with galaxies showing no obvious signature of AGN activity in their optical spectra. In deep near–infrared observations two out of the three sources reveal a nuclear point–like excess with respect to the galaxy starlight.

Key words: active galaxies; X-rays; surveys.

## 1. INTRODUCTION

One of the most interesting findings of the recent Chandra and XMM-*Newton* surveys consists in the discovery of luminous ($L_{2-10keV} \simeq 10^{41-43}$ erg s$^{-1}$) hard X–ray sources hosted by normal galaxies whose optical spectra are relatively featureless (i.e. without any obvious emission lines like $H\alpha$, $H\beta$, $[OIII]$; Barger et al. 2001; Comastri et al. 2002). The X–ray luminosities, the X–ray-to-optical flux ratio[1] ranging between that of truly normal galaxies (X/O∼–2) and that of AGN (X/O∼0) and their hard X–ray spectra, as inferred from the X–ray colors, all suggest that some kind of activity is taking place in their nuclei.

In order to explain the lack of optical emission lines and the multiwavelength properties of XBONGS, different interpretations have been suggested:

- Heavy obscuration by Compton–thick gas covering almost $4\pi$ at the nuclear X–ray sources prevents ionizing optical and UV photons from escaping, thus hampering the formation of the Narrow Line Regions (NLRs). Such a possibility is favoured by Comastri et al. (2002) to explain the multiwavelength behaviour of P3, the XBONG prototype.
- In a Radiatively Inefficient Accretion Flow (RIAF) model, a featureless hard X–ray spectrum is expected, with a negligible contribution in the optical and UV bands, which are therefore dominated by the host galaxy stellar light (Yuan & Narayan 2004).
- Diffuse emission, associated with a small group of galaxies or a close pair, unresolved by XMM observations.
- Dilution of nuclear emission from the host galaxy starlight (Georgantopoulos and Georgakakis 2005). Such an effect might be important if the ground-based spectroscopic observations are performed with relatively wide slits (Severgnini et al. 2003), or the sources are at high redshifts (Moran et al. 2002).

Although some of the above mentioned explanations provide a good description of the observed properties of a few objects, the nature of XBONGS is still subject of debate.

In order to search for weak AGN signatures, we have pursued an alternative approach which is based on deep near–infrared (NIR) imaging of relatively bright XBONGS. In the NIR the nuclear emission (either obscured or reddened) should rise over the stellar light. We present the results obtained applying the surface brightness decomposition tecnique to $J$ and $K_s$ good–quality images of a small sample of XBONGS.

## 2. THE SAMPLE

The sample presented here includes three sources, serendipitously detected in the 2–10 keV band, from the

[1] $X/O = \log \frac{f_X}{f_R} = \log f_X + C + \frac{R}{2.5}$

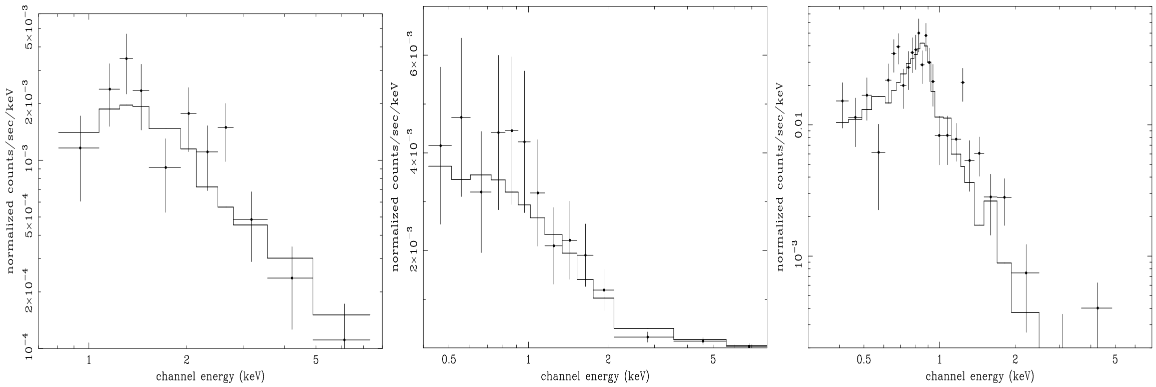


*Figure 1. XMM-Newton (pn) spectra of the sources PKS 03120018, PKS 03120017 and Abell 2690013. The X-ray parameters after fitting the spectra with an absorbed power–law model (PKS 03120018 and PKS 03120017) and with a thermal model (Abell 2690013) are reported in Table 1.*

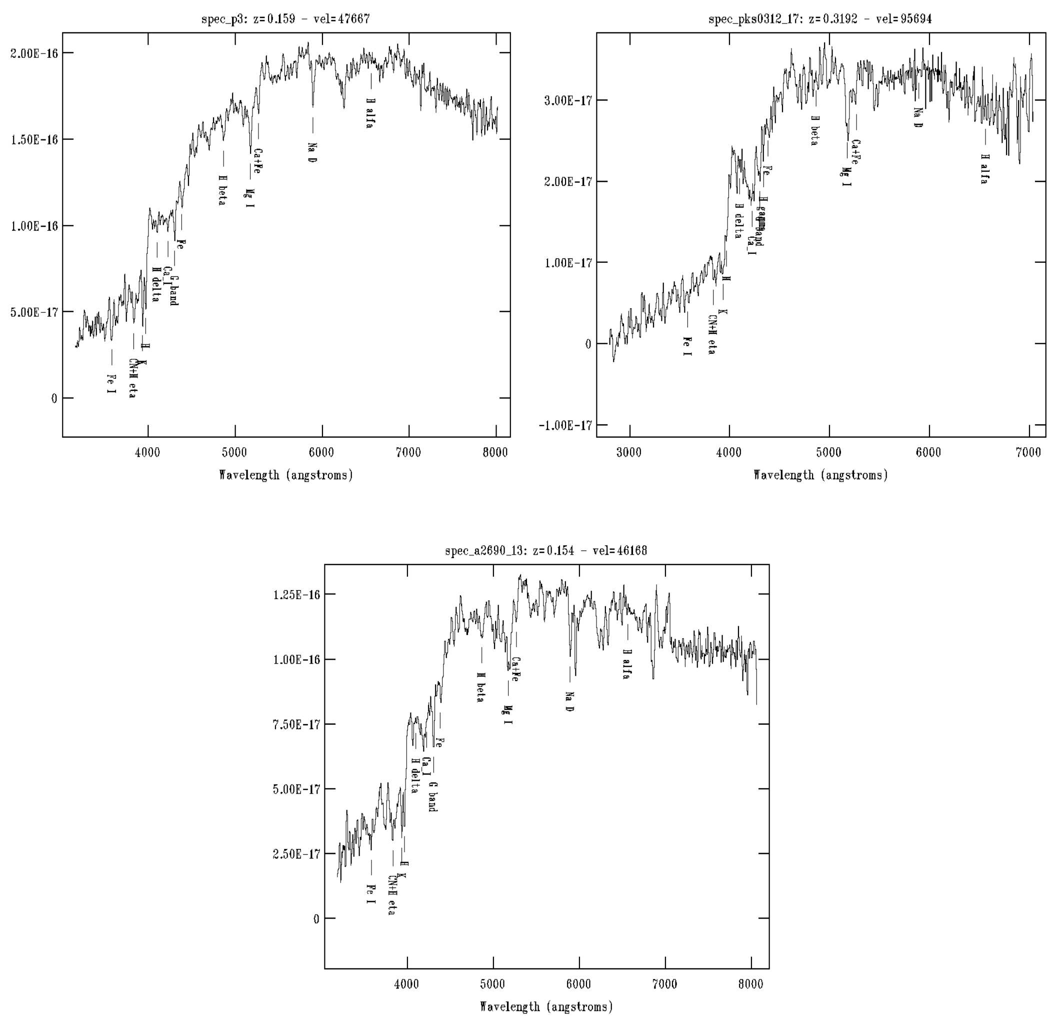


*Figure 2. Optical spectra of the sources PKS 03120018, PKS 03120017 (top) and Abell 2690013 (bottom) taken with the ESO 3.6m telescope.*

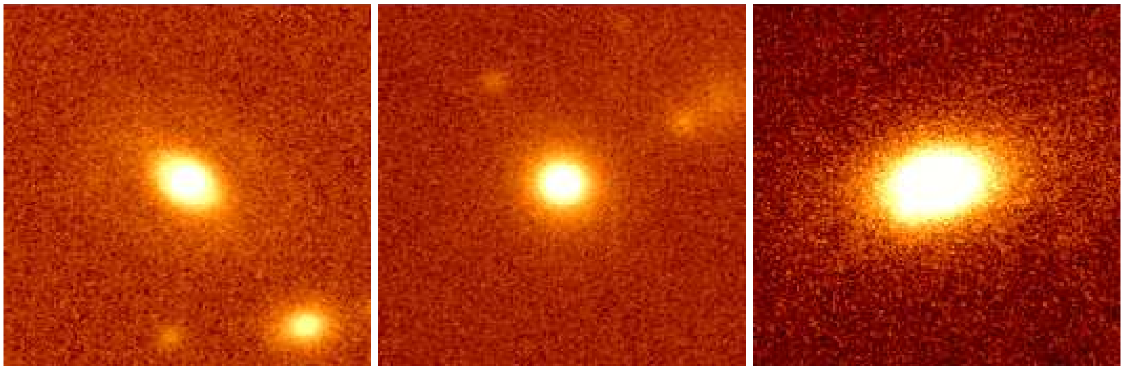

*Figure 3.* $K_s$*–band images: PKS 03120018, PKS 03120017 and Abell 2690013. The image size is 15"× 15".*

*Table 1. X–ray spectral analysis parameters.*

| id | $\Gamma$ | $N_H$ (cm$^{-2}$) | $\chi^2_{d.o.f}$ |
|---|---|---|---|
| PKS 03120017 | $2.11^{+0.82}_{-0.36}$ | $6.86^{+7.94}_{-4.58}\times 10^{21}$ | 9.6/9 |
| PKS 03120018 | $2.40^{+0.62}_{-0.40}$ | $< 2.11\times 10^{21}$ | 3.7/11 |
| id | $kT$ (keV) | $-$ | $\chi^2_{d.o.f}$ |
| Abell 2690013 | 0.75± 0.06 | | 42.5/27 |

HELLAS2XMM 1dF sample: two objects in the PKS 0312 field (03120018 and 03120017) and one in the Abell 2690 field (2690013). The source redshfits are 0.159, 0.319 and 0.154, respectively. Their X–ray and optical properties are discussed in Fiore et al. (2003) and Perola et al. (2004). The X–ray spectral parameters are reported in Table 1 and the spectra are shown in Figure 1; a careful X-ray analysis will be present in Civano et al. (2006). The optical spectra (Figure 2) have been taken with the ESO 3.6m telescope (slit width 1.5"–2"). The upper limits on the typical AGN optical emission line $[OIII]$ in our good signal-to-noise ratio spectra are $F[OIII]_{5007\mathring{A}} < 4\times 10^{-18}$ erg cm$^{-2}$ s$^{-1}$, one order of magnitude fainter than that expected from the X–ray luminosities for typical AGN emission (see also Cocchia et al. in prep. and references therein).

## 3. NEAR INFRARED ANALYSIS

The near–infrared observations have been carried out using the VLT (Very Large Telescope) with the Infrared Spectrometer and Array Camera (ISAAC). The ISAAC images were taken in two near–IR bands (the $J$ and $K_s$ filters) and were reduced using the DIMSUM[2] package, following standard procedures. Total exposure times for each galaxy were 600 sec in $J$ and 1800 sec in $K_s$. The effective seeing on the final frames ranges between 0.5 and 0.8 arcsec (FWHM). The $K_s$ images obtained for the three sources are shown in Figure 3.

[2]Deep Infrared Mosaicing Software, developed by P.Eisenhardt, M.Dickinson, A.Stanford and J.Ward., and available at the site `ftp://iraf.noao.edu/contrib/dimsumV2`

The surface brightness decomposition has been performed with GALFIT (Version 2.0.3b, Peng et al. 2002), a two dimensional algorithm that extracts structural parameters from galaxy images combining several analytical models. The fitting procedure was performed in both the $J$ and $K_s$ bands which allows to cross-check the results and search for a possible color trend. In order to better constrain the galaxy structural parameters, the fit was first performed in the $J$ band, where the AGN contribution is resulted to be lower. Then we fitted the $K_s$ band where the AGN contribution (if present) to the total light is expected to be more important.

For the analysis we proceed as follows. The host galaxy surface brightness was modeled with a de Vaucouleurs profile

$$\mu(r) = \mu_e\, \mathrm{e}^{-7.67\left[\left(\frac{r}{r_e}\right)^{1/4}-1\right]} \quad (1)$$

where $r_e$ is the effective radius and $\mu_e$ is the surface brightness at the effective radius. If a residual emission in the innermost region is still present after the fitting procedure, we added the contribution of a point-like source. The latter is modeled by the average profile of several stars in the field nearby each source. For both bands we performed the GALFIT analysis without and with the central unresolved component down to the images magnitude limit for point-like sources ($J$(lim)=22 and $K_s$(lim)=21.5).

In two out of the three sources the addition of a nuclear unresolved component significantly improves the statistical quality of the fit. The residual images of PKS 03120018 and 03120017 are shown in Fig. 4 and the fitting results are reported in Table 2. There is no evidence of a point-like source in Abell 2690013. This result is consistent with X–ray spectral and spatial analysis: the X–ray spectrum of Abell 2690013 is well represented by a thermal model (see Table 1) and the X–ray contours are suggestive of diffuse emission centered on the optical galaxy (see Fig. 5).

Once the nuclear component is subtracted, the host galaxy parameters (m$_{host}$, r$_e$) and the $J$–$K_s$ colors are in good agreement with the $K_s$–band luminosity–radius relation (Pahre 1999) and the color for elliptical galaxies

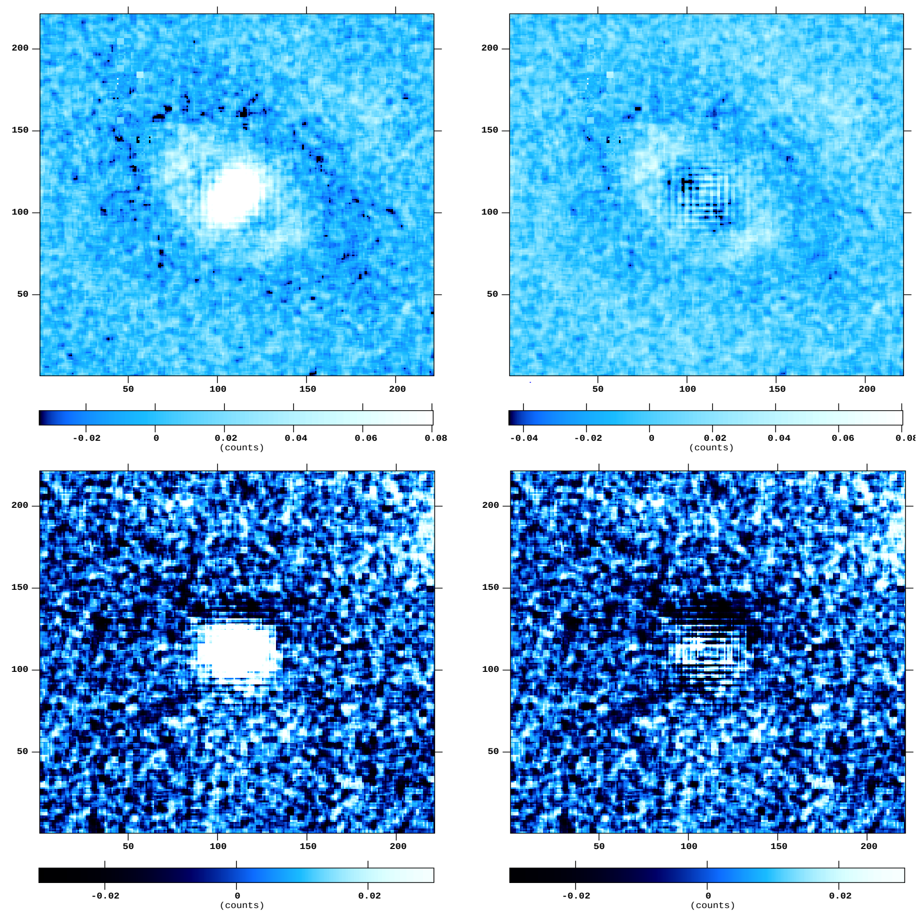


*Figure 4. Residual images (galaxy – model) of PKS 03120018 (bottom) and PKS 03120017 (top) obtained applying a model without (on the left) and with (on the right) a central unresolved component.*

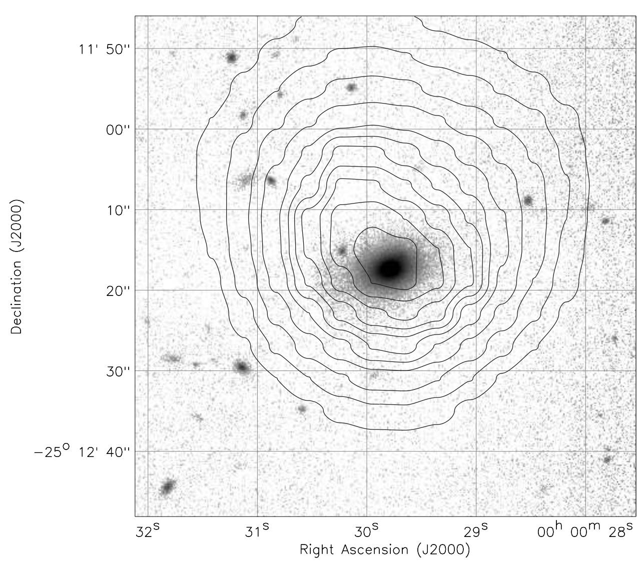


*Figure 5. X–ray contours obtained from the 0.5-10 keV adaptively smoothed pn image of source Abell2690013 overlaid on the $K_s$–band image.*

*Table 2. Results of the morphological fit performed in the $K_s$ band.*

| id | $m_{host}$ | $r_{eff}$ (kpc) | $m_{nucleus}$ |
|---|---|---|---|
| PKS 03120017 | 15.25±0.04 | 5.57±0.80 | 18.47±0.27 |
| PKS 03120018 | 15.20±0.01 | 3.75±0.15 | 18.07±0.12 |
| Abell 2690013 | 14.28±0.02 | 6.76±0.20 | – |

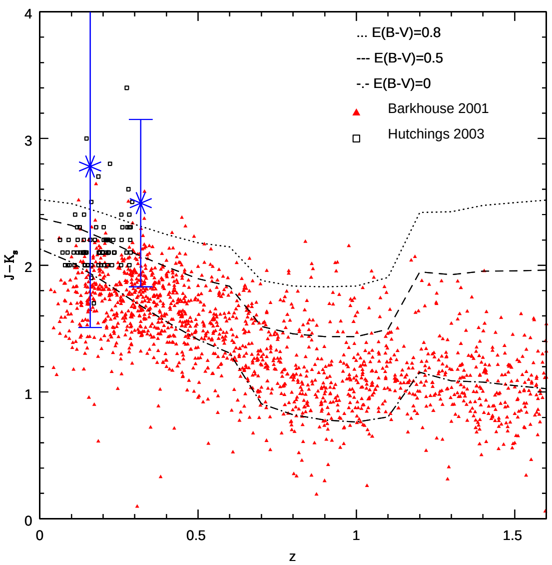


*Figure 6. Near–infrared color obtained for the AGNs hosted in PKS 03120018 and 03120017 compared with literature data.*

(Cutri et al. 2000), respectively, lending further support to the morphological analysis.

The nuclear $J$–$K_s$ color of PKS 03120018 and 03120017 is reported in Figure 6 compared with literature data. Red triangles represent the optically selected quasars with near–infrared counterparts in the 2MASS (Barkhouse et al. 2001), the open black squares are the 2MASS selected red quasars from Hutchings et al. (2003) in a redshift range ($0.1 < z < 0.3$) similar to that of our sources. Even if affected by large errors, due to the extremely faint $J$–band magnitudes, the $J$–$K_s$ colors are consistent with those of 2MASS red quasars. The tracks plotted in Fig.6 represent the color redshift relations for a quasar template (the composite spectrum from the Large Bright Quasar Survey extended to the near–IR using the mean radio–quiet quasar energy distribution; Francis et al. 2001; Elvis 1994). We have included the effect of internal dust attenuation on the quasar template, using a dust screen model and the SMC extinction law (Pei 1992). The curves represent different extinction values ($E(B-V)$=0, 0.5, 0.8 from bottom to top). At the face value the best fit $J$–$K_s$ color of the nuclei implies $E(B-V) \simeq 0.8$ which corresponds to $N_H \simeq 5 \times 10^{21}$ cm$^{-2}$ for a standard Galactic dust to gas ratio (Bohlin et al. 1978), in fairly good agreement with the X–ray spectral analysis (see Table 1).

## 4. SUMMARY

A detailed analysis of deep near–infrared images has allowed us to uncover a weak and red unresolved component in the central region of two bright XBONGs. The red nuclear $J$-$K_s$ colors suggest the presence of a mildly obscured AGN responsible of the observed X–ray emission. The broad–band properties of two XBONGs are explained by the presence of a mildly obscured nucleus hosted by a bright galaxy. The X–ray luminosity of the third object is most likely due to diffuse emission from hot gas possibly originating in a galaxy group. A more detailed analysis of the XBONG multiwavelength properties, including optical spectral simulations, is currently underway (Civano et al. 2006 in preparation).

## ACKNOWLEDGMENTS

Partial support from MIUR Cofin 03–02–23 and INAF/270/2003 grants is acknowledged.

## REFERENCES


Barger, A. J., Cowie, L. L., Bautz, M. W., Brandt, W. N., Garmire, G. P., Hornschemeier, A. E., Ivison, R. J., & Owen, F. N. 2001, AJ, 122, 2177

Barkhouse, W. A., & Hall, P. B. 2001, AJ, 121, 2843

Bohlin, R. C., Savage, B. D., & Drake, J. F. 1978, ApJ, 224, 132

Comastri, A., et al. 2002, ApJ, 571, 771

Cutri, R.M., et al., 2000, Explanatory Supplement to the 2MASS Second Incremental Data Release (Pasadena: IPAC)

Elvis, M., et al. 1994, ApJS, 95, 1

Fiore, F., et al. 2003, A&A, 409, 79

Francis, P. J., Hewett, P. C., Foltz, C. B., Chaffee, F. H., Weymann, R. J., & Morris, S. L. 1991, ApJ, 373, 465

Georgantopoulos, I., & Georgakakis, A. 2005, MNRAS, 358, 131

Hornschemeier, A. E., et al. 2001, ApJ, 554, 742

Hutchings, J. B., Maddox, N., Cutri, R. M., & Nelson, B. O. 2003, AJ, 126, 63

Moran, E. C., Filippenko, A. V., & Chornock, R. 2002, ApJ, 579, L71

Pahre, M. A. 1999, ApJS, 124, 127

Pei, Y. C. 1992, ApJ, 395, 130

Peng, C. Y., Ho, L. C., Impey, C. D., & Rix, H. 2002, AJ, 124, 266

Perola, G. C., et al. 2004, A&A, 421, 491

Severgnini, P., et al. 2003, A&A, 406, 483

Yuan, F., & Narayan, R. 2004, ApJ, 612, 724

# THE ACCRETION DISK SCALE WARM ABSORBER IN NGC 4051

**M. Elvis[1], Y. Krongold[1,2], F.Nicastro[1], N.Brickhouse[1] & L.Binette[2]**

1. *Harvard-Smithsonian Center for Astrophysics,60 Garden St., Cambridge MA 02138, USA*
2. *IA-UNAM, Mexico City, Mexico*

**ABSTRACT**

The warm absorber (WA) of NGC4051 is found to respond rapidly to the changing continuum in XMM EPIC-pn data, requiring high densities in the WA gas, so restricting the WA location

The two components of the WA in NGC4051 – required by RGS - the 'low' and 'high' ionization phases, are determined to lie a few light-days from the ionizing continuum source, equivalent to 2200-4400 $R_g$. The implied mass loss rates are a few percent of the accretion rate. This suggests that AGN winds are not capable of affecting galaxy-AGN co-evolution.

## 1. WARM ABSORBERS

Ionized, or 'Warm' Absorbers (WAs) are a common signature of winds in AGNs, seen in both UV and X-rays for ~50% of AGNs (Crenshaw, Kraemer & George 2003). Depending on the mass outflow rate of these winds they may influence their host galaxies, potentially controlling the 'co-evolution' that is required by the M-σ relation. While we know the line-of-sight velocity of these winds (~500- ~2000 km $s^{-1}$), their mass flux is uncertain by a factor $10^6$, due to our lack of knowledge of where the wind arises, as the two are proportional.

Suggested locations range from the kpc-scale narrow emission line region (Kinkhabwala et al. 2002) , to the pc-scale obscuring molecular torus (Krolik & Kriss 2001), to the ~1000 $R_g$ scale of the accretion disk (Elvis 2000, 2004). This ignorance can be lifted by employing non-equilibrium photoionization models to time variable AGNs (Nicastro et al. 1999). Figure 1 illustrates how a step function change in the continuum produces a rapid, though not instantaneous, change in dense gas, and a slow change in low density gas. Early attempts used primitive models of the WA that used only a few bound-free transitions and relatively low signal-to-noise spectra. We now have far more complete WA models including large numbers of bound-bound transitions (Figure 2, Krongold et al.) from extensive databases (APED, Smith, Brickhouse & Liedahl, 2003).

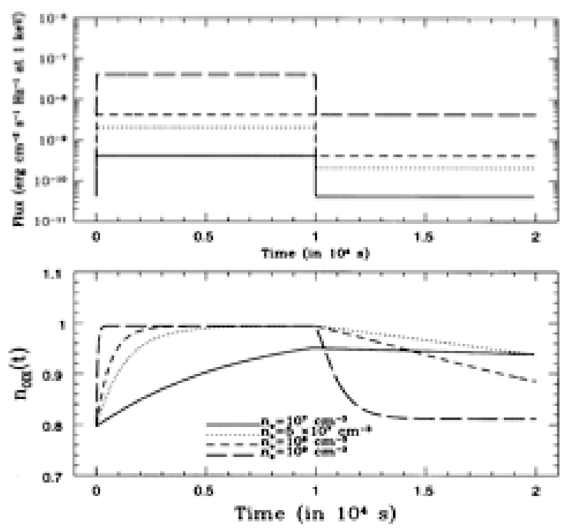


*Figure 1: Response of photoionized gas to a step function change in the ionizing continuum for various densities (Nicastro et al. 1999).*

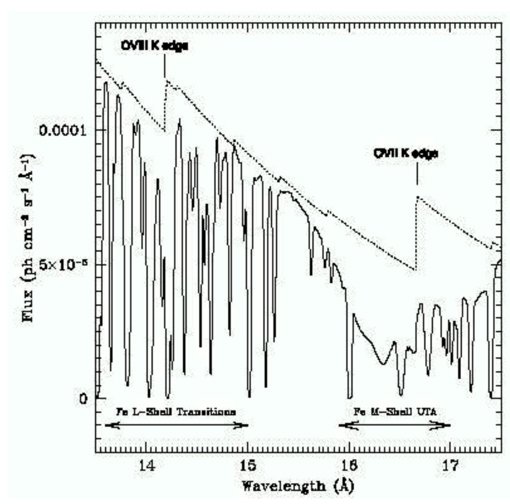


*Figure 2: Comparison of full PHASE photoionized absorber model with the component due just to bound-free transitions (Krongold et al. 2003).*

## 2. NGC 4051

NGC4051 varies rapidly (<1hour) and with large amplitude (factor 3-10). This makes NGC4051 an excellent test case for determining the density and hence location of a warm absorber (WA), using the timescale on which the WA gas responds to changes in the ionized continuum. As NGC 4051 has a known black hole mass ($2x10^6 M_o$) from reverberation mapping (Peterson et al. 2004) we can further restrict the WA location in Schwartzchild radii.

XMM-Newton observed NGC4051 for 117 ksec in 2001 May. We have reanalyzed the archival data for this observation using the PHASE code (Krongold et al. 2003) to determine the WA properties.

## 3. NGC 4051 XMM-NEWTON SPECTRA

The XMM-Newton RGS data in the high state required a two-component WA in order to fit the spectrum. The ionization state of the low and high ionization phases (LIP, HIP) are similar to those of NGC3783 (Krongold et al. 2003) but with smaller column densities.

Using these two components we then fitted the EPIC-pn data for 21 separate intervals along the
light curve, chosen to have roughly constant flux during each interval. We found that two components were required for EPIC too, but that the derived ionization parameters, $U_X$ (Netzer 1996), changed systematically with the continuum flux. Figure 3 shows the light curve, the binned light curve, and the derived values of $U_X$ for the two components.

## 4. RAPID RESPONSE OF THE WARM ABSROBERS

Clearly the ionization parameters track the ionizing flux close to the way expected for gas in photoionization equilibrium. This can be seen more precisely by noting the squares in the two $U_X$ plots, which show the values expected for gas keeping precisely to photoionization equilibrium.

This behavior immediately requires a dense and, as the column density is fixed, compact WA. A NELR origin is thus ruled out. Moreover continuous flow models are also ruled out. In these models the WA is a continuous medium extending over a factor of several in radius with gradually decreasing ionization parameter. Such a WA will not respond strongly to changes in the continuum as gas ionized up from state *i* to *i+1* is compensated for by gas ionized from *i-1* to *i*. This result has already been found to apply to NGC 3783 (Krongold et al. 2004).

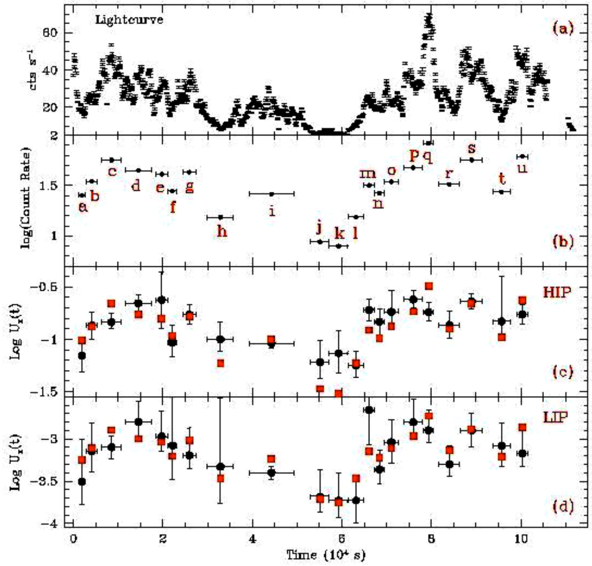


*Figure 3: (a) XMM-Newton light curve of NGC4051 and (b) binned in 21 intervals; (c)(d) ionization parameters, $U_X$, for the high (HIP) and low (LIP) ionization WA required by the RGS. The squares show $U_X$ for gas in photoionization equilibrium.*

We can make more quantitative estimates of the WA gas density for each phase. Figure 4 shows $U_X$ vs. continuum count rate for the high low ionization phase (LIP) of the WA fits. As one would expect from the light curves, the two are well correlated. The normalization of these plots determines the WA density-radius-squared product, $n_e R^2$, robustly.

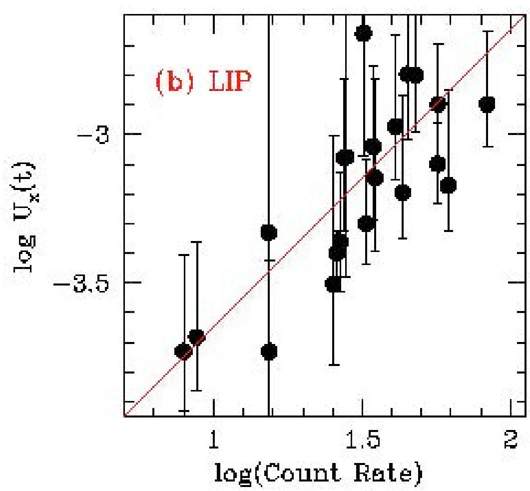


*Figure 4: UX versus continuum count rate for the low ionization WA phase (LIP).*

For the LIP there is no departure from ionization equilibrium even at extreme fluxes and down to the shortest timescale of variability of 3 ksec. This implies $n_e(LIP) > 8.1x10^7$ cm$^{-3}$. But $n_e R^2 = 6.6x10^{39}$ cm$^{-1}$. So we derive an upper limit on the distance of the LIP from the ionizing continuum of *r(LIP)* <$8.9 \times 10^{15}$ cm, which is <0.0029 pc, or <3.5 light-days.

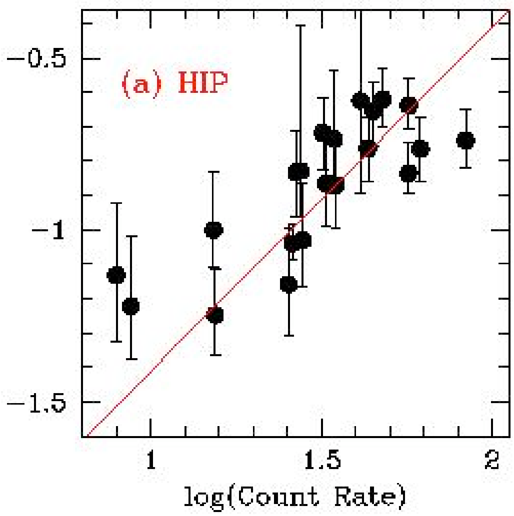


*Figure 5: UX versus continuum count rate for the low ionization WA phase (LIP).*

The high ionization phase (HIP) presents a different and more constraining picture (figure 5). Here the HIP is out of photoionization equilibrium at the highest and lowest continuum fluxes, but in equilibrium at intermediate fluxes. In this observation we are just resolving the ionization and recombination times of the HIP. It is reasonable that it is the HIP which has a resolved response time: if the HIP and LIP are co-spatial then the higher ionization phase will have lower density and so should be slower to respond to continuum changes.

Quantitatively we find that the HIP density is tightly constrained to about a factor 2: $n_e(HIP)$ = (0.6-2.1) x$10^7$ cm$^{-3}$. This translates into a radius, *r(HIP)* = (1.3-2.6) x$10^{15}$ cm, which is (0.5-1.0) light-days.

The first thing to note is that the LIP and HIP are consistent with being at the same radius and so could be co-spatial as assumed in previous studies. Moreover, as PHASE also determines a temperature, we can determine the HIP and LIP pressures independent of assuming co-spatiality.

Again the pressures turn out to be consistent with pressure equilibrium between the two phases: *P(HIP)* = (2.9-10.5) x $10^{12}$ K cm$^{-1}$, while *P(LIP)* > 2.4 x $10^{12}$ K cm$^{-1}$.

The thickness of the two WA phases (assuming each is continuous) can also be found as $\Delta R = 1.23 N_H/n_e$. $\Delta R(LIP) < 9 \times 10^{12}$cm; $\Delta R(HIP)$ – (1.9-7.2) x $10^{14}$cm. This yields surprisingly thin radial extents compared with their radii: $(\Delta R/R)HIP$ = 0.1-0.2, $(\Delta R/R)$LIP < $10^{-3}$. The particularly thin LIP $\Delta R/R$ suggests that this phase is either a boundary layer around the HIP, or is mixed within the HIP in pressure equilibrium – which may be preferred given the consistency with pressure balance of the two phases.

## 5. THE LOCATION OF THE AGN WIND

We already ruled out the kpc-scale NELR as the location of the AGN wind seen in the WA. These quantitative distance determinations allow us to go much further (figure 6).

For a source with the continuum luminosity of NGC 4051 the minimum dust sublimation radius is 12-170days (Barvainis 1987). As both WA components lie within 3.5 light-days this rules out the inner edge of the dusty molecular torus (Krolik & Kriss 2001) of unification models (Urry & Padovani 1995 as the source of the AGN wind, at least in this AGN. Reverberation mapping also locates the Hβ emitting broad emission line region (BELR) outside the WA location, at 5.9 light-days (Peterson et al. 2000).

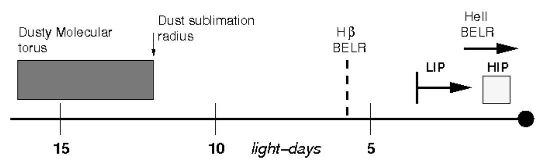


*Figure 6: Location of nuclear features in NGC4051 on a light-days scale.*

Zooming in closer to the AGN (figure 7), we recall that the BELR in AGNs is stratified, with higher ionization lines being closer to the nucleus (Clavel e al. 1991). In NGC4051 the high ionization line HeII (4686A) comes from a region <2 light-days from the continuum source. The high ionization BELR is thus consistent with the location of the WA wind. Interestingly the HeII emission line has a blue asymmetry of ~400 km s$^{-1}$, suggestive of an outflow at a velocity similar to that of the WA wind (600– 2400 km s$^{-1}$, Collinge et al. 2001).

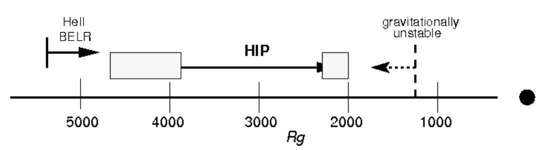


*Figure 7: Location of features in NGC4051 on a Schwartzchild radii, Rg, scale.*

Because NGC4051 has a measured black hole mass of (1.9 +/- 0.78) x $10^6$ $M_o$ (Peterson et al. 2004), we can convert the WA HIP location into Schwartzchild radii: 2200 – 4400 $R_g$. This location suggests a connection with the accretion disk gravitational instability radius which, is $r_{grav}=1330(\kappa/\kappa_{es})^{2/3}r_g$ (Goodman 2003), for nominal standard parameters. However as the disk opacity, κ, could well be 1000 times the electron scattering opacity, $\kappa_{es}$, this may be merely a coincidence.

## 6. GEOMETRY OF THE AGN WIND

The thinness of the wind might suggest that AGN winds consist of a series of repetitive impulsive outbursts. However, given the thinness of the WA-HIP these would have a duty cycle of no more than 10-20%. However WAs are seen in at least 50% of all AGNs, leading to an apparent paradox.

This problem was encountered before in the puzzle of the 20-year persistence of the CIV narrow absorption line (NAL) in NGC5548 by Mathur, Elvis & Wilkes (1995). These authors suggested that the solution was to discard spherical symmetry. They proposed instead that the outflow velocity we see is just a component of the true space velocity of the wind, which is moving primarily *across* our line of sight. Higher resolution observations of the WA wind in the UV (Arav, Korista & deKool 2002) make a strong case for a transverse flow dominating the AGN WA wind. The simplest geometry is then a bi-conical flow (Elvis 2000).

## 7. MASS LOSS RATE IN THE AGN WIND

With the assumption of a conical flow, we can derive a mass loss rate in the WA wind:

$$M_{out} = 0.8\pi\, m_p\, N_H\, v_r\, R\, f(\theta) \sim (4\text{-}9) \times 10^{-5}\ M_o\ yr^{-1}$$

As NGC4051 has an accretion rate of $0.05M_{Edd}$ (Peterson ett al. 2000), this outflow rate corresponds to 2% - 5% of $M_{acc}$. [The function *f(θ)* has a value close to unity except for extreme viewing angles.]

This contrasts sharply with the far larger mass loss rates obtained by previous studies which assumed *R* of order parsecs.

We note that if viewed along the flow direction the wind in NGC4051 would have a 10 times larger column density ($Rn_e$~$5x10^{22}$ cm$^{-2}$), and a larger velocity by up to factor 10. The NGC4051 wind would then approach the observed properties of a BAL (Broad Absorption Line) quasar wind (Elvis 2000). The uncertainty in the correct terminal velocity means that we have only a lower limit to the total kinetic power of the wind, which is only ~$2.5x10^{37}$ erg s$^{-1}$. Assuming the wind achieves escape velocity (else it is not a wind) from 2200Rg, we get a ~100 times larger kinetic power.

## 8. IMPLICATIONS & CAVEATS

With a mass loss rate of 2%-5% $M_{acc}$ integrating over a somewhat generous $10^8$yr lifetime for an AGN outburst, gives a total ejected mass of (0.4-2) x $10^4 M_o$ and the total energy carried by the wind is $10^{45}$-$10^{47}$ erg.

If all AGN winds arise at the same value of $R_g$ then the mass loss rate scales with the black hole mass and, for more typical masses of $10^8$-$10^9 M_o$, the total ejected mass per quasar is $10^6$-$10^7 M_o$. This is comparable to that ejected by a ULIRG (Bland-Hawthorn 2005).

Similarly the total energy deposited by a quasar wind would be $10^{47}$-$10^{49}$ erg.

This observation fits 5 separate predictions of the 'funnel wind' model of Elvis (2000, 2004). The AGN wind in NGC4051 is found to be:

1. on the accretion disk scale;
2. consistent with the location of the high ionization BELR;
3. consistent with pressure balanced phases;
4. non-spherical and consistent with conical;
5. similar to a BAL quasar if viewed in the wind flow direction.

This gives us some confidence in this model.

NGC4051 is only one AGN, and has somewhat unusual properties, which must lead to caution in accepting this result as typical of the whole AGN population:

- Low black hole mass;
- Unusually distant BELR (NGC4051 is a narrow line Seyfert 1);
- Unusually weak wind? (as judged from eigenvector 1).

The EPIC-pn is not sensitive to higher ionization WA phase, e.g. one shown only by Fe-K absorption. Some quasars appear to have fast winds with high $N_H$ in this highest WA state (Pounds et al. 2003). In this sense our wind mass loss rate and kinetic luminosity values are lower limits.

## 9. CONCLUSIONS

We have used the non-equilibrium photoionization technique of Nicastro et al. (1999) to make the first measurement of the density and location of an AGN warm absorber wind. We demonstrate that:

- AGN WA winds arise on accretion disk scales;
- NELR or molecular torus origins are ruled out;
- Continuous flow models are ruled out;

- A spherical geometry is unlikely, while a bi-cone is favored
- Multiple predictions of the Elvis (2000) model are upheld;
- The mass loss rate is small, a few percent of $M_{acc}$.
- The kinetic power may be small, but depends on the unobserved terminal velocity of the wind.

We can test the spherical flow model by re-observing NGC4051 with XMM-Newton. As the line-of-sight velocity is close to 1 light-day/year, repeating the same experiment will give a clear distinction between a transverse flow (*R*~1 light-day, always) and a radial flow (*R*~4 light-days after 3 years).

We also need to establish wind locations, densities, mass loss rates and kinetic powers for more typical AGNs. The less dramatic and reliable variability of other AGNs will require long monitoring campaigns. Without this investment however, the extrapolation to the total mass and energy available from AGN winds to affect galaxy evolution will remain too uncertain to test co-evolution models.

NASA grant GO4-5126X (*Chandra*) and grant UNAM-PAPIIT IN118905 partially supported this work.

**REFERENCES**

Arav N., Korista K., & deKool M., 2002 ApJ, 566, 699
Barvainis R., 1987, ApJ, 320, 537
Bland-Hawthorn J., 2005, AnnRevA&A, 43, 769
Clavel, J., 1991, MNRAS, 246, 668
Collinge M.J., et al. 2001, ApJ, 557, 2
Crenshaw D.M., Kraemer S.B., & George I.M., 2003, Ann.Rev.A&A, 41, 117
Elvis M., 2000, ApJ, 545, 63
Elvis M., 2004, ASP Conf. Proc. 311, 109
Goodman, J., 2003, MNRAS, 339, 937
Kinkhabwala et al., 2002, ApJ, 575, 732
Krolik J.H., & Kriss G.A., 2001, 447, 512
Krongold Y., et al., 2003, ApJ, 597, 832
Krongold Y., et al., 2004, ApJ, 622, 842
Mathur S., Elvis M., & Wilkes B.J., 1995, ApJ, 452, 230
Netzer H., 1996, ApJ, 473, 781
Peterson B.M., et al., 2000, ApJ, 542, 161
Peterson B.M., et al., 2004, ApJ, 613, 682
Urry M., & Padovani P., 1995, PASP, 107, 803

# A CONSTANT TOTAL PRESSURE MODEL FOR THE WARM ABSORBER IN NGC 3783

**A. C. Gonçalves**[1,2], **S. Collin**[2], **A.-M. Dumont**[2], **A. Różańska**[3], **M. Mouchet**[2,4], **L. Chevallier**[2,3], **and R. Goosmann**[2]

[1]CAAUL, Observatório Astronómico de Lisboa, Tapada da Ajuda, 1349-018 Lisboa, Portugal
[2]LUTH, Observatoire de Paris-Meudon, 5 Place Jules Janssen, 92195 Meudon Cedex, France
[3]Copernicus Astronomical Center, Bartycka 18, 00-716 Warsaw, Poland
[4]APC, Université Denis Diderot Paris 7, 75005 Paris, France

## ABSTRACT

Many AGN exhibit X-ray absorption features caused by the presence of highly ionized gas located on the line-of-sight of the central continuum. Such a material is called "Warm Absorber" (WA) and displays zones of different density, temperature and ionization. Our approach to the study of the WA relies on the assumption of pressure equilibrium, resulting in the natural stratification of the medium, which allows us to explain the presence of lines from different ionization states in many AGN observed by *Chandra* and *XMM-Newton*. Among the best WA observations available are those of NGC 3783, which we have analyzed.

We have used the photoionization code TITAN, developed by our team, to calculate a grid of constant total pressure models dedicated to fit the WA in NGC 3783. Our study shows that the WA can be modelled in pressure equilibrium. Finally, this work provides a good example of the application of the TITAN code to the study of the WA in AGN, and opens perspectives for its use by the community, through a larger grid of constant total pressure models to be made available via XSPEC and/or via Virtual Observatory facilities.

Key words: active galactic nuclei: NGC 3783; warm absorber.

## 1. INTRODUCTION

Many Active Galactic Nuclei (AGN) exhibit important X-ray absorption features caused by the presence of highly ionized gas located on the line-of-sight of the central continuum; such a material is called "Warm Absorber" (hereafter WA).

The first observations of WA gas in AGN were reported by Halpern et al. (1984) in the *Einstein Observatory* spectrum of MR 2251−178, a quasar displaying a large absorption feature around 1 keV; this feature has been attributed to the O VII (739 eV) and O VIII (871 eV) photoelectric absorption edges (*e.g.* George et al. 1995) and is consistent with the presence of gas photoionized by the hard X-rays produced near the central engine of the active nucleus.

Early *ASCA* observations have revealed the presence of ionized soft X-ray absorption in $\sim 50\%$ of type 1 Seyferts; evidence for a WA was also found in type 2 Seyferts, Narrow Line Seyfert 1s, BAL QSOs and even some BL Lacs. With the advent of space X-ray observatories such as *XMM-Newton* and *Chandra*, carrying aboard high-resolution grating spectrographs, an important set of high quality data became available providing valuable information on the WA. Spectra of type 1 objects revealed the presence of tens of absorption lines, covering a wide range of ionization states, and blueshifted by a few hundreds to thousands $\mathrm{km\,s^{-1}}$ (an indication that the absorbing material is outflowing); in type 2 AGN, the data have shown the presence of emission lines.

Despite the undeniable improvements in our knowledge of the WA, some important issues remain a subject of debate, namely: *(i)* the location and geometry of the WA, *(ii)* the physical conditions of the absorbing/emitting gas, and *(iii)* the implications of the WA in the energetics of AGN. Trying to solve these questions requires not only high quality observations, as the ones provided by *XMM-Newton* and *Chandra*, but also an adequate treatement of the X-ray data through the use of reliable photoionization codes, calculating the full radiative transfer.

We have addressed the above mentioned points through the study of the Warm Absorber in NGC 3783, for which unmatching quality *Chandra* archive data are available; we have modelled the data using our photoionization code TITAN (*e.g.* Dumont et al. 2000; Collin et al. 2004), which supports the assumption of pressure equilibrium and allows for a multi-angle analysis of the spectra.

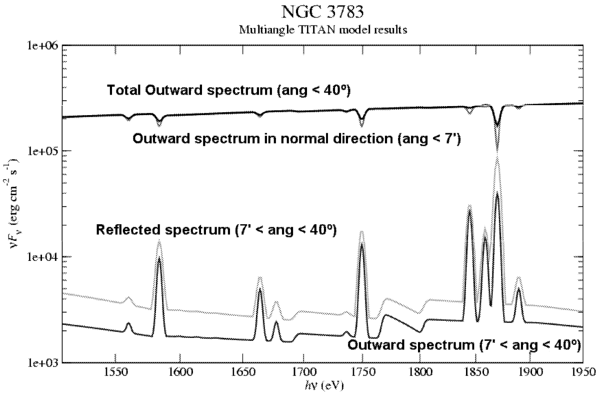


*Figure 1. Absorption (outward spectrum inside an opening cone of $7'$) and emission components (outward and reflected spectra in a cone comprised between $7'$ and $40°$). This figure illustrates how an absorption feature can be partially, or totally filled in by an underlying emission component, and stresses the importance of a separate analysis of the absorption and emission spectra.*

## 2. THE WARM ABSORBER IN NGC 3783

NGC 3783 is a bright ($V$~13.5), nearby ($z$=0.0097) Seyfert 1.5 galaxy observed in the Optical, UV and X-rays. The WA in this object has been discussed by several authors (*e.g.* Kaspi et al. 2001, 2002; Netzer et al. 2003; Krongold et al. 2003; Behar et al. 2003) based on *Chandra* data (56 ks and 900 ks spectra) and *XMM-Newton* observations (40 ks and 280 ks spectra). These studies seem to agree on the presence of a 2 (or more)-phase gas (a cold Low-Ionization Phase and a hot High-Ionization Phase) and on the absorbing and emitting plasma being manifestations of the same gas. Concerning the kinematics of the WA, two or more velocity systems have been identified in *Chandra* observations; they are compatible with those observed in UV spectra. A single velocity system ($v_{out} \sim$ 600–800 km s$^{-1}$) seems enough to describe *XMM-Newton* observations. There is no consensus in what concerns a possible correlation between the velocity shifts or the *FWHMs* with the ionization potentials of the ions.

Although the WA in NGC 3783 has been the object of many studies, these have assumed constant density (*e.g.* Netzer et al. 2003) or a dynamical state (Chelouche & Netzer 2005) for the modelling. In addition, they all require multiple zones of different density, temperature and ionization; these are invoked to explain the large span in ionization observed in the WA spectrum. Furthermore, when plotted on the S-curve of thermal equilibrium $log(T)$ *vs.* $log(\xi/T)$ (where $T$ is the temperature of the medium and $\xi$ is the ionization parameter[1]), these clouds lie on a vertical line of roughly the same gaseous pressure. However, a stratified medium can be obtained naturally if we assume the gas to be in pressure equilibrium.

[1]The ionization parameter $\xi$ is defined as $L/n_{\rm H}R^2$, where $L$ is the luminosity integrated over the total spectrum, $n_{\rm H}$ is the hydrogen density and $R$ is the distance from the WA to the illuminating source.

Our approach to the study of the WA relies therefore on the assumption of constant total pressure, which allows us to explain the presence of lines from different ionization states, and accounts naturally for the other properties of a model composite of multiple constant density clouds.

## 3. DATA REDUCTION AND MODELLING

We have searched the *Chandra* archives for the HETG data used to build the 900 ks spectrum published by Kaspi et al. (2002), which is a combination of MEG and HEG observations. In this study, we have only considered HEG data. The retrieved spectra were treated in the standard way using the CIAO software (vs. 3.2.1) and corresponding threads. We have then used our photoionization code TITAN to model the observations and to constrain the physical conditions of the WA gas in NGC 3783.

TITAN is well suited for the study of optically thick and thin media; it computes the gas structure in thermal and ionization equilibrium, both locally and globally; it can work under constant density, constant gaseous pressure or constant total pressure. Our atomic data includes ~1000 lines from ions and atoms of H, He, C, N, O, Ne, Mg, Si, S and Fe; more lines should be added soon.

The photoionization code TITAN accounts for Compton heating and cooling corresponding to photons with energies inferior to 25 keV; when coupled with the Monte-Carlo code NOAR, it can also account for the Compton heating and cooling corresponding to photons with energies larger than 25 keV.

Another important aspect of TITAN, is its multi-angle treatment of the transfer allowing, in particular, for the separate study of the emission and absorption components. As an example, Fig. 1 displays the calculated outward (absorption and emission), reflected (emission only) and total spectra (corresponding to the sum of the absorption and emission components) for NGC 3783, in the conditions of our best model described further down. This figure shows the importance of a separate analysis of the absorption and emission components, and illustrates how an absorption feature can be partially, or totally filled in by an underlying emission component; one can also see that the emission-line spectra corresponding to the reflected and outward flux are not similar, displaying different line-ratios.

We have calculated a grid of 16 constant total pressure models dedicated to fit the WA in NGC 3783; the 16 models cover the combinations between 4 possible values of the ionization parameter $\xi$ ($2000 < \xi < 3500\ {\rm erg\,cm\,s^{-1}}$) and of the total column density ($3\,10^{22} < N_{\rm H} < 6\,10^{22}\ {\rm cm^{-2}}$); the density at the face of the cloud ($n_{\rm H}$) was set to $10^5\ {\rm cm^{-3}}$ and the turbulent velociy to $150\ {\rm km\,s^{-1}}$. Our study shows that the WA can be modelled in pressure equilibrium conditions, providing a best model with $\xi = 2500$ and $N_{\rm H} = 4\,10^{22}$.

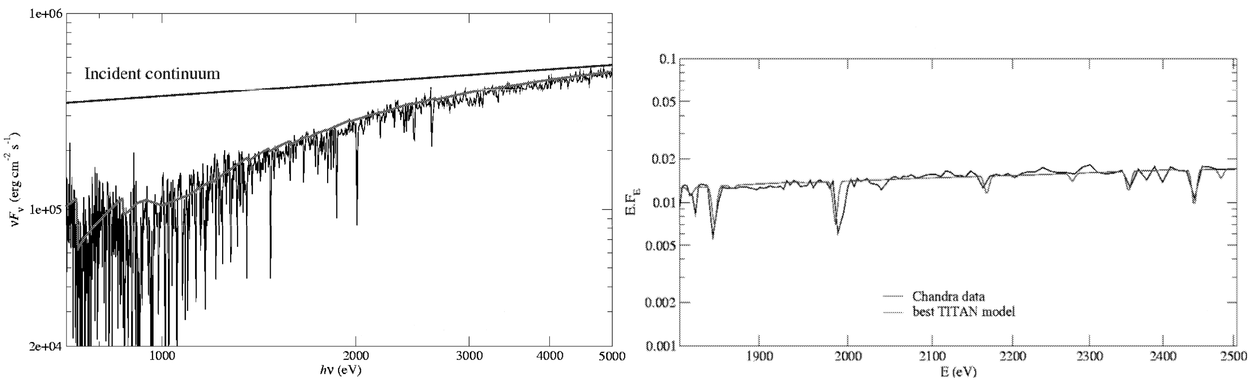


*Figure 2. NGC 3783 observations and TITAN model. Left panel: incident and emergent continua plotted over the observations. Righ panel: zoom on the observed and modelled spectra. The "unfitted" features correspond to Al lines (not present in the atomic data).*

This model gives a good fit to the observed data (Fig. 2), both for the continuum (following its overall shape up to 10000 eV and reproducing the O VII and O VIII edges) and the lines (both from high and low ionization); these are blueshifted by $\sim 810\,\mathrm{km\,s^{-1}}$. The observed and modelled spectra will be presented in detail in a forthcoming paper (Gonçalves et al., in preparation).

## 4. CONSTANT DENSITY VERSUS CONSTANT TOTAL PRESSURE MODELS

Our results can be compared to those of Netzer et al. (2003), who found three constant density clouds: a "low-ionization" cloud ($\xi = 68$ and $N_{\rm H} = 8\,10^{21}$), a "medium-ionization" cloud ($\xi = 1071$, $N_{\rm H} = 1\,10^{22}$), and a "high-ionization" one ($\xi = 4265$, $N_{\rm H} = 2\,10^{22}$).

We have studied the behaviour of the temperature, pressure and density for both constant density and constant total pressure models. In Fig. 3 we give the temperature for the three constant density clouds in Netzer et al. (2003) and for our WA in pressure equilibrium. As an example, Fig. 4 shows the Oxygen ionization fractions for both cases. Our results show that the WA in NGC 3783 can be modelled by a single medium in pressure equilibrium, instead of a composite medium of multiple constant density clouds.

As a good illustration of the agreement between an unique constant total pressure model and the composition of several constant density models, one can compare the values of the "observed" ionic column densities (*i.e.* those which have been determined through a curve of growth analysis in Netzer et al. 2003), with those deduced from our best model, and from the composite model of Netzer et al. (2003). Fig. 5 displays the computed column densities *vs.* the observed ones for both cases. One can see that both models give very similar results, even if these do not agree perfectly with the observations.

Based on our best model results and on the object's luminosity and black hole mass, we were able to make some preliminary estimates of physical quantities related to the WA. Assuming $n_{\rm H} = 10^5~\mathrm{cm}^{-3}$, the size of the WA medium achieves $\Delta R \sim 2\,10^{17}$ cm. We should note here that constant pressure models vary only proportionally with $n_{\rm H}$ varying in the range $10^5$ to $10^{12}$; however, assuming a higher value of $n_{\rm H}$ at the face of the cloud would imply a smaller size for the WA medium. For a WA size of $\sim 2\,10^{17}$ cm, and in order to keep the amount of outflowing material within reasonable limits ($\dot{M}_{\rm out}/\dot{M}_{\rm Edd} < 1$), the WA should be located closer than $\sim 2\,10^{18}$ cm (*i.e.* before the Narrow Line Region). This is in agreement with the values put forward by Netzer et al. (2003) and Krongold et al. (2003).

Based on the absence of variability on timescales of 1 to 4 days, Netzer et al. (2003) conclude that the aborbers in NGC 3783 are located far from the central source, and that their densities are small, at most of the order of $n_{\rm H} = 10^5~\mathrm{cm}^{-3}$. Accordingly, the thickness of the WA should be large ($\Delta R \geq 2\,10^{17}$ cm). The dynamical time scale of the WA is of the order of at least $\Delta R/c_{\rm s}$, where $c_{\rm s}$ is the sound velocity. If the gas pressure dominates, $c_{\rm s}$ is very roughly (since it varies by almost one order of magnitude) of the order of $10^7$ cm s$^{-1}$, which means that the dynamical timescale in this object is of the order of $10^3$ years.

If radiation pressure dominates (as it is the case in our model), $c_{\rm s}$ is larger, and the dynamical timescale is reduced in proportion. Nevertheless, it would stay far much longer than the timescale for the flux variations. It can thus be objected that the medium cannot reach a state where it is in pressure equilibrium with the illuminating source; this is actually not true at the zeroth order. Indeed, the medium would then adopt a "quasi-pressure equilibrium" corresponding to a flux averaged over a long time, and the flux variations would induce rapid, but relatively small changes of the temperature and of the ionization equilibrium, keeping the same density structure, and the spectrum would not be strongly modified (work in preparation).

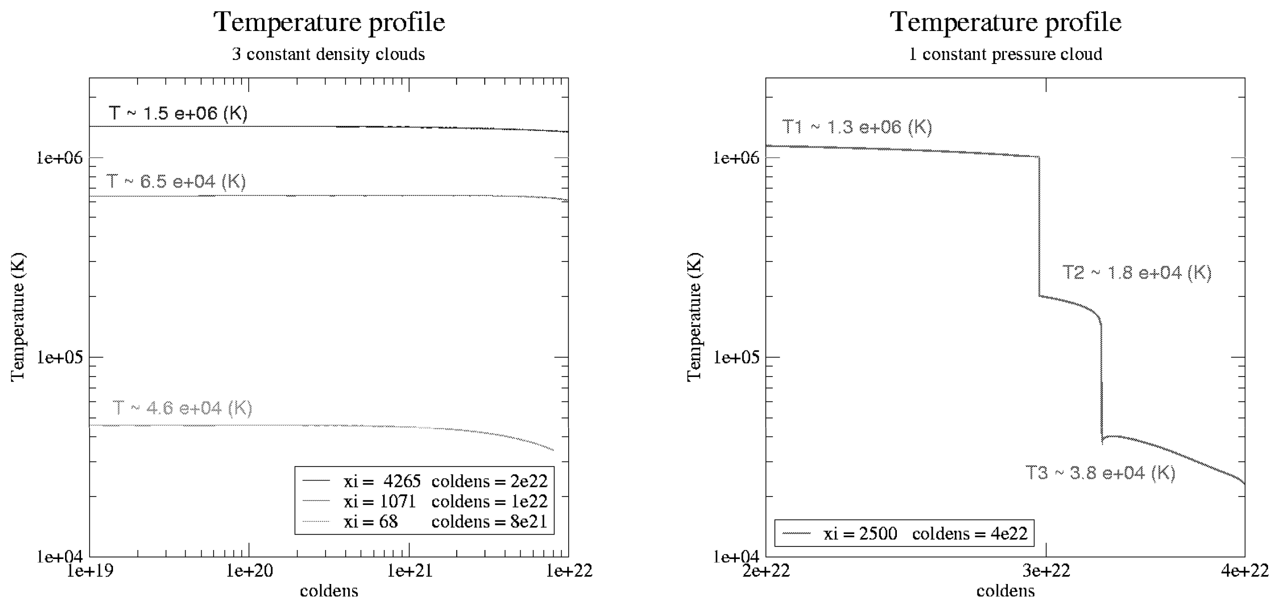


*Figure 3. Left-hand panel: Temperature profiles calculated for the three constant density WA clouds described in Netzer et al. (2003). The top curve corresponds to the "high-ionization" cloud, the intermediate curve to the "medium-ionization" cloud, and the bottom curve, to the "low-ionization" cloud. Right-hand panel: Temperature profile resulting from our modelling of the WA as a single medium in total pressure equilibrium; notice that in this case, the temperature discontinuities arise naturally.*

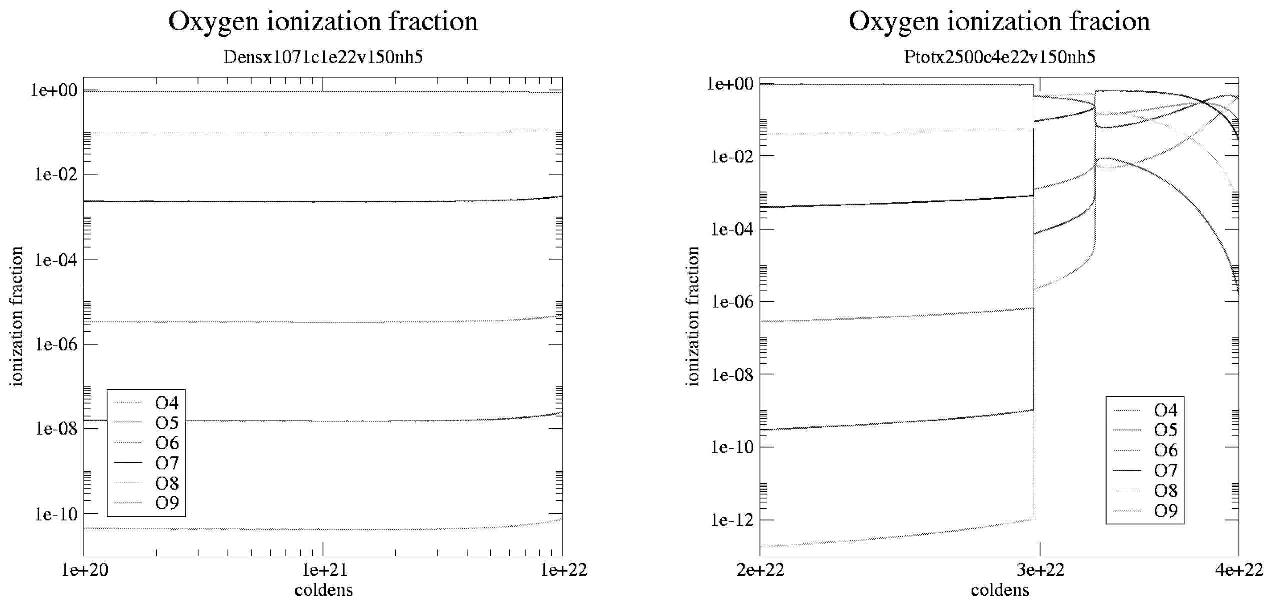


*Figure 4. Ionization fraction of the oxygen ions ("Oi" stands for Oxygen ionized "i-1" times); from top to bottom, the curves correspond to the ions* O IX, O VIII, O VII, O VI, O V *and* O IV*. Left-hand panel: ionization fractions for the "medium-ionization" constant density cloud described in Netzer et al. (2003); we note that in this case, only 2 species (*O VII *and* O VIII*) contribute significantly to the final spectrum. Right-hand panel: ionization fractions resulting from our modelling of the WA as a single medium in total pressure equilibrium; we note that in this case all ionic species contribute to some extent to the final spectrum, justifying the wide range in ionization species observed in this object.*

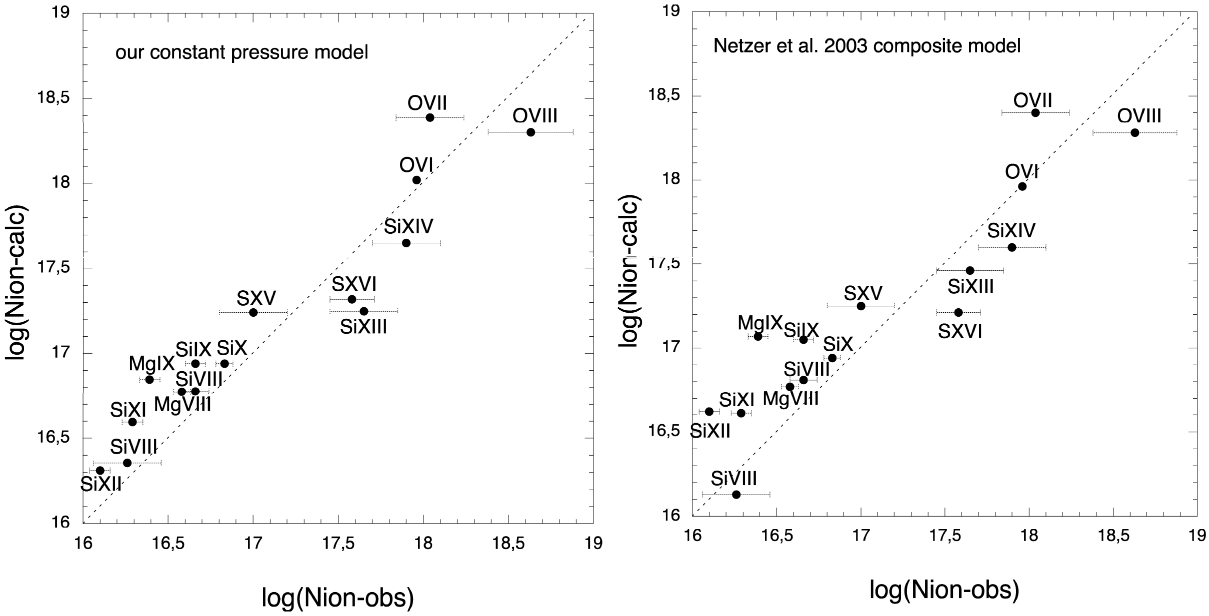


*Figure 5. Ionic column densities for the Netzer et al. (2003) composite constant density model (right panel), and for our constant total pressure model (left panel), vs. the "observed" column densities determined through a curve of growth analysis (Netzer et al. 2003). The observed* O VI *column density value corresponds to a lower limit, only; it was therefore replaced by the Netzer et al. (2003) computed value, which explains the absence of an error bar for this ion. The dotted line shows the diagonal on which the calculated ionic column densities equal the observations.*

Moreover, we observe that the three constant density components of the Netzer et al. (2003) model are located on the thermal stability S-curve at positions corresponding to roughly the same gas pressure (for the same radiative pressure). Therefore, even in the composite constant density model of Netzer et al. (2003), there should also exist a mechanism able to maintain a state of pressure equilibrium (different from our own state, as it does not involve a modification of the ionizing continuum accross the slabs).

Finally, one should take into account that the location of the WA absorber in NGC 3783 is still a controversial matter. A careful analysis of the emission lines and/or P Cygni-like features observed in the spectrum of NGC 3783 (probably due to both outward and reflection components) could help constraining the covering factor in this WA, and provide important information on its geometry and location.

As an example of the studies one can carry on such high-resolution spectra, Fig. 6 shows the absorption/emission blending for the O VIII $\lambda 18.969$ line, as described in Krongold et al. (2003); superposed to the data, we show our own modelling of the P Cyg-like profile (thick line), obtained with a combination of absorption and emission spectra calculated with a turbulent velocity of 200 $\mathrm{km\,s^{-1}}$; we note here that a lower turbulent velocity (*e.g.* 150 $\mathrm{km\,s^{-1}}$) does not provide a satisfactory fit. In this tentative modelling of the O VIII line, the absorption component has a resolution of 300 and is represented at rest wavelength, while the emission component has a resolution of 600 and is resdshifted with respect to the absorption. Such a preliminary result suggests that the WA medium is rather complex; it could be that the absorption and emission gas do not originate on the same region, or even that the reflection flux could contribute to some ex-

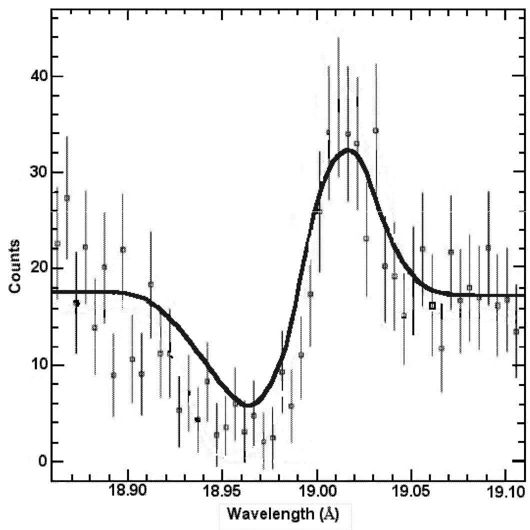


*Figure 6. Absorption/emission blending for the* O VIII $\lambda 18.969$ *line, as described in Krongold et al. (2003); superposed to the data, we show our own modelling of the P Cyg-like profile (thick line), obtained with a combination of absorption and emission spectra calculated with a turbulent velocity of 200* $\mathrm{km\,s^{-1}}$.

tent to the final (total) observed spectrum. These subjects are still under study and will be discussed in more detail in a forthcoming paper (Gonçalves et al., in preparation).

In addition, this preliminary work shows the importance of the turbulent velocity in the description of the observed spectral features. Our grid of models was calculated for a turbulent velocity of $150\,\mathrm{km\,s^{-1}}$; a new grid is now being calculated for a higher value of the turbulent velocity, for comparison.

## 5. CONCLUSIONS AND FUTURE WORK

Our work demonstrates that the TITAN code is well adapted to the study of the WA in Active Galactic Nuclei. In particular, its multi-angle treatement of the transfer will be useful in the study of the emission-line spectrum of NGC 3783, and hopefully provide important information on the geometry and location of the Warm Absorber in this object.

We have shown that the WA in NGC 3783 can be modelled by a single medium in total pressure equilibrium; this is probably the case for all WA presently described by multiple zones of constant density. Such a pressure equilibrium can be reached if we assume the flux to be averaged over a long time.

In the case of NGC 3783, our grid of models has provided a best result corresponding to $\xi = 2500\,\mathrm{erg\,cm\,s^{-1}}$ and $N_{\mathrm{H}} = 4\,10^{22}\ \mathrm{cm^{-2}}$. This model fits the observations well, both for the continuum and the lines; these are blueshifted by $\sim 810\ \mathrm{km\,s^{-1}}$. Our grid of constant total pressure models, dedicated to the study of NGC 3783, is now ready to be inserted into XSPEC; this analysis will provide a more quantitative appreciation of our fit to the *Chandra* data, and will be discussed in more detail in a forthcoming paper (Gonçalves et al., in preparation).

In addition, our work opens perspectives for the future use of the TITAN code by the community, through a larger grid of constant total pressure models to be made available via XSPEC and/or via Virtual Observatory facilities.

## ACKNOWLEDGEMENTS

A. C. Gonçalves acknowledges support from the *Fundação para a Ciência e a Tecnologia* (FCT), Portugal, under grant BPD/11641/2002.

Part of this work was supported by the Laboratoire Européen Associé Astrophysique Pologne-France.

## REFERENCES

Behar E., Rasmussen A. P., Blustin A. J., et al. 2003, ApJ, 598, 232

Chelouche D., & Netzer H. 2005, ApJ, 625, 95

Collin S., Dumont A.-M., & Godet O. 2004, A&A, 419, 877

Dumont A.-M., Abrassart A., & Collin S. 2000, A&A, 357, 823

George I. M., Turner T. J., & Netzer H. 1995, ApJ, 438, 67L

Halpern J. P. 1984, ApJ, 281, 90

Kaspi S., Brandt W. N., Netzer H., et al. 2001, ApJ, 554, 216

Kaspi S., Brandt W. N., George I. M., et al. 2002, ApJ, 574, 643

Krongold Y., Nicastro F., Brickhouse N. S., et al. 2003, ApJ, 597, 832

Netzer H., Kaspi S., Behar E., et al. 2003, ApJ, 599, 933

# NEW XMM-NEWTON SPECTROSCOPY OF THE MOST LUMINOUS AND DISTANT QUASARS

**O. Shemmer and W. N. Brandt**

Department of Astronomy and Astrophysics, Pennsylvania State University, 525 Davey Laboratory, University Park, PA 16802, USA

**ABSTRACT**

In the two parts of this contribution we describe two related *XMM-Newton* programs. The first part summarizes our study of the X-ray spectral properties and variability of $z>4$ quasars (Shemmer et al. 2005). The second part presents preliminary results from our ongoing *XMM-Newton* program to investigate the X-ray spectral properties and variability of luminous, high accretion-rate quasars at $z\sim2$–3. We find that the X-ray photon index does not depend on luminosity or redshift, and there is suggestive evidence that it may depend on the accretion rate. None of our quasars is significantly absorbed, and none shows signatures of reflection. By jointly fitting high-quality spectra of eight radio-quiet $z>4$ quasars, including three from our *XMM-Newton* observations, we place tight constraints on the mean X-ray spectral properties of such sources. Most of our quasars are significantly X-ray variable on timescales of months–years, but none shows rapid ($\sim$1 hr timescale) variations.

## 1. *XMM-NEWTON* SPECTROSCOPY OF $Z>4$ QUASARS

### 1.1. Introduction

Quasars at $z>4$ are valuable cosmological probes of the physical environment in the $\sim$1 Gyr old Universe. In particular, the most distant quasars known, at $z\sim6$, have enabled tracing of the physical conditions in the Universe at the end of the re-ionization epoch with implications for large-scale structure formation (e.g., Fan et al. 2002). The study of $z>4$ quasars therefore has become one of the main themes in astrophysics during the past few years. One of the lines of research in this field is to determine whether the energy production mechanism of quasars is sensitive to the significant large-scale evolution the Universe has experienced over cosmic time. A central question in this context is whether black holes (BHs) in distant quasars feed and grow in the same way as BHs in local active galactic nuclei (AGN). Recent radio–optical observations of $z>4$ quasars have found that their spectral energy distributions (SEDs) are not significantly different from those of lower redshift sources implying no SED evolution, and hence no significant changes in the energy production mechanism of AGN are observed (e.g., see Carilli et al. 2001 and Petric et al. 2003 for radio observations; Pentericci et al. 2003 and Vanden Berk et al. 2001 for UV–optical observations).

X-rays from distant quasars are especially valuable for studying the energy production mechanism, since they provide information on the innermost regions of the central engine, where most of the nuclear energy is produced. Until fairly recently, only a handful of $z>4$ quasars were detected in X-rays, and the data only provided basic X-ray photometry. During the past five years over 100 quasars have been detected by *Chandra* and *XMM-Newton*, allowing reliable measurements of their mean X-ray spectral properties (e.g., Brandt et al. 2002; Bechtold et al. 2003; Grupe et al. 2004, 2006; Vignali et al. 2003a,b, 2005). However, the different X-ray studies of $z>4$ quasars often led to conflicting conclusions. For example, while Bechtold et al. (2003) reported that the X-ray power-law photon indices ($\Gamma$) of $z>4$ quasars are *flatter* than those of nearby AGNs, Grupe et al. (2006) reported that their $\Gamma$ are rather *steep*; Vignali et al. (2005) found that $\Gamma$ does not undergo significant evolution and is not luminosity dependent.

The different conclusions, frequently based upon the same X-ray data, were reached mainly due to the small number of photons collected in the observations that were intended to detect $z>4$ quasars; this led to large uncertainties in the basic X-ray spectral properties and hence to several possible interpretations. This motivated us and other authors to solve the puzzle and obtain high-quality X-ray spectra of several X-ray bright $z>4$ quasars. High-quality X-ray spectra (with $\gtrsim 500$ [$\gtrsim 100$] photons obtained by *XMM-Newton* [*Chandra*]) are currently available for 10 $z>4$ radio-quiet and radio-moderate quasars (Ferrero & Brinkmann 2003; Farrah et al. 2004; Grupe et al. 2004, 2006; Schwartz & Virani 2004; Shemmer et al. 2005, hereafter S05). Below we summarize the results of the recent set of five of those spectra, which are described in detail in S05.

### 1.2. High-Quality Spectra of $z>4$ Quasars

We obtained high-quality *XMM-Newton* spectra of five $z>4$ quasars during *XMM-Newton* AO3; the detailed data-reduction and analysis procedures are described in S05. Each quasar was previously detected in *Chandra* snapshot observations (Vignali et al. 2001, 2003a,b). The basic properties of the quasars, as well as their measured X-ray properties, are given in Table 1. Three of the quasars are radio-quiet, one quasar, PSS 0121+0347, is radio loud ($R$=300; Vignali et al. 2003a), and another quasar, SDSS 0210−0018, is radio moderate ($R$=80; Vignali et al. 2001) following the radio-loudness definition of Kellermann et al. (1989). We detected ∼500–1500 photons from each quasar in a net exposure time of ∼20–30 ks per source. These exposures enabled accurate measurements of $\Gamma$ (with $\Delta\Gamma$=0.15) and upper limits on the intrinsic neutral column densities for each quasar. The *XMM-Newton* data, best-fit spectra, and residuals appear in Fig. 1. In Fig. 1 we also plot confidence contours in the $\Gamma$–$N_{\rm H}$ plane for each quasar.

To extend our analysis, we added to our sample high-quality X-ray spectra of five additional $z>4$ radio-quiet quasars (RQQs) from the archive; these are Q 0000−263 (Ferrero & Brinkmann 2003), SDSS 1030+0524 (Farrah et al. 2004), BR 0351−1034 and BR 2237−0607 (Grupe et al. 2004, 2006), from *XMM-Newton* observations, and SDSS 1306+0356 which was observed with *Chandra* (Schwartz & Virani 2004). The spectra of all 10 $z>4$ quasars were reduced and analyzed uniformly to obtain the basic X-ray spectral properties for each source.

### 1.3. X-ray Spectral Properties of $z>4$ Radio-Quiet Quasars

The best-fit X-ray spectral properties for our sources appear in Table 1. The photon indices and the upper limits on the neutral intrinsic absorption in each quasar were obtained by fitting the spectra with intrinsically (redshifted) absorbed power-law models, including Galactic absorption. The constraints we obtained on the intrinsic absorption in each quasar (Table 1) show that our $z>4$ RQQs are not significantly absorbed. In Fig. 2 we plot $\Gamma$ (above 2 keV in the rest-frame) for samples of radio-quiet AGN, including our expanded sample of $z>4$ quasars, against optical luminosity and redshift. We find that $\Gamma$ takes a typical value of ∼1.9, and it does not depend significantly on either optical luminosity or redshift. We also note that there is no significant intrinsic dispersion in $\Gamma$ values within our sample of eight $z>4$ RQQs.

We have also computed optical–X-ray spectral slopes ($\alpha_{\rm ox}$, e.g., Tananbaum et al. 1979; see Table 1) for our sources and found that our measurements are consistent with the Strateva et al. (2005) and Steffen et al. (2006) conclusions that $\alpha_{\rm ox}$ strongly correlates with ultraviolet luminosity and does not evolve over cosmic time (out to $z$∼6).

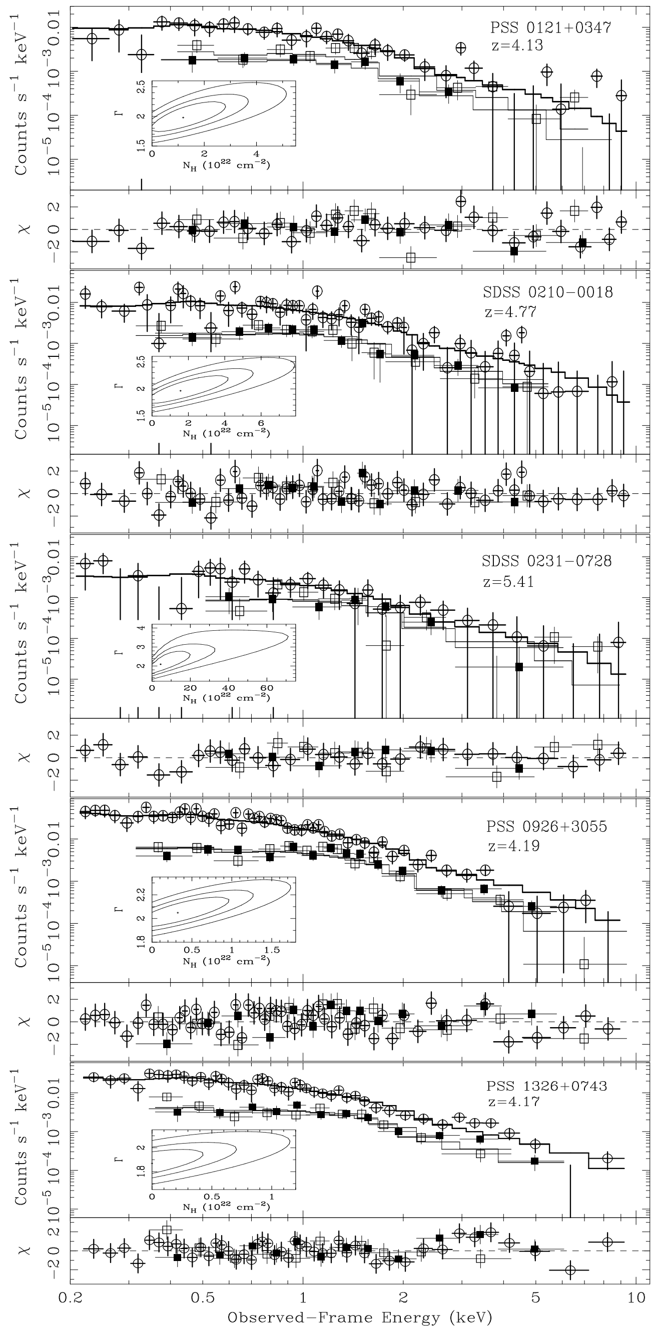


*Figure 1. Data, best-fit spectra, and residuals for our new XMM-Newton observations of five z>4 AGNs. Open circles, filled squares, and open squares represent the pn, MOS1, and MOS2 data, respectively. Solid lines represent the best-fit model for each spectrum, and the thick line marks the best-fit model for the pn data. The $\chi$ residuals are in units of $\sigma$ with error bars of size 1. The inset in each panel shows 68%, 90%, and 99% confidence contours for the intrinsic absorption and photon index.*

*Table 1. Optical and X-ray properties of our z>4 quasar sample.*

| Quasar | $z$ | $M_{\rm B}$[a] | $\Gamma$ | $N_{\rm H}$[b] ($10^{22}$ cm$^{-2}$) | $\log L_{2-10\ \rm keV}$[a] (erg s$^{-1}$) | $\alpha_{\rm ox}$ |
|---|---|---|---|---|---|---|
| PSS 0121+0347 | 4.13 | −28.3 | $1.81^{+0.16}_{-0.16}$ | $\leq 2.91$ | 45.5 | $-1.65^{+0.03}_{-0.03}$ |
| SDSS 0210−0018 | 4.77 | −27.7 | $1.81^{+0.15}_{-0.14}$ | $\leq 4.17$ | 45.3 | $-1.54^{+0.03}_{-0.02}$ |
| SDSS 0231−0728 | 5.41 | −27.9 | $1.85^{+0.33}_{-0.31}$ | $\leq 19.90$ | 45.2 | $-1.62^{+0.06}_{-0.06}$ |
| PSS 0926+3055 | 4.19 | −30.1 | $1.99^{+0.08}_{-0.08}$ | $\leq 1.02$ | 45.9 | $-1.76^{+0.03}_{-0.01}$ |
| PSS 1326+0743 | 4.17 | −29.6 | $1.87^{+0.10}_{-0.10}$ | $\leq 0.47$ | 45.7 | $-1.76^{+0.03}_{-0.02}$ |

[a]Luminosity distances were computed using the standard “concordance” cosmological parameters $\Omega_\Lambda$=0.7, $\Omega_M$=0.3, and $H_0$=70 km s$^{-1}$ Mpc$^{-1}$.
[b]Neutral intrinsic column density.

To obtain the mean X-ray spectral properties of the RQQ population at $z$>4, we fitted jointly our new *XMM-Newton* spectra of three RQQs and the five archival high-quality spectra of $z$>4 RQQs with several models; this is roughly equivalent to fitting a single mean spectrum composed of $\sim$7000 photons. The number of photons in our combined spectrum is larger by an order of magnitude than the number of photons previously used in such analyses (e.g., Vignali et al. 2005). By fitting the spectra jointly we obtained a mean photon index $\Gamma$=$1.97^{+0.06}_{-0.04}$. We also obtained the strongest constraint to date on the mean neutral intrinsic column density in such sources, $N_{\rm H} \lesssim 3\times10^{21}$ cm$^{-2}$ (Fig. 3), showing that optically selected RQQs at $z$>4 are, on average, not more absorbed than their lower-redshift counterparts. All this suggests that the X-ray production mechanism and the central environment in radio-quiet AGN have not significantly evolved over cosmic time. We also used the combined spectrum to constrain the mean equivalent width of a putative neutral narrow Fe K$\alpha$ line to $\lesssim$ 190 eV, and similarly to constrain the mean Compton-reflection component to $R \lesssim$ 1.2; these constraints are consistent with the expected strength of a reflection component given the high luminosities of our sources (e.g., Page et al. 2004).

### 1.4. X-ray Variability of $z$>4 Radio-Quiet Quasars

We applied Kolmogorov-Smirnov tests to the photon arrival times in our new *XMM-Newton* observations to search for rapid ($\sim$1 hr timescale in the rest frame) variations, but none was detected.

To look for long-term (months–years) X-ray variations in our sample, we compared the fluxes of our sources in the observed-frame 0.5–2 keV band in the first epoch (*Chandra* snapshot observations) with those in the second epoch (*XMM-Newton* or *Chandra* observations). Seven $z$>4 quasars from this study have high-quality (i.e., *Chandra* or *XMM-Newton* data to minimize cross-calibration uncertainties) two-epoch X-ray data for our comparison. Using $\chi^2$ statistics, we found that five of the seven quasars varied significantly between the two epochs (Fig. 4); the two sources that did not vary significantly between the two epochs are PSS 1326+0743 and SDSS 1030+0524.

While most quasars varied by no more than a factor of $\approx$2 between the two epochs, one source, SDSS 0231−0728, faded by a factor of $\sim$4 between the first observation (*Chandra*) and the second one (*XMM-Newton*). This flux change occurred over a rest-frame period of 73 d. This is the largest change in X-ray flux observed for a $z$>4 RQQ. Given the UV–optical flux of the source, and using the Strateva et al. (2005) relation between UV luminosity and $\alpha_{\rm ox}$, it is likely that this source was caught in an X-ray high state in the first epoch (Vignali et al. 2003b), since its X-ray flux in the second epoch (S05) agrees with the value predicted from its optical flux (assuming the optical flux is nearly constant). Vignali et al. (2003b) also noted that SDSS 0231−0728 was X-ray brighter than expected (see their Fig. 5). The spectral slope of the source also shows a possible indication of flattening from $\Gamma$=$2.8^{+1.10}_{-0.95}$ to $\Gamma$=$1.85^{+0.33}_{-0.31}$ between the two epochs, but the significance is only $\sim$1 $\sigma$ due to the limited number of counts ($\sim$25) in the first *Chandra* snapshot observation. This is a tentative indication for a transition from a soft/high state to a hard/low state in this source, as has been seen for a few local AGN (e.g., Guainazzi et al. 1998; Maccarone et al. 2003).

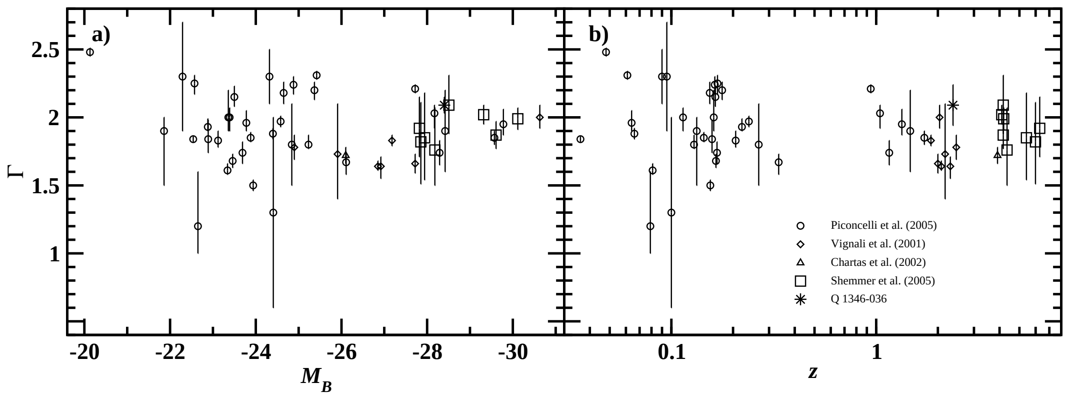


*Figure 2. The X-ray photon index versus (a) absolute $B$ magnitude and (b) redshift; adapted from S05. Note the lack of a clear dependence of the photon index on either luminosity or redshift, although considerable scatter in $\Gamma$ is observed in local AGN. Our new XMM-Newton observation of Q 1346−036, a luminous, high accretion-rate quasar at z=2.37 is represented by a star; our ongoing XMM-Newton observations of similar sources may determine whether $\Gamma$ depends on the accretion rate (see § 2)*

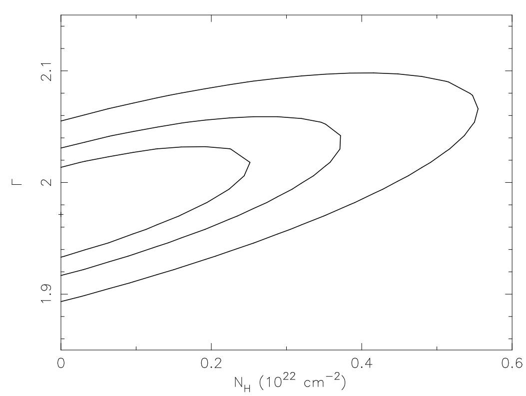


*Figure 3. 68%, 90%, and 99% confidence regions for the photon index vs. intrinsic column density derived from joint spectral fitting of our sample of eight RQQs.*

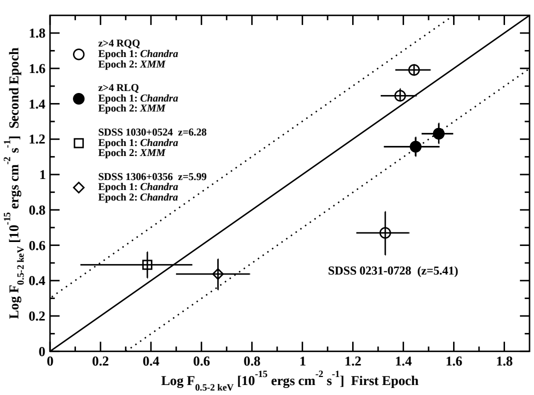


*Figure 4. Two-epoch Galactic-absorption corrected 0.5–2 keV fluxes for seven of the z>4 quasars in our sample. The solid line marks the 1:1 flux ratio, and the two dotted lines mark 1:2, and 2:1 flux ratios, to guide the eye. SDSS 0231−0728 clearly varied by more than a factor of two between the two epochs. The second and third most variable sources, PSS 0121+0347 and SDSS 0210−0018, are radio loud and radio moderate, respectively, and are marked with filled circles.*

## 2. *XMM-NEWTON* SPECTROSCOPY OF LUMINOUS, HIGH ACCRETION-RATE QUASARS AT REDSHIFT ∼2–3

### 2.1. Is $\Gamma$ an Accretion Rate Indicator?

In § 1 we have shown that the X-ray photon index in RQQs appears to be constant, with a typical value of ∼1.9, regardless of redshift or luminosity. This result has also been confirmed and strengthened by other recent studies (e.g., Mateos et al. 2005; Page et al. 2005; Risaliti & Elvis 2005). However, inspection of Fig. 2 shows considerable scatter in $\Gamma$, in particular at low redshifts ($z \lesssim 0.5$). This scatter may be attributed to a fundamental physical parameter, which controls the X-ray spectral shape in AGN.

Boller et al. (1996) have found that the soft (*ROSAT* band) X-ray power-law photon index is anti-correlated with FWHM(H$\beta$), and hence narrow-line Seyfert 1 (NLS1s) galaxies (which meet the FWHM[H$\beta$] $\lesssim$ 2000 km s$^{-1}$ criterion of Osterbrock & Pogge 1985) have significantly steeper X-ray spectral slopes than broad-line Seyfert 1 galaxies. This trend is observed in the hard (*ASCA*) X-ray band as well (e.g., Brandt et al. 1997; Leighly 1999). Strong correlations between FWHM(H$\beta$) and the X-ray photon index in both the soft and hard bands are also exhibited by higher luminosity nearby ($z \lesssim 0.5$) quasars (e.g., Laor et al. 1997; Porquet et al. 2004).

Brandt & Boller (1998) and Laor (2000) have suggested that the strong $\Gamma$–FWHM(H$\beta$) correlation may be a consequence of a fundamental correlation between $\Gamma$ and the accretion rate, since FWHM(H$\beta$) is considered to be an accretion-rate indicator in AGN (e.g., Boroson & Green 1992; Porquet et al. 2004). Such a correlation may be expected if the bulk of the emitted optical–X-ray energy is shifted into higher energies for higher accretion rates.

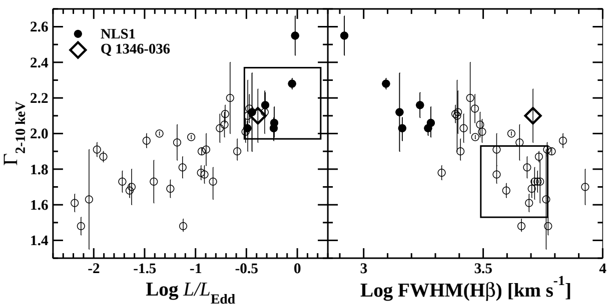


*Figure 5. X-ray photon index in the rest-frame 2–10 keV band versus $L/L_{\rm Edd}$ (left) and FWHM(H$\beta$) (right). Circles mark AGN at z<0.5. NLS1s are marked with filled symbols, and Q 1346−036, a luminous, z=2.37 quasar from the S04 sample and recently observed by XMM-Newton, is marked with a diamond; it is the only high-$z$ source on this diagram. Both $L/L_{\rm Edd}$ and FWHM(H$\beta$) are significantly correlated with $\Gamma$ for z<0.5 AGN. Boxes mark the expected positions of the S04 quasars on each correlation.*

The use of FWHM(H$\beta$) as an accretion-rate indicator relies on reverberation-mapping studies that found a strong correlation between the broad-line region (BLR) size and luminosity in AGN (e.g., Kaspi et al. 2000). By assuming Keplerian motion of the BLR gas around the central BH and using the BLR size–luminosity relation, the BH mass becomes $M_{\rm BH}= c_1[\lambda L_\lambda(5100)]^{c_2}$ [FWHM(H$\beta$)]$^2$, and the accretion rate (in terms of the Eddington ratio) is therefore $L/L_{\rm Edd}\propto[\lambda L_\lambda(5100)]^{1-c_2}$ [FWHM(H$\beta$)]$^{-2}$, where $\lambda L_\lambda(5100)$ is the monochromatic luminosity at 5100Å, $L_{\rm Edd}$ is the Eddington luminosity, and $c_1$ and $c_2$ are constants determined by reverberation mapping (e.g., Kaspi et al. 2000, 2005; see the specific equations in Shemmer et al. 2004, hereafter S04). FWHM(H$\beta$) is perhaps the best accretion-rate indicator, and the use of other emission lines as proxies to H$\beta$, such as C IV, can lead to spurious estimates of $L/L_{\rm Edd}$ (e.g., Baskin & Laor 2005). NLS1s are the highest accretion-rate sources among low-luminosity AGN, with $L/L_{\rm Edd}$ approaching, and in extreme cases even exceeding, unity.

## 2.2. X-ray Properties of Luminous, High Accretion Rate Quasars at High Redshift

The recent study of S04 has found that in at least two respects, accretion rate (determined from H$\beta$) and metallicity, extremely luminous ($L \gtrsim 10^{47}$ erg s$^{-1}$, where $L$ is the bolometric luminosity) quasars at 2<$z$<3.5 resemble NLS1s with $L \lesssim 10^{45}$ erg s$^{-1}$. Motivated by this study, we have initiated an *XMM-Newton* program to look for unusual X-ray properties in the S04 quasars and to determine whether they are the luminous, high-$z$ analogs of local NLS1s (frequently termed narrow-line type 1 quasars). Specifically, we intend to measure $\Gamma$ accurately (to within $\pm$0.15) for these sources and to look for rapid (on a $\sim$1 hr rest-frame timescale) X-ray variations, since steep photon indices and rapid X-ray variations are two well-known NLS1 characteristics. The X-ray photon indices obtained for the S04 sources will allow us to test whether $\Gamma$ can be considered a reliable accretion-rate indicator for all AGN, including luminous, high-$z$ quasars, with important implications for accretion disk and corona models in AGN (e.g., Haardt & Maraschi 1993).

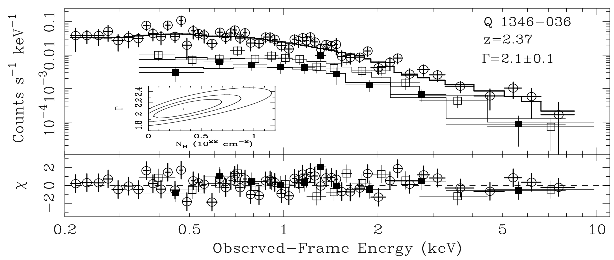


*Figure 6. Data, best-fit spectrum, and residuals for our new XMM-Newton observation of Q 1346−036, a luminous z=2.37 quasar from S04. Symbols are similar to those in Fig. 1. We find a photon index $\Gamma$=2.1$\pm$0.1, which seems to support the hypothesis that the accretion rate is the underlying physical driver for steep X-ray spectra in AGN (see Fig. 5).*

This test is portrayed in Fig. 5, where we have plotted $\Gamma$ versus FWHM(H$\beta$) and $L/L_{\rm Edd}$ (which is a combination of FWHM(H$\beta$) and $L$). In this plot we consider archival data for AGN with high-quality X-ray spectra (obtained from Reeves et al. 1997; Reynolds 1997; George et al. 1998, 2000; Piconcelli et al. 2005) and with reliable FWHM(H$\beta$) measurements. All but one of the sources in Fig. 5, Q 1346−036, are AGN at $z \lesssim 0.5$ (and therefore have low–moderate luminosities), since at higher redshift H$\beta$ is not present in the optical band and near-IR measurements of FWHM(H$\beta$) are difficult to obtain. Although there are significant correlations between $\Gamma$ and both FWHM(H$\beta$) and $L/L_{\rm Edd}$ for the nearby sources, the S04 quasars are predicted to have significantly different values of $\Gamma$ in each case. Based on their FWHM(H$\beta$), these quasars are expected to have a mean $\Gamma$ of $\sim$1.7, but when their high accretion rates are considered, the mean expected $\Gamma$ is $\sim$2.2, which is only observed in extreme NLS1s. The first S04 quasar observed in our ongoing *XMM-Newton* program, Q 1346−036, shows a moderately steep X-ray spectrum (see Fig. 6) and suggests that the $\Gamma$–$L/L_{\rm Edd}$ correlation may still hold when luminous, high-$z$ quasars are included (Fig. 5).

**ACKNOWLEDGMENTS**

We wish to thank all of our collaborators who contributed to these projects: X. Fan, S. Kaspi, R. Maiolino, H. Netzer, G. T. Richards, D. P. Schneider, M. A. Strauss, and C. Vignali.

## REFERENCES


Baskin, A., & Laor, A. 2005, MNRAS, 356, 1029

Bechtold, J., et al. 2003, ApJ, 588, 119

Boller, T., Brandt, W. N., & Fink, H. 1996, A&A, 305, 53

Boroson, T. A., & Green, R. F. 1992, ApJS, 80, 109

Brandt, W. N., Mathur, S., & Elvis, M. 1997, MNRAS, 285, L25

Brandt, N., & Boller, T. 1998, Astronomische Nachrichten, 319, 163

Brandt, W. N., et al. 2002, ApJ, 569, L5

Carilli, C. L., et al. 2001, ApJ, 555, 625

Fan, X., Narayanan, V. K., Strauss, M. A., White, R. L., Becker, R. H., Pentericci, L., & Rix, H. 2002, AJ, 123, 1247

Farrah, D., Priddey, R., Wilman, R., Haehnelt, M., & McMahon, R. 2004, ApJ, 611, L13

Ferrero, E., & Brinkmann, W. 2003, A&A, 402, 465

George, I. M., Turner, T. J., Netzer, H., Nandra, K., Mushotzky, R. F., & Yaqoob, T. 1998, ApJS, 114, 73

George, I. M., Turner, T. J., Yaqoob, T., Netzer, H., Laor, A., Mushotzky, R. F., Nandra, K., & Takahashi, T. 2000, ApJ, 531, 52

Grupe, D., Mathur, S., Wilkes, B., & Elvis, M. 2004, AJ, 127, 1

Grupe, D., Mathur, S., Wilkes, B., & Osmer, P. 2006, AJ, in press (astro-ph/0501521)

Guainazzi, M., et al. 1998, A&A, 339, 327

Haardt, F., & Maraschi, L. 1993, ApJ, 413, 507

Kaspi, S., Brandt, W. N., & Schneider, D. P. 2000, AJ, 119, 2031

Kaspi, S., Maoz, D., Netzer, H., Peterson, B. M., Vestergaard, M., & Jannuzi, B. T. 2005, ApJ, 629, 61

Kellermann, K. I., Sramek, R., Schmidt, M., Shaffer, D. B., & Green, R. 1989, AJ, 98, 1195

Laor, A., Fiore, F., Elvis, M., Wilkes, B. J., & McDowell, J. C. 1997, ApJ, 477, 93

Laor, A. 2000, New Astronomy Review, 44, 503

Leighly, K. M. 1999, ApJS, 125, 317

Maccarone, T. J., Gallo, E., & Fender, R. 2003, MNRAS, 345, L19

Mateos, S., et al. 2005, A&A, 433, 855

Osterbrock, D. E., & Pogge, R. W. 1985, ApJ, 297, 166

Page, K. L., O'Brien, P. T., Reeves, J. N., & Turner, M. J. L. 2004a, MNRAS, 347, 316

Page, K. L., Reeves, J. N., O'Brien, P. T., & Turner, M. J. L. 2005, MNRAS, 898, in press (astro-ph/0508524)

Pentericci, L., et al. 2003, A&A, 410, 75

Petric, A. O., Carilli, C. L., Bertoldi, F., Fan, X., Cox, P., Strauss, M. A., Omont, A., & Schneider, D. P. 2003, AJ, 126, 15

Piconcelli, E., Jimenez-Bailón, E., Guainazzi, M., Schartel, N., Rodríguez-Pascual, P. M., & Santos-Lleó, M. 2005, A&A, 432, 15

Porquet, D., Reeves, J. N., O'Brien, P., & Brinkmann, W. 2004, A&A, 422, 85

Reeves, J. N., Turner, M. J. L., Ohashi, T., & Kii, T. 1997, MNRAS, 292, 468

Reynolds, C. S. 1997, MNRAS, 286, 513

Risaliti, G., & Elvis, M. 2005, ApJ, 629, L17

Schwartz, D. A., & Virani, S. N. 2004, ApJ, 615, L21

Shemmer, O., Netzer, H., Maiolino, R., Oliva, E., Croom, S., Corbett, E., & di Fabrizio, L. 2004, ApJ, 614, 547

Shemmer, O., Brandt, W. N., Vignali, C., Schneider, D. P., Fan, X., Richards, G. T., & Strauss, M. A. 2005, ApJ, 630, 729

Steffen, A. T. et al. 2006, AJ, submitted

Strateva, I. V., Brandt, W. N., Schneider, D. P., Vanden Berk, D. G., & Vignali, C. 2005, AJ, 130, 387

Tananbaum, H., et al. 1979, ApJ, 234, L9

Vanden Berk, D. E., et al. 2001, AJ, 122, 549

Vignali, C., Brandt, W. N., Fan, X., Gunn, J. E., Kaspi, S., Schneider, D. P., & Strauss, M. A. 2001, AJ, 122, 2143

Vignali, C., Brandt, W. N., Schneider, D. P., Garmire, G. P., & Kaspi, S. 2003a, AJ, 125, 418

Vignali, C., et al. 2003b, AJ, 125, 2876

Vignali, C., Brandt, W. N., Schneider, D. P., & Kaspi, S. 2005, AJ, 129, 2519

# X-RAY EVOLUTION OF ACTIVE GALACTIC NUCLEI IN HIERARCHICAL GALAXY FORMATION

**N. Menci**

INAF-Osservatorio Astronomico di Roma, Via di Frascati 33, 00040 Monteporzio (Roma), Italy

## ABSTRACT

We have incorporated the description of the X-ray properties of Active Galactic Nuclei (AGNs) into a semi-analytic model of galaxy formation, adopting physically motivated scaling laws for accretion triggered by galaxy encounters. Our model reproduces the level of the cosmic X-ray background at 30 keV; we predict that the largest contribution (around $2/3$) comes from sources with intermediate X-ray luminosity $10^{43.5} < L_X/\mathrm{erg\,s^{-1}} < 10^{44.5}$, with 50 % of the total specific intensity produced at $z < 2$. The predicted number density of X-ray AGNs is characterized by a "downsizing" effect: for luminous X-ray AGNs ($L_X > 10^{44.5}$ erg/s in the 2-10 keV band) it peaks at $z \approx 2$ with a decline of around 3 dex to $z = 0$; for the low luminosity sources ($10^{43} < L_X/\mathrm{erg\,s^{-1}} < 10^{44}$) it has a broader and less pronounced maximum around $z \approx 1.5$, and a smoother decline at lower $z$. We compare our results with recent observations.

Key words: galaxies: active – galaxies: formation – X-rays: galaxies – galaxies: evolution.

## 1. INTRODUCTION

Connecting the evolution of AGNs to that of their host galaxies is a major goal of present "ab initio" galaxy formation models within a cosmological context (see, e.g., Haiman & Loeb 1998; Wyithe & Loeb 2002; Hatziminaoglou et al. 2003; Volonteri, Hardt & Madau 2003; Kauffmann & Haehnelt 2000, 2002). However, a common problem of the models proposed so far is that they do not match the observed steep decline of the QSO density at redshifts $z \lesssim 1$ and its dependence on the AGN luminositiy.

Recently, Menci et al. (2003) developed a physical model to connect the BH accretion to the galaxy evolution in the hierarchical scenario. The accretion is triggered by galaxy encounters, not necessarely leading to bound merging, in common host structures like clusters and especially groups; these events destabilize part of the galactic cold gas and hence feed the central BH, following the physical modelling developed by Cavaliere & Vittorini (2000). The amount of the cold gas available, the interaction rates, and the properties of the host galaxies are derived through the SAM developed by Menci et al. (2002).

As a result, at high $z$ the protogalaxies grow rapidly by hierarchical merging; meanwhile, much fresh gas is imported and also destabilized, so the BHs are fueled at their full Eddington rates. At lower $z$, the dominant dynamical events are galaxy encounters in hierarchically growing groups; now refueling peters out, as the residual gas is exhausted while the destabilizing encounters dwindle. With no parameter tuning other than needed for star formation in canonical SAMs, the model naturally produces in the bright QSO population a rise for $z > 3$, and for $z \lesssim 2.5$ a drop as steep as observed. In addition, the results closely reproduce the observed luminosity functions of the optically selected QSOs, their space density at different magnitudes from $z \approx 5$ to $z \approx 0$, and also the local $m_{BH} - \sigma$ relation.

Here we report the implications of this model for the X-ray AGNs (Menci et al. 2004) to derive their contribution to the X-ray background and their intrinsic luminosity function.

## 2. THE GALAXY FORMATION MODEL

The model we adopt is described in detail in Menci et al. (2003; 2004). Here we recall the basic points:

We follow the merging histories of DM clumps, adopting the Extended Press & Schechter description (see, e.g., Lacey & Cole 1993. When two haloes merge, the contained galaxies merge on a longer timescale, either with the central dominant galaxy (due to the orbital decay produced by dynamical friction) or with other "satelite" galaxies orbiting the same DM halo ("binary aggregations"). We describe the potential depth of the DM halo associated to a single galaxy through its circular velocity $v$, while the circular velocity of the halos hosting the galaxies (groups and clusters) is $V$; the model also computes the tidal radius $r_t$ associated to galaxies with given $v$.

The properties of the gas and stars contained in the galactic DM clumps are computed following the standard recipes commonly adopted in SAMs. Starting from an initial gas amount $m\,\Omega_b/\Omega$ ($m \propto v^3$ being the DM mass of the galaxies) at the virial temperature of the galactic halos, we compute the mass $m_c$ of cold baryons which are able to radiatively cool in the densest, central regions. This settles is a rotationally supported disk whose radius $r_d$ and rotation velocity $v_d$ is computed after Mo, Mao & White (1998). Stars form with rate $\dot{m}_* \propto (m_c/t_d)$ with the disk dynamical time evaluated as $t_d = r_d/v_d$. Finally, a mass $\Delta m_h = m_*\,(v/v_h)^{\alpha_h}$ is returned from the cool to the hot gas phase due to the energy fed back by canonical type II Supernovae associated to $m_*$. The values adopted for the free parameters $\alpha_* = -1.5$, $\alpha_h = 2$ and $v_h = 150$ km/s fit both the local B-band galaxy LF and the Tully-Fisher relation, as illustrated by Menci et al. (2002). The model also matches the bright end of the galaxy B-band LFs up to redshifts $z \approx 3$ and the resulting global star formation history is broadly consistent with that observed up to redshift $z \approx 4$ see Menci et al. (2005).

At each merging event, the masses of the different baryonic phases are replenished by those in the merging partner; the further increments $\Delta m_c$, $\Delta m_*$, $\Delta m_h$ from cooling, star formation and feedback are recomputed on iterating the procedure described above.

The resulting star formation rate (for a given $v$) is convolved with the spectral energy distribution $\phi_\lambda$ obtained from population synthesis models Bruzual & Charlot 1993) to obtain the integrated galactic stellar emission $S_\lambda(v,t)$ at the wavelength $\lambda$.

## 3. ENCOUNTERS TRIGGERING STARBURSTS AND BH ACCRETION

A quantitative model to derive the fraction $f$ of cold gas destabilized by the encounters has been worked out by Cavaliere & Vittorini (2000) and has been inserted into a SAM by Menci et al. (2003, 2004, 2005).

For a galactic halo with given circular velocity $v$ inside a host halo (group or cluster) with circular velocity $V$ and virial radius $R$, grazing encounters occur at a rate $\tau_r^{-1} = n_T(V)\,\Sigma(v,V)\,V_r(V)$, where $n_T = 3\,N_T/4\pi R^3$, and the cross section $\Sigma(v,V) \approx \pi\,\langle r_t^2 + r_t^{'2}\rangle$ is averaged over all partners with tidal radius $r_t'$ and circular velocity $v'$ in the same halo $V$. The membership $N_T(V)$ (i.e., the number of galaxies contained in a group or cluster with circular velocity $V$), the distributions of $v'$, $r_t'$, and the relative velocity $V_r = \sqrt{2}\,V$ are computed from the SAM. The duration of each encounter is defined as $\tau_e = \langle (r_t + r_t^{'})/V\rangle$ (with an upper limit given by $\tau_r$).

The fraction of cold gas which is destabilized in each interaction event and feeds the starbursts is derived from eq. A3 of Cavaliere & Vittorini (2000) in terms of the variation $\Delta j$ of the specific angular momentum $j \approx Gm/v_d$ of the gas;

$$f(v,V) \approx \frac{1}{2}\left|\frac{\Delta j}{j}\right| = \frac{1}{2}\left\langle \frac{m'}{m}\,\frac{r_d}{b}\,\frac{v_d}{V}\right\rangle. \qquad (1)$$

The average runs over the probability of finding a galaxy with mass $m'$ in the same halo $V$ where the galaxy $m$ is located, and the impact parameter $b$ is computed in the SAM. The prefactor accounts for the probability 1/2 of inflow rather than outflow related to the sign of $\Delta j$.

We assume that $1/4$ of the destabilized fraction $f$ feeds the central BH (whose intial seeds are asssumed to have a mass $10^2\,M_\odot$, see Madau & Rees (2000), while the remaining fraction is assumed to kindle circumnuclear starbursts, see Sanders & Mirabel (1996). Thus, the average gas accretion rate onto the central black hole as

$$\dot{m}_{acc}(v,z) = \left\langle \frac{f(v,V)\;m_c(v)}{4\,\tau_r(v,V)}\right\rangle, \qquad (2)$$

where the average over all host halos with circular velocity $V$ is computed from the SAM. The bolometric luminosity so produced by the QSO hosted in a given galaxy is then given by

$$L(v,t) = \frac{\eta\, c^2 \Delta m_{acc}}{\tau_e}\,, \qquad (3)$$

where $\Delta m_{acc}$ is the gas accreted at the rate given by eq. (3). and we adopt the standard mass-to-energy conversion efficiency $\eta \approx 0.1$ (see Yu & Tremaine 2002). Here $\tau_e \approx t_d \sim 5\,10^7\,(t/t_0)$ yrs is the duration of the accretion episode, i.e., the timescale for the QSO to shine; $\Delta m_{acc}$ is the gas accreted at the rate given by eq. (2). The blue luminosity $L_B$ is obtained by applying a bolometric correction 13 (Elvis et al. 1994), while for the unabsorbed X-ray luminosity $L_X$ (2-10 keV) we adopt a bolometric correction $c_{2-10} = 100$ following Elvis, Risaliti & Zamorani (2002); for simplicity, this is assumed to be constant with $z$. The shape of the X-ray spectrum $I(E)$ is assumed to be a power law with a slope $\alpha = 0.9$ (see Comastri 2000 and references therein), with an exponential cutoff at an energy $E_c = 300$ keV (see e.g. Perola et al. 2002 and references therein); in view of the present data situation we shall keep this as our fiducial shape.

## 4. RESULTS

We first compute the predicted contribution to the cosmic X-ray background (CXB) from AGNs at different redshifts and luminosity. The result is shown in Fig. 1, for the hard CXB at $E_0 = 30$ keV obtained by integrating all the prdicted sources out to running redshift $z$. We show both the global value, and the fraction contributed by AGNs in three classes of luminosity. The predicted background with the chosen parameters for the spectrum

($\alpha = 0.9$, $E_c = 300$ keV, $c_{2-10} = 100$) exceeds the value measured by HEAO1-A2 by no more than 50 %. Note that the value of the observed background is appreciabely affected by the presence of sources in a Compton thick phase of obscuration, not included in the model.

At the present state of our observational knowledge, the substantial agreement is very encouraging, especially if the following points are taken into account: a) the available evidence (at $E < 10$ keV, Lumb et al. 2002; Vecchi et al. 1999) that the CXB normalization from the HEAO1-A2 experiment may be underestimated by as much as 30 %; b) the bolometric correction need take on the fixed value we adopted for all values of $L$ and $L/L_{edd}$; c) the incidence of a Compton thick phase along the active phase of a galactic nucleus, as a function of $L$ and $z$, is not known, except that locally it may amount as much as 50 % (Risaliti, Maiolino & Salvati 1999) of the so-called type 2 AGNs, namely those with a substantial obscuration both in the optical as well as in the X-ray band. The essential features of our predictions are shown in Figs. 2 and 3.

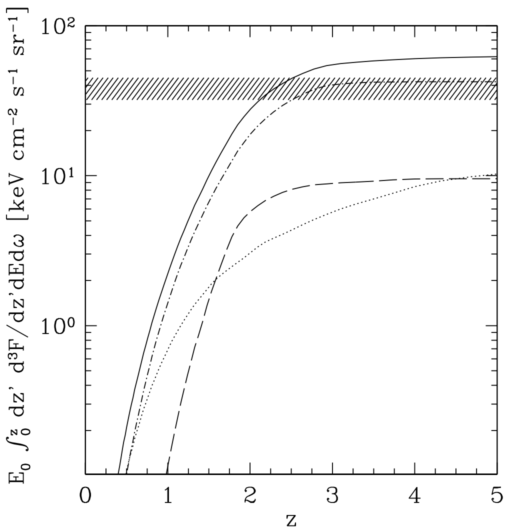

Fig. 2. - The cumulative contruibution (multiplied by the energy $E_0$) to the predicted CXB at $E_0 = 30$ keV, yielded by sources at progressively larger redshifts. The solid line shows the total CXB produced by sources with all luminosities. The other lines show the contributions of AGNs with luminosities $L_x$ (in units of erg $s^{-1}$ in the band 2-10 keV) in the ranges $42 < logL_X < 43.5$ (dotted), $43.5 < logL_X < 44.5$ (dot dashed), and $44.5 < logL_X$ (long-dashed). The shaded strip is the value 43 keV cm$^{-2}$ s$^{-1}$ sr$^{-1}$ measured by HEAO1-A2 (Gruber et al. 1999).

Fig. 1 shows that in our model the CXB is mainly contributed by AGNs with intermediate luminosities $L_X = 10^{43.5} - 10^{44.5}$ erg/s, which provide $\approx 50\%$ of the total value. High luminosity ($L_X > 10^{44.5}$ erg/s) and low luminosity ($L_X < 10^{43}$ erg/s) sources contribute a fraction $\sim 25\%$ each. The population with intermediate luminosities strikes the best tradeoff between larger luminosity and smaller number of sources. Thus, in this picture high luminosity highly absorbed objects (the so-called type 2 QSOs) would not give a dominant contribution to the hard CXB. In fact, although recent XMM and Chandra surveys are providing a sizeable number of QSO2 (Barger et al. 2002, Fiore et al. 2003, Hasinger 2003), these are likely to constitute a relatively minor fraction of sources down to the fluxes where the bulk of the hard CXB is resolved into sources.

In Fig. 2 we compare our predictions with the evolution of the number and luminosity densities of AGNs in three luminosity bins, estimated by Fiore et al. (2003). All the predicted densities drop substantially from $z \approx 2$ to the present. The agreement with the data is excellent for the highest luminosity bin, and confirms that, at least for the very luminous AGNs, the bolometric corrections adopted in the B and in the X-ray band are fully consistent.

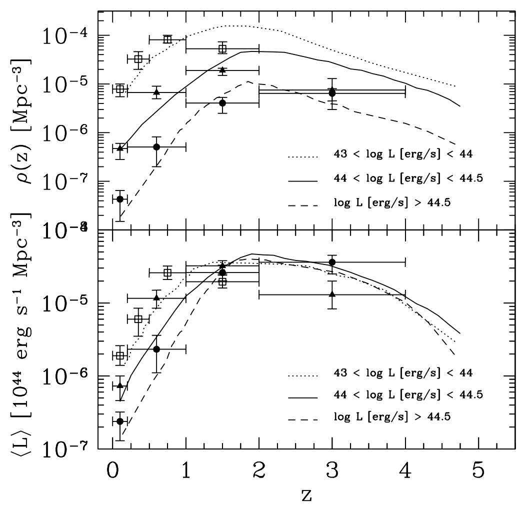


Fig. 2. - Top: The evolution of the number density of X-ray AGNs in three bins of luminosity (in units of erg/s, in the band 2-10 keV): $43 < logL_X < 44$ (dotted line), $44 < logL_X < 44.5$ (solide line), $44.5 < logL_X$ (dashed line). The data for the above luminosity bins (squares, triangles, and circles, respectively) are taken from Fiore et al. (2003). Bottom: The evolution of the X-ray luminosity density for the same luminosity bins.

At lower luminosities, the decline for $z < 1 - 2$ is less pronounced in the predictions as well as in the observations. In the former, this is due to the larger quantity of galactic cold gas left available for accretion in the less massive galaxies. Such a downsizing effect is a natural feature in hierachical scenarios, since more massive potential wells originate from clumps collapsed earlier in *biased* regions of the primordial perturbation field; the higher densities then prevailing allowed for earlier condensation and hence enhanced star formation at high redshifts. Thus, at low $z$ a larger fraction of cold gas will have already been converted into stars, and both star formation and BH accretion are considerably suppressed. We note though that the decrease of the peak redshift with decreasing luminosity appears to be significantly smaller than indicated by the data. In particular, at z$= 1 - 2$ the observed density of Seyfert-like AGNs is a factor $\approx 2$

lower than predicted by the model; a similar difference is present also for the intermediate luminosity objects ($L_{2-10} = 10^{44-44.5}$ erg s$^{-1}$) in the redshift bin $z = 2{-}4$.

The reason for such a discrepancy can be traced back to the shape of the high-$z$ X-ray luminosity function. This is shown in Fig. 3, where we compare our model results with the observational LFs derived by Fiore et al. (2003, upper panel) and by Ueda et al. (2003, lower panel), which are obtained from a combination of HEAO1, ASCA and *Chandra* data, and extend down to lower luminosities. The above observational results concur to indicate that the LFs at $z \gtrsim 2$ are appreciably flatter than at $z = 0.5 - 1$. When the above data are compared to our results, a substantial agreement is found at low $z$, while at $z \gtrsim 1.5 - 2$ the model overestimates the number of low luminosity objects found in both the observational analysis. Such a mismatch can not be reduced by tuning the bolometric correction $c_{2-10}$ adopted in our model, since the latter affects only the normalization of the luminosities.

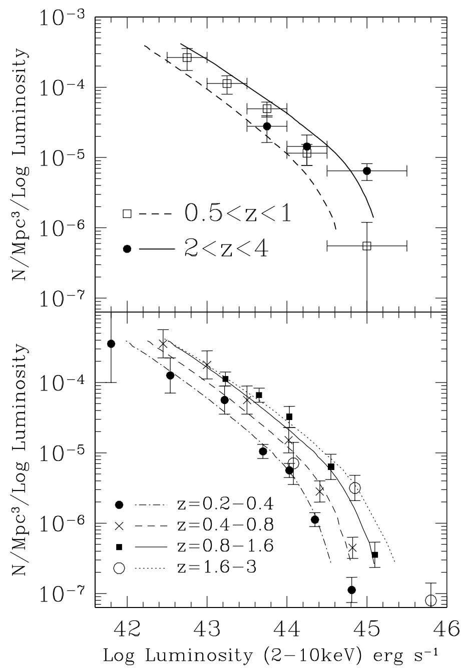


Fig. 3. - Upper panel. The predicted LFs in the energy range 2-10 keV at low redshifts $0.5 < z < 1$ (dashed line) and high redshifts $2 < z < 4$ (solid line) are compared with observational values derived from the same sample used in Fiore et al. (2003) to derive the densities in Fig. 2. Bottom panel. The predicted LFs are compared with data bu Ueda et al. (2003).

## 5. DISCUSSION

We have incorporated the description of the X-ray properties of AGNs into the hierarchical picture of galaxy evolution. Our semi-analytic model, already proven to match the observed evolution of luminous optically selected QSOs over the redshift range $0 < z < 6$ (Menci et al. 2003), is here extended to bolometric luminosities $L$ a factor 10 lower. So we describe the history of accretion down to $L \sim 10^{45}$ erg/s, for which the main observational information comes from the X-ray band.

We have compared our model with X-ray observations either corrected for gas obscuration, or performed in the hard ($E > 30$ keV) band not affected by photoelectric absorption.

We find that our model is encouragingly able to match the level of the cosmic X-ray background (CXB) at 30 keV (Fig. 1). We predict that the largest contribution (around 2/3) to the CXB comes from intermediate luminosity sources $43.5 < log(L_X/erg\, s^{-1}) < 44.5$, and that 50 % of its total specific intensity is produced at $z < 2$.

When compared to the observed evolution of the number and luminosity density of AGNs with different $L_X$ (Fig. 2), our model agrees with the observations concerning all luminosities $L_X > 10^{43}$ erg/s for low or intermediate redshifts $z \lesssim 1.5 - 2$. In particular, the density of luminous ($L_X > 10^{44.5}$ erg/s) AGNs peaks at $z \approx 2$, while for the low luminosity sources ($10^{43} < L_X/\mathrm{erg\,s^{-1}} < 10^{44}$) it has a broader maximum around $z \approx 1.5$; the decline from the maximum to the value at the present epoch is around 3 dex for the former class, and 1.5 dex for the latter class. At larger redshifts $z \gtrsim 2$, the model still reproduces the observed number and luminosity densities of AGNs stronger than $10^{44.5}$ erg/s, but at z= $1 - 2$ the predicted density of Seyfert-like AGNs is a factor $\approx 2$ larger than observed; a similar difference is present also for the intermediate luminosity objects ($L_{2-10} = 10^{44-44.5}$ erg s$^{-1}$) in the redshift bin $z = 2 - 4$. We next discuss our interpretation of both the low-$z$ and the high-$z$ results.

For $z \lesssim 2$, the model results agree with the observed number and luminosity densities in indicating a drop of the AGN population for $z < 2$ which is faster for the strongest sources. Such a *downsizing* effect in our picture is due to the combined effect of: 1) the decrease of the galaxy merging and encounter rates which trigger the gas destabilization and the BH feeding in each galaxy; 2) of the decrease of the galactic cold gas, which was already converted into stars or accreted onto the BH. The faster decline which obtains in massive galaxies (and hence for luminous AGNs) is related in particular to the latter effect. Indeed, in hierarchical clustering scenarios the star formation history of larger objects peaks at higher $z$, since massive objects originate from progenitors collapsed in biased regions of the Universe where/when the higher densities allowed for earlier star formation; so, at low $z$ such objects have already exhausted most of their gas. On the other hand, less massive galaxies are continuously enriched by low-mass satellites, whose star formation is more smoothly distributed in $z$, and which retain even at $z \approx 0$ an appreciable fraction of cold gas available for BH accretion.

Although the model naturally yields a downsizing effect, we note though that the decrease of the peak redshift with decreasing luminosity appears to be smaller than indicated by the data. Such mismatch is even larger if the model predictions for the AGN number density are compared with the recent data by Hasinger, Miyaji & Schmidt (2005; see also this volume). However, it must be considered that our model does not include absorption: thus, the comparision with the abosrption-corrected data by Fiore et al. (2003) in the harder 2-10 keV band constitutes a more solid baseline for probing the model predictions.

A real improvement in the modeling requires the inclusion of additional physical processes in the SAM (and in particular in the sector concerning the feedback) rather than the tuning of the parameters in the existing framework. One such process could be well constituted by the inclusion into SAMs of the feedback produced by the AGNs emission itself. Since the AGN activity strongly increases with redshift, this could significantly contribute to expell/reheat part of the galactic cold gas reservoir in low-mass systems at high $z$. While the modeling of such impulsive processes is particulary delicate, some steps in this direction have already been taken (see, e.g., Haenhelt, Natarajan & Rees 1998; Silk & Rees 1998; Wyithe & Loeb 2003; Cavaliere, Lapi & Menci 2002; and references therein). We shall investigate the effects of such processes on the evolution of the AGN population in a next paper.

In sum, the present model provides a baseline to include the evolution of galaxies and AGNs in the same global picture, being supported by a remarkable agreement with the observations of its predictions for brighter sources in a wide range of redshifts (from $0 < z < 6$) and of wavelengths (from optical to X-rays). The most distinctive feature of such a picture is the dramatic decrease of the AGNs luminosities at $z \lesssim 2$ especially in massive galaxies (see Fig. 1), naturally resulting from to the exhaustion of cold gas necessary for feeding both the accretion and the star formation; relatedly, massive galaxies are predicted to undergo a nearly passive evolution from $z \approx 2$ to the present. The relevance of such an exhaustion in determining the observed properties of the AGN population (in both the optical and the X-rays) is confirmed by recent N-body simulations (Di Matteo et al. 2003). The above picture thus naturally explains the parallel evolution of BH accretion and star formation in spheroidal systems; this, originally discussed by Monaco, Salucci & Danese (2000) and Granato et al. (2001), is supported by recent works (see Franceschini, Hasinger, Miyaji, Malquori 1999; Haiman, Ciotti & Ostriker 2003) which also enlightened its simultaneous consistence with the evolution of the optical and the X-ray luminosity functions of AGNs (Cattaneo & Bernardi 2003). The physical origin of such a parallel evolution is here clarified and shown to arise as a natural outcome of hierarchical galaxy formation.

**REFERENCES**


Barger, A., Cowie L., Brandt, W.N., Capak, P., Garnire, G.P., Hornschemeier, A.E., Steffen, A.T., & Wehner, E.H. 2002, AJ, 124, 1839

Bruzual, A.G., & Charlot, S., 1993, ApJ, 105, 538

Cattaneo, A., & Bernardi, M. 2003, MNRAS, 344, 45

Cavaliere, A., Vittorini, V., 2000, ApJ, 543, 599

Cavaliere, A., Lapi, A., & Menci, N. 2002, ApJ, 518, L1

Comastri, A. 2000, in Stellar Endpoints, AGN, and the Diffuse X-ray Background, Ed. N. White, G. Malaguti, G.G.C. Palumbo, AIP conference proceedings, 599, 73

Comastri, A., Fiore, F., Vignali, C., Matt, G., Perola, G.C., La Franca, F., 2001, MNRAS, 327, 781

Di Matteo, T., Croft, R.A.C., Springel, V., Hernquist, L. 2003, ApJ, 593, 56

Fiore, F. et al. 2003, A&A, 409, 79

Franceschini, A., Hasinger, G., Miyaji, T., Malquori, D., 1999, MNRAS, 310, L5

Granato, G.L., Silva, L., Monaco, P., Panuzzo, P., Salucci, P. De Zotti, G., Dbibitem, 2001, MNRAS, 324, 757

Gruber, D.E. et al., 1999, ApJ, 520, 124

Haehnelt, M., & Rees, M.J., 1993, MNRAS, 263, 168

Haehnelt, M., Natarajan, P., & Rees, M.J., 1998, MNRAS, 300, 817

Haiman. Z., Loeb, A. 1998, ApJ, 503, 505

Haiman. Z., Ciotti, L., Ostriker, J.P., 2003, preprint [astro-ph/0304129]

Hasinger, G. 2003, proceedings of the Conference: The Emergence of Cosmic Structure, Maryland, Stephen S. Holt and Chris Reynolds (eds), astro-ph/0302574

Hatzminaoglou, E., Mathez, G., Solanes, J.-M., Manrique, A., Salvador-Sole', E., 2003, MNRAS, 343, 692

Kauffmann, G., Haehnelt, M., 2000, MNRAS, 311, 576

Kauffmann, G., Haehnelt, M., 2002, MNRAS, 332, 529

Lacey, C., & Cole, S., 1993, MNRAS, 262, 627

Lumb, D.H., Warwick, R.S., Page, M., De Luca, A., 2002, A&A, 389, 93

Madau, P., & Rees, M.J., 2000, ApJ, 551, L27

Menci, N., Cavaliere, A., Fontana, A., Giallongo, E., Poli, F., 2002, ApJ, 578, 18

Menci, N., Cavaliere, A., Fontana, A., Giallongo, E., Poli, F., Vittorini, V. 2003, ApJ, 587, L63

Menci, N., Fiore, F., Perola, G.C., Cavaliere, A., 2004, ApJ, 606, 58

Menci, N., Fontana, A., Giallongo, E., Salimbeni, S. 2005, ApJ, 632, 49

Mo, H.J., Mao, S., & White, S.D.M., 1998, MNRAS, 295, 319

Monaco, P., Salucci, P., Danese, L. 2000, MNRAS, 317, 488

Perola, G.C., Matt, G., Cappi, M., Fiore, F., Guainazzi, M., Maraschi, L., Petrucci, P.O., Piro, L. 2002, A& A, 389, 802

Poli, F. et al. 2003, ApJ, 593, L1

Risaliti, G. Maiolino, R. & Salvati, M. 1999, ApJ, 522, 157

Sanders, D.B., & Mirabel, I.F. 1996, ARA&A, 34, 749

Silk, J., & Rees, M.J. 1998, A&A, 331, 1

Ueda, Y., Akiyama, M., Ohta, K., Miyaji, T., 2003, preprint [astro-ph/0308140]

Vecchi, A., Molendi, S., Guakinazzi, M., et al. 1999, A&A, 349, L73

Volonteri, M., Haardt, F., Madau, P., 2003, ApJ, 582, 559

Yu, Q., & Tremaine, S., 2002, MNRAS, 335, 965

Wyithe, J.S., Loeb, A. 2002, ApJ, 581, 886

Wyithe, J.S., Loeb, A. 2003, ApJ, 595, 614

# THE SPECTRAL ENERGY DISTRIBUTION OF NEW TEV BLLACS

**L. Costamante**

Max-Planck-Institute für Kernphysik, Heidelberg, Germany

## ABSTRACT

Tev blazars studies have been hindered until now by the uncertainties in reconstructing the intrinsic TeV spectra due to absorption from the the diffuse Extragalactic Background Light (EBL), and by the small number of sources. The most recent H.E.S.S. results have now changed this situation, with the discovery of 3 new objects, and providing strong circumstantial evidence for a low intensity of the EBL. Here we present some first results of XMM and RXTE observations performed in coordination with H.E.S.S., which give information on the overall Spectral Energy Distribution of these objects during the epoch of the TeV detections, and discuss some implications of the absorption-corrected TeV spectra in the context of the leptonic SSC scenario.

Key words: LaTeX; XMM; X-rays; TeV; BL Lacs.

## 1. INTRODUCTION

TeV blazars are presently the most interesting and challenging objects to test the emission models and the physical conditions in blazars jets, since they are characterized by the most energetic electrons in the whole class (synchrotron radiation dominating and often peaking in the X-ray band) and by peculiar phenomenology (e.g. rapid variability at high energies, wide changes in the synchrotron peak energy, and different types of correlation between the synchrotron and inverse Compton emissions). Simultaneous X-ray–TeV observations represent therefore a fundamental diagnostic tool, since the bulk of the luminosity is emitted in those bands and they are supposed to sample electrons of similar energy (radiating through synchrotron and IC processes).

Such studies however have been hindered by the uncertainties in the reconstruction of the intrinsic TeV spectra due to absorption by $\gamma - \gamma$ collisions and pair production on the diffuse Extragalactic Background Light (EBL), and by the small number of objects (until very recently only 4 were well studied).

With the start of operations in 2004 of the Cherenkov telescope H.E.S.S. in full array, the situation is now changing, and 3 new TeV BLLacs have been recently discovered, two of which at relatively high redshift.

The hard spectra of the two most distant sources have provided the strongest constraints up to date on the level of the EBL (Aharonian et al. (2005c), which can now be used to reconstruct and study the blazars SED with less uncertainty than in the past.

## 2. EBL ABSORPTION

The EBL SED at Opt–NIR frequencies is dominated by thermal radiation produced by stars (which is then partly absorbed and re-emitted by dust at longer wavelengths) over the entire history of evolution of galaxies. Gamma-ray photons from 0.1 up to few TeV (the band detected in these objects) are mainly absorbed by (and thus sample) the EBL up to few microns, whose SED is shown in Fig. 1. The energy dependence of the optical depth $\tau(E_\gamma$ gives origin to a strong modification of the incident spectrum (see Fig. 2), resulting in a steepening of the original slope up to 2-3 TeV (for all expected EBL SEDs, i.e. peaked around 1-2$\mu$m). This creates a direct link between the blazar spectrum and the EBL SED: for a given observed TeV spectrum, higher O–NIR EBL fluxes requires harder source spectra. Unfortunately, the large uncertainties on the EBL knowledge (see Fig. 1) leave room to a wide range of possible source spectra, while conversely data from the synchrotron peak alone are not sufficient to univocally constrain the blazars TeV emission, thus hindering the possibility to disentangle absorption from intrinsic features.

A breakthrough in this classic "one equation – two variables" problem is now provided by the H.E.S.S. results on 1ES 1101-232 and H 2356-309 Aharonian et al. (2005c): their observed spectra are unexpectedly hard for their given redshifts. As described in Aharonian et al. (2005c), with the high O–NIR values suggested by the "direct" EBL measurements (i.e. after modelling and subtraction of the much brighter foregrounds, in particular zodiacal light), the reconstructed spectra are extremely hard (pho-

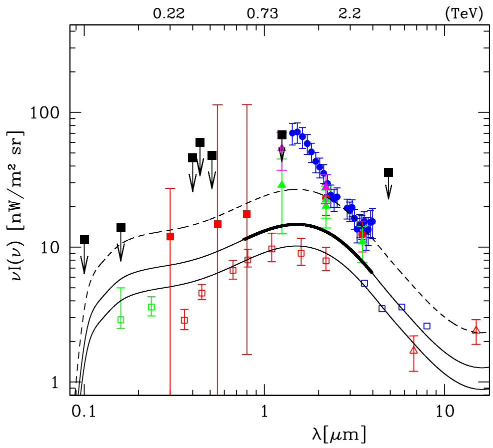


*Figure 1. EBL Spectral Energy Distribution. Open points: integrated light from resolved galaxy counts, and thus has to be considered lower limits for the EBL. Full points, direct estimates (see Aharonian et al. (2005c)). The two filled lines correspond to the range of the EBL flux levels used to deabsorb the TeV data. Details in Aharonian et al. (2005c). The dashed line, as well as the NIR peak over galaxy counts, are considered very unlikely since imply intrinsic TeV spectra with photon indexes $\Gamma < 0$. The upper axix shows the TeV energies corresponding to the peak of the $\gamma - \gamma$ cross-section.*

ton index $\Gamma \lesssim 0$). Such values have never been previously seen in the blazar emission, are not explained with the accelerated particle spectra obtained in the standard shock acceleration models, and are generally difficult to reproduce in the standard leptonic or hadronic scenarios.

They are not impossible in principle (and in fact some mechanisms have already been envisaged, seeAharonian (2001)), but if they were a real, newly discovered feature of the blazar TeV emission, they should become directly visible in the observed spectra of the closer, less absorbed objects like Mkn 421 and Mkn 501 ($\Gamma_{obs} \lesssim 0.5$), so far not seen. Unless assuming an improbable fine tuning of the source parameters with redshift, so that such "line-like" features always disappear due to EBL absorption.

High EBL fluxes in the NIR band, if due to redshifted UV radiation from Pop III stars in the early universe, are also disfavoured by recent theoretical results on this scenario (Madau & Silk (2005); Dwek et al. (2005)), due to the extreme energetic requirements and fine-tuning necessary not to overproduce the mean metallicity or the soft X-ray background presently observed.

A lower EBL intensity, instead, in agreement with the expectations from standard galaxy evolution models (e.g. Primack et al. (2005)), would avoid such problems.

Given also the fact that the "direct" EBL estimates can be affected by large systematic uncertainties due to the difficulties in the accurate modelling of the bright foregrounds, in particular zodiacal light (which has the same

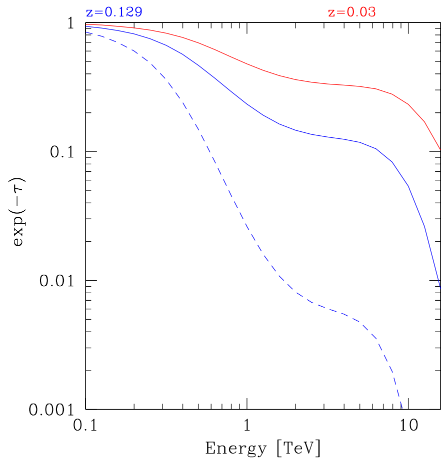


*Figure 2. Attenuation factors for two different redshifts for the lowest curve in Fig 1 (full lines), and for the same redshift (z=0.129) but with the higher EBL curve in Fig. 1 (dashed line). The above curves can be thought as the observed spectrum resulting after absorption if the incident one is a power-law with flat slope.*

spectrum of the NIR excess between 1 and 4 micron, Dwek et al. (2005)), a low EBL intensity seems at present the simplest and most natural conclusion.

Although not yet the "smoking gun", the H.E.S.S. results on these two objects provide strong circumstantial evidence for a very low EBL. Therefore, unless/untill further data will change this picture (e.g., the direct measurement of very hard spectra in nearby TeV blazars, or the detection of spectra of objects at high redshift, z=0.3-0.5, incompatible even with the galaxy counts limits), we will adopt for the TeV spectra reconstruction the range between the upper limit derived in Aharonian et al. (2005c), and the lower limits represented by the integrated light from resolved galaxies.

## 3. X-RAY DATA

The XMM observations were performed as simultaneous campaigns with H.E.S.S. at fixed epochs (given the narrow overlap of the visibility windows for simultaneous coverage), while the XTE observation was performed as ToO, but the campaign was hindered by bad weather conditions (thus the short exposures). Strict simultaneity has been possible only for the XMM observation of 1ES 1101-232, while for the others only within 1-2 days, due to bad atmospheric conditions on the H.E.S.S. site. The TeV flux levels however were not high enough to allow a study of the flux or spectral properties within one night of data.

The XMM data were analysed with the SAS 6.5 (6.0 for OM), according to the XMM Handbook and calibration instructions (and correspondingly for the XTE data), with

*Table 1. Main parameters of the H.E.S.S. observations and campaigns, with the results of a single powerlaw fit. Errors are 1 sigma statistical. H.E.S.S. results taken from Aharonian et al. (2005a,b,c); Benbow et al. (2005); Pita et al. (2005); Tluczykont et al. (2005)*

| Name | z | X-ray obs. | TeV obs. | H.E.S.S. results detection | livetime | $\Gamma_{obs}$ | $N_0$ ($cm^{-2}s^{-1}TeV^{-1}$) |
|---|---|---|---|---|---|---|---|
| PKS 0548-322 | 0.069 | XMM 20/10/04 | 10 2004 | (2.1$\sigma$) | 4.1 hrs | - | $<$ 2.2% Crab |
| PKS 2005-489 | 0.071 | XMM 4/10/04 | 6-7/8-9 2004 | 6.7$\sigma$ | 24.3 hrs | $4.0 \pm 0.4$ | 1.9e-13 |
| H 2356-309 | 0.165 | XTE 11/11/04 | 6-12 2004 | 10$\sigma$ | 40 hrs | $3.06 \pm 0.21$ | 4.4e-13 |
| 1ES 1101-232 | 0.186 | XMM 8/6/04 | 3-6 2004-05 | 12$\sigma$ | 43 hrs | $2.88 \pm 0.17$ | 3.1e-13 |

*Table 2. X-ray data spectral parameters of the best fit models, for single and broken powerlaw ones. Preliminary analysis, full details in Aharonian et al. 2006, Costamante et al. 2006, in preparation. The column density was fixed at the galactic values. Errors are at 90% confidence level for 1 and 3 parameter of interests. The last column gives the range of possible slopes for the intrinsic TeV spectrum using the limits in Fig. 1, as derived in Aharonian et al. (2005c).*

| Name | exposure ks | $\Gamma_1$ | $E_{break}$ keV | $\Gamma_2$ | Flux (2-10 KeV) erg $cm^{-2}$ $s^{-1}$ | intrinsic TeV $\Gamma$ |
|---|---|---|---|---|---|---|
| PKS 0548-322 | 35 | $1.76 \pm 0.05$ | $0.81 \pm 0.1$ | $1.99 \pm 0.01$ | 3.28 e-11 | - |
| PKS 2005-489 | 12 | $3.09 \pm 0.02$ | - | - | 1.03 e-12 | 3.5-3.6 |
| H 2356-309 | 2.8 | $2.44 \pm 0.25$ | - | - | 1.0 e-11 | 2.0-2.3 |
| 1ES 1101-232 | 18 | $1.97 \pm 0.04$ | $1.3 \pm 0.1$ | $2.19 \pm 0.03$ | 3.88 e-11 | 1.5-1.8 |

the standard recipies for exclusion of background flares intervals, pile-up and background subtraction (details in Costamante et al. 2006, Aharonian et al. 2006, in preparation). The spectra were then analysed with XSPEC V11.3.1. The observations were performed in *small window* mode for MOS2, and in *timing* for PN. The main X-ray and TeV data parameters are summarized in Table 1.

No variability has been observed in these objects: all X-ray and OM light curves for the different filters are well fitted by a constant, as well as the hardness ratios among different energy bands. We therefore fitted the whole datasets, with free normalization between the the MOS2 and PN spectra. The preliminary results of single and broken-powerlaw fits are shown in Table 2. The $N_H$ was fixed to the galactic values, but no evidence for higher values was found with free $N_H$.

## 4. TEV BLAZARS SEDS

We used all the available data (optical, X-ray and TeV) to build the source SEDs corresponding to the overall epoch of the TeV detections. Although derived from very different timescales (hours for the X-ray data, average over several months for the TeV data), the lack of significant variability also in the TeV band, and the fact that the X-ray data were taken in an epoch corresponding to the average TeV flux, suggests that these SEDs can likely represent the status of the source during a relatively quiescent period, even if of course variability in the unobserved epochs cannot be excluded (although not high enough).

The H.E.S.S. data were corrected for absorption as decribed in in Aharonian et al. (2005c): i.e. between the EBL upper limit corresponding to $\Gamma_{\rm TeV} \geq 1.5$ for 1ES 1101-232 and the absolute lower limit represented by the resolved galaxy counts (P0.4). The range of the derived spectra is shown in Table 2.

The OM data taken in the different filters (V, B, U, UVW1,UVM2) were corrected for galactic extinction according to the Cardelli's curve, and using the $A_B$ values from NED (Schlegel et al. 1998), but no host galaxy subtraction was performed.

### 4.1. PKS 0548-322

This source was not detected by H.E.S.S. around the XMM pointing, so only an upper limit is derived Aharonian et al. (2005b), but given the short exposure (4 hrs) and assuming that the observed excess of 2.5$\sigma$ is not due to background fluctuations, the detection level ($\sigma/\sqrt{hr}$) and flux estimate is comparable to that of the other objects (around 1% of the Crab).

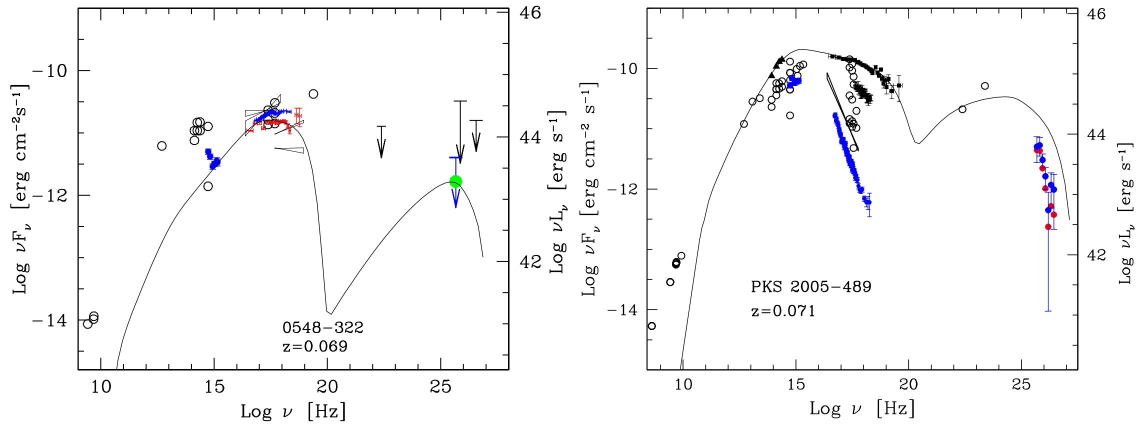


*Figure 3. SED of the two HBL with very similar redshifts ($\sim 0.07$). The new "sam epoch" data are shown in blue. In the TeV range: left, the point corresponds to the flux estimate on the excess, assuming it's not a fluctuation; right, the data are corrected with the middle curve in Fig. 1 (i.e. the one that implies $\Gamma = 1.5$ for the 1ES 1101-232 TeV spectrum). In black, historical data. The lines correspond to an old SSC modelling to the BeppoSAX data (see Costamante et al. (2001); Tagliaferri et al. (2001); Perlman et al. (1999)). An updated modelling is in preparation. The Y axis on the right shows the luminosity scale for these objects. For all calculations, a flat ΛCDM cosmology with $H_0 = 70$ km/s/Mpc, $\Omega_m = 0.3$, $\Omega_\Lambda = 0.7$ is adopted.*

The X-ray spectrum (see Fig. 3, left) shows that the source was characterized by an extreme state, with the synchrotron peak $\approx 5keV$. Compared with the past *Beppo*SAX and ASCA data, the source was in a higher state in the hard X-ray band, approaching the hard spectrum seen with EINSTEIN. Given the nearly identical redshift as PKS 2005-489 (z=0.069 vs 0.071; so that the EBL absorption effects are exactly the same), and the very different X-ray and SED properties (Fig. 3), the comparison between the TeV emission in these two objects will be very interesting, shedding light on the most efficient TeV production conditions. These two objects in fact are characterized by very different ratios between X-ray (tracing TeV electrons) and optical-UV fluxes (giving the seed photons for IC).

Quite interestingly, the spectrum derived from the OM data in the different filters is concave, suggesting that we are seeing the transition zone between the tail of the host galaxy (thermal) emission, and the emerging of the jet synchrotron radiation.

### 4.2. PKS 2005-489

With PKS 2155-304, this HBL is one of the X-ray brightest BL lacs in the southern emisphere, and is characterized historically by a very large amplitude variability. The X-ray spectrum however has always been steep, even during the exceptional flare of 1998 Tagliaferri et al. (2001); Perlman et al. (1999), locating the peak below the X-ray band (Fig. 3, right)

Quite surprisingly, the X-ray state corresponding to the H.E.S.S. TeV detection is one of lowest and steepest ever observed in this object (2 orders of magnitude less than for the 1998 flare, in the hard X-ray band), suggesting similar properties also in the TeV range, which would explain the very steep TeV spectrum. Given the huge potential dynamic range for the X-ray flux (which traces TeV electrons), this object seems in fact a "dormant TeV vulcano", potentially capable of $10^{-10}$ erg cm$^{-2}$ s$^{-1}$ TeV fluxes even if the TeV emission would follow only linearly the X-ray one during flares. It is therefore one of the best objects to investigate the correlated variability in the two bands, both on the shortest timescales (thanks to the large fluxes expected in high states), and for long term monitoring studies, since the H.E.S.S. array seems capable to detect it also in a very low state.

The $\Gamma < 2$ slope indicated by the OM photometric data constraints the peak of the synchrotron emission to be located in the UV, around $10^{16}$ Hz.

### 4.3. H 2356-309

Compared to the past *Beppo*SAX data (Costamante et al. (2001)), these short XTE PCA observations reveal a significantly steeper spectrum in the hard X-ray band, and at a lower flux level by a factor $\sim 3$. The TeV spectrum, instead, once corrected for absorption, is flat ($\Gamma = 2.0$) up to 1 TeV using the upper limit EBL, while it is more similar to the X-ray one (within errors) if the EBL is as low as the galaxy counts limit. In the first case, for the usual

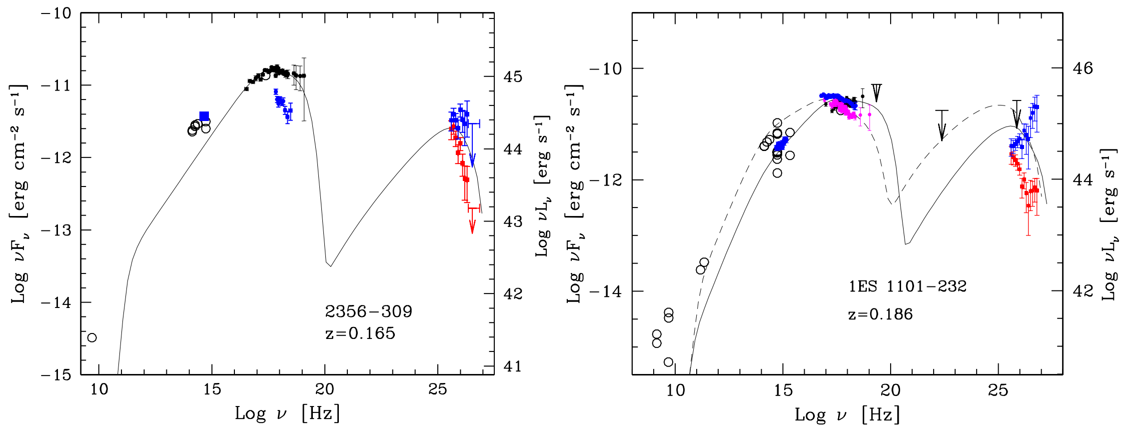


*Figure 4. SED of the two most distant TeV blazars presently detected with spectral information. Same labels as in Fig. 3. In the TeV range, the lower point are the observed data, the higher ones are absorption corrected according to Aharonian et al. (2005c).*

leptonic SSC scenarios, the IC peak would be located in the TeV band (unless such slope is due to a second component emerging above 200 GeV), and the electrons producing the TeV emission would not correspond to the observed X-ray ones. In the second case, instead, they can be the same electrons, but to avoid the steepening in the TeV band due to the Klein-Nishina effects, the scattering of these electrons has to occur around the Thomson limit and with a sufficiently constant energy density of seed photons, as given for example by a flat slope ($\Gamma 1.9 - 2$) down to the optical band.

### 4.4. 1ES 1101-232

Recognized by Wolter et al. (2000), using *Beppo*SAX observations, as an extreme BLLac (with $\nu_{peak} > 10$ keV) and promising TeV source, this object is revealed by the new H.E.S.S. and XMM results as one of the most interesting and puzzling cases for the blazars physics, even after assuming the lowest values for EBL absorption (i.e. galaxy counts). With all possible EBL levels, the intrinsic spectrum is always rather hard (see Table 2). The X-ray spectrum instead, as measured by XMM (at a flux level very similar to the old *Beppo*SAX data in high state), is characterized by a softer slope, nearly flat from 0.2 up to 1 keV and then steepening. The two emissions correspond therefore to two different particle spectra (KN effects tend to steepen the gamma-ray spectrum with respect ot the X-ray one, see e.g. Tavecchio et al. (1998)).

The natural question that arises is therefore: where is the synchrotron emission of the TeV electrons responsible for the TeV spectrum ? From simple energy conservation law, these electrons have

$$\gamma \gtrsim \frac{(1+z)}{\delta} \, \frac{(0.2-3)\mathrm{TeV}}{m_e c^2} \qquad (1)$$

corresponding to $\gamma \gtrsim 2 \cdot 10^6/\delta$ around 1 TeV. They emit by synchrotron at $h\nu_{sync} \gtrsim 50B(Gauss)/\delta$ keV. So the issue is to find an energy band in the SED with spectra as hard as the TeV ones. The OM data do indicate that the spectrum in the optical-UV band is quite hard, but to shift the TeV electrons synchrotron emission in the O-UV band would require very large beaming factors, $\delta \geq 100$. The alternatives within the SSC scenario are not many, but they can be effectively tested with further simultaneous observations:

- two populations/components, one of which characterized by lower fluxes but higher Compton dominance, so that its (hard) synchrotron spectrum remains hidden below the brighter (and softer) one. This hypothesis has already been proposed to explain the “orphan flares” in 1ES 1959+650 (Krawczynski et al. (2004)). In such case one should not expect correlated variability in the two bands, except for very low amplitude variations in X-rays, and more prominent in the hard bands;

- an electron population with a hard component rising above 10 kev, characterized by a spectrum similar to the TeV one (as in fact not excluded by the *Beppo*SAX PDS data). Such case can be tested with simultaneous observations in the hard X-ray band, although the problem remains on how to avoid the steepening of the gamma-ray spectrum due to the KN effect, since the Optical slope seems rather hard (meaning a rapidly decreasing seed photon energy density for higher energy electrons).

## 5. CONCLUSIONS

The new results obtained by H.E.S.S. on the high energy emissions of HBLs have opened a new vista on the blazars SED and EBL problems, as well as on the physics of the blazar emission itself. With the universe more transparent to $\gamma$-rays than previously thought, detections at larger redshifts become more likely also with the present generation instruments, and the the peculiar SED properties revealed by these X-ray – TeV observations make these objects excellent and very promising laboratories for a deeper understanding of the radiation mechanisms in blazars.

## ACKNOWLEDGMENTS

L.C. thanks the H.E.S.S. Collaboration for all the work which allowed to obtain the TeV data, and F. Aharonian, G. Ghisellini, F. Tavecchio, D. Horns, & L. Ostorero for insightful discussions.

## REFERENCES

Aharonian, F.A., Highlight Talk at Proc. 27th ICRC (Hamburg), 2001, astro-ph/0112314

Aharonian F. et al. (HESS Coll.) 2005, A&A, 436L, 17

Aharonian F. et al. (HESS Coll.) 2005, A&A, 441, 465

Aharonian F. et al. (HESS Coll.) 2005, submit. to Nature, astro-ph/0508073

Benbow W. et al, 2005, proc. ICRC 2005 Conference

Costamante L. et al., 2001, A&A, 371, 512;

Costamante, L. & Ghisellini, G., 2002, A&A, 384, 56

Dwek, E., Arendt, R.G., Krennrich, 2005, submit. to Apj, astro-ph/0508262

Krawczynski, H. et al. 2004, ApJ, 601, 151

Madau, P. & Silk, J., 2005, MNRAS, 359L, 37

Perlman E. et al., 1999, ApJ, 523, L11

Pita S. et al, 2005, proc. ICRC 2005 Conference

Primack, J.R., Bullock, J.S., Somerville R.S., 2005, AIP Conf. Proc. 745, 23

Tagliaferri G. et al., 2001, A&A, 368, 38

Tavecchio. F. et al., 1998, ApJ 509, 608

Tluczykont M. et al, 2005, proc. ICRC 2005 Conference

Wolter A., et al. 2000, A&A, 357, 429

# CHANDRA OBSERVATION OF THE LOW ENTROPY REGION IN THE RADIO LOBE GALAXY NGC 1316

**Makoto Tashiro[1], Kouichi Ito[1], Keiichi Abe and Naoki Isobe[2]**

[1]*Department of Physics, Saitama University, 255 Shimo-Okubo, Sakura, Saitama, 338-8570, Japan*
[2]*Institute of Physical and Chemical Research (RIKEN), 2-1 Hirosawa, Wako, Saitama, 351-0198, Japan*

**ABSTRACT**

NGC 1316 hosts the classical double lobe radio galaxy Fornax A. Recently, Kim and Fabbiano (2003) revealed with *Chandra* a 'blob' like emission associated with the optical dark lane, suggesting heating by the galaxy-merging. In this paper, we show a detail analysis focusing into the ‘blob’ to show significantly low temperature and low entropy. The significantly lower entropy in comparison with the other inter-stellar medium structures supports that the ‘blob’ are produced at the past galaxy merging. Comparing with those of non-thermal electrons in the radio lobes, we discuss a possible history of the nucleus activity and show its estimated kinetic luminosity during its active phase.

Key words: X-ray: galaxies --- X-rays: active nucleus ---galaxies: individual (NGC 1316)

## 1. INTRODUCTION

Formation of super massive black holes and history of the resultant active galactic nuclei is a crucial issue to evaluate total energy flow from galaxies and galactic medium heating. Some observational constraints, based on black hole merging models, estimate the lifetime of active galactic nuclei (AGNs) to be 0.01 to 0.1 Gyr (e.g. Yu & Tremaine 2002). In addition, recent observational results show that kinematic energy flows from the AGNs could be comparable to those of radiative energy (e.g. Isobe et al. 2005; I05 hereafter). That estimation implies that AGNs with large scale jets may have injected kinetic energy of $10^{58\text{-}61}$ergs into the inter-galactic space through their life. It suggests that it is important to estimate the lifetime of outflow activity independently from their electromagnetic radiation to evaluate total energy output from AGN to the inter-galactic medium.

In this paper, we present X-ray observation results from the radio galaxy Fornax A (NGC 1316), having prominent double lobes with the dimmed nucleus. The host galaxy NGC 1316 is a disturbed elliptical galaxy with numerous tidal tails. Schweizer (1980) suggested that the morphology is caused by several low-mass, gas-rich merging over the last 2 Gyr (see also Ekers et al. 1983; Kim, Fabbiano, & Mackie 1998; Mackie & Fabbiano 1998). Fornax A (NGC 1316) has been extensively observed in a wide range of wavelengths. In the radio band, Fornax A is the third brightest object in the sky, with giant radio lobes (Wade 1961; Ekers et al. 1983), separated by 200 kpc, consisting of polarized filaments (Fomalont et al. 1989) and S-shaped nuclear radio jets (Geldzahler & Fomalont 1984). In X-ray band, the galaxy was observed intensively so far with *Einstein* (Fabbiano, Kim, & Trinchieri 1992), *ROSAT* PSPC(Feigelson et al. 1995), *ASCA* (Kaneda et al. 1995; Iyomoto et al. 1998; Tashiro et al. 2001), *ROSAT* HRI (Kim, Fabiano & Makie 1998), *Chandra* (Kim & Fabbiano 2003: KF03 hereafter) and *XMM-Newton* (Isobe et al. 2005: I05 hereafter).

In particular, the *ROSAT* observations revealed $\sim 10^9$ $M_{\rm solar}$ of hot ISM, with an inhomogeneous distribution. Although the substructures of the ISM were not highly significant, given the *ROSAT* HRI data quality, KF03 confirmed the presence of fine substructures in the hot interstellar medium (ISM) with *Chandra*. Some of the substructures are likely to result from interaction with the radio jets, while others placed free from the jet directions should be related to a complex intermingling of different phases of the ISM. They also confirmed the dimmed nucleus with $L_x = 5\times10^{39}$ ergs s$^{-1}$ (in 0.3 to 8 keV band) and a $\Gamma$=1.7 power-law energy spectrum, which is consistent with the results reported by Iyomoto et al. (1998).

X-ray observations with *ASCA* (Kaneda et al. 1995; Iyomoto et al. 1998; Tashiro et al. 2001), *ROSAT* (Feigelson et al. 1995), and *XMM-Newton* (I05) have also been unveiling the inverse-Compton X-rays from the lobes. In particular, I05 summarized them and revised electron energy and the energy density spectrum based on the latest X-ray and radio results.

In this paper we reanalyze the *Chandra* observation results on the possible merging induced ISM to compare its cooling time scale with the suggested history of the lobes. Also discussion on the lobe cooling time derived from the X-ray observation of

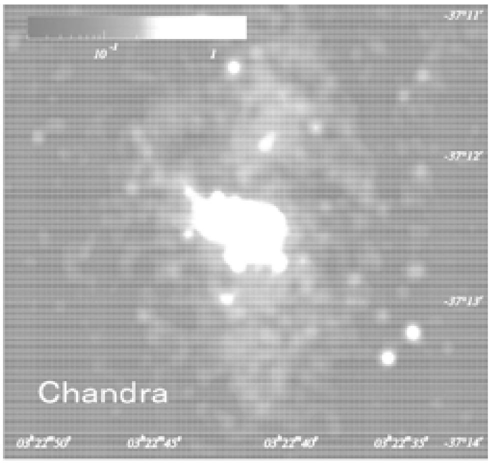


*Figure1. Chandra 0.2-7keV image of NGC1316*

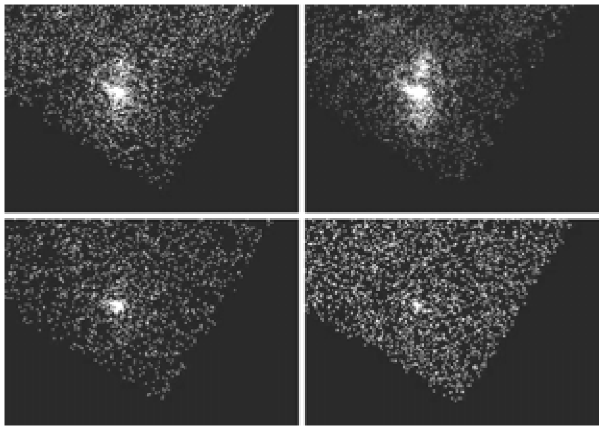

*Figure 2. Chandra X-ray band images from NGC1316 (a)0.2-0.7, (b) 0.7-1.2, (c) 1.2-2.0, (d) 2.0-7.0 keV (see text).*

lobes is presented in comparison with the newly estimated cooling time of the ISM structure.

## 2. OBSERVATION AND RESULTS

### 2.1 Observation

NGC 1316 was observed for 30 ks on 2001 April 17 (Observation ID 2022), with the *Chandra* Advanced CCD Imaging Spectrometer (ACIS; Garmire 1997), and details are described by KF03. We reanalyzed the archive data and processed them thoroughly with the latest processing tools and calibration files.

### 2.1 Results from Point Sources

We show the obtained 0.2 to 10 keV X-ray image in Fig. 1, in which we smoothed the image with two-dimensional Gaussian function of $\sigma = 4$ pixels. We see elongated emission in the north-south direction. It extends within the optical galaxy and the direction is perpendicular to the lobe axis (east-west). KF03 noticed the 'blob' like ISM substructure, exhibiting a prominent peak emission in the north of the galaxy centre.

We show the X-ray band images in Fig. 2. They are labelled with (a) to (d) each of which represent 0.2-0.7, 0.7-1.2, 1.2-2.0 and 2.0-5.0 keV band images, respectively. We see the significant substructures at the galaxy centre and the north-south extension in the softer two band images, although no significant diffuse emission in the harder bands.

Before investigating the diffuse emission structure, we note we see no prominent peak at the centre of the galaxy. In order to evaluate the possible active nucleus emission, we accumulate photons within 250 pc from the centre. Although the obtained spectrum is well described with power-law model, the best-fit photon index of $2.8 \pm 0.24$ is too soft to be attributed to the typical AGN emission. The derived upper limit of the luminosity from the centre region is up to $10^{40}$ erg s$^{-1}$, which is consistent with the reported values by Iyomoto et al. (1998) and KF03. We conclude that we observe no significant nucleus activity of the radio galaxy.

### 2.2 Results from Diffuse Emissions

Point sources in the field are investigated and reported by KF03. In order to focus into the diffuse emissions, here we remove all the point sources and evaluate the residual diffuse X-ray spectrum. As described by the previous report (e.g. Kaneda et al. 1995), whole galaxy is covered with wide spread emission from a relative hot component $kT = 0.83$ keV, which is known to be extended outside of the galaxy. Here we subtracted the large-scale thermal emission by employing background spectrum region outside but near the optical galaxy. In the following, we examine the spectra from the ISM substructures by employing regions shown in Fig. 3.

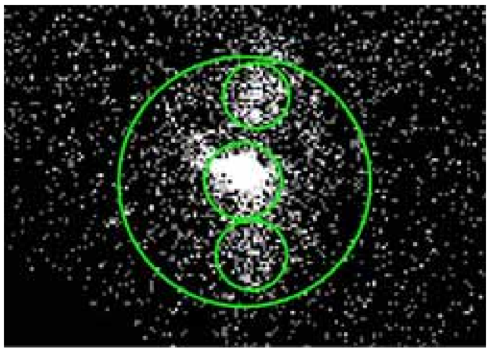

*Figure 3. Spectrum accumulating regions for: (1) the north 'blob'; (2) the centre; (3) the south 'blob'; (4) diffuse ISM.*

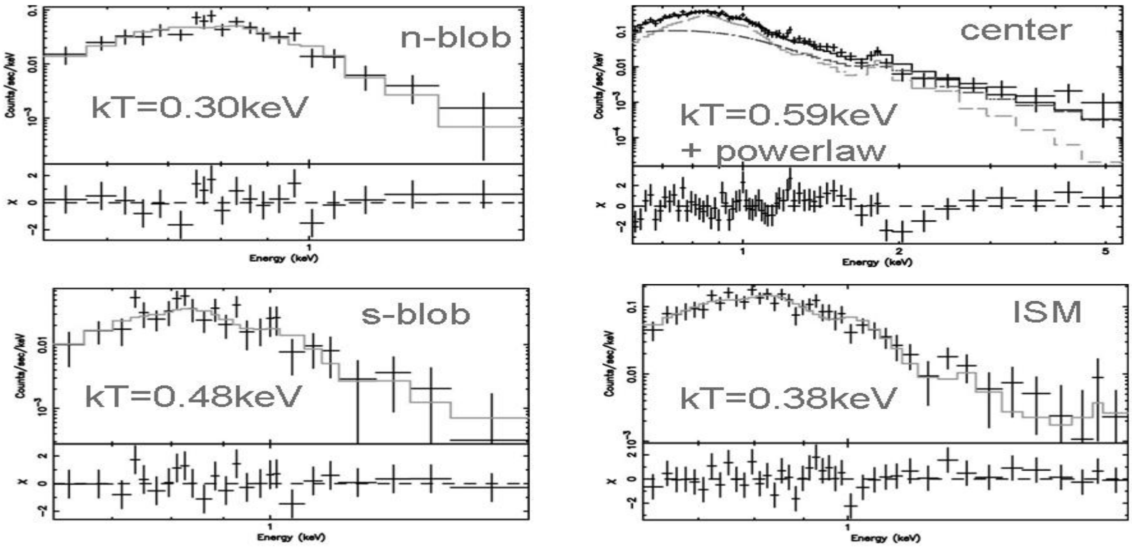


*Figure 4. X-ray spectra obtained from the four regions.*

The regions are; (1) north 'blob'; (2) central region of the galaxy; (3) southern extension also 'blob' like structure; and (4) diffuse ISM in the galaxy.

Thus integrated X-ray spectra are presented in Fig. 4. We used "mekal" model to evaluate the thermal emission and summarized the best-fit parameters in Table 1. All but the centre region spectra are well described with thermal plasma emission model. Only from the centre we detected an additional hard component. The hard component is here described with a power-law model, although it is thought to represent unresolved point sources including low mass X-ray binaries in the centre region.

*Table 1. Summary of the spectral fitting for the diffuse emission regions*

| Region | kT (keV) | $\chi^2_{red}$ |
|---|---|---|
| 1 | 0.30 +/- 0.02 | 0.87 |
| 2 | 0.59 +/- 0.02 | 1.12* |
| 3 | 0.48 +/- 0.06 | 0.64 |
| 4 | 0.38 +/- 0.03 | 0.74 |

*: with additional power-law component (text).

## 3. DISCUSSION

### 3.1 Entropy of the ISM Substructures

We observed NGC 1316 having a large-scale double lobe without large-scale radio jets or active nucleus. We confirmed the ISM substructures suggested to be related with the past galaxy merging. Interestingly, the measured temperatures of the substructures are not homogeneous. We observed the hot plasmas in the centre and in the south extension, while we found the relative cool plasmas in the north blob and from the diffuse ISM region. The brightness and temperature profile imply inhomogeneous entropy distributions in the ISM substructures, and suggests different origins of each substructure. In this section, we calculate the 'entropy' to discuss a possible history of the nucleus activity in the following subsection. We here adopted the definition of 'entropy' (or adiabat) as,

$$S = n^{-2/3}kT\ , \qquad (1)$$

according to Tozzi and Norman (2001). The calculated $S$ for each region (region 1, 2 and 4) is summarized in Fig. 5 in reference to the radial distance from the centre of the galaxy. The grey line indicates the extrapolation from the outer ISM region in the case of gravitational cooling only ( $S \propto r$ ). We note the derived entropy value for the central region exceeds the line. It might be caused by the heating at the merging or by subsequent nucleus activity. On the other hand, the lowest entropy of the north blob is consistent of the extrapolation if the blob were at the centre. The fact might hint that the blob used be at the centre.

### 3.2 Electron Energy in the Lobes

Referring to I03 presenting a new estimation of stored energy in the lobes, we adopt the derived energy densities of the relativistic electrons and the magnetic fields are $u_e = 2.8 \pm 0.3$ erg cm$^{-3}$ and $u_m = 0.3^{+0.08}_{-0.06}$ erg cm$^{-3}$, respectively. Employing these values with estimated emission volume of the two lobes, we obtained a cooling time of 0.2 Gyr for both synchrotron and Compton processes.

### 3.3 Possible History of the Nucleus Activity

Indices of the end time of activity of the nucleus are given by those facts that the jets are extinguished; yet the relativistic electrons in the lobes have not been cooled. These give the lower and the upper limits of the time intervals from the end of activity to the present time, such as 0.1 Myr and 0.2 Gyr, respectively.

On the other hand, cooling times of the ISM sub-structures suggest the age of the merging galaxy. We calculate it as 1 Gyr from the cooling time of the north blob. Adopting these indices as the duration of the activity of the nucleus, we could conclude that it last, at the longest case, from 1 Gyr to 0.1 Myr ago at the rest frame of the galaxy.

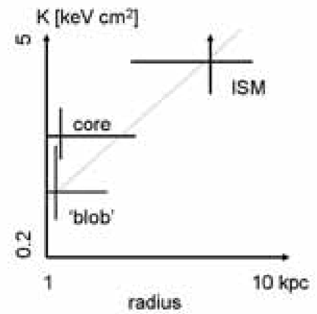


*Figure 5. Radial entropy profile of the radio galaxy*

The estimated total electron energy in the lobes is $1.0 \times 10^{58}$ erg (I05). If we adopt the cooling time of the lobes as the integration time of the energy injection into the lobes, we estimated the average kinetic luminosity of $2 \times 10^{45}$ erg s$^{-1}$. We note that it is comparable to the typical radiation luminosity of the radio galaxy.

## 4. SUMMARY

We confirmed the hot ISM and substructures (KF03). Their 'entropy' analysis shows that (1) heating in the galaxy centre ('core'); (2) cooled 'blob' in the north. These results suggest that the lifetime of AGN of 1 Gry. We estimated the average kinetic luminosity in the lifetime of the nucleus.

## REFERENCES

Ekers, R. D., Gross, W. M.,Wellington, K. J., Bosma, A., Smith, R. M., & Schweizer, F. 1983, A&A, 127, 361
Fabbiano, G., Kim, D.-W., & Trinchieri,G. 1992, ApJS, 80, 531
Feigelson, E. D., Laurent-Muehleisen, S. A., Kollgaard, R. I., & Fomalont, E. B. 1995, ApJ, 449, L149
Fomalont, E. B., Ebnerter, K. A., van Breugel, J.M., &
Garmire,G. P. 1997, BAAS, 190, 3404
Geldzahler, B. J., & Fomalont, E. B. 1984, AJ, 89, 1650
Isobe, N., Makishima, K., Tashiro, M., 2005 this issue (I05)
Iyomoto, N., Makishima, K., Tashiro, M., Inoue, S., Kaneda, H., Matsumoto, Y., & Mizuno, T. 1998, ApJ, 503, L31
Kaneda, H., Tashiro, M., Ikebe, Y., Ishisaki, Y., Kubo, H., Makshima, K., Ohashi, T., Saito, Y., Tabara, H., 1995, ApJ, 453, L13
Kim, D.-W., Fabbiano, G., & Mackie, G. 1998, ApJ, 497, 699
Kim, D.-W., Fabbiano, G., & Trinchieri,G. 1992, ApJ, 393, 134
Kim & Fabiano, 2003, (KF03)
Mackie,G., & Fabbiano, G. 1998, AJ, 115, 514
Schweizer, F. 1980, ApJ, 237, 303
Tashiro, M., Makishima, K., Iyomoto, N., Isobe, N., & Takahashi, T., 2001, ApJ 546, L19–L23
Wade, C. M. 1961, Publ. NRAO, 1, 99
Yu & Tremaine, 2002, MNRAS 335, 965

# FRII SOURCES AT $Z > 0.5$: X-RAY PROPERTIES OF THE CORE AND EXTENDED EMISSION

**E. Belsole[1], J.H. Croston[2,3], D.M. Worrall[1], and M. J. Hardcastle[3]**

[1]H.H. Wills Phyisics Laboratory, University of Bristol, Tyndall Avenue, Bristol BS8 1TL, UK
[2]Service d'Astrophysique, bat 709 CEA- Saclay, L'orme des Merisiers, 91191 Gif sur Yvette Cedex, France
[3]School of Physics, Astronomy and Mathematics, University of Hertfordshire, College Lane, Hatfield, Hertfordshire AL10 9AB, UK

**ABSTRACT**

Active galaxies are the most powerful engines in the Universe for converting gravitational energy into radiation, and their study at all epochs of evolution is therefore important. Powerful radio-loud quasars and radio galaxies have the added advantage that, since their radio jets need X-ray-emitting gas as a medium in which to propagate, the sources can be used as cosmological probes to trace significant atmospheres at high redshift. The radio emission can be used as a measure of source orientation, and sensitive X-ray measurements, especially when used in combination with multi-wavelength data, can be used to derive important results on the physical structures on a range of sizes from the cores to the large-scale components. In this paper we present new results on a significant sample of powerful radio galaxies and quasars at $z > 0.5$, drawn from the 3CRR catalogue and selected to sample a full range of source orientation. Using high-quality observations from *XMM-Newton* and *Chandra*, we discuss the X-ray properties of the cores, jets, lobes and cluster gas, and, through the incorporation of multi-wavelength data, draw conclusions about the nature of the emission from the different components.

Key words: active galaxies, radio galaxies, high redshift, quasars, general, X-ray, synchrotron, inverse Compton.

## 1. INTRODUCTION

Powerful ($P_{178\mathrm{MHz}} > 5 \times 10^{24}$ W s$^{-1}$ Hz$^{-1}$) radio sources are visible across the Universe and can thus be used to probe a number of physical conditions at high redshift, from accretion processes to Active Galactic Nucleus (AGN) environments at early epochs. On small scales, X-ray emission from the central AGN can be used to probe the process of converting gravitational energy into radiation, as spectral and variability studies have shown that at least some of the X-ray emission comes from regions very close to the central engine. At least part of the X-ray emission is expected to be anisotropic as a result of relativistic beaming and anisotropic absorption. In particular, Unification Models explain the observed differences among AGNs as the result of their orientation with respect to the line of sight (e.g. Barthel 1989; Urry & Padovani 1995), and an optically thick obscuring torus is invoked to hide the nucleus of objects (namely radio galaxies) viewed at large angles to the jet axis (e.g. Barthel 1989).

To understand the accretion mechanism(s) we need to understand orientation effects, especially in X-ray selected samples. In the simple picture of an obscuring torus, quasar light heats the gas and dust of the torus and thermal radiation is re-emitted isotropically in the mid/far-infrared in order to maintain energy balance in the inner regions. Thus, in principle, far-infrared radiation should provide an orientation-independent measure of the emitted power from the central engine. The sensitivity in the mid/far-infrared of the *Spitzer* satellite provides for the first time the possibility to test this hypothesis for a large number of objects.

On larger spatial scales, extended X-ray emission is observed from spatial regions coincident with the radio lobes, and the combination of the X-ray and radio radiation can be used to measure the particle content and magnetic field in the radio lobes. In addition, the well collimated relativistic jets associated with these sources, require a medium in which to propagate. As a result powerful high redshift radio galaxies are potential tracers of the formation and evolution of the most massive galaxies and clusters (e.g., Crawford & Fabian 2003; Hardcastle & Worrall 1999; Worrall et al. 2001). Powerful radio sources are thus key objects to understand the cosmological evolution of accretion/radiation mechanisms, relativistic effects and plasma physics in the early Universe (e.g., Brunetti et al. 2001; Hardcastle, Birkinshaw & Worrall 2001; Marshall et al. 2005; Overzier et al. 2005).

In this paper we present high-quality X-ray observations obtained with *Chandra* and *XMM-Newton* of 19 sources in the redshift range $0.5 < z < 1.0$, which are mostly part of a larger sample of Faranoff-Riley type II (FRII) radio galaxies and quasars currently being observed with *Spitzer*. We discuss the properties of the core and particle content of the radio lobes and we present preliminary results on the cluster-like environment of these sources.

Throughout this paper we use the concordance cosmology with $h_0 = H_0/100$ km s$^{-1}$ Mpc$^{-1}$ $= 0.7$, $\Omega_{\rm M} = 0.3$, $\Omega_\Lambda = 0.7$. If not otherwise stated, quoted errors are $1\sigma$ for one interesting parameter.

## 2. THE SAMPLE

Low-radio-frequency optically-thin synchrotron radiation from the radio lobes of radio-loud sources should be isotropic. Thus, selection of objects via their low-frequency radio emission represents the most reliable method for selecting an orientation-unbiased sample. The sample discussed in this paper is composed of 19 sources at redshift $0.5 < z < 1.0$, selected from the 3CRR catalogue (Laing, Riley & Longair, 1983) at 178 MHz, and having *Chandra* or *XMM-Newton* observations. This work does not aim at statistically testing unification models, for which a random selection from the parent sample would be necessary. Instead we intend to look for differences in the X-ray emitting components between quasars and radio galaxies, as would be expected in unification schemes. The sources are also being observed with *Spitzer* and their selection as part of a larger sample was based on convenient scheduling of *Spitzer* observations.

*Chandra* or *XMM-Newton* observations of 9 sources (3C 184, 3C 200, 3C 220.1, 3C 228, 3C 263, 3C 275.1, 3C 292, 3C 330, 3C 334) were awarded to us in support of various projects, while data for the remaining sources were extracted from the *Chandra* archive. Table 1 lists the sources used in this work. Our analysis of the lobe emission was performed with a larger sample, including sources at lower and higher redshift to those detailed in Table 1. For a full list of these sources see Croston et al. (2005).

## 3. THE PROPERTIES OF THE CORES

High-frequency nuclear radio emission probes sub-arcsecond scales of radio-loud sources, and is explained as synchrotron radiation from the unresolved bases of relativistic jets, which is anisotropic due to relativistic beaming. The correlation found using *ROSAT* data between the nuclear, soft X-ray emission and the core radio emission of powerful radio-loud AGN (e.g. Hardcastle & Worrall 1999; Brinkmann, Yuan & Siebert 1997) suggests that at least part of the soft X-ray emission is also relativistically beamed and originates at the base of the jet. The correlation is very tight for core-dominated quasars (CDQs), i.e. those source having jets pointing to small angles to the line of sight. Another sub-class of

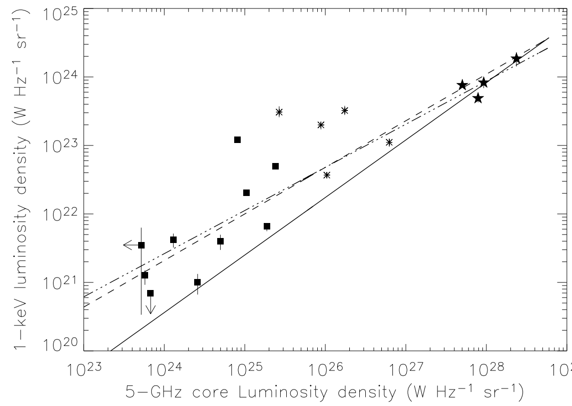


*Figure 1. Luminosity-Luminosity relation. Filled boxes are RGs, asterisks are LDQs and star CDQs. Errors bars show 1$\sigma$ uncertainties. When these are not visible it is because errors are smaller than symbols. Upper limits are at the 3$\sigma$ level. The continuous line is the best-fit regression to the sample of CDQs only. The dot-dashed line is the regression to the whole sample, while the dashed line fits the sample composed of CDQs and RGs*

object, lobe-dominated quasars (LDQs), were found to lie above the flux-flux correlation valid for CDQs (Worrall et al., 1994), supporting the idea that lobe-dominated quasars are viewed at an angle to the line of sight such that the observer sees in X-ray both the jet-dominated component and a more isotropically emitted, probably nucleus-related component, with the two components being more similar in flux density than for the CDQs. For those sources viewed on the plane of the sky (thus strongly obscured by a torus) the picture is less clear. Worrall et al. (1994) found that the core soft X-ray emission of the galaxy 3C 280 lies on an extrapolation of the correlation obtained for CDQs, and interpreted the result as due to X-ray emission from a jet-related component, with the nucleus-related component being obscured by a torus. In this picture, nucleus-related X-ray emission in radio galaxies would be seen only at hard ($> 2.5$ keV) energies and its characteristics have been essentially unknown before *Chandra* and *XMM-Newton* observations.

### 3.1. Results

*Chandra* and *XMM-Newton* observations allow us to answer some of the still open questions about the nature of X-ray emission from the nuclear region of high-redshift radio sources:

1. **Do RGs have more absorbed cores than QSOs?** Spectral analysis of 10 radio galaxies in the sample show that 70% of them display an absorbed nuclear component with intrinsic absorption ranging from 0.2 to 50 $\times 10^{22}$ cm$^{-2}$. We do not find absorption above Galactic value for any of the quasars in the sample.

*Table 1. The sample. Galactic column density is from Dickey & Lockman (1990); NRLG means Narrow Line Radio Galaxy; LERG means low-excitation radio galaxy. Redshifts and positions are taken from Laing et al. (1983)*

| Source | RA(J2000) h m s | Dec(J2000) ° ′ ″ | redshift | scale arcsec/kpc | type | $N_{\mathrm{H}}$ $10^{20}$ cm $^{-2}$ |
|---|---|---|---|---|---|---|
| 3C 6.1 | 00 16 30.99 | +79 16 50.88 | 0.840 | 7.63 | NLRG | 14.80 |
| 3C 184 | 07 39 24.31 | +70 23 10.74 | 0.994 | 8.00 | NLRG | 3.45 |
| 3C 200 | 08 27 25.44 | +29 18 46.51 | 0.458 | 5.82 | NLRG | 3.7 |
| 3C 207 | 08 40 47.58 | +13 12 23.37 | 0.684 | 7.08 | QSO | 4.1 |
| 3C 220.1 | 09 32 39.65 | +79 06 31.53 | 0.61 | 6.73 | NLRG | 1.8 |
| 3C 228 | 09 50 10.70 | +14 20 00.07 | 0.552 | 6.42 | NLRG | 3.18 |
| 3C 254 | 11 14 38.71 | +40 37 20.29 | 0.734 | 7.28 | QSO | 1.90 |
| 3C 263 | 11 39 57.03 | +65 47 49.47 | 0.656 | 6.96 | QSO | 1.18 |
| 3C 265 | 11 45 28.99 | +31 33 49.43 | 0.811 | 7.54 | NLRG | 1.90 |
| 3C 275.1 | 12 43 57.67 | +16 22 53.22 | 0.557 | 6.40 | QSO | 1.99 |
| 3C 280 | 12 56 57.85 | +47 20 20.30 | 0.996 | 8.00 | NLRG | 1.13 |
| 3C 292 | 13 50 41.95 | +64 29 35.40 | 0.713 | 6.90 | NLRG | 2.17 |
| 3C 309.1 | 14 59 07.60 | +71 40 19.89 | 0.904 | 7.80 | GPS-QSO | 2.30 |
| 3C 330 | 16 09 34.71 | +65 56 37.40 | 0.549 | 6.41 | NLRG | 2.81 |
| 3C 334 | 16 20 21.85 | +17 36 23.12 | 0.555 | 6.38 | QSO | 4.24 |
| 3C 345 | 16 42 58.80 | +39 48 36.85 | 0.594 | 6.66 | core-dom QSO | 1.13 |
| 3C 380 | 18 29 31.78 | +48 44 46.45 | 0.691 | 7.11 | core-dom QSO | 5.67 |
| 3C 427.1 | 21 04 06.38 | +76 33 11.59 | 0.572 | 6.49 | LERG | 10.90 |
| 3C 454.3 | 22 53 57.76 | +16 08 53.72 | 0.859 | 7.68 | core-dom QSO | 6.50 |

2. **If soft X-ray emission is jet-related, a correlation should exist between core radio emission and a soft X-ray unabsorbed component of RGs and CDQs.**

   We correlate core radio luminosity density at 5 GHz to soft, 1-keV X-ray luminosity density of an unabsorbed component in all the sources in our sample (Figure 1). We confirm previous results found with *ROSAT* about the tight correlation valid for CDQs, and the position above the correlation for LDQs. The 1-keV emission from the 10 RGs, which is interpreted as jet-related in CDQs, lies above the correlation valid for CDQs, suggesting that the mechanism responsible for the unabsorbed X-ray emission in the two subclasses of sources may be different.

3. **Are the two populations (RGs and QSOs) different in their X-ray spectral properties?**

   Radio-loud (core-dominated or blazar-type) quasars are found to have flatter spectral index , i.e. $\Gamma \sim 1.5$ (e.g., Worrall & Wilkes 1990, Brinkmann et al. 2000) in comparison to the values of $\Gamma \sim 2$ more commonly found in their radio-quiet counterparts (e.g. Brinkmann et al. 2000, Reeves & Turner 2000, Galbiati et al. 2005). The flat spectrum has been interpreted as the result of beamed emission from the jet. However, for RGs it is in principle possible to separate X-ray emission which is unobscured and jet-related from obscured (possibly) accretion-related emission. From our analysis we find that the average spectral index (Figure 2; the absorbed component is here considered for RGs) for all sources is $<\Gamma> = 1.55 \pm 0.05$, for RGs alone is $<\Gamma_{RG}> = 1.57\pm0.03$, for CDQs $<\Gamma_{CDQ}> = 1.45\pm0.06$, and for LDQs $<\Gamma_{LDQ}> = 1.59\pm0.09$. This shows that RGs absorbed emission behaves more similarly to the spectral behaviour of radio-loud quasars (RLQs) than radio-quiet quasars (RQQs).

   Interestingly, the spectral index of the RG unabsorbed X-ray emission at low energy is rather steep, with a average of $<\Gamma> = 2.05 \pm 0.25$. This is indication that the emission mechanism responsible for the unabsorbed emission in RGs and QSOs may be different.

### 3.2. Conclusions

Several results support a simple unification model to explain the X-ray emission from high-redshift radio loud sources:

- RGs display higher intrinsic absorption than QSOs (as expected if a torus is present);
- the unabsorbed X-ray component observed in RGs (and QSOs) correlates with the radio core, implying that this emission is most likely jet related. However the steeper spectrum observed in RGs is con-

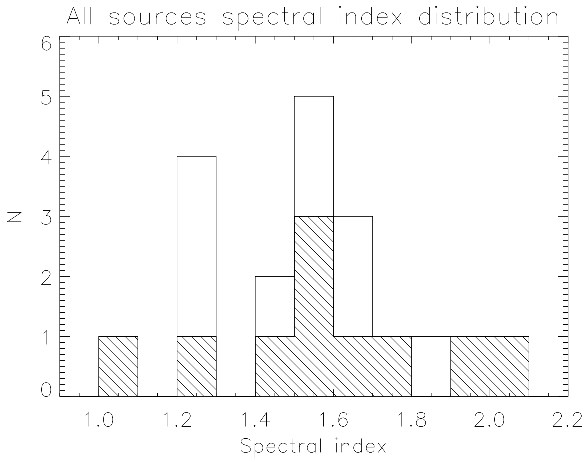


*Figure 2. Spectral index distribution for the whole sample. The dashed histogram illustrates the distribution of the absorbed components of radio galaxies, and empty boxes represent quasars.*

sistent with synchrotron emission as the mechanism responsible for this emission in RGs. On the other hand,

- the flattening of the flux-flux relation (as well as the luminosity-luminosity relation) for CDQs, i.e. the source is under-luminous in X-ray for a given radio flux, is consistent with IC becoming dominant with decreasing angle to the line of sight;
- LDQs have more X-ray emission than would be expected from a jet component alone suggesting a possible contribution to the spectrum from both jet-related and accretion-related emission mechanisms.

The new and surprising result we find from our analysis is the flat slope describing the absorbed X-ray spectrum of RGs. In particular its value is flatter than that observed for RQQs. This seems to indicate that jet emission dominates over a possible more heavily absorbed core, as verified by simulations (Belsole, Worrall & Hardcastle, 2006). However, we cannot rule out that RLQs and RQQs engines are different.

## 4. EXTENDED EMISSION FROM THE RADIO LOBES

Radio synchrotron emission from radio lobes is a function of electron density and magnetic field strength. The combination of radio observations with resolved X-ray observations allows us to decouple these two quantities since electron density is directly measurable from the inverse Compton (IC) emission observed in the X-rays. This may help in solving the issue of particle content and magnetic field strength in radio lobes.

The particle content in radio galaxies and quasars is still under debate. Possible interpretations are electron-proton jets (e.g., Celotti & Fabian 1993) and electron-positron jets (e.g., Wardle et al. 1998; Kino & Takahara 2004). Although relativistic protons are not directly observable by IC emission, results consistent with equipartition between the magnetic field and electron energy densities represent an indirect means to disfavour models in which a substantial contribution to the energy density is provided by a population of protons (e.g., Hardcastle et al. 2004; Croston et al. 2004).

In this paper we summarise the results obtained from the analysis of *Chandra* and *XMM-Newton* observation of 33 classical double radio galaxies and their radio lobes. Detail of this work are described in Croston et al. (2005).

### 4.1. Results

The X-ray observations available allow us to resolve emission from 38 lobes and upper limits for another 16 lobes. Of the 38 lobes with detection, 8 have sufficient counts to perform spectral analysis.

The properties of the lobes in our sample were investigated by computing the ratio ($R$) of the observed to predicted X-ray flux at equipartition. The predicted flux was obtained by modelling of the IC and synchrotron emission using the radio flux densities at different frequencies to normalise the synchrotron spectrum. A broken power law electron distribution with initial electron energy index $\delta = 2$, $\gamma_{\rm min}$ =10 and $\gamma_{\rm max} = 10^5$, and a break energy in the range $\gamma_{\rm break} = 1200 - 10,000$ was used. The prediction for the CMB IC and SSC at 1 keV was determined on the basis of the modelled synchrotron spectrum for each source assuming equipartition between radiating particles and magnetic field. In this definition $R = 1$ means that the CMB and SSC model with an equipartition magnetic field and a filling factor of unity can explain the observed X-ray flux. $R > 1$ indicates that either the magnetic field is lower than the equipartition value, i. e., the lobes are electron dominated, or an additional photon field is present. $R < 1$ implies magnetic field domination.

Figure 3 shows the histogram of $R$ for the detected lobes. The majority of sources have $R > 1$ and appear to be distributed around $R \sim 2$.

We also examined whether the observed $R$-value is related to the type of radio source by comparing the distribution of $R$ for narrow-line and broad-line objects. We observe that broad-line quasars have a tendency to display higher value of $R$ (Figure 3). We demonstrated (Croston et al., 2005) that projection effects are likely to be important in explaining the distribution of the observed $R$-values, although other possibilities cannot be ruled out.

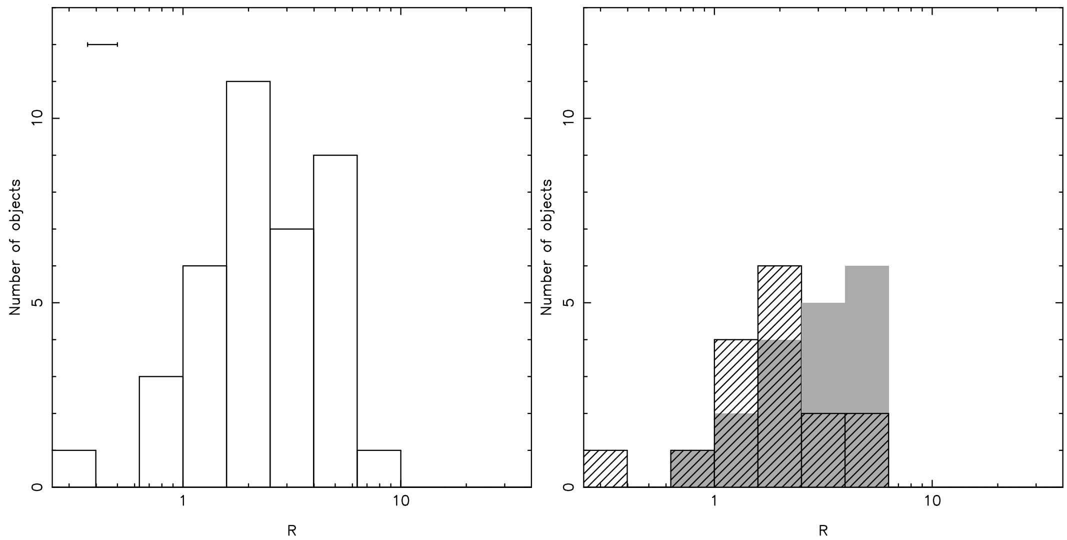


*Figure 3. Distribution of $R$-parameter for the detected lobe sample (Left), and $R$ distribution of the narrow-line (hatched rectangles) and broad line (filled rectangles) objects discussed in Croston et al. (2005) (Right).*

### 4.2. Conclusions

Our study shows that more than 70% of the sources in the sample are at equipartition or electron dominated. The distribution of the $R$-values, with a peak around $R \sim 2$ indicates that most of the source magnetic fields are within 35% of equipartition, or electron dominance ($U_e/U_b$) by a factor of $\sim 5$. Some sources can be magnetically dominated by at least a factor of 2. These results disfavour models in which FRII lobes have an energetically dominant population of relativistic protons which are also in equipartition with the magnetic field.

## 5. ENVIRONMENT OF RADIO SOURCES AND THE SEARCH OF HIGH-REDSHIFT CLUSTERS

Because of the propagation of radio jets, radio galaxies are expected to lie in an external medium dense enough to confine their relativistic jets. The combination of this hypothesis with the visibility of radio galaxies at high redshift suggested that these objects can be used as tracers of high-redshift galaxy clusters, by looking for hot intracluster medium around them in X-rays.

Observations with the *ROSAT* satellite were promising in this context (e.g., Crawford & Fabian 1993; Worrall et al. 1994; Crawford et al. 1999; Hardcastle & Worrall 1999), with detection of cluster-like emission around some of the $z > 0.5$ sources in the 3CRR catalogue.

*Chandra* and *XMM-Newton* make it now possible to detect and study the environment of high redshift radio galaxies in great detail, and to separate spatially and spectrally the different components (core, lobes, jets) responsible for the X-ray emission from these sources. The picture from *Chandra* and *XMM-Newton* is rather different from that of previous satellites.

### 5.1. The current picture: results from *Chandra* and *XMM-Newton*

Preliminary results for sources analysed so far are shown in Figure 4. Published work in the literature, and here assembled, shows that most of the radio galaxies and quasars in the redshift range $0.5 < z < 1.0$ show a tendency to lie in extended environments with luminosities of few $10^{43} h_{70}^{-2}$ erg s$^{-1}$ (e.g. Hardcastle et al. 2002; Crawford & Fabian 2003; Donahue, Daly & Horner 2003; see Fig. 4). Only few objects have been confirmed spectroscopically (3C220.1 - Worrall et al. 2001, 3C184 and 3C292 - Belsole et al. 2004). Indeed most of the X-ray emission associated with these and other sources was found to be elongated in the direction of the radio lobes (Carilli et al., 2002; Hardcastle et al., 2002; Donahue, Daly & Horner, 2003; Croston et al., 2005)

Despite the low surface brightness emission from these objects, most of these environments are sufficient to confine the radio lobes (e.g. Hardcastle et al. 2002; Donahue, Daly & Horner 2003; Belsole et al. 2004).

The preliminary picture we observe from our study is suggesting that radio sources at high redshift trace a particular type of environment, i.e. they prefer poor environments at high redshift. This also supports that they may represent a means to built up a more unbiased sample for structures in the high-redshift Universe, where massive clusters are expected to be fewer in the hierarchical formation paradigm.

This calls for a systematic study of a well selected sample of radio sources, and the 3CRR catalogue is a good

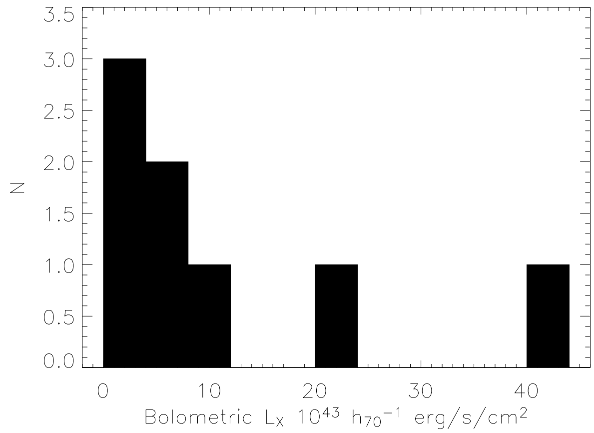


*Figure 4. Distribution of the bolometric X-ray luminosity of 3CRR sources with detected extended, cluster-like emission.*

starting point.

Work on the detection of extended emission from the sources in Table 1 is under way. Our full study will allow us not only to probe the characteristics of the extended emission, but also to constrain the physical state of the radio source itself by comparing the internal and external pressure of the radio lobes.


## ACKNOWLEDGEMENTS

We are very grateful to the organisers of this conference for allowing us to present the work described in the paper. This well-organised meeting was enjoyable for the richness of results presented. This paper is based on observations obtained with *XMM-Newton*, an ESA science mission with instruments and contributions directly funded by ESA Member States and the USA (NASA). This research has made use of the NASA's Astrophysics Data System.


## REFERENCES


Barthel P.D., 1989, ApJ, 336, 606

Belsole, E., Worrall, D.M., Hardcastle, M.J., Birkinshaw, M., Lawrence, C.R., 2004, MNRAS, 352,924

Belsole,E., Worrall, D.M., Hardcastle, M.J., 2006, MNRAS, submitted

Brinkmann W., Yuan W., Siebert J., 1997, A&A, 319, 413

Brinkmann W., Laurent-Muehleisen S. A., Voges W., Siebert J., Becker R. H., Brotherton M. S., White R. L., Gregg M. D., 2000, A&A, 356, 445

Brunetti, G., Cappi, M., Setti, G., Feretti, L., Harris, D. E., 2001, A&A, 372, 755

Carilli, C. L., Harris, D. E., Pentericci, L., Röttiger, H. J. A., Miley, G. K., Kurk, J. D., van Breugel, W., 2002, ApJ, 567, 781

Celotti, A. & Fabian, A.C, 1993 MNRAS, 264, 228

Crawford, C. S. & Fabian, A. C., 1993, MNRAS, 260, 15

Crawford, C. S., Lehmann, I., Fabian, A. C., Bremer, M. N., Hasinger, G.,1999, MNRAS, 308,1159

Crawford, C. S. & Fabian, A. C., 2003, MNRAS, 339, 1163

Croston J.H., Birkinshaw M., Hardcastle, Worrall D.M., 2004, MNRAS, 353, 879

Croston J.H., Hardcastle M. J., Harris D. E., Belsole E., Birkinshaw M., Worrall, D.M., 2005, ApJ, 626,733

Dickey J.M. & Lockman F.J., 1990, ARA&A, 28, 215

Donahue, M., Daly, R. A., Horner, D. J., 2003, ApJ, 584, 643

Galbiati E., et al., 2005, A&A, 430, 927

Hardcastle, M. J., Worrall, D. M., 1999, MNRAS, 309, 969

Hardcastle M. J., Birkinshaw M., Worrall D. M., 2001, MNRAS, 326, 1499

Hardcastle, M. J., Birkinshaw, M., Cameron, R. A., Harris, D. E., Looney, L. W., Worrall, D. M., 2002, ApJ, 581, 948

Hardcastle, M.J., Harris, D.E., Worrall, D.M., Birkinshaw, M., 2004, ApJ, 612, 729

Kino, M., & Takahara, F., 2004, MNRAS, 349, 336

Laing R. A., Riley J. M., Longair M. S., 1983, MNRAS, 204, 151

Marshall H. L., et al., 2005, ApJS, 156, 13

Overzier, R. A., Harris, D. E., Carilli, C. L., Pentericci, L., Röttgering, H. J. A., Miley, G. K., 2005, A&A, 433, 87

Reeves J.N. & Turner M.J.L., 2000, MNRAS, 316, 234

Urry C. M. & Padovani P., 1995, PASP, 107, 803

Wardle, J.F.C, Homan, D.C., Ojha, R., Roberts, D.H., 1998, Nature, 395, 457

Worrall D.M. & Wilkes B.J., 1990, ApJ, 360, 396

Worrall, D. M., Lawrence, C. R., Pearson, T. J., Readhead, A. C. S., 1994, ApJ, 420, L17

Worrall, D. M., Birkinshaw, M., Hardcastle, M. J., Lawrence, C. R., 2001, 326, 1127

# THE REMARKABLE X-RAY JET IN THE QUASAR 4C 20.24

**D.A. Schwartz[1], H.L. Marshall[2], J. Gelbord[2], E.S. Perlman[3], M. Georganopoulos[3], M. Birkinshaw[4], D. M. Worrall[4], J.E.J. Lovell[5], D.L. Jauncey[5], L. Godfrey[6], G.V. Bicknell[6], D.W. Murphy[7], and S. Jester[8]**

[1]Harvard-Smithsonian Center for Astrophysics,60 Garden St., Cambridge, MA, 02138, USA
[2]Kavli Institute for Astrophysics and Space Research, Massachusetts Institute of Technology, 77 Massachusetts Avenue, Cambridge, MA 02139, USA
[3]Department of Physics, Joint Center for Astrophysics, University of Maryland-Baltimore County, 1000 Hilltop Circle, Baltimore, MD 21250, USA
[4]Department of Physics, University of Bristol, Tyndall Avenue, Bristol BS8 1TL, UK
[5]CSIRO Australia Telescope National Facility, PO Box 76, Epping NSW 1710, Australia
[6]Research School of Astronomy and Astrophysics, Australian National University, Cotter Road, Weston Creek, Canberra, ACT72611, Australia
[7]Jet Propulsion Laboratory, 4800 Oak Grove Drive, Pasadena, CA 91109, USA
[8]Fermi National Accelerator Laboratory, P.O. Box 500, Batavia, IL, 60510, USA

## ABSTRACT

The Chandra X-ray telescope has observed a jet in 4C 20.24 (= PKS B1055+201) for which the de-projected length is inferred to be greater than 1 Mpc. The arcsec scale X-ray and 1.46 GHz jets initially follow the direction of the VLBA jet emanating N from the 0.2 mas core, but then curve to the NNW through a total change in angle of about 45 degrees. The 22 arcsec length of the jet gives us one of the best opportunities to study independent spatial elements, in order to infer how the magnetic field and relativistic beaming factor change with distance from the core. We find a constant Doppler factor of about 6, up until the radio structure bends through two 90 degree turns. The remarkable feature of this jet is that we detect extended X-ray emission of about 14 arcsec full width, symmetric about the jet. Furthermore, a similar extended X-ray feature extends to the south, where no radio or X-ray jet is visible, terminating just before the south radio lobe. At the redshift z=1.11 of this quasar, the extended X-ray emission has a luminosity 3E44 ergs per second, comparable to a luminous X-ray cluster. This system gives us a laboratory where we can observe both the jet, and the medium with which it is interacting.

Key words: jets; quasars; X-rays; 4C 20.24; PKS 1055+201.

## 1. INTRODUCTION

The FR II radio source 4C20.24 is identified as a quasar at redshift z=1.11 (Bolton, Kinman, & Wall, 1968). This quasar, which is also cataloged as PKS 1055+201, was observed by *Chandra* as part of a snapshot survey of radio jets (Marshall et al., 2005a). The survey, which is on-going, consists of 56 flat spectrum quasars, selected from two samples. One is by Murphy, Browne, & Perley (1993), of radio sources at declination angles above 0°, with core flux densities at 5 GHz greater than 1 Jy, and the other by Lovell (1997) of Parkes catalog sources below declination -20°, with core flux densities at 2.7 GHz greater than 0.34 Jy. From their radio maps, we selected sources with radio jets longer than $2''$ and for which we expected that 5 ks *Chandra* observations would yield X-ray detections for objects having as large a ratio of X-ray to radio flux as was observed for the jet in PKS 0637-752 (Schwartz et al., 2000; Chartas et al., 2000).

*Chandra* obsid 4889 acquired 4.7 ks data in an initial survey of 4C 20.24. This gave a clear detection, showing an X-ray jet extended about $20''$ along the radio jet to the north (Marshall et al., 2006). The X-ray flux was roughly 6.5 $\mu$Jy, only about 20% of that predicted based on the radio emission. We proposed a longer followup *Chandra* observation, motivated by the angular extent in X-rays. The $21''$ length could in principle be divided into 25 independent angular resolution elements, based on the $0.77''$ full width half maximum (FWHM) response. This could allow a detailed study of the change of magnetic field and Doppler factor vs. distance from the quasar. At the redshift z=1.11, an angular size of $1''$ corresponds to 8.24 kpc in the plane of the sky[1].

In this talk we will present some of the remarkable X-ray features revealed in the 31.6 ks *Chandra* obsid 5733. In

[1]We use a flat, accelerating cosmology, with $H_0$=71 km $s^{-1}$ $Mpc^{-1}$, $\Omega_m = 0.27$ , and $\Omega_\Lambda = 0.73$

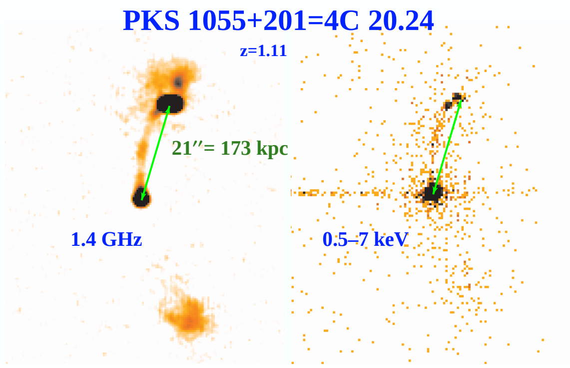


*Figure 1. Left panel shows the 1.46 GHz radio image reconstructed with a 1.64″ × 1.5″ beam size, and the right panel the 0.5 – 7 keV X-ray image. The 21″ lines connect the same celestial coordinates in each panel. There is a clear X-ray jet to the north of the quasar, coincident with the radio jet, until the latter makes sharp bends to the west and then north. The horizontal feature on the X-ray image is the readout streak artifact. The X-ray image shows enhanced emission well beyond the width of the jet, and similar emission extending to the south.*

particular, we detect extended X-ray emission surrounding the jet structure, and similar X-ray emission to the south surrounding an assumed, unseen counter-jet. In Section 2 we summarize some of the properties which 4C 20.24 shares in general with the other radio and X-ray jets we have studied, including the interpretation of the X-ray emission as inverse Compton (IC) scattering off the cosmic microwave background (CMB), (Tavecchio et al., 2000; Celotti et al., 2001). In Section 3 we present the unique X-ray features of this system. The final Section 4 discusses some possible mechanisms for the X-ray emission from the extended "tube" region.

## 2. WHAT IS NORMAL ABOUT THE 4C 20.24 JET?

In Fig. 1 we show the radio and X-ray images of 4C 20.24. The two images are to scale, and the double arrow is 21″ long which corresponds to 173 kpc in the plane of the sky. The arrow connects the same coordinates in each panel. The radio and X-ray jets are extremely similar, at least out to the point where the X-ray jet appears to end. In Fig. 1, the horizontal streak in the X-ray image is an artifact due to the fact that the ACIS CCD camera is not shuttered while a frame is being read out. Past the northern end of the arrow, the radio image appears to bend at nearly right angles to the west, and then again at a right angle to the north, where it terminates in a hotspot and lobe.

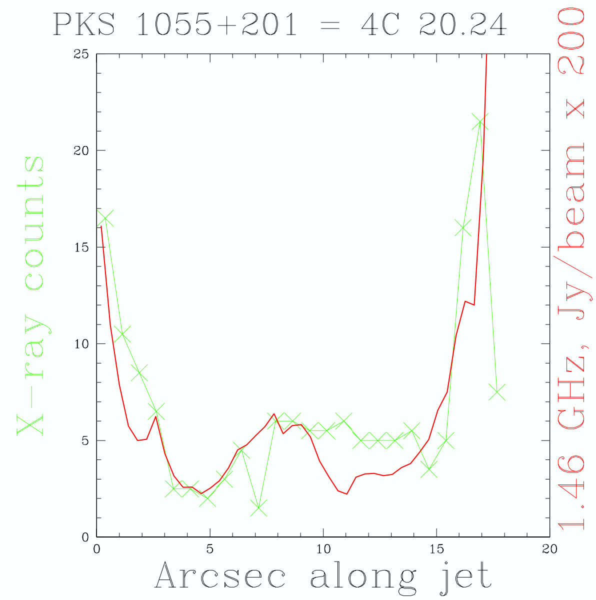


*Figure 2. X-ray counts, crosses, sorted into 0.75″ bins, compared to the radio, solid line, 1.46 GHz flux density per beam, along a 4″ × 18″projection box. The X-ray counts have Poisson errors, but adjacent bins are correlated as the counts were split from the original 0.492″ bins. The radio flux density is arbitrarily multiplied by 200 to better compare to the X-ray profile.*

### 2.1. Correlation to Radio emission

Fig. 2 compares the X-ray and radio profiles in more detail. Both images project identical areas of the sky, starting about 2″ from the quasar and extending 18″ along the jet; i.e., extending to where the radio emission bends toward the west. The projection is 4″ i.e., approximately ±2″ perpendicular to the jet. The crosses are the X-ray data, given in counts per bin.The heavier solid line is the 1.46GHz radio data. The radio emission in Jy/beam is multiplied by a factor of 200, to better compare to the X-ray profile. In Fig. 3 the radio data is given to the same scale of absolute physical units as the X-rays.

Over the range of 18″ corresponding to 148 kpc in the plane of the sky, the ratio of X-ray to radio flux does not change by more than a factor of 2. Since we infer from relativistic beaming that the jet is tilted no more than 9° from our line of sight, this would actually be a minimum distance of 948 kpc. In the range 2.5″ to 9.5″ the coincidence is even tighter. Such a similar ratio is hard to explain when the X-rays are due to either synchrotron or IC/CMB emission. In the synchrotron case both the radio and X-ray emission depend on the same magnetic field, but the lifetime of the X-ray emitting electrons is so short compared to the scale of the jet that a very fine tuned balance of high energy electron acceleration would be needed, and this acceleration must not simultaneously

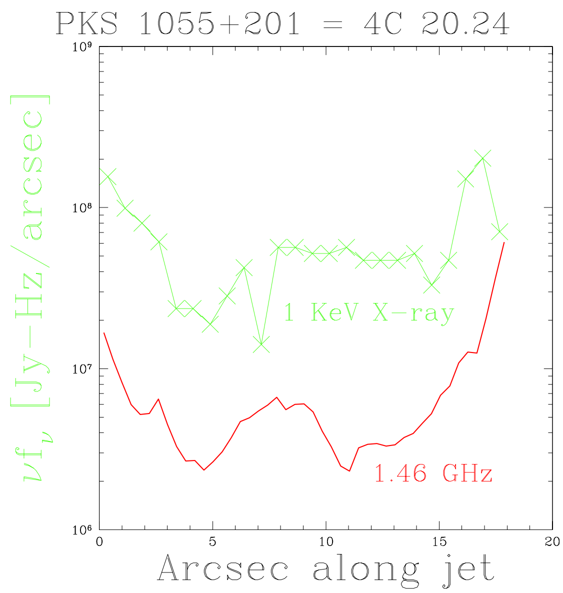


*Figure 3. Both X-ray (crosses) and radio (solid line) are converted to absolute physical units of Jy-Hz arcsec$^{-1}$ to show that the energy radiated in X-rays dominates over that radiated in the GHz band.*

increase the number of longer lived radio emitting electrons. In the IC/CMB case, the X-rays result from electrons with lower energies than the radio, and both are longer lived than in the synchrotron case, but since the X-ray emission then does not depend on the magnetic field the latter would have to be finely tuned to be relatively constant. The naive prediction for IC/CMB would be for the X-ray emission to persist downstream of the radio emission, due to the longer life of the lower energy electrons, and we may be seeing this in the region around 10″ to 13″ along the jet. (The apparent X-ray dip at 7″ is not significant, due to the Poisson statistical errors.)

Fig. 3 plots $\nu f_\nu$ per arcsec along the jet. For the X-rays, we estimate a flux density at $\nu$=2.4 $\times 10^{17}$ Hz, or 1 keV, by assuming an energy spectral index of $\alpha$=0.7. The radio frequency is $\nu$=1.46 GHz. We see the radiated energy in X-rays dominating that in radio by an order of magnitude, in the region shown. In contrast, the radio energy flux surpasses the X-ray beyond the terminal shocks, i.e., past the north end of the arrow in Fig. 1. In the sense that radio dominates X-ray at the end of the jet there is a similarity to the case of 3C 273, although for that object we see a constant decrease of the X-ray to radio ratio along the ≈10″ length of that jet.

### 2.2. Interpretation as Inverse Compton X-rays

Inverse Compton scattering of electrons by the cosmic microwave background photons (IC/CMB) has been widely inferred as the most plausible mechanism of X-ray emission from powerful, radio-loud quasars (Marshall et al., 2001; Sambruna et al., 2001, 2002, 2004; Harris & Krawczynski, 2002; Siemiginowska et al., 2002, 2003a,b; Schwartz et al., 2006) following the suggestion by Tavecchio et al. (2000) and Celotti et al. (2001) to explain the X-ray jet found in PKS 0637-752 (Schwartz et al., 2000; Chartas et al., 2000). Typically this is motivated by optical detection or upper limits which do not allow extrapolation of a single synchrotron spectrum from the radio to X-ray range. We will adopt the IC/CMB scenario here, although noting that other models have been constructed to try to produce the X-rays via synchrotron emission (e.g., Dermer & Atoyan (2002); Stawarz et al. (2004); Atoyan & Dermer (2004)).

We apply this formalism to the jet of 4C 20.24. We divide the X-ray jet into six distinct regions, each of 1.6″ radius, so that they enclose greater than 95% of the point spread function. The model assumes that the synchrotron emission arises from a region uniformly filled with a constant magnitude, randomly oriented magnetic field, and with minimum energy conditions between the particles and magnetic field. We assume an equal energy density of protons and electrons, and that the observed radio emission would extend over the range $10^6$ Hz to $10^{12}$ Hz. This allows calculation of the magnetic field strength, $B_1$, required to generate the observed radio emission under the minimum energy condition. Such a magnetic field strength is typically much greater than the field one would calculate by assuming that the X-rays arise via IC/CMB from a volume at rest with respect to the CMB. However, Tavecchio et al. (2000) and Celotti et al. (2001) both pointed out that if the jet were in bulk relativistic motion with Lorentz factor $\Gamma$ at an angle $\cos(\theta)$ to our line of sight, then in the rest frame of the jet the actual magnetic field would be $B=B_1/\delta$, where the Doppler factor $\delta = (\Gamma(1-\beta\cos(\theta))^{-1}$. Furthermore, the apparent CMB energy density seen by the photons in the jet is enhanced by a factor $\Gamma^2$ (Dermer & Schlickeiser, 1994). By assuming that $\Gamma = \delta$, which is the value of $\Gamma$ for the maximum angle which can occur at any fixed $\delta$ we have only the two unknowns B and $\delta$, which can then be estimated from the radio and X-ray flux densities.

Fig. 4 shows the results of this modeling. For the five innermost regions, labeled *a* through *e*, the magnetic fields are in the range 1 to 16 $\mu$Gauss, and the Doppler factors in the range $\delta$=5.5 to 6.5. Such values of $\delta$ imply that the angle to our line of sight cannot be greater than $\theta$=9°. The values of B and $\delta$ are consistent with being constant, within the statistics of the X-ray counts, and especially due to the systematic uncertainties underlying the model assumptions. The final region, at the apparent terminal shock around the northern arrow point in Fig. 1, shows a significantly higher magnetic field and lower Doppler factor. This presumably is due to deceleration of the jet, and conversion of the bulk kinetic energy into magnetic field and relativistic particles. At 1.46 GHz, this region outshines the quasar by a factor of about three. However, it seems clear that the formalism is not self-consistent in interpreting both this region and the inner five regions. This can be seen by the deviation of point *f* from the solid line in Fig. 4. That line represents a constant kinetic energy flux, of about $3{\times}10^{45}$ ergs s$^{-1}$, averaged over the

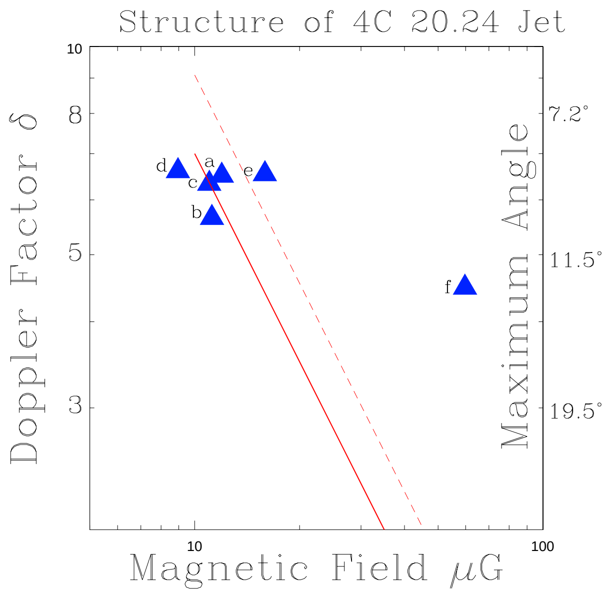


*Figure 4. The effective Doppler factor and the magnetic field strength in the jet rest frame for six regions along the jet, labeled alphabetically away from the quasar. The solid line is the locus of kinetic luminosity $3{\times}10^{45}$ergs $s^{-1}$ of the five innermost regions, assuming equal proton and electron energy densities. The dashed line would represent the average of all six regions. The right hand scale shows the maximum possible angle at which the corresponding Doppler factor can be achieved. This occurs when $\Gamma = \delta$.*

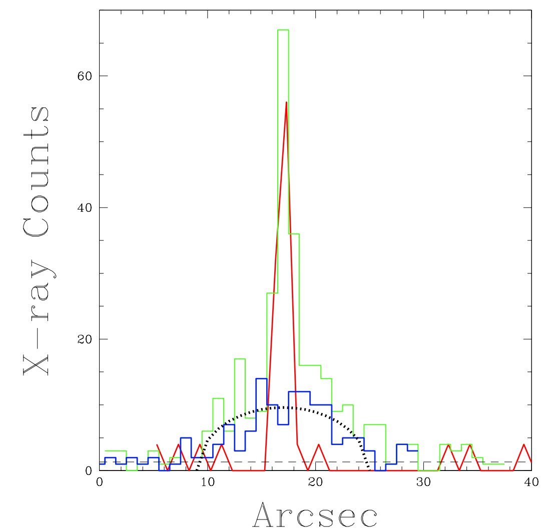


*Figure 5. The two histograms show the X-ray profile along the jet (larger values, lighter line) and counter jet (smaller values, darker line) directions, plotted vs. angle across the jet. The continuous line is the scaled profile of the readout streak, which shows how an unresolved line source would appear. The dashed horizontal line shows the background level. The dotted profile is that expected from uniform emission of a cylinder.*

five inner regions. The outermost region would require a minimum energy flux ten times greater. Possible solutions are that the kinetic flux is really about $3{\times}10^{46}$ ergs $s^{-1}$ through out the jet, e.g., due to a much greater proton to electron ratio than assumed or to conditions deviating from equipartition; or that the region *f* is at a non-relativistic velocity and not emitting X-rays via minimum energy IC/CMB.

## 3. WHAT IS REMARKABLE ABOUT THE 4C 20.24 JET?

4C 20.24 shows at least two remarkable features which have not previously been noted for FRII/quasar X-ray jets. One is the broad, about 16″ wide tube-like region of enhanced X-ray emission following the narrow X-ray and radio jet to the north and terminating at the same distance that the X-ray jet ends. The other is a similar symmetric feature to the south, following what might be assumed to be an unseen counter-jet.

Both tube regions appear to be curved to the west of the quasar. This can be substantiated; e.g., against the hypothesis that only one jet is deflected from an initial straight line, by considering the VLBI image. Kellerman et al. (2004) report six years of VLBA monitoring, where the core at 15 GHz is clearly extended by about 3 mas at position angle -5°. Within a few degrees uncertainty, this is the same initial angle that each of the radio and X-ray jet follows for the first few arcsecond north of the quasar.

An impression of the enhanced X-ray tubes can be seen directly in Fig. 1. A more quantitative result can be derived from Fig. 5. The figure presents two histograms which show the X-ray profile across the jet north and south of the core. These are constructed by integrating along 17″ lengths parallel to the jet and counter-jet directions. The horizontal dashed line close to zero counts represents the background measured in an identical projection in a nearby, source-free region. The continuous line results from a projection region that straddles the readout streak; it represents the width of an unresolved source and has been rescaled for comparison with the component of the northern histogram resulting from the projection of the narrow jet. Emission in each of the northern and southern regions extends at least from 10″ to 26″ in the plot, and hints at even broader extension which is fainter than the sensitivity of the present observation.

In the north and south regions of the X-ray tube, excluding the narrow jet, we have 310 X-ray counts. The spectrum of these counts allow a fit to a power law, with energy index $\alpha$=0.66±0.2, Fig. 6. More complex models cannot be ruled out; for example, a power law with $\alpha$=$0.4^{+0.7}_{-3.3}$ plus a thermal spectrum with kT=$1.3^{+4.4}_{-1.2}$, Fig. 7. We include this latter model since it is relevant to discuss whether the X-ray tube emission arises from thermal bremsstrahlung. The X-ray spectrum of the jet can be fit with a power law of energy index $\alpha$=0.98±0.25. Formally the two regions may therefore have the same spectrum; however, the spectrum of the narrow jet is somewhat softer than that of the tube. This can be seen simply from the integral distribution of photons in Fig. 8. A K-S test rejects these distributions being equal at the 99.95% confidence level. The spectral fit to the jet is based on 241 photons. However, from the profile of the extended X-rays, we can estimate that 40 of these are from the tube region projected in front and behind the jet and which has a harder spectrum, so that the residual jet spectrum will be even somewhat softer.

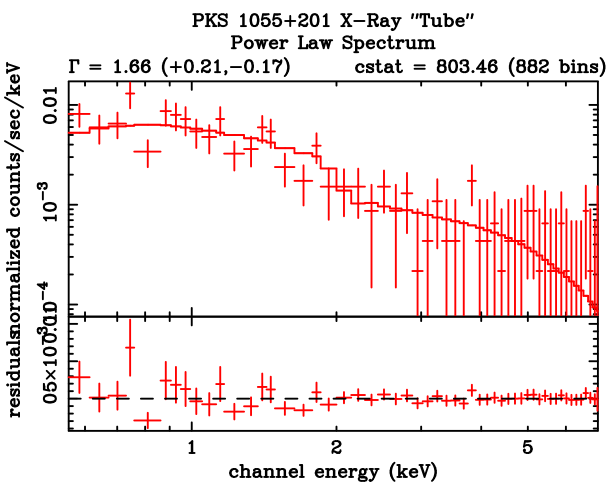


*Figure 6. X-ray spectrum of the extended tube region, fit to a single power law. Residuals are shown in the bottom panel.*

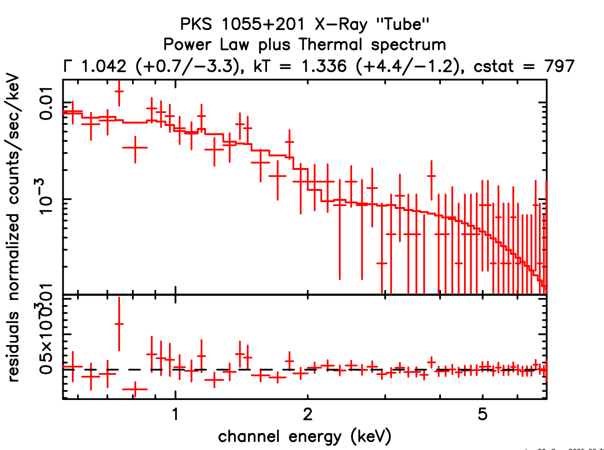


*Figure 7. X-ray spectrum of the extended tube region, fit to the sum of a power law and a mekal thermal spectrum.*

## 4. DISCUSSION

We discuss the extended X-ray tube in terms of thermal vs. non-thermal emission. Although a simple non-thermal power law is indicated by the X-ray spectrum, a

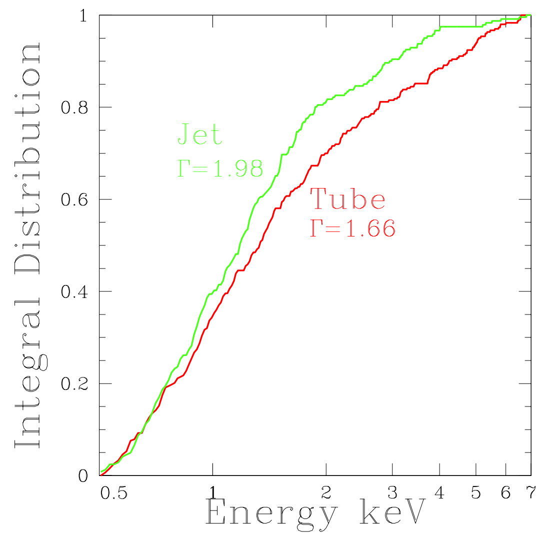


*Figure 8. Integral distributions of the counts from the narrow jet and from the extended X-ray tube. The maximum absolute difference of 0.1317 at 1.9 keV shows that the two spectra cannot be identical, according to a two-tail K-S test.*

thermal component cannot be strongly limited. In either case we model the tube as two uniformly filled cylinders, each of 65 kpc radius and 1 Mpc in length. The dotted curve in Fig. 5 shows the expected projection of such an emission region. The numbers here may be rough, pending more detailed spectral and spatial analysis.

From the fit to a thermal mekal model plus a power law, the thermal normalization implies an X-ray luminosity of $2.5\times10^{44}$ergs s$^{-1}$ emitted in the 1 to 15 keV band in the source frame. We note that this would be grossly overluminous if it were thought to arise in a cluster of galaxies with such a low temperature kT=1.34 keV. At that gas temperature, the density would be $n_e$=0.0054 cm$^{-3}$ to produce the luminosity. The total energy content of the gas would be of order $10^{61}$ ergs, requiring our estimated kinetic flux of $3\times10^{45}$ ergs s$^{-1}$ to be maintained for $\approx 10^8$ years and to be efficiently converted into heating the gas. However, the cooling time scale of the gas is of order $4\times10^9$ years, so that it is conceivable that several different epochs of radio-activity could contribute to the thermal reservoir. Gas at such a cool temperature will show a very strong complex of Fe-L line emission, observable in the 0.45 to 0.55 keV range. With of order ten times as many X-ray photons, one should be able to observe a temperature gradient whose hot end would point to the location of interaction. The jet energy might be dissipated laterally, e.g., through entrainment of material or lateral shocks. However, since we do not see evidence for deceleration out to at least 17″ from the quasar, the dissipation may be taking place at the terminal shock. In this case the base of the tubes, nearest the quasar, would show the coolest temperatures. The mass of gas required to fill the cylinders in the thermal scenario is of order 2 ×

$10^{12}$ solar masses.

Non-thermal emission allows many scenarios for the origin of the relativistic electrons. We consider a case where the electrons diffuse out of the jet and into a region of low magnetic field which is not in bulk relativistic motion with respect to the microwave background. In this case the entire X-ray emission is produced by IC/CMB, giving an X-ray luminosity of $5.4 \times 10^{44}$ ergs $s^{-1}$. The required density of relativistic electrons is of order $3 \times 10^{-8}$ $cm^{-3}$, comparable to the density in the jet. Their lifetime against IC/CMB emission is of order $10^8$ years, so a diffusion velocity of $\approx$ 300 km $s^{-1}$ would be required to propagate 65 kpc away from the jet. This scenario gives a clear prediction of low frequency radio emission. Since we may still conjecture magnetic fields of order 0.1 to 1 $\mu$Gauss we may detect the tube region in the few 100 MHz range. We should see a steeper X-ray spectrum laterally away from the jet, at distances comparable to the electron lifetimes. Alternately, if the relativistic electrons are back-streaming from the terminal hotspot, the steeper spectra will be toward the base of the jet.

4C 20.24 gives us an opportune system for deducing the spatial structure of the magnetic fields and Doppler factors in an X-ray/radio jet. The relativistic beaming IC/CMB scenario can explain the X-ray and radio emission along the length of the jet, but we require a scenario with non-relativistic motion to explain the terminal shock. The extended X-ray emitting “tubes” surrounding this jet are unique. There are problems explaining them as either thermal gas, or electrons diffusing out of the jet. The situation requires a much deeper X-ray image to further elucidate the spatial emission profile and the spatially dependent spectral shape, and low frequency radio observations. In any event, the southern X-ray structure provides new evidence for the presence of unseen counter jets, which hitherto have been inferred by the presence of radio lobes.

## ACKNOWLEDGMENTS

This work was supported by NASA contract NAS8-39073 to the *Chandra* X-ray Center, and SAO SV1-61010 to MIT, and NASA grant GO2-3151C to SAO. E.S.P. acknowledges support from NASA LTSA grant NAG5-9997. Part of this research was performed at the Jet Propulsion Laboratory, California Institute of Technology, under contract to NASA. This research used the NASA Astrophysics Data System Bibliographic Services, and the NASA/IPAC Extragalactic Database (NED) which is operated by the Jet Propulsion Laboratory, California Institute of Technology, under contract with the National Aeronautics and Space Administration.

## REFERENCES

Atoyan, A. & Dermer, C. D. 2004, ApJ, 613, 151

Bolton, J. G., Kinman, T. D., & Wall, J. V. 1968, ApJ, 154, L105

Celotti, A., Ghisellini, G., & Chiaberge, M. 2001, MNRAS, 321, L1

Chartas, G., et al. 2000, ApJ, 542, 655

Dermer, C. D. & Atoyan, A. M. 2002, ApJ, 568, L81

Dermer, C. D. & Schlickeiser, R. 1994, ApJS, 90, 945

Harris, D. E., & Krawczynski, H. 2002, ApJ, 565, 244

Kellerman, K. I. et al. 2004, ApJ, 609, 539

Lovell, J. 1997, Ph.D. Thesis, U. of Tasmania

Marshall, H. L., et al. 2001, ApJ, 549 L167

Marshall, H. L., et al. 2005a, ApJS, 156, 13

Marshall, H. L., et al. 2006, in preparation

Murphy, D.W., Browne, I.W.A., & Perley, R.A. 1993, MNRAS, 264, 298

Sambruna, R.M., Urry,C.M. Tavecchio, F., Maraschi, L., Scarpa, R., Chartas, G., & Muxlow,T. 2001, ApJ, 549, L161

Sambruna, R. M., Maraschi, L., Tavecchio, F., Urry, C. M., Cheung, C. C., Chartas, G., Scarpa, R., & Gambill, J. K. 2002, ApJ, 571, 206

Sambruna, R. M., Gambill, J.K., Maraschi, L., Tavecchio, F., Cerutti, R., Cheung, C. C., Urry, C. M., & Chartas, G., 2004, ApJ, 608, 698

Schwartz, D. A., et al. 2000,ApJ, 540, L69

Schwartz, D. A., et al. 2006, ApJ, in press

Siemiginowska, A, Bechtold, J., Aldcroft, T. L., Elvis, M., Harris, D. E., Dobrzycki, A. 2002, ApJ, 570, 543

Siemiginowska, A., et al. 2003a, ApJ, 595, 643

Siemiginowska, A., Smith, R. K., Aldcroft, T. L., Schwartz, D. A., Paerels, F., & Petric, A. O. 2003b, ApJ, 598, L15

Stawarz, Ł., Sikora, M., Ostrowski, M., & Begelman, M. C. 2004, ApJ, 608, 95

Tavecchio, F., Maraschi, L., Sambruna, R. M., Urry, C. M. 2000, ApJ, 544, L23

# THE ELECTRON AND MAGNETIC FIELD ENERGIES IN THE EAST LOBE OF THE RADIO GALAXY FORNAX A, MEASURED WITH XMM-NEWTON.

**N. Isobe[1], K. Makishima[1,2], M. Tashiro[3], K. Ito[3], N. Iyomoto[4], and H. Kaneda[5]**

[1]The Institute of Physical and Chemical Research (RIKEN), 2-1 Hirosawa, Wako, Saitama, 351-0198, Japan
[2]Department of Physics, University of Tokyo, 7-3-1, Hongo, Bunkyo, 113-0033, Japan
[3]Department of Physics, Saitama University, Shimo-Okubo, Saitama, 338-8570, Japan.
[4]Laboratory for High Energy Astrophysics, Code 662, NASA Goddard Space Flight Center, Greenbelt, MD 20771, USA
[5]Institute of Space and Astronautical Science, Japan Aerospace Exploration Agency (ISAS/JAXA), 3-1-1, Yoshinodai, Sagamihara, Kanagawa, 229-8510, Japan

## ABSTRACT

In an XMM-Newton observation of the east lobe of nearby radio galaxy Fonrax A, we have significantly detected the diffuse X-ray emission, which was originally discovered by *ASCA* and *ROSAT*. The X-ray spectrum of the diffuse emission is described by a single power-law model, modified with the Galactic absorption toward the object. The best-fit X-ray photon index, $1.62^{+0.25}_{-0.15}$, agrees well with the synchrotron radio index, $1.68 \pm 0.05$, between 29.9 MHz and 5 GHz. Therefore, the inverse Compton interpretation for the diffuse X-ray emission is justified. A comparison between the radio and X-ray flux densities gives a moderate electron-energy dominance over in the east lobe of Fornax A, in spite of the dormancy of its nucleus. We also reexamined the ASCA result on the west lobe, to find that both lobes share the similar physical condition.

Key words: radiation mechanisms: non-thermal — magnetic fields — X-rays: galaxies — radio continuum: galaxies — galaxies: individual (Fornax A) .

## 1. INTRODUCTION

Inverse Compton (IC) X-ray emission associated with the lobes of radio galaxies and quasars is a very useful probe to investigate the energetics in jet-lobe systems, once the seed photon source is usually identified with the cosmic microwave background (CMB) radiation (Harris & Grindlay, 1979), or infra-red photons from the nucleus (Brunetti et al., 1997). The recent detections of the these lobe-IC X-rays with *ASCA*, *Chandra* and *XMM-Newton* frequently claim an electrons dominance of $u_{\rm e} \sim 10 u_{\rm m}$ in the lobes (Croston et al., 2005; Isobe et al., 2005), where $u_{\rm e}$ and $u_{\rm m}$ is energy density of electrons and magnetic fields in the lobes, respectively.

The lobe-IC X-ray emission was originally discovered from the nearby radio galaxy Fornax A. with *ROSAT* (Feigelson et al., 1995) and *ASCA* (Kaneda et al., 1995). Fornax A is the fourth brightest radio source all over the sky in the GHz band, located at the southern hemisphere. Although the radio images of Fornax A show a prototypical double-lobe morphology (Ekers et al., 1983), which naturally suggests a past activity of the jets from the nucleus, recent X-ray observations indicate a current dormancy of the nucleus (Iyomoto et al., 1998; Kim & Fabianno, 2003). Therefore, Fornax A is one of the most important target to study the evolution of energetics in lobes of radio galaxies, associated with the activity of the jets from the nucleus. Actually, the *ASCA* result (Kaneda et al., 1995; Tashiro et al., 2001) dose not conflict with an equipartition between $u_{\rm e}$ and $u_{\rm m}$, though with lightly large errors.

We report here, the *XMM-Newton* observation of Fornax A, in which the IC X-ray emission from the east lobe was confirmed with significantly improved signal statistics. We adopted the distance to Fornax A to be 18.6 Mpc (Madore et al., 1999), At the distance, $1'$ corresponds to a physical size of $5.41$ kpc.

## 2. OBSERVATION AND RESULTS

We conducted a 60 ksec observation of the east lobe of Fornax A, and obtained about 26 ksec of good exposure for the MOS camera. However, we diceded to reject all the PN data, because the background was found to be unstable, even after we carefully removed so-called background flare periods. The details on the data reduction and the background rejection will be presented elsewhere (Isobe et al., submitted to ApJ).

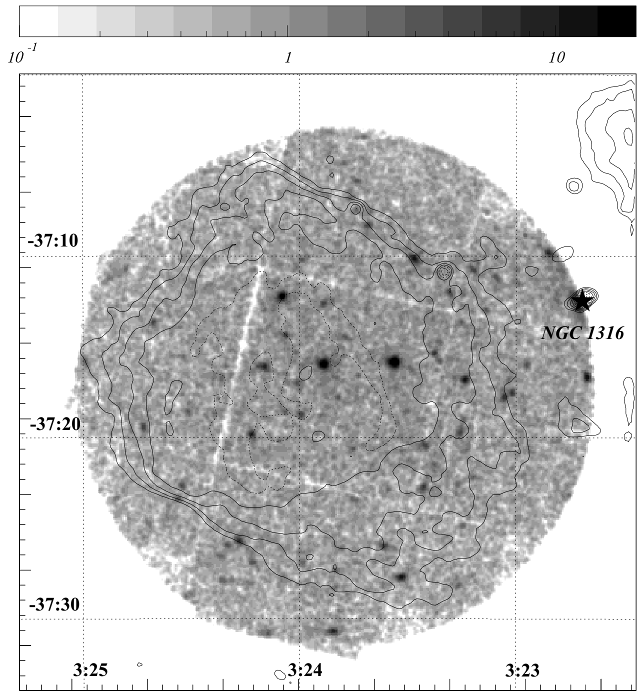


*Figure 1. The 0.3 – 10 keV MOS image of the east lobe of Fornax A, smoothed with a two dimensional Gaussian of* $5''$ *radius. The backgound is not subtracted. The 1.5 GHz VLA contour image (Fomalont et al., 1989) is overlaid. The center of the host galaxy, NGC1316, is shown with the filled star at the edge of the MOS VOV. The east lobe is fully contained in the MOS field of view.*

### 2.1. X-ray Image

We show a raw 0.3 – 10 keV MOS image in the left panel of Figure 1, The 1.5 GHz radio image (Fomalont et al., 1989) is superposed with contours on the X-ray image, to visualize that the east lobe is fully contained within the MOS field of view (FOV). However, the center of the host galaxy, NGC 1316, locates near the FOV edge. We have detected, in total, 59 X-ray sources in this image, almost all of which were not able to be resolved with the *ASCA*.

In order to search for the diffuse X-ray emission associated with the east lobe, we removed all the detected point sources. The right panel of Figure 2 shows the source-removed, background-subtracted MOS image in 0.3 – 10 keV. The image is heavily smoothed with a two dimensional Gaussian of $\sigma = 1'$, after the exposure correction is performed. Diffuse X-ray emission has been clearly detected almost all over the east lobe.

### 2.2. X-ray spectrum

The MOS spectrum of the east lobe, integrated within the smaller circle ($10'$ raduis) in the right panel of Figure 1, is shown in Figure 3. The X-ray signals are highly significant (about $24\sigma$) in the 0.3 – 6 keV range. We removed all the detected point sources in the same manner as for the X-ray image. The spectrum appears relatively featureless and hard. t is successfully reproduced by a single power-law (PL) model modified with a free absorption. The best-fit spectral parameteds are summarised in Table 1 (Fit 1). The photon index becomes $\Gamma_{\rm X} = 1.62^{+0.24}_{-0.15}$, which is consistent with the *ASCA* result (Kaneda et al., 1995). The flux density at 1 keV, $S_{\rm 1keV} = 86^{+18}_{-9}$ nJy, becomes slightly smaller than the *ASCA* result of $110 \pm 50$ nJy. The absorption column density coincides with the Galactic value toward Fornax A, $2.06 \times 10^{20}$ cm$^{-2}$ (Stark et al., 1992), within the sta-

*Table 1. The best-fit PL spectral parameters*

| Parameter | Fit1 | Fit2 |
|---|---|---|
| $N_{\rm H}(10^{20}$ cm$^{-2})$ | $1.2^{+5.5}_{-1.2}$ | $2.4^{+2.8}_{-2.4}$ |
| $\Gamma_{\rm X}$ | $1.62^{+0.24}_{-0.15}$ | 1.68 (fix) |
| $S_{\rm 1keV}$(nJy)$^a$ | $86^{+18}_{-9}$ | $90^{+8}_{-9}$ |
| $F_{\rm X}(10^{-13}$ erg cm$^{-2}$ s$^{-1})^b$ | $5.9^{+0.6}_{-0.5}$ | |
| $L_{\rm X}(10^{40}$ erg s$^{-1})^c$ | $2.4^{+0.3}_{-0.2}$ | |
| $\chi^2$/d.o.f | 26.5/29 | 26.7/30 |

$^a$Flux density at 1 keV. $^b$Absorption-corrected flux in 0.5 – 5 keV. $^c$Absorption-corrected luminosity in 0.5 – 5 keV.

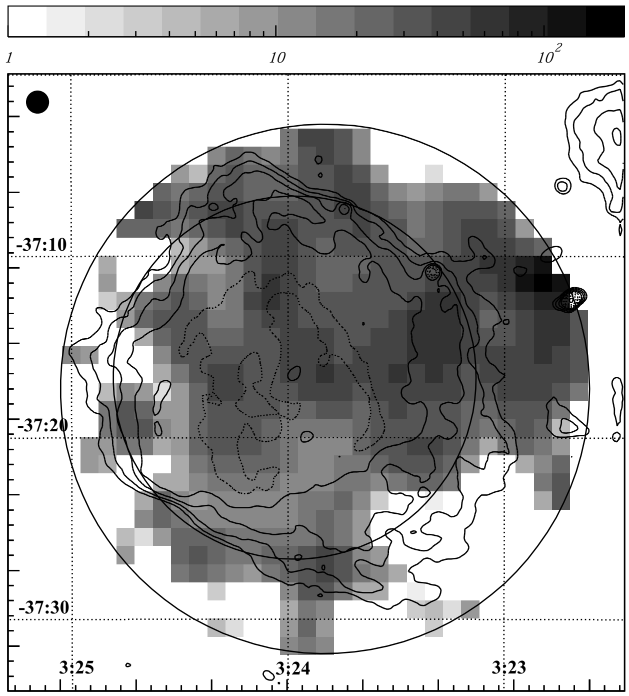


*Figure 2. The background-subtracted MOS image in 0.3 – 10 keV, which is heavily smoothed with a two dimensional Gaussian of $1'$ radius. The exposure is corrected, after all the detected X-ray sources (circles of 36" radius) are rejected. The two colid circles indicate the MOS FOV and the integration region of the spectrum of the east lobe. The same contour radio image is overlaid.*

tistical uncertainty. Thanks to the careful removal of contaminating point sources, these parameters can be considered to represent the "true" spectrum of the diffuse X-ray emission of the east lobe.

## 3. DISCUSSION

We show the radio and X-ray spectral energy distribution of Fornax A in Figure 4 (reference therein). The radio spectrum between 29.9 MHz and 5 GHz is almost successfully descrived by a PL model with a photon index of $\Gamma_{\rm R} = 1.68 \pm 0.05$. Although we have found only two data points for the east lobe at 1.4 and 2.7 GHz, the index between the two data points agrees well with $\Gamma_{\rm R}$, as shonw with the dashed line in Figure 4. Then, we think that this $\Gamma_{\rm R}$ also represents the radio spectrum of the east lobe. The best-fit X-ray index $\Gamma_{\rm X}$ of the east lobe is consistent with $\Gamma_{\rm R}$, within the statistical uncertainty. Therefore, we have concluded that the diffuse X-ray emission is of IC origin, and the seed photon source is of no doubt the CMB radiation, as already discussed in detail by KEA95.

According to Harris & Grindlay (1979), we estimated the physical parameters in the east lobe of Fornax A. We here, re-evaluated the X-ray flux density at 1 keV by the PL fitting with a photon index fixed at $\Gamma_{\rm R} = 1.68$ (see Fit 2 in Table 1). The relevant parameters are summarised in Table 2. We have safely rejected an energy equipartition between the electrons and magnetic field, and instead, revealed a moderate electron dominance of $u_{\rm e}/u_{\rm m} \sim 5$ in the east lobe. Correspondingly, the magnetic field is found to be about 20% weaker than the equipartition value $B_{\rm me}$.

The *ASCA* value of the IC X-ray index of the west lobe, $\Gamma_{\rm X} = 1.74 \pm 0.1$ (Tashiro et al., 2001), well coincides with the radio synchrotron index, $\Gamma_{\rm R} = 1.68$. But Tashiro et al. (2001) adopted the radio index of $\Gamma_{\rm R} = 1.9 \pm 0.2$, based only on three data points between 843 MHz and 2.7 GHz, in the evaluation of the energetics in the west lobe. Therefore, we re-evaluated $u_{\rm e}$ and $u_{\rm m}$ in the west lobe of Fornax A, by using $\Gamma_{\rm R} = 1.68$. As shown in Table 2, it is found that both lobes share similar physical condition.

The nucleus of Fornax A is reported to have been already faded out (Iyomoto et al., 1998; Kim & Fabianno, 2003). This means that the electrons and magnetic field in the lobes of Fornax A are thought to be no longer supplied with sufficient energy by the jets from the nucleus. Therefore, it reasonable that both $u_{\rm e}$ and $u_{\rm m}$ in the lobes of Fornax A is found to be lower than the typical values in the lobes of radio galaxies; $u_{\rm e} = 10^{-12\sim-9}$ erg cm$^{-3}$ and $u_{\rm m} = 10^{-13\sim-10}$ erg cm$^{-3}$ (Croston et al., 2005; Isobe

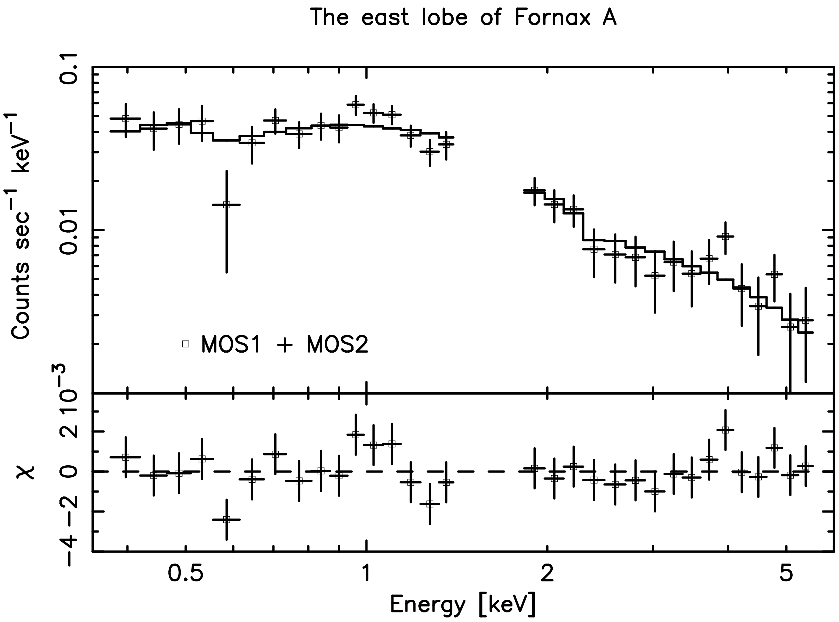


*Figure 3. The background-subtracted MOS spectrum of the east lobe of Fornax A, in the 0.3 – 6 keV range. The data between 1.4 and 1.8 keV are rejected, due to a severe contamination from a prominent instrumental background feature. The histogram indicates the best-fit PL model spectrum modified with a free absorption (Fit1 in Table 1).*

et al., 2005). However, we have confirmed the electron dominance even in the lobes of Fornax A, with a relatively moderate degree of $u_\mathrm{e}/u_\mathrm{m} \sim 5$. Because the electrons in the lobes of Fornax A currently only lose their energy continuously through IC X-ray and synchrotron radio radiation, they will evolve to achieve the equipartition condition within a few Gyr, considering the cooling time of electrons in the lobes.

The *ASCA* result (Tashiro et al., 2001) also indicated a rim-strengthened magnetic field feature in the west lobe of Fornax A, in spite of a nearly uniform distribution of electrons. The same tendency was found in several lobes of radio galaxies (Tashiro et al., 1998; Isobe et al., 2002; Comastri et al., 2003). Figure 2 apparently shows the relatively uniform brightness of the IC X-rays with a slight brightening toward the host galaxy in the east lobe of Fornax A, in contrast to the radio distribution. The X-ray and radio distribution imply a slight discrepancy between the spatial structures of the energy densities of electrons and magnetic field in the lobe. However the limited statistics of our *XMM-Newton* data prevent us from investigating in detail.

*Table 2. Physical quantities in the lobes of Fornax A.*

| Parameters | East lobe | West lobe$^a$ |
|---|---|---|
| Radius(arcmin) | 10 | 11 |
| $S_\mathrm{R}$(Jy)$^b$ | 44 | 50 |
| $\Gamma_\mathrm{R}{}^c$ | $1.68 \pm 0.05$ | |
| $S_\mathrm{1keV}$(nJy) | $90\ ^{+8}_{-9}$ | $100 \pm 10$ |
| $B_\mathrm{me}(\mu\mathrm{G})^d$ | 1.55 | 1.59 |
| $B(\mu\mathrm{G})$ | $1.23\ ^{+0.08}_{-0.06}$ | $1.22 \pm 0.07$ |
| $u_\mathrm{m}(10^{-13}$ erg cm$^{-3})$ | $0.60\ ^{+0.08}_{-0.06}$ | $0.59^{-0.08}_{-0.06}$ |
| $u_\mathrm{e}(10^{-13}$ erg cm$^{-3})^e$ | $3.0 \pm 0.3$ | $2.6^{+0.3}_{-0.2}$ |
| $u_\mathrm{e}/u_\mathrm{m}$ | $5.0\ ^{+1.1}_{-1.0}$ | $4.4^{+1.1}_{-0.9}$ |

$^a$The parameters re-evaluated after TEA01. $^b$Flux density at 1.4 GHz. $^c$Energy index of synchrotron radio emission. $^d$Magnetic field calculated under the minimum energy condition, excluding proton contribution (Miley, 1980). $^e$calculated for electrons with a Lorentz factor of $\gamma_\mathrm{e} = 10^3$ to $10^5$.

## ACKNOWLEDGMENTS

We thank Dr. I. Takahashi for his guidance of the *XMM-Newton* data analysis, especially the background estimation. This result is based on the observation obtained with *XMM-Newton*, an ESA science mission with instruments and contributions directly funded by ESA Member States and NASA.

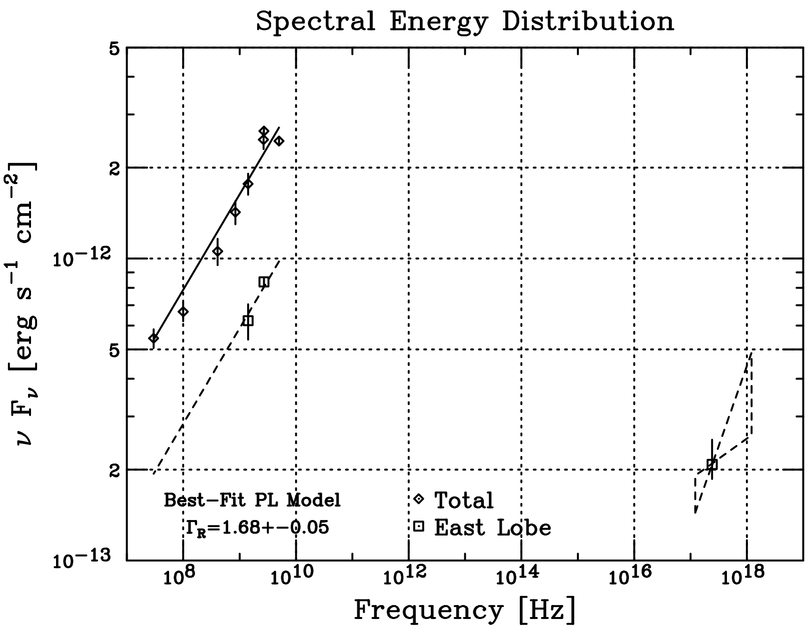


*Figure 4. The spectral energy distribution of Fornax A. The diamonds and boxes refer to the data for the whole radio structure and those for the east lobe, respectively. The dashed tie represents the best-fit X-ray PL model of the east lobe. The solid line shows the best-fit PL model of* $\Gamma = 1.68$ *to the radio spectrum of the whole structure, and the dashed one also shows the similar PL model, with the flux normalized by 0.36 to fit the east lobe spectrum. The radio data are taken from Ekers (1969), Ekers et al. (1983), Finlay & Jones (1973), Jones & McAdam (1992), Kühr et al. (1981), Robertson (1973), and Shimmins (1971)*

## REFERENCES


Brunetti, G., Setti, G., & Comastri, A., 1997, A&A, 325, 898

Comastri, A., Brunetti, G., Dallacasa, D., Bondi, M., Pedani, M., Setti, G., 2003, MNRAS, 304, L52

Croston, J.H., Hardcastle, M.J., Harris D.E., Belsole, E., Birkinshaw, M., & Worrall, D. M., 2005, ApJ, 626, 733

Ekers, J.A., 1969, Australian J. Phys. Suppl., 7, 3

Ekers, R.D., Goss, W.M., Wellington, K.J., Bosma, A., Smith, R.M., & Schweizer, F., 1983, A&A, 127, 362

Feigelson, E.D., Laurent-Muehleisen, S.A., Kollgaard, R.I., & Fomalont, E.B., 1995, ApJ, 449, L149

Finlay E.A., & Jones B.B., 1973, Australian J. Phys., 26, 389

Fomalont, E.B., Ebneter, K.A., van Breugel, W.J.M. & Ekers, R.D., 1989, ApJ, 346, L17

Harris, D.E., and Grindlay, J.E., 1979, MNRAS, 188, 25

Isobe, N, Makishima, K., M., Tashiro, & S. Hong 2005, ApJ, 632, 781

Isobe, N., et al., 2002, ApJ, 581, L111

Isobe, N., Makishima, K., Tashiro, M., Itoh, K., Iyomoto, N., Takahashi, I., & Kaneda, H., submitted to ApJ.

Iyomoto, N. Makishima, K., Tashiro, M., Inoue, S., Kaneda, H., Matsumoto, Y., & Mizuno, T., 1998, ApJ, 503, 31

Jones, P.A., McAdam, W.B., 1992, ApJS, 80, 137

Kaneda, H., Tashiro, M., Ikebe, Y., Ishisaki, Y., Kubo, H., Makshima, K., Ohashi, T., Saito, Y., et al. 1995, ApJ, 453, L13

Kim, D-W, & Fabbiano, G., 2003, ApJ, 586, 826

Kühr, H., Witzel, A., Pauliny-Toth, I.I.K., & Nauber, U., 1981, A&AS, 45, 367

Madore, B.F., et al., 1999, ApJ, 515, 29

Miley, G., 1980, ARA&A, 18, 165

Robertson, J.G., 1973, Australian J. Phys., 26, 403

Shimmins, A.J., 1971, Australian J. Phys. Astrophys. Suppl., 21, 1

Stark, A.A., Gammie, C.F., Wilson, R.W., Bally, J., Linke, R.A., Heiles, C. & Hurwitz, M., 1992, ApJS, 79, 77

Tashiro, M., et al., 1998, ApJ, 499, 713

Tashiro, M., Makishima, K., Iyomoto, N. Isobe, N., & Kaneda, H. 2001, ApJ, 546, L19

# A COMBINED XMM-NEWTON AND CHANDRA STUDY OF THE ULIRG MRK 273

**I. Balestra, Th. Boller, L. Gallo, D. Lutz, and S. Hess**

Max-Planck-Institut für extraterrestrische Physik, Postfach 1312, 85741 Garching, Germany

## ABSTRACT

We present a compared analysis of a 23 ks XMM-*Newton* and a 47 ks *Chandra* observation of the Ultraluminous Infrared Galaxy Mrk 273. The hard X–ray spectrum can be modelled by a highly absorbed ($\sim 7 \times 10^{23}$ cm$^{-2}$) power law plus a Fe K$\alpha$ emission line. The Fe line is broad ($\sigma = 260^{+370}_{-170}$ eV), suggesting possible superposition of a neutral line at 6.4 keV and a blend of ionized iron lines from Fe XXV and XXVI. The broad band spectrum requires three collisionally ionized plasma components, which may be associated with star–forming regions, having temperatures of about 0.3, 0.8 and 5 keV. The thermal emission at $\sim 0.3$ keV extends on $\sim 45$ kpc embracing the long tidal tail of the merger. Interestingly, thermal emission at $\sim 0.7$ keV seems to be ubiquitous in ULIRGs, probably associated with circumnuclear starburst. A high temperature ($kT > 5$ keV) thermal component is also detected in two other ULIRGs (namely NGC 6240 and Arp 220). The absorption corrected X–ray luminosity ($L_{2-10\,keV} \sim 7 \times 10^{42}$ erg s$^{-1}$) is $\sim 0.2$% of the far–IR luminosity, similar to typical values found in pure starbursts. The thermal contribution to the soft X–ray luminosity is approximately $0.2 - 0.7 \times 10^{42}$ erg s$^{-1}$, comparable to those found in NGC 6240 and other starburst dominated ULIRGs.

Key words: galaxies: individual: Mrk 273 - galaxies: individual: Mrk 273x - galaxies: Seyfert - X-rays: galaxies.

## 1. XMM-NEWTON

The XMM-*Newton* spectrum can be modelled by three collisionally ionized plasma components, a highly absorbed ($\sim 7 \times 10^{23}$ cm$^{-2}$) power law and a neutral Fe K$\alpha$ line (Fig. 1). The highest spectral resolution and collecting area of XMM-*Newton* has allowed to resolve the iron line complex profile, which may originate by a superposition of two unresolved components: a neutral Fe K$\alpha$ line at 6.4 keV, probably associated with a Compton–thick torus, and a blend of Fe XXV and XXVI lines at 6.7 and 6.97 keV respectively. The ionized iron lines can be, indeed, produced by an optically thin hot

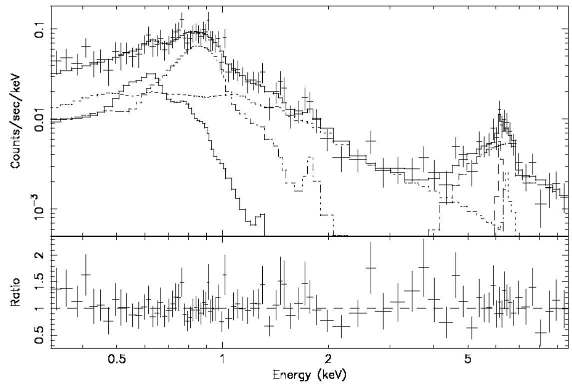


*Figure 1. The EPIC–PN spectrum of Mrk 273 fitted with three different temperature thermal emission models, a highly absorbed power law and a neutral Fe K$\alpha$ line. Each model component is displayed.*

($kT > 5$ keV) plasma, as observed at least in two other ULIRGs: namely NGC 6240 (Boller et al., 2003) and Arp 220 (Iwasawa et al., 2005). The best fit to the $0.3-10$ keV PN spectrum is obtained using three thermal plasma components with temperatures of $0.31^{+0.09}_{-0.07}$, $0.78 \pm 0.08$ and $5.4^{+2.6}_{-1.3}$ keV, a highly absorbed power law and a neutral Fe K$\alpha$ line (Fig. 1). According to this model the emission below about 4 keV is of thermal origin.

## 2. CHANDRA

From the *Chandra* image a soft, extended ($\sim 45$ kpc) X–ray halo, surrounding the nucleus and embracing the long tidal tail of the merger, is clearly apparent (Fig. 2). The spectrum of the X–ray halo is that of a hot diffuse plasma with a temperature of $0.38 \pm 0.04$ keV (Fig. 3). While the spectrum of the nuclear region (Fig. 4) is best fitted by two thermal components, a highly absorbed power law and a neutral Fe K$\alpha$ line. For Mrk 237 the unobscured X–ray luminosity is a more modest fraction of the bolometric luminosity than in typical AGNs, suggesting additional star formation, in agreement with the detection from mid–infrared spectroscopy of very powerful star formation in this source.

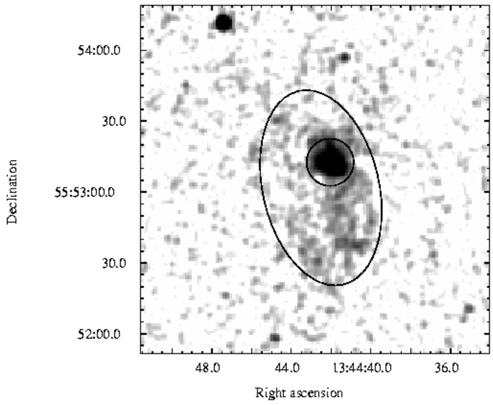


*Figure 2. Adaptively smoothed* $0.3 - 10$ *keV Chandra image of Mrk 273 with a smoothing scale of 2 pixels (*$\sim 1''$*). The circle has a radius of* $10''$ *and is centered at the peak of the hard X–ray emission. The ellipse has a size of* $42'' \times 25''$.

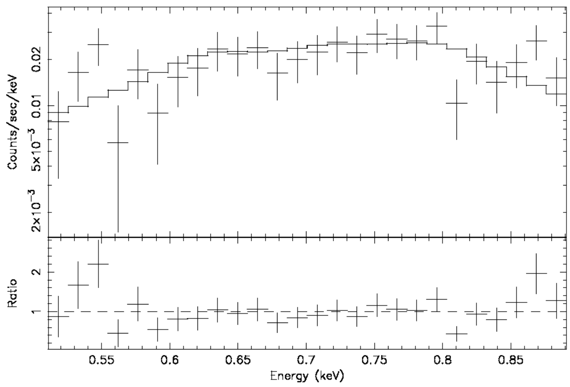


*Figure 3. The* $0.5 - 0.9$ *keV unbinned spectrum of the extended hot gas halo. A single APEC model with a temperature of* $0.38 \pm 0.04$ *keV provides a satisfactory fit.*

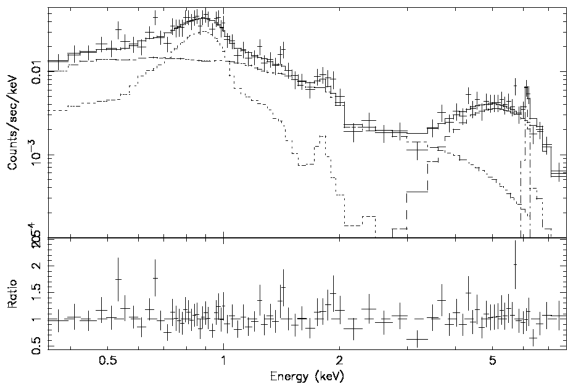


*Figure 4. The* $0.3 - 8$ *keV ACIS–S spectrum of the inner* $10''$ *region fitted with two thermal plasma components, a highly absorbed power law and a narrow Fe K*$\alpha$ *line at 6.4 keV.*

## 3. DISCUSSION AND CONCLUSIONS

The temperatures of the three plasma components found in Mrk 273 are remarkably similar to those observed in other ULIRGs (e.g. NGC 6240 and Arp 220) and in the local starburst galaxy NGC 253 (Pietsch et al., 2001). The thermal emission at $\sim 0.3$ keV, as clearly shown from the *Chandra* image, extends on a large scale ($\sim 45$ kpc) and embraces the long tidal tail of the merger. Therefore, it must be associated with hot gas distributed in the halo. Interestingly, thermal emission at $\sim 0.7$ keV seems to be ubiquitous in the spectra of ULIRGs, probably being associated with a nuclear or circumnuclear starburst (Franceschini et al., 2003). The presence of a high temperature ($> 5$ keV) thermal component is less frequently observed, but not so unusual, being also detected in the XMM-*Newton* spectra of NGC 6240 (Boller et al., 2003) and Arp 220 (Iwasawa et al., 2005). The ratio of the $2 - 10$ keV unabsorbed X–ray luminosity of the highest temperature thermal component to the bolometric luminosity in Mrk 273 is $L_{2-10\,\mathrm{keV}}/L_{FIR} \simeq 7 \times 10^{-5}$ ($L_{FIR} = L(8 - 1000\,\mu\mathrm{m} \sim L_{bol}$), a factor of 20 smaller than in NGC 6240 and a factor of 5 larger than in Arp 220.

We analyzed the X–ray spectral properties of Mrk 273 combining the high throughput of XMM-*Newton* with the high spatial resolution of *Chandra*.

*Chandra* spatial resolution allowed to study separately the hot gas halo extended emission from the nuclear one. The spectral analysis of the two regions has revealed that the temperature of the extended hot gas halo is $0.38 \pm 0.04$ keV and in very good agreement with XMM-*Newton* results. From the XMM-*Newton* spectrum we found a broad Fe K$\alpha$ emission line with a high statistical significance (>99% c.l.). We suggested the superposition of multiple unresolved iron line features: one from neutral iron at 6.4 keV ($EW \sim 170$ eV) and one from a blend of Fe XXV at 6.7 keV ($EW \sim 120$ eV) and Fe XXVI at 6.97 keV ($EW < 85$ eV). The emission below about 4 keV can be interpreted in terms of purely thermal emission, therefore involving the presence of a hot gas associated with regions of intense star formation.

## REFERENCES

Boller, T., Keil, R., Hasinger, G., et al. 2003, A&A, 411, 63

Franceschini, A., Braito, V., Persic, M., et al. 2003, MNRAS, 343, 1181

Iwasawa, K., Sanders, D. B., Evans, A. S., et al. 2005, MNRAS, 357, 565

Pietsch, W., Roberts, T. P., Sako, M., et al. 2001, A&A, 365, L174

# BLACK HOLE MASSES AND EDDINGTON RATIOS OF AGNS CONTRIBUTING MOST OF THE XRB

**L. Ballo[1], S. Cristiani[2], L. Danese[1], G. Fasano[3], F. Fontanot[4], M. Nonino[2], P. Tozzi[2], and E. Vanzella[2]**
[1]SISSA/ISAS, International School for Advanced Studies - Trieste, Italy
[2]INAF - OAT - Trieste, Italy
[3]INAF - OAPd - Padova, Italy
[4]DAUT - Trieste, Italy

## ABSTRACT

The discovery of relationships between the masses of the local supermassive black holes and their spheroidal host components has revealed a connection between the formation and evolution of galaxies and the formation and growth of supermassive black holes. To gain insight into this process we have investigated the properties of a sample of X-ray selected active nuclei and of their host galaxies in the framework of the Great Observatory Origins Deep Survey. Here we present the results of a morphological and photometric analysis of the ACS-HST images in four bands, based on bidimensional deconvolution. Our findings on black hole masses, nuclear bolometric luminosities and Eddington ratios indicate that these systems are already formed objects in which we see a renewal of low level activity, in an environment poor of gas.

Key words: Active Galactic Nuclei; X-ray background.

## 1. INTRODUCTION AND SAMPLE SELECTION

Recent deep surveys have resolved most of the $2-10$ keV X-ray background (XRB), showing that it is produced by a mixture of obscured and unobscured Active Galatic Nuclei (AGNs) with a redshift distribution peaking at $z \sim 0.7$. To investigate the galaxy evolution in the redshift domain in which a major fraction of the black hole (BH) mass observed in the local universe is expected to be accreted, we began studying the nuclear activity of a sample of AGNs at redshift between $0.4$ and $1$.
The starting point is the deep high-resolution optical imaging performed in the F435W ($B$), F606W ($V$), F814W ($i$) and F850LP ($z$) bands with ACS onboard HST in the framework of the GOODS program (Giavalisco et al., 2004). X-ray sources are selected by cross-correlating the GOODS optical catalogs with the CDFS and the HDFN X-ray catalogs (Alexander et al., 2003; Giacconi et al., 2002; Tozzi et al., 2005). To bracket the bulk of the sources making the XRB and at the same time to have a sufficient signal–to–noise ratio, we pick out only sources with spectroscopic or photometric redshift between $0.4$ and $1$ (Barger et al., 2003; Szokoly et al., 2004; Zheng et al., 2004). Finally, *bona fide* AGNs are selected by imposing a cut in X-ray luminosity, $L_{\text{2-8 keV}} > 10^{42}$ ergs s$^{-1}$. This lead to an initial sample of $74$ sources.
To carry out a morphological analysis, the simultaneous availability of high-quality, non-crowded $B$, $V$, $i$ and $z$ ACS images is necessary. We further concentrate only on X-ray sources with *spectroscopic* redshifts. Thus, the final sample is made of 30 objects; taking into account their redshift and the luminosity distributions, we can conclude that our sample is representative of the AGNs contributing the XRB at $z \leq 1$.

## 2. MORPHOLOGICAL ANALYSIS

To disentangle the main galactic components for the AGNs in our sample, we carry out two-dimensional fits to galaxy profiles (performed using the image decomposition program GALFIT; Peng et al. 2002). We assume a galaxy model composed by a bulge, a disk and a nuclear source (described by a De Vaucouleur model, an exponential function and a pointlike profile, respectively).
Having images in four bands, where the three model components have different weight, we set up a three-step procedure (details will be reported in Ballo et al. 2005, in prep.). The initial guesses for the parameters are drawn from the GOODS ACS public catalog. Thus we derive magnitudes in four bands for the three galactic components.

## 3. AGN PROPERTIES

The information provided by the deconvolution allows us to study the nuclear activity of the analysed galaxies. Using the magnitudes of the bulge component we can estimate the **mass of the central BH**. In order to use the

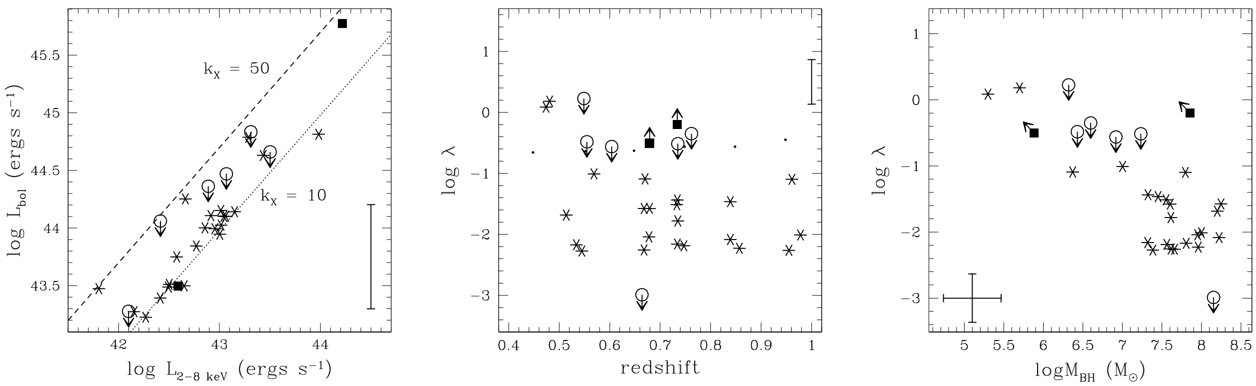


*Figure 1. Distributions of derived $M_{BH}$, $L_{bol}$ and $\lambda$; stars refer to sources for which we are confident that the results from the morphological deconvolution are reliable; filled squares and open circles mark nucleus–dominated and host–dominated sources, for which we can provide only upper limits on $M_{BH}$ and $L_{bol}$ respectively. The error bars reported represent the mean uncertainties in the derived quantities.*

*local* $M_{R,\,\mathrm{bulge}}$–$M_{\mathrm{BH}}$ relation found by McLure & Dunlop (2002), we fit an integrated Single Stellar Population (SSP) spectrum at the redshift of the source to the deconvolved bulge magnitudes. A template of local elliptical galaxy, normalized from this fit, provides the rest-frame *evolved* $R$-band bulge magnitude (assuming *passive evolution*).

Fitting the nuclear SED (de-absorbed X-ray emission + deconvolved optical magnitudes) with a library of templates of type 1 AGNs for a set of X-ray–to–optical ratios (see Monaco & Fontanot, 2005) we draw the **nuclear bolometric luminosity**.

## 4. RESULTS

From the estimated black hole masses and nuclear bolometric luminosities, and the consequent **Eddington ratios** $\lambda = L_{\mathrm{bol}}\ [\mathrm{ergs\ s^{-1}}]/\left(1.3 \times 10^{38} M_{\mathrm{BH}}\ [M_\odot]\right)$, we found that:

1. the ratios $k_{\mathrm{X}} = L_{\mathrm{bol}}/L_{\mathrm{X}}$ are lower than previous claims (Barger et al., 2005), but in agreement with Fabian (2004); see Fig. 1, *left panel*;
2. the Eddington ratios are lower than at higher redshift; a similar trend is also suggested by observations (even if optically selected quasars show higher mean values, see McLure & Dunlop 2004 – dots in Fig. 1, *central panel*), and proposed by Shankar et al. (2004) to match the accretion mass function and the local supermassive BH mass function.

The wide range of $M_{\mathrm{BH}}$ and the low values of $\lambda$ (Fig. 1, *right panel*) suggest that we are observing a **renewal** of activity in previously formed objects. This finding is consistent with the antihierarchical behaviour already found in AGN evolution and expected on the basis of a bimodal scenario for the cosmic mass accretion history (Cavaliere & Vittorini, 2000; Granato et al., 2004).

## REFERENCES


Alexander, D. M., et al. 2003, AJ, 126, 539

Ballo, L., et al. 2005, in preparation

Barger, A. J., et al. 2003, AJ, 126, 632

Barger, A. J., et al. 2005, AJ, 129, 578

Cavaliere, A., & Vittorini, V. 2000, ApJ, 543, 599

Fabian, A. C. 2004, Coevolution of Black Holes and Galaxies, 447

Giacconi, R., et al. 2002, ApJS, 139, 369

Giavalisco, M., et al. 2004, ApJ, 600, L93

Granato, G. L., De Zotti, G., Silva, L., Bressan, A., & Danese, L. 2004, ApJ, 600, 580

McLure, R. J., & Dunlop, J. S. 2002, MNRAS, 331, 795

McLure, R. J., & Dunlop, J. S. 2004, MNRAS, 352, 1390

Monaco, P., & Fontanot, F. 2005, MNRAS, 359, 283

Peng, C. Y., Ho, L. C., Impey, C. D., & Rix, H. 2002, AJ, 124, 266

Shankar, F., Salucci, P., Granato, G. L., De Zotti, G., & Danese, L. 2004, MNRAS, 354, 1020

Szokoly, G. P., et al. 2004, ApJS, 155, 271

Tozzi, P., et al. 2005, A&A in press

Zheng, W., et al. 2004, ApJS, 155, 73

# PRINCIPAL COMPONENT ANALYSIS OF THE X-RAY VARIABILITY IN NGC 7469

**A. J. Blustin[1], S. V. Fuerst[1,2], G. Branduardi-Raymont[1], M. J. Page[1], E. Behar[3], and J. S. Kaastra[4]**

[1]UCL Mullard Space Science Laboratory, Holmbury St. Mary, Dorking, Surrey, RH5 6NT, UK
[2]KIPAC, Stanford University, Menlo Park, CA 94025, USA
[3]Physics Department, Technion, Haifa 32000, Israel
[4]SRON National Institute for Space Research, Sorbonnelaan 2, 3584 CA Utrecht, The Netherlands

## ABSTRACT

We apply Principal Component Analysis (PCA) to study the variability of the X-ray continuum in the Seyfert 1 galaxy NGC 7469. The PCA technique is used to separate out linear components contributing to variability between multiple datasets; the technique is often used in analysis of optical spectra, but has rarely been applied to AGN X-ray spectroscopy. Running a PCA algorithm on 0.3−10 keV EPIC data from a 150 ks XMM-Newton observation of NGC 7469, we describe the spectral components extracted and evaluate the usefulness of the PCA technique for understanding the X-ray continuum in AGN.

Key words: AGN; X-rays; PCA; spectroscopy.

## 1. INTRODUCTION AND METHODOLOGY

Principal Component Analysis (PCA) is a technique which finds linear combinations of the spectral components that produce most of the variability in a time series of spectra. Using only the first few of these components (the 'principal ones') one can describe the time series with a greatly reduced number of parameters. These components may correspond to physical parameters of the system that are changing, so the method may be used to discover how many parameters there are, and how they change with time.

In order to calculate the components, first the mean of each variable is subtracted. This corresponds to the zero$^{\rm th}$ order component. Next, each variable is scaled by its standard deviation. Generally, the correlation matrix of these shifted, scaled variables is then obtained. The mathematics is simplified, however, by using the method of singular value decomposition to find the eigenvalues and eigenvectors. With this technique, the correlation matrix is not explicitly required, and the raw data matrix is used instead (Mittaz et al., 1990). The output of the PCA consists of a set of principal components, a matrix of coefficients and a set of eigenvalues. Each input spectrum can be reconstructed from the components once they have been multiplied by the appropriate set of coefficients which determine how much of an effect each component has in a given spectrum.

A problem with Principal Component Analysis is that it strictly only works when the signal is a superposition of linear components. If there is a non-linear interaction between components then it will 'incorrectly' separate them. For example, if the time series consists of the spectrum of a Gaussian line profile which changes width over time, then the components will be similar to Fourier modes. These modes can be combined to produce a line of any width, but do not individually correspond to physical reality. If there is a combination of non-linear effects operating simultaneously within the system, then interpretation can be difficult. Statistical noise in the data is another potential source of confusion. This introduces extra principal components to describe the noise fluctuations, which obviously need to be removed as they do not describe physical processes of interest. This can be done by truncating the list of components in the correct place, by assuming that the weaker components (those with smaller eigenvalues) correspond to the Fourier modes for the broad-band noise.

NGC 7469 is a bright nearby Seyfert (z = 0.0164) which was observed for 150 ks by XMM-Newton in November/December 2004. The total exposure time was split into two parts over consecutive orbits. This long observation was obtained primarily for the purposes of high resolution spectroscopy with the RGS; this spectrum contains evidence of absorption by outflowing material with at least two different levels of ionisation. In order to correctly model the soft X-ray spectral features, we need to understand the continuum underlying them. Fig. 1 shows the EPIC-pn spectra from the whole of the observation and from both parts separately. The solid line is a power-law model with galactic absorption fitted to the 3−5.5 keV and 7−10 keV ranges. The lower panel of this plot shows the ratios of the three observed spectra to

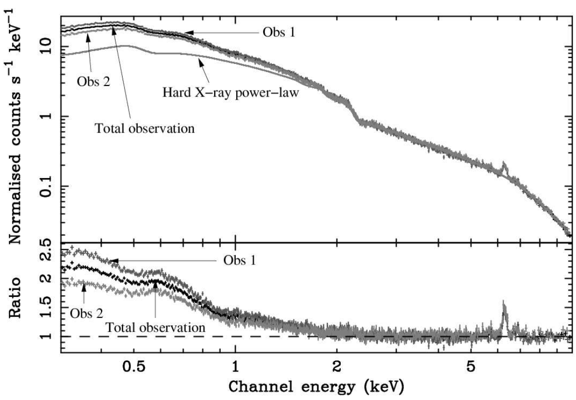


*Figure 1. EPIC-pn spectrum of NGC 7469 from the first and second part of the observation, and from the whole observation combined. Also the ratios of these spectra to a Galactic-absorbed power-law model fitted to the 3−5.5 keV and 7−10 keV ranges.*

the power-law fit. The soft excess is clearly variable, so we applied PCA to see if it could separate out different varying components in the EPIC-pn spectrum (see e.g. Vaughan & Fabian, 2004). We ran a PCA code (based on that of Francis & Wills 1999) on a series of twelve $\sim$ 10 ks EPIC-pn spectra (six from each part of the observation). This exposure time was chosen as a compromise between obtaining good time resolution to look for changing components in the spectrum and having sufficient signal-to-noise in each spectrum.

## 2. RESULTS AND DISCUSSION

The PCA code generates as many principal components as there are input datasets, in this case twelve. The eigenvalues for each component indicate how much of the spectral variability that particular component is responsible for. In this case, the first two principal components seem to be significant, being responsible for $\sim$18% and $\sim$13% of the variability respectively. The other ten components appear to be noise. Fig. 2 and 3 show components 1 and 2 added to the mean spectrum (for clarity, only the components plus mean showing the greatest extent of the variability are plotted). These plots indicate the presence of a variable hard power-law and a variable soft power-law, with the hard power-law being more variable than the soft. The iron K$\alpha$ line seems only to be present in the constant mean spectrum but not in the individual components, thus implying that it is not variable on these timescales − or that any variability is below the level of the statistical noise in the input spectra.

Since PCA will reduce a non-linear variability to a series of Fourier-type components, are these two components genuinely physical or simply Fourier deconstructions of a much more complicated reality? A good sign

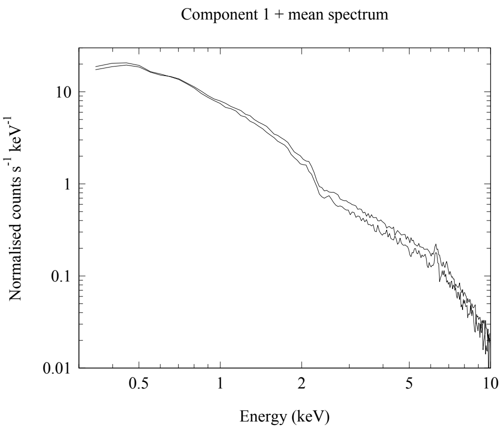


*Figure 2. Maximum and minimum spectra (added to the mean) for the most variable component.*

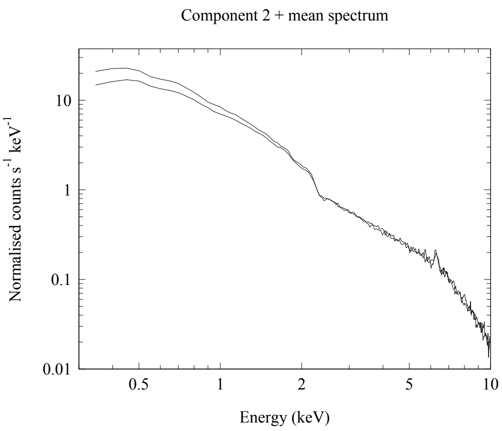


*Figure 3. Maximum and minimum spectra (added to the mean) for the second most variable component.*

may be that there are only two apparently non-noise components; if the spectrum had been varying in a more complicated way, a larger number of power-law type components might have been generated than the two plausible ones we see here. On the subject of whether PCA tells us anything about the spectrum of NGC 7469 that we did not already know via less sophisticated methods (there is a soft and a hard component, varying in different ways), we conclude that it does not provide us with new information; the method does however give a model-independent confirmation of current knowledge.

## REFERENCES

Francis, P. J. & Wills, B. J. 1999, in Quasars and Cosmology, ASP Conference Series 162, p. 363

Mittaz, J. P. D., Penston, M. V. & Snijders, M. A. J. 1990, MNRAS, 242, 370

Vaughan, S. & Fabian, A. C. 2004, MNRAS, 348, 1415

# *XMM-NEWTON* OBSERVATIONS OF THE LAOR ET AL. SAMPLE OF PG QUASARS

**C.Brocksopp[1], R.L.C Starling[2], P.Schady[1], K.O.Mason[1], E.Romero-Colmenero[3], and E.M.Puchnarewicz[1]**

[1]Mullard Space Science Laboratory, University College London, Holmbury St. Mary, Dorking, Surrey RH5 6NT
[2]Astronomical Institute "Anton Pannekoek", University of Amsterdam, Kruislaan 403, 1098 SJ Amsterdam
[3]South African Astronomical Observatory, PO Box 9, Observatory 7935, Cape Town

## ABSTRACT

We present *XMM-Newton* EPIC and OM observations of the Laor et al. sample of the Palomar Green quasars. A power-law provides a reasonable fit to the 2–5 keV region of the X-ray spectra; extrapolation of this power-law to the full *XMM*/EPIC range reveals a soft excess below 2 keV in most objects. A single power-law provides a poor fit to the full range and instead a broken power-law is used. We show that the low- and high-energy components of this broken power-law are tightly-correlated ($r = 0.97$, to within $99\%$ confidence), suggesting a common origin. This result places important constraints on attempts to fit the soft X-ray emission with a thermal model. Finally, preliminary study of the broad-band (optical–X-ray) spectral energy distribution suggests that accretion disc models are not able to represent the soft X-ray region of the spectrum, adding support to the conclusion that the soft X-ray emission may be non-thermal in origin.

Key words: Multiwavelength; Quasars; SED.

## 1. INTRODUCTION

The Laor et al. (1997) sample of PG quasars is a subset of the optically-selected Bright Quasar Survey which, in order to create a sample which is complete and representative of most quasars in terms of their X-ray properties, has been further constrained by redshift ($z \leq 0.4$) and column density ($nH_{Gal} < 1.9 \times 10^{20}$). *ROSAT* observations in the 0.2–2.0 keV range were obtained and presented by Laor et al. (1997). We have used *XMM-Newton* to update the *ROSAT* observations, providing a much wider X-ray spectral coverage (0.3–10.0 keV, although we note that we were able to use only 0.7–10.0 keV for the MOS cameras due to calibration problems at low energy), higher energy resolution and a high S/N ratio, and also providing simultaneous optical and UV data from the Optical Monitor.

We note that full details of the results of this study are presented in Brocksopp et al. 2005.

## 2. RESULTS

We find that a simple absorbed power-law is a good fit to the 2–5 keV region of the spectrum and that extrapolation to low energies reveals the presence of a soft excess in most objects. Such a power-law provides a poor fit to the full *XMM*/EPIC range (0.3–10.0 keV). Instead we use a broken power-law plus Galactic absorption and iron line, which is a successful fit to the spectra in most cases. Four of the quasars show evidence for additional (presumably intrinsic) absorption. Twelve of the sources show evidence for an iron line, but with low significance ($< 2\sigma$) in most cases. An example of one of the fits, for PG 1115+407, is shown in the top left corner of Fig. 1.

We have plotted various combinations of spectral parameters and line and continuum luminosities for comparison with the plots in Laor et al. (1997). We confirm the correlations found by these authors. But our most significant correlation is the extremely tight relationship (Spearman rank correlation coefficient, $r = 0.97$ to $> 99\%$ confidence) between the photon indices of the low- and high-energy components of the broken power-law. There are a number of discrepant points (labeled in the bottom left panel of Fig. 1 but we find that these objects are atypical, containing a warm absorber and/or are labelled as "X-ray weak" by Laor et al. (1997). The bottom left panel of Fig. 1 shows an expanded view of the same plot, with the best-fit straight line drawn through the points.

In addition to the EPIC X-ray spectra, we have obtained *XMM*/OM data for each of the Laor et al. quasars. All optical–X-ray broad-band spectra have been plotted and a sample plot (again for PG 1115+407) is shown in the top right panel of Fig. 1. The spectrum is in the observed-frame of the quasar, the vertical dotted line represents the position of the Lyman break and all points have been corrected for Galactic absorption.

Also plotted are four accretion disc models; best-fit

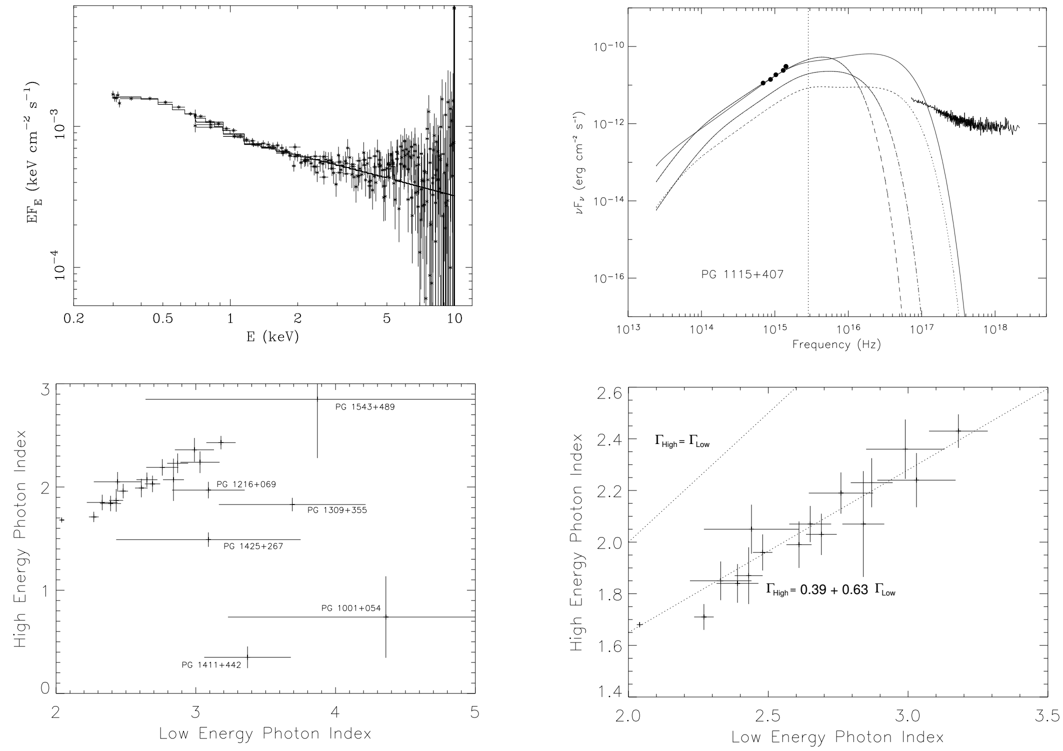


*Figure 1. Top row: Sample EPIC (left) and OM–EPIC (right) spectra for one of the Laor et al. quasars, PG 1115+407. Both are plotted in $\nu F_\nu$-space (or equivalent) in the observed-frame of the quasar. The EPIC spectrum is over-plotted by an absorbed broken power-law model. The broad-band spectrum is over-plotted by four accretion disc models: best-fit Kerr (solid), best-fit Schwarzschild (dashed), published mass Kerr (dotted), published mass Schwarschild (dot-dashed), all of which have been fit to the OM data-points. The vertical dotted line represents the Lyman limit. Bottom row: The tight correlation ($r = 0.97$) between the high- and low-energy photon-indices of the broken power-law for each quasar in the sample. The discrepant points in the left-hand plot are mainly those which contain warm absorbers and/or defined as "X-ray weak" (Laor et al., 1997). The right-hand plot shows an expanded view of the same correlation and the equation of the best-fit straight line through the points.*

Kerr (solid line), best-fit Schwarzschild (dashed line), best-fit Kerr using published mass estimate (dotted line) and best-fit Schwarzschild using published mass estimate (dot-dashed line). These models are modified Czerny & Elvis (1989) accretion disc curves (Siemiginowska et al. 1995) and are parametrised in terms of black hole mass, angle of inclination and mass accretion rate (Kerr models) or luminosity (Schwarzschild models). They have been fit to the OM photometry alone and the best fit obtained by minimising $\chi^2$.

In all cases we find that the disc models which fit the OM data most successfully are not able to represent the soft X-ray excess. We also find that fitting the disc model predicts masses which are significantly different from the estimates published in the literature; indeed a number of the published masses provide very poor fits to the OM data. In general the Schwarzschild models provide better fits than the Kerr models. Furthermore some of the Kerr models overpredict the soft-X-ray flux (e.g. PG 1402+261).

## 3. CONCLUSIONS

By using simple phenomenological models to fit these data, we are able to place important constraints on which physical models are appropriate for describing the spectra of the Laor et al. sample of quasars. The tight correlation between the low- and high-energy components of the broken power-law suggest that both components are produced in the same region of the system and by the same emission mechanism. This would appear to rule out thermal disc emission, particularly given the failure of the disc models to represent the soft X-ray excess in the SEDs above. Instead models invoking non-thermal mechanisms should be used. Detailed investigation of these alternative models will be the subject of future work, including consideration of the radio emission and jet models often used to describe the SEDs of black hole X-ray binaries.

## REFERENCES


Brocksopp C., Starling R.L.C., Schady P., Mason K.O., Romero-Colmeno E., Puchnarewicz E., 2005, MNRAS in press (astroph/0510776)

Czerny B., Elvis M., 1987, ApJ, 321, 305

Laor A., Fiore F., Elvis M., Wilkes B., McDowell C., 1997, ApJ, 477, 93

Siemiginowska A., Kuhn O., Elvis M., Fiore F., McDowell J., Wilkes B.J., 1995, ApJ, 454, 77

# X-RAYING RELATIVISTIC QUASAR OUTFLOWS

**G. Chartas[1], W. N. Brandt[1], S. C. Gallagher[2], and D. Proga[3]**

[1]Pennsylvania State University, 525 Davey Lab, University Park, PA 16802
[2]University of California – Los Angeles, Mail Code 154705, 475 Portola Plaza, Los Angeles, CA 90095-1547
[3]University of Nevada, 4505 South Maryland Parkway, Las Vegas, NV 89154

## ABSTRACT

Recent *XMM-Newton* and *Chandra* observations of the gravitationally lensed BAL quasars PG 1115+080 and APM 08279+5255 have provided new insights into the structure of quasar outflows and the enrichment of the intergalactic medium by quasar winds. The confirmation of relativistic outflows in most quasars would imply that these energetic winds have a significant impact in regulating the growth of the black hole, perhaps explaining the $M_{\rm BH}$-$\sigma$ relation, and halting star formation and shaping the evolution of their host galaxies. We present new results from multi-epoch spectral analysis of BAL quasar PG 1115+080 with *XMM-Newton*. We find significant variability in the properties of the outflowing absorbers. Relativistic outflow velocities are inferred from the blueshifted highly ionized Fe lines detected in our analysis of the EPIC spectra. The depths of the Fe X-ray BALs in PG 1115+080 show a significant decrease between the first two observation epochs. We constrained the fraction of the total bolometric energy released by quasars PG 1115+080 and APM 08279+5255 into the IGM in the form of kinetic energy to be $\epsilon_{\rm k}$= $0.3^{+0.1}_{-0.2}$, and $\epsilon_{\rm k}$ = $0.09^{+0.03}_{-0.07}$, respectively. According to recent theoretical studies this range of efficiencies is large enough to influence significantly the formation of the host galaxy and regulate the growth of the central black hole. An analysis of the RGS spectra indicates the possible presence of two absorption lines at rest-frame energies of 3.36 keV and 3.73 keV.

Key words: Gravitational Lenses; X-rays; Quasar Outflows.

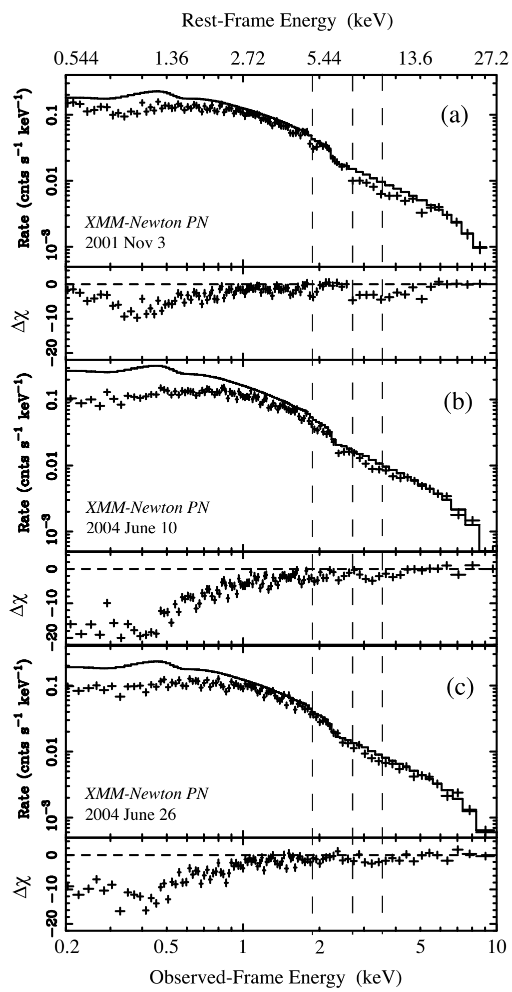


*Figure 1. (a) The top panel shows the PN spectrum of the combined images of PG1115+080 for Epoch 1 fit with Galactic absorption and a power-law model to events with energies lying within the range of 5–10 keV. The lower panel shows the residuals of the fit in units of 1$\sigma$ deviations. Several absorption features from 1.5–5.2 keV are noticeable in the residuals plot. (b) Same as (a) for Epoch 2. (c) Same as (a) for Epoch 3.*

## 1. INTRODUCTION

In recent years there has been mounting evidence from both theoretical and observational studies for the importance of quasar outflows in regulating the growth of the supermassive black hole, controlling the formation of the host galaxy, and enriching the intergalactic medium. Recently, the potential importance of quasar outflows has been explicitly demonstrated in theoretical models of structure formation and galaxy mergers that incorporate the effects of quasar outflows [e.g., Scannapieco & Oh 2004 (SO04); Granato et al. 2004 (G04); Springel, Di Matteo, & Hernquist 2005 (SDH05)]. Recent X-ray observations of two BAL quasars have suggested the presence of relativistic outflows of X-ray absorbing material with velocities of up to $0.4c$ (Chartas et al. 2002, 2003). The inferred hydrogen column densities of the outflowing absorbers of about $10^{23}$ cm$^{-2}$ and relativistic velocities of these outflowing X-ray absorbers imply mass-outflow rates that are comparable to the estimated accretion rates of a few $M\odot$ yr$^{-1}$. Additional observational evidence to support the presence of quasar feedback came with the detection of high-velocity blueshifted absorption-line features in the X-ray spectra of several quasars and Narrow-Line Seyfert 1 galaxies (Reeves et al. 2003; Pounds et al. 2003a, 2003b).

In this work we present recent results from monitoring X-ray observations of the BAL quasar PG 1115+080 ($z$ = 1.72). The goal of these observations was to monitor the time variability of the absorption features and thereby constrain the kinematic, ionization, and absorbing properties of the quasar outflows in these X-ray-bright BAL quasars. Throughout this paper we adopt a $\Lambda$-dominated cosmology with $H_0$ = 70 km s$^{-1}$ Mpc$^{-1}$, $\Omega_\Lambda$ = 0.7, and $\Omega_M$= 0.3.

## 2. OBSERVATIONS AND RESULTS

PG 1115+080 was observed with XMM-Newton on 2001 Nov 25 (Epoch 1), 2004 June 10 (Epoch 2), and 2004 June 26 (Epoch 3), for 62.9 ks, 81.2 ks and 86.3 ks, respectively. A variety of models were fit to the spectra of PG 1115+080. For clarity we only show the higher S/N ratio PN data in Figure 1; however, all fits were performed simultaneously to the PN and MOS1+2. High-energy X-ray absorption lines are detected in three epochs of monitoring observations of BAL quasar PG1115+080. The energies and inferred outflow velocities of the lines are listed in Table 1. To quantify the variability of the high-energy absorption features we took ratios of the spectra. We find significant variability of the X-ray BALs in PG1115+080 between epochs 1 and 2 separated by 0.92 yr (rest-frame) and marginal variability of the X-ray BALs between epochs 2 and 3 separated by 5.9 d (rest-frame). Motivated by the apparent detection of high-energy absorption lines in the EPIC spectra we investigated the presence of absorption lines in the RGS. We report the possible detection of absorption lines at 3.36 keV and 3.73 keV (rest-frame) We caution that due to the low S/N of the present RGS spectra the significance of these features is relatively low and additional higher quality data are required to confirm this result. A plausible, but not unique, interpretation of these lines is that they arise from blueshifted S XVI Lya absorption. We have estimated the mass outflow rates and efficiency of the outflows in PG1115+080 and APM08279+5255 and listed our results in Table 2. The systematic uncertainties in estimating the outflow efficiencies are one sided in the sense that they lead to underestimates of the outflow efficiencies.

*Table 1. Energies and Outflow Velocities of Absorption Lines Detected in PG 1115+080 During Epoch 1*

| Line | $E_{\rm obs}$ (keV) | $\sigma_{\rm rest}$ (keV) | $v_{\rm abs}$ ($c$) |
|---|---|---|---|
| Fe XXV 1s–2p | $2.67^{+0.14}_{-0.04}$ | <0.44 | $0.09^{+0.05}_{-0.02}$ |
| Fe XXV 1s–2p | $3.60^{+0.29}_{-0.46}$ | $3.07^{+1.82}_{-0.83}$ | $0.40^{+0.09}_{-0.11}$ |
| S XVI Ly$\alpha$ | $1.24^{+0.02}_{-0.02}$ | <0.024 | $0.26^{+0.01}_{-0.01}$ |
| S XVI Ly$\alpha$ | $1.38^{+0.07}_{-0.07}$ | < 0.23 | $0.37^{+0.01}_{-0.04}$ |

*Table 2. Mass-Outflow Rates and Efficiencies of PG 1115+080 and APM 08279+0552*

| Line | $\dot{M}$ ($M_\odot\ yr^{-1}$) | $\epsilon_{\rm k}$ |
|---|---|---|
| PG 1115+080 Outflow | | |
| Fe XXV 1s–2p | $0.006^{+0.004}_{-0.005}$ | $3.4^{+2.1}_{-2.8} \times 10^{-4}$ |
| Fe XXV 1s–2p | $0.27^{+0.17}_{-0.22}$ | $3.0^{+1.9}_{-2.5} \times 10^{-1}$ |
| S XVI Ly$\alpha$ | $0.026^{+0.016}_{-0.015}$ | $1.3^{+0.8}_{-0.7} \times 10^{-2}$ |
| S XVI Ly$\alpha$ | $0.025^{+0.015}_{-0.014}$ | $2.4^{+1.5}_{-1.4} \times 10^{-2}$ |
| APM 08279+5255 Outflow | | |
| Fe XXV 1s–2p | $1.7^{+1.0}_{-1.0}$ | $0.9^{+0.6}_{-0.6} \times 10^{-2}$ |
| Fe XXV 1s–2p | $3.3^{+2.0}_{-2.4}$ | $0.8^{+0.5}_{-0.6} \times 10^{-1}$ |

## REFERENCES


Chartas et al., 2002, ApJ, 579, 169

Chartas et al., 2003, ApJ, 595, 85

Granato et al., 2004, ApJ, 600, 580

Pounds et al., 2003, MNRAS, 345, 705

Pounds et al., 2003, MNRAS, 346, 1025

Reeves at al., 2003, MNRAS, 593, 65

Scannapieco & Oh, 2004, ApJ, 608, 62

Springel et al., 2005, ApJ, 620, 79

# *INTEGRAL* AND *XMM-NEWTON* OBSERVATIONS OF 3C 273 IN 2003 – 2005

**M. Chernyakova[1,2], T. J.-L. Courvoisier[1,2], M. Türler[1,2], A. Neronov[1,2], S. Soldi[1,2], and K. Page[3]**

[1]*INTEGRAL* Science Data Center, 16 Ch. d'Ecogia, CH-1290 Versoix, Switzerland
[2]Observatoire de Gèneve, 51 chemin des Maillettes, 1290 Sauverny, Switzerland
[3] University of Leicester, University Road, Leicester, LE1 7RH, UK

## ABSTRACT

We present INTEGRAL and quasi-simultaneous XMM-Newton observations of 3C 273 during 2003 – 2005. These data are part of a program meant to monitor the high-energy emission of this bright quasar in order to measure the different components contributing to the emission above 0.2 keV and their respective variability. 3C 273 was found to be in a weak and rather soft state compared to the historical record of high-energy observations. Here we describe our results and discuss their possible physical interpretation.

Key words: X-rays, AGN:individual:3C 273.

## 1. INTRODUCTION

3C 273 is a radio loud quasar, with a jet showing superluminal motion, discovered at the very beginning of quasar research (see review by Courvoisier 1998). Being the brightest and the nearest (z=0.158) quasar, 3C 273 was intensively studied at different wavelengths. In the current work we present the analysis of the quasi-simultaneous *INTEGRAL* (Winkler et al. 2003) and *XMM-Newton* observations in 2003 – 2005.

## 2. OBSERVATIONS

The details of the analysed data are given in Table 1. In order to increase the statistics for *INTEGRAL* data we have combined all data taken at appproximately the same time. Analysis were done with OSA 5.0 (*INTEGRAL*) and SAS 6.5 (*XMM-Newton*). JEM-X 2 and JEM-X 1 were alternatively operated during periods 1 – 3 , and 4 – 5, respectively. No simultaneous observations are available for the third period of *INTEGRAL* observations.

*Table 1. Journal of INTEGRAL and XMM-Newton observations of 3C 273.*

| Period | Observation Epoch | ISGRI/JEMX Exposure(ks) |
|---|---|---|
| 1 | 2003-01-05 – 2003-01-18 | 182.5/12.4 |
| 2 | 2003-06-01 – 2003-07-23 | 308.9/40.3 |
| 3 | 2004-01-01 – 2004-01-02 | 15.2/13.8 |
| 4 | 2004-06-23– 2004-06-24 | 67.1/29.2 |
| 5 | 2005-05-28– 2005-07-11 | 269.1/68.7 |
| *XMM-Newton* observations. | | PN Exp (ks) |
| 1 | 2003-01-05 – 2003-01-07 | 5.97 |
| 2 | 2003-07-07 – 2003-07-08 | 40.60 |
| 4 | 2004-06-30 – 2004-06-30 | 13.93 |
| 5 | 2005-07-10 – 2005-07-10 | 19.33 |

## 3. SPECTRAL AND TIMING ANALYSIS

It has been found in previous X-ray observations that the high energy continuum could be fitted by a hard power law with a variable photon index. Observations by *EXOSAT* first indicated the existence of a soft excess, at energies $<$ 1 keV (Turner et al. 1985). Using a model with two power laws, modified by Galactic absorption, we obtain good fit to the combined (0.2 – 100 keV) *INTEGRAL* and *XMM-Newton* spectra of periods 1, 2, 4, and 5, see Table 2.

The quality of the model fit for the second data set can be improved by adding a Fe line at 5.72$\pm$0.06 keV (which corresponds to the dereddened value of 6.622$\pm$0.07 keV) with a half width of about 300 eV. This is the only observation where the Fe line is observed. Surprisingly enough during this observation the flux in the 2 – 10 keV energy band was the highest. As it is clearly seen from the Table 2 and Figure 1, the slope of the soft excess was found to be more variable than the slope of the harder component.

*Table 2. Two power law fit to PN, JEM-X, and ISGRI 3C 273 spectra. The fit was done leaving free intercalibration factors for ISGRI ($C_i$) and JEM-X ($C_j$) with respect to the PN camera. Flux is given in $10^{-11}$erg cm$^{-2}$ s$^{-1}$ units.*

| Set | $N_H$(cm$^{-2}$) | $\Gamma_1$ | $\Gamma_2$ | F(0.1-2) | F(2-10) | F(20-60) | $C_i$ | $C_j$ | chi2/dof(dof) |
|---|---|---|---|---|---|---|---|---|---|
| 1 | 1.79e-20(fix) | 2.79±0.06 | 1.66±0.03 | 9.47±1.08 | 8.76±0.53 | 6.53±0.40 | 0.6 | 1.09 | 0.98(1374) |
| 2 | 1.79e-20(fix) | 2.40±0.03 | 1.66±0.02 | 9.97±0.78 | 10.13±0.53 | 12.10±0.65 | 1.31 | 1.05 | 1.12(1984) |
| 3 | 1.79e-20(fix) | | 1.57±0.1 | | | 13.3±5.64 | 1.(fix) | 1.25 | 0.95(162) |
| 4 | 1.79e-20(fix) | 2.70±0.06 | 1.63±0.02 | 6.05±0.74 | 6.73±0.35 | 7.91±0.41 | 0.88 | 0.36 | 0.97(1627) |
| 5 | 1.79e-20(fix) | 2.88±0.04 | 1.57±0.01 | 6.87±0.43 | 8.46±0.18 | 13.92±0.30 | 1.06 | 0.68 | 1.07(2103) |

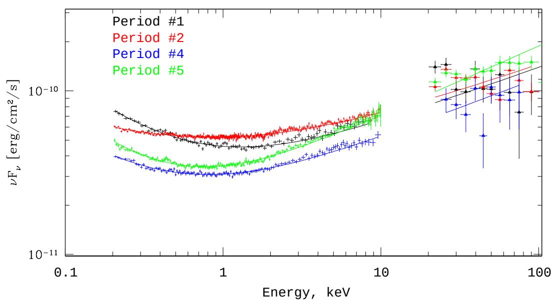


*Figure 1. PN and ISGRI spectra at different epochs.*

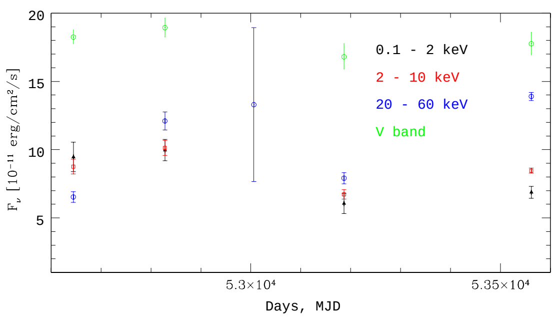


*Figure 2. Lightcurves in 0.2 – 2 keV (black, PN data), 2 – 10 keV (red, PN data), 20 – 60 keV (blue, ISGRI data), and Johnson V-filter (green, OMC data) bands.*

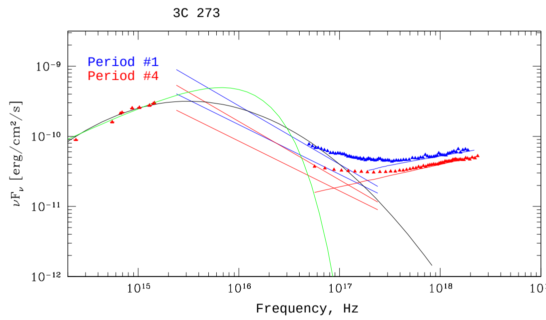


*Figure 3. June 2004 broadband spectra of 3C 273 (red triangles), along with the January 2003 data (blue triangles) and various models, see text.*

## 4. DISCUSSION

The overall spectra of blazars (plotted as $\nu F_\nu$) have two pronounced continuum components: one peaking between infrared and X-rays, and the other in the $\gamma$-ray regime. The radiation is emitted from a relativistic jet, directed close to our line of sight. 3C 273 is not an exception to this picture, but an additional 'big blue bump' dominates the optical emission. Although its origin is far from being understood, it is believed that it could be due to the thermal emission from the surface of the accretion disk, although the analysis of the blue bump variability supposes that two components, variable on different time scales, must contribute to the total emission at these wavelengths (Paltani et al. 1998). The observed soft excess is often explained as a hard tail of the blue bump. To test it we have fitted the observed soft excess with simple model described above (Table 2). On the Figure 3 the example of such a fit is shown for the first (blue points) and fourth periods (red points), along with the multiwavelength spectrum, almost simultaneous to the period 4. Taking into account small variations in the optical flux (Figure 2), it seems that it is not easy to explain the observed variations of the soft excess if as hard tail of the blue bump. For the illustration we have fitted optical data with a standard $E^{-1/3}exp(-E)$ model (green line), and a quadratic approximation (black line) often used in literature.

## REFERENCES

Courvoisier T. J.-L. 1998, A&A Rev., 9, 1

Paltani S., Courvoisier T. J.-L.,Walter R., 1998, A&A, 340, 47

Turner M.J.L., Williams O. R., Courvoisier T. J.-L.,et al. 1990, MNRAS 244, 310

Winkler C., Courvoisier T.J.-L., Di Cocco G., et al. 2003, A&A, 411, L1

# THE ROLE OF ABSORPTION AND REFLECTION IN THE X-RAY SPECTRUM OF ACTIVE GALACTIC NUCLEI

**Chevallier, L.[1,2], Collin, S.[1], Dumont, A. M.[1], Czerny, B.[2], Mouchet, M.[3], Gonçalves, A. C.[1,4], and Goosmann, R.[1]**

[1]LUTH, Observatoire de Paris, Section de Meudon, F-92195 Meudon Cedex, France; email: loic.chevallier@obspm.fr & suzy.collin@obspm.fr & anne-marie.dumont@obspm.fr, & anabela.goncalves@obspm.fr & rene.goosmann@obspm.fr
[2]Copernicus Astronomical Center, Bartycka 18, 00-716 Warsaw, Poland;, email: bcz@camk.edu.pl
[3]APC, Université Denis Diderot, F-75005 Paris, France; email: martine.mouchet@obspm.fr
[4]CAAUL, Observatório Astronómico de Lisboa, Tapada da Ajuda, 1349-018 Lisboa, Portugal

## ABSTRACT

In the 2-10 keV range, the AGN continuum is generally well represented by a single power law but at lower energies it displays an excess with respect to the extrapolation of this power law, called the "soft X-ray excess"; the nature of this component is still under discussion. Until now the soft X-ray excess was attributed either to the reflection of the hard X-rays on the accretion disk, or to the presence of an additional Comptonizing medium. This feature could also be due to the absorption of an intrinsically steep power law source (whose origin is not clear) by a medium with a very large dispersion velocity (as a relativistic wind). Understanding the nature of the soft X-ray excess is essential for our knowledge of the Warm Absorber, the primary spectrum, and the accretion flow process. We have therefore examined the pros and cons of the reflection and absorption models. The observed soft X-ray spectra may probably be modeled by an "hybrid" model: absorption and reflection.

Key words: galaxies: active, Seyfert; X-rays: general.

## 1. INTRODUCTION

Now more than 50% of well studied Seyfert 1 (Sy1) galaxies and many quasars are known to possess absorbers (e.g., Blustin et al. 2005). One main issue is to explain the apparent change of slope in the overall X-ray spectrum at $\sim 1$ keV in Sy1s and QSOs. When fitting an observed X-ray spectrum with a power law plus absorption plus the Compton reflection component plus the iron line and narrow spectral features, the model usually underpredicts the observed spectrum in the soft X-ray range. An additional component – a soft X-ray excess – is needed (Wilkes & Elvis 1987). Apart from an usual additional continuum or a strongly ionized reflection, this component is well modeled by absorption of an originally rather soft power law intrinsic spectrum due to an absorber having a random or bulk velocity of several thousands of km s$^{-1}$ (Gierliński & Done 2004). We consider the advantages and drawbacks of the reflection vs. absorption models (Chevallier et al. 2005), using our code TITAN (Dumont et al. 2003).

## 2. RESULTS

Gierliński & Done (2004) modeled the X-ray spectrum of the Narrow Line Sy1 PG 1211+143 by a steep power law continuum between 0.1 and 20 keV, absorbed by an ionized slab of constant density. Note that the observed spectrum is smeared by a large (Gaussian) velocity dispersion $v/c = 0.2$ in order to get a "quasi-continuum" without narrow features. This high velocity can be due to an accelerated outflow, or to a disk wind with Keplerian motion and produced very close to the black hole.

We have computed the absorption spectra (primary source of radiation complete covered) for a grid of constant density models. Any small variation of the column-density $N$, the ionization parameter $\xi = L/n_{\rm H}R^2$ , or the slope $\alpha$ of the primary continuum, would induce a strong variation on the shape of the X-ray spectrum.

Such a variation is not observed from one object to the other. It is more appropriate to assume that the absorbing medium is in total – gas and radiation – pressure equilibrium owing to the short dynamical time scale needed to reach again an equilibrium (less than one day, for $R \sim 10\ R_{\rm G}$, where $R_{\rm G} = GM/c^2$, and $M \sim 10^7\ M_{\odot}$). The thickness of the slab cannot then exceed a maximum value for a given $\xi$, due to thermal instabilities. A consequence is the existence of a "maximum absorption trough", which cannot be exceeded.

Figure 1 shows as an exemple the comparison of the X-ray spectrum of PG 1307+085 (Piconcelli et al. 2005) with that obtained with an absorbing slab of constant total pressure. This spectrum is well fitted, considering that the narrow emission feature around 0.5 keV – the OVII complex – must be provided by another emitting region.

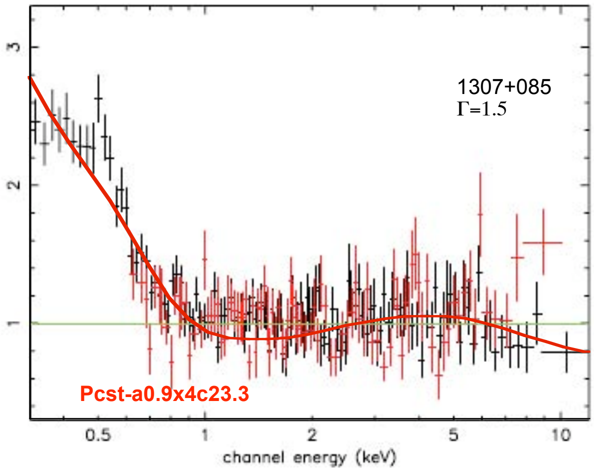


*Figure 1. Comparison between the observed X-ray spectra for PG 1307+085 (Piconcelli et al. 2005, Fig. 2) and the computed spectrum (arbitrary units) of a power law primary continuum* $\alpha = 0.9$ *absorbed by a constant total pressure slab (*$\xi = 10^4$*,* $N = 2\ 10^{23}$*,* $v/c = 0.2$*, CGS units). The observed and computed spectra have been both divided by the observed power law of photon index* $\Gamma = 1.5$ *over the 2–10 keV range.*

Absorption models are not very satisfactory from a physical point of view. Owing to its large column density ($\sim 10^{23}$ cm$^{-2}$), the wind implies too massive outflows (near the Eddington limit). Both the wind and the accretion models require an additional UV emission, which has to be provided by a geometrically thin accretion disk. The coexistence of a spherical accretion flow at about 25 $R_{\rm G}$ and a thin disk seems quite artificial. So we come back now to the "traditional" reflection models, including a "cold" accretion disk emitting the UV, surrounded by a hot corona emitting X-rays which are reflected by the disk (Haardt & Maraschi 1993). We notice that the soft X-ray excess almost disappears when the reflection spectrum is added to the primary continuum. Either $\xi$ is small and the reflection spectrum displays a strong X-ray excess, but it is negligible as compared to the primary one; or $\xi$ is large, and the reflection spectrum is comparable in flux to the primary one, but it has a small X-ray excess. A strong excess requires to hide the primary continuum (Fabian et al. 2002, Crummy et al. 2005).

Since both the absorption and the reflection models seem inadequate, we propose an "hybrid model", including the traditional reflection model, plus a high velocity absorbing medium with a modest thickness. The small soft X-ray excess is increased when it is absorbed by such a wind and becomes comparable to the observations. The mass outflow rate is thus 30 times smaller than in the previous absorption model.

## 3. CONCLUSION

Absorption models could account for some strong soft X-ray excesses, but require a kind of "fine tuning" in order to constrain the 1 keV trough, which otherwise could have any strength (e.g., constant density models). We have suggested a medium in total – gas and radiation – pressure equilibrium, which leads to a maximum intensity of the trough, as well as a "universal" shape of this maximum trough, due to the thermal instability mechanism. A complete grid of constant total pressure models, very demanding in computation time, is necessary to pursue this study. In the absorption model, either a thick accretion flow, or a relativistic wind is required. None of them seem realistic from a physical point of view, and moreover both require an additional source of UV emission, like a geometrically thin accretion disk. On the other hand, the "traditional" reflection models cannot account for the observations, unless the X-ray source is hidden from our view. Therefore we favor an "hybrid" model, where the primary UV-X source could be produced by a disk-corona system, and then absorbed by a modest relativistic wind.

## ACKNOWLEDGEMENTS

A. C. Gonçalves acknowledges support from the *Fundação para a Ciência e a Tecnologia*, Portugal, under grant no. BPD/11641/2002. Part of this work was supported by the Laboratoire Européen Associé Astrophysique Pologne-France.

## REFERENCES

[1] Blustin, A. J., Page, M. J., Fuerst, S. V., Branduardi-Raymont, G., & Ashton, C. E. 2005, A&A, 431, 111

[2] Chevallier, L., Collin, S., Dumont, A.-M., Czerny, B., Mouchet, M., Gonçalves, A. C., & Goosmann, R., A&A, accepted, astro-ph/0510700

[3] Crummy, J., Fabian, A. C., Brandt, W. N., & Boller, Th. 2005, MNRAS, 361, 1197

[4] Dumont, A.-M., Collin, S., Paletou, F., Coupé, S., Godet, O., & Pelat, D. 2003, A&A, 407, 13

[5] Fabian, A. C., Ballantyne, D. R., Merloni, A., Vaughan, S., Iwasawa, K., & Boller, T. 2002, MNRAS, 331, L35

[6] Gierliński, M., & Done, C. 2004, MNRAS, 349, L7

[7] Haardt, F., & Maraschi, L. 1993, ApJ, 413, 507

[8] Piconcelli, E., Jimenez-Bailón, E., Guainazzi, M., Schartel, N., Rodríguez-Pascual, P. M., & Santos-Lleó, M. 2005, A&A, 432, 15

[9] Wilkes, B. J., & Elvis, M. 1987, ApJ, 323, 243

# SPECTRAL STACKING ANALYSIS OF AN *XMM-NEWTON* INTERNATIONAL SURVEY (AXIS)

**A. Corral, X. Barcons, F.J. Carrera, and M.T. Ceballos**

Instituto de Física de Cantabria, 39005 Santander, Spain

## ABSTRACT

We have performed an X-ray spectral stacking analysis over the identified *Active Galactic Nuclei* (AGN) from the *XMM-Newton* International Survey (AXIS). We have processed the data for 22 of the 36 fields of the sample ($\sim$ 200 identified AGN) using the latest available *XMM-Newton* software and calibration. Moreover, we optimised the spectral source extraction to maximise the signal to noise ratio. We separated *Broad Line Active Galactic Nuclei* (BLAGN) and *Narrow Emission Line Galaxies* (NELGs) spectra and constructed rest frame average spectra for both types. In this way, we can examine the overall spectra shape and features of both AGN types. We obtained that the NELGs average spectrum shows a much harder spectral slope than the BLAGN, likely due to a major absorption. However, only in the NELG average spectrum we can see a feature that could be the emission line Fe K$\alpha$. We also see a bump over 10keV, but it is possibly caused by a normalisation effect.

Key words: galaxies:active; galaxies: Seyfert; X-rays: galaxies.

## 1. INTRODUCTION

Attending to their optical characteristics, *Active Galactic Nuclei* (AGN) are often separated in two groups, type 1 and 2 AGN. In a simple manner, for type 1 AGN we usually see broad emission lines in their optical spectrum and an unabsorbed X-ray spectrum. On the other side, for type 2 AGN we only see narrow emission lines and an absorbed X-ray spectrum. The *Unified Model for AGN* considers both types to have the same basic structure but they are observed through different amounts of absorbing material due to different inclination angles. Following this model, the observed *X-ray Background* (XRB) have been reproduced using AGN spectra with different absorptions, since it has been found that the major contribution to the XRB at medium fluxes is due to a combination of type 1 and type 2 AGN. See for example Comastri et al. (1995), Gilli et al. (2001) and Ueda et al. (2003). Besides, the X-ray sources flux distribution shows that most of the XRB is generated by medium flux sources.

We report here preliminary results on the construction of an average spectrum of AGN over a well defined sample of the more representative sources in the XRB, the medium flux sources of the AXIS sample.

## 2. X-RAY SPECTRAL EXTRACTION

We processed the data for 22 fields of the 36 fields in the AXIS sample, but only considered in our analysis those AGN that are optically identified in these fields (about 260 sources) and with fluxes above $2 \times 10^{-14}\mathrm{ergs}^{-1}\mathrm{cm}^{-2}$. The good time intervals for the observations in these fields range from 10 to 100ks. In some cases, there are more than one observation of the same field, so we can obtain a rather good quality spectrum.

We processed the newest refinalised ODFs from the *XMM-Newton* archive using the *Science Analysis Software* (SAS) version 6.1.0, the latest software and calibration available at the time of our analysis. We processed the ODFs in order to obtain the calibrate images and event lists using the SAS pipeline chains `emchain` and `epchain` for the MOS and pn data, respectively. Then, we performed the source detection using the SAS tasks `eboxdetect` and `emldetect`. For the fields that have more than one observation, we use `emosaic` to merge the images and optimise the source detection.

We extracted the source spectra in circular regions maximising the *signal to noise ratio* (SNR) for all detectors. The background spectra were taken in annular regions centred in the source position. If any other source falls within this region, we excluded the source region from the background region. If the resulting background was statistically small or fell near bright sources, we substituted it by a circular source-free region. We merged the MOS1 and MOS 2 spectra for each observation and the spectra for the MOS and pn, separately, from different observations to maximise the SNR.

*Table 1. Number of sources and redshift ranges*

| Source Type | Number of sources | Redshift range |
|---|---|---|
| BLAGN | 168 | 0.17-2.99 |
| NELGs | 33 | 0.04-2.98 |

## 3. IDENTIFIED SAMPLE

After the spectral extraction, we selected only the sources with more than 100 source MOS+pn counts. That reduced the sample to 201 sources. Using the optical identifications from the AXIS programme, we divided the sample in two groups: BLAGN and NELGS in order to obtain their spectral characteristics separately. The samples characteristics are in Table 1.

## 4. STACKING PROCESS

At this point, we have the source and background spectra and the response matrices for each source. To perform our analysis we needed the unfolded spectra, i.e., the source spectra before entering the detectors. To obtain the unfolded spectrum for each source, we used XSPEC. We set a single power law model with a fixed spectral slope of 2. We applied this model to the non grouped spectra so the model does not affect significantly the resulting spectrum thanks to the narrow energy bins.

Then, we shifted each spectrum to the rest frame using the redshifts given by the optical identifications from the AXIS program. We need each spectrum to contribute in the same manner to the final average spectrum, so we need to normalise them. To achieve this, we forced the 2-10 keV fluxes to be the same for all the spectra. We excluded the 5-8 keV range in the 2-10 keV range because the Fe K$\alpha$ line is expected to fall between these energies.

Since each spectrum has a different energy bins grid, we constructed a new one for the final spectrum. To select these new bins, we used the source spectra in counts, rebinned them to the new bins and added them all together without normalisation. Then, we chose the grid that distributes the counts in the most uniform way so as to assure a minimum number of real source counts ($\sim$ 100) in each new bin. We used this method as a quality check of the final grid.

Once we have the rest frame, normalised and rebinned spectra, we simply averaged them in a simple manner. Because of the quite large dispersion in the redshift distribution, some high energies could be reached only by a few spectra. We have only taken into account those spectral ranges to which at least 10 spectra contributed. The error bars were computed as the standard deviation of each bin divided by the square root of the number of spectra that contributes to that bin.

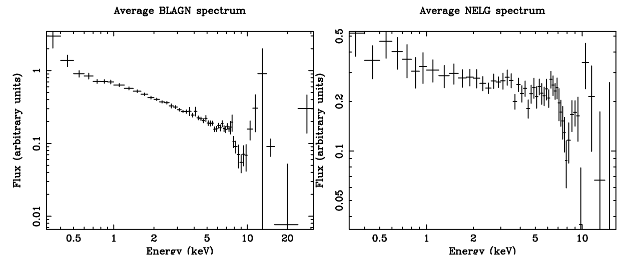


*Figure 1. Average BLAGN and NELGs spectra in the full covered range*

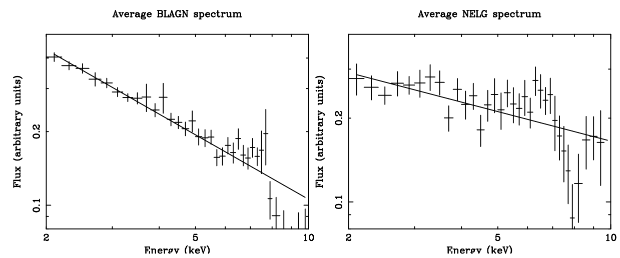


*Figure 2. Average BLAGN and NELGs spectra in the 2-10 keV range along with the power law fit*

## 5. PRELIMINARY RESULTS

The optimisation of the stacking process is still in progress. Our preliminary results are shown in Figure 1. The BLAGN average spectra extends up to 28 keV but NELGs spectrum only to 15 keV. This is due to the imposed restriction about the minimum number of spectra that has to contribute to each energy bin. For BLAGN we have many spectra with redshifts above 1, while most NELGs have redshifts below 1.

For the BLAGN average spectrum we fit a power law in the 2-10 keV obtaining an spectral slope of $\sim$ 1.9 (see Figure 2). We see no clear evidence of the Fe K$\alpha$ emission line. For the NELGs spectrum, we obtain a much flatter spectral slope of $\sim$ 1.4 (see Figure 2) as expected due to absorption if NELGs correspond to type 2 AGN , with absorbed X-ray spectrum. We see a feature around 6.4 keV that could correspond to the Fe K$\alpha$ line. In both spectra we see a bump starting at $\sim$ 10keV in BLAGN and at a little lower energy in NELGs. We have to test if this is a real spectral feature.

## REFERENCES

Comastri A., Setti G., Zamorani G., Hasinger G., 1995, A&A, 296, 1

Gilli R., Salvati M., Hasinger G., 2001, A&A, 366, 407

Ueda Y., Akiyama M., Ohta K., Miyaji T., 2003, ApJ, 598, 886

# EMISSION PROCESSES INVOLVED IN THE HARD X/$\gamma$ RAY EMISSION OF GALACTIC AND EXTRAGALACTIC COMPACT OBJECTS

**Sandrine Deluit, Laurent Bouchet, Elisabeth Jourdain**

Centre d'Étude Spatiale des Rayonnements (CESR/CNRS/UPS), 9 av. du Colonel Roche, 31 028 Toulouse, France

## ABSTRACT

Most compact objects, in particular X-ray Binaries (XRBs) and Active Galactic Nuclei (AGN), are characterised by X and $\gamma$-ray radiation, leading to investigate the physical processes occurring in their high energy emission and how their properties scale with different observables like the accretion rate, presence/absence of jets...
We perform various studies on the high energy emission of several Galactic and Extragalactic compact objects. In particular, using the spectrometer SPI on board INTEGRAL, we detect for the first time an emission above 200 keV and even up to 350 keV for a neutron star binary, GS 1826-24, suggesting the presence of another contribution to the classical thermal emission extending until $\sim$150 keV. The processus associated can still have a thermal origin but we favor a non thermal processus, similar to that found in black hole candidates and AGNs. We thus evoke the hypothesis that both thermal (corona) and non thermal (jet or not) emission processes could be involved ubiquitously in the high energy emission of Galactic and extragalactic compact objects.

Key words: X-ray Binaries; Active Galactic Nuclei.

## 1. GALACTIC COMPACT OBJECTS: X-RAY BINARIES

### 1.1. The neutron star binary GS 1826-24 with INTEGRAL/SPI: discovery of an emission above 200 keV

X-ray binaries present an emission extending up to X/$\gamma$ rays making them ideal candidates for the INTEGRAL satellite. We analyzed one year of Galactic Centre Deep Exposure (GCDE) by INTEGRAL, in particular with the Spectrometer SPI (20 keV-8 MeV), giving the unique opportunity to study the hard tail of X-ray bursters like GS 1826-24. GS 1826-24 has been discovered with GINGA while BeppoSAX revealed its neutron star nature showing regular type I bursts.
The BeppoSAX satellite set the detection limit of GS 1826-24 at 150 keV (Di Salvo, 2002), with a cutoff energy found at $\sim$50 keV. The hard X-ray emission of a neutron star system when a cutoff is detected is explained by a thermal comptonisation of soft photons in a hot region (corona) probably placed between the neutron star and the accretion disk.

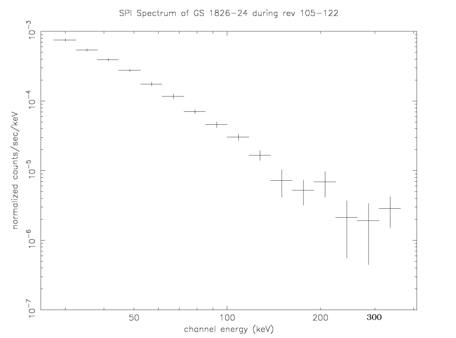


*Figure 1. SPI Spectrum of GS 1826-24*

With SPI, we reveal for the first time a significative emission extending up to 350 keV (Figure 1). The SPI spectrum still requires the classical thermal cutoff component at 60 keV (Deluit et al. 2006), but the large extension of the emission up to 350 keV, well reproduced by a power law, suggests the presence of an additional contribution. A thermal origin is possible but we favor a non thermal emission since the radiation up to 350 keV would request a hot plasma region, hardly compatible with the Compton cooling expected to reproduce the soft X-ray emission.
The discovery of this new contribution to the classical thermal emission up to 100-150 keV known for neutron star binaries naturally leads to a comparison with other types of compact objects.

### 1.2. Black Hole Candidates

The spectrum of GS 1826 revealed by SPI, for which several components seem to be present, naturally reminds the one found for BHCs in the hard X/$\gamma$ ray domain. As an example, Cyg X-1 presenting an emission at much higher energies than for GS 1826-24, shows however similarities with the state for which its emission extends

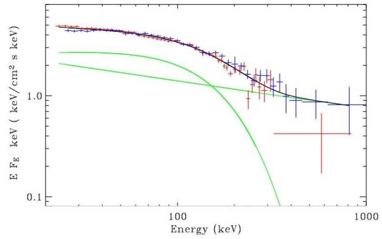


*Figure 2. IBIS and SPI spectra of Cyg X-1 in June 2003. From Malzac et al. (2005)*

far above the cutoff energy found in the X-ray domain and is composed of both a thermal (cutoff) and non thermal component (power law) extending up to the MeV domain (Figure 2). The presence of a jet in Cyg X-1 makes it the ideal candidate to produce the non thermal emission observed in the $\gamma$-ray domain. Moreover, a clear correlation is found between the radio and hard X-ray/$\gamma$ domain in Cyg X-1, but also for most of BHCs in the low/hard state where the jet is dominant.

## 2. EXTRAGALACTIC COMPACT OBJECTS: ACTIVE GALACTIC NUCLEI

BHCs have often be compared to AGNs, and in the last decade, an AGN/BHC binary paradigm has even emerged (Figure 3).

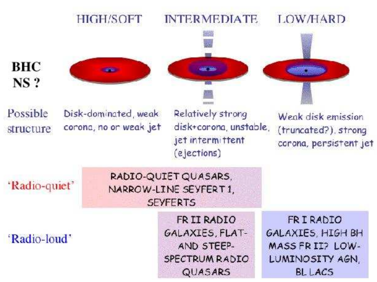


*Figure 3. Black Hole Grand Unification (Uttley, astro-ph/0508060)*

AGNs are composed of several classes, mainly radio quiet (e.g. Seyfert) and radio loud (e.g. blazar) objects. Their emission extension differs following the class considered, in particular if a jet is present. The Seyfert galaxies emission is presumed to be due to a pure thermal process with a cutoff detected between 100-300 keV, whereas for blazars, a dominant non thermal emission from the jet reaches MeV or GeV domains.

In Deluit et al. (2003) and Deluit (2004), we show that Sy 1 and Sy 2 with Polarized Broad Lines (PBLs hereafter) present common properties with a clear detection of a cutoff. On the other hand, Sy 2 without PBLs detected do not seem to exhibit a cutoff, leading us the hypothesis that another emission process, probably non thermal, could occur in this kind of Sy 2 and in Sy in general.

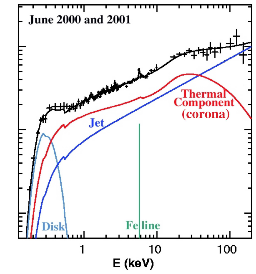


*Figure 4. Schematic view of 3C 273 X-ray spectrum in June 2000 and 2001*

Conversely, in Deluit et al. (2005), studying the 1996-2004 X-ray emission of the quasar 3C 273, usually largely dominated by the non thermal emission from the jet, we constrain a thermal cutoff in June 2000 and June 2001 observations (Figure 4), corresponding (with June 2004) to the lowest X-ray flux and jet activity states ever observed in the 3C 273 history. That proves that a thermal process is involved in addition to the well known non thermal emission from the jet.

## 3. DISCUSSION

Studying the high energy emission of different compact objects like neutron star binaries, black hole candidate binaries and AGNs, we emphasize the emergence of a more complex picture of their emission, but also great similarities between all these classes of compact objects.

Indeed, it appears that both thermal and non thermal processes could occurred in their high energy emission. The thermal component is well explained by the "accretion disk+hot corona" system. The non thermal component is natural in the case of a jet presence, like e.g. for 3C 273. But for Seyfert galaxies and neutron star binaries for which no jets are observed ? We evoke the possibility that collimated outflows or more probably jets extended in small distance scale (i.e. "mini-jet") could be omnipresent in radio-quiet AGNs and X-ray binaries presenting an emission above 200 keV.

Our various investigations thus suggest that an ubiquitous "thermal+non thermal" origin would be drawn for the high energy emission of galactic and extragalactic compact objects.

## REFERENCES


Deluit, S., et al., 2003, A&A, 399, 277

Deluit, S.J., 2004, A&A, 415, 39

Deluit, S., Stuhlinger, M., & Staubert R., 2005, submitted to A&A

Deluit, S., Bouchet L., Jourdain, E., et al., 2006, in preparation

Di Salvo, 2002, astro-ph/0207219

Malzac, J., et al., 2005, submitted to A&A

# EXTENDED INVERSE COMPTON EMISSION FROM DISTANT POWERFUL RADIO GALAXIES

**M. C. Erlund[1], A. C. Fabian[1], K. M. Blundell[2], A. Celotti[3], and C. Crawford[1]**

[1]Institute of Astronomy, University of Cambridge, Madingley Road, Cambridge, CB3 0HA, UK
[2]Department of Astrophysics, University of Oxford, Oxford, OX1 3RH, UK
[3]SISSA/ISAS, via Beirut 4, 34014 Trieste, Italy

## ABSTRACT

*Chandra* observations of 3C 432, 3C 191 and B2 0902+34 are presented as part of an ongoing search for inverse-Compton scattering of the cosmic microwave background (CMB) from high redshift radio sources (Schwartz, 2000). The energy density of the CMB increases with redshift, $z$, as $(1 + z)^4$, so the relatively high redshift of these powerful radio galaxies makes them good candidates for detecting extended inverse-Compton scattering along the radio jet axis: we do indeed detect radio-aligned X-ray emission.

Key words: inverse-Compton; powerful radio galaxies; high redshift.

## 1. INTRODUCTION

Inverse-Compton scattering of the cosmic microwave background (hereafter CMB) in high-redshift radio sources should be detectable, since the energy density of the CMB increases steeply with redshift, $z$, counter-balancing surface brightness dimming (Schwartz, 2000). Most high-redshift radio galaxies should therefore have extended X-ray emission produced by inverse-Compton scattering of the CMB, thus tracing an older relativistic electron population (with Lorentz factor $\gamma \sim 10^3$) compared with those producing the radio synchrotron emission ($\gamma \sim 10^5 - 10^6$). Several such sources have been detected (Schwartz, 2000, Belsole et al., 2004, Overzier et al., 2005, Scharf et al., 2003, Sambruna et al., 2004, and Blundell et al., 2005).

Here, *Chandra* observations of three high-redshift radio galaxies (3C 432, 3C 191 and B2 0902+34) are analysed with the aim of detecting and characterising their extended X-ray emission.

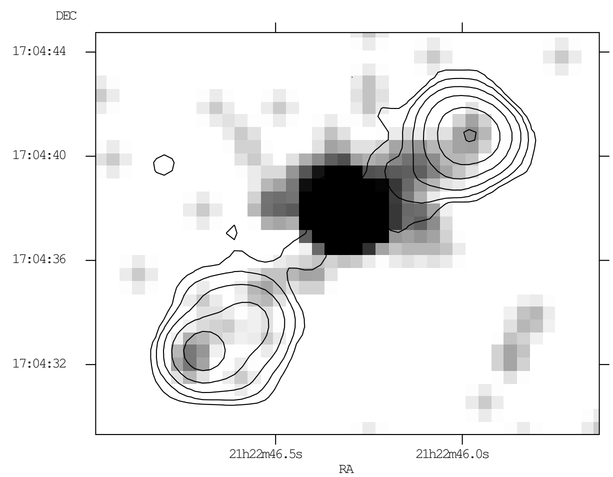


*Figure 1. Image of 3C 432, Gaussian-smoothed by 0.49", with 1.54* GHz *radio contours overlaid (0.001, 0.003, 0.012, 0.042, 0.144, 0.5* Jy/beam*).*

## 2. 3C 432

A 19.77 ks-long observation of 3C 432 ($z = 1.785$, RA 21h22m46.2s Dec +17d04m38s) was taken by *Chandra* on 2005 January 7 in VFAINT (very faint) mode. Fig. 1 clearly shows extended X-ray emission lying along the radio jet, not only in the lobes but also in the bridge. Spectra were extracted from the nucleus; the total extended X-ray emission (i.e. that within a $8'' \times 18''$ region aligned along the radio axis); the emission within the 1.54 GHz radio contours, excluding the central source, and the background. The nucleus has a photon index of $\Gamma = 1.84^{+0.09}_{-0.11}$ and intrinsic absorption $N_H = 2.1^{+0.36}_{-0.21} \times 10^{21}\,\mathrm{cm}^{-2}$ assuming a Galactic absorption of $7.4 \times 10^{20}\,\mathrm{cm}^{-2}$. The total extended emission has $\Gamma = 1.57^{+0.27}_{-0.36}$, and the extended emission within the 1.54 GHz contours has $\Gamma = 1.52^{+0.27}_{-0.48}$. These values were calculated using C-statistics, however $\chi^2$-statistics gives consistent values.

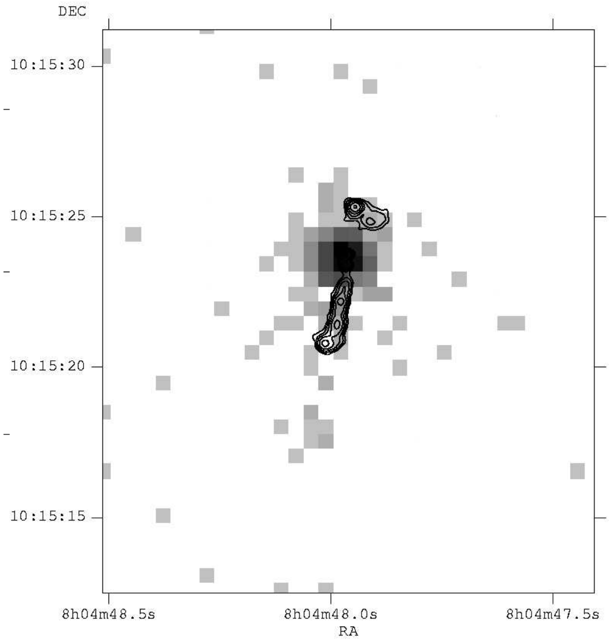


*Figure 2. X-ray image of 3C 191 with 8.46* GHz *radio contours overlaid (0.0005, 0.0012, 0.0029, 0.0069, 0.0167, 0.04* Jy/beam*).*

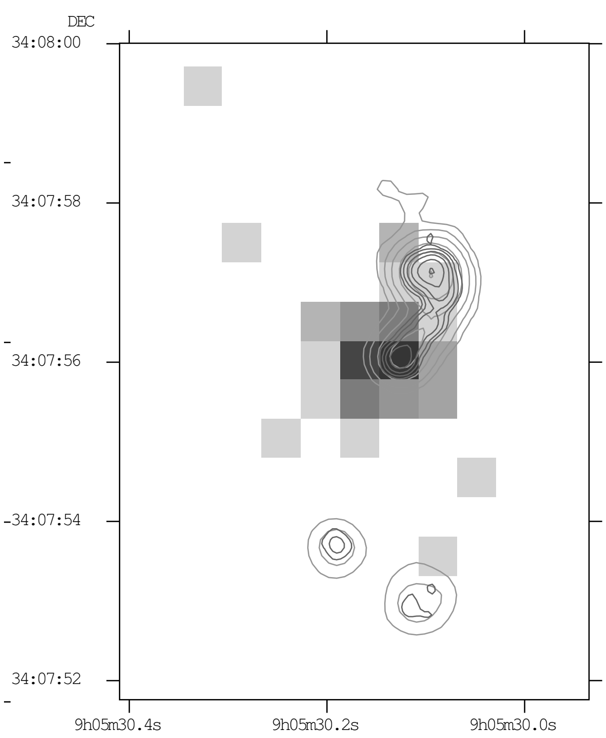


*Figure 3. X-ray image of B2 0902+34, overlaid with 8.09* GHz *radio contours (0.00015, 0.00042, 0.0012, 0.0033, 0.0093, 0.26* Jy/beam*) in dark grey and 4.54* GHz *radio contours (0.0003, 0.00088, 0.0026, 0.0076, 0.022, 0.065* Jy/beam*) in light grey.*

## 3. 3C 191

Two observations of 3C 191 have been analysed ($z = 1.965$, RA 08h04m47.9s Dec +10d15m23s): the first is 8.32 ks-long (Sambruna et al., 2004), taken with *Chandra* in FAINT mode on 2001 March 7 and the second is 19.77 ks-long, taken on 2004 December 12 in VFAINT mode. Fig. 2 is the sum of the two observations and shows extended X-ray emission aligned along the radio jet which appears to extend beyond the radio emission to the south. The nucleus has an intrinsic absorbed power law with $N_H = 0.46^{+0.29}_{-0.35} \times 10^{22}\,\mathrm{cm}^{-2}$ and $\Gamma = 1.79^{+0.12}_{-0.12}$. The total extended emission ($6.5'' \times 10.5''$ region excluding the central source) has $\Gamma = 1.66^{+0.32}_{-0.29}$, and the emission within the contours of the lowest $8.46$ GHz radio contour, shown in Fig. 2, has $\Gamma = 1.95^{+0.44}_{-0.20}$ (using C-statistics).

## 4. B2 0902+34

The *Chandra* image of B2 0902+34 ($z = 3.382$) is centred on the active nucleus. There are indications that the X-ray emission is slightly extended along the radio jet to the north (Fabian et al., 2002).

## REFERENCES


Schwartz, D. A. 2002, ApJ, 569, 23

Fabian, A. C., Crawford, C. S., & Iwasawa, K. 2002, MNRAS, 331, 57

Blundell, K. M., Fabian, A. C., Crawford, C. S., et al., 2005, MNRAS, submitted

Sambruna, R. M., Gambill, J. K., Maraschi, L., et al., 2005, ApJ, 608, 698

Belsole, E., Worrall, D. M., Hardcastle, M. J., et al., 2004, MNRAS, 352, 924

Overzier, R. A., Harris, D. E., Carilli, C. L., et al., 2005, A&A, 433, 87

Scharf, C., Smail, I., Ivison, R., et al., 2003, ApJ, 596, 105

# HIGH-RESOLUTION X-RAY SPECTROSCOPY OF THE ACTIVE GALACTIC NUCLEUS NGC 4051 WITH CHANDRA

**M. Feňovčík[1,2], J.S. Kaastra[1], E. Costantini[1,2], K.C. Steenbrugge[3], and F. Verbunt[2]**

[1]SRON Netherlands Institute For Space Research, Sorbonnelaan 2, 3584 CA Utrecht, the Netherlands
[2]Astronomical Institute, Utrecht University, P.O. BOX 80000, 3508 TA Utrecht, the Netherlands
[3]Harvard-Smithsonian Center for Astrophysics, 60 Garden Street Cambridge, MA 02138

## ABSTRACT

The narrow line Seyfert 1 galaxy NGC 4051 is one of the most variable Active Galactic Nuclei. During our 94 ks Chandra LETGS observation, the source was first rapidly variable at a high flux and then more quiescent when at a low flux level. The spectrum is rich in absorption and emission features some of which are significantly responding to the luminosity changes. In the high state we resolve three X-ray absorption systems of photo-ionized gas with different ionization states and outflow velocities. After the rapid ($< 3\,500$ s) transition from the high to the low flux level the emission spectrum shows Radiative Recombination Continua (RRCs). The fast observed response of the RRCs to the continuum flux change indicates that they originate very close to the central source.

Key words: NGC 4051; warm absorber; Radiative Recombination Continuum.

## 1. INTRODUCTION

The stupendous amount of energy emitted by an Active Galactic Nucleus (AGN) is released by gas that flows towards a super–massive black hole in the center of the galaxy. The structure and the size of the AGN environment are inferred through spectral emission features like the relativistically broadened, "classical" broad and narrow emission lines and Radiative Recombination Continua (RRCs). In addition to the accretion flow into the super–massive black hole, there is also gas flowing away from it. The mass loss rate and the accretion/mass–loss ratio play an important role in many processes (e.g. enrichment of the intergalactic medium, evolution of the host galaxy).
We present here the results of an observation of the nearby (z=0.0023) narrow line Seyfert 1 galaxy NGC 4051. The source was observed by Chandra LETGS for 94 ks.
This results will be published in Feňovčík et al. (2006).

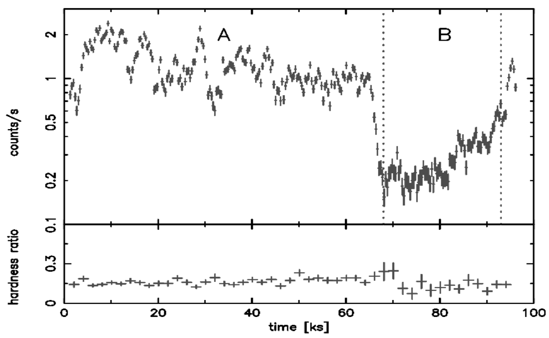


*Figure 1. The light curve (upper panel) and hardness ratio (lower panel) of NGC 4051. The hardness ratio is defined as the ratio of 2—8 and 8—32 Å count rate. The upper panel has a bin size of 350 s and the bottom panel has a bin size of 2 000 s. Dotted lines denote the different flux states during the observation.*

## 2. THE LIGHT CURVE

Looking at the light curve (Figure 1) we can distinguish two different states. At the beginning of the observation (65 ks) the source flux is characterized by a high flux level and fast variability (part A). Then the flux rapidly decreases (in $< 3\,500$ s) by a factor of $\sim 5$ and on short time scales stays almost constant (part B). At the end the flux rises slowly again to the previous flux level.
The hardness ratio does not vary significantly throughout the observation. This fact indicates that the soft and hard energy spectral components respond to the flux change in the same way.

## 3. WARM ABSORBER

Many absorption and emission lines from different elements in various ionization states are present in the spectrum (Figure 2).
In part A three absorption systems are evident: two low

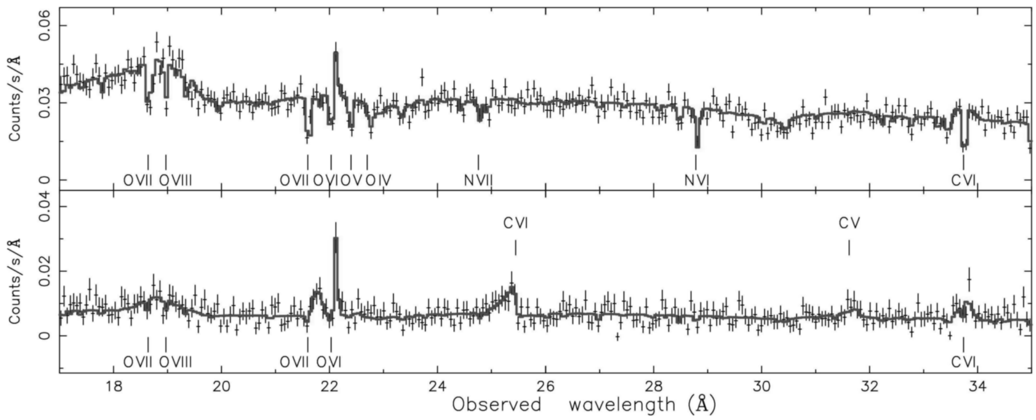


*Figure 2. Chandra LETGS spectra of part A (top) and of part B (bottom). Note the strong Radiative Recombination Continuum of C VI in the spectrum of part B.*

velocity components at $-400\ \mathrm{km\,s^{-1}}$ and $-800\ \mathrm{km\,s^{-1}}$ and the highest velocity outflow ever detected in a Seyfert 1 galaxy at $-4810\ \mathrm{km\,s^{-1}}$ (van der Meer et al., 2003). With increasing outflow velocity, the ionization parameter and column density of individual components are increasing as well (Table 1). In part B only one outflow component is clearly detected. It has similar physical parameters as the intermediately ionized system with outflow velocity of $-800\ \mathrm{km\,s^{-1}}$, detected in part A (Table 1), except for a lower ionization parameter.
We note that in our data the absorption system with outflow velocity $-2340\ \mathrm{km\,s^{-1}}$, observed by Collinge et al. (2001), is not significantly detected. The presence of a low velocity component was previously reported also by Collinge et al. (2001) and later by Ogle et al. (2004).

*Table 1. Properties of the warm absorber in the high state (part A) and in the low state (part B)*

| | | $N_{\mathrm{H}}$ ($\times 10^{25}$ m$^{-2}$) | $\log\xi$ ($\times 10^{-9}$ W m) | $\mathrm{v_{out}}$ (km s$^{-1}$) |
|---|---|---|---|---|
| | 1 | $0.41 \pm 0.04$ | $0.74 \pm 0.06$ | $-420 \pm 20$ |
| **A** | 2 | $1.9 \pm 1.0$ | $2.44 \pm 0.08$ | $-820 \pm 40$ |
| | 3 | $15^{+10}_{-6}$ | $3.2 \pm 0.1$ | $-4810 \pm 120$ |
| **B** | 2 | $3.5 \pm 1.0$ | $1.54 \pm 0.10$ | $-790 \pm 40$ |

## 4. RADIATIVE RECOMBINATION CONTINUA

In part B (Figure 1), where the flux decreased by a factor of $\sim 5$, strong narrow RRCs of C VI (25.39 Å) and C V (31.64 Å) appear in the spectrum. The inferred temperature of the recombining photo–ionized gas is $\sim$ 5 eV. In addition, the RRCs show a redshift of $\sim$ 1 000 km s$^{-1}$ with respect to the rest frame of the AGN. Interestingly, the RRCs from other abundant ions such as O VII and O VIII are not visible in the spectrum.
If we consider that the RRC is somehow linked to the warm absorber, the most natural question is, to which particular component? The best candidate is the second absorption system in part A, with outflow velocity $-820$ km s$^{-1}$ and $N_{\mathrm{H}} = 1.9{\times}10^{25}\mathrm{m^{-2}}$. With a fivefold drop in the continuum, we expect a $\log\xi = 1.74$, which is close to the value observed in part B (Table1). Moreover, the gas temperature will decrease from 21 eV to 6 eV which is, within the error bars, the temperature of the gas producing the C VI and C V RRC.
By taking $\log\xi = 1.54$ we expect only a small fraction of gas recombining to O VIII. On the contrary, for this ionization parameter we expect a lot of gas producing an O VII RRC at 16.77 Å, but this feature is not clearly observed. However in this spectral region absorption from Fe IX may mask the O VII RRC emission.
The fact that we see the fast response to the flux change means that the distance of the gas from the central source has to be less than $1.5 \times 10^{12}$ m. As a consequence, given the mass of the black hole of NGC 4051 ($3 \times 10^5 \mathrm{M_\odot}$, McHardy et al. (2004) ) we expect a keplerian velocity broadening of at least $5\,200$ km s$^{-1}$ in the RRC, which is not observed.
From the observed C VI RRC emission measure we can derive a lower limit for the recombining gas column density: $N_{\mathrm{H}} > 10^{26}\ \mathrm{m^{-2}}$. This value is 3 – 5 times higher than the column density of the warm absorber. Therefore the hypothesis that the warm absorber and the RRC are produced by the same gas is not straightforwardly confirmed. Other effects (e.g. geometry) may play an important role in the emission/absorption process of the system.

## REFERENCES

Collinge, M. J., et al. 2001, ApJ, 557, 2

Feňovčík et al. 2006, A&A (in preparation)

McHardy, I. M., et al. 2004, MNRAS, 348, 783

Ogle, P. M., et al. 2004, ApJ, 606, 151

van der Meer, R. L. J., et al. 2003, ASP CS, 290, 133

# THE $XMM-NEWTON$ VIEW OF $\gamma-$RAY LOUD ACTIVE NUCLEI

**L. Foschini[1], G. Ghisellini[2], C.M. Raiteri[3], F. Tavecchio[2], M. Villata[3], M. Dadina[1], G. Di Cocco[1], G. Malaguti[1], L. Maraschi[2], E. Pian[4], and G. Tagliaferri[2]**

[1]INAF/IASF-Bologna, Via Gobetti 101, 40124 Bologna, Italy
[2]INAF/Osservatorio Astronomico di Brera, Via Bianchi 46, 23807 Merate, Italy
[3]INAF/Osservatorio Astronomico di Torino, Via Osservatorio 20, 10025 Pino Torinese, Italy
[4]INAF/Osservatorio Astronomico di Trieste, Via G.B. Tiepolo 11, 34131 Trieste, Italy

## ABSTRACT

Notwithstanding the big efforts devoted to the investigation of the mechanisms responsible for the high-energy ($E > 100$ MeV) $\gamma-$ray emission in active galactic nuclei (AGN), the definite answer is still missing. The X-ray energy band ($0.4 - 10$ keV) is crucial for this type of study, since both synchrotron and inverse Compton emission can contribute to the formation of the continuum. Within an ongoing project aimed at the investigation of the $\gamma-$ray emission mechanism acting in the AGN detected by the EGRET telescope onboard CGRO, we firstly focused on the sources for which X-ray and optical/UV data are available in the *XMM-Newton* public archive. The preliminary results are outlined here.

Key words: Galaxies: active – BL Lacertae objects: general – Quasars: general – X-rays: galaxies.

## 1. INTRODUCTION

The discovery of $\gamma-$ray loud AGN dates back to the dawn of $\gamma-$ray astronomy, when the European satellite *COS-B* ($1975 - 1982$) detected photons in the $50 - 500$ MeV range from 3C273 (Swanenburg et al. 1978). However, 3C273 remained the only AGN detected by *COS-B*.

A breakthrough in this research field came later with the Energetic Gamma Ray Experiment Telescope (EGRET) on board the *Compton Gamma-Ray Observatory* (CGRO, 1991-2000). The third catalog of point sources contains $271$ sources detected at energies greater than $100$ MeV and $93$ of them are identified with blazars (66 at high confidence and 27 at low confidence), and 1 with the nearby radiogalaxy Centaurus A (Hartman et al. 1999). Therefore, EGRET discovered that the blazar type AGN are the primary source of high-energy cosmic $\gamma-$rays (von Montigny et al. 1995).

Later on, Ghisellini et al. (1998) and Fossati et al. (1998) proposed a unified scheme for $\gamma-$ray loud blazars, based on their physical properties (see, however, Padovani et al. 2003). Specifically, the blazars are classified according to a sequence going from BL Lac to flat-spectrum radio quasar depending on the increase of the observed luminosity, which in turn leads to a decrease of the synchrotron and inverse Compton peak frequencies, and an increase of the ratio between the emitted radiation at low and high frequencies. In other words, the spectral energy distribution (SED) of blazars is typically composed of two peaks, one due to synchrotron emission and the other to inverse Compton radiation. Low luminosity blazars have the synchrotron peak in the UV-soft X-ray energy band and therefore are “high-energy peaked” (HBL). As the synchrotron peak shifts to low energies (near infrared, “low-energy peaked”, LBL), the luminosity increases and the X-ray emission can be due to synchrotron or inverse Compton or a mixture of both. For the Flat-Spectrum Radio-Quasars (FSRQ), the blazars with the highest luminosity, the synchrotron peak is in the far infrared and the X-ray emission is due to inverse Compton.

Moreover, the two-peaks SED is a dynamic picture of the blazar behaviour: indeed, these AGN are characterized by strong flares during which the SED can change dramatically. The X-ray energy band can therefore be crucial to understand the blazars behaviour and to improve the knowledge of high-energy emission.

## 2. SAMPLE SELECTION AND DATA ANALYSIS

To investigate the X-ray and optical/UV characteristics of $\gamma-$ray loud AGN in order to search for specific issues conducive to the $\gamma-$ray loudness, we cross correlated the 3$^{\rm rd}$ EGRET Catalog (Hartman et al. 1999), updated with the identifications performed to date, with the public observations available in the *XMM-Newton* Science Archive to search for spatial coincidences within $10'$ of the boresight of the EPIC camera. Fourteen AGN have

*Table 1. Main characteristics of the observed AGN.*

| 3EG | Counterpart | Type* | Redshift |
|---|---|---|---|
| $J0222+4253$ | $0219+428$ | LBL | $0.444$ |
| $J0237+1635$ | AO $0235+164$ | LBL | $0.94$ |
| $J0530-3626$ | PKS $0521-365$ | FSRQ | $0.05534$ |
| $J0721+7120$ | S5 $0716+714$ | LBL | $>0.3$ |
| $J0845+7049$ | S5 $0836+710$ | FSRQ | $2.172$ |
| $J1104+3809$ | Mkn 421 | HBL | $0.03002$ |
| $J1134-1530$ | PKS $1127-145$ | FSRQ | $1.184$ |
| $J1222+2841$ | ON 231 | LBL | $0.102$ |
| $J1229+0210$ | 3C 273 | FSRQ | $0.15834$ |
| $J1324-4314$ | Cen A | RG | $0.00182^{**}$ |
| $J1339-1419$ | PKS $1334-127$ | FSRQ | $0.539$ |
| $J1409-0745$ | PKS $1406-076$ | FSRQ | $1.494$ |
| $J1621+8203$ | NGC 6251 | RG | $0.0247$ |
| $J2158-3023$ | PKS $2155-304$ | HBL | $0.116$ |

* LBL: low frequency peaked BL Lacertae Object; HBL: high frequency peaked BL Lacertae Object; FSRQ: flat-spectrum radio quasar; RG: radio galaxy.

** This redshift is not indicative and the distance of $3.84$ Mpc is adopted here.

been found (Table 1) as of April $14^{\rm th}$, 2005, for a total of $43$ observations. For three of them there are several observations available: 15 for 3C $273$, 6 for Mkn $421$, 9 for PKS $2155-304$. The data from $6$ sources of the present sample are analyzed here for the first time and, among them, one has never been observed in X-rays before (PKS $1406-706$).

Data from the EPIC camera (MOS, Turner et al. 2001; PN, Strüder et al. 2001) and the Optical Monitor (Mason et al. 2001) have been analyzed with `XMM SAS 6.1` and `HEASoft 6.0`, together with the latest calibration files available at April $14^{\rm th}$, 2005, and by following the standard procedures described in Snowden et al. (2004). In addition, the Optical Monitor makes it possible to have optical/UV data simultaneous to X-ray for most of the selected sources, with the only exception of PKS $0521-365$, Mkn $421$, and Cen A.

## 3. MAIN RESULTS

The main findings of this study can be summarized as follows:

(i) the EGRET blazars studied here have spectral characteristics in agreement with the unified sequence of Ghisellini et al. (1998) and Fossati et al. (1998);

(ii) no evident characteristics conducive to the $\gamma-$ray loudness have been found: the photon indices are generally consistent with what is expected for this type of sources, with FSRQ that are harder than BL Lac; there are hints of some differences in the photon indices when compared with other larger catalogs (e.g. *BeppoSAX* Giommi et al. 2002), particularly for FSRQ: the sources best fit with a simple power law model show a harder photon index ($1.39\pm0.09$ vs $1.59\pm0.05$); however, the statistics is too poor to make firm conclusions (3 sources vs 26 in the *BeppoSAX* catalog);

(iii) three sources show Damped Lyman $\alpha$ systems along the line of sight (AO $0235+164$, PKS $1127-145$, S5 $0836+710$), but it is not clear if the intervening galaxies can generate gravitational effects altering the characteristics of the blazars so to enhance the $\gamma-$ray loudness;

(iv) no evidence of peculiar X-ray spectral features has been found, except for the emission lines of the iron complex in Cen A.

More details of the analysis will be available in Foschini et al. (2005).

## ACKNOWLEDGMENTS

This work is based on public observations obtained with *XMM–Newton*, an ESA science mission with instruments and contributions directly funded by ESA Member States and the USA (NASA). This work was partly supported by the European Community's Human Potential Programme under contract HPRN-CT-2002-00321 and by the Italian Space Agency (ASI).

## REFERENCES

Foschini L. et al., 2005, submitted

Fossati G. et al., 1998, MNRAS 299, 433

Ghisellini G. et al., 1998, MNRAS 301, 451

Giommi P. et al., 2002, astro-ph/0209596

Hartman R.C. et al., 1999, ApJS 123, 79

Mason K.O. et al., 2001, A&A 365, L36

Padovani P. et al., 2003, ApJ 588, 128

Snowden S. et al., 2004. An introduction to XMM-Newton data analysis. Version 2.01, 23 July 2004.

Strüder L. et al., 2001, A&A 365, L18

Swanenburg B.N. et al., 1978, Nature 275, 298

Turner M.J. et al., 2001, A&A 365, L27

von Montigny C. et al., 1995, ApJ 440, 525

# ANGULAR CLUSTERING OF X-RAY POINT-LIKE SOURCES IN THE XMM LARGE SCALE STRUCTURE SURVEY

**O. Garcet[1], P. Gandhi[2], E. Gosset[1], A. Gueguen[3], F. Pacaud[3], M. Pierre[3], and J. Surdej[1]**

[1]Institut d'Astrophysique et de Géophysique, Université de Liège, Belgium
[2]European Southern Observatory, Casilla 19001, Santiago, Chile
[3]CEA/DSM/DAPNIA Service d'Astrophysique, Saclay, F-91191 Gif sur Yvette, France

## ABSTRACT

We present the log(N)-log(S) diagram and an angular clustering analysis of point-like X-ray sources for the XMM-Newton Large Scale Structure (XMM-LSS) Survey. Though designed to study the properties and evolution of distant X-ray clusters up to $z \sim 1$, the large contiguous area planned for the full XMM-LSS survey is ideal for studying X-ray-selected AGN and their clustering properties. Our goal is to test the AGN unified scheme paradigm by studying the clustering of X-ray point-like sources. A clustering analysis of a 4.2 $deg^2$ contiguous region in the soft ([0.5-2] keV) and hard ([2-10] keV) energy bands is presented here. The angular correlation function and the nearest neighbour test have been performed in each band. Both tests only reveal a weak clustering in the soft X-ray band.

## 1. THE XMM-LSS SURVEY

The XMM-LSS observations consist presently of 51 overlapping pointings with exposure time between 10 and 20 ks, which cover a total contiguous area of 6 $deg^2$. Full details of the detection pipeline and source classification will be presented in Pacaud et al. (2005).

## 2. SELECTION OF POINT-LIKE SOURCES

Only those sources that lie within 10 arcmin of the optical axis centres of each pointing were retained. This was done in order to minimize biases due to the PSF distortion at large off-axis angles. Confirmed extended X-ray sources were removed from the [0.5-2] keV (soft) sample, while for the [2-10] keV (hard) sample, every source was considered as point-like. Finally, all samples in this analysis have been defined with $S/N > 3$.

## 3. GENERATION OF RANDOM (UNCORRELATED) CATALOGUES

Significant variation in sensitivity and irregular holes are present in our survey. That is why it has been crucial to simulate selection effects accurately. Due to mirror vignetting, the minimum detectable flux at an off-axis distance of 10 arcmin is higher by a factor of 2 as compared to the optical-axis centre. We generated an ensemble of random and initially uniform catalogues to correctly simulate the selection effects of the sample, each catalogue containing the same number of sources as the parent data sample. These random catalogues have been generated in the following way : first, sky positions over the central inner 10 arcmin regions of each pointing are randomly chosen. Second, source flux are randomly chosen, according to the logN-logS of the parent data sample. Finally, the source flux at a given position is compared to the limiting flux at that location. If the limiting flux at that position is higher, the random source is discarded and another sky position is again randomly chosen.

## 4. RESULTS

Results concerning the logN-logS are shown in Fig 1. and Fig 2. for the soft and hard band, respectively. We systematically find significantly less bright sources (only shown for the hard band, compared to the HELLAS2XMM). Clustering analysis results are gathered in Fig 3. to Fig 6. Both tests (ACF and nearest neighbour test) only reveal a weak clustering in the soft band, and no hint for clustering in the hard band.

## 5. DISCUSSION AND CONCLUSION

We presented a clustering analysis over a region covering 4.2 $deg^2$ in the soft and hard energy bands. In the soft band, both the two-point angular correlation function and

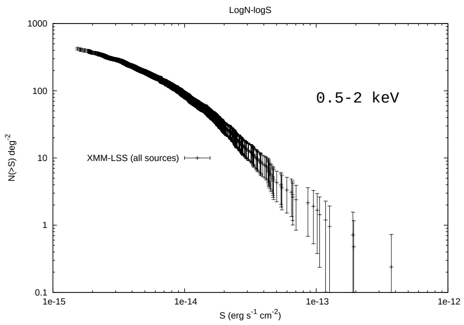


*Figure 1. LogN-logS for the soft sample, in the [0.5-2] keV band. The logN-logS is shown here for all sources (clusters have a minor contribution, except at very bright fluxes). The error bars denote 1 $\sigma$ Poisson uncertainties.*

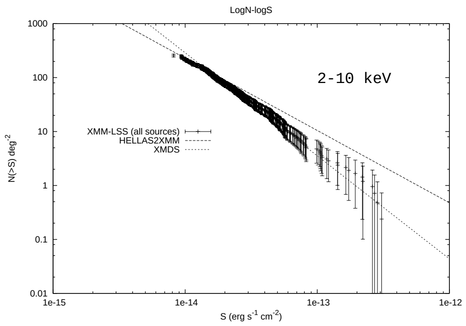


*Figure 2. LogN-logS for the hard sample, in the [2-10] keV band. The logN-logS is shown here for all sources. The error bars denote 1 $\sigma$ Poisson uncertainties.*

the nearest neighbour test show a positive clustering signal, though with low significance, around 2 $\sigma$, which is consistent with measurements of Basilakos (2005) within the error bars. However, the results of the same analysis in the hard band is consistent with a random and uniform distribution, which is at odds with measurements of Basilakos (2004). Full details of this clustering analysis are presented in Gandhi et al. (2005).

## REFERENCES


Baldi A., Molendi S., Comastri A., et al. 2002, ApJ, **564**, 190

Basilakos S., Georgakakis A., Plionis M., et al. 2004, ApJL, **607**, L79

Basilakos S., Plionis M., Georgakakis A., et al. 2005, MNRAS, **356**, 183

Chiappetti L., Tajer M., Trinchieri G., et al. 2005, A&A, **439**, 413

Gandhi P., Garcet O., Disseau L., et al., submitted to MNRAS

Hamilton A. J. S., 1993, ApJ, **417**, 19

Pacaud F., Pierre M., Gueguen A., et al. 2005, to be submitted to MNRAS


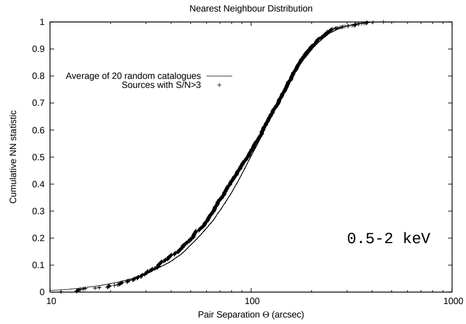


*Figure 3. Cumulative first nearest-neighbour distribution function in the [0.5-2] keV band, for point-like sources, compared to the average distribution function of random catalogues.*

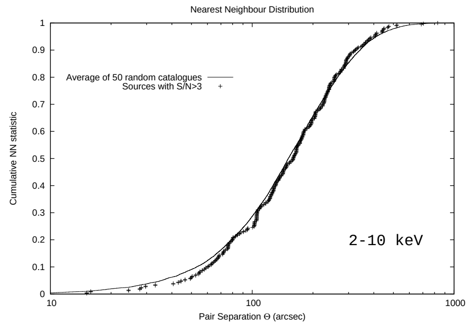


*Figure 4. Cumulative first nearest-neighbour distribution function in the [2-10] keV band, for point-like sources, compared to the average distribution function of random catalogues.*

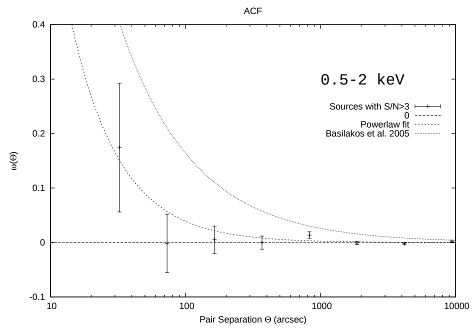


*Figure 5. ACF, as defined by Hamilton (1993) and measured for the soft (1163 sources) point-sources. The dashed line is the best-fit powerlaw model. Literature determination of the best-fit powerlaw ACF from Basilakos (2005) is shown.*

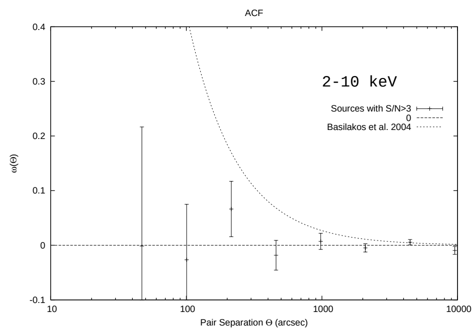


*Figure 6. ACF, as defined by Hamilton (1993) and measured for the hard (413 sources) point-sources. Literature determination of the best-fit powerlaw ACF from Basilakos (2004) is shown.*

# X-RAY EVIDENCE FOR MULTIPLE ABSORBING STRUCTURES IN SEYFERT NUCLEI

**J. M. Gelbord[1], K. A. Weaver[2], and T. Yaqoob[3]**

[1]MIT Kavli Institute, 77 Massachusetts Ave., Cambridge, MA 02140, USA
[2]NASA GSFC, Code 662, Greenbelt, MD 20771, USA
[3]Department of Physics and Astronomy, Johns Hopkins University, 3400 N Charles St., Baltimore, MD 21218, USA

## ABSTRACT

We have discovered a correlation between the X-ray absorbing column densities within Seyfert galaxies and the relative alignment between the central engines and their host galactic disks. This correlation carries several implications for Seyfert unification models. (1) In addition to small-scale circumnuclear absorbers, there are absorbing systems associated with the host galactic plane that are capable of obscuring the broad line region emission. (2) The misalignment between the central engine axis and that of the host galaxy arises on intermediate scales between these absorbers. (3) The small-scale absorbers have systematically higher column densities and may be universally Compton-thick.

Key words: galaxies: active, galaxies: Seyferts.

## 1. THE DUAL-ABSORBER MODEL

Seyfert galaxies are generally subdivided into two spectroscopic classifications: type 1's have extremely broad permitted emission lines, less broad forbidden lines, and strong non-thermal continua, while type 2 Seyferts exhibit only the narrow forbidden lines. Unification models assert that all Seyferts are intrinsically similar but have different appearances in different directions. The canonical model invokes a parsec-scale torus that hides the innermost, energetic regions from some lines of sight. Observers with an unimpeded view of the central region see a Seyfert 1 and those with line-of-sight obscuration see a type 2. To hide the central continuum source and the broad line region (BLR), the screen must have $N_{\rm H} > 10^{21}$ cm$^{-2}$ to attenuate soft X-rays and be dusty to effectively staunch IR/optical/UV continuum.

The distribution of host galaxy inclinations ($i$) amongst Seyfert types indicates that a model consisting of a single torus is incomplete. If such a torus is the universal source of obscuration, then one of two scenarios are expected: either it is aligned with the host galactic plane, causing Seyfert 1's to be found in face-on hosts and Seyfert 2's in edge-on galaxies, or it is misaligned with the galaxy, in which case there would be no correlation between Seyfert types and $i$. Neither is the case. Several studies have instead established that type 2 Seyferts are found with any $i$ while type 1's are not found in edge-on galaxies (e.g., Maiolino & Rieke, 1995). The distribution of Seyfert 2's suggests an obscuring medium that is misaligned with the host galaxy, but the dearth of edge-on Seyfert 1 hosts indicates that there is always sufficient material in the galactic plane to hide the broad line region.

The distribution of $i$ values can be explained with the introduction of a second absorber (Fig. 1). In this model, the small-scale "nuclear absorber" or NA (presumably the torus although other models are possible, e.g., Elvis, 2000) is randomly oriented with respect to the host galaxy; the second absorber lies at larger scales and is aligned with the galactic plane, hence the "galactic absorber" or GA. Such a model has been proposed by numerous authors (e.g., McLeod & Rieke, 1995; Maiolino & Rieke, 1995; Kinney et al., 2000). Several lines of evidence suggest an absorbing medium on 100 pc scales, including: missing edge-on Seyferts of any type from optical, UV and soft X-ray selected surveys suggesting a large-scale absorber that covers much of the narrow line region (NLR; McLeod & Rieke, 1995); IR reprocessing by dust (Granato et al., 1997); and direct imaging of dust lanes on few-hundred pc scales (Malkan et al., 1998; Pogge & Martini, 2002). The relative alignment of the absorbers is an important parameter of this model. When the absorbers are misaligned, the shadow of the NA covers less of the GA and the combined covering fraction of the absorbers increases. Seyfert 1's should tend to be in well-aligned systems and Seyfert 2's attenuated by the GA and not the NA should prefer poorly-aligned ones.

The two absorbers should differ in their mean column densities. A significant fraction of Seyfert 2 galaxies exhibit Compton thick absorption ($N_{\rm H} > 10^{24}$ cm$^{-2}$). To provide marginally Compton-thick absorption over a covering fraction $f$ requires $10^9 M_\odot f (r_{100\ \rm pc})^2$; a reasonable quantity for the NA but an excessive amount for the GA. Dynamical mass measurements of some nearby

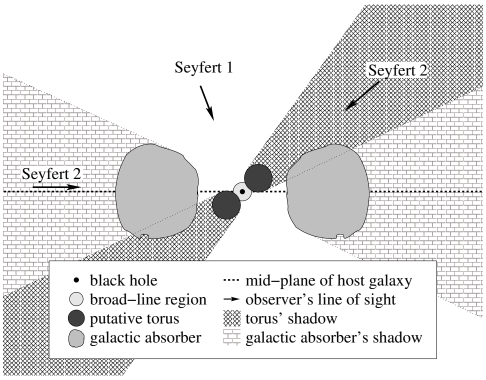


*Figure 1. The dual absorber framework. One absorber lies near the nucleus and may be identified with the putative torus, while the other is on much larger scales and is aligned with the host galactic plane. A type 2 Seyfert is observed if either lies along the line of sight to the BLR.*

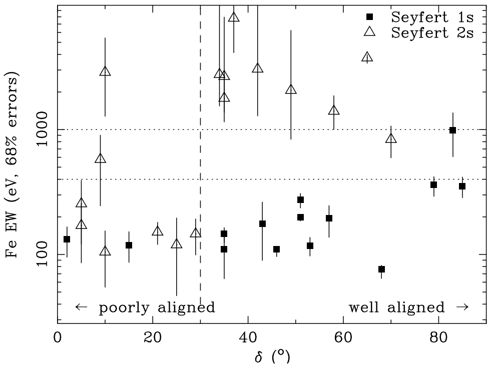


*Figure 2. The distribution of the alignment parameter $\delta$ amongst the Seyfert classes. Heavily obscured sources are defined as those with Fe EW $>$ 1 keV and modestly obscured sources have EW $<$ 400 eV. The preferences of low-EW Seyfert 2's for low $\delta$ values and Seyfert 1's for high values is predicted by the dual-absorber model.*

Seyferts can rule out any appreciable Compton-thick covering fraction at $\sim$100 pc scales (e.g., Maiolino et al., 1998). Thus, most if not all Compton thick Seyferts are attenuated by their NA, and typical lines of sight through the GA will have much lower column densities.

To test the dual-absorber model we combine measurements of the line of sight attenuation with geometric constraints on the internal alignment. We divide the Seyferts into three classes: unobscured (optically-defined Seyfert 1's), modestly obscured (Compton-thin Seyfert 2's), and heavily obscured (Compton-thick or nearly so), with the latter two differentiated by X-ray spectroscopy. We assume that these respectively correspond to lines of sight that are unobstructed, intercept only the GA, and intercept the NA. Rather than model $N_{\rm H}$ values, we rely upon the equivalent width (EW) of the Fe K$\alpha$ line to avoid an ambiguity of models fitted to low S/N data. When the continuum around 6 keV is repressed (if $N_{\rm H} > 10^{23.5}$ cm$^{-2}$) the EW of the 6.4 keV Fe line skyrockets, providing a robust indicator of heavy obscuration. As an alignment measure, we use published values of $\delta$, the angle between the radio jet and the host galaxy major axis (Kinney et al., 2000): misaligned systems have low values and perfectly aligned ones have $\delta = 90°$.

## 2. RESULTS FROM THE ASCA SAMPLE

We analyzed all 31 Seyferts with ASCA detections and published $\delta$ values, classifying each as heavily, modestly, or not obscured (Fig. 2). We find that (1) modestly obscured Seyfert 2's all have $\delta < 30°$; (2) unobscured systems prefer moderate-to-high $\delta$ values ($\delta > 30°$); (3) heavily obscured systems have no strong correlation with $\delta$; and (4) when taken together, systems with modest or no obscuration are uncorrelated with $\delta$. These distributions all agree with the dual-absorber model (points 3 & 4 *should* be independent of $\delta$ because they depend only upon whether our line of sight intercepts the NA). A KS test shows the $\delta$ distributions of unobscured and modestly obscured Seyferts to differ with 99.8% confidence. The strength of the correlation of modestly obscured sources and $\delta$ is surprising; we would expect some misaligned systems to have low $\delta$ values due to projection effects.

These observations allow us to make some inferences about Seyfert structures. If the misalignment must be severe before we see GA-only attenuation, then the GA must have a much smaller covering fraction than the NA (contrary to Fig. 1). The fact that we have any correlations with $\delta$ means that the radio jet is a reliable indicator of the direction of the NA. Thus, the misalignment between the central engine and the host galaxy must take place on intermediate scales. The NA seldom if ever has a column density below $10^{23}$ cm$^{-2}$. Otherwise some fraction of modestly absorbed systems would be observed through the NA and hence shouldn't correlate with $\delta$. The strength of the correlation argues against this but needs to be tested with a larger, more complete sample.

## REFERENCES

Elvis, M. 2000, ApJ, 545, 63

Granato, G. L., Danese, L., & Franceschini, A. 1997, ApJ, 486, 147

Kinney, A. L., Schmitt, H. R., Clarke, C. J., et al. 2000, ApJ, 537, 152

Maiolino, R. & Rieke, G. H. 1995, ApJ, 454, 95

Maiolino, R., Salvati, M., Bassani, L., et al. 1998, A&A, 338, 781

Malkan, M. A., Gorjian, V., & Tam, R. 1998, ApJS, 117, 25

McLeod, K. K. & Rieke, G. H. 1995, ApJ, 441, 96

Pogge, R. W. & Martini, P. 2002, ApJ, 569, 624

# SWIFT MULTI-WAVELENGTH OBSERVATIONS OF NGC5548 : A SEYFERT 1 IN A VEGETATIVE LOW-STATE.

**M.R. Goad, K.L. Page**

Dept. of Physics and Astronomy, University of Leicester, UK

## ABSTRACT

*Swift* observed the archetypal Seyfert 1 galaxy NGC5548 during April-May 2005, as an integral part of a co-ordinated ground- and space-based multi-wavelength monitoring campaign aimed at measuring the interband continuum time-delays, and thereby the mass accretion rate in a small sample of nearby, low-luminosity, radio-quiet AGN. Here we report on the X-ray/ultra-violet/optical temporal and spectral characteristics of this source as observed by *Swift* during the course of this campaign.

Key words: NGC5548; multi-wavelength monitoring.

## 1. NGC5548 : THE ARCHETYPAL SEYFERT 1

NGC5548 is by far the best observed of all nearby AGN. In the ultra-violet and optical bands NGC5548 displays highly correlated continuum and broad emission-line variations which may be used to map the spatial distribution and physical properties of the emission-line gas on size scales (< a few microarcseconds) currently unachievable by more conventional means (ie. direct imaging). In the 3-10 keV band, the high soft-state spectrum of NGC5548 can be fitted with an absorbed power-law of photon index $\Gamma = 1.75$ together with reflection (Pounds et al. 2003) and a weak narrow FeK$\alpha$ emission-line (EW$\sim$60 eV). Below 0.7 keV the X-ray spectrum shows a clear soft-excess which can be best described as either Comptonised thermal emission or enhanced reflection from a highly ionised accretion disc. The X-ray spectral variations appear to be correlated with continuum flux, with the X-ray spectrum being significantly softer when brighter.

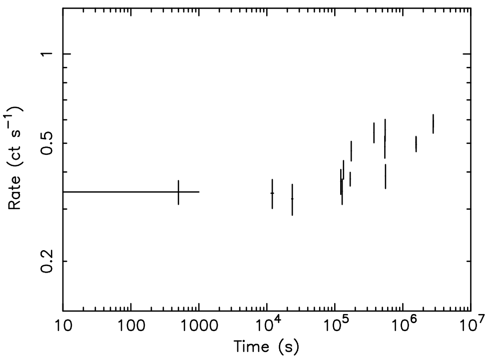


*Figure 1. XRT 0.2-10.0 keV PC mode light-curve for NGC5548.*

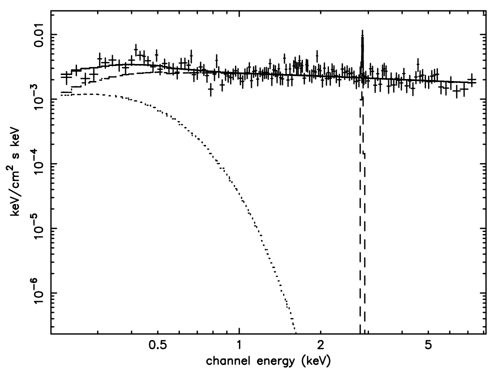


*Figure 2. XRT PC mode spectrum of NGC5548. The spectrum is well-fit by an absorbed power-law $\Gamma = 1.2$, $n_{\rm H} = 1.69 \times 10^{20}$ cm$^{-2}$, a soft excess which we model as a simple blackbody with temperature $kT = 0.1$ keV and an emission-line at 2.85 keV.*

### 1.1. Swift XRT monitoring of NGC5548

*Swift* XRT observed NGC5548 on 14 separate occasions from April 8th to May 10th 2005, with a total on-source exposure of 13 ks. The high count rate, a result of numerous hot pixels, meant that some source on-time was lost due to mode switching (Hill et al. 2004), with the majority of the observations in Photon Counting (PC) mode. The cleaned event lists contain a total on-source exposure of 9.385 ks (PC) and 3.646 ks in Windowed Timing (WT) mode. Figure 1 shows the XRT PC mode 0.2-10 keV light-curve of NGC5548. For clarity all counts in a single observation have been grouped into one bin. The source shows significant variability on timescales of a few hundred seconds, with a mean observed count rate of 0.3 ct s$^{-1}$ and variance 0.44 ct s$^{-1}$. Figure 2 shows the best-fit model to the PC mode data. The spectrum is well-fit by a single absorbed power-law with photon index $\Gamma = 1.2$, $n_{\rm H}$ fixed at the Galactic value of $1.69 \times 10^{20}$ cm$^{-2}$, a soft excess which we model as a blackbody with temperature $kT = 0.1$ keV and an as yet unidentified emission-line at 2.85 keV. We find a mean 2.0-10.0 keV unabsorbed flux of $1.6 \times 10^{-11}$ erg cm$^{-2}$ s$^{-1}$, a factor of 3 lower that that reported in Pounds et al. (2003) for *XMM*/EPIC MOS observations of this source.

## 2. SWIFT UVOT GRISM OBSERVATIONS

*Swift* UVOT grism observations of NGC5548 were taken on 14 separate occasions constituting 8 distinct epochs with a total on-source exposure time of 12 ks (U-grism) and 7 ks (V-grism). The grism observations were processed to remove the modulo-8 fixed pattern noise, cleaned of hot pixels and flat-fielded. Source and background spectra were extracted using the widest possible extraction slit (>35 pixels) avoiding where possible contamination by other sources in the field. For the effective area curves we use those derived from model fits to white dwarf spectra (Wayne Landsman, private communication) taken as part of the UVOT calibration phase verification. We note that individual spectra are affected by 2nd order contamination at wavelengths $>$3600Å (U-grism), $>$5600Å (V-grism).

Figure 3 shows the combined XRT/UVOT U-grism multi-wavelength spectrum for NGC5548.

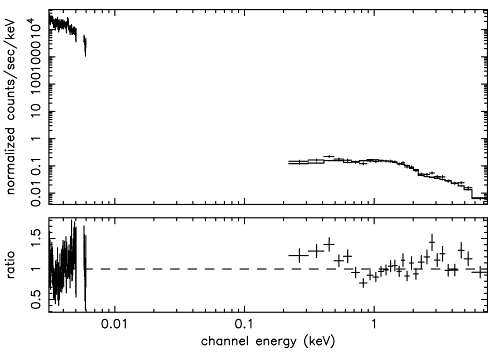


*Figure 3. The combined XRT/UVOT U-grism spectrum of NGC5548. The V-grism observations await further calibration of the effective area file.*

The *Swift* combined multi-wavelength spectrum of NGC5548 is markedly different from that reported in Walter et al. (1993), from simultaneous IUE, GINGA and ROSAT observations, with a considerably harder X-ray photon index ($\Gamma = 1.2$ c.f. 1.9). The X-ray spectrum is also much harder than that reported in Pounds et al. (2003; $\Gamma = 1.75$). This startling result suggests that

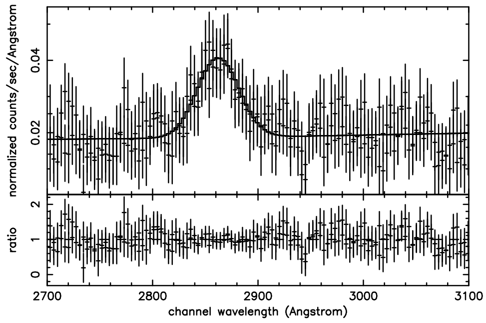


*Figure 4. A fit to the continuum and MgII$\lambda 2800$Å emission-line of NGC5548. The line remains broad (FWHM=4610 km $s^{-1}$).*

NGC5548 has undergone spectral evolution from a high soft-state to a low hard-state. State changes of this nature have been reported for other sources, notably the NLS1 NGC4051 (Pounds et al. 2004). Possible causes include a reduction in the mass accretion rate, and/or obscuration of the steep powerlaw X-ray continuum by intervening gas.

We note that, while the X-ray continuum is relatively weak, the strong UV low ionisation emission-line MgII$\lambda 2800$Å remains broad with a FWHM of 44.6Å equivalent to a velocity of 4610 km s$^{-1}$, broader than that measured for the narrow line in the 1992 *HST*/FOS low-state spectrum (Crenshaw et al. 1993), and similar in width to the semi-broad MgII component reported by Goad et al. (1998). We further note that the MgII line EW (58.2Å) is similar to that derived for the semi-broad component (60.9Å; Goad et al. 1998). Interestingly, the broad UV emission-lines of Ly$\alpha$ and CIV$\lambda 1550$Å are totally absent from an HST/STIS spectrum of NGC5548 taken in early 2004, when the UV continuum was in an historical low-state. In fact the broad lines are so weak that the narrow CIV doublet is clearly resolved. If the frequency of changes in state are related to black hole mass and/or accretion rate, then it is entirely possible that NGC5548 will remain in this vegetative low-state for many years.

## ACKNOWLEDGMENTS

MRG and KLP acknowledge support from PPARC.

## REFERENCES

Crenshaw, D.M. Boggess, A. and Wu, Chi-Chao 1993, ApJ 416, L67.

Goad, M.R. and Koratkar, A. 1998, ApJ 495, 718.

Pounds, K. A.; Reeves, J. N.; King, A. R.; Page, K. L. 2004, MNRAS 350, 10.

Pounds, K. A.; Reeves, J. N.; Page, K. L.; Edelson, R.; Matt, G.; Perola, G. C. 2003, MNRAS 341, 953.

Walter, R.; Fink, H. H. 1993 A&A 274, 105.

# X-RAY EMISSION OF A SAMPLE OF LINER GALAXIES

**O. González-Martín[*], J. Masegosa & I. Márquez**
Instituto de Astrofísica de Andalucía (CSIC), Apdo 3004, 18080 Granada, Spain

## ABSTRACT

We report the results from an homogeneous analysis of the X-ray (ACIS-S/Chandra) data available for a sample of 52 LINER galaxies. The X-ray morphology has been classified attending to their nuclear compactness in the hard band (4.5–8.0 keV), into 2 categories: AGN-like nuclei (with a clearly identified unresolved nuclear source) and Starburst-like nuclei (without a clear nuclear source). 60% of the total sample are classified as AGNs, with a median luminosity of $L_X(2.0 - 10.0\ \mathrm{keV}) = 2.5 \times 10^{40}\ \mathrm{erg\ s^{-1}}$, which is an order of magnitud higher than that for SB-like nuclei. All X-ray morphology, spectral fitting and Color-Color diagrams allow to conclude that a high percentage of LINER galaxies host AGN nuclei.

Key words: galaxies, AGN, LINER, X-ray, Chandra.

## 1. INTRODUCTION

LINERs are very common in the nearby universe. Pioneering works already estimate that at least 1/3 of all the spiral galaxies are LINERs (Heckman et al. 1980). More than two decades after they were clasified, there is still an ongoing strong debate on the origin of the energy source in LINERs, with two main alternatives for the ionizing source being explored: either a low luminosity AGN (Filippenko & Halpern, 1984), or a thermal origin from massive star formation (Filippenko & Terlevich, 1992) and/or from shock heating mechanisms resulting from the massive stars evolution (Fosbury et al. 1978 and Dopita 1976). The search for a compact X-Ray nucleus in LINERs is indeed one of the most convincing evidences about their AGN nature. The excellent resolution of Chandra allows an investigation of the X-Ray nuclear properties of these galaxies.

[*] e-mail address: omaira@iaa.es

## 2. SAMPLE & DATA PROCESS

All the 476 LINER galaxies in the compilation by Carrillo et al. (1999) have been searched by coordinates in Chandra archives. The final sample comprises 52 galaxies with high S/N ratio and optically reidentified.

The data products were analyzed in an uniform, self-consistent, manner using *CXC Chandra Interactive Analysis of Observations* (CIAO ) software version 3.1. The spectral analysis was done with *XSPEC* (version 11.3.2). Level 2 event data from ACIS instrument have been extracted from Chandra archive. Time intervals with high background levels have been excluded.

## 3. SPECTRAL FITTING & LUMINOSITIES

For the source selection, we made use of the nuclear positions from NVSS and 2MASS data base. Nuclear spectra were extracted using regions defined to include as many photons coming from the source as possible, but at the same time minimizing contamination from nearby sources and background. The background region was defined as either a source-free circular annulus or several circles surrounding each source, to take into account the spatial variations of the diffuse emission and to minimize effects related to the spatial variation of the CCD response. In order to use the $\chi^2$ statistic, the data were grouped to include at least 20 counts per spectral bin, before background substraction. For the spectral fitting any events with energies above 10.0 keV or below 0.5 keV have been excluded. The spectra in the 0.5-10.0 keV passband were modelled with a single [MEKAL (ME), Raymond-Smith (RS) or Power Law (PL)] component first and second with a two component [ME+PL or RS+PL] model. Single models are representative for sources dominated either by thermal emission, or non-thermal emission, and two component models correspond to composite objects. Note that number counts were sufficient to employ detailed spectral fitting in 24 out of 52 objects.

The luminosities and fluxes of the individual nuclear

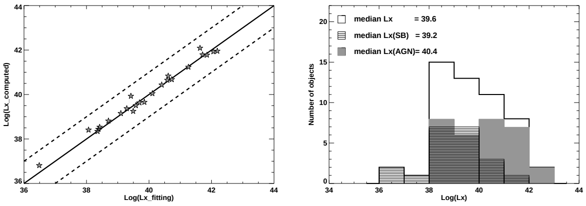


*Figure 1. (left): Luminosity estimation versus real luminosity. (right): Luminosity histogram for the whole sample and clasified objects.*

sources have been computed based on the best-fit model for the 24 galaxies above. We have done an empirical calibration from these 24 objects with high signal-to-noise ratio from flux estimation, assuming an intrinsic power law slope of 1.8, corrected for Galactic absortion. In Fig. 1 (left) our estimated luminosity is plotted versus the value obtained from the direct integration of the spectral energy distribution. The 2.0–10.0 keV luminosities are therefore provided for the whole sample, using the spectral energy distribution fit, when it is available, and from this calibration otherwise.

## 4. MORPHOLOGICAL CLASSIFICATION

We have classified the nuclear morphology attending to the compactness in the hard band (4.5 to 8.0 keV):

- **AGN-like nuclei:** Clearly identified unresolved nuclear source in the hard band. 59.6% (31/52) has been clasified as AGN-like nuclei in our sample and their median luminosity is $L_X(2-10\ \mathrm{keV}) = 2.5 \times 10^{40} \mathrm{erg\ s^{-1}}$.
- **Starburst-like nuclei (SBs):** Objects without a clear nuclear source in the hard band. 40.4% of the sample of LINERs fall in this classification and their median luminosity is $L_X(2-10\ \mathrm{keV}) = 1.0 \times 10^{39}\ \mathrm{erg\ s^{-1}}$.

## 5. COLOR-COLOR DIAGRAMS

The colors of the nuclear sources have been defined as the ratio of counts observed in the following energy bands: 0.6 to 0.9, 0.9 to 1.2, 1.2 to 1.6, 1.6 to 2.0, 2.0 to 4.5, and 4.5 to 8.0 keV. The bands were chosen in order to maximize the detection as well as to obtain a good characterization of the spectra. In the last energy band, the range from 6.0 to 7.0 keV has been excluded to avoid the possible contamination due to the FeK emission line. Therefore, 3 colors has been defined ($Q_A$, $Q_B$ and $Q_C$) as Q=(Hard-Soft)/(Hard+Soft). Sinthetic colors were computed for PL, RS and PL+RS models (see Fig.2). We have only considered the data with error less than 30%. In the $Q_B$ versus $Q_C$ plot (Fig. 2, bottom) we can see that

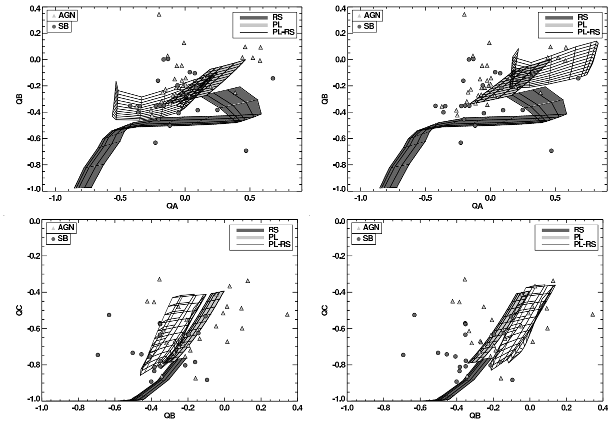


*Figure 2. Color-color diagrams for a RS model , PL model and combinated model for* $N_H = 10^{20}\ \mathrm{cm^{-2}}$ *(left) and* $N_H = 10^{22}\ \mathrm{cm^{-2}}$ *(right). QB versus QA (top) and QC versus QB (bottom).*

$Q_C$ is a good AGN activity estimator. Objects classified as AGN-like nulcei have high values of $Q_C$. However, not only a few objects classified as SB-like have a high $Q_C$, but also most of the objects classified as SB are not in the thermal model grid. Therefore, the use of Color-Color diagrams allows to also analyze the properties of the nuclear sources for which the spectral fitting is not possible.

## 6. CONCLUSIONS

Morphologically, 60% of LINERs have been classified as AGN-like candidates, with median luminosity 10 times higher than that of SB-like objects (Fig. 1, right). Color-Color diagrams are a valid tool to estimate physical parameters, specially interesting to be used when the spectral fit is not possible. Both thermal and non-thermal contributions are required for the spectral fitting of most of the objects. Color-Color diagrams have confirmed this result. An empirical calibration for estimating X-ray luminosities ($L_X(2.0-10.0\ \mathrm{keV})$) has been done based on total counts, which allows a reliable estimation when the spectral fitting is not possible.

## REFERENCES

Carrillo R. et al., 1999, Rev. Mex. A&A, 35, 18.

Dopita M.A., 1976 ApJ, 209, 395.

Filippenko A. V. & Halpern, J. P. 1984 ApJ, 285, 458.

Filippenko, A. V., & Terlevich, R. 1992 ApJ, 397, L79.

Fosbury R. A. E. et al. 1978 MNRAS, 183, 549.

Heckman T.M. et al., 1980, A&AS, 40, 295.

Ho L. C. et al., 1985, ApJ, 549, L51.

# X-RAY PROPERTIES OF MAGNETIC FLARES ORBITING ABOVE THE ACCRETION DISK IN ACTIVE GALACTIC NUCLEI

**R. W. Goosmann[1], M. Mouchet[1,2], M. Dovčiak[3], V. Karas[3,4], B. Czerny[5], A.-M. Dumont[1], and A. Różańska[5]**

[1]LUTH, Observatoire de Paris, 92190 Meudon, France
[2]APC, UMR 7164, Université Denis Diderot, 75005 Paris, France
[3]Astronomical Institute, Academy of Sciences, 141 31 Prague, Czech Republic
[4] Faculty of Mathematics and Physics, Charles University, 180 00 Prague, Czech Republic
[5]Nicolaus Copernicus Astronomical Center, 00-716 Warsaw, Poland

## ABSTRACT

We present radiative transfer modeling of the X-ray emission from magnetic compact flares in Active Galactic Nuclei (AGN). In this model the hard X-ray primary radiation coming directly from the flare source illuminates the accretion disk, which is supposed to stay in hydrostatic equilibrium. A Compton reflection/reprocessed component coming from the disk surface is computed for several flare locations and for different emission directions. This modeling takes into account the variations of the incident radiation across the hot-spot underneath the flare source. Time-dependent spectra and light curves for orbiting flares at various distances from the black hole are computed using a full general relativity ray-tracing technique. The computations are carried out for black holes of different masses and accretion rates. Rms-variability spectra for large flare distributions across the disk are also computed and compared to observed X-ray data of the Seyfert-1 galaxy MCG-6-30-15.

Key words: active galactic nuclei; flares; X-rays.

## 1. INTRODUCTION

X-ray spectra of Active Galactic Nuclei (AGN) exhibit a Compton reflection/reprocessed component due to hard X-ray radiation illuminating an optically thick medium at a temperature of $T = 10^5$ K —$10^6$ K. This medium is commonly identified with the accretion disk (e.g. Collin, 2001). One way to explain the incident hard X-rays is by assuming the existence of magnetic flares similar to solar flares. Due to reconnecting magnetic fields above the disk, compact regions of optically thin plasma are created. These plasma blobs emit the primary X-ray component partly reaching the observer directly, and partly shining toward the disk to form a hot-spot, which emits the Compton reflection/reprocessed component.

We investigate time-dependent properties of the reprocessed spectrum of a hot-spot orbiting around the black hole in Keplerian motion. We take into account the varying ionization profile across the spot and include relativistic effects. Then we perform Monte-Carlo simulations of spot distributions to model the variability spectra of the Seyfert-1 galaxy MCG -6-30-15.

## 2. LOCAL REPROCESSED SPECTRA

We perform detailed radiative transfer simulations using the codes TITAN and NOAR (Dumont et al., 2000; 2003) to obtain the locally emitted Compton reflection/reprocessed spectra across the hot-spot. We assume a plane-parallel atmosphere with the initial density structure of a non-irradiated disk in hydrostatic equilibrium (Różańska et al., 1999). The incident flux spectrum is modeled as a power-law with a photon index of 1.9 over 0.1 keV —100 keV. We limit the size of the hot-spot to a flare half-opening angle of $60°$. The main parameters of the model are the Schwarzschild black hole mass $M$, the Eddington accretion rate $(dm/dt)_{\rm disk}$, the distance $r$ of the spot to the disk center (in $R_{\rm g} = GM/c^2$), and the ratio between incident flux $F_{\rm inc}$ and disk flux $F_{\rm disk}$.
The reflection spectra contain typical features of Compton reflection and reprocessing, like an iron $K_\alpha$-line and a Compton hump. Seen face-on and at high energies, they are similar for all rings. At low energies the spectrum from the spot center is softer than from the limb. For higher inclinations, significant changes in the hard X-rays are observed, with the Compton hump being stronger in the outer parts of the spot than closer-in.

## 3. SPECTRUM DURING THE ENTIRE ORBIT OF A SPOT

We investigate the time evolution for a hot-spot completing a whole Keplerian orbit using the relativistic

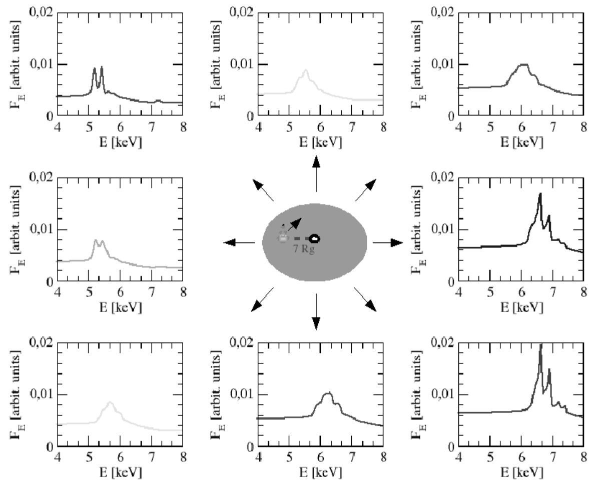


*Figure 1. Profile of the iron line complex as a function of the orbital phase; disk at $i = 30°$; other parameters: $M = 10^8\ M_\odot$, $(dm/dt)_{\rm disk} = 0.001$, $r = 7R_{\rm g}$.*

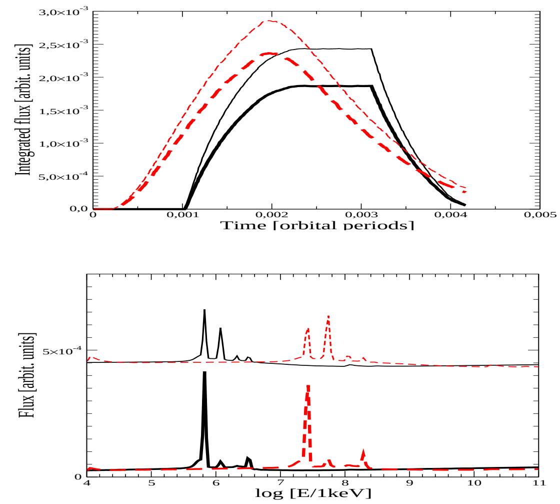


*Figure 2. Light curves (top) and spectra (bottom) at the maximum of the light curves for a short lasting hot-spot at $r = 18R_{\rm g}$ moving toward the observer; disk inclination $i = 0°$ (solid lines), and $i = 60°$ (dashed lines); models: $M = 10^8\ M_\odot$, $(dm/dt)_{\rm disk} = 0.001$ (thin lines, offset), and $M = 10^7 M_\odot$, $(dm/dt)_{\rm disk} = 0.02$ (thick lines).*

ray-tracing program KY (Dovčiak et al., 2004). Although, the accretion disk atmosphere does not remain at the same hydrostatic equilibrium during such a long time scale, the case is instructive to understand the influence of the relativistic effects at various orbital phases.

In Fig. 1 we show the evolution of the iron $K_\alpha$-line complex during one orbit in a disk seen at the viewing angle $i = 30°$. The relativistic effects have a strong impact on the line profile, changing its strength by a factor of 2 and shifting the centroid in a range of 1.5 keV. The different line components can only be resolved at specific orbital phases, and the relative fluxes of these components change with phase, indicating a predominance of highly ionized iron when the spot is moving away from the observer. The model assuming the Schwarzschild metric cannot reproduce a broad red line wing as observed in MCG -6-30-15. This would require a Kerr black hole.

## 4. LIGHT CURVES AND SPECTRAL EVOLUTION OF SHORT-LASTING FLARES

We also consider short lasting flares, having a duration comparable to the light-crossing time of the hot-spot. In this case, the varying ionization and temperature structure across the spot becomes more important for the variability. We investigate the resulting spectra and light curves at two inclinations, a face-on view at $i = 0°$ and an intermediate viewing angle at $i = 60°$. In addition to the previous model with $M = 10^8$ $M_\odot$ and $(dm/dt)_{\rm disk} = 0.001$, we investigate a model with a smaller black hole mass $M = 10^7 M_\odot$, a higher accretion rate $(dm/dt)_{\rm disk} = 0.02$, and a lower ratio $F_{\rm inc}/F_{\rm disk}$. In Fig. 2, we show X-ray light curves, obtained over the energy range of 1.3 keV —82.0 keV, for a short-lasting hot-spot located at the distance $r = 18R_{\rm g}$ and moving toward the observer. The light curves of the two models differ mainly in normalization. Their shape depends on the inclination - no symmetric shape of the light curve can be obtained for a face-on viewing angle. The components of the iron-line indicate a different ionization state of the medium for the two models.

We attempt to model the variability of MCG -6-30-15 sampling random flare distributions across the disk and including relativistic line tracing of the reflected photons. The method is given by Czerny et al. (2004). A good fit of the fast (point-to-point) variability around the iron line can be obtained for 750 flares and a fast-rotating black hole. The observed dip of the rms-spectrum around the $K_\alpha$-line is well reproduced (see Goosmann et al., 2005).

## REFERENCES


Collin S., in "Advanced lectures on the starburst-AGN connection", eds. I. Aretxaga, D. Kunth, R. Mjica, World Scientific, 2001, p. 167

Czerny B., Różańska A., Dovčiak M., Karas V., Dumont A.-M., 2004, A&A, 420, 1

Dovčiak M., Karas V., Yaqoob T., 2004, ApJS, 153, 205

Dumont A.-M., Abrassart A., Collin S., 2000, A&A, 357, 823

Dumont A.-M., Collin S., Paletou F., et al. 2003, A&A, 407, 13

Goosmann R.W., Czerny B., Mouchet M. et al., 2005, A&A, submitted

Różańska A., Czerny B., Zycki P. T., Pojmanski G., 1999, A&A, 305, 481

# X-RAY JETS AND HOTSPOTS IN EXTRAGALACTIC RADIO SOURCES

**M.J. Hardcastle**

School of Physics, Astronomy and Mathematics, University of Hertfordshire, College Lane, Hatfield AL10 9AB, UK

## ABSTRACT

X-ray emission has now been detected from a large number of jets and hotspots of radio galaxies and radio-loud quasars. This paper asks, and attempts to provide answers to, a fundamental question: what are the emission mechanisms for these X-rays, and how do we know?

## 1. LOW-POWER JETS

The X-ray emission from low-power jets in Fanaroff- Riley class I radio sources is thought to be synchrotron. The primary motivation for this belief is the detection of optical synchrotron emission at a level that allows a smooth spectrum to be constructed through the radio, optical and X-ray data (e.g. Hardcastle et al. 2001). Synchrotron X-ray emission, in the typical fields estimated for a low-power jet, implies very highenergy electrons ($\gamma > 10^7$) and correspondingly short loss lifetimes (tens of years). Thus X-ray synchrotron emission traces the current location of high-energy particle acceleration. The fact that the X-ray emission is often associated with the region where the jet is decelerating suggests that the acceleration mechanism must involve the tapping of the jet kinetic energy. In Cen A, the brightest compact X-ray regions are associated with stationary radio knots, suggesting that we are seeing small internal shocks in the jets (Hardcastle et al. 2003). A more diffuse particle acceleration process is probably also required. There are still unanswered questions in this model: why do the overall spectra of jets resemble one-zone synchrotron models, although the acceleration mechanism must be very localized? And what determines the characteristic steep high-energy spectral index ($\alpha$ = 1.0–1.5)? But the basic picture seems clear: these low-power radio galaxies at least have synchrotron jets.

## 2. HIGH-POWER JETS

The situation is less clear for the jets in powerful FRII radio galaxies and quasars. The earliest new discoveries of X-ray jets in this type of object (e.g. Schwartz et al. 2000) were unlike the FRI jets in that their radio through X-ray spectra were not consistent with a one-zone synchrotron model: where optical constraints existed, they lay below a straight line connecting the radio and X-ray fluxes. This led to the widespread adoption of the beamed inverse Compton model for these jets (Tavecchio et al. 2000; Celotti et al. 2001). In this model the jets are travelling at highly relativistic speeds and the CMB's energy density in the jet frame is boosted by a factor $\sim \Gamma^2$, where $\Gamma$ is the bulk Lorentz factor. In this model the electrons producing the X-rays by the inverse-Compton process have very low energies, and the electron spectrum must extend down to $\gamma \sim 10$. Typical bulk Lorentz factors needed to produce the X-rays are $\sim 10$, similar to what is observed on pc scales.

One problem with this model is that it is inconsistent with the existing constraints on the bulk speeds of the kpc-scale jets from beaming studies. These tend to give bulk speeds of $\sim 0.6c$ (e.g. Wardle & Aaron 1997, Hardcastle et al. 1999, Mullin et al. in prep.). The distribution of observed jet parameters is inconsistent with even moderately high jet speeds. If the core-dominated quasars that show X-ray jets are the same objects as the lobe-dominated radio galaxies that dominate the radio samples, then there must be some velocity structure in the jets, e.g. a fast central spine with $\Gamma \sim 10$ and a slower sheath with $v = 0.5c$. More recently some FRII sources have been shown to have jet X-ray components that are likely to be synchrotron in origin: examples include Pictor A (Hardcastle & Croston 2005) and 3C403 (Kraft et al. 2005). So it is clear that the X-ray emission in these sources can be synchrotron emission. In the beamed inverse-Compton model, perhaps the X-ray synchrotron emission originates in the slow sheath.

Is there any way of testing the beamed inverse-Compton model? One interesting approach comes from considering those jet X-ray sources that can be resolved into more than one jet X-ray component. The bulk Lorentz factor can then be calculated for each X-ray region, allowing us to plot quantities as a function of position along the jet. I have carried out this analysis for a small sample of objects from the literature (Hardcastle, 2005, MN submitted. Almost all of these show a systematic de-

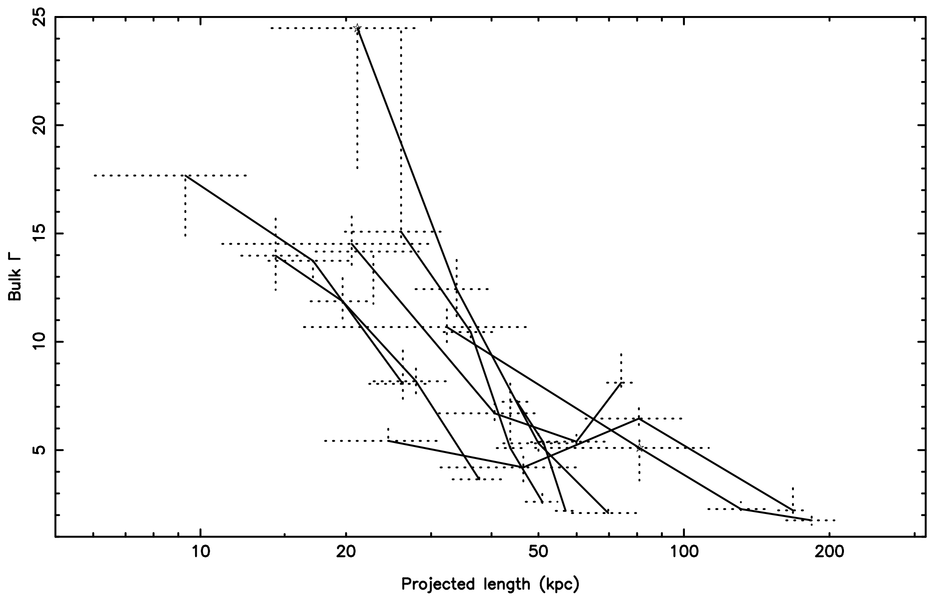


*Figure 1. Bulk Lorentz factor as a function of projected distance for 9 X-ray jet sources, showing apparent jet deceleration.*

crease in X-ray to radio ratio. It has already been pointed out (e.g. Georganopoulos & Kazanas 2004) that this obvious strong trend could be attributed to bulk deceleration: however, this has so far not been tested quantitatively against real data until now. My analysis (Fig. 1) shows that the required bulk Lorentz factor (for a fixed but reasonable choice of angle to the line of sight, 4°) systematically decreases as a function of distance along the source, not just in general, but also for most individual sources. The decrease in Γ is large, so that there are some interesting physical problems involved in getting the jet to decelerate (particularly as the deceleration must happen on scales of 100 kpc–1 Mpc). More importantly, there is no corresponding evidence for deceleration in the jets in radio galaxies on these scales – if the spine-sheath model discussed above were true, then we would expect the sheath to decelerate, with observable changes in jet prominence as a function of length, which are not seen.

If deceleration is not viable, what is? Possible ways to explain the radio/X-ray properties of these jets in the framework of the beamed IC model include changing magnetic field strength as a function of length and/or a synchrotron contribution to the inner part of the jet. Such a synchrotron model would not be a one-zone model, but we know (Jester et al. 2002) that the optical-UV spectrum of the best-studied object in this sample, 3C 273, is not described by a one-zone model anyway. There is some evidence for X-ray synchrotron emission in the hotspots of powerful sources (Hardcastle et al. 2004) although space restrictions preclude a detailed discussion here. At present we have to conclude that the emission mechanism for the jets in these sources is not clear, although inverse-Compton is a required process that must come to dominate at large redshifts. More work is needed before inverse-Compton jet X-ray emission can reliably used as a diagnostic of jet physical conditions.

## REFERENCES

Celotti, A., Ghisellini, G., & Chiaberge, M., 2001, MNRAS, 321, L1

Georganopoulos, M., & Kazanas, D., 2004, ApJ, 604, L81

Hardcastle, M.J., & Croston, J.H., 2005, MNRAS in press, astro-ph/0507694

Hardcastle, M.J., Alexander, P., Pooley, G.G., & Riley, J.M., 1997, MNRAS, 288, 859

Hardcastle, M.J., Alexander, P., Pooley, G.G., & Riley, J.M., 1999, MNRAS, 304, 135

Hardcastle, M.J., Birkinshaw, M., & Worrall, D.M., 2001, MNRAS, 326, 1499

Hardcastle, M.J., Harris, D.E., Worrall, D.M., & Birkinshaw, M., 2004, ApJ, 612, 729

Hardcastle, M.J., Worrall, D.M., Kraft, R.P., Forman, W.R., Jones, C., & Murray, S.S., 2003, ApJ, 593, 169

Jester, S., Röser, H.-J., Meisenheimer, K., & Perley, R., 2002, A&A, 385, L27

Kraft, R.P., Hardcastle, M.J., Worrall, D.M., & Murray, S.S., 2005, ApJ, 622, 149

Schwartz, D.A., et al., 2000, ApJ, 540, L69

Tavecchio, F., Maraschi, L., Sambruna, R.M., & Urry, C.M., 2000, ApJ, 544, L23

Wardle, J.F.C., & Aaron, S.E., 1997, MNRAS, 286, 425

# INTEGRAL AND BLAZARS

**R. Hudec**[1], **F. Munz**[1], **M. Basta**[1], **P. Kubanek**[1,2], **E. Pian**[3]

[1]Astronomical Institute, Academy of Sciences of the Czech Republic, CZ–251 65 Ondrejov, Czech Republic

[2]ISDC, Versoix, Switzerland

[3] INAF, Trieste, Italy

## ABSTRACT

We refer on analysis of the ESA INTEGRAL satellite data for blazars, promising sources to be observed during their active states.

Key words: Active Galactic Nuclei, Blazars, INTEGRAL.

## 1. INTRODUCTION

Blazars represent the most extreme class of active galaxies. They are observed in all wavelength bands - from radio through VHE gamma frequencies, with maximum spectral output and largest variability often at gamma ray energies. It is obvious that blazars represent suitable targets for INTEGRAL satellite (Winkler et al. 2003) especially during active states (flares).

## 2. INTEGRAL OBSERVATIONS

The INTEGRAL observations are divided into the following categories: (i) AO-1,2,3 Program (allocated pointed observations), (ii) Core Program CP (Galactic Plane Scans, Galactic Center Deep Exposure,...), and (iii) Objects inside FOV of AO-1,2,3 observations. Blazars in the INTEGRAL Galactic Plane Scans (GPS) represent a promising group of objects for the study within the INTEGRAL CP.

The GPS zone is usually neglected by extragalactic astronomers due to heavy obscuration: in optical, ∼20% of the sky is obscured by our Galaxy, while the gamma–ray telescopes on board INTEGRAL allow detectability of up to few mCrabs in the most exposed GPS regions. Seven optically bright (with V$\leq$17 mag, to be detected by the INTEGRAL OMC camera) blazars were

*Figure 1. The IBIS INTEGRAL telescope total exposure times for blazars, CP data, revolutions 1-250.*

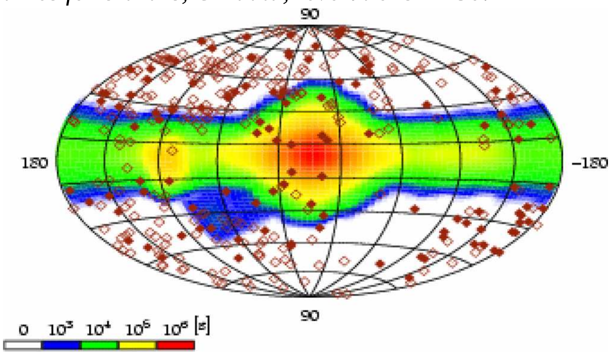


*Figure 2. The IBIS INTEGRAL telescope total exposure times for blazars, all data, revolution 1-250.*

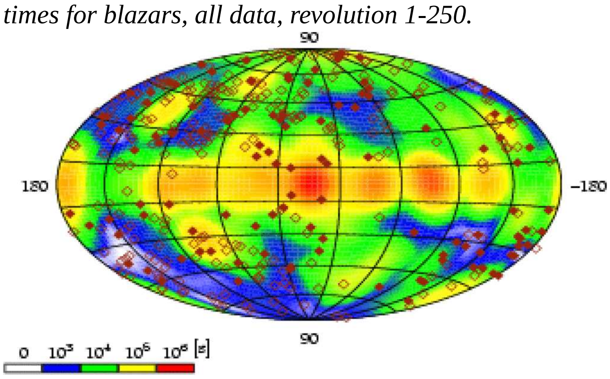

identified within galactic scans of INTEGRAL, namely: 1ES 0647+250, PKS 0823-223 (no gamma from EGRET, grav. lensing candidate), 1ES 2344+514 (TeV gamma ray source, very close), 8C 0149+710 (BL Lac candidate?), 4C 47.08, 87GB 02109+5130 (poorly understood blazar, TeV candidate), and BL Lac (the prototype). While the prototype object BL Lac is well studied, most of the INTEGRAL GPS blazars are poorly investigated and poorly understood so far. The study with Sonneberg Observatory Archival Plates reveals that most of these objects are optically variable, hence a gamma ray variability can be expected. Below the detection limit of the INTEGRAL OMC on board camera is blazar NRAO530 (1730-130), which is an example of blazar with violent optical activity (4 mag within 1 month). In flare, the object is expected to be much brighter also in gamma. This strengthens the role of optical monitoring and ToO program - the flare can be recognized by optical monitoring with small (D $\sim$50 cm) telescopes. All the above mentioned blazars in INTEGRAL GPS have been investigated with INTEGRAL CP data (IBIS and JEM-X telescopes). We have no positive detection by high energy instruments on board INTEGRAL yet (except marginal detection of 1ES 0647+250). The targets quiet level is still below the sensitivity threshold of the instruments. However, the positive detection may be possible in the future as (i) there will be more cumulative time available and (ii) the probability to see a blazar during a flare (and hence much brighter) will also increase with time. Additional blazars have been identified in the fields represented by the AO-1 and AO-2 observations of other scheduled targets, covered by up to 400 ksec cumulative exposure time. The analysis of these objects is in progress. There is a hope that one can detect additional gamma-ray blazars (to the list detected by EGRET) not detected by EGRET due to the fact that they were inactive during the time period of EGRET observations but active during the INTEGRAL coverage.

Regarding the pointed observations of blazars by INTEGRAL, the AO-2 ToO blazar observation No. 220049 by Pian et al. (2005) has provided promising results. This collaborative proposal was based on extended optical and/or X-ray monitoring (RXTE ASM and others) of flaring activity of a large list of blazars and, alternatively, on soft gamma-ray monitoring by INTEGRAL itself (serendipitous detection of a flaring blazar in the IBIS FOV). Then ToO INTEGRAL observation was activated meeting the trigger criteria (major flaring event). Blazar S5 0716+714 was the target of this ToO observation. This is a BL Lac object, intensively monitored at radio and optical wavelengths. The ToO was triggered by optical activity - 2 outbursts up to the extreme level of R = 12.1 mag (historical maximum, light increase by 1 mag in 2 weeks and 2 magnitudes in 4 months) and, consequently, the INTEGRAL ToO observation was performed in the time interval 2004 April 2–7 (Pian et al. 2005). More recently, an INTEGRAL AO-3 ToO observation of 3C454.3 (z=0.859) was performed, with preliminary results given by L. Foschini et al. 2005 (PI E. Pian with a large collaboration). This ToO was triggered by high optical (T. Balonek, VSNET alert) and X-ray (BAT Swift) activity of the source. The INTEGRAL observation started 2005 May 15, at 18:40 UT, with exposure of 200 ksec. The source was clearly detected by IBIS/ISGRI in the 20-40 and 40-100 keV energy bands, with a significance of 20 and 15 sigma. This confirm the importance of blazar observations by INTEGRAL of blazars in flaring state (ToO observations).

*Figure 3. The optical light curve of 3C454.3 around the time of the INTEGRAL AO–3 ToO observation*

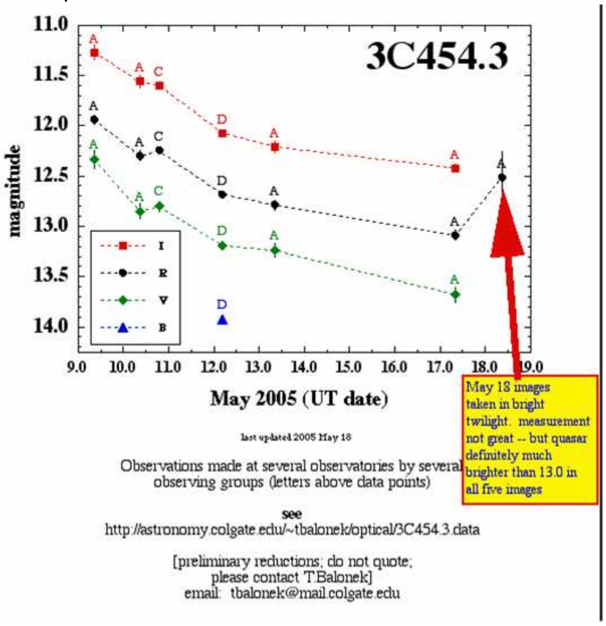


## 3. ACKNOWLEDGMENTS

The International Gamma-Ray Astrophysics Laboratory (INTEGRAL) is an European Space Agency mission with instruments and science data center funded by ESA member states (especially the PI countries: Denmark, France, Germany, Italy, Spain, Switzerland), Czech Republic and Poland, and with the participation of Russia and the USA. We acknowledge the suppport provided by ESA Prodex (project 90108) and ESA PECS (project 98023). This study is partly linked to the grant A3003206 by the Grant Agency of the Academy of Sciences of the Czech Republic.

## REFERENCES

Winkler, C. et al. 2003, A&A, 411, 7.

Foschini, L. et al. 2005, ATEL 497.

Pian, E. et al. 2005, A&A 429, 427.

# ASTROPHYSICS WITH DIGITIZED ASTRONOMICAL PLATES: SEARCH FOR SUPERMASSIVE BLACK HOLE BINARIES

**R. Hudec**[1], **M. Basta**[1], **L. Hudec**[1,2]

[1]Astronomical Institute, Academy of Sciences of the Czech Republic, CZ–251 65 Ondrejov, Czech Republic

[2]Department of Informatics, Faculty of Mathematics and Physics, Charles University, Prague, Czech Republic

## ABSTRACT

In the history of X–ray astronomy, astronomical archival plates, mostly those from two major plate collections (Harvard and Sonneberg) helped to identify and to analyse first stellar X–ray sources. Novaday, there are efforts to digitise the astronomical plate archives and to use these data for various scientific projects. These data may easily provide monitoring over very extended time intervals (up to more than 100 years) with limiting magnitudes up to 23 and are expected to provide very valuable supplementary information to recent and even to future satellite data from various spectral bands.

Key words: Astronomical archives, astronomical plates, astronomical photography.

## 1. INTRODUCTION

At the early stages of stellar X–ray astronomy, astronomical archival plates helped to identify and to analyse optical counterparts of celestial X–ray sources such as Sco X-1/V 818 Sco, Her X-1/HZ Her, and others (e.g. Hudec and Wenzel, 1976, 1986, Hudec and Meinunger, 1977). The nearly 3 millions astronomical archival plates located at different observatories (Hudec, 1999) still represent a unique database for various scientific projects including X–ray astronomy as well as satellite experiments. The plates represent thousands of exposures for any celestial position, reaching monitoring intervals of up to few years of continuous monitoring - i.e. tens of thousands of hours. Each of the plates cointains valuable information about thousands and often even tens of thousands star images recorded on the plate. The photographic sky monitoring is available for more than 100 years and some of the archives have very high quality plates with limiting magnitudes of up to 20 ... 23 (direct imaging) and /or 17....19 (spectral with objective prism). However, only the recent development of photographic scanners and powerful computers allows an efficient extraction of scientific data. Some of the archives already have devices for digitisation of plates and few of them have already started extended digitisation of the plates (e.g. Sonneberg Observatory - about 180 000 plates already scanned). There are attempts to create an European Plate Centre in Brussels, Belgium (the UDAPAC project, see de Cuyper et al., 2001). Analogous efforts exist also in the US (Castelaz and Cline, 2005).

## 2. THE SCIENCE WITH ASTRONOMICAL PLATES

Archival and sky patrol plates represent a valuable tool in investigations and identifications of various types of high energy sources such as blazars/quasars, X-ray binaries, X- and gamma-ray transients, cataclysmic variables, etc. Many of X-ray sources emit also optical light and can be hence analysed on archival plates. It is obvious that the automated evaluation of sky patrol plates has large potential in: (i) providing extended (more than 10 years) monitoring intervals with good (daily or weekly measurements) sampling, (ii) allowing long-term evolution and changes to be studied, (iii) searching for optically variable AGNs-QSOs-blazars and other objects, (iv) providing their light curves with good sampling, (v) searching for their flares, (vi) providing simultaneous and quasi-simultaneous optical data for satellite campaigns, even back in time, (vii) monitoring of objects as base for proposals for ToO (Target of Opportunity) for satellite high energy observations, and (viii) providing extended database for identification and classification of sources.

The detection and investigation of very large amplitude flares from AGNs may serve as an example. There is increasing evidence that some AGNs may exhibit very large amplitude flares exceeding mag 10 (Hudec et al. 1999). These large flares are however rare so very large fractions of monitoring times (of order of thousands hrs or more) are required to detect them. This can be accessed easily on plates but hardly by other methods.

Identification of high-energy sources is another example of use of archival plates. The recent high-energy satellites, especially those observing in X-rays, provide a large number of detected sources. The identification of them is an important but not easy task. Astronomical plate archives can help essentially. Some of the X-ray objects detected by recent analyses can be very easily rediscovered and further studied - even back in the history - on high quality direct and spectral archival plates.

## 3. THE SOFTWARE FOR PLATE ARCHIVES

Until recently, the data recorded on archival plates were accessible only by special procedures. The recent wide digitisation of plate collections offers significantly easier access by computers. However, there is still a gap between the digitised archive and the scientific use. Special software is required to fill this gap. The robust program able to provide realiable and automated astrometry and photometry of all objects on the plates is a difficult tasks and still a matter of further development.

The second type of plate software is specific to particular plate type and particular project. For example, if we search for optical prompt emission (including orphans) from GRBs, we need to look for short-living transient phenomena lasting minutes or less, analogous to the event observed for the GRB990123. However, on long-exposed deep images and plates, it is very difficult to look for brief transients since the OT image is hidden by typically tens to hundreds of thousands stellar images with similar appearance. The methods of comparing plates and/or comparison with catalogues is still not very effective and reliable. We have developed novel method using multiply exposed astronomical plates and based solely on the information recorded in the plate itself. Such plates are available and are relatively numerous in various sky plate archives, e.g. at the Royal Observatory Brussels. These plates contain several (typically 2 to 10) identical star field images on the same plate. This means, each star inside the FOV of the telescope, is represented several times. Such plates have been obtained by multiple exposures on the same plate with tiny shifts between the exposures. It is difficult to find transient objects on these plates by classical methods. However, using digitisation, dedicated novel algorithms and software programs, and powerful computers, it is relatively easy, effective and reliable to identify the OT candidates.

## 4. SEARCHES FOR SUPERMASSIVE BLACK HOLE BINARIES

The project of searches for supermassive black hole binaries represent another example of an dedicated scientific project of recent astrophysics based on the astronomical plates. In this project, we have gathered data from the literature and observational campaigns in order to establish long-term optical light curves of the selected blazars - binary black hole candidates - to study periodic behavior in their light curves and other interesting features (intense outbursts, flares, quiescent level behavior). However, there are several crucial data gaps that disable to confirm periodicity or a BBH model (that has already been built up for several of these blazars). Therefore we intend to go to databases of astronomical plates (e.g. Sonneberg Observatory, Germany (about 280,000 plates), Harvard College Observatory, USA (about 500,000 plates),UKSTU plate collection ROE Edinburgh, UK (18,000 very deep plates), and Observatory Leiden, NL (40,000 plates)) to fill in these gaps. Within this project, we intend to reach the following results: (i) improve historical light curves of candidates, (ii) periodicity and light curve analysis, (ii) confront the new light curve of the selected blazars with the corresponding theories, (iii) establish a detailed model at least of one of the candidates, (iv) draw statistical conclusions, (v) provide the data to wide scientific community. The nature of the project requires the availability of data sets covering very long time intervals, hence digitized archival plates are the obvious choice (Hudec, 1999).

## 5. CONCLUSION

The astronomical plate archives represent a very important data source for various aspects of astrophysics in general and for X–ray astronomy in particular. The recent efforts to scan the plates and to develop related software packages for scientific evaluation of plates represent a promising basis for future computer-based analyses.

## 6. ACKNOWLEDGMENTS

We acknowledge the support provided by the Grant Agency of the Academy of Sciences of the Czech Republic, grant A3003206.

## REFERENCES

Hudec R., Vrba F. J. and Luginbuhl C. B. 1999, BL Lac Phenomenon, ASP Conference Series, 159, 115.

Hudec R. and Wenzel W. 1976, Bull. Astron. Inst. Czech., 27, 325.

Hudec R. and Wenzel W. 1986, Astron. Astroph., 158, 396.

Hudec R. and Meinunger L. 1977, Mitt. Veraend. Sterne, 8, 10.

Hudec R. 1999, Acta Historica Astronomiae, 6, 28.

Castelaz M. V. and Cline J. D. 2005, Bull. Amer. Astron. Soc., 206, 2404.

de Cuyper J.-P. et al. 2001, ASP Conference Proceedings, 238, 125.

# X-RAY EMISSION PROPERTIES OF LARGE SCALE JETS, HOTSPOTS AND LOBES IN ACTIVE GALACTIC NUCLEI

**Jun Kataoka**[1] **and Łukasz Stawarz**[2]

[1]Tokyo Institute of Technology, Meguro, Tokyo, Japan
[2]Max-Planck-Institut fur Kernphysik, Heidelberg, Germany

## ABSTRACT

We examine a systematic comparison of jet-knots, hotspots and radio lobes recently observed with $Chandra$ and $ASCA$. The data was compiled at radio (5 GHz) and X-ray frequencies (1keV) for more than 40 radio galaxies. We examined three models for the X-ray production: synchrotron (SYN), synchrotron self-Compton (SSC) and external Compton on CMB photons (EC). For the SYN sources, X-ray photons are produced by ultrarelativistic electrons with energies $10-100$ TeV that must be accelerated in situ. For the other objects, a simple formulation of calculating the "expected" SSC or EC fluxes under an equipartition hypothesis is presented. We confirmed that the observed X-ray fluxes are close to the expected ones for non-relativis tic emitting plasma velocities in the case of radio lobes and majority of hotspots, whereas considerable fraction of jet-knots is too bright at X-rays to be explained in this way. We concluded, if the inverse-Compton model is the case, the X-ray bright jet-knots are most likely far from the minimum-power condition. We however prefer the other possibility, namely that the observed X-ray emission from all of the jet-knots is synchrotron in origin.

Key words: galaxies: jets — magnetic fields — radiation mechanism: non-thermal.

## 1. INTRODUCTION

The excellent spatial resolution of $Chandra$ X-ray Observatory has opened a new era to study the large scale jets in powerful extragalactic radio sources. More than 40 radio-loud AGNs are known to possess X-ray counterparts of radio jets on kpc to Mpc scales (Harris & Krawczynski 2002, Kataoka & Stawarz 2005). Bright X-ray knots are most often detected, but the X-ray emissions from the hotspots and radio lobes are also reported in a number of FR II radio galaxies and quasars. It is believed that the relativistic jet is decelerated in a hotspot converting part of its energy into relativistic electrons and part in magnetic field. Then the shocked plasma moves inside the head region just behind the hotspot, and expands almost adiabatically to form diffuse, extended radio lobes. Even though this picture appears to be simple, much of the fundamental physics behind it remains unclear (see, e.g., recent monograph by de Young 2002).

Unfortunately, present radio-to-X-ray observations are not sufficient to discriminate conclusively between different models proposed in order to explain multiwavelength emission of the large-scale structures of powerful radio sources, and of their kpc/Mpc jets in particular. However, we believe that a systematic comparison between jet-knots, hotspots, and lobes will provide important clues to dynamics and the physics of large scale jets, and to put some constraints on the theoretical models.

## 2. DATA AND MODEL APPLICATION

We collected all existing data of "X-ray jet sources" at well sampled radio (5 GHz) and X-ray (1 keV) frequencies and analyzed them in a systematic manner (see Kataoka & Stawarz 2005). This gives a large number of objects known to us as of 2004 June, which contains 44 X-ray jet sources (56 jet-knots, 24 hotspots, and 18 radio lobes). Fig 1 presents the correlation between radio and X-ray luminosities, in two dimensional space. One finds several important tendencies which cannot be accounted by the sampling bias effect. First, hotspots and radio lobes occupy only the high-luminosity part of the plot, namely $\geq 10^{40}$ erg s$^{-1}$. Secondly, low-luminosity hotspots tend to be brighter in X-ray, as has been pointed out by Hardcastle et al. (2004). Thirdly, $L_{\rm R} \geq L_{\rm X}$ for most of the hotspots and radio lobes, but most of the jet-knots show an opposite trend.

In order to determine the X-ray emission properties of large scale jets, we first derive a simple formulation of computing an equipartition magnetic field strength $B_{\rm eq}$ from an observed radio flux $f_{\rm R}$ measured at a radio frequency $\nu_{\rm R}$. Next, we calculate the "expected" inverse

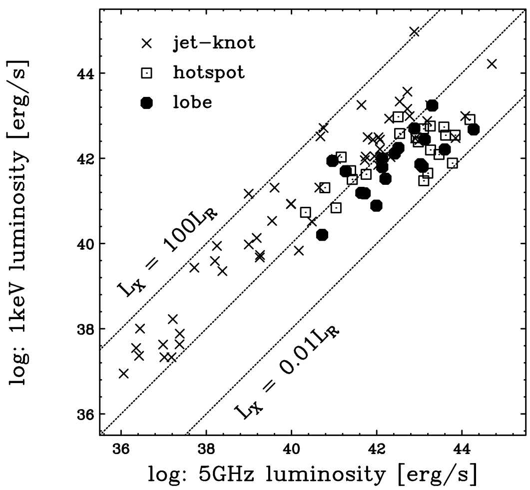


*Figure 1. Relation between $L_{5\mathrm{GHz}}$ and $L_{1\mathrm{keV}}$*

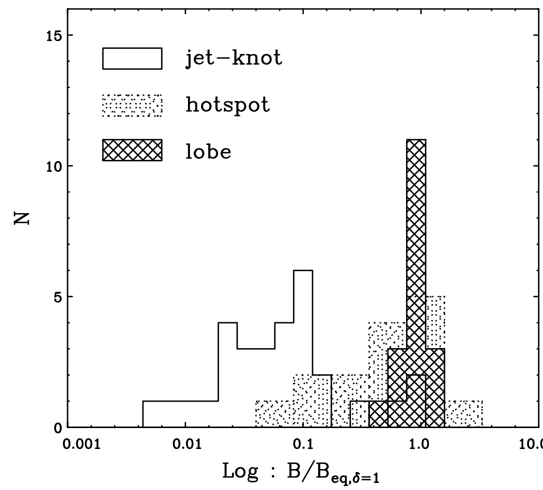


*Figure 2. Distribution of the ratio between the magnetic field $B$ (for $\delta$ = 1) and the equipartition value $B_{\mathrm{eq},\,\delta=1}$.*

Compton luminosities for $B_{\mathrm{eq}}$, to compare them with the observed X-ray luminosities. In the analysis, we include possible relativistic bulk velocity of the jet plasma. Taking the obtained results into account, and analyzing additionally the observed broad-band spectral properties of the compiled sources, we follow the "conservative" classification of the compiled X-ray sources into three groups, namely (i) synchrotron involving single/broken power-law electron energy distribution (SYN), (ii) synchrotron self-Compton (SSC) and (iii) external Compton of CMB photons (EC). Full details are given in Kataoka & Stawarz (2005).

## 3. DISCUSSION

One formal possibility of understanding extremely bright jet-knots is that equipartition hypothesis may not be valid in the considered jet-knots. For a given synchrotron luminosity $L_{\mathrm{sync}} \propto u_{\mathrm{e}} u_B$ and for a given emitting region volume $V$, an expected SSC luminosity is $L_{\mathrm{SSC}} \propto u_{\mathrm{e}}$. We therefore expect ratio $R_{\mathrm{SSC}} \propto L_{\mathrm{SSC}}^{-1} \propto u_B$. Similarly, for the EC case, $R_{\mathrm{EC}} \propto L_{\mathrm{EC}}^{-1} \propto u_B$. Hence, in both models, the expected X-ray luminosity will be increased by decreasing the magnetic field strength. Fig 2 shows the ratio of $B$ to the equipartition value. Interestingly, $B$ in the lobe and most of the hotspots are almost consistent with the equipartition ($B/B_{\mathrm{eq},\delta=1} \sim 1$), whereas that of the non-SYN jet-knots and of some of the hotspots is much weaker from what is expected ($B/B_{\mathrm{eq},\delta=1} \sim$ 0.01−0.1). It must be noted, however, that the idea of sub-equipartition magnetic field is often rejected since it implies a very high kinetic power of the jets.

As an alternative, we also consider a case when the difference between the "expected" and "observed" X-ray fluxes is due to the relativistic beaming effect, and the minimum-power condition is fulfilled. Again, the lobes and the hotspots exhibit relatively narrow distribution at $\delta \sim 1$, whereas for most of the jet-knots large beaming factors of $\sim$ 10 are required. Such a large beaming factor is indeed expected for some of blaza-type objects, but is very unlikely for most of the radio galaxies observed with $Chandra$. Furthermore, it is well known that the $VLA$ studies of the large-scale jets in quasars and FR IIs indicate that bulk Lorentz factors of the radio-emitting plasma in these sources cannot be much greater than $\Gamma_{\mathrm{BLK}} \sim 3$ (Wardle & Aaron 1997). If one insists on applying the homogeneous one-zone model (as a zero-order approximation), as presented in this paper, self-consistency requires a consideration of $\Gamma_{\mathrm{BLK}} \leq 5$. In such a case, a departure from the minimum power conditions within the non-SYN X-ray jets is $inevitable$.

We have discussed two different versions of the EC model to account for extremely bright X-ray jet-knots: (1) non-equipartition case and (2) significant relativistic beaming case. Both of these options are in many ways problematic. We may therefore suggest a new idea that the X-ray photons from the powerful quasar jets are not inverse-Compton, but the synchrotron emission in origin. Recent detailed re-analysis of the $Chandra$ data for 3C 120, again "conservatively" classified as an EC source, strongly support this idea (Harris et al. 2004).

## REFERENCES

De Young, D. S., 2002a, *'The Physics of Extragalactic Radio Sources'*, University of Chicago Press

Hardcastle, M. J., et al, 2004, ApJ, 612, 729

Harris, D. E. & Krawczynski, H. 2002,ApJ, 565, 244

Harris, D. E., Mossman, A. E., & Walker, R. C. 2004 , ApJ, 615, 161

Katakoka, J. & Stawarz, L. 2005, ApJ, 622, 797

Wardle, J. F. C., & Aaron, S. E., 1997, MNRAS, 286, 425

# ACTIVITY OF BL LACERTAE DURING 1997-2005:LONG-TERM AND INTRADAY VARIABILITY

**O.M. Kurtanidze[1,2,3], M.G. Nikolashvili[1,2], S.M. Chanturiya[1], G.N. Kimeridze[1], L.A. Sigua[1], B.Z. Kapanadze[1], R.Z. Ivanidze[1], G.N. Jimsheleishvili[1], N.B. Ograpishvili[1], and D.G. Zarqua[4]**

[1]Abastumani Observatory, 383792 Abastumani, Georgia
[2]Landessternwarte Heidelberg, Koenigstuhl, D-69117 Heidelberg, Germany
[3]Astrophysikalisches Institute Potsdam, 14482 Potsdam, Germany
[4]Physics Department, Sukhumi Branch of Tbilisi State University, Tbilisi, Georgia

**ABSTRACT**

We present the results of optical observations of BL Lacertae from August 1997 to May 2002 carried out with ST-6 CCD Camera attached to the Newtonian focus of the 70-cm meniscus telescope of Abastumani Observatory.

The long-term, intraday and intrahour variabilities of BL Lacertae were studied on the bases of 600 and 440 nights, respectively. The variability patterns showed by BL Lacertae are very complex.

The maximum amplitude of the long-term variability in B band equals to $3^{m}_{\cdot}0$ (rms=0.03), while the variation in V and R bands are within $2^{m}_{\cdot}71$ (0.02) and $2^{m}_{\cdot}53$ (0.01), respectively. This means that variations are larger at shorter wavelength or the object become bluer in the active phase.

It were also demonstrated that BL Lacertae shows intraday variability within $0^{m}_{\cdot}30$ (0.02), while intrahour variability within $0^{m}_{\cdot}10$ (0.01) magnitudes.

Key words: BL Lacertae; CCD Photometry; Variability.

## 1. INTRODUCTION

BL Lacertae is the prototype of one of the most extreme subclass of AGNs. It was discovered in 1929 by Guno Hoffmeister, who found it to vary by more than a factor two in one week and classified it as a short period variable star (Hoffmeister, 1990). Since its identification as an extragalactic source it was the subject of numerous studies in many frequency bands.

Historically, BL Lac is known to show $5^{m}_{\cdot}0$ variation in optical band with episodic outbursts (Fan (1998), Webb (1988), Maesano (1997)). Maximum variation in the infrared K band is $3^{m}_{\cdot}0$ (Fan, 1999). During the summer 1997 outburst it showed a very strong activity including intranight ones (Nesci (1998), Clements (2001)). The strong activity was also detected in the radio, X-ray and $\gamma$-ray bands (Bloom (1997), Sambruna (1999), Madejiski (1999), Tanihata (2000), Bottcher (2000)).

| Observational Periods | | | | | Nights | $\delta m(R)$ |
|---|---|---|---|---|---|---|
| Aug | 1997 | - | May | 1998 | 74 | 2.53 |
| May | 1998 | - | Aug | 1998 | 39 | 1.10 |
| Aug | 1998 | - | Jan | 1999 | 50 | 0.80 |
| July | 1999 | - | Aug | 1999 | 78 | 0.90 |
| Aug | 1999 | - | June | 2000 | 72 | 1.85 |
| June | 2000 | - | Nov | 2000 | 69 | 1.40 |
| May | 2001 | - | Nov | 2001 | 83 | 1.80 |

## 2. OBSERVATION AND DATA REDUCTION

We are intensively monitoring BL Lacertae at Abastumani Observatory since Aug 1997, when it remained in a high state for more than two months. Rapid and large amplitude flux variations characterized the source during this period. Here we present observations carried out from Aug 1997 to Nov 2001. All observations were carried out with 70-cm meniscus telescope and ccd camera ST-6 attached to the Newtonian focus (1/3). To study the long-term variability we observed BL Lacertae during 317 nights, collected 320 frames in every of the BVI bands and 465 frames in R band. More than 16 000 frames were obtained in R band during 259 nights to study intraday variability (Wagner (1995), Wagner (2001)) and intrahour variability ( (Miller, 1989)).

The duration of observational runs varied from two hours to six hours. The exposure times varied from 60 to 180 sec depending on the brightness of the object and the filter used. Instrumental differential magnitudes were calculated relative comparison stars C and H, that have nearly the same colours as the object under study (Smith et al. 1985). The images are reduced using Daophot-II (Stetson, 1987). The highest differential photometric accuracy reached in R band is $0^{m}_{.}005$ (rms) magnitude at $m_r$=$14^{m}_{.}00$ during 180 sec. Magnitudes are calculated relative comparison stars C and H, that have nearly the same colours as the object under study (Smith et al. 1985). To eliminate the effects of seeing induced spirious IDV and IHV (Cellone, 2000) the apertures are taken to include the whole host galaxy.

## 3. RESULTS AND CONCLUSIONS

The constructed long-term variability lightcurves have shown that maximum variation in B band was observed during August 1997 and equals to $3^{m}_{.}0$ (rms=0.03), while the maximum amplitude in R band equals to $2^{m}_{.}53$ (0.01). The amplitudes of variation in R band of the other observing seasons are presented in the table.

The results of optical observations of BL Lacertae during great summer 1997 outburst are presented by different blazar monitoring groups (Webb (1998), Sobrito (1999), Speziali (2000), Fan (2001), Clements (2001), Villata (2002), Villata (2003), Villata (2004)). On the basis of observations of BL Lacertae during the period from August 1997 to November 2001 it was clearly demonstrated that variations are larger in B band or the object become bluer in the active phase (Nikolashvili (1999), Kurtanidze (2001), Nesci (2001)), that were also confirmed by other groups (Clements (2001), Fan (2001)).

The significant statistical evidences of intraday and intrahour variabilities are found during many nights of observations. The typical intraday and intrahour variability amplitudes in R band are within $0^{m}_{.}30$ (0.02) and $0^{m}_{.}10$ (0.01) magnitudes, respectively. Detailed study of BL Lacertae during multiwavelength campains carried out in the frame of WEBT collaboration are most extensive study of this prototype source ever conducted (Villata (2003), Villata (2004)).

## ACKNOWLEDGMENTS

O.M.K. and M.G.N. grateffully acknowledge the hospitality, invaluable financial support and the kind collaboration of many years with Dr. G.M. Richter (Astrophisikalisches Institute Potsdam) and Prof. S.J. Wagner (Landesternwarte Heidelberg) without which this Programm would never have been conducted.

We thank European Astronomical Society for donation of the ST-6 CCD camera.

## REFERENCES

Bloom S. D., et al. 1997, ApJ, 490, L145

Bottcher M., Bloom S. D. 2000, AJ, 119, 469

Cellone S. A., et al. 2000, AJ, 121, 90

Clements S.D., Carini M.T. 2001, AJ, 9, 534

Fan J. H., et al. 1998, ApJ, 507, 173

Fan J. H., et al. 1999, A&AS, 133, 217

Fan J. H., et al. 2001, A&A, 369, 758

Hoffmeister G., et al. 1990, Veranderlichte Sterne, Leipzig

Kurtanidze O.M., et al. 2001, in 6th Compton Symp., eds. Ritz S., et al. 2001, AIP CP. 587, 333.

Madejiski G. M., et al. 1999, ApJ, 521, 145

Maesano M., et al. 1997, A&AS, 122, 267

Miller H. R., et al. 1989, Nature, 337, 627

Nesci R., et al. 1998, Pubbl. Osserv. Astron. Univ. de Perugia, 3, 189

Nesci R., et al. 2001, ASP CS, 227, 144

Nikolashvili M. G., et al. 1999, in Blazar Monitoring Towards the Third Millenium, eds. Raiteri C., et al., Osservatorio Astronomico di Torino, 33.

Sambruna R. M., et al. 1999, ApJ, 515, 140

Stetson P.B. 1987, PASP, 99, 191

Sobrito G., et al. 1999, Blazar Data, 1, no.5

Speziali R., Natali G. 2000, A&AS, 339, 382

Tanihata S., et al. 2000, ApJ, 543, 124

Villata M., et al. 2002, A&A, 390, 407

Villata M., et al. 2003, A&A, 421, 103

Villata M., Raiteri C.M., et al. 2004, A&A, 424, 497

Wagner S.J., Witzel A. 1995, ARA&A, 35, 607

Wagner S. J. 2001, in Blazar Demographics and Physics, eds., P. Padovani and M. Urry, ASP CS, 227, 112

Webb J. R., et al. 1988, AJ, 95, 374

Webb J. R., et al. 1998, AJ, 115, 2244

# CCD PHOTOMETRY OF X-RAY SELECTED BLAZARS

**O.M. Kurtanidze[1,2,3], M.G. Nikolashvili[1,2], S.M. Chanturiya[1], G.N. Kimeridze[1], L.A. Sigua[1], B.Z. Kapanadze[1], R.Z. Ivanidze[1], G.N. Jimsheleishvili[1], N.B. Ograpishvili[1], and D.G. Zarqua[4]**

[1]Abastumani Observatory, 383792 Abastumani, Georgia
[2]Landessternwarte Heidelberg, Koenigstuhl, D-69117 Heidelberg, Germany
[3]Astrophysikalisches Institute Potsdam, 14482 Potsdam, Germany
[4]Physics Department, Sukhumi Branch of Tbilisi State University, Tbilisi, Georgia

## ABSTRACT

We present optical R band photometry of nine X-ray selected BL Lac objects: 1ES 0229+200, 1ES 0323+022, 1ES 502+675, 1ES 0647+250, 1ES 0806+524, 1ES 0927+500, 1ES 1028+511, 1ES 1959+650, 1ES 2344+514. Variability on long time scales within one magnitude in R band was found for all of the observed objects, except 1ES 0229+200 and 1ES0927+500. Largest variation was detected for 1ES 0502+675 and equals to $1^{m}_{\cdot}07$. Only few objects show statistically significant variation on Intraday scale.

Key words: X-Ray Blazars; CCD Photometry; Variability.

## 1. OBSERVATION AND DATA REDUCTION

Blazar Monitoring Program at Abastumani Observatory was started in the May 1997 and is carried out with ST-6 CCD Camera attached to the Newtonian focus of the 70-cm meniscus telescope (1/3, 14.9x10.7 sq. arcmin). All observations are performed using combined filters of glasses that match the standard B, V (Johnson) and Rc, Ic (Cousins) bands well (Kurtanidze, et al., 1999). Reference sequences in the blazar fields are calibrated using the equatorial standard stars (Landolt, 1992).

List of target objects was compiled from Einshtein Slew survey Sample of BL Lacertae objects (Perlman, et al., 1996). During more than 200 nights about 1400 ccd frames were obtained in R band to study long-term and intraday variability of selected objects. In the Table the list of the target X-ray BL Lacertae objects, along with the number of nights observed and frames obtained in R band are given. Last column shows the number of frames obtained to study the intraday (IDV) variability. Most frequently observed object, as on long-term as well as on intraday scales, is 1ES 1959+650. The duration of observational runs varied from two hours to six hours and exposure times varied from 60 to 180 sec depending on the brightness of the object and the filter used. The images are reduced using Daophot-II (Stetson, et al., 1987). To eliminate the effects of seeing induced spirious IDV and IHV varianility (Cellone, et al., 2000) the apertures are taken to include the whole host galaxy.

## 2. RESULTS AND CONCLUSIONS

### 2.1. 1ES 0323+022 and 1ES 0502+675

1ES 0323+022 is the most frequently studied object. Brightest state R=$15^{m}_{\cdot}0$. 62 was detected in Dec 1982 (Feigelson, et al., 1986). Largest amplitude $0^{m}_{\cdot}67$ in R band was detected during three years (23.10.1996-23.01.1999) of observation by Torino group with a maximum R = $16^{m}_{\cdot}60$ (Villata, et al., 2000). Our observations include the period from 04 Oct 1997 to 04 Feb 2002. There were two dramatic changes of brightness: first, up to $0^{m}_{\cdot}43$ from 31 Aug 1998 to 23 Nov 1998 and second one from 12 Sept 1999 to 23 July 2000 about $0^{m}_{\cdot}26$, while the maximum amplitude was $\Delta R0^{m}_{\cdot}45$.

Early observations of 1ES 0502+675 (31.10.1996-22.02.1997) show that maximum amplitude in R band equals to $0^{m}_{\cdot}58$ (Raiteri,et al., 1998). Our observations include the period from 09 Nov 1997 to 12 Feb 2000. Dramatic chages R=$15^{m}_{\cdot}67$-$16^{m}_{\cdot}74$ was detected before 23 Nov 1998 with an amplitude $1^{m}_{\cdot}07$. After the minimum it rapidly increases again and reach a mean state characterised by R=$16^{m}_{\cdot}40$ and $\Delta R=0^{m}_{\cdot}36$.

*Table 1. A list of X-Ray selected blazars*

| Source | $RA_{2000}$ | $DEC_{2000}$ | $N^{Nights}_{LTV}$ | $N^{Frames}_{LTV}$ | $N^{Nights}_{IDV}$ | $N^{Frames}_{IDV}$ | $\Delta R$ |
|---|---|---|---|---|---|---|---|
| 1ES 0229+200 | 02 32 48.6 | 20 17 17 | 13 | 23 | | | $0\overset{m}{.}00$ |
| 1ES 0323+022 | 03 26 13.9 | 02 25 15 | 27 | 37 | | | $0\overset{m}{.}45$ |
| 1ES 0502+675 | 05 07 56.2 | 67 37 24 | 32 | 37 | | | $1\overset{m}{.}07$ |
| 1ES 0647+250 | 06 50 46.5 | 25 03 00 | 09 | 13 | | | $0\overset{m}{.}30$ |
| 1ES 0806+524 | 08 09 49.2 | 52 18 58 | 33 | 36 | | | $0\overset{m}{.}88$ |
| 1ES 0927+500 | 09 30 37.6 | 49 50 26 | 06 | 07 | | | $0\overset{m}{.}00$ |
| 1ES 1028+511 | 10 31 18.5 | 50 53 36 | 28 | 32 | | | $0\overset{m}{.}60$ |
| 1ES 1959+650 | 19 59 59.9 | 65 08 55 | 43 | 48 | 23 | 732 | $0\overset{m}{.}40$ |
| 1ES 2344+514 | 23 47 04.8 | 51 42 18 | 13 | 25 | 10 | 373 | $0\overset{m}{.}10$ |

### 2.2. ES 0647+250, 1ES 0806+524 and 1ES 1028+511

The previous observation of 1ES 1028+511 during Dec 3,1996 - May 8, 1997 revealed variation $\Delta R=0\overset{m}{.}18$ and maximum brightness $R=16\overset{m}{.}53$ (Villata, et al., 2000). Our observations of these objects include the period from 25 Nov 1997 to 25 Jan 2002. All three objects show significant light variations that are equal to $0\overset{m}{.}37$ (25Nov 1997-13 Dec 1998), $0\overset{m}{.}88$ (28 Dec 1997-06 June 2000) and $0\overset{m}{.}60$ (28 Jan 1998-25 Jan 2002), respectively.

### 2.3. 1ES 1959+650 and 1ES 2344+514

Observations of 1ES 1959+650 from February 29,1996 to May 30, 1997 shows that the light curve in the R band is characterized by rapid flickering, a decrease of $0\overset{m}{.}28$ in 4 days ( (Villata, et al., 2000). Both objects during our observations show light variations bellow $0\overset{m}{.}4$ in R band. Largest one is observed for 1ES 1959+650 Kurtanidze (et al.). 1ES 2344+514 show obvious long-term variability trend over the observing period at $\Delta R=0\overset{m}{.}1$ level (Fan, et al., 2004). Consequently, the intraday variability is very week bellow $0\overset{m}{.}05$ and may only be detected in exceptional cases of very high photometric accuracy. More higher level activity of 1ES 1959+650 in comparison with 1ES 2344+514 may be attributed to its higher radio luminosity (Raiteri,et al., 1998).

### 2.4. Conclusion

Seven of the nine X-Ray BL Lacertae object studied show variability on long-term scale. Three of them show variation over $0\overset{m}{.}5$ (1ES 0502+675, 1ES 0806+524 and 1ES 1028+511), while other four bellow $0\overset{m}{.}5$ (1ES 0323+022, 1ES 0647+250, 1ES 1959+650 and 1ES 2344+514). Long-term variability was not detected for two BL Lacertae 1ES 0229+200 and 1ES 0927+500.

Intraday variability of 1ES 1959+650 and 1ES 2344+514 is bellow $0\overset{m}{.}05$. In general, X-ray selected blazars show week optical variability in comparison with radio selected blazars.

## ACKNOWLEDGMENTS

O.M.K. and M.G.N. grateffully acknowledge the hospitality, invaluable financial support and the kind collaboration of many years with Dr. G.M. Richter (Astrophisikalisches Institute Potsdam) and Prof. S.J. Wagner (Landesternwarte Heidelberg) without which this Programm would never have been conducted.

We thank European Astronomical Society for donation of the ST-6 CCD camera.

## REFERENCES

Cellone S. A., et al. 2000, AJ, 121, 90

Fan J, Kurtanidze O.M., Nikolashvili M.G., et al. 2004, ChAA, 4, 133

Feigelson E.D., et al. 1986, ApJ, 302, 337

Kurtanidze O. M. and Nikolashvili M. G. 2001, AIP Conf. Proc., 587, 333

Kurtanidze O. M. and Nikolashvili M. G. 1999, in Blazar Monitoring Towards the 3rd Millenium, eds. Raiteri C., et al. (Osservatorio Astron. di Torino), 29

Landolt A.U. 1992, AJ, 104, 340

Perlman E., et al. 1996, ApJS, 104, 251

Raiteri C.M., et al. 1998, A&A, 132, 361

Stetson P.B. 1987, PASP, 99, 191

Villata M., et al. 2000,A&A, 144, 481

# THE RESULTS OF LONG-TERM MONITORING OF BLAZARS AT ABASTUMANI OBSERVATORY

**O.M. Kurtanidze[1,2,3], M.G. Nikolashvili[1,2], S.M. Chanturiya[1], G.N. Kimeridze[1], L.A. Sigua[1], B.Z. Kapanadze[1], R.Z. Ivanidze[1], G.N. Jimsheleishvili[1], N.B. Ograpishvili[1], and D.G. Zarqua[4]**

[1]Abastumani Observatory, 383792 Abastumani, Georgia
[2]Landessternwarte Heidelberg, Koenigstuhl, D-69117 Heidelberg, Germany
[3]Astrophysikalisches Institute Potsdam, 14482 Potsdam, Germany
[4]Physics Department, Sukhumi Branch of Tbilisi State University, Tbilisi, Georgia

## ABSTRACT

We give a brief summary of the ongoing Abastumani Active Galactic Nuclei Monitoring Program started in the May of 1997. More than 110 000 frames are obtained during more than 1300 nights of observation for about 50 target objects, among them $\gamma$-ray, X-ray and optical blazars. All observations were done in the BVRI bands using ST-6 CCD based Photometer attached to the Newtonian focus of 70-cm meniscus telescope.

Key words: Blazars; CCD Photometry; Variability.

## 1. INTRODUCTION

Among active galactic nuclei (AGNs), blazars are objects most dominated by non thermal continuum emission, which extends from radio to $\gamma$-rays, and whose properties are best explained by emitting plasma in relativistic motion towards the observer, closely aligned with the line of sight (Urry, 1995). One of the distinguishing characteristics of the blazars which includes BL Lacertae type objects, high polarization quasars (HPQ) and optical violently variable (OVV) quasars is that their flux densities are highly variable at all wavelength from radio to $\gamma$-rays. Therefore the optical multiband monitoring along with other ones gives unique clues into the size and structure of the radiating region. Variability time scales have been derived for many blazars from monitoring programs which attain a time resolution of days and to years (Wagner, 1995). Unfortunately, existing multiwavelength data are not adequate yet to permit definite conclusions to be drawn about the nature of blazars due to the optical coverage in the previous campaigns has been much too sparse. We started systematic multiband optical monitoring of blazars at Abastumani Observatory in the May of 1997. In the late of October 1997 we joined the Whole Earth Blazar Telescope (WEBT, http://www.to.astro.it/blazars/webt). The aim of the programme is to study short-term and long-term variability of blazars and their correlations with that in radio, X-ray and $\gamma$-ray bands.

## 2. OBSERVATION AND DATA REDUCTION

Abastumani Observatory is located in the South-Western part of Georgia at a latitude of $41^{\circ}\!.8$ and a longitude of $42^{\circ}\!.8$ on the top of the Mt. Kanobili at 1700 m above mean sea level. The weather and seeing are very good in Abastumani (150 nights per year, 1/3 with seeing $<$1 arcsec). The mean values of the night sky brightness are B=$22^{m}\!.0$, V=$21^{m}\!.2$, R=$20^{m}\!.6$ and I=$19^{m}\!.8$. Blazar Monitoring Program at Abastumani Observatory was started in the May 1997 and is carried out with Peltier cooled ST-6 CCD Imaging Camera attached to the Newtonian focus of the 70-cm meniscus telescope (1/3). The pointing accuracy of the meniscus telescope is one-two arcminutes and it is good enough to locate target object inside of the full frame field of view 14.9x10.7 sq. arcminute. The ST-6 Imaging Camera uses the TC241 chip (375x242, 23x27 sq.micron) with a maximum quantum efficiency 0.7 at 675 nm. All observations are performed using combined filters of glasses which match the standard B, V (Johnson) and Rc, Ic (Cousins) bands well. Reference sequences in the blazar fields are calibrated using the Landolt's equatorial standard stars (Landolt, 1992). In photometric nights at least one equatorial field is observed with different exposures. Because of the scale of CCD and resolution of the meniscus telescope are equal to 2.3x2.7 sq. arcsec per pixel and 1.5 arcsec respectively, the images are undersampled, therefore to improve sampling it is needed to defocus frames slightly. Unfortunately, the high dark current limits the exposure time to 900 sec. The images are reduced using Daophot-II (Stetson, 1987). The highest differential photometric accuracy reached in R band is $0^{m}\!.005$ (rms) magnitude at $m_r$=$14^{m}\!.00$ during 180 sec.

| RA (2000) | DEC (2000) | Name | Nights | Observations $N_B$ | $N_V$ | $N_R$ | $N_I$ | $N_{IDV,Nights}$ |
|---|---|---|---|---|---|---|---|---|
| 01 12 05.7 | 22 44 38 | S2 0109+22 | 88 | 107 | 87 | 198 | 83 | 602, 11 |
| 02 19 42.8 | 02 19 42 | 3C 66A | 137 | 129 | 111 | 284 | 85 | 1443, 17 |
| 02 38 38.8 | 16 36 59 | AO 0235+164 | 147 | 71 | 81 | 683 | 52 | 1102, 15 |
| 07 21 53.4 | 71 20 36 | S5 0716+714 | 440 | 390 | 323 | 1300 | 600 | 15470, 360 |
| 08 54 48.9 | 20 06 31 | OJ 287 | 135 | 111 | 103 | 196 | 92 | 647, 18 |
| 09 58 47.2 | 65 33 55 | S4 0954+658 | 89 | 65 | 79 | 132 | 88 | 249, 14 |
| 11 04 27.3 | 38 12 32 | MKR421 | 156 | 192 | 180 | 647 | 163 | 3906, 79 |
| 11 59 32.1 | 29 14 42 | 4C 29.45 | 91 | 85 | 85 | 218 | 112 | 380, 12 |
| 12 21 31.7 | 28 13 58 | ON 231, W Com | 142 | 135 | 193 | 495 | 160 | |
| 12 56 11.2 | -05 47 22 | 3C 279 | 96 | 120 | 98 | 196 | 85 | 332, 9 |
| 16 42 58.8 | 39 48 37 | 3C 345 | 96 | 87 | 95 | 178 | 106 | 600, 19 |
| 16 53 52.1 | 39 45 36 | MRK 501 | 93 | 143 | 105 | 185 | 91 | 373, 12 |
| 17 28 18.5 | 50 13 11 | I ZW 187 | 83 | 76 | 85 | 179 | 96 | |
| 18 00 45.7 | 78 28 04 | S5 1803+784 | 147 | 78 | 74 | 500 | 57 | |
| 18 06 50.7 | 69 49 28 | 3C 371 | 120 | 137 | 99 | 164 | 118 | |
| 19 59 59.9 | 65 08 55 | 1ES1959+650 | 160 | 142 | 175 | 275 | 194 | 1790, 38 |
| 22 02 43.2 | 42 16 40 | BL Lacertae | 600 | 583 | 1189 | 1700 | 453 | 28227, 439 |
| 22 57 17.3 | 07 43 12 | S2 2254+074 | 110 | 65 | 68 | 193 | 74 | |
| 23 47 04.8 | 51 42 18 | 1ES2344+514 | 147 | 124 | 156 | 242 | 95 | 467, 12 |

## 3. RESULTS AND CONCLUSIONS

List of target objects was compiled using two Catalogues of AGNs (Padovani (1996), Perlman (1996)). In the period from May 1997 to September 2005, during about 1300 observing nights, more than 110 000 frames were obtained. In the Table the list of the target objects along with the number of nights observed and frames obtained in every of the BVRI bands in excess of one hundred fifty in R band are given. Last column shows the number of frames obtained to study the intraday and intrahour variability. Among most frequently observed objects are BL Lacertae, S5 0716+714, AO 0235+164 and Mkr 421. So far we took part in many international multiwavelength campaigns conducted during outburst and post-outburst era of BL Lacertae, S5 0716+71, 3C 279, Mrk 241, AO 0235+164, 4C 29.45, OJ 287, S4 0954+65 and ON 231. The main part of the results are already published (Hartmann (2001), Raiteri (2003), Massaro (2003), Osterman (2003), Villata (2004), Krawczynski (2004), Jorstad (2004), Raiteri (2005), Bottcher (2005)). Most objects under study show light variations over one magnitude in the optical band. Largest one was observed for AO 0235+164 and equals to $4^{m}_{.}0$ in R band. A few faint variable stars (B$\sim$$16^{m}_{.}5$) with amplitude $0^{m}_{.}3$-$0^{m}_{.}4$ and periods 3-5 hours were also identified.

## ACKNOWLEDGMENTS

O.M.K. and M.G.N. gratefully acknowledge the hospitality, invaluable financial support and the kind collaboration of many years with Dr. G.M. Richter (Astrophisikalisches Institute Potsdam) and Prof. S.J. Wagner (Landesternwarte Heidelberg) without which this Programm would never have been conducted.

## REFERENCES

Bottcher M., Harvey J., et al. 2005, ApJ, 631, 169

Hartmann R.C., Villata M., et al. 2001, ApJ, 558, 583

Jorstad S., Marscher A., et al. 2004 AIPC, 714, 202

Krawczynski H., et al. 2004, ApJ, 601, 151

Landolt A.U. 1992, AJ, 104, 340

Massaro E., Giommi P., et al. 2003, A&A, 399, 33

Osterman M.A., et al. 2003, AAS, 203, 7903

Padovani P., Giommi P. 1996, MNRAS, 277, 1477

Perlman E., et al. 1996, ApJS, 104, 251

Raiteri C.M., Villata M., et al. 2003, A&A, 402, 151

Raiteri C.M, Villata M., et al. 2005, A&A, 438, 39

Stetson P.B. 1987 PASP, 99, 191

Urry C.M., Padovani P. 1995, PASP, 107, 803

Villata M., Raiteri C.M., et al. 2004, A&A, 424, 497

Wagner S.J., Witzel A. 1995, ARA&A, 35, 607

# XMM-NEWTON OBSERVATIONS AND SIMULTANEOUS OPTICAL SPECTROSCOPY OF THE GRAVITATIONAL LENS SYSTEM SDSS J1004+4112

**G. Lamer, A. Schwope, L. Wisotzki, and L. Christensen**

Astrophysikalisches Institut Potsdam, Potsdam, Germany

## ABSTRACT

We report on observations of the large separation gravitational quasar lens SDSS J1004+4112 obtained simultaneously with *XMM-Newton* and the integral field spectograph *PMAS* at Calar Alto observatory. The XMM X-ray and UV images show that the 4 lens images differ significantly in their spectral energy distributions. The optical spectra of the 2 brightest lens components show a reappearance of a previously observed excess in the blue wing of the C IV emission line. We discuss microlensing and intrinsic variability as causes for these unusual observations. The extended emission of the lensing cluster of galaxies is clearly detected in the *EPIC* images, providing an estimate of its X-ray luminosity and mass.

Key words: gravitational lensing; quasars; X-rays.

## 1. INTRODUCTION

The lensed quasar SDSS J1004+4112 (RBS 825, Schwope et al. 2000) has been found by Inada et al. (2004) in a survey of large separation lenses using the Sloan Digital Sky Survey (SDSS). Optical imaging revealed 4 images of the quasar, with a maximum separation of 14.6" it is the largest separation gravitational lens known so far. The lensing object is a cluster of galaxies at z=0.68, the quasar itself has a redshift of z=1.73. SDSS J1004+4112 is the first multiple quasar, where the lensing gravitational potential is dominated by a cluster of galaxies, and not a single galaxy. Modelling of the lensing potential gives only a rough estimate of the cluster mass ($M \geq 10^{14} h^{-1} M_{\odot}$, Oguri et al. 2004) . The predictions for the time delays between the images are similarly uncertain, the delay between the closest components A and B can be up to $37h^{-1}$ days, the largest delay C-D could be up to $3000h^{-1}$ days (Oguri et al. 2004). Optical spectroscopy of the individual components has revealed significant differences in the emission line profiles of the components (Richards et al. 2004), which have been attributed to microlensing of lens image A. Specifically, the blue wings of the emission lines are enhanced in the spectra of component A. This feature has been observed in May 2003 and then disappeared. The blue line wing excess has again been observed in our *PMAS* spectra of SDSS J1004+4112 which were taken simultaneously with the *XMM-Newton* data (Fig. 1).

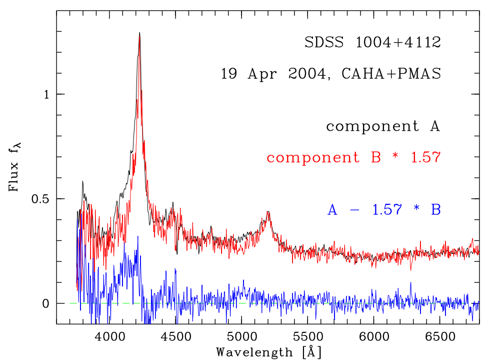


*Figure 1. Optical spectra of SDSS J1004+4112 A and B taken almost simultaneously with the XMM data on 19/04/2004. The lower line is the difference spectrum (A - 1.57 · B) and shows that the blue wings of the emission lines are enhanced in component A.*

## 2. XMM-NEWTON RESULTS

We observed SDSS J1004+4112 for 60 ksec with the XMM EPIC and OM instruments. Inspection of the EPIC images reveals that lens image A appears much fainter in X-rays than expected from its optical brightness (Figs. 2, 3 ). A deconvolution using PSF fitting with the SAS task *emldetect* results in a flux ratio B/A $\sim$ 2, component A is more than 3 times weaker than expected from the optical/UV fluxes. The flux deficit of component A is constant over the XMM EPIC energy range, hence we can exclude that it is caused by photoelectric absorption. The simultaneous UV imaging of the XMM Optical Monitor (OM) shows that the UV continuum of the close components A and B is much brighter and harder than in images C and D (Fig. 4).

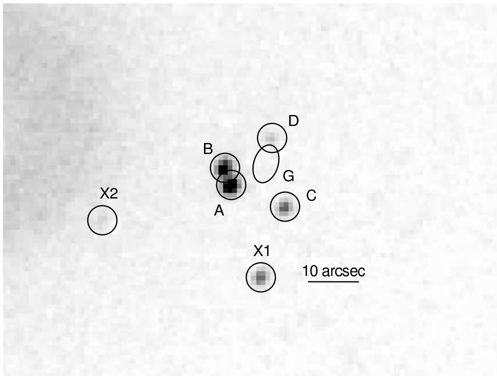


*Figure 2. U-band image of SDSS J1004+4112 from the XMM optical monitor on 20/04/2004. Here the order of the components in brightness is the same as in previous optical observations.*

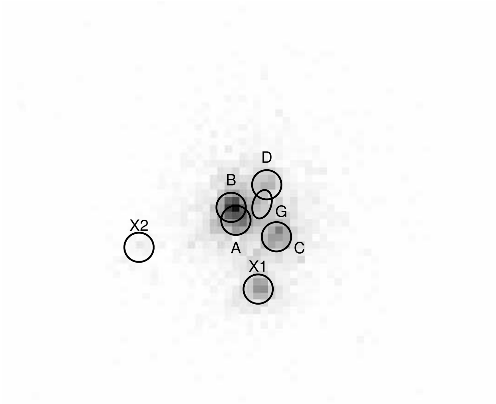


*Figure 3. EPIC MOS image of SDSS J1004+4112 on 20/04/2004. It is obvious that the optically brightest component A is significantly fainter in X-rays than expected. Sources X1 and X2 are not related to the lensed quasar.*

The following scenario could explain both the variable line profiles in image A and the unusual SEDs in the UV/X-ray wavebands: The UV and X-ray continuum of the lensed quasar is intrinsically very variable, during the time of the XMM observations the close images A and B were very bright. The variable continuum gives rise to variability of the optical lines, image A is probably affected by microlensing, which amplifies parts of the broad line region and causes the selective, repeated brightening of the blue line wing. The X-ray deficit of image A is still puzzling. Intrinsic variability is an unlikely cause, since the time lag to component B is relatively small. If caused by microlensing, this would be an extreme case of flux attenuation induced by microlensing. Repeated X-ray observations of SDSS J1004+4112 are needed to clarify this case.

Multiple PSF fitting with the XMM SAS *emldetect* task yielded a significant detection of the extended emission of the lensing cluster. We measure a 0.5-2.0 keV luminosity of $1.4 \cdot 10^{44} \mathrm{erg/s}$, and from the count rates in the 5 standard EPIC energy bands a gas temperature of

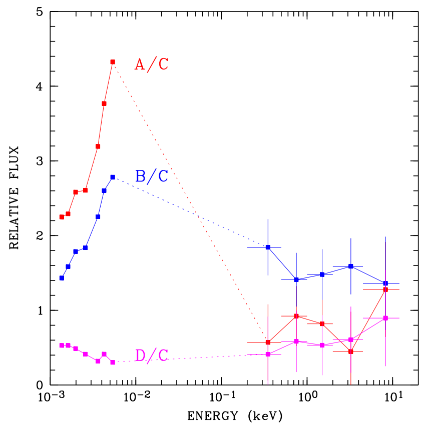


*Figure 4. Relative spectral energy distributions of the lens components, normalized to image C. The SEDs include (non-simultaneous) optical Subaru data and XMM-OM and EPIC data.*

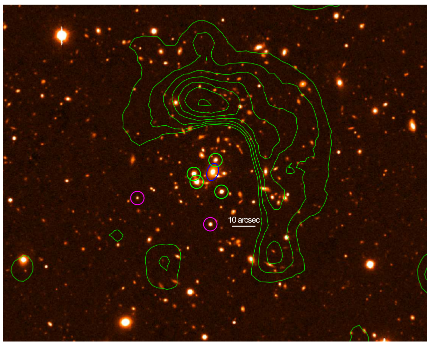


*Figure 5. X-ray contours after subtraction of the point sources plotted over a Subaru I-band image. The extended emission of the cluster is clearly detected.*

$T = 4.3^{+2.1}_{-1.0}$ could be derived. With the scaling relations for clusters of this redshift (Kotov & Vikhlinin 2005) this puts the cluster in the mass range $3 - 6 \cdot 10^{14} \mathrm{M}_{\odot}$, consistent with, and improving the estimates from lensing models. Fig. 2b shows, that the extended cluster emission is asymmetric with respect to the brightest cluster galaxy and the lensing centre, tracing the distribution of cluster galaxies.

## REFERENCES

Inada, N, Oguri, M, Pindor, B. et al., 2003, Nature 426, 810

Kotov, O., and Vikhlinin, A., 2005, ApJ, in press

Richards, T.G., Keeton, C.R., Pindor, B., et al. 2004, ApJ 610, 679

Oguri, M., Inada, N., Keeton, C.R., et al. 2004, ApJ 605, 78

Schwope, A., Hasinger, G., Lehmann, I., Schwarz, R., Brunner, H., et al., 2000, Astron. Nachr., 321, 1

# X-RAY EMISSION FROM THE 3C 273 JET

**H.L. Marshall[1], S. Jester[2], D.E. Harris[3], and K. Meisenheimer[4]**

[1]MIT Kavli Institute, MIT, Cambridge, MA, 02139, USA
[2]Southampton University, Southampton SO17 1BJ, UK
[3]Smithsonian Astrophysical Observatory, Cambridge, MA, 02138, USA
[4]Max-Planck-Institut fur Astronomie, D-69117 Heidelberg, Germany

**ABSTRACT**

We present results from four recent *Chandra* monitoring observations of the jet in 3C 273 using the ACIS detector, obtained between November 2003 and July 2004. We find that the X-ray emission comes in two components: unresolved knots that are smaller than the corresponding optically emitting knots and a broad channel that is about the same width as the optical interknot region. We compute the jet speed under the assumption that the X-ray emission is due to inverse Compton scattering of the cosmic microwave background, finding that the dimming of the jet X-ray emission to the jet termination relative to the radio emission may be due to bulk deceleration.

Key words: X-rays; quasars, jets; 3C 273.

## 1. INTRODUCTION

Marshall et al. (2001) showed that X-rays from the 3C 273 jet follow the optical emission fairly well. However, the X-ray emission is significantly brighter at the beginning of the jet than at the end while the optical knots are of similar brightness along the jet. Optically, the width of the jet is well resolved at the 0.1″ level using the Hubble Space Telescope (HST) and we find that it is now resolved in the X-ray band in the cross-jet direction. Assuming that the X-ray emission arises from inverse Compton scattering of cosmic microwave background photons (IC-CMB) (Tavecchio et al., 2000; Celotti et al., 2002), we can compute the jet speed for a given (small) angle to the line of sight that is approximately constant along the jet.

## 2. CROSS-JET PROFILE

Results from fits of Gaussians to the X-ray cross-jet profiles are shown in Fig. 1. The profiles are adaptively binned to maintain $> 15$ counts per bin so there are 7-30 bins per profile. For comparison, the ACIS readout streak from the quasar core was fit to a Gaussian, providing a good value for the Gaussian width, $\sigma = 0.34''$ (or FWHM = 0.80″), of a point source. Except in the centers of knots A and B (about 13″ and 15.5″ from the core), the jet is resolved. The reduced $\chi^2$ is near unity except at the positions of the X-ray bright knots because the 1D profile of a point source does not match a Gaussian function. The residuals of the Gaussian fits are very similar to those of unresolved sources, confirming that knots A and B are point-like. The size of knot A's X-ray emission region ($< 0.2''$ FWHM) is distinctly smaller than found optically, where knot A was easily resolved using HST to be about 0.4″ across and 0.7″ long (Bahcall et al., 1995). The physical size differences between optical and X-ray emission regions are not expected in the IC-CMB model.

For an average observed $\sigma$ of 0.45″ and the value for a point source of 0.35″, the inferred intrinsic FWHM of the X-ray emission outside knots A and B is 0.62″. This width is comparable to that of the optical emission between knots (Bahcall et al., 1995). Thus, the X-ray emission comes in two components: unresolved knots that are smaller than the corresponding optically emitting knots and a broad channel that is about the same size as the optical interknot region.

## 3. JET SPEED

We use the profile of the X-ray emission from the jet, which we compare to the radio profile to obtain the flow speed along the jet if we accept the hypothesis that the X-rays are produced by inverse Compton scattering of microwave background photons in a relativistic jet. Following Harris & Krawczynski (2002), Marshall et al. (2005) showed that the beaming parameters - the cosine of the angle to the line of sight $\cos\theta = \mu$ and the jet speed $\beta c$ - are related to a function, $K$, of the observables. See Marshall et al. (2005) for details. We can solve their Equation 4 for $\beta$, giving

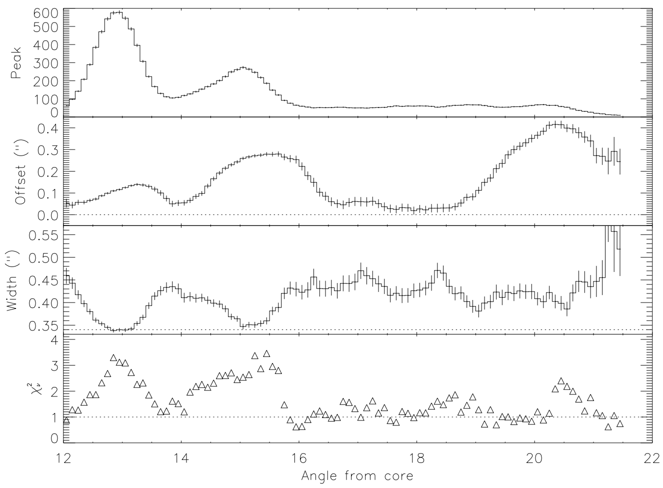


*Figure 1. Results from fitting Gaussians to the X-ray cross-jet profiles. From the top, the panels are: Gaussian normalization (counts per 0.1″ bin), angular deviation from PA=-137.5°, the Gaussian dispersion parameter ($\sigma \equiv$ FWHM/2), and the reduced $\chi^2$. The dotted line in the width panel shows the Gaussian dispersion obtained for an unresolved source. Except at 13″ and 15.5″ from the core (knots A and B), the jet is resolved in the cross-jet direction.*

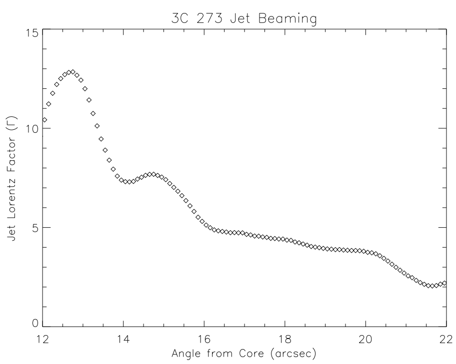


*Figure 2. Jet beaming factor assuming the IC-CMB model of the X-ray emission. The X-ray to radio flux ratio is used as in the anaysis by Marshall et al. (2005) but using equation 1 to compute the jet speed and Lorentz factor. In this model, the jet dimming results from bulk deceleration.*

$$\beta = \frac{-1-\mu+2K\mu \pm (1+2\mu-4K\mu+\mu^2+4K\mu^3)^{1/2}}{2K\mu^2} \tag{1}$$

Using the ratio of the X-ray and radio fluxes as a function of position along the jet and Equation 1 above, we compute the jet $\Gamma = (1-\beta^2)^{(-1/2)}$ upon setting the angle to the line of sight and using the magnetic field from Jester et al. (2002), which seems to be nearly constant along the jet. We find a good solution for a very small angle to the line of sight, 2.5°, where the jet bulk $\Gamma$ drops from a maximum of 18 down to 2 at the terminal hotspot. Thus, the dimming of the jet to the end relative to the radio emission may be due to bulk deceleration.

**ACKNOWLEDGMENTS**

This work was supported in part by U.S. Dept. of Energy under contract No. DE-AC02-76CH03000, Smithsonian Astrophysical Observatory (SAO) contract SVI-73016 for the Chandra X-Ray Center (CXC), and NASA contract NAS8-39073.

**REFERENCES**

Bahcall et al. 1995, ApJ, 452, L91

Celotti, A., Ghisellini, G., and Chiaberge, M. 2001, MNRAS, 321, L1

Jester, S. et al., 2002, A&A, 385, L27

Harris, D. E. & Krawczynski, H. 2002, ApJ, 565, 244

Marshall, H.L., et al. 2001, ApJ, 549, L167

Marshall, H.L., et al. 2005, ApJS, 156, 13.

Tavecchio, et al. 2000, ApJ, 544, L23

# A NEW XMM-NEWTON OBSERVATION OF PICTOR A RADIO LOBES CONFIRMS THE NON-THERMAL ORIGIN OF THE X-RAY EMISSION

**G. Migliori[1,2], P. Grandi[1], G. G. C. Palumbo[2], G. Brunetti[3], G. Malaguti[1], M. Guainazzi[4]**

[1]INAF/IASF Bologna, Italy [2]Bologna University, Italy [3]INAF/IRA Bologna, Italy [4]XMM-Newton SOC Vilspa, Spain

## ABSTRACT

X-ray emission from the eastern radio lobe of the FRII Radio Galaxy Pictor A was serendipitously discovered by a short observation of XMM-Newton in 2001. The X-ray spectrum, accumulated on a region covering about half of the entire radio lobe, was well described by both a thermal model and a power law, making non-univocal the physical interpretation. A new XMM-Newton observation performed in 2005 has allowed the detection of the X-ray emission from both radio lobes and unambiguously revealed its non-thermal origin. The X-ray emission is due to Inverse Compton (IC) of the cosmic microwave background photons by relativistic electrons in the lobe. We confirm the discrepancy between the magnetic field, as deduced from the comparison of the IC X-ray and radio fluxes, and the equipartition value.

Key words: Radio-galaxies - radio lobes - radiation mechanism.

## 1. INTRODUCTION

Pictor A is a nearby ($z$=0.035) double lobe radio source with a Fanaroff Riley II (FRII) morphology. VLA observations (Perley et al. 1997) show two nearly circular radio lobes with hot spots and a faint radio jet connecting the nucleus to the west hot spot. The spectral indices are fairly uniform throughout each lobe $<\alpha_{\rm R}>= 0.8$. XMM-Newton discovered X-ray radiation associated to the extended radio lobes (Grandi et al. 2003). In spite of the relatively short exposure time ($\sim$ 15 ks), and the very high background, a quite good spectrum was obtained from a circular region centered on the east lobe. However, the data interpretation was not univocal, as the X-ray spectrum could be described by both a power law ($\alpha_{\rm X} = 0.6 \pm 0.2$) and a thermal model ($kT \sim 5$ keV). The presence of an extended emission, most likely to be ascribed to non-thermal processes, has been recently confirmed (Hardcastle & Croston 2005). To definitely solve the ambiguity on the nature of the radio-lobes X-ray emission, a new XMM-Newton 50 ks observation was performed on 14 January 2005. Here we present the preliminary results.

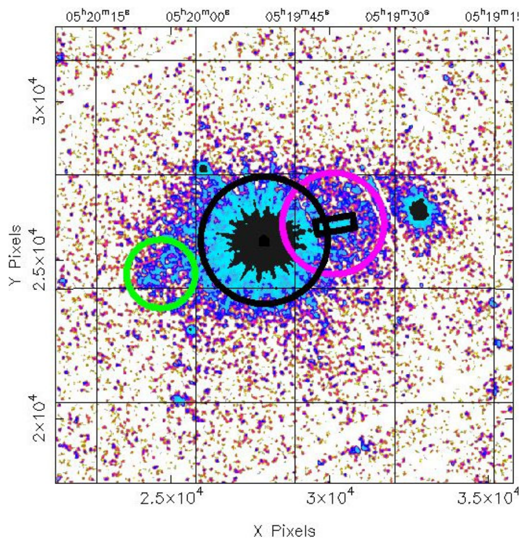


*Figure 1. XMM/MOS1 image (0.2-10 keV) of Pictor A observed on 14 January 2005. Several components are visible: the bright nucleus, the west hot spot, the jet, and the two lobes. The green and the pink circles (excluding the nuclear and the jet contributions), represent the extraction regions of the east and west lobe spectra, respectively.*

## 2. SPECTRAL ANALYSIS

Figure 1 shows the observed MOS1 image (0.2-10 keV) of Pictor A. The X-ray counterparts of radio lobes are clearly visible as asymmetric diffuse emission around the bright nucleus. Unlike the previous XMM-Newton observation, performed in 2001, spectra of good quality can be extracted from both lobes. This has allowed a spatially resolved X–ray spectral analysis. The green circle

*Table 1. East lobe spectral fit results*

| Power Law | | Thermal Emission | |
|---|---|---|---|
| $\Gamma$ | $1.80^{+0.17}_{-0.14}$ | $kT$(keV) | $4.94^{+3.01}_{-1.47}$ |
| $F^{(a)}$ | $1.09^{+0.21}_{-0.12}$ | $F^{(a)}$ | $1.00^{+0.01}_{-0.01}$ |
| $\chi^2$/dof | 19/23 | $\chi^2$/dof | 28/23 |

$(a)$: 2–10 keV flux in $10^{-13}$ erg cm$^{-2}$ s$^{-1}$

*Table 2. West lobe spectral fit results*

| Power Law | | Thermal Emission | |
|---|---|---|---|
| $\Gamma$ | $1.75^{+0.17}_{-0.17}$ | kT$(keV)$ | $5.59^{+3.18}_{-1.62}$ |
| $F^{(a)}$ | $1.58^{+0.16}_{-0.16}$ | $F^{(a)}$ | $1.48^{+0.12}_{-0.12}$ |
| $\chi^2$/dof | 34/30 | $\chi^2$/dof | 42/30 |

$(a)$: 2–10 keV flux in $10^{-13}$ erg cm$^{-2}$ s$^{-1}$

indicated in Figure 1 represents the selected accumulation region for the east lobe spectrum. The spectrum of the west lobe was instead extracted from the pink circle, after subtraction of the nuclear and the jet contributions (black circle and rectangle, respectively).

Following the previous work (Grandi et al. 2003) we tested both a power law and a thermal model to fit the data. For both lobes, a non-thermal emission is preferred to a thermal process, as shown in Tables 1 and 2. This appears also evident in Figure 2 where the two spectral models to the east lobe data are compared. The residuals result clearly larger for the thermal model fit. The comparison between Table 1 and 2 indicates that the X-ray photon index value is $\Gamma \sim 1.8$ ($\alpha_{\rm X} = 0.8$) independently of the position of the extraction region. The X-ray spectral index, $\alpha_{\rm X}$ is thus in very good agreement with the radio slope ($\alpha_{\rm R} \sim 0.8$). Moreover, the non-thermal X-ray flux of the east lobe is in agreement with the previous value reported in Grandi et al. (2003).

## 3. DISCUSSION

This new observation solves the ambiguity on the nature of the extended X-ray emission. Radio emitting electrons in the lobes upscatter local cosmic microwave background, producing the observed X-ray emission. We assume $k = 1$, where $k$ is the ratio between electron and proton energy density in the lobes, and an electron spectrum $N(\gamma) \propto \gamma^{-(2\alpha_{\rm R}+1)}$, with a low energy cut-off

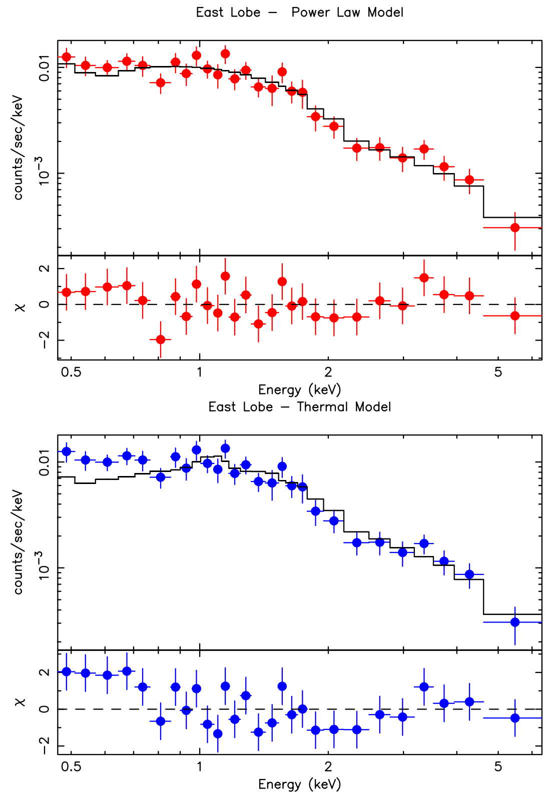


*Figure 2. XMM/MOS1 spectrum of the east lobe: a power law (upper panel) is clearly preferred to a thermal model (bottom panel).*

$\gamma_{\rm min} = 50$. Following Brunetti et al. (1997) and Blumenthal & Gould (1970), we find $B_{\rm EQ}/B_{\rm IC} \simeq 2.7$, which implies a ratio between the particle and magnetic field energy density equal to (Brunetti 2004): $(\omega_{\rm (e+p)}/\omega_{\rm B}) \sim [2/(\alpha_{\rm R}+1)](B_{\rm EQ}/B_{\rm IC})^{(3+\alpha_{\rm R})} \sim 50$, thus showing a strong particle dominance in the radio lobes.

## REFERENCES


Blumnethal., G. R. & Gould, R.J. 1970, Rev. Mod. Phys., 42, 237

Brunetti G., Setti, G. & Comastri, A., 1997, A&A, 325, 898

Brunetti G. 2004, in The Role of VLBI in Astrophysics, Astrometry and Geodesy, Mantovani & kus eds, p. 29.

Grandi, P. et al. 2003, ApJ, 586, 123

Hardcastle. M., J. & Croston, J. H. 2005, MNRAS, 363, 649

Miley, G., 1980 ARA&A, 18, 165

Perley R.A., Roser H.J. & Meisenheimer K. 1997 A&A, 328, 12

# THE NATURE OF X-RAY ABSORBED STARBURST QSOS AND THE QSO EVOLUTIONARY SCHEME

**M.J. Page[1], F.J. Carrera[2], J. Ebrero[2], J.A. Stevens[3], and R.J. Ivison[4]**

[1]UCL, Mullard Space Science Laboratory, Holmbury St. Mary, Dorking, Surrey RH5 6NT, UK
[2]Instituto de Física de Cantabria, Avenida de los Castros, 39005 Santander, Spain
[3]Centre for Astrophysics Research, University of Hertfordshire, College Lane, Hatfield AL10 9AB, UK
[4]UK Astronomy Technology Centre, Royal Observatory, Blackford Hill, Edinburgh, EH9 3HJ, UK

## ABSTRACT

In contradiction to the simple AGN unification schemes, there exists a significant population of broad line, $z \sim 2$ QSOs which have heavily absorbed X-ray spectra. These objects have luminosities and redshifts characteristic of the sources that produce the bulk of the QSO luminosity in the universe. Our follow up observations in the submillimetre show that these QSOs are embedded in ultraluminous starburst galaxies, unlike most unabsorbed QSOs at the same redshifts and luminosities. The radically different star formation properties between the absorbed and unabsorbed QSOs implies that the X-ray absorption is unrelated to the torus invoked in AGN unification schemes. The most puzzling question about these objects is the nature of the X-ray absorber. We present our study of the X-ray absorbers based on deep (50–100ks) XMM-Newton spectroscopy. The hypothesis of a normal QSO continuum, coupled with a neutral absorber is strongly rejected. We consider the alternative hypotheses for the absorber, originating either in the QSO or in the surrounding starburst. Finally we discuss the implications for QSO/host galaxy formation, in terms of an evolutionary sequence of star formation and black hole growth. We propose that both processes occur simultaneously in the gas-and-dust-rich heavily obscured centres of young galaxies, and that absorbed QSOs form a transitional stage, between the main obscured growth phase, and the luminous QSO.

Key words: X-rays; submillimetre; galaxies: active.

## 1. INTRODUCTION

The prevalence of black holes in present day galaxy bulges, and the proportionality between black hole and spheroid mass (Merritt & Ferrarese, 2001) implies that the formation of the two components are intimately linked. One way to probe star formation in distant QSOs is to observe them at submillimetre wavelengths, and so measure the amount of radiation from young stars which is absorbed and re-emitted by dust in the far infrared. With this in mind, we have observed matched samples of X-ray absorbed and unabsorbed QSOs at 850$\mu$m with SCUBA. These observations revealed a remarkable dichotomy in the submillimetre properties of these two groups of sources: X-ray absorbed QSOs are often ultraluminous infrared galaxies, while X-ray unabsorbed QSOs are not. This suggests that the two types are linked by an evolutionary sequence, whereby the QSO emerges at the end of the main star-forming phase of a massive galaxy (Page et al., 2004; Stevens et al., 2005, Carrera et al. 2006, this volume).

However, the nature of the X-ray absorption remains puzzling. It could be due to gas located within the AGN structure, or from more distant material in the host galaxy. These objects are characterised by hard, absorbed X-ray spectra, but they have optical/UV spectra which are typical for QSOs, with broad emission lines and blue continua. Assuming that their hard X-ray spectral shapes result from photoelectric absorption from cold material with solar abundances, the column densities are $\sim 10^{22}$ cm$^{-2}$. These properties are surprising: for a Galactic gas/dust ratio, the restframe ultraviolet spectra would be heavily attenuated by such large columns of material. Therefore in order to investigate the X-ray absorption, we have obtained deep (50–100ks) *XMM-Newton* observations of three submillimetre bright, X-ray absorbed QSOs from our sample of hard-spectrum *Rosat* sources (Page, Mittaz & Carrera, 2001).

## 2. RESULTS

The *XMM-Newton* spectra were first fitted with a power law and fixed Galactic absorption. Surprisingly, the power law produces reasonable $\chi^2$ values. However, the photon indices are unusually hard for QSOs, and the data show a deficit of counts relative to the model at the softest energies, indicating that absorption is present. The original *Rosat* PSPC spectra and the *XMM-Newton* spectra show excellent agreement (see Fig. 1).

The hypothesis of a normal ($\Gamma = 2$) AGN X-ray spectrum and a cold absorber is strongly rejected for RXJ121803

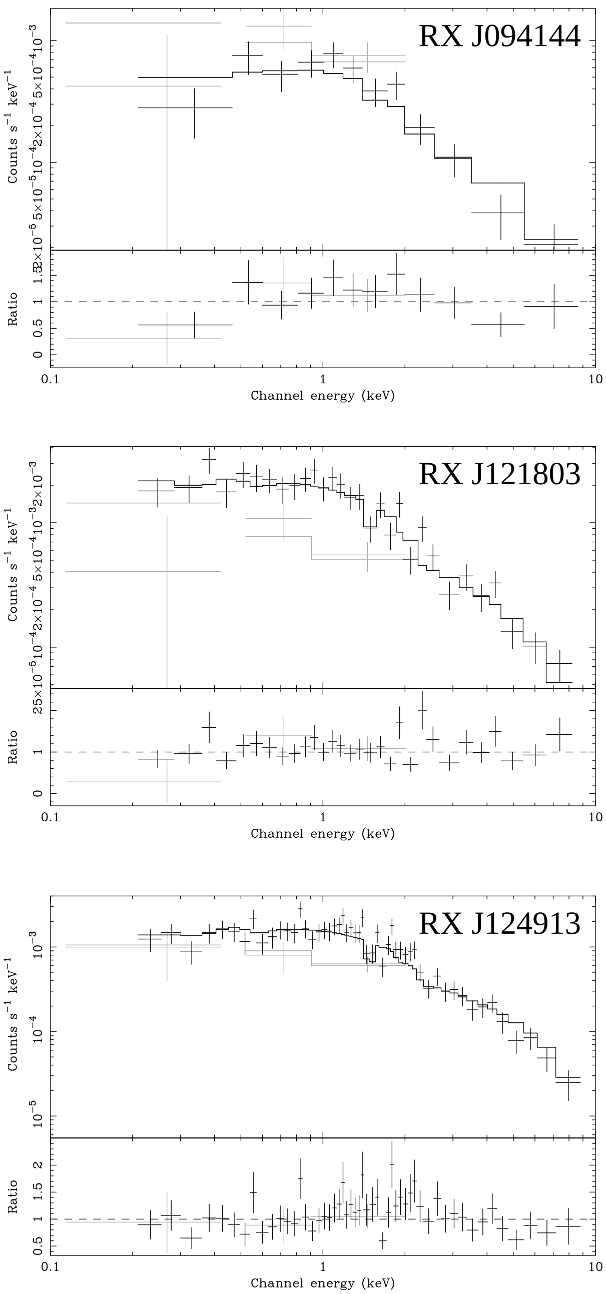


*Figure 1.* XMM-Newton *EPIC spectra (black) and* Rosat *PSPC spectra (grey) of three X-ray absorbed QSOs. The model is a simple power law with fixed Galactic absorption. The best-fit power law photon indices* $\Gamma$ *are* $1.3 \pm 0.1$, $1.4 \pm 0.1$ *and* $1.4 \pm 0.1$ *for RX J094144, RX J121803, and RX J124913 respectively. Such photon indices are unusually hard for radio-quiet AGN. In all three objects there is a deficit of counts at the lowest energy, indicating that absorption is responsible for the hard spectral shape; this is also seen in the* Rosat *data. Furthermore, RX J094144 and RX J124913 show some systematic curvature relative to the power law model.*

and RXJ124913. Therefore we considered ionised absorber models for the X-ray absorption, using the 'xabs' model in SPEX, which includes both photoelectric and line absorption. For all three AGN an acceptable fit can be obtained with a $\Gamma = 2$ power law and an absorber with an ionisation parameter log $\xi \sim 2$ and column densities of $10^{22.5}$–$10^{23.5}$ cm$^{-2}$. These absorbers have similar properties to the high-ionisation absorber phases seen as outflows in some nearby Seyfert 1 galaxies and QSOs such as NGC3783 and PG1114+445 (Ashton et al., 2004).

At these ionisation parameters and column densities, the absorbers are likely to originate in the AGN themselves, rather than in the host galaxies. This solution is attractive, because it is compatible with the lack of optical extinction in these objects: if the absorber is driven as a wind, either from the accretion disc or from evaporation of the inner edge of the molecular torus, then dust will be sublimated before (or as) it enters the flow.

## 3. IMPLICATIONS FOR AGN AND GALAXY EVOLUTION

The low space density of X-ray absorbed QSOs relative to unabsorbed QSOs and to distant ultraluminous galaxies detected in blank field SCUBA surveys, implies that the X-ray absorbed QSOs are caught during a short-lived transitional phase. Before this brief phase, AGN must be weak, and heavily obscured (Alexander et al., 2005); after this phase the host galaxy is essentially fully formed, and the naked QSO shines brightly until its fuel is consumed. A number of theoretical models predict a very similar evolutionary pattern. In many of these models, the QSO terminates the star formation in the host galaxy by driving a powerful wind (e.g. Fabian, 1999; Di Matteo Springel & Hernquist, 2005). The EPIC spectra of our X-ray absorbed QSOs suggest that the absorbers are ionised winds driven by the AGN, and therefore that the transition between buried AGN and naked QSO is mediated by a radiatively driven wind from the AGN, as predicted by these models.

## REFERENCES

Alexander D.M., et al., 2005, Nature, 433, 604

Ashton C.E., et al., 2004, MNRAS, 355, 73

Di Matteo T., Springel V. & Hernquist L., 2005, Nature, 433, 604

Fabian A.C., 1999, MNRAS, 308, L39

Merritt D. & Ferrarese L., 2001, MNRAS, 320, L30

Page M.J., Mittaz J.P.D. & Carrera F.J., 2001, MNRAS, 325, 575

Page M.J., Stevens J.A., Ivison R.J., Carrera F.J., 2004, ApJ, 611, L85

Stevens J.A., et al., 2005, MNRAS, 360, 610

# PROBING LOCAL SEYFERT GALAXIES: CONSISTENT WITH UNIFIED MODELS, BUT NOT WITH STANDARD ACCRETION?

**F. Panessa**[1], **M. Cappi**[2], **and L. Bassani**[2]

[1]Instituto de Fisica de Cantabria (CSIC-UC), 39005 Santander, Spain
[2]INAF-IASF, sez. Bologna, 40129 Bologna, Italy

## ABSTRACT

Results obtained from an X-ray survey of a complete sample of Seyfert galaxies using XMM-Newton and Chandra are reported. The sample, which has been selected from the Palomar optical spectroscopic survey of nearby galaxies (Ho et al. 1997), covers a wide range of nuclear power from $L_{2-10keV} \sim 10^{42}$ erg/s down to very low luminosities ($L_{2-10keV} \sim 10^{37}$ erg/s). A high fraction of Compton thick sources has been identified (>30%), confirming previous studies. After taking into account the effect of heavy absorption, we have found that the X-ray and multiwavelength properties of our sources are consistent between type 1 and type 2 Seyferts, as expected from 'unified models', and consistent with those of brigther AGNs, with exceptions at a $\sim$ 10% level. However, when we consider black hole mass estimates, it appears that Seyferts are accreting at very low Eddington ratios which are more typical of ADAF-like regimes, rather than of radiative efficient accretion.

Key words: X-rays:galaxies; galaxies: Seyfert.

## 1. INTRODUCTION

The fundamental paradigm on which our understanding of AGN activity is based is the accretion onto a supermassive black hole. In the last decades, unification of different classes of AGN has been based on orientation of the line of sight. It has been shown that X-ray observations of Seyfert galaxies are key to verifying the predictions and, thus, the validity of unified models of AGN. Several studies seem to suggest that the standard unified model for Seyfert galaxies (Antonucci 1993) may not hold down to very low luminosities (Ho et al. 2001, Panessa & Bassani 2002). Fundamental parameters, such as black hole mass, Eddington ratio, and perhaps the black hole spin, might help in the comprehension of the whole AGN phenomenon. By studying the X-ray properties, their correlation to other wavebands and to black hole masses of a sample of nearby Seyfert galaxies, we aim at testing the applicability of unification models and verifying standard accretion disk theories down to the lowest ($L_B$=$10^8$-$10^{11}$ $L_\odot$) nuclear luminosities.

## 2. STARTING POINT: XMM-NEWTON SURVEY OF A DISTANCE LIMITED SAMPLE OF 27 SEYFERT GALAXIES

An X-ray spectral survey has been performed on a well defined sample of Seyfert galaxies taken from Ho, Filippenko & Sargent (1997, hereafter HFS97) using *XMM–Newton* (Cappi et al. 2005). The optically selected sample is complete in B magnitude and distance limited: it consists of the nearest (D $\leq$ 22 Mpc) 27 Seyfert galaxies (9 of type 1, 18 of type 2). Hard X-ray nuclear spectra have been assembled for all the sources except two Seyfert 2s which are not detected between 2 and 10 keV. Nuclear luminosities reach values down to $10^{38}$ erg s$^{-1}$. A high fraction of Compton-thick (CT) objects ($\geq$ 30% among type 2s) affects the shape of the distribution of X-ray parameters. CT sources have been identified either directly from their intense FeK line and flat X-ray spectra, or indirectly with flux diagnostic diagrams which use isotropic indicators. A correction factor has been applied to the column density and X-ray luminosity values of the identified CT 'candidates'. After taking into account these highly absorbed sources, we find that the intrinsic X-ray spectral properties (i.e., spectral shapes and luminosities above 2 keV) are consistent between type 1 and type 2 Seyferts, as expected from "unified models". The column density distribution (see Fig.1) shows that Seyfert galaxies as a whole are distributed fairly continuously over the entire range of $N_{\rm H}$, between $10^{20}$ and $10^{25}$ cm$^{-2}$, and while Seyfert 1s tend to have lower $N_{\rm H}$ and Seyfert 2s tend to have the highest, we find 30% and 10% exceptions, respectively.

With the exception of a few cases, the average instrinsic properties of nearby Seyfert galaxies are consistent with predictions of 'unified models' of Seyfert galaxies and extend their validity down to low luminosities.

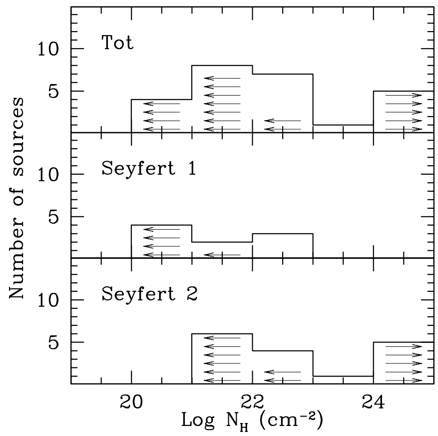


*Figure 1. Column density distribution after correction for Compton thick candidates (Cappi et al. 2005). Upper and lower limits are indicated with arrows.*

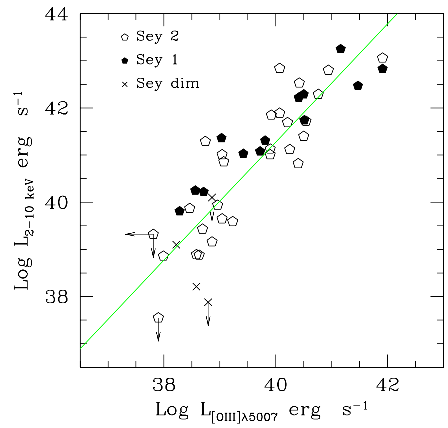


*Figure 2. 2-10 keV luminosity versus [OIII] luminosity corrected for Galactic and NLR extinction. The solid line shows the best fit linear regression line (Panessa et al. in prep.)*

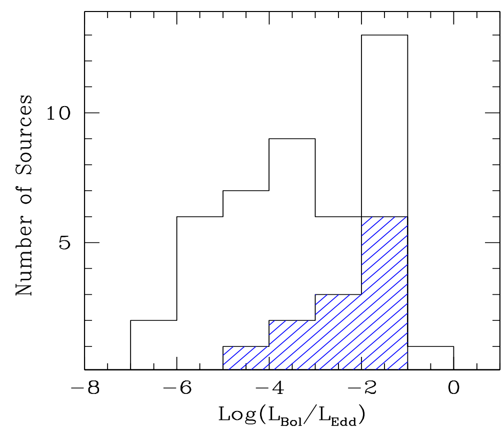


*Figure 3. Distribution of the bolometric luminosity (derived using the conservative assumption that $L_{Bol}/L_X \sim 30$) over the Eddington luminosity. Type 1 Seyfert's distribution is marked with a shaded area.*

## 3. EXTENDED SAMPLE: XMM-NEWTON & CHANDRA SURVEY OF A COMPLETE SAMPLE OF 60 SEYFERT GALAXIES

The X-ray spectral analysis has also been performed on the extended version of the Cappi et al. (2005) Seyfert sample: all the sources classified as Seyferts galaxies in the HFS97 sample have been selected without limitations in distance. The total sample of 60 Seyfert galaxies includes, 39 type 2 (type 2, 1.8 and 1.9), 13 type 1 (type 1.0, 1.2, 1.5) and 8 "dim Seyferts"[1]. Nuclear X-ray spectra have been obtained using both *Chandra* and *XMM–Newton* observations. Similarly to Cappi et al. (2005), we have investigated the issue related to the distribution of the absorption among objects in our sample. The fraction of identified CT 'candidate' objects ranges from 20% up to 50% in good agreement with Cappi et al (2005).

To verify the physical continuity between our sample and bright AGNs, the X-ray luminosities have been correlated with the $H_\alpha$ and the [OIII]$\lambda$5007 luminosities, which are both often considered to be absorption independent quantities and good tracers of the nuclear emission. Both $L_X$ vs. $L_{H_\alpha}$ and $L_X$ vs. $L_{[OIII]}$ correlations are highly significant in our sample (see Fig.2), expecially when the Cappi et al. (2005) correction factor is applied to the X-ray luminosities of Compton thick 'candidates', indicating that a common nuclear process is involved in the production of multi-wavelength radiation. Both correlations scale with luminosity, i.e. they have similar slopes to those of more powerful objects (Ho et al. 2001). It is therefore likely that low-luminosity Seyfert galaxies are powered by the same physical processes which operates in brighter AGNs such as QSOs.

Black hole masses estimates are available for 44 objects from literature. They have been obtained from gas, stellar and maser kinematics, or from reverberation mapping.

[1]Objects in which the Seyfert classification was not dominant but still present (L2/S2, H/S2 or T2/S2) have been included in the present sample.

No correlation is found between X-ray or optical emission and black hole masses. A large range of accretion rates is present (see Fig.3). Surprisingly, these sources are accreting at very low accretion rates (down to $\sim 10^{-7}$) which are more typical of ADAF-like regimes than of Standard Accretion Disk regime. Possible explanations will be discussed in a forthcoming paper, Panessa el al. in prep.

## REFERENCES

Antonucci, R. R. J. 1993, ARAA, 31, 473

Cappi, M. et al. 2005, A&Ain press, (astro-ph/0509584)

Ho, L. C., Filippenko, A. V., & Sargent, W. L. W. 1997a, ApJS, 112, 315 (HFS97a)

Ho, L. C. et al. 2001, ApJ, 549, L51

Panessa, F. & Bassani, L. 2002, A&A, 394, 435

# THE XMM-NEWTON LOOK AT MKN 841

**P.O. Petrucci[1], G. Henri[1], G. Matt[2], C. Perola[2], P. Nandra[3], P. Ferrando[4], L. Koch[4], M. Mouchet[5], A.M. Dumont[5], L. Maraschi[6], and F. Haardt[7]**

[1]Laboratoire d Astrophysique de Grenoble, Grenoble, France
[2]Dipartimento di Fisica, Universit'a degli Studi Roma tre, Roma, Italy
[3]Astrophysics Group, Imperial College, London, UK
[4]Service d Astrophysique, DSM/DAPNIA/SAp, Gif-sur-Yvette, France
[5]DAEC/LUTH, Observatoire de Paris, Meudon, France
[6]Osservatorio Astronomico di Brera, Milano, Italy
[7]Istituto di Astrofisica Spaziale, CNR, Roma, Italy

## ABSTRACT

Mkn 841 has been observed during 3 different periods (January 2001, January 2005 and July 2005) by XMM-Newton for a total cumulated exposure time of ~108 ks. In January 2001, the iron line in this source was rapidly variable, the variability being interpreted either by a change in line flux (Petrucci et al., 2002) or by a change in line width (Longinotti et al., 2004). Here we present preliminary results of the whole XMM-Newton data concerning this source, focusing on the line complex and the broad-band continuum.

Key words: LaTeX; ESA; X-rays; Galaxies: Mkn 841.

## 1. THE DATA

Mkn 841 has been observed 5 times by XMM-Newton. The date and exposure time of the different observations are summarized below: We have divided the observation

| Obs. | Date | Duration (ks) | 3-10 keV Flux ($10^{-11}$ erg.s$^{-1}$.cm$^{-2}$) |
|---|---|---|---|
| 1 | 13 Jan. 2001 | 8.5 | 1.05 |
| 2 | 13 Jan. 2001 | 10.9 | 1.17 |
| 3 | 14 Jan. 2001 | 13.3 | 1.24 |
| 4 | 16 Jan. 2005 | 46.0 | 0.85 |
| 5 | 17 Jul. 2005 | 29.1 | 0.95 |

done in Jan. 2005 in 3 sub-observations of ~ 15 ks so that we have 7 spectra with about the same exposure.

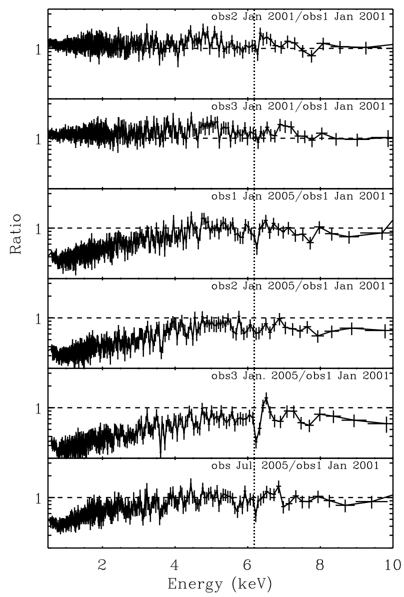


*Figure 1. Ratios of the different PN spectra to the first XMM observation. The dashed line indicates the 6.4 keV position in source frame.*

## 2. FLUX CONTINUUM VARIABILITY

During each observation, the flux smoothly varies, with a maximum amplitude (between min and max) of ~40% in Jan 2005. From January 2001 to July 2005, the flux of the source has decreased by a factor 3. We have reported in Fig. 1 the ratios of the different PN observations to the first XMM pointing of Jan 13th. We clearly see strong spectral variability between January 2001 and the others, especially below 5 keV and around 6.4 keV.

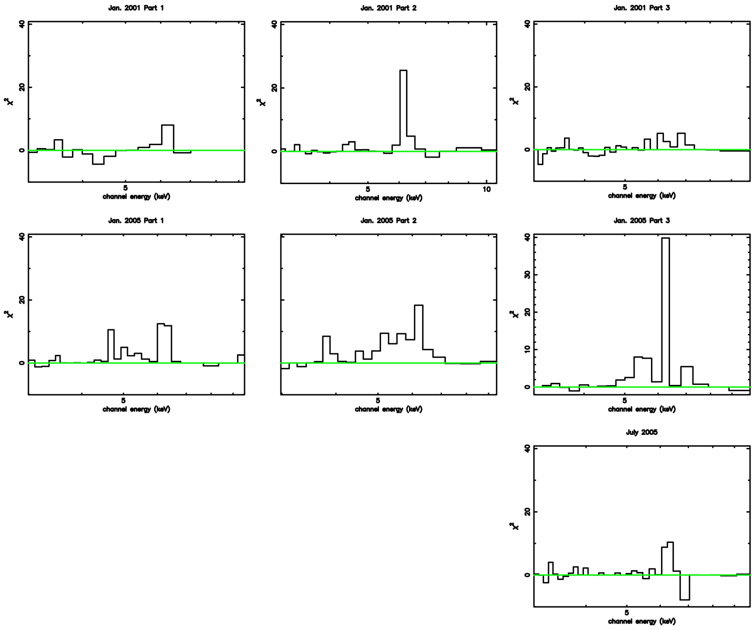


*Figure 2. $\chi^2$ distributions when fitting the different observations with a power law between 3 and 10 keV but excluding the data between 4 and 7 keV.*

## 3. LINE VARIABILITY

We have plotted in Fig. 2 the contribution to the $\chi^2$ distributions (positive and negative values of $\chi^2$ correspond to positive and negative residuals of the best fit) when fitting the different observations with a power law between 3 and 10 keV but excluding the data between 4 and 7 keV. Data have been rebinned to reach a significance of at least 15 $\sigma$ per bin. The line complex variability is clearly visible especially on short (∼10-15 ks) time scale.

## 4. PCA ANALYSIS

We use a principal component analysis (PCA) to seek for variability patterns. As shown in Fig 3, most of the variability (>99% for the broad band continuum and >80% for the iron line complex) is explained by the two first components. The first one (PC 1) consists in a variability mode dominated by flux variations in the soft energy range. It seems also to explain part of the line wings variability. The second PCA component (PC 2) can be described roughly as a pivoting of the spectrum around 1-2 keV. It should be noticed that most of the (neutral) line core variability is also explained by this component.

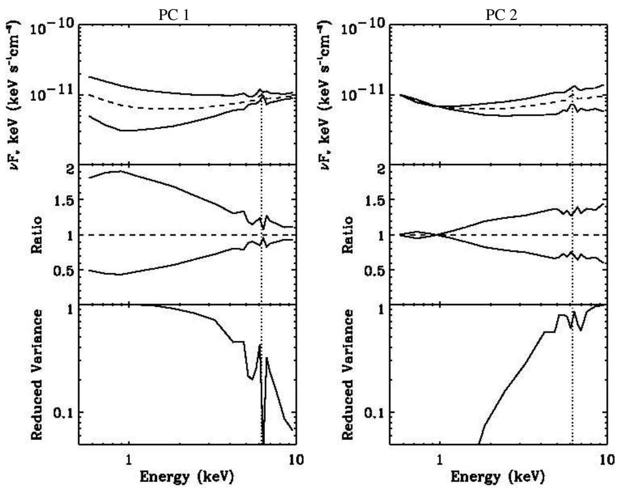


*Figure 3. The 2 first principal components of variability. The upper panels illustrate the effects of each component on the shape and normalisation of the spectrum: time average spectrum (dashed line) and spectra obtained for the maximum and minimum observed values of the normalisation parameter. The middle panels show the ratio of the maximum and minimum spectra to the average one. The bottom panels show the contribution of each component to the total variance as a function of energy.*

## REFERENCES

Longinotti, A. L., Nandra, K., Petrucci, P. O., & O'Neill, P. M. 2004, MNRAS, 355, 929

Petrucci, P. O., Henri, G., Maraschi, L., et al. 2002, A&A, 388, L5

# THE HIGHLY RED-SHIFTED FE K$\alpha$ LINE IN ESO 113-G010

**D. Porquet**[1], **J. N Reeves**[2,3], **P. Uttley**[2], **and T. J. Turner**[2,4]

[1]Max-Planck-Institut für extraterrestrische Physik, Garching, Germany
[2]Laboratory for High Energy Astrophysics, NASA Goddard Space Flight Center, Greenbelt, USA
[3]Universities Space Research Association, Seabrook, USA
[4]Joint Center for Astrophysics, Physics Department, University of Maryland, Baltimore, USA

## ABSTRACT

We present a spectral analysis of the Seyfert 1.8 ESO 113-G010 observed with XMM-Newton for 4 ks. The spectrum shows a soft excess below 0.7 keV and more interestingly a narrow emission Gaussian line at 5.4 keV (in its rest-frame), most probably originating from a red-shifted iron K$\alpha$ line. No significant line at or above 6.4 keV is found contrary to other objects showing red-shifted lines, ruling out a strong blue-wing to the line profile. The line is detected at 99% confidence, from performing Monte Carlo simulations which fully account for the range of energies where a narrow iron line is likely to occur. The energy of the line could indicate emission from relativistic (0.17–0.23 $c$) ejected matter moving away from the observer, as proposed for Mrk 766 by Turner et al. (2004). Alternatively, the emission from a narrow annulus at the surface of the accretion disk is unlikely due to the very small inclination angle (i.e. less than 10 degrees) required to explain the narrow, red-shifted line in this intermediate Seyfert galaxy. However emission from a small, localized hot-spot on the disk, occurring within a fraction of a complete disk orbit, could also explain the redshifted line. This scenario would be directly testable in a longer observation, as one would see significant variations in the energy and intensity of the line within an orbital timescale.

Key words: X-rays; Seyfert; Emission line.

## 1. INTRODUCTION

In Active Galactic Nuclei (AGN), from Seyfert galaxies to quasars, the analysis of several X-ray features can help us to understand the central region of these powerful objects. Especially in the hard X-ray band, the Fe K$\alpha$ line complex observed in the 6–7 keV range is an important spectral diagnostic tool to probe dense matter from the inner disk out to the Broad Line Region and the molecular torus (see review Reynolds & Nowak 2003; Fabian & Miniutti 2005). Recently, narrow spectral features in the 5–6 keV energy range were discovered with *XMM-Newton* and *Chandra* in a few AGN: NGC 3516 (Turner et al., 2002); NGC 7314 (Yaqoob et al., 2003); Mrk 766 (Turner et al., 2004, 2005); IC 4329A (McKernan & Yaqoob, 2004); AX J0447-0627 (Della Ceca et al., 2005). Localized spots or narrow annuli which occur on the surface of an accretion disk following its illumination by flares has been proposed to explain these features (e.g., Nayakshin & Kazanas 2001; Turner et al. 2002; Dovčiak et al. 2004). An alternative scenario has been proposed by Turner et al. (2004) for Mrk 766 for which the first evidence for a significant line energy shift has been observed over a few tens of ks. They proposed that this shift could be also interpreted as deceleration of an ejected blob of gas traveling close to the escape velocity.

## 2. THE CASE OF ESO 113-G010

This intermediate Seyfert 1.8 has been observed for the first time above 2 keV by XMM-Newton on May 2001 during a PN net exposure of 4 ks (Porquet et al., 2004). The spectrum shows a significant positive deviation near 5.4 keV (Fig. 1). The line is detected at 99% confidence from performing Monte Carlo simulations which fully account for the range of energies where a narrow iron line is likely to occur. For our null hypothesis, we assumed that the spectrum is simply an absorbed power-law continuum, with the same parameters as the absorbed power-law model fitted to the real data. We used the XSPEC FAKEIT command to create 1000 fake EPIC-pn spectra corresponding to this model, with photon statistics expected from the 4 ks exposure, and grouped each spectrum to a maximum of 20 counts per bin. Following the procedure used to test the real data for the presence of a narrow line, we fitted each fake spectrum with an absorbed power-law (absorption fixed at Galactic, but power-law photon index and normalisation left free to vary), to obtain a $\chi^2$ value. We then added a narrow line ($\sigma = 0.1$ keV) to the fit, restricting the line energy to be between 4–7 keV. Furthermore we stepped the line over

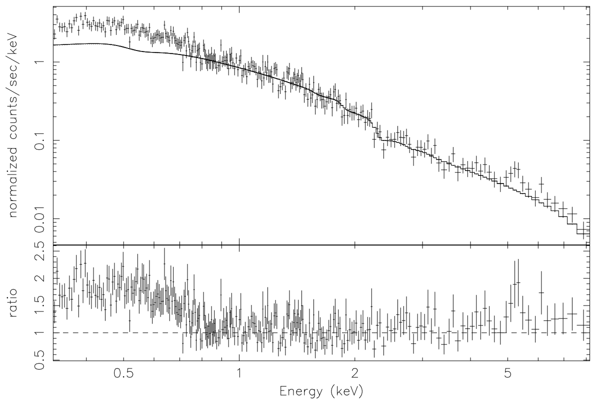


*Figure 1. PN spectrum of ESO 113-G010 (observer frame). A power-law has been fitted to the 1–4 keV energy band and extrapolated to lower and higher energies. A soft X-ray excess is clearly seen extending to about 0.7 keV, as well as a positive deviation near 5.4 keV (quasar frame).*

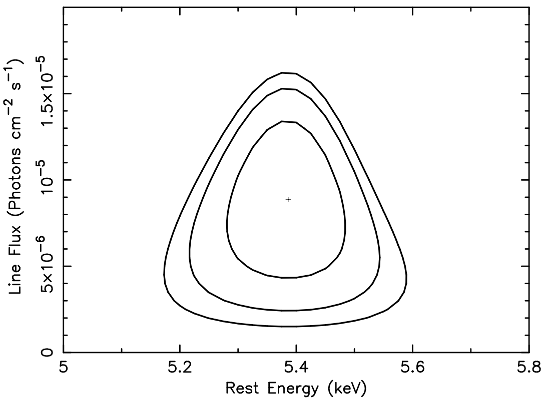


*Figure 2. Contour plot showing the 68%, 90% and 95% (from the inner to outer curves) confidence level for values of line rest-energy (keV) and line flux.*

the 4–7 keV energy range in increments of 0.1 keV, whilst fitting separately each time to ensure the lowest $\chi^2$ value was found. We then recorded the minimum $\chi^2$ obtained from these multiple line fits for each fake spectrum, and compared with the corresponding $\chi^2$ of the null hypothesis fits, to obtain 1000 simulated values of the $\Delta\chi^2$, which we used to construct a cumulative frequency distribution of the $\Delta\chi^2$ expected for a blind line search in the 4–7 keV range, assuming the null hypothesis of a simple power-law with no line is correct. We find only 1.4% of fake power-law spectra fitted with a line show a larger $\Delta\chi^2$ than observed in the real data, implying that the line detection is significant at approximately 99% confidence (see Fig. 4. in Porquet et al. 2004).

Fitting the data above 1 keV with a Gaussian line ($\sigma$=0.1 keV) we obtain a good fit for the feature with: E=5.38$\pm$0.11 keV and EW=$265^{+147}_{-145}$ eV. Figure 2 shows the confidence contour plot for the rest-energy of the line.

### 2.1. Possible origins for this highly red-shifted Fe K$\alpha$ line

• Emission from relativistic (v $\sim$ 0.17–0.23 $c$) ejected matter moving away from the observer.

• Emission from an annulus at the surface of the accretion disk BUT a very small inclination angle, less than 10 degrees, is required to explain the line in this intermediate Seyfert galaxy !

• Emission from a small, localized hot-spot of the disk, occurring within a fraction of a complete disk orbit (see modelisation e.g., by Nayakshin & Kazanas 2001 and Dovčiak et al. 2004).

• A longer X-ray observation is necessary to disentangle between these possible origins of this highly red-shifted line. This will be done with a 103 ks XMM-Newton observation (AO4, PI: D. Porquet) in order to perform time-resolved spectroscopy.

## REFERENCES

McKernan B. & Yaqoob T. 2004, ApJ, 608, 157

Dovčiak M., Karas V., Yaqoob T. 2004, ApJS, 153, 205

Fabian A. C. & Miniutti G. 2005, in ”Kerr Spacetime: Rotating Black Holes in General Relativity”, eds. D.L. Wiltshire, M. Visser and S.M. Scott, Cambridge Univ. Press, in press, [astro-ph/0507409]

McKernan B. & Yaqoob T. 2004, ApJ, 608, 157

Nayakshin S., Kazanas D. 2001, ApJ, 553, L141

Porquet D., Reeves J. N., Uttley P., Turner T. J. 2004, A&A, 427, 101

Reynolds C. S., Nowak M. A. 2003, Physics Reports, 377, 389.

Turner T. J., Mushotzky R. F., Yaqoob T. et al. 2002, ApJ, 574, L123

Turner T. J., Kraemer S. B. & Reeves J. N. 2004, ApJ, 603, 62

Turner T. J., Miller L., George I. M., Reeves J. N. 2005, A&A, in press, [astro-ph/0506223]

Yaqoob T., George I. M., Kallman T. R. et al. 2003, ApJ, 596, 85

# EXTREME X-RAY VARIABILITY AND ABSORPTION IN NGC 1365

**G. Risaliti[1,2], M. Elvis[1], G. Fabbiano[2], A. Baldi[2], A. Zezas[2], S. Bianchi[3], G. Matt[4]**

1: Harvard-Smithsonian Center for Astrophysics, 60 Garden St, Cambridge MA 02138, USA

2: INAF - Osservatorio Astrofisico di Arcetri, L. go E. Fermi 5, I-50125 Firenze, Italy

3: XMM-Newton SOC, European Space Astronomy Center, ESA, Apartado 50727, E-28080 Madrid, Spain

4: Dipartimento di Fisica, Università degli Studi "Roma Tre", Via della Vasca Navale 84, I-00146 Roma, Italy

## ABSTRACT

We present multiple Chandra and XMM-Newton observations revealing extreme X-ray absorption properties in the Seyfert Galaxy NGC 1365. We observe changes from reflection-dominated ($N_H > 10^{24}$ cm$^{-2}$) to transmission - dominated ($N_H \sim 10^{23}$ cm$^{-2}$) states in time scales as short as three weeks; moreover, we clearly measure column density variations in the Compton thin states of $\sim 10^{23}$ cm$^{-2}$ in time scales of $\sim 20,000$ sec.

Key words: Galaxies: X-rays.

## 1. INTRODUCTION

NGC 1365 (z=0.0055) is an optically type 1.8, X-ray absorbed, Seyfert Galaxy, which has shown in the past extreme variations of its spectral state: it was observed in a reflected-dominated state by ASCA in 1995 (Iyomoto et al. 1995), then in a Compton-thin state by BeppoSAX in 1998 (Risaliti et al. 2000).

Given the long time interval between the two observations, it was not possible to understand whether the variations were due to switching on and off of the central source, or to column density variations $\Delta(N_H) > 10^{24}$ cm$^{-2}$ (Guainazzi et al. 2005).

In order to further investigate this issue, NGC 1365 has been the target *Chandra* and XMM-*Netwon* observational campaign during the years 2002-2004. The source was caught in a Compton-thick state by Chandra, then in a Compton-thin state by XMM-*Newton* three weeks later, and again in a Compton-thick state three more weeks later. This rapid variability implies the presence of a clumpy absorber on a smaller scale (of the order of that of the Broad Line Region or slightly larger) than usually assumed for the circumnuclear torus (a few parsecs). These results are discussed in detail in Risaliti et al. 2005a. These three observations are all relatively short ($\sim 10$ ksec), therefore a variability analysis of the single observations is not possible. Two, longer ($\sim 60$ ksec) XMM observations were obtained in 2004, allowing an analysis of the intra-day variability. Here we summarize the results regarding the variability studies. Another interesting result obtained from these two observations is the detection of four strong absorption lines in the 6.7-8.3 keV spectral range, identified as FeXXV and FeXXVI $K\alpha$ and $K\beta$. These lines imply the presence of a highly ionized, compact absorber with a column density of several $10^{23}$ cm$^{-2}$, and are discussed in Risaliti et al. 2005b.

## 2. ANALYSIS OF THE ABSORPTION VARIABILITY

In order to search for column density variations within the single observations, we performed a two-steps analysis. We first calculated a hardness-ratio (HR) light curve, which is sensitive to variations in spectral shape. A non-constant HR light curve can be due to several different phenomena: column density variations, changes in the continuum slope, flux variability of a spectral component in a multi-component spectrum. As a second step, a complete spectral analysis of the single HR states is needed in order to distinguish between these cases. We show in Fig. 1 the HR light curve for the first of our two long XMM observations. Three different spectral states are clearly present. We extracted the spectrum from each of these three intervals, and performed three fits to a multi-component model, consisting of an absorbed power law, a cold reflection component, an iron emission line, and a soft thermal component. In each fit all the parameters were left free, therefore any of the above-mentioned variation mechanisms could be investigated. We obtained a good fit for all the single spectra, with all the parameters compatible with a constant value, except for the column density, which was found to vary with a significance higher than 99% (Fig. 2).

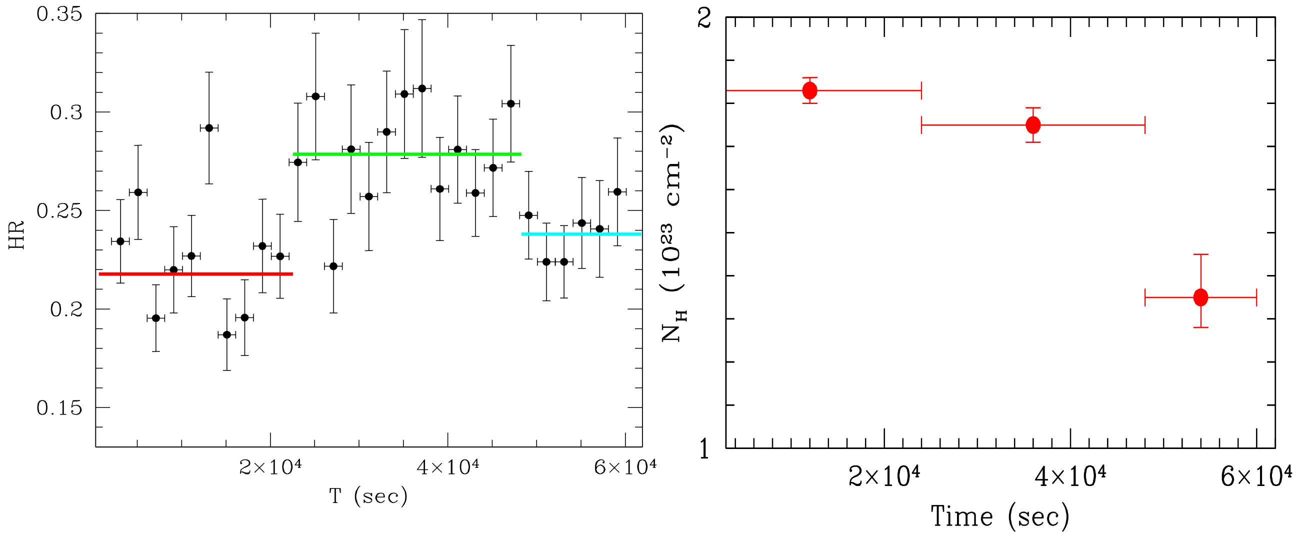


*Figure 1. Left panel: hardness ratio light curve for a 60 ksec XMM observation of NGC 1365. The three intervals labeled with the three horizontal lines have been separately analyzed. The best fit column density values for the three spectra are shown in the right panel.*

Our results put strong constraints on the location of the X-ray absorber. Assuming that the absorption is due to clouds moving with Keplerian velocity, $v_K = \sqrt{GM_{BH}/R}$, we can derive a relation between the cloud density $\rho$ and its distance $R$ from the central source simply identifying the linear dimension of the cloud, $D = N_H/\rho$, with the distance covered by the cloud in the typical variation time scale, $\Delta(T)$. The limits put by our observations are shown in Fig. 2. A parsec scale torus is completely ruled out, unless unphysically high densities ($\rho > 10^{12}$ cm$^{-3}$) are allowed.

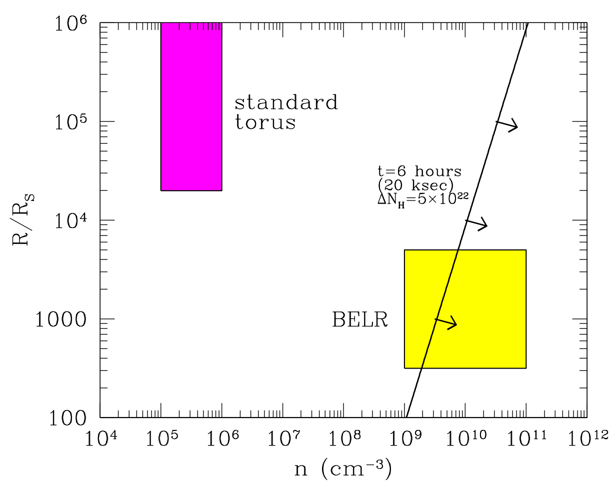


*Figure 2. Distance of the absorber from the central source versus its density. Our observations exclude a parsec-scale torus, and suggest that the absorber is located at the Broad Line Region scale.*

This result is in agreement with the studies performed by our group on other bright Seyfert Galaxies, such as NGC 4151 (Puccetti et al. 2004) and NGC 4388 (Elvis et al. 2004) and suggests that the X-ray absorber is located as close to the center as the Broad Line Region.

## ACKNOWLEDGMENTS

This work has been supported by NASA grants NAG5-13161, NNG04GF97G, and NAG5-16932.

## REFERENCES


Elvis, M., Risaliti, G., Nicastro, F., Miller, J. M., Fiore, F., & Puccetti, S. 2004, ApJ, 615, L25

Guainazzi, M., Fabian, A. C., Iwasawa, K., Matt, G., & Fiore, F. 2005, MNRAS, 356, 295

Iyomoto, N., Makishima, K., Fukazawa, Y., Tashiro, M., & Ishisaki, Y. 1997, PASJ, 49, 425

Puccetti, S., Risaliti, G., Fiore, F., Elvis, M., Nicastro, F., Perola, G. C., & Capalbi, M. 2004, Nuclear Physics B Proceedings Supplements, 132, 225

Risaliti, G., Maiolino, R., & Bassani, L. 2000, A&A, 356, 33

Risaliti, G., Bianchi, S., Matt, G., Baldi, A., Elvis, M., Fabbiano, G., & Zezas, A. 2005a, ApJ, 630, L129

Risaliti, G., Elvis, M., Fabbiano, G., Baldi, A., & Zezas, A. 2005b, ApJ, 623, L93

# *INTEGRAL/RXTE* OBSERVATIONS OF CEN A

**Richard E. Rothschild, John Tomsick[1], Jörn Wilms[2], Rüdiger Staubert, Sara Benlloch[3], Werner Collmar[4], Greg Madejski[5], Sandrine Deluit[6], and Harish Khandrika[7]**

[1]Center for Astrophysics and Space Sciences, University of California, San Diego, La Jolla, CA, USA
[2]Department of Physics, University of Warwick, Coventry, UK
[3]Institut für Astronomie und Astrophysik, Tübingen, Germany
[4]Max-Planck-Institut für extraterrestrische Physick, Garching, Germany
[5]Stanford Linear Accelerator Center, Menlo Park, CA, USA
[6]Centre d'Etude-Spatiale des Rayonnements, Toulouse, France
[7]Department of Physics, University of California, Berkeley, Ca, USA

## ABSTRACT

*INTEGRAL* and *RXTE* performed three simultaneous observations of the nearby radio galaxy Centaurus A in March, 2003, January, 2004 and February, 2004. When combined with earlier archival *RXTE* results, we find the power law continuum flux and the line-of-sight column depth varied independently by 60% between 2000 January and 2003 March. Taking X-ray spectral measurements from satellite missions since 1970 into account, we discover a variability in the column depth between (1 and 1.5)$\times 10^{23}$ cm$^{-2}$, and suggest that variations in the edge of a warped accretion disk viewed nearly edge-on might be the cause. Direct comparison of *INTEGRAL* and *RXTE* results finds that all instruments agree, except for *INTEGRAL*/ISGRI which consistently finds a power law index greater by $\sim$0.2.

Key words: Radio galaxies; Centaurus A; X-rays.

## 1. INTRODUCTION

The three *RXTE* observations of Cen A — the nearest radio galaxy — in 1996, 1998, and 2000 (Rothschild et al., 1999; Benlloch et al., 2001) and five from *BeppoSAX* in 1997-2000 (Grandi et al., 2003) found the spectrum to be characterized by an absorbed (N$_H$ $\sim 10^{23}$ cm$^{-2}$) power law ($\Gamma$ $\sim$1.80) with Fe line emission and no evidence for a reflection component. These multiple observations yielded evidence for $\sim$50% flux variations from one observation to the next with little if any spectral shape changes.

## 2. OBSERVATIONS AND RESULTS

*INTEGRAL* and *RXTE* observed Cen A three times as part of the *INTEGRAL* AO-1 and *RXTE* AO-7 proposal cycles in March, 2003 and early 2004 with the goal of intercalibration and extension of the measurement of the continuum beyond 200 keV. The *INTEGRAL* analysis was based upon release OSA 4.2 from the *INTEGRAL* Science Data Center. Approximately 20% systematics errors have been added to the JEM-X data and 3–9% systematics have been added to ISGRI data to represent the level of understanding of the instrument response, while none have been added to SPI. PCA data for all observations were limited to PCU2. Systematic errors of 0.3% have been included in the PCA data along with additions to the spectral model for known systematic effects. None have been added to the HEXTE data.

Table 1: Mean Cen A Spectral Parameters

| | PCU2 | HEXTE | JEM-X | ISGRI |
|---|---|---|---|---|
| $\langle N_{\rm H}\rangle$ | $15.9^{+0.3}_{-0.2}$ | | $13.8^{+5.5}_{-4.6}$ | |
| $\langle\Gamma\rangle$ | 1.83±0.01 | 1.83±0.07 | 1.80±0.17 | 2.01±0.09 |
| | SPI | *RXTE* | *INTEGRAL* | |
| $\langle N_{\rm H}\rangle$ | | 15.8±0.2 | $17.7^{+3.6}_{-3.3}$ | |
| $\langle\Gamma\rangle$ | 1.78±0.17 | 1.82±0.01 | 1.94±0.07 | |

$\langle N_{\rm H}\rangle$ in units of $10^{22}$ cm$^{-2}$

The two missions' data sets were fit separately to the spectral model const*phabs*(power + gauss). JEM-X did not detect the iron line whereas PCA did. Fig. 1 shows the best fit spectral histograms for the two *RXTE* and three *INTEGRAL* instruments, and Table 1 gives the mean best fit values for $N_{\rm H}$ and $\Gamma$. We have observed factor of two flux variability in Cen A without correlated spectral changes. The column density varied by 50% independently of the flux or power law index. No break in the power law continuum is detected below $\sim$140 keV.

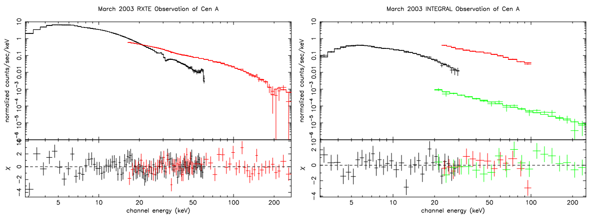


*Figure 1. The March 2003 Cen A counts histograms from RXTE (Left) with PCA in black and HEXTE in red, and INTEGRAL (Right) with JEM-X in black, ISGRI in red, and SPI in green. The chi per energy bin versus energy for fitting to an absorbed power law is displayed below each histogram. The relative normalizations are with respect to PCA and JEM-X, respectively.*

The ISGRI best fit power law indices were 0.2±0.1 larger than the indices found by the *RXTE* instruments.

## 3. VARIABLE OBSCURATION

Over the last 3 decades, Cen A has been observed from space by nearly all X-ray and gamma ray missions. Fig. 2 shows the measured values of the inferred column density, $N_{\rm H}$, since 1975 (see also Risaliti, Elvis, & Nicastro, 2002). The lower value of $\sim 10\times 10^{22}$ cm$^{-2}$ is seen to occur twice in this time period, with the higher value of $\sim 15\times 10^{22}$ cm$^{-2}$ seen the rest of the time. The first occurrence of the lower value was detected by only HEAO-1 in 1978, while the second was was seen by *RXTE*, *Chandra*, and *BeppoSAX*. The range of high values of $N_{\rm H}$ seen from $\sim$(13.5 to 17)$\times 10^{22}$ cm$^{-2}$ is broader than the range of lower values, (9.5 to 10.2)$\times 10^{22}$ cm$^{-2}$, and this might indicate that the lower values represent the baseline for judging variations in column depth. The times of increased absorption could represent dense ($\sim 10^{22}$ cm$^{-2}$) clouds transiting the line of sight, or variable structure in the outer edges of the obscuring accretion disk or molecular torus.

If the $\sim$9 year duration of the higher level of absorption seen in the center of Fig. 2 represents a cloud, and if, as discussed by Wang et al. (1986), it resides in the broad line region at $10^{17}$ cm from the central object and has velocity of 500–1000 km/s, its diameter would be $\sim 10^{17}$ cm — the size of the entire broad line region. If we assume a more reasonable cloud of diameter of $10^{13}$ cm and $N_{\rm H} = 5\times 10^{22}$ cm$^{-2}$, then its velocity would be a meager 0.3 km/s and would place the cloud far beyond the core region. A cloud-based explanation appears to be untenable.

The second possibility is variable structure in the outer edge of the disk. This could be characterized as a non-uniform edge structure that rotated through the line of sight as the outer disk rotated or just stochastic variations in disk structure. Assuming a $2\times 10^8 M_\odot$ black hole (Silge et al. , 2005), 20 pc radius accretion disk (Schreier et al., 1998), and Kelperian motion, the velocity of the outer edge of the disk is $\sim 7\times 10^6$ cm s$^{-1}$ and the circumference is $\sim 4\times 10^{21}$ cm. A point on the edge will travel $2\times 10^{15}$ cm in 8 years, or less than a millionth of the circumference. Thus, the required structure is quite small with respect to the disk, and is not out of the question.

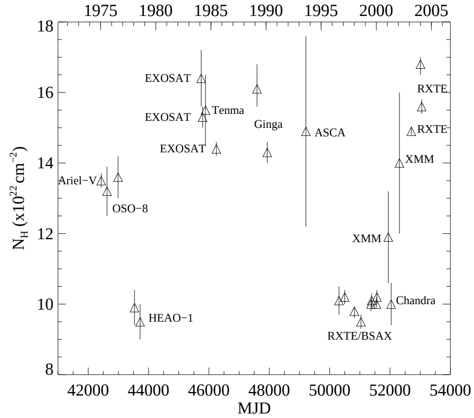


*Figure 2. History of line of sight column depth to Cen A from 1975 to the present utilizing* Ariel-V, OSO-8, HEAO-1, EXOSAT, Tenma, Ginga, ASCA, BeppoSAX *(Grandi et al., 2003),* RXTE *(present paper),* Chandra, *and* XMM-Newton.

Another possible explanation is precession of the warped accretion disk (Schreier et al., 1998) creating a variable absorption. The lower column depth would represent the time when the edge of the disk raised or lowered to allow a more direct view of the emission region, and the higher values could be associated with the edge of the disk returning to attenuate the X-ray emission.

## ACKNOWLEDGMENTS

RER acknowledges the support of NASA contract NAS5-30720 and NSF international grants NSF_INT-9815741 and NSF_INT-0003773 for fostering the UCSD/Tübingen collaboration.

## REFERENCES

Benlloch, S. et al. 2001, A&Ap, 371, 858.

Grandi, P. et al. 2003, ApJ, 593, 160.

Risaliti, G., Elvis, M., & Nicastro, F. 2002, ApJ, 571, 234.

Rothschild, R.E. et al. 1999, ApJ, 510, 651.

Schreier, E.J. et al. 1998, ApJ, 499, L143.

Silge, J.D. et al. 2005, astro-ph/0501446.

Wang, B. et al. 1986, PASJ, 38, 685.

# AN XMM-NEWTON STUDY OF HYPER-LUMINOUS INFRARED GALAXIES

**A. Ruiz, F.J. Carrera, and F. Panessa**

Instituto de Física de Cantabria (CSIC-UC), 39005 Santander, Spain

## ABSTRACT

We have selected a sample of Hyper-Luminous Infrared Galaxies (HLIRGs) with public observations in the XMM-Newton archive. This is the first time that a systematic study of this type of objects is carried out in this spectral band. Their X-ray spectra are characterized by the presence of a power-law continuum, associated to the AGN, and, in a few cases, of a thermal component probably associated to the starburst (SB). We have looked up for relationship between the X-ray and far-IR luminosities. We find that most HLIRGs are "mixed" sources: their X-ray luminosity is too high to be produced by a SB, and their infrared luminosity is too high to be produced by an AGN, assuming a standard SED for QSOs as in Elvis et al. (1994). The X-ray to IR luminosity ratio is constant with redshift, indicating that their respective power sources could be physically related.

Key words: galaxies:infrared; galaxies:starburst; galaxies:evolution; galaxies:active; HLIRG.

## 1. INTRODUCTION

Hyper-Luminous Infrared Galaxies (HLIRGs, $L_{IR} \geq 10^{13} L_{\odot}$) are the most luminous objects in the Universe. They exhibit extremely high star formation rates, and most of them seem also to harbour an AGN. HLIRGs are strong candidates for being primeval galaxies (Rowan-Robinson, 2000), in the process of a major episode of star formation. As they represent the most vigorous stage of galaxy formation, they are unique laboratories to investigate extremely high star formation, and its connection to supermassive black hole growth. X-ray studies of HLIRGs have the potential to unravel the AGN contribution to the bolometric output from these bright objects.

The main objective of this study is to determine the relative contribution of starburst (SB) and AGN emission to the bolometric luminosity and their interplay. The dependence of the SB versus AGN contribution with cosmic time has been investigated. We have also studied the relation of HLIRGs with their lower IR luminosity version, Ultra-Luminous Infrared Galaxies (ULIRGs) (Franceschini et al., 2003).

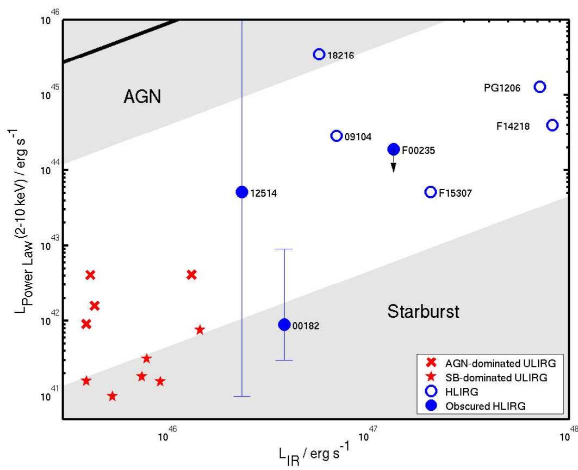


*Figure 1. 2-10 keV $L_X$ of the power-law component versus $L_{IR}$. The top grey area indicates the $L_{IR}$ expected (at 90% of confidence) for an AGN with the corresponding $L_X$ (Elvis et al., 1994). The bottom grey area indicates the $L_X$ expected for a SB with the corresponding $L_{IR}$ (Persic et al., 2004; Kennicutt, 1998). IRAS F00235 X-ray data are upper limits from Wilman et al. (2003).*

## 2. SAMPLE AND RESULTS

Our sample has been selected from Rowan-Robinson (2000) sample of HLIRGs with redshift between ~0.3 and ~1.5, and with public data in XMM-Newton archive. The EPIC spectra extracted from this data have been modelled, revealing an heterogeneous spectral properties for this objects.

All the sources present a power-law continuum, probably associated to the AGN. We have included a thermal (two sources), reflection (one source) and/or absorption (one source) component where it was needed. In two spectra we have also found K$\alpha$ iron lines. A detailed description

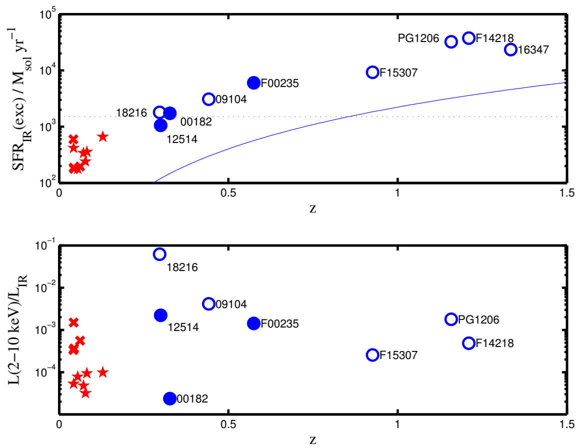


*Figure 2.* ***Top:*** *SFR derived from $L_{IR}$ (Kennicutt, 1998), versus z. The dotted line represents the SFR limit corresponding to the HLIRGs definition. The solid line is the SFR for a source with IRAS fluxes equals to the IRAS FSC sensitivity limits (Moshir et al., 1990).* ***Bottom:*** *2-10 keV X-ray to IR luminosities ratio versus z.*

of the sample and data analysis will be presented in Ruiz et al.(in prep.).

We have calculated the X-ray luminosities ($L_X$), using XMM-Newton data, and far-IR (8-1000 $\mu$m) luminosities ($L_{IR}$), using IRAS fluxes (Pérault, 1987). We have also estimated the star formation rate (SFR) for each source using its far-IR luminosity (Kennicutt, 1998).

## 2.1. X-ray PL vs Far-Infrared: Starburst or AGN?

In Fig. 1 HLIRGs seem to follow the same tendency as AGN-dominated ULIRGs, although no significant correlation is observed. Most of HLIRGs and all AGN-dominated ULIRGs seem to be “mixed” sources: their X-ray luminosity is too high to be produced only by a SB, and their infrared luminosity is too high to be produced by only an AGN. Note that IRAS 18216+6418 is the only source that clearly shows AGN-dominated properties.

Compton thick obscuration could in principle move up some HLIRGs from the “mixed zone” to the “AGN zone” (see Wilman et al. 2003, Iwasawa et al. 2006, this volume).

## 2.2. Redshift evolution?

Higher SFR at higher redshift is observed in upper plot of Fig. 2. However this could be due to a selection effect. We can see in bottom plot that the ratio of hard X-ray to IR luminosity remains constant with z, suggesting that AGN and SB are physically connected at least below z$\sim$1.5. A sample at higher z is needed to check this issue.

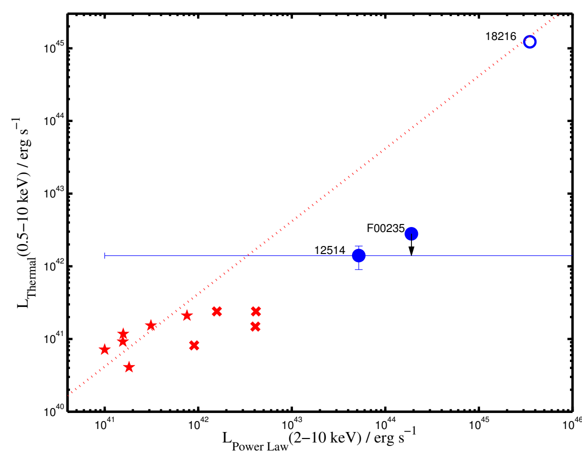


*Figure 3. $L_X$ (0.5-10 keV) of the thermal component versus $L_X$ (2-10 keV) of the power-law component. The dotted line is a correlation obtained by Franceschini et al. (2003) for SB-dominated ULIRGs. IRAS F00235 X-ray data are upper limits from Wilman et al. (2003).*

## 2.3. X-ray thermal vs PL: Where is thermal emission?

As shown in Fig. 3, only two HLIRGs present intrinsic thermal emission, while in all ULIRGs a thermal component has been observed. Also, IRAS 18216+6418, whose emission is clearly AGN-dominated, follows the same correlation as starburst-dominated ULIRGs (Franceschini et al., 2003), but the limited statistics of the samples prevent from further discussion.

## REFERENCES

Elvis, M., Wilkes, B. J., McDowell, J. C., et al. 1994, ApJS, 95, 1

Franceschini, A., Braito, V., Persic, M., et al. 2003, MNRAS, 343, 1181

Kennicutt, R. C. 1998, ApJ, 498, 541

Moshir, M., Kopan, G., Conrow, T., et al. 1990, in IRAS Faint Source Catalogue, version 2.0 (1990), 0–+

Pérault, M. 1987, PhD thesis, Université de Paris VII

Persic, M., Rephaeli, Y., Braito, V., et al. 2004, A&A, 419, 849

Rowan-Robinson, M. 2000, MNRAS, 316, 885

Wilman, R. J., Fabian, A. C., Crawford, C. S., & Cutri, R. M. 2003, MNRAS, 338, L19

# PROBING THE PHYSICAL CONDITIONS IN THE CIRCUMNUCLEAR REGION OF NGC 4151

**H. R. Schmitt[1], S. B. Kraemer[2], D. M. Crenshaw[3], and J. B. Hutchings[4]**

[1]Naval Research Laboratory, Code 7210, Washington, DC 20375; and Interferometrics Inc., Herndon, VA 20171, USA
[2]Catholic University of America, Washington, DC 20064; and Laboratory for Astronomy and Solar Physics, GSFC, Code 681, Greenbelt, MD 20771, USA
[3]Department of Physics and Astronomy, Astronomy Offices, Georgia State University, Atlanta, GA 30303, USA
[4]Dominion Astrophysical Observatory, National Research Council of Canada, Herzberg Institute of Astrophysics, Victoria, BC V9E 2E7, Canada

## ABSTRACT

We present a study of high resolution HST images of the Seyfert 1 galaxy NGC 4151 in the emission lines [OII]$\lambda$3727Å and [OIII]$\lambda$5007Å. These images were used to study the ionization structure of the gas in the Narrow Line Region (NLR), through the emission line ratio [OIII]/[OII]. We find that gas located along the region perpendicular to the torus axis has much lower ionization than the gas located along the torus axis. This result, indicates that the gas along the torus equator is being ionized by radiation filtered through its outer regions. This scenario is consistent with the detection, by X-ray observations, of a high column density along the line of sight, corroborating the previously suggested nuclear geometry of this AGN.

Key words: Emission Lines; Seyfert; NGC 4151.

## 1. INTRODUCTION

NGC 4151 is a nearby Seyfert 1 galaxy that has been extensively studied throughout the electromagnetic spectrum. Narrow band images of this galaxy (Evans et al. , 1993) show that the [OIII] emission has the shape of a bi-cone with the axis aligned along PA$=60°$. The bi-cone is caused by the shadowing of the nuclear radiation by the circumnuclear torus, postulated by the unified scheme Antonucci (1993). Based on the orientation of the NLR relative to the host galaxy and the radio jet, Evans et al. (1993) suggested a geometry where the nucleus of this AGN is observed through the torus wall. Although this geometry would suggest that NGC 4151 should be classified as a Seyfert 2 object, our line of sight to the nucleus may pass only through regions of the torus that are mostly ionized, or have a small dust content. Support for this interpretation comes from previous X-ray studies with ASCA and Chandra (e.g. George et al. 1998), which detected a high column density of ionized gas in front of the nucleus of this galaxy, with column densities in the range $2-5\times10^{22}$ cm$^{-2}$.

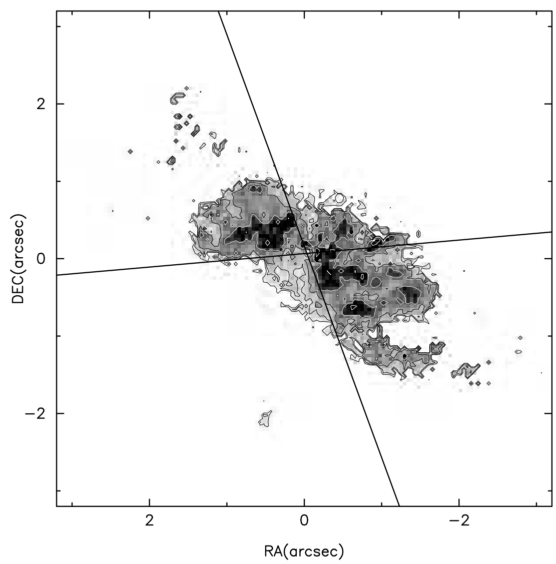


*Figure 1. The [OIII]/[OII] ratio image of NGC 4151. The solid lines highlight the ionization bi-cone described by Evans et al. (1993), which has a projected opening angle of 75°, aligned along PA$=60°$. The range of values covered by the image goes from [OIII]/[OII]=0.5 in the lighter regions, low ionization, to 8 in the darker ones, high ionization. The contour levels correspond to [OIII]/[OII]=0.5, 1, 2, 4 and 8.*

Here we present further evidence in favor of the geometry proposed by Evans et al. (1993), based on high resolution HST images. We used narrow-band images centered on the emission lines [OIII] and [OII], observed with the planetary camera on WPFC2. The images were reduced, calibrated and continuum subtracted using standard procedures. In order to study the ionization of the NLR gas we clipped the continuum free images at the $3\sigma$ level and created a [OIII]/[OII] image (Figure 1). This image shows the ionization bi-cone seen in the single emission line images, with the high ionization gas located along the bi-cone axis. A feature of particular interest in this Figure is the wedge of low ionization gas along the direction perpendicular to the bi-cone axis (PA 150).

The difference in the ionization state of the gas along the bi-cone axis and in the perpendicular direction can be seen better in the radial profiles presented in Figure 2. In the case of the profile along PA$= 221°$, we can do a direct comparison to the STIS long slit spectrum presented by Nelson et al. (2000). We find a good agreement between the two measurements, with the strongest [OIII]/[OII] located close to the nucleus, indicating higher excitation, decreasing toward to outer regions of the NLR. On the other hand, the profile along the direction perpendicular to the bi-cone axis (PA$= 150°$) confirms that [OIII]/[OII] is lower along this direction, particularly toward the SE, where it reaches a factor of $\sim$5 lower than along the bi-cone axis. The emission toward the NW has slightly higher values, but still lower then the ones seen in the cone. Notice that this ratio should actually be considered an upper limit, since the effect of reddening is strong in [OII], which suggests that the excitation of the gas can be even lower along this direction.

The result presented in Figures 1 and 2 can be understood in the geometry proposed by Evans et al. (1993). A natural consequence of this scenario is that the torus filters part of the ionizing radiation, resulting in the low [OIII]/[OII] seen along PA$= 150°$ (torus equator). Further confirmation of this model comes from the comparison between the predictions from simple photo-ionization models with the [OIII]/[OII] along this direction. We find that the observed line ratios can be explained if the continuum ionizing this gas is first absorbed by a column density of $\sim 10^{21}$ cm$^{-2}$.

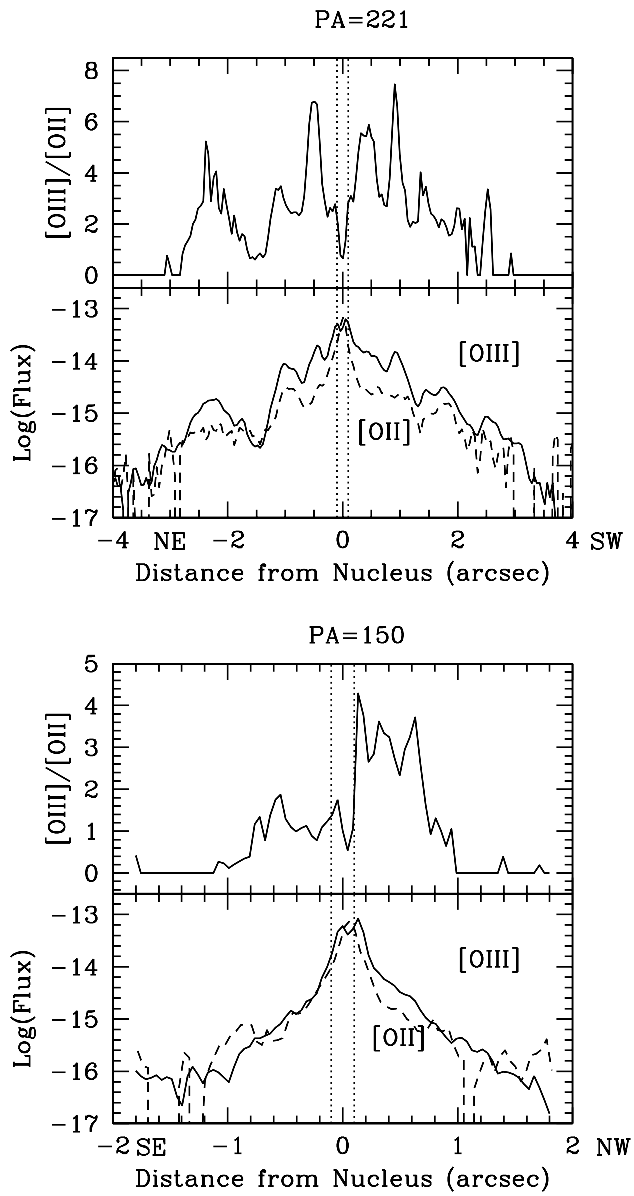


*Figure 2. Radial profiles along PA$= 221°$ (top panels), corresponding to the direction along the bi-cone/torus axis, and along PA$= 150°$ (bottom panels), corresponding to the direction along the torus equator. Top panel shows the [OIII]/[OII] ratio and the bottom one shows the [OIII] (solid line) and [OII] (dashed line). The vertical dotted lines show the region around the nucleus that should be disregarded because of image saturation. Profiles were extracted by adding 3 pixels ($\sim 0.14''$) along the direction perpendicular to the one being studied.*

## ACKNOWLEDGMENTS

Results based on observations made with the NASA/ESA Hubble Space Telescope, operated by the Association of Universities for Research in Astronomy, Inc., under NASA contract NAS5-26555. Basic research at the US Naval Research Laboratory is supported by the Office of Naval Research.

## REFERENCES

Antonucci, R. 1993, ARA&A, 31, 473

Evans, I. N., et al. 1993, ApJ, 417, 82

George, I., et al. 1998, ApJS, 114, 73

Nelson, C. H., et al. 2000, ApJ, 531, 257

# X-RAY EMITTING EROS AND OBSCURED QSOS

**P. Severgnini[1], V. Braito[2], A. Caccianiga[1], R. Della Ceca[1], T. Maccacaro[1], and P. Saracco[1]**

[1]INAF- Osservatorio Astrofisico di Brera, via Brera 28, I-20121 Milano, Italy
[2]Johns Hopkins University, 3400 N. Charles Street, Baltimore, MD 21218,USA
**on behalf of the XMM-Newton SSC collaboration**

## ABSTRACT

We present XMM-Newton data along with optical and near-infrared photometric properties of one of the X-ray emitting EROs (XBS J0216-0435) with the highest F(2-10 keV)/F(R) ratio (>200) among those present in the literature. This ERO has been discovered in the XMM-Newton Bright Serendipitous Survey and it is an excellent candidate to be a high redshift (z>0.6, possibly z∼2) X–ray obscured and optical type 2 QSO.

Key words: Extremely Red Objects - Active Galactic Nuclei - QSO.

## 1. INTRODUCTION

X-ray obscured (NH>$10^{22}$ cm$^{-2}$) and optically absorbed QSOs (hereafter QSO2) represent an important ingredient for the X-ray Cosmic Background (Gilli et al. 2001, Ueda et al. 2003) and many efforts have been made so far by the scientific community to find them and to study their properties. Extremely red objects (R-K>5, EROs) with X-ray fluxes Fx>$5\times10^{-15}$ erg s$^{-1}$ cm$^{-2}$ and with X-ray-to-optical flux ratios equal or larger than 10 are among the best candidates to host QSO2. Indeed, in these latter sources, the UV and optical emission could be totally suppressed by the large amount of dust producing red optical-NIR colors, while the X-ray emission is less affected by the absorbing medium producing high F(2-10 keV)/F(opt). We present here recent results obtained for an X-ray emitting ERO (XBS J0216-0435) discovered in the XMM-BSS survey and characterized by an extremely high X-ray-to-optical flux ratio. Hereafter, we assume $H_0$=65 km s$^{-1}$ Mpc$^{-1}$ and $\Omega_M$=0.3, $\Omega_\Lambda$=0.7. All the magnitudes are in Vega system.

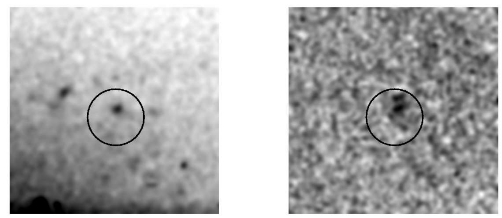

*Figure 1. R–band image (30″×30″, left panel) and K–band image (30″×30″, right panel) of XBS J0216-0435. North is up and east to the left. The circle of 4″of radius marks the X–ray position of XBS J0216–0435.*

## 2. XBS J0216-0435

**Broad-band properties –** The XMM-BSS (XMM-Newton Bright Serendipitous Survey) is a project carried out by the XMM-Newton Survey Science Center (Watson et al. 2001). The source sample is composed by two subsamples of high Galactic latitude (|bII|>20°) and bright (Fx∼$10^{-13}$ erg cm$^{-2}$ s$^{-1}$) serendipitous XMM sources selected in two complementary energy bands: 0.5-4.5 and 4.5-7.5 keV (see Della Ceca et al. 2004 and Caccianiga et al. 2004). Here we focus on the optical, near-infrared and X-ray properties of one of these sources: XBS J0216-0435 (Fx∼$10^{-13}$ erg cm$^{-2}$ s$^{-1}$).

Our own R–band and K–band photometric observations have been performed at the ESO New Technology Telescope (NTT) using the ESO Multi-Mode Instrument (EMMI, 1 hour of exposure time) and at the Telescopio Nazionale Galileo (TNG) using the Near Infrared Camera Spectrometer (NICS, 15 minutes of exposure) respectively (see Fig. 1). A weak (R∼24.5 mag) optical counterpart is visible within 4″ from the X-ray position of XBS J0216-0435 (see the circle in Fig. 1, left panel). Within the same distance from the X-ray position two possible weak near-infrared objects are visible (K'∼19.5 mag, Fig. 1, right panel). All the sources appear extended in the optical and NIR images. We find that the optical source is spatially coincident with the southern near-infrared source. This latter is also the near-infrared

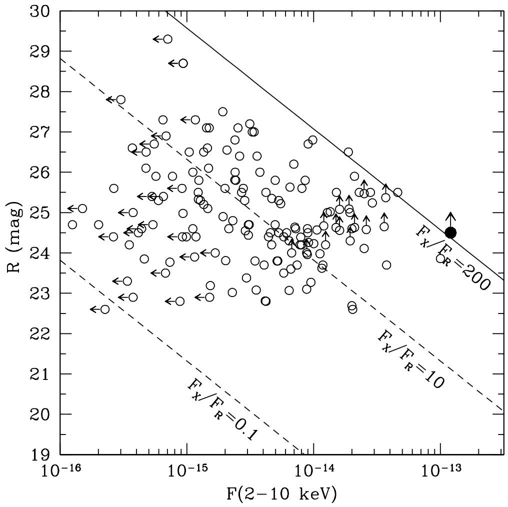


*Figure 2. R–magnitude vs. 2–10 keV flux for XBS J0416–0435 (filled circle) and for other X–ray emitting EROs (empty circles) taken from the literature (see Severgnini et al. 2005, Brusa et al. 2005). Upper and lower limits of the 2–10 keV fluxes and R magnitudes are marked with arrows. The two dashed lines define the region where unobscured type 1 AGN typically lie.*

source closest to the X-ray position (less than 1″). Given the colour of the two sources (R-K'∼5 for the southern source and R-K'>6 for the northern one) XBS J0216–0435 turn out to be an ERO.

XBS J0216-0435 is the X-ray source with the highest F(2-10 keV)/F(R) ($\gtrsim$220) among the XMM-BSS objects. Moreover, it is one of the X-ray emitting EROs in the literature with the highest X-ray flux among those with the highest F(2-10 keV)/F(R) ratio. This is shown in Fig. 2 where R–magnitudes are reported as a function of 2-10 keV flux for XBS J0216-0435 (filled circle) and for other X–ray emitting EROs (empty circles) taken from the literature (see Severgnini et al. 2005, Brusa et al. 2005).

**X-ray spectral analysis –** A single absorbed power-law model (typical of obscured AGN) gives a good description of the overall X-ray spectrum of XBS J0216-0435 ($\chi^2$/dof∼1, see Fig. 3). Under the hypothesis that the object lies at z>0.6, i.e. the minimum z for extra-Galactic EROs with such high F(2-10 keV)/F(opt) and F(2-10 keV)/F(K), we find an intrinsic NH>$10^{22}$ cm$^{-2}$ and a de-absorbed rest–frame L(2-10 keV)>$10^{44}$ erg s$^{-1}$. If we associate the 2 keV excess shown in Fig. 3 to the neutral iron K$\alpha$ line at 6.4 keV rest-frame the source is placed at z∼2 with an intrinsic L(2-10 keV)∼$6\times10^{45}$ erg s$^{-1}$.

**Conclusion –** The X-ray spectral analysis of the XMM–BSS X-ray emitting EROs (XBS J0216-0435) suggests the presence of an high redshift (z>0.6, possibly z∼2) obscured QSOs in this source. The extended appearance in the optical and near-infrared bands along with the extremely high X-ray to optical and X–ray to near-infrared flux ratios support the idea that the host galaxy dominates the emission at these wavelengths and that this QSO is heavily absorbed also in the optical band.

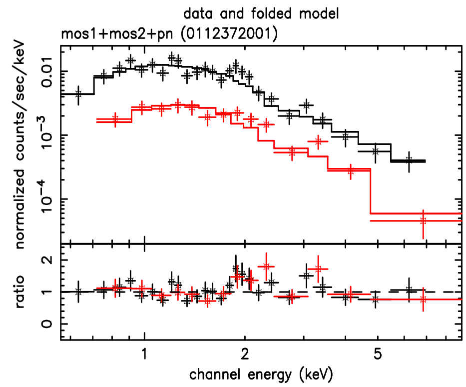


*Figure 3. Mos+pn folded X–ray spectra of XBS J0216-0435 (upper panel, solid points) and the best–fit model (single absorbed power–law model at z=0.6, continuous lines). Ratio between data and model is plotted in the lower panel as a function of energy.*

Our result suggests that relatively bright X-ray emitting EROs with high X-ray to optical and X–ray to near-infrared flux ratios are very good candidates to be QSO2. This scenario is also supported by the few examples already present in the literature of X-ray emitting EROs with high F(2-10 keV)/F(opt) ratios and with an estimate of the spectroscopic redshift (i.e. Severgnini et al. 2005, Maiolino et al. 2005).

## ACKNOWLEDGMENTS

We acknowledge partial financial support by ASI (grants: I/R/062/02 and I/R/071/02), by MURST (Cofin-03-02-23) and by INAF. We thank the staff members of the TNG and the ESO telescopes for their support during the observations.

## REFERENCES

Brusa, M., et al. 2005, A&A 432, 69

Caccianiga, A., et al. 2004, A&A 416, 901

Della Ceca, R., et al. 2004, A&A 428, 383

Gilli, R. et al. 2001, A&A 366, 407

Maiolino, R., et al. 2005, A&A in press [astro-ph/0509244]

Severgnini, P., et al. 2005, A&A 431, 87

Ueda, Y., et al. 2003, ApJ 598, 886

Watson, M., et al. 2001, A&A 365, L51

# OUTFLOWS FROM HIGH ACCRETION RATE AGN

**M. Simpson and P.T. O'Brien**

Department of Physics and Astronomy, University of Leicester, Leicester, LE1 7RH, UK

## ABSTRACT

X-ray spectral analysis for three high accretion rate AGN, observed by *XMM-Newton*, has been carried out to determine whether they contain evidence for highly-ionised, high-velocity outflows, like that of PDS 456. The results from this analysis is that there are no such outflows present in the three objects. However, there is evidence of absorption from a warm absorber along the line of sight, in one of the objects, with the others being modelled well with a standard power law and blackbody emission to describe the soft excess found.

Key words: AGN; outflows, high-accretion rate.

## 1. INTRODUCTION

The discovery of high-mass, high-velocity outflows from active galactic nuclei (AGN) in recent years has been a source of great dicussion. The well known target PDS 456 (Reeves et al. 2003) is the best known candidate to exhibit such an outflow. It shows clear evidence for out flowing material in both x-rays and the ultraviolet. Along with PDS 456 there are a small number of other targets that also appear to manifest this type of outflow. Some examples are: PG 1211+143 (Pounds et al. 2003a), APM 08279+5255 (Chartes et al. 2002), PG 0844+349 (Pounds et al. 2003b), PG 1115+080 (Chartes et al. 2003), IRAS 13197-1627 (Dadina & Cappi 2004) and RXJ0136.9-3510 (Ghosh et al. 2004); all appear to be high accretion rate objects.

The signatures of these outflows within the x-ray spectrum of the object, are in the form of absorption due to ionised atoms, H- and He-like in some cases, that have been blue shifted relative to the rest frame of the object. The main absorption features are in the Fe K band, with other prominent absorption features being produced by ionised Mg, O, C, Ne and S. However, the mechanisms behind this phenomenon are unclear.

In an attempt to better constrain the characteristics of the outflow phenomena, and with the assumption that they are found in high accretion rate AGN, a sample of three high accretion rate (super-Eddington) objects were observed with *XMM-Newton*. The three targets are MS 2254.9-3712, PG 1351+640 and QSO 0204+292. All are local ($z < 0.11$), radio quiet AGN. The three targets were taken from a paper by Wang (2003), in which author derives a limit realtionship between the black hole mass and the H$\beta$ line width that is being emitted from the broad-line region. It is concluded that the three targets are all supper-Eddington accretors.

## 2. SPECTRAL ANALYSIS

Spectral analysis was performed using XSPEC version 11.3. An inital absorbed powerlaw was simultaneously fitted to the hard band, 2.0-10.0 keV, of the spectra from the EPIC cameras, then extended across the whole band-pass, 0.3-10.0 keV. The ratio of the EPIC pn and MOS data sets to the model fit are shown in Fig.'s 1 to 3, for MS 2254.9-3712, PG 1351+640 and QSO 0204+292 respectively.

In the case of MS 2254.9-3712, the intial absorbed powerlaw fit (Fig. 1) shows a clear soft excess below 2 keV and excess around 6.2 keV (observed) but no obvious absorption lines or edges due to the Fe K band. Further modelling resulted in a best fit model of two black body components with temperatures of $\sim 0.04$ keV and $\sim 0.14$ keV to descibe the soft excess, a gaussian emission line at $\sim 6.40$ keV (rest-frame) from neutral iron, and an underlying power-law with $\Gamma \sim 2.00$.

For PG 1351+640, as with MS 2254.9-3712, soft excess can seen from the inital absorbed powerlaw fit (Fig. 2) and there are no obvious absorption or emission features in the hard band. The best model fit comprised of a black body component with a temperature of $\sim$ 0.14 keV, a powerlaw with $\Gamma \sim 1.83$ and an aborption edge at $\sim 0.71$ keV with an optical depth, $\tau \sim 0.63$.

Finally, the initial fit to QSO 0204+292 (Fig. 3) revealed that there is absorption of the powerlaw that the Galactic absorption cannot account for between 0.6 and 1.4 keV, suggesting the presence of absorbing material intrinsic to the object. This absorption is modelled well using the ABSORI model. The final model has an absorbing material with a column denisty of $N_H = 2.96$ x $10^{21}$ cm$^{-2}$ and ionisation parameter, $\xi \sim 0.36$, an aborption edge at $\sim 0.75$ keV with $\tau \sim 0.77$, an undying powerlaw of $\Gamma \sim 1.62$ and guassian emission at $\sim 6.36$ (rest-frame) from a Fe K$\alpha$ transition. The inclusion of an aborption edge is needed to model further absorption believed to be associated with the unresolved transmition array (UTA) of ionised iron.

## 3. DISCUSSION

The best fit models for the three data sets do not show evidence for high-mass, high velocity outflows, e.g. Fe K-band absorption. MS 2254.9-3712 and PG 1351+640 show emmision common to type 1 AGN. Whereas the third target QSO 0204+292 exhibits the presence of a warm absorbing material along the line of sight. The lack of any outflow poses some questions. Are the three targets really accreting above the Eddington limit?; Could the outflow have become completely ionised, such that we can no longer see the absorbing column?; Is having a high accretion rate the only pre-requisit?

## 4. CONCLUSIONS

The analysis of the x-ray spectra from three suspected high accretion objects was carried out to determine the presence of (or lack of), a high-mass, high-velocity outlow. No clear evidence for such outflows were found using EPIC data.

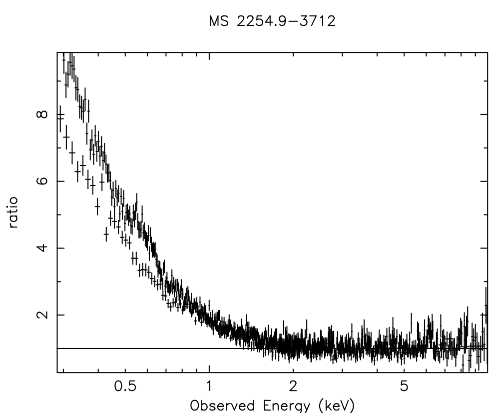


*Figure 1. Ratio plot of EPIC spectral data for MS 2254.9-3712 to a simple power-law fit between 2-10keV, extended down to 0.3keV. It clearly shows strong soft excess below 2 keV.*

## ACKNOWLEDGMENTS

MS acknowledges support from a PPARC studentship.

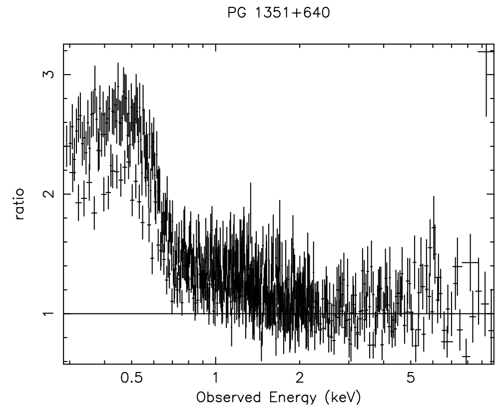


*Figure 2. Ratio plot of EPIC spectral data for PG 1351+640 to a simple power-law fit between 2-10keV, extended down to 0.3keV. It clearly shows strong soft excess below 2 keV.*

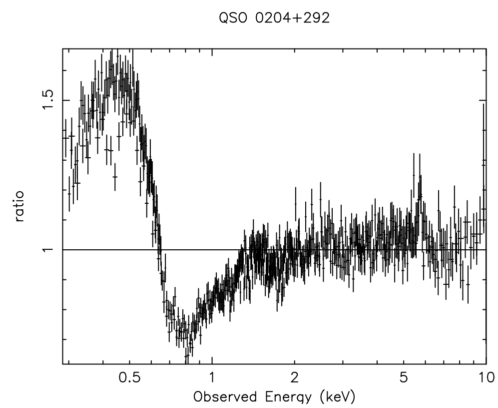


*Figure 3. Ratio plot of EPIC spectral data for QSO 0204+292 to a simple power-law fit between 2-10keV, extended down to 0.3keV. It reveals absorption between 0.6 and 1.4 keV.*

## REFERENCES

Chartes,G. et al. 2002, ApJ, 579, 169

Chartes,G. et al. 2003, ApJ, 595, 85

Dadina,M. & Cappi,M. 2004, A&A, 413, 921

Ghosh,K.K. et al. 2004, ApJ, 607, L111

Pounds,K.A. et al. 2003, MNRAS, 345, 705

Pounds,K.A. et al. 2003, MNRAS, 346, 1025

Reeves,J.N. et al. 2003, ApJ, 593, 65

Wang,J.-M. 2003, AJ, 125, 2859

# *INTEGRAL* OBSERVATIONS OF SIX AGN IN THE GALACTIC PLANE

**S. Soldi[1,2], V. Beckmann[3,4], L. Bassani[5], T. J.-L. Courvoisier[1,2], R. Landi[5,6], A. Malizia[5], A. J. Dean[7], A. De Rosa[8], A. C. Fabian[9], and R. Walter[1,2]**

[1]INTEGRAL Science Data Centre, Chemin d'Écogia 16, 1290 Versoix, Switzerland
[2]Observatoire de Genève, 51 chemin des Mailletes, 1290 Sauverny, Switzerland
[3]NASA Goddard Space Flight Center, Code 661, Greenbelt, MD 20771, USA
[4]Joint Center for Astrophysics, Department of Physics, University of Maryland, Baltimore County, MD 21250, USA
[5]IASF, CNR/INAF, via Gobetti 101, 40129 Bologna, Italy
[6]Dipartimento di Fisica, Università di Bologna, Viale C. Berti Pichat 6/2, 40127, Italy
[7]School of Physics and Astronomy, University of Southampton, Highfield, Southampton, SO17 1BJ, UK
[8]IASF, CNR/INAF, Via Fosso del Cavaliere 100, 00133 Rome, Italy
[9]Institute of Astronomy, Madingley Road, Cambridge CB3 0HA, UK

## ABSTRACT

We present results on one year of *INTEGRAL* observations of six AGN detected during the regular scans of the Galactic Plane. The sample is composed by five Seyfert 2 objects (MCG –05–23–16, NGC 4945, the Circinus galaxy, NGC 6300, ESO 103–G35) and the radio galaxy Centaurus A. The continuum emission of these sources is well represented by a highly absorbed ($N_{\rm H} > 10^{22}\,{\rm cm}^{-2}$) power law, with average spectral index $\Gamma = 1.9 \pm 0.3$. The Circinus Galaxy presents a high energy exponential cut-off at $E_c \sim 50\,{\rm keV}$ whereas a lower limit of 130 keV has been found for NGC 4945 and no cut-off has been detected for NGC 6300. A factor 2 of variability in the flux of Centaurus A is accompanied by a spectral change, which can be modelled equally well by an increase of the absorption ($N_{\rm H}$ from 17 to $33 \times 10^{22}\,{\rm cm}^{-2}$) or by the presence of a cut-off at $\geq 120$ keV in the low state spectrum. A comparison with recently reprocessed *BeppoSAX*/PDS data shows a general agreement with *INTEGRAL* results.

Key words: Galaxies: active – Galaxies: Seyfert – Gamma rays: observations – X-rays: galaxies.

## 1. INTRODUCTION

X-ray and $\gamma$-ray emission in AGN comes from the regions close to the nucleus and its study enables us to constrain the geometry and the state of the matter in the heart of an AGN. The emission in the soft X-ray domain is rather well known (up to $\leq 10$ keV), whereas many questions are still open for the hard X-rays/soft $\gamma$-ray range. For many objects, a high-energy cut-off is required to reproduce the data between 60 and 300 keV, but the shape and the energy of this feature is not yet well known.
The sources in this sample were selected from among the 10 previously known AGN detected during the first year of Core Program observations performed by *INTEGRAL* (Bassani et al. 2004). We focussed our attention on the 6 AGN (MCG –05–23–16, NGC 4945, Centaurus A, Circinus galaxy, NGC 6300, ESO 103–G35) which were previously studied by different hard X-ray missions, in particular by *BeppoSAX*, allowing us to compare the *INTEGRAL* results with previous ones.

## 2. OBSERVATIONS AND DATA ANALYSIS

Each source of this sample was first detected during the *INTEGRAL* Core Program observations performed between 2003 February 28 and October 10, by the IBIS/ISGRI instrument. In order to perform a detailed analysis, we used all the data that were public at the time of this study, specifically all the data in revolutions 1–136 (October 2002–November 2003) and 142–149 (December 2003–January 2004) and we analysed them using the version 4.2 of the ISDC's Offline Science Analysis (OSA) package. Extraction of ISGRI spectra has been performed for all sources but MCG –05–23–16 because of a low detection significance (2.4$\sigma$, $F < 1.9$ erg cm$^{-2}$ s$^{-1}$ in the 20-100 keV range). For NGC 4945, Centaurus A and Circinus SPI spectra have been extracted and Centaurus A and Circinus have been detected also by JEM-X. Within 10 months, the hard X-ray flux of Centaurus A has changed by a factor of $\sim 2$ in *INTEGRAL* data. We split our data set according to the flux level, choosing three main periods: high state (March 7–9, 2003), intermediate state (July 18 – August 22, 2003) and low state

(January 2–4, 2004), and we analysed them separately.

## 3. *INTEGRAL* RESULTS

Due to the lack of *INTEGRAL* data below 20 keV, with the exception of Centaurus A, during our analysis $N_{\rm H}$ was fixed to the values found in the literature.
A single power law corrected by photoelectric absorption is the best fit model for the *INTEGRAL* spectra of NGC 6300, ESO 103–G35 and NGC 4945, with photon indices $\Gamma = 2.2{\pm}0.5, 1.4{\pm}0.4$ and $1.9{\pm}0.1$, respectively. The introduction of a high energy cut-off component does not improve the quality of the fit for NGC 4945 and a lower limit of $E_c \sim 130$ keV can be given at $1\,\sigma$ level, in agreement with previous studies which have found $E_c$ in the 100-300 keV range (Madejski et al. 2000).
The *INTEGRAL* spectrum of Circinus is best fitted with a high absorbed power law with $\Gamma = 1.8^{+0.4}_{-0.5}$ and a high energy exponential cut-off at $50^{+51}_{-18}$ keV. A high energy cut-off at $E_c \sim$ 35–55 keV, required in both *INTEGRAL* and *BeppoSAX* data (Matt et al. 1999, Soldi et al. 2005), results in a temperature of $T \sim 4{-}6{\times}10^8$ K for the distribution of thermal electrons in the Comptonizing medium. The presence of a cut-off supports the scenario in which the X-ray emission of Seyfert galaxies originates where soft photons emitted by a cold optically thick disk are Comptonized in a hot region (Haardt & Maraschi 1993). A Compton reflection component observed in the broad band *BeppoSAX* data (Matt et al. 1999) has not been detected by *INTEGRAL* because of the lack of data below 20 keV.
Centaurus A is known to be a highly variable object on both long and short time scales. The flux variation by a factor of 2 in *INTEGRAL* data is associated with spectral variation, which can be modelled equally well by an increase by a factor of 2 of the absorption ($N_{\rm H}$ from 17 to $33 \times 10^{22}\,{\rm cm}^{-2}$) with flux decrease or by the presence of a high energy cut-off at $E_c \geq 120$ keV in the low state spectrum. Variations of the absorption are a common characteristic in Seyfert 2 galaxies, with changes of 20–80% on a one year time scales. Hints for a break or a cut-off in the hard X-ray and soft $\gamma$-ray spectra have been found by OSSE, *BeppoSAX*, and *RXTE* data (Steinle et al. 1998, Grandi et al. 2003, Benlloch et al. 2001), but these studies place this feature in the 300–700 keV range. *INTEGRAL* observations confirm the lack of a Compton reflection (Rothschild et al. 1999, Grandi et al. 2003), as adding this component does not improve the fits and results in a reflection fraction <0.1. Only a $3\sigma$ upper limit of $f_{\rm K\alpha} = 3.0$ and $5.5 \times 10^{-3}$ ph cm$^{-2}$ s$^{-1}$ (high and low state) can be derived for the fluorescence iron line.

## 4. CONCLUSIONS

The spectral characteristics of our *INTEGRAL* sample can be generally summarized as follows: a hard X-ray continuum emission described by a power law with a wide range of photon indices ($\Gamma \sim 1.4 - 2.3$) and, in the case of Circinus and Centaurus A the presence of a high energy cut-off. The average photon index $\Gamma = 1.9 \pm 0.3$ obtained from *INTEGRAL* spectra is consistent with the values found for other samples of Seyfert 2 galaxies in *BeppoSAX* (Malizia et al. 2003), OSSE (Zdziarski et al. 2000) and *Ginga* (Smith & Done 1996) data.
Studies of single objects confirm that the cut-off in the 100–300 keV range is not a universal characteristic of all Seyfert 2, and the results for our sample support these findings. *INTEGRAL* confirms the presence of a cut-off at ∼50 keV for the Circinus galaxy, a lower limit of 130 keV for NGC 4945 and the lack of this feature for NGC 6300, in agreement with what has been found in PDS spectra. A poorly constrained cut-off at $\geq$ 120 keV has been detected for Centaurus A during the *INTEGRAL* low state, but this feature has not been seen in the other *INTEGRAL* observations reported in this work and in the PDS spectrum. Cut-offs below 100 keV have been found for MCG –05–23–16 and ESO 103–G35 by PDS, but could not be studied by *INTEGRAL* because of the short exposure time of those observations.

## REFERENCES


Bassani, L., Malizia, A., Stephen, J., et al. 2004, Proc. of the 5th INTEGRAL Workshop, ESA SP-552, astro-ph/0404442

Benlloch, S., Rothschild, R. E., Wilms, J., et al. 2001, A&A, 371, 858

Grandi, P., Fiocchi, M., Perola, C. G., et al. 2003, ApJ, 593, 160

Haardt, F. & Maraschi, L. 1993, ApJ, 413, 507

Madejski, G., Życki, P., Done, C., et al. 2000, ApJ, 535, L87

Malizia, A., Bassani, L., Stephen, J. B., et al. 2003, ApJ, 589, L17

Matt, G., Guainazzi, M., Maiolino, R., et al. 1999, A&A, 341, L39

Rothschild, R. E., Band, D. L., Blanco, P. R., et al. 1999, ApJ, 510, 651

Smith, D. A. & Done, C. 1996, MNRAS, 280, 355

Soldi, S., Beckmann, V., Bassani, L., et al. 2005, A&A accepted, astro-ph/0509123

Steinle, H., Bennett, K., Bloemen, H., et al. 1998, A&A, 330, 97

Zdziarski, A. A., Poutanen, J., & Johnson, W. N. 2000, ApJ, 542, 703

# WHY ARE THEY NOT AGN?

**Roberto Soria[1], Alister W. Graham[2], Giuseppina Fabbiano[1], Alessandro Baldi[1], Martin Elvis[1], Helmut Jerjen[2], Silvia Pellegrini[3], and Aneta Siemiginowska[1]**

[1]Harvard-Smithsonian Center for Astrophysics, 60 Garden st, Cambridge, MA 02138, USA
[2]RSAA, Australian National University, Cotter Rd, ACT 2611, Australia
[3]Astronomy Department, Bologna University, Italy

## ABSTRACT

We have studied the X-ray luminosity of the nuclear SMBH of a sample of quiescent early-type galaxies, and the inflow rate of the hot gas, feeding the SMBH. We have also studied the additional contribution of warm gas from stellar winds. Assuming an ADAF-like radiative efficiency, we find that only a fraction $\sim$ 1–10% of the gas is accreted onto the SMBH; the rest must be removed or used to form new stars. Self-regulated feedback from the SMBH can provide the power necessary to remove the gas. Slow outflows can remove most of the mass, while a fast jet can carry out most of the accretion power.

Key words: galaxies: nuclei — X-rays: galaxies.

## 1. NUCLEAR X-RAY EMISSION FROM QUIESCENT EARLY-TYPE GALAXIES

Most of the galaxies in the nearby universe have inactive nuclei (X-ray luminosities $\lesssim 10^{40}$ erg s$^{-1}$). This may be due to an interplay of different factors: low rate of gas injection/inflow inside the “sphere of influence” of the supermassive black hole (SMBH); low fraction of the available gas being accreted onto the SMBH; low radiative efficiency of accretion, with the rest of the accretion power being advected, or carried out as mechanical luminosity by a jet or an outflow. Our goal is to estimate these factors quantitatively, to discriminate between different radiatively-inefficient scenarios, and to outline the power and mass budget inside the sphere of influence. To do so, we have selected a sample of six quiescent early-type galaxies with known SMBH mass (Table 1). Using new *Chandra* data, we have determined: the X-ray luminosity of the nuclear sources; the radial profile, average temperature and central density of the surrounding hot interstellar medium (ISM); and the classical Bondi rate ($\dot{M}_{\rm B}$) of inflow of the hot ISM into the SMBH sphere of influence (Soria et al. 2006a, 2006b). Typical hot-gas densities are $\sim 0.01$–$0.03$ cm$^{-3}$. The other main results are summarized in Table 1. We found that the nuclear sources are much fainter than predicted by the standard-disk scenario (which is also ruled out by other theoretical considerations at such low accretion rates). However, they are brighter than predicted by radiatively-inefficient models, in particular by the advection-dominated accretion flow (ADAF) model. This suggests that, when we take into account only the X-ray emitting gas, we are underestimating the true accretion rate $\dot{M}$ (Soria et al. 2006a). We then considered another eighteen galaxies for which the SMBH X-ray luminosity and the Bondi inflow rate have been calculated or constrained from previous work (Pellegrini 2005, and references therein). For most of these galaxies, the SMBH X-ray luminosity is lower than predicted by the standard ADAF model, suggesting that the true accretion rate $\dot{M} \ll \dot{M}_{\rm B}$. Overall, there is little or no correlation between Bondi rate and X-ray luminosity of the SMBH (Fig. 14 in Soria et al. 2006a).

## 2. HOW MUCH OF THE GAS AVAILABLE IS ACCRETED?

To make sense of these contradictory findings, we need to keep in mind that the hot, X-ray emitting ISM may represent only a small fraction of the gas fuelling the SMBH. That can be the case in systems where gas can cool efficiently (cooling timescale $<$ accretion timescale), or, vice versa, if gas is injected into the inner regions in a cool or warm phase and is accreted before it has time to virialize. We use optical brightness profiles to obtain a complementary estimate of the gas injection rate into the SMBH sphere of influence (Soria et al. 2006b). The stellar contribution can be estimated by deprojecting the optical brightness profiles to obtain the volumetric luminosity densities, and applying standard relations between optical luminosity, stellar densities and ages, and mass loss rates. We found typical stellar mass loss rates $\sim 10^{-4}$–$10^{-3} M_\odot$ yr$^{-1}$; on the other hand, the hot gas content varies greatly, leading to X-ray-estimated Bondi rates from $\lesssim 10^{-5}$ to $\sim 10^{-2} M_\odot$ yr$^{-1}$ over the full sample of galaxies.

*Table 1. Mass accretion rate and X-ray luminosity of the SMBH in our target galaxies.*

| Galaxy | Distance (Mpc) | $M_{\rm BH}$ ($M_\odot$) | $\log(\dot{M}_{\rm B}/\dot{M}_{\rm Edd})$ | $\log L_{\rm X}$ (erg s$^{-1}$) | $\log(L_{\rm X}/L_{\rm Edd})$ | $\dot{M}_*/\dot{M}_{\rm B}$ | $\log L_{\rm X}^{\rm A}$ (erg s$^{-1}$) | $\dot{M}/\dot{M}_{\rm t}$ |
|---|---|---|---|---|---|---|---|---|
| (1) | (2) | (3) | (4) | (5) | (6) | (7) | (8) | (9) |
| N821 | 24.1 | $0.85^{+0.35}_{-0.35}$ | $-4.7$ | $< 38.7$ | $< -7.3$ | 19 | 41.3 | $< 7\%$ |
| N3377 | 11.2 | $1.0^{+0.9}_{-0.1}$ | $-4.9$ | 38.5 | $-7.6$ | 93 | 42.5 | 2% |
| N4486B | 16.9 | $0.5^{+0.5}_{-0.2}$ | $< -5.0$ | 38.4 | $-7.4$ | $> 2$ | 39.0 | 50% |
| N4564 | 15.0 | $0.56^{+0.03}_{-0.08}$ | $-5.4$ | 38.9 | $-7.0$ | 74 | 41.0 | 12% |
| N4697 | 11.7 | $1.7^{+0.2}_{-0.1}$ | $-4.4$ | 38.6 | $-7.7$ | 6 | 41.2 | 7% |
| N5845 | 25.9 | $2.4^{+0.4}_{-1.4}$ | $-4.7$ | 39.4 | $-7.0$ | 31 | 42.1 | 7% |

Notes: Col. 4: $\dot{M}_{\rm B}$ is the classical Bondi inflow rate estimated from BH mass, density and temperature of the X-ray emitting gas; Col. 5: 0.3–10 keV luminosity of the nuclear source; Col. 7: $\dot{M}_*$ is the estimated warm gas inflow rate from stellar winds, inside the SMBH sphere of influence; Col. 8: predicted X-ray luminosity if all the inflowing hot and warm gas were accreted at ADAF efficiency; Col. 9: fraction of the inflowing gas that has to be accreted, assuming ADAF efficiency, to reproduce the observed SMBH X-ray luminosity. See details in Soria et al. (2006a, 2006b).

We have added these two components ($\dot{M}_{\rm B}$ and $\dot{M}_*$) to estimate the total mass injection rate $\dot{M}_{\rm t}$. Only an *a priori* unknown fraction of this gas reaches the SMBH (the rest being re-ejected, stored, or turned into new stars), which adds another parameter to the model. And only an *a priori* unknown fraction of the accretion power is released as X-ray flux (the rest being advected or carried out as mechanical luminosity, in a radio jet or a wind). Various accretion flow solutions (standard disk, ADAF, etc.) have different predictions for the fraction of gas accreted by the BH, and for its radiative efficiency. Assuming the ADAF radiative efficiency $\eta \approx 10\dot{M}/\dot{M}_{\rm Edd}$, the observed X-ray luminosities imply that, for most galaxies, only $\sim 1$–$10\%$ of the inflowing gas is accreting onto their SMBHs (Table 1, Col. 9). We suggest that the intrinsic scatter in $\dot{M}_*$ and in the accretion fraction is the main reason for the lack of correlation between the Bondi rate and the X-ray luminosity of the SMBH.

## 3. MASS AND ENERGY BUDGET OF THE NUCLEAR SMBH

What are the conditions for mass equilibrium inside the SMBH sphere of influence, and the fate of the gas that does not sink into the SMBH? It is possible that in some cases (most notably in NGC 5845), part of the excess gas may cool down, settle into a dusty/stellar disk, and eventually form new stars, even inside the Bondi accretion radius. In our current work (Soria et al. 2006b), we have used the simplifying assumption that star formation is negligible, and most of the gas is removed from the nuclear region by slow, massive outflows. Soria et al. (2006b) discuss possible sources of energy that can remove that amount of gas. To reach a steady state, avoiding an implausible degree of fine-tuning between injection, accretion, and outflow rates, both the accretion rate and the outflow rate must be self-regulating. This happens, for example, if the accretion rate is proportional to the gas density or total mass inside the sphere of influence of the SMBH, and the power carried by the outflow is proportional to the accretion power. In this case, the system can reach an asymptotic equilibrium; this mechanism relies on the idea of SMBH feedback.

We have estimated what fraction of the accretion power has to be used to drive away the excess gas. Pure ADAF solutions require a highly efficient feedback coupling, essentially because most of the accretion power is lost into the BH. Other radiatively inefficient solutions (e.g., the ADIOS model) only require that $\lesssim 1\%$ of the available accretion power be used for the feedback. Hence, a fast jet may still carry outwards $\gtrsim 99\%$ of the accretion power. If the jet is fully relativistic, it can carry outwards $\sim 0.1\%$ of the inflowing mass, with the rest being either accreted or removed by feedback-driven, slow outflows. If the jet is only midly relativistic ($v_{\rm w} \lesssim 0.5c$), it can carry away an amount of mass comparable to what sinks into the SMB, $\sim 10\%$ of the inflowing gas, with the difference being removed by a slower outflow component.

## REFERENCES

Pellegrini, S. 2005, ApJ, 624, 155

Soria, R., Fabbiano, G., Graham, A. W., et al. 2006a, ApJ, in press

Soria, R., Graham, A. W., Fabbiano, G., et al. 2006b, ApJ, in press

# IONIZATION STRUCTURE OF THE WARM WIND IN NGC 5548

**K. C. Steenbrugge[1,2], J. S. Kaastra[2], D. M. Crenshaw[3], S. B. Kraemer[4,5], N. Arav[6], I. M. George[7,8], D. A. Liedahl[9], F. B. S. Paerels[10], T. J. Turner[7,8], and T. Yaqoob[8,11]**

[1]SRON National Institute for Space Research, Sorbonnelaan 2, 3584 CA Utrecht, The Netherlands
[2]now at Harvard-Smithsonian Center for Astrophysics, 60 Garden street, Cambridge, MA 02138, USA
[3]Department of Physics and Astronomy, Georgia State University, Astronomy Offices, One Park Place South SE, Suite 700, Atlanta, GA 30303, USA
[4]Catholic University of America, USA
[5]Laboratory for Astronomy and Solar Physics, NASA's Goddard Space Flight Center, Greenbelt, MD 20771, USA
[6]CASA, University of Colorado, 389 UCB, Boulder, CO 80309-0389, USA
[7]Joint Center for Astrophysics, University of Maryland Baltimore County, 1000 Hilltop Circle, Baltimore, MD 21250, USA
[8]Exploration of the Universe Division, Code 662, NASA's Goddard Space Flight Center, Greenbelt, MD 20771, USA
[9]Physics Department, Lawrence Livermore National Laboratory, PO Box 808, L-41, Livermore, CA 94550, USA
[10]Columbia Astrophysics Laboratory, Columbia University, 538W. 120th Street, New York, NY 10027, USA
[11]Department of Physics and Astronomy, Johns Hopkins University, Baltimore, MD 21218, USA

## ABSTRACT

We present the results from our 140 ks XMM-*Newton* and 500 ks *Chandra* observation of NGC 5548. The velocity structure of the X-ray absorber is consistent with the velocity structure measured in the simultaneous UV spectra. In the X-rays we can separate the highest outflow velocity component, $-1040$ km s$^{-1}$, from the other velocity components. This velocity component spans at least three orders of magnitude in ionization parameter, producing both highly ionized X-ray absorption lines (Mg XII, Si XIV) and UV absorption lines. A similar conclusion is very probable for the other four velocity components. We show that the lower ionized absorbers are not in pressure equilibrium with the rest of the absorbers. Instead, a model with a continuous distribution of column density versus ionization parameter gives an excellent fit to our data.

Key words: AGN, Seyfert 1, NGC 5548, X-ray spectroscopy.

## 1. INTRODUCTION

Over half of all Seyfert 1 galaxies exhibit signatures of photoionized outflowing gas in their X-ray and UV spectra. Studying these outflows is important for a better understanding of the enrichment of the Inter Galactic Medium (IGM) as well as the physics of accretion of gas onto a super-massive black hole. Arav et al. (Arav et al., 2003) and Steenbrugge et al. (Steenbrugge et al., 2003) concluded that there is substantially more lowly ionized gas than has been claimed from previous UV observations. It was concluded that the X-ray and UV warm absorbers are different manifestations of the same phenomenon.

## 2. OBSERVATION AND DATA REDUCTION

The XMM-*Newton* RGS data was reduced using the standard threads of the SAS version 5.3. For the *Chandra* HETGS data we used the threats in CIAO version 2.2. For the LETGS the 1.5 event file was obtained using CIAO version 2.2, but further data reduction was done using the pipeline described by Kaastra et al. (2002a), which includes an empirical correction for the known wavelength problem in the LETGS and fitted it with responses that include the first 10 positive and negative orders. The data were analyzed using the *spex* package (Kaastra et al., in press).

## 3. VELOCITY STRUCTURE

The five velocity components measured in the UV (Crenshaw et al., 2003) are listed in Table 1. Each velocity component can have a different ionization parameter and hydrogen column density. Also the variability detected in the ionization parameter is different for the five outflow velocities. Using the MEG, HEG and LETGS data we

*Table 1. The outflow velocity, the velocity broadening and ionization parameter as measured for the five components detected in the UV (Crenshaw et al., 2003).*

| Outflow km $s^{-1}$ | broadening km $s^{-1}$ | U | $N_H$ log $m^{-2}$ |
|---|---|---|---|
| −1040 | 94 | 0.03 | 22.8 |
| −667 | 18 | 0.03 | 22.6 |
| −530 | 68 | 0.24 | 24.3 |
| −336 | 62 | 0.03 | 23.3 |
| −160 | 90 | 0.03 | 22.6 |

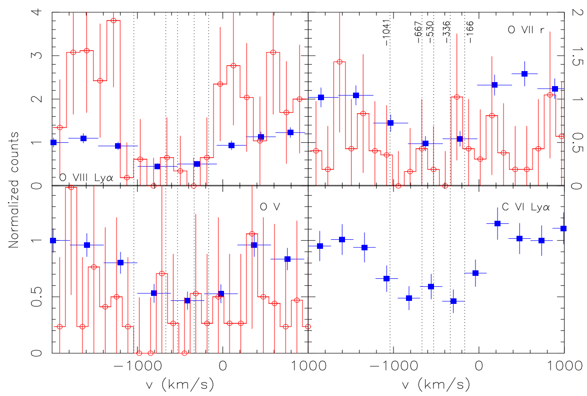

*Figure 1. The MEG (open circles) and LETGS (filled squares) data for the O VIII Ly$\alpha$, O VII resonance, O V and C VI Ly$\alpha$ lines. The dotted lines indicate the outflow velocity measured from UV spectra.*

were able to resolve the -1040 km $s^{-1}$ component from the 4 other velocity components in the 6 strongest lines (see Fig 1). This clearly indicates that this velocity component spans an ionization range of at least 3 orders of magnitude, from low ionization UV lines to Si XIV.

## 4. IONIZATION STRUCTURE

Fig. 2 shows the S-curve, with superimposed the five ionization parameters measured from the RGS spectra. The two lowest ionized components measured from the X-ray spectra cannot be in pressure equilibrium with the higher ionized components. This means that if the absorber is due to clouds in an outflow, they need to be magnetically confined. An equally good fit to the spectra is obtained with a continuous ionization parameter distribution, i.e. an outflow with a density gradient (Steenbrugge et al., 2005). The lowest ionization component measured in the X-rays has a very similar ionization parameter as the ionization parameter measured from UV spectra: log $\xi_{\rm X-ray}$ = − 0.03 versus log $\xi_{\rm UV}$ = 0.05. However, most of the gas is highly ionized. Assuming a continuous outflowing stream, we derive a power law slope for the column density of 0.4 with ionization parameter.

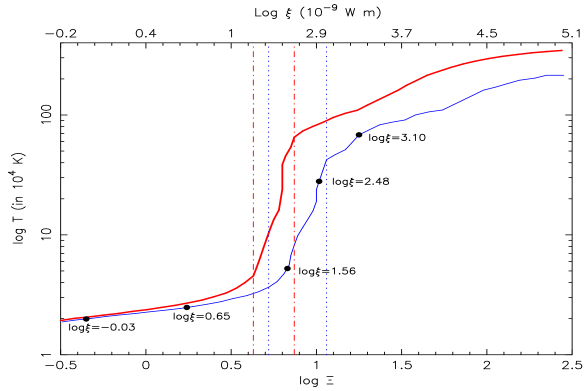

*Figure 2. The temperature versus ionization parameter for constant pressure. Points: the ionization paramters measured from the RGS spectra. The ionization parameter $\xi$ for the spectral energy distribution (SED) assumed in the upper curve is indicated on the top x-axis. The dotted and dashed lines indicate the boundaries for the marginally stable branch for the two different SEDs assumed.*

## 5. ACKNOWLEDGEMENTS

SRON National Institute for Space Research is supported financially by NWO, the Netherlands Organization for Scientific Research.

## REFERENCES

Arav, N., Kaastra, J., Steenbrugge, K., et al. 2003, ApJ, 590, 174

Crenshaw, D. M., Kraemer, S. B., Gabel, J. R., et al. 2003, ApJ, 594, 116

Kaastra, J. S., Mewe, R., & Raassen, A. J. J. in press, Proc. Symp. New Visions of the X-ray Universe in the XMM-*Newton* and *Chandra* era

Kaastra, J. S., Steenbrugge, K. C., Raassen, A. J. J., et al. 2002a, A&A, 386, 427

Steenbrugge, K. C., Kaastra, J. S., Crenshaw, D. M., et al. 2005, A&A, 434, 569

Steenbrugge, K. C., Kaastra, J. S., de Vries, C. P., & Edelson, R. 2003, A&A, 402, 477

# X-RAY PROPERTIES OF DOUBLE-PEAKED BALMER-LINE ACTIVE GALAXIES

**I. Strateva, W. Brandt, M. Eracleous, G. Chartas, and D. Schneider**

Pennsylvania State University, 525 Davey Lab., University Park, PA 16802

## ABSTRACT

We study the X-ray properties of 39 AGN (24 radio-quiet [RQ] and 15 radio-loud [RL]) with double-peaked Balmer emission lines. 28 of them are Sloan Digital Sky Survey (SDSS) AGN serendipitously observed with *ROSAT*, *XMM-Newton*, or *Chandra*; an additional 11 previously studied double-peaked RL AGN are considered for comparison purposes. Double-peaked Balmer lines originate in the accretion disk and are an important diagnostic of the accretion flow. We find that the ratio of UV-to-X-ray emission, $\alpha_{\rm ox}$, of RQ double-peaked AGN are similar to those of normal RQ AGN with comparable UV luminosities. Most RL double-peaked AGN are more X-ray luminous than normal RQ AGN, as expected for RL objects. For both RL and RQ double-peaked AGN a few notable exceptions appear X-ray underluminous for their UV luminosity. The spectral shapes of double-peaked AGN are also consistent with those of other objects with similar radio properties.

Key words: active galaxies; X-ray and UV emission; disk-emission AGN.

## 1. INTRODUCTION

A small fraction of active galaxies (~3% of optically selected AGN and up to ~20% of broad line radio galaxies [BLRGs]) have double-peaked Balmer-line shapes indicative of accretion-disk line emission. The class of disk-emission AGN is rather heterogeneous – it includes BLRGs, LINERs (low-ionization nuclear emission-line region galaxies), and luminous Seyferts, spanning a range of radio-loudness, luminosity, black-hole mass, and accretion rate. It is clear that the association of Balmer line disk-emission in AGN with a subsample of radiatively inefficient accretion-flow AGN is not sufficient to explain all double-peaked AGN. Since most of the double-peaked AGN have strong Balmer-line emission, which could not have been produced by the release of gravitational energy locally without invoking unrealistic radiative efficiency, X-ray illumination from the inner thick disk is deemed necessary to produce the observed signatures. In search

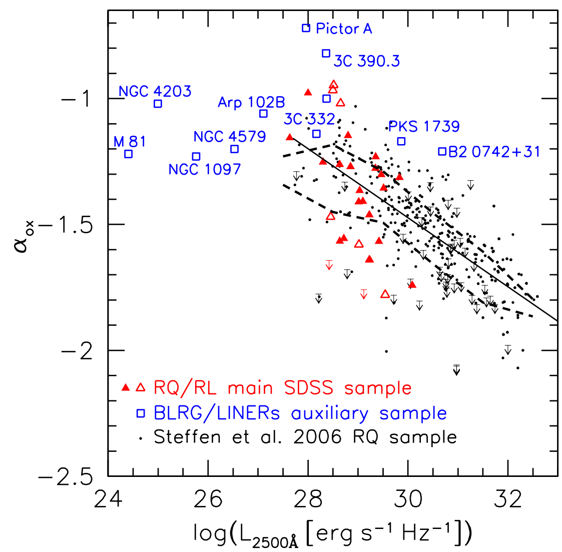


*Figure 1. $\alpha_{\rm ox}$ vs. $L_{2500\,\mathring{A}}$ for disk-emission AGN in comparison with normal AGN from [St06]. The solid line is the best-fit bisector and the dashed lines connect the 25th- and 75th-percentiles estimated for each magnitude bin by [St06].*

of clues to the nature of the luminous double-peaked AGN, we embarked on a detailed study of the 0.5–10 keV X-ray properties of this class.

## 2. SAMPLE

We selected a new sample of double-peaked AGN from SDSS areas with overlapping *ROSAT* PSPC, *Chandra*, or *XMM-Newton* archival exposures. Our main sample consists of 28 double-peaked Hα-line AGN, 80% of which lie in pointings with effective exposure times of $> 2$ ks. Using a variety of statistical tests (on the redshift, luminosity, radio-loudness, Hα-line width, and centroid distributions) we confirmed that this sample is representative of the sample of disk-emission AGN presented in Strateva et al. (2003) [hereafter the S03 sample]. We also con-

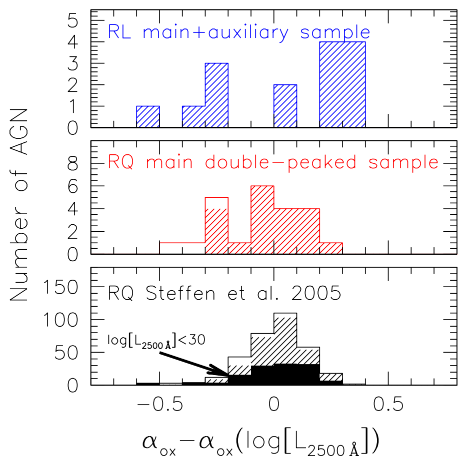


*Figure 2.* $\alpha_{ox}$ *residual distributions, after subtraction of the best-fit* $\alpha_{ox}$–$\log[L_{2500\,\text{Å}}]$ *relation from St06.*

sider 11 previously studied double-peaked BLRGs and LINERs with high-quality UV and X-ray data (the auxiliary sample), which are at lower luminosity and redshift than the S03 sample and are all RL. The full sample consists of 39 double-peaked AGN, 24 radio quiet (RQ) and 15 RL. Since RL AGN are known to differ in their X-ray properties from RQ AGN (with flatter power-law photon indices, Γ, and higher X-ray fluxes), we study the X-ray properties of RL and RQ double-peaked AGN separately.

## 3. X-RAY PROPERTIES OF DISK-EMISSION AGN

Figure 1 presents the ratio of UV-to-X-ray luminosity densities, $\alpha_{\rm ox} \equiv -0.384\log[L_{2500\,\text{Å}}/L_{2\,\rm keV}]$, as a function of the UV monochromatic luminosity, $L_{2500\,\text{Å}}$. A strong correlation exists between $\alpha_{\rm ox}$ and $L_{2500\,\text{Å}}$ in optically selected RQ AGN samples (e.g., Steffen et al., 2006, hereafter St06), and RQ disk-emission AGN also follow this correlation. The apparent lack of high-luminosity objects with double-peaked lines in Figure 1 is probably a result of the selection procedure, which is volume limited to SDSS AGN with $z < 0.33$. The distribution of $\alpha_{\rm ox}$ residuals for RQ disk-emission AGN (obtained by subtracting the best fit relation from St06, $\alpha_{\rm ox} = -0.137\log[L_{2500\,\text{Å}}] + 2.637$) is presented in Figure 2. It is statistically consistent with the distributions of the full St06 sample and a luminosity matched St06 subsample (e.g., a Kuiper test returns $D = 0.27$, with a 49% probability that the two distributions are indistinguishable). The Kaplan-Meier estimated mean of the RQ subsample residuals for the disk-emission AGN is $\langle\alpha_{\rm ox} - \alpha_{\rm ox}(L_{2500\,\text{Å}})\rangle = -0.07 \pm 0.06$, consistent within the errors with that of the St06 luminosity matched subsample, $\langle\alpha_{\rm ox} - \alpha_{\rm ox}(L_{2500\,\text{Å}})\rangle = -0.01 \pm 0.02$. The RL disk-emission AGN have $\alpha_{\rm ox}$ residuals[1] which are sta-

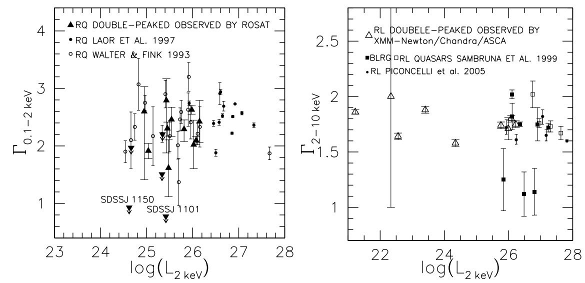


*Figure 3. Power-law photon indices for simple absorbed power-law fits of the RQ double-peaked AGN in the 0.1–2 keV band (left) and the RL double-peaked AGN in the 2.0–10.0 keV band in comparison with appropriate normal AGN samples.*

tistically different from those of both RQ disk-emission AGN and normal AGN. As expected for RL AGN, the majority of RL disk-emission AGN are more X-ray luminous relative to their UV emission. Despite the agreement of the overall RQ distributions of $\alpha_{\rm ox}$ residuals for double-peaked and normal AGN, a few RQ and RL disk-emission AGN are clearly X-ray weak relative to their UV emission. Figure 3 shows the power-law photon indices, Γ, for the RQ disk-emission AGN measured in the 0.1–2.0 keV band and the RL disk-emission AGN measured in the 2.0–10.0 keV in comparison with carefully matched normal AGN samples. The Γ's of the RQ disk-emission AGN, all but two of which were observed in the soft band only, were estimated using the standard *ROSAT* hardness ratio, HR1, assuming no intrinsic absorption above Galactic. The Γ's of the RL disk-emission AGN were obtained using direct 2.0–10.0 keV spectral fits. With the exception of the two SDSS RQ disk-emission AGN whose very flat Γ's suggest the presence of absorption above Galactic, the Γ's of both RL and RQ AGN agree well with those of normal AGN.

We conclude that the soft X-ray emission of double-peaked AGN as a class does not differ substantially from that of other AGN with comparable radio and UV emission and is thus unlikely provide a simple explanation for the incidence of disk-emission in AGN.

## REFERENCES

Laor, A., et al. 1997, ApJ, 477, 93

Piconcelli, E., et al. 2005, A&A, 432, 15

Sambruna, R. M., et al. 1999, ApJ, 526, 60

Steffen, A., et al. 2006, AJ, submitted [St06]

Strateva, I. V., et al. 2003, AJ, 126, 1720 [S03]

Walter, R., & Fink, H. H. 1993, A&A, 274, 105

[1] Note in Figure 1 that the $\alpha_{\rm ox}(L_{2500\,\text{Å}})$ relation is not well defined for $\log(L_{2500\,\text{Å}}) < 27.5$, rendering the $\alpha_{\rm ox}$ residuals of the lowest luminosity RL disk-emission AGN very uncertain.

# THE UV-TO-X-RAY EMISSION RATIO IN AGN: LUMINOSITY DEPENDENCE AND NO REDSHIFT EVOLUTION

**I. Strateva[1], A. Steffen[1], W. Brandt[1], D. Alexander[2], A. Koekemoer[3], B. Lehmer[1], D. Schneider[1], and C. Vignali[4]**

[1]Pennsylvania State University, 525 Davey Lab., University Park, PA 16802, USA
[2]Institute of Astronomy, Madingley Road, Cambridge CB3 0HA, UK
[3]Space Telescope Science Institute, 3700 San Martin Drive, Baltimore, MD 21218, USA
[4]Dipartimento di Astronomia, Via Ranzani 1, 40127 Bologna, Italy

**ABSTRACT**

We compiled a relatively homogeneous sample of 332 optically-selected, radio-quiet, unabsorbed AGN with the largest redshift range coverage ($0 < z < 6$) and X-ray detection fraction to date (88%). Using partial-correlation analysis, we confirm that the soft X-ray emission from AGN is strongly correlated with their UV emission (partial Kendall's $\tau = 0.52$ at $15.4\sigma$) despite the dependence of luminosity on redshift in flux-limited samples. The UV-to-X-ray emission ratio, $\alpha_{\rm ox} \equiv -0.384 \log[L_{2500\,\text{Å}}/L_{2\,\rm keV}]$, is related to the AGN luminosity (in the sense that less luminous AGN emit more soft X-rays per unit UV), but remains unchanged with cosmic time.

Key words: active galactic nuclei; X-ray/UV/optical emission of AGN; AGN evolution.

## 1. INTRODUCTION

Precise knowledge of the relationship between UV and X-ray emission in Active Galactic Nuclei (AGN) is important for testing energy generation models of AGN, deriving bolometric corrections, identifying X-ray weak AGN, and for proper comparison between the AGN evolution scenarios derived independently in the UV and X-ray bands.

### 1.1. Sample

We assembled a sample of 332 optically-selected, radio-quiet (RQ) AGN with correspondingly deep soft X-ray coverage. The largest subsample (155 objects) contains Sloan Digital Sky Survey (SDSS) AGN serendipitously observed in medium-deep *ROSAT* PSPC exposures. In order to increase the coverage of the luminosity-redshift plane without sacrificing X-ray detection fraction, which is crucial for determining the relation between UV and X-ray emission, we include subsamples of 52 COMBO-17 AGN with $R < 23$ (Wolf et al., 2003; Steffen et al., 2006), 46 BQS AGN with $M_{\rm B} < -23$ (Brandt et al., 2000), 25 Seyfert 1 galaxies from Walter & Fink (1993), and 54 high-redshift AGN (Steffen et al., 2006). Optical/UV spectra were used, when available, to subtract the host-galaxy continua and to identify and remove AGN with broad UV absorption lines (BALs). We explored the effect of any remaining BALs through Monte-Carlo simulations and found it statistically insignificant. By removing the radio-loud (RL) and BAL AGN we ensure that our observations measure the intrinsic rest-frame UV and soft X-ray emission of AGN, unaffected by nuclear absorption or jet emission. Figure 1 shows the luminosity-redshift plane coverage of the full sample. To our knowledge, this is the cleanest (controlling for RL, BAL, host-galaxy contribution, etc.) large sample of optically-selected AGN with the highest X-ray detection fraction (88%) to date.

### 1.2. Statistical Methods

While our sample provides good coverage of the luminosity-redshift plane, both the UV and X-ray luminosities are still correlated with redshift. To measure the strengths of correlations between $L_{2500\,\text{Å}}$, $L_{\rm 2keV}$, $\alpha_{\rm ox}$, and redshift, we use partial-correlation methods, which allow us to determine the correlation between any two variables while controlling for the effects of a third variable. We use rank-correlation coefficient analysis, developed by Akritas & Siebert (1996), which also accounts for the presence of upper/lower limits.

To obtain the linear-regression parameters of the correlations, we use the Astronomy Survival Analysis package (ASURV; Isobe et al., 1986). We used Monte Carlo simulations to confirm the robustness of the present correlations (see La Franca et al., 1995; Strateva et al., 2005).

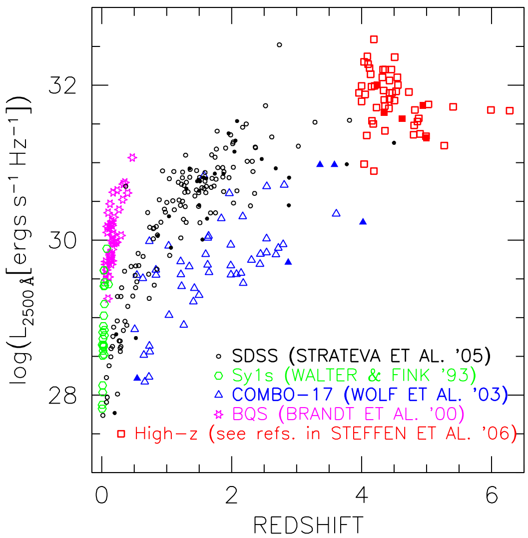


*Figure 1. Distribution of rest-frame UV monochromatic luminosity with redshift. The inclusion of both large-area and deep, pencil-beam samples allows us to break the strong dependence of luminosity on redshift, characteristic of flux-limited samples without compromising the X-ray detection fraction. X-ray upper limits are indicated with solid symbols in this plot only.*

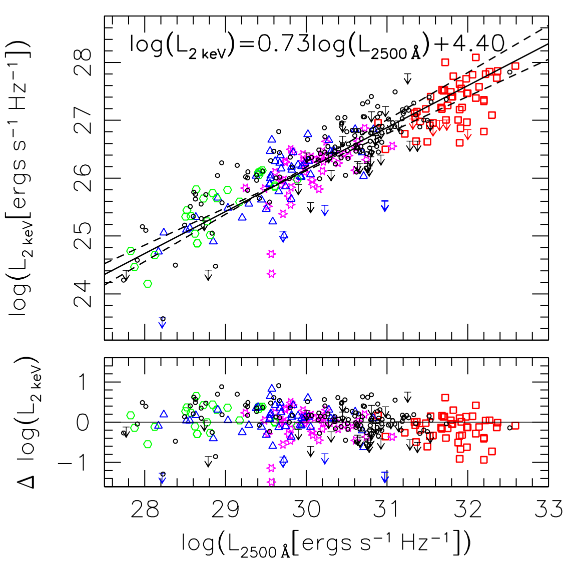


*Figure 2. The soft X-ray and UV monochromatic luminosities are strongly correlated (partial Kendall's $\tau = 0.52$ with 15.4$\sigma$ significance) with slope less than one. Symbols are as in Figure 1, except for the X-ray upper limits which are indicated with arrows. The solid line is the best-fit bisector line, with parameters given above and residuals plotted below; the two dashed lines are the best-fit linear regressions minimizing the x- or y-axis residuals.*

## 2. RESULTS

– We confirm that rest-frame soft X-ray and UV emission of AGN are strongly correlated (partial Kendall's $\tau = 0.52$, significant at 15.4$\sigma$, see Figure 2).

– The slope of the $\log(L_{2500\,\text{Å}})$–$\log(L_{2\,\text{keV}})$ correlation is less than one, which means that less luminous AGN emit relatively more X-ray emission (in comparison with their UV emission) than their more luminous counterparts. The best bisector line fit for the $\log(L_{2500\,\text{Å}})$–$\log(L_{2\,\text{keV}})$ relation is: $\log(L_{2\,\text{keV}}) = 0.73\log(L_{2500\,\text{Å}}) + 4.40$. To estimate the X-ray emission from the UV emission, the linear regression minimizing the X-ray residuals must be used: $\log(L_{2\,\text{keV}}) = 0.64\log(L_{2500\,\text{Å}}) + 6.87$. Conversely to obtain the best UV emission estimate from X-ray data, the linear regression minimizing the UV residuals must be used: $\log(L_{2\,\text{keV}}) = 0.82\log(L_{2500\,\text{Å}}) + 1.71$.

– The primary dependence of $\alpha_{\text{ox}}$ is on $\log(L_{2500\,\text{Å}})$: $\alpha_{\text{ox}} = -0.14\log(L_{2500\,\text{Å}}) + 2.64$, significant at 13.6$\sigma$. There is no dependence on redshift (1.2$\sigma$).

– We find a weaker, but significant (3.1$\sigma$) correlation between $\alpha_{\text{ox}}$ and $\log(L_{2\,\text{keV}})$.

– Using the $\alpha_{\text{ox}}$ residuals as a function of redshift, we estimate that the ratio of UV to soft X-ray emission of AGN has not changed by more than 30% since the Universe was $\sim$1 Gyr old.

For more detailed results, we refer the reader to Steffen et al. (2006) and Strateva et al. (2005).

## ACKNOWLEDGMENTS

We gratefully acknowledge support from NASA LTSA grant NAG5-13035 (I.S. and W.N.B.), CXC grant G04-5157A (A.T.S., W.N.B., B.D.L., and D.P.S), NSF CAREER award AST-9983783 (A.T.S. and W.N.B.), and MIUR COFIN grant 03-02-23 (C.V.).

## REFERENCES

Akritas, M. G. & Siebert, J. 1996, MNRAS, 278, 919

Brandt, W. N., et al. 2000, ApJ, 528, 637

Isobe, T., et al. 1986, ApJ, 306, 490

La Franca, et al. 1995, A&A, 299, 19

Steffen, A., et al. 2006, AJ, submitted

Strateva, I. V., et al. 2005, AJ, 130, 387

Walter, R., & Fink, H. H. 1993, A&A, 274, 105

Wolf, C., et al. 2003, A&A, 408, 499

# LOG-PARABOLIC SSC SPECTRA IN HBL SOURCES. A NEW ANALYSIS OF THE APRIL 1997 LARGE OUTBURST OF MKN 501.

**A. Tramacere[1], E. Massaro[1], M. Perri[2], P. Giommi[2], and G. Tosti[3]**

[1]Dipartimento di Fisica, Università La Sapienza, Piazzale A. Moro 2, I-00185 Roma, Italy
[2]ASI Science Data Center, ESRIN, I-00044 Frascati, Italy
[3]Dipartimento di Fisica, Università di Perugia, via A. Pascoli, Perugia, Italy

## ABSTRACT

Broad band X-ray observations of HBL sources (e.g. Mkn 421 and Mkn 501) were found well described by a log-parabolic law in which the second degree term measures the curvature. Log-parabolic energy spectra of relativistic electrons can be obtained by means of a statistical acceleration mechanism having an energy dependent probability of acceleration. We compute by means of an accurate numerical code, the spectra radiated by an electron population via synchrotron and synchro-self Compton (SSC) processes to derive the relations between the log-parabolic parameters. We applied our results to the simultaneous X and TeV spectra of Mkn 501 during the large outburst of April 1997 and found that SSC emission from an electron population with a log-parabolic distribution is able to reproduce the observed synchrotron X-ray and inverse Compton TeV spectra with the proper curvatures. This implies that pair production absorption of very energetic gamma rays against the extragalactic background can be lower that usually modelled.

Key words: radiation mechanisms: non-thermal - galaxies: active - galaxies: BL Lacertae objects, X-rays: galaxies: individual: Mkn 501.

## 1. INTRODUCTION

Log-parabola represents in a natural way the spectral shape with a mild curvature symmetric around the maximum. A log-parabolic spectrum can be written as

$$F(E) = K(E/E_1)^{-(a\ +\ b\ Log(E/E_1))} \qquad (1)$$

and needs just one parameter $(b)$ to represent the curvature around the peak, while in other models, like the continuous combination of power laws, it is a function of more parameters. Massaro et al. (2004a, 2004b) have shown that log-parabolic spectra can describe very well observational data, and that in a statistical acceleration process where the probability of energetic gain is not constant but a function decreasing with energy the resulting electron distribution can be described by:

$$N(>\gamma) = N_0(\gamma/\gamma_0)^{-[s-1+rLog(\gamma/\gamma_0)]} \qquad (2)$$

where $\gamma_0$ is the initial electron Lorentz factor. The parameter $r$ is the curvature term, and both $r$ and $s$ are linked to the statistic of acceleration precess (see Massaro et al (2004) for further details). In this paper we will evaluate the relations between the curvature parameters, not by analytical $\delta$ approximation, but numerically and using the exact spectral distribution, and will extend this study to Inverse Compton (IC) emission. We consider two electron distributions: a log-parabola (LP) and a mixed distribution (LPPL), where the probability of energy gain is constant up to a critical energy corresponding to a Lorentz factor $\gamma_a$, and for $\gamma > \gamma_a$ decreases with energy. The resulting electron distribution can be described by:

$$\begin{aligned} N(\gamma) &= N_0\ (\gamma/\gamma_0)^{-s_0} \quad \gamma \le \gamma_0 \\ N(\gamma) &= N_0\ (\gamma/\gamma_0)^{-(s_0+r\ Log(\gamma/\gamma_0))} \quad \gamma > \gamma_0. \end{aligned} \qquad (3)$$

where we take $\gamma_0$=$\gamma_a$.

## 2. NUMERICAL CALCULATION OF $b-r$ RELATION FOR SYNCHROTRON AND IC

The $b-r$ relation for synchrotron radiation (SR) emission, evaluated numerically using the exact SR spectral frequency distribution and in frequency intervals higher then the peak is linear with $b/r \simeq 0.22$, while around the peak it is $b/r \simeq 0.18$ for the both LP and LPPL cases. Both ratios are smaller than that of $\delta$ approximation equal to 0.25
IC spectra were evaluated using the exact Klein-Nishina (KN) cross section, in the approximation of isotropic photon seed distribution (Blumenthal & Gould 1970). The relations between SR and IC peak frequencies shows the transition between Thomson (TH) and Klein-Nishina

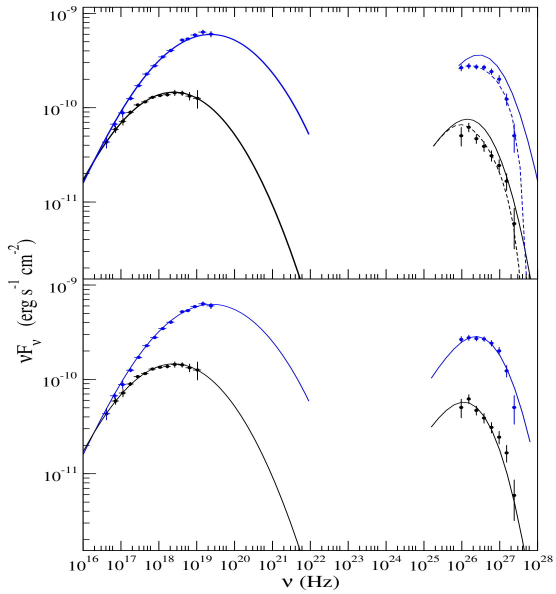


*Figure 1. Two SED of Mkn 501 during the low and high states observed on 7 and 16 April 1997, respectively. X-ray points are from Massaro et al. (2004a), TeV points are simultaneous CAT data (Djannati-Atai et al. 1999). Solid lines are the spectra computed in a 1-zone SSC model for the SR and IC components. In the upper panel IC spectra have been absorbed (dashed lines) by interaction with infrared EBL photons according to the LLL model by Dwek & Krennich (2005). In the lower panel EBL absorption was neglected. Details about the model parameters can be found in Massaro et al. (2005)*

(KN) regime: IC peak frequency increases slower and slower as we increase the peak electron energy. IC curvature ($b_{IC}$) has a more complex behaviour and there is not a univoque relation between $r$ and $b_{IC}$. This is due mainly to the fact that the shape is log-parabolic, only over limited ranges, and the resulting curvatures depend both on seed SR photons and electron distributions. Our computations show that $b_{IC}$ values are close to $b_{SR}$ or lower in TH regime, and approach to $r$ values as the diffusion enters in KN regime. A detailed description of these results is given in Massaro et al. (2005).

## 3. THE LARGE FLARE OF MKN 501 DURING APRIL 1997

We applied results found above to study the evolution of SED of Mkn 501 during the large flare of April 1997. In reproducing TeV spectra we took into account the photon-photon interaction with the photons of the diffuse infrared extragalactic background (EBL). We considered first a single zone SSC model. The spectrum of the emitting electrons was chosen with a curvature parameter $r = b/0.22 \simeq 0.75$. The TeV curvature measured around the peak was about 0.4 for the low state and 0.45 for the high state (Djannati-Atai et al. 1999) and, for $\gamma_0$ of the order of $10^4$ and even higher, we expect a value of r in the range 0.5-0.8. The EBL model used was the LLL model by Dwek and Krennich (2005). In both cases TeV data were well fitted in both the peak position and spectral curvature. This suggests that this curvature could be partly intrinsic rather then to be entirely produced by EBL absorption. Another possibility is that of two zone SSC model which gives again spectra in a good agreement with data. More details can be found in Massaro et al. (2005).

## 4. DISCUSSION

A log-parabolic law reproduces well the SED of blazars over several frequency decades. We present the exact relations, computed using a precise numerical code, between the spectral parameters of the energy distributions of relativistic electrons and their SR and IC emission. We also calculate SR and IC spectra of Mkn 501 observed by Beppo Sax and CAT during the large outburst of April 1997. We found a spectral curvature at TeV energies consistent with that observed in X-ray range and therefore it can be mostly intrinsic. This interpretation is in agreement with a previous work by Krawczynski et al. (2000) and is also supported by a recent paper by H.E.S.S. team (Aharonian et al. 2005a), who found that the time averaged cut-off energy of Mkn 421 is at about 3.1 TeV, lower than Mkn 501 (about 6.2 TeV). Considering the nearly equal redshifts of the these two blazars, they conclude that the cut-off is not due to EBL attenuation but it is intrinsic to the sources, in agreement with our conclusion about the IC curvature. The extragalactic space is likely more transparent to TeV photons than previously assumed and more blazars could be detected in this range at redshifts higher than previously thought, in agreement with recent detection of 1ES 1101-232 at $z$=0.186 (Aharonian et al. (2005b).

## REFERENCES


Aharonian F., Akhperjanian A.G. et al., 2005a, A&A 437, 95

Aharonian F., Akhperjanian A.G. et al., 2005b, astro-ph/0508073

Blumenthal G.R., Gould R.J., 1970, Rev. Mod. Phys. 42, 237

Djannati-Atai A., Piron F., Barrau A. et al., 1999, A&A 350, 17

Dwek E., Krennich F.,2005, ApJ 618, 657

Krawczynski, H., Coppi, P.S., Maccarone, T., Aharonian, F.A. 2000, A&A 353, 97

Massaro E., Perri M. et. al., 2004a, A&A 413, 489

Massaro E., Perri M. et. al., 2004b, A&A 422, 103

Massaro E., Tramacere A. et. al., 2005, A&A in press

# ANALYSIS OF THE OBSERVED APPARENT CORRELATION OF LINE LUMINOSITY WITH REDSHIFT FOR FR TYPE II AGNs

**A. C. Ugwoke**

*Department of Industrial Physics*
*Enugu State University of Science and Technology*
*Enugu – Nigeria*

## ABSTRACT

We investigate the reported correlation of emission line luminosity with redshift in radio-loud FR II elliptical galaxies. This is with a view to testing if this relationship is real or merely an artefact of luminosity selection effects, since the condition is ubiquitously absent in the lower redshift, FR I elliptical galaxies.

## 1. INTRODUCTION

Most classes of Active Galactic Nuclei (AGNs) exhibit strong emission lines which are photonoized by the UV continuum of the central continuum source which is probably powered by accretion of matter into a massive balckhole. Current classification groups objects with strong broad permitted lines as belonging to type I AGNs while those with narrow emission lines are designated as type II AGNs. While the type I AGNs have both broad permitted and narrow forbidden lines, type II AGNs have only narrow forbidden lines in their spectra. The emission line width is also used to classify these objects into broad line radio galaxies (BLRGs) and narrow line radio galaxies (NLRGs). The radio loud type II AGNs (i.e. NLRGs) include two distinct morphological types: the low luminosity FR I (Fanaroff and Riley, 1974) type radio galaxies and their high luminosity FR II counterparts. Generally, there exists a strong correlation between luminosity (P) and redshift (z) in extragalactic sources at both high and low z. However, for the emission-line luminosity ($L_{line}$) data, while the P-z correlationship is observed for the high luminosity FR II radio-loud elliptical galaxies, it is absent in the low z, FR I counterparts. In the subsequent analysis, we estimate the contribution of luminosity selection effects to the observed strong $L_{line}$-z correlation for the FR II galaxies in our sample to check if this correlation is significant or merely artificial. Our data is taken from Zirbel and Baum (1995) and contains 136 FR II galaxies but we excluded those sources without spectral index ($\alpha$) and/or $L_{line}$ values in our analysis.

## 2. ANALYSIS AND RESULT

Previous investigations of radio loud objects have revealed a flattening of their spectral slopes with increasing z for both radio-loud and radio-quiet types up to $z \leq 2$ (Schartel et al.,1996). Studies of the variation of $\alpha$ with z independent of P is normally performed using samples of sources which have approximately the same median P but a wide range in z (Ubachukwu et al., 1996). This arrangement will enable some quantitative assessments to be provided for the contribution of luminosity selection effects in the observed $\alpha$-z relationship. Ubachukwu et al. (1996) have shown that if $\alpha$ correlates with both z and P (here emission-line luminosity, $L_{line}$) the functional relationship can be parametized respectively as,

$$\alpha(z) = a_1 + m \log(1+z) \tag{1}$$
$$\alpha(L_{line}) = a_2 + n \log(L_{line}) \tag{2}$$

However, it has further been shown that a power-law variation of P with z exists (which is only applicable above some z cut-off; Ubachukwu et al. (1993)) of the sort,

$$L_{line} = L_{line(o)} (1+z)^{\beta} \tag{3}$$

where $\beta$ is a constant arising largely as a consequences of luminosity selection effects (if the P-z relation is entirely attributable to it). Hence, incorporating Eq. (3) into Eq. (2) we have,

$$\alpha(L_{line}, z) = a_2 + n\beta \log(1+z) + n \log_{line\,(o)} \tag{4}$$
$$= a_3 + n\beta \log(1+z) \tag{5}$$

where $L_{line(o)} = L_{line}$ (z = 0) and $a_3 = a_2 + n\log L_{line(o)}$.
Eqs. (1) and (2) will enable us to estimate the contribution of luminosity selection effects in the source sample since if the observed $L_{line}$-z correlation is attributable to it, then $m \approx n\beta$; else the residual z dependence, x can be estimated as

$$x = m - n\beta \tag{6}$$

We analyze the emission-line fluxes for a large sample of radio-loud, high z (z > 0.5) type II AGNs as compiled by Zirbel and Baum (1995). The sample consists of narrow emission-line luminosities measured in H$\alpha$ + (N II) $\lambda\lambda$ 6584, 6548 and excludes all measurements of broad emission-lines. This implies that for the BLRGs we only considered their narrow emission fluxes and for those sources measured at (O II) $\lambda$ 3727 or in (O III) $\lambda$ 4959/$\lambda$5005 their fluxes were converted to H$\alpha$ flux by using the empirical relation H$\alpha$/(O II) = 4.0 and H$\alpha$(O III) = 1.1 (McCarthy, 1987). Our analysis is carried out using the steep radio spectra ($\alpha$ > 0.5) components since inclusion of the flat spectra ($\alpha$<0.5) components is likely to complicate interpretation of the resultant numerical results (Kapahi and Kulkari ,1990). We have adopted $H_o$ = 50 Km/h/Mpc, $q_o$ = 0.0 and $S_\nu = S_o\nu^{-\alpha}$ where $S_o$ is the monochromatic flux. We shall first investigate the dependence of $\alpha$ on z and $L_{line}$ independent of each other by fitting the observed data to Eqs. (1) and (2). This produced the following empirical relationships,

$$\alpha\ (z) = -\ 0.17 + 0.26 \log (1+z) \qquad (7)$$

$$\alpha\ (L_{Line}) = 0.26 + 0.06 \log L_{line} \qquad (8)$$

with correlation coefficients, $\gamma$ = 0.6 and 0.66, respectively. These correlations are significant. However, to investigate the effect of luminosity, on the above relationships we fitted the observed log $L_{line}$ – log (1+z) data into Eq. (3) and obtained,

$$\alpha(z) = 34.2 + 3.80 \log (1+z) \qquad (9)$$

Eq.(9) implies that $\beta$ = 3.8, agreeing closely with $\beta$ 4.0 found by Ubachukwu et al. (1996). Therefore, using $\beta$ = 3.8 plus m = 0.26 and n = 0.06 (from Eqs. (8) and (9) respectively) Eq. (6) which expresses the expected redshift dependence, x yields,

$$x = 0.26\text{-}0.06 \times 3.80 \sim 0.032 \qquad (10)$$

Equation (10) is expected to give a null result if m = n $\beta$. This condition is virtually true here as the difference is negligible and indicates that only ~12% of the observed $\alpha$ - z correlation is intrinsic with the rest contributed by luminosity selection effects.

In conclusion, we have demonstrated in the foregoing analysis that the reported (artificial) correlation in emission-line luminosity with redshift for FR II radio-loud elliptical galaxies is not true but is merely an artefact induced by luminosity selection effects in the sample. It seems rather more correct that there is no correlation in the emission-line luminosity with z for both the FR II and FR I radio-loud elliptical galaxy types.

**REFERENCES**


Fanaroff, B. L. & Riley, J. M. 1974, MNRAS, 167, 31

Kapahi, V. K. & Kulkarni, V. K. 1990, AJ, 91, 1

McCarthy, P. J. 1998, Ph.D. Thesis University of California at Berkeley

Schartel, N., Brinkmann, W., Fink, H. H., Trüper, J. & Wamsteker, W. 1996, A & A, 307, 33

Ubachukwu, A. A., Okoye, S. E. & Onuora, L. I. 1993, Proc. Nig. Acad. Sci., 5, 62

Ubachukwu, A. A., Ugwoke, A. C. & Ogwo, J. N. 1996, Astrophys. Space Sci., 238, 151

Zirbel, E. L. & Baum, S. A. 1995, ApJ, 448, 521

# PHYSICAL PROPERTIES OF THE X-RAY ABSORBER IN APM 08279+5255 AND THE SEARCH FOR SPECTRAL VARIABILITY

**Chen Zheng, Masao Sako, and Roger Blandford**

Kavli Institute for Particle Astrophysics and Cosmology/ Stanford University, Stanford, CA 94305, USA

## ABSTRACT

BALQ X-ray absorption features provide an important opportunity to study powerful gas outflows from quasars. Recently, Chartas et al. (2002) and Hasinger, Schartel & Komossa (2002) have reported the detections of a deep X-ray absorption trough at a centroid of $E = 1.67$ keV (corresponding to a rest-frame energy of $E = 8.1$ keV) in both the *Chandra* and *XMM-Newton* observations of BALQ APM 08279+5255 at a redshift $z = 3.91$. Our analysis of both the *Chandra* and *XMM-Newton* spectra of APM 08279+5255 is consistent with a model in which either Fe XXVI or Fe XXV outflowing with relativistic velocities which range from $0.15$ c to $0.19$ c, in agreement with the conclusions of Chartas et al. (2002). The presence of a highly ionized iron implies the existence of other ions, including Ni XXVI, Ni XXVII, Ni XXVIII, Ca XX and Ar XVIII that also absorb in the observed X-ray band pass, and thus suggests a high mass-loss rate which can be used to estimate the launch radius of X-ray BAL gas. Our best-fit model yields a total iron column density of $\sim 10^{18}\ cm^{-2}$. Over a period of $18$ months covered by these observations, the data do not exhibit significant variability in the structure of the absorption troughs, which suggests that the jets are launched from relatively large radius.

Key words: BALQ; APM 08279+5255; Absorption lines; Outflows; X-rays.

## INTRODUCTION

Broad absorption lines are observed in approximately $20\%$ of radio-quiet quasars (Hewett & Foltz, 2003; Reichard et al., 2003). These are interpreted as signs of large mass outflow with speeds $\sim 0.03c$ from the accretion disks orbiting massive black holes. As such, they provide insight into the fueling mechanisms in quasars and its interaction with the host galaxy, e.g. (Scannapieco & Oh, 2004; Springl et al., 2005; Pounds et al., 2003; Reeves et al., 2003).

Recently, broad X-ray absorption features have been seen with velocities of $\sim 0.2c$, suggesting that these outflows may be even more powerful than estimated from optical observations and may provide active feedback to the surrounding gas e.g. (Chartas et al., 2002; Reeves et al., 2003; Pounds et al., 2003). As both the velocities and the level of ionization is higher, the X-ray absorbing gas is expected to originate from smaller radii than UV-absorbing gas. Detailed study of this gas may therefore be quite prescriptive concerning the outflow acceleration mechanism. These outflows are generally believed to be accelerated through resonance scattering of UV continuum photons by highly ionized ions e.g. (Arav & Li, 1994; Murray et al., 1995; Proga et al., 2000; Chelouche & Netzer, 2001). Many of these models predict the BAL clouds to be launched near the supermassive black hole at $r_{\rm launch} \approx 10^{16}$ cm (Murray et al., 1995). However, one problem with this model is that the outflows might be expected to vary on timescales of order the orbital period at the launch radius, $\sim 0.1(M_{\rm hole}/10^8{\rm M}_\odot)^{-1/2}(R/100AU)^{3/2}(1+z)$ yr. Such variations appear to be rare in optical observations (Weymann, 1997). There is therefore considerable interest in the variability of the X-ray lines.

We have independently analyzed data of APM 08279+5255 from the *Chandra* observations on 2000 October 11 and 2002 February 24 (Chartas et al., 2002) and those by *XMM-Newton* on 2001 October 30 and 2002 April 28-29 (Hasinger et al., 2002), and have searched for spectral variability of the X-ray BALs in APM 08279+5255 among these epochs. We chose this source because it has a large gravitational lensing magnification of  100 and high redshift of $z = 3.91$, which makes it a unique object with high signal-to-noise X-ray spectra. Chartas et al. (2002) modeled the *Chandra* data of APM 08279+5255 using gaussian absorption lines and interpreted it as due to a blueshifted absorption line from either Fe XXV K $\alpha$ or Fe XXVI K $\alpha$ , which requires a presence of a relativistic outflow. On the other hand, Hasinger et al. (2002) interpreted this feature as an absorption edge from Fe XV - Fe XVIII with zero bulk velocity in the quasar's frame.

## SPECTRAL ANALYSIS

We studied both the *Chandra* and *XMM-Newton* spectra using spectral/atomic models, which contain line and continuum absorption that are computed with the Flexible Atomic Code (Gu, 2003) in the low-density limit. The detection of a deep resolved discrete feature at a centroid of $E = 1.67$ keV (corresponding to a rest-frame energy of $E = 8.1$ keV) in APM 08279+5255 is statistically significant and strongly suggests the presence of highly ionized iron (Fe XXVI and/or Fe XXV). To model the spectra, we assumed a uniform absorber with ionization parameter in the range $\log \xi \sim 3 - 5$. Other ions are likely to be present, such as Ni XXVIII, Ni XXVII, Ni XXVI, Ca XX, Ar XVIII and contribute to the total absorption. In addition, we included cold local and Galactic absorption components and a single power-law continuum. During the fitting, the intrinsic absorption column density, the normalization and the slope of the power-law component, the column densities of ions, the turbulent velocity and the outflow velocity of the absorber were allowed to vary and the bulk velocities of the individual ions were assumed to be identical to each other.

This model provides a reasonable fit to the data from both *Chandra* and *XMM-Newton* . The results reveal a detection of $1 \sim 2 \times 10^{18}\ cm^{-2}$ of either Fe XXVI or Fe XXV and other elements with column densities that are an order of magnitude or more lower, which are more or less consistent with solar abundances. The outflow velocities are estimated to be either $0.15\ c$ or $0.18\ c$ for *Chandra* and $0.17\ c$ or $0.19\ c$ for *XMM-Newton* observations, in agreement with Chartas et al. (2002). The ambiguity in the redshift is a result of whether the single absorption trough is interpreted as either Fe XXV or Fe XXVI. Contributions from other lines, like Ni XXVII and Ni XXVIII, are expected as well, as predicted for example by Monte Carlo radiative transfer calculations of Sim (2005). The relative strength of the iron feature to the other lines can be used to constrain both the mass-loss rate and opening angle of the outflow. Based on the computed spectra by Sim (2005), the appearance of Ar XVIII and Ca XX in the hard X-ray band suggests a mass-loss rate near or higher than $6M_\odot/yr$. Adopting the best-fit hydrogen column density of $N_H \sim 5 \times 10^{22}\ cm^{-2}$, a global covering factor of $0.2$, a outflow velocity of $0.2$ c and the ratio of the distance to the absorber thickness $R/\Delta R \sim 1$ (Chartas et al., 2002), the launch radius of the X-ray BAL gas would be larger than $3 \times 10^{17}\ cm$, which corresponds to a variability time scale of roughly four months in the source frame. We have searched for spectral variability in observations of APM 08279+5255 separated by $2 - 18$ months, which correspond to timescales of a few weeks to three months in the quasar's rest frame. All of the data are consistent with the same spectral model suggesting that the the variability is not significant over timescales of $\sim 3$ months in the quasar's rest frame.

## REFERENCES


Arav, N., & Li, Z. Y. 1994, ApJ, 427, 700

Chartas, G. Brandt, W. N., Gallagher, S. C., & Garmire, G. P. 2002, ApJ, 579, 169

Chelouche D. & Netzer H. 2001, MNRAS, 326, 916

Granato, G. L., De Zotti, G., Silva, L., et al. 2004, ApJ, 600, 580

Gu, M. F. 2003, ApJ, 582, 1241

Hasinger, G. Schartel, N., & Komossa, S. 2002, ApJ, 573, L77

Hewett, P. C., & Foltz, C. B. 2003, AJ, 125, 1784

Murray, N., Chiang, J., Grossman, S. A., & Voit, G. M. 1995, ApJ, 451, 498

Pounds, K. A., Reeves, J. N., King, A. R., et al. 2003, MNRAS, 345, 705

Proga, D., Stone, J. M., & Kallman,T.R. 2000, A&A, 543, 686

Reeves, J. N., O'Brien, P. T., & Ward, M. J. 2003, ApJ, 593, L65

Reichard, T. A., et al. 2003, AJ, 125, 1711

Scannapieco, E., Oh, S. P. 2004, ApJ, 608, 62

Sim, S. A. 2005, MNRAS, 356, 531

Springl, V., Di Matteo, T., Hernquist, L. 2005, ApJ, 620, L79

Weymann, R. 1997, Mass Ejection from AGN : proceedings of a workshop held at the Carnegie Observatories in Pasadena